PHYSIK-DEPARTMENT

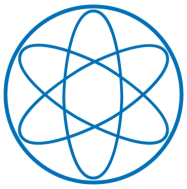

Two-Dimensional Partial-Wave Analysis of Exclusive 190 GeV $\pi^- p$ Scattering into the $\pi^-\pi^-\pi^+$ Final State at COMPASS (CERN)

Dissertation von Florian Haas

TECHNISCHE UNIVERSITÄT
MÜNCHEN

TECHNISCHE UNIVERSITÄT MÜNCHEN
Physik-Department E18

Two-Dimensional Partial-Wave Analysis of Exclusive 190 GeV $\pi^- p$ Scattering into the $\pi^-\pi^-\pi^+$ Final State at COMPASS (CERN)

Florian Haas

Vollständiger Abdruck der von der Fakultät für Physik der Technischen Universität München zur Erlangung des akademischen Grades eines

Doktors der Naturwissenschaften (Dr. rer. nat.)

genehmigten Dissertation.

Vorsitzende: Univ.-Prof. Dr. Nora Brambilla

Prüfer der Dissertation:

1. Univ.-Prof. Dr. Stephan Paul
2. Univ.-Prof. Dr. Walter Henning

Die Dissertation wurde am 17.12.2013 bei der Technischen Universität München

eingereicht und durch die Fakultät für Physik am 30.01.2014 angenommen.

Summary

The dynamics of strong interaction in the regime of low energies, i.e. large distances, is still not understood. Given its simplicity the non-relativistic simple quark model (SQM) describes successfully the observed hadronic spectra. QCD-inspired models, however, predict hadronic states where the gluonic content contributes to the hadron quantum numbers. These so-called hybrids cannot be explained within the SQM. A solid experimental proof of the existence of such systems would be the observation of spin-exotic states, with spin-parity quantum numbers, not allowed in the SQM. The study of mesons, the simplest hadrons, permits to gain insight into the realm of strong interaction where hadrons are the relevant degrees of freedom. The most promising spin-exotic meson candidate is the $\pi_1(1600)$, which was claimed in several experiments and in particular in data taken during a previous hadron campaign of the COMPASS experiment.

The hadron spectroscopy program of the COMPASS experiment at CERN focuses on the investigation of the light-meson spectrum in order to enlighten this rarely understood regime of strong interaction. During the 2008 data taking an unprecedented statistical precision has been reached in peripheral interactions of 190 GeV/c pions with a proton target leading to the $\pi^-\pi^-\pi^+$ final state. A spin-parity analysis in the kinematical region of the squared four-momentum transfer $0.1 \leq t' \leq 1.0$ GeV$^2/c^2$ was carried out based on a model of 88 partial waves up to a total angular momentum of 6. Besides the precise determination of properties of known resonances, a new axial-vector state, the $a_1(1420)$, was observed for the first time in a mass region where neither model nor lattice calculations predict mesons with this quantum numbers. Noteworthy is the very small intensity of this signal and that it only couples to the $f_0(980)$ isobar which is assumed to have a large strangeness content. The spin-exotic $\pi_1(1600)$ was observed albeit as a broad component dominated by non-resonant contributions. The simultaneous analysis in bins of the three-pion invariant mass and the squared four-momentum transfer t' allowed to study resonant and non-resonant contributions in more detail. Of special interest is the Deck effect, a non-resonant production mechanism, leading to the same final state and assumed to contribute to the partial waves that also contain the $a_1(1260)$ and the spin-exotic $\pi_1(1600)$. The hybrid nature of the two established states $\pi(1800)$ and $\pi_2(1880)$ was investigated. In addition the $\pi_2(1880)$ was confirmed as a resonance separate from the $\pi_2(1670)$. For the first time a study of the t' dependence on the level of partial waves was undertaken. These findings will serve as input for future models of light-meson production. The same spin-parity analysis was applied to a smaller data set taken in 2009 with a lead target. The aim was to compare the result with the 2004 analysis and to learn more about the production by a direct comparison with the 2008 proton data set.

In order to improve the tracking close to the high-intensity hadron beam, five GEM (Gas Electron Multiplier) detectors with pixelised readout were developed and constructed for the 2008 data-taking. Similar detectors with strip readout and inactive areas around the beam axis were already installed in COMPASS and proved their high-rate capability in combination with a small interaction length. These new detectors replaced parts of the inner tracking system and were the backbone of the Small Angle Tracker (SAT) system during the 2008/2009 hadron campaign.

Zusammenfassung

Die Dynamik der starken Wechselwirkung im Bereich kleiner Energien, d.h. großer Abstände, ist bis heute nicht verstanden. In Anbetracht seiner Einfachheit beschreibt das nicht-relativistische Konstituentenquark-Modell das gemessene hadronische Spektrum sehr erfolgreich . Andererseits sagen Modelle, angelehnt an die QCD, hadronische Zustände vorraus, bei denen Gluonen zu den Quantenzahlen der Hadronen beitragen. Diese Zustände gehen über das Konstituentenquark-Modell hinaus. Ein experimenteller Beweis der Existenz solcher Systeme wäre eine Beobachtung spin-exotischer Zustände mit Quantenzahlen, welche im Konstituentenquark-Modell verboten sind. Die Untersuchung von Mesonen, den einfachsten Hadronen, erlaubt es neue Erkenntnisse zu gewinnen in einem Gebiet der starken Wechselwirkung, in der Hadronen die relevanten Freiheitsgrade sind. Der vielversprechendste Kandidat für ein spin-exotisches Meson ist das $\pi_1(1600)$, welches von mehreren Experimenten behauptet, beobachtet worden zu sein, insbesondere in Daten einer früheren COMPASS Hadron Kampagne.
Das Hadronenspektroskopie Programm des COMPASS Experiments am CERN konzentriert sich auf die Untersuchung von leichter Mesonen mit Massen um 2 GeV/c^2, um diesen kaum verstandenen Bereich der starken Wechselwirkung etwas zu erhellen. Die in 2008 genommenen Daten zur diffraktiven Streuung eines 190 GeV/c Pion-Strahls an einem Proton-Target haben eine nie zuvor erreichte statistische Präzision. Basierend auf einem Modell, bestehend aus 88 Partialwellen mit Gesamtdrehimpulsen bis zu 6 wurde eine Partialwellenzerlegung im kinematischen Bereich des quadrierten Vierimpuls-Übertrags von $0.1 \leq t' \leq 1.0$ GeV$^2/c^2$ durchgeführt. Neben der präzisen Bestimmung von Eigenschaften bekannter Resonanzen wurde ein neuer Axialvektor-Zustand, das $a_1(1420)$, zum erstenmal beobachtet, in einer Massen Region, in welcher weder Modelle noch Gittereich Rechnungen Mesonen mit diesen Quantenzahlen vorhersagen. Bemerkenswert ist die sehr kleine Intensität dieses Signals und die Tatsache, dass es nur an das $f_0(980)$ Isobar koppelt, bei dem man einen großen Strangeness Anteil vermutet. Das spin-exotische $\pi_1(1600)$ wurde beobachtet, wenn auch nur als eine breite Komponente neben dominanten nicht-resonanten Beiträgen. Eine gleichzeitige Analyse in Bins der invarianten Drei-Pionen Masse und des quadrierten Viererimpulsübertrags t' ermöglichte es resonante und nicht-resonante Beiträge eingehend zu untersuchen und besser voneinander zu trennen. Von speziellem Interesse ist hierbei der Deck-Effekt, ein nicht-resonanter Produktionsmechanismus, der zum gleichen Endzustand führt und höchstwahrscheinlich zu den Partialwellen beiträgt, die das $a_1(1260)$ und das spin-exotische $\pi_1(1600)$ beinhalten. Die hybride Natur der zwei bekannten Zustände $\pi(1800)$ und $\pi_2(1880)$ wurde untersucht. Zusätzlich wurde das $\pi_2(1880)$ als eine Resonanz getrennt vom $\pi_2(1670)$ bestätigt. Zum ersten Mal wurde die t' Abhängikeit auf der Ebene der Partialwellen studiert. Diese Resultate werden als Grundlage für zukünftige Modelle der Produktion leichter Mesonen dienen. Die gleiche Spin-Paritäts Analyse wurde auf einen kleineren Datensatz angewandt, der 2009 mit einem Blei-Target aufgezeichnet worden ist. Ziel war es, dieses Resultat mit der 2004 Analyse zu vergleichen und, mittels einem direkten Vergleich mit den 2008 Proton Daten, mehr über den Produktionsmechanismus zu lernen.
Um die Spurrekonstruktion in der Nähe des hochintensiven Hadronen-Strahls zu verbesseren, wurden fünf GEM(Gas Electron Multiplier)-Detektoren mit Pixelauslese für die 2008 Datennahme entworfen und gebaut. Ähnliche Detektoren mit Streifenauslese und inaktiven Bereichen um die Strahl-Achse waren schon in COMPASS installiert und überzeugten durch ihre Standfestigkeit bei hohen Raten zusammen mit einer kleinen Wechselwirkungslänge. Die neuen Detektoren ersetzten Teile des Spurrekonstruktionssystems im Innenbereich und waren das Rückgrat des Small Angle Tracker (SAT) Systems während der Datennahme 2008/2009.

Contents

Preamble

It's fair to say that Joseph von Fraunhofer (1787-1826) can be regarded as the archetype of a modern experimental physicist. His scientific work is known to be based on the development and construction of precise tools and measuring instruments on the one hand and detailed analysis and discussions of his observations on the other. He was not the first to describe the absorption spectrum of the sun, named after him the *Fraunhofer Lines* (see Fig. 1). But in contrast to William Hyde Wollaston, who found in 1802 seven dark lines in the solar spectrum, Fraunhofer reported 570 lines in 1814 and he also determined the corresponding wavelengths. He can also be seen as a pioneer in the sense that he used his observations primarily for commercial applications (he used his method of spectroscopy to check the quality of the glass products, manufactured at his factory). But he also measured the spectrum of the brightest stars (e.g. Sirius, Betelgeuse) seen in the night and found that their spectrum differs from that of the sun. The explanation of the absorption lines was given by Bunsen and Kirchoff 50 years later and revealed for the first time the power of spectroscopy.

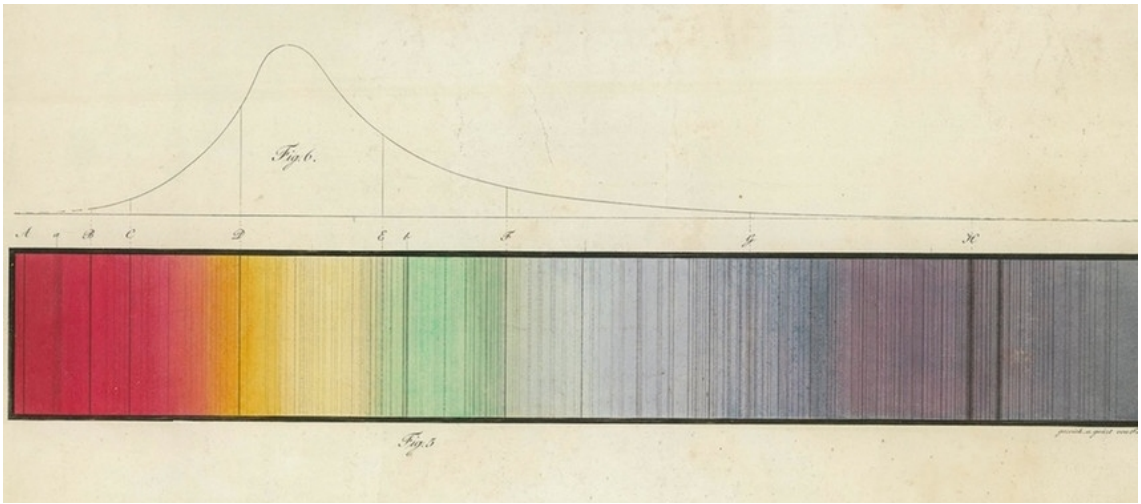

Figure 1 The solar absorption spectrum documented by Jospeh von Fraunhofer (who served as eponym for this spectrum later).

The analysis of the hydrogen spectrum and especially the observation of a shift of the corresponding atomic levels (Lamb shift) finally lead to a first mathematically satisfactory description of quantum electrodynamics (QED) by Hans Bethe in 1947. Based on his concept of renormalisation and the experimental results, the modern formulation of QED was developed by Feynman, Schwinger and others.
In modern physics spectroscopy is still a powerful tool; from determining the composition of

stellar objects to the exploration of hadron dynamics, the latter being the topic of this thesis. The idea of hydrogen spectroscopy, to investigate the simplest system (an electron orbiting around a proton) with spectroscopic methods, inspired physicists since decades in order to learn more about the behavior of quantum chromodynamics (QCD) at low energies or large distances. Thus it is only logical to examine the spectrum of the simplest hadronic system, mesons (a quark and a anti quark bound system) in order to enlight the hadronic territory which cannot be calculated within the QCD (yet).

The structure of this thesis follows the road map of a modern scientific experiment:

- **What is the goal of the experiment?** This question sounds simple, but to clearly define the problem, which one wants to investigate, is essential. In that sense it is also important to check, what was already achieved in the field, where are the obstacles and how one can overcome these. This will be attacked in the first chapter.
- **What are the underlying reaction mechanisms?** The second chapter gives a short introduction to *Regge* theory, which is able to describe in a certain kinematic range the scattering of light mesons. By this it is possible to understand the different production mechanisms, which contribute to the final state of interest.
- **How can the process of interest be meassured?** The COMPASS experiment and its key components of hardware as well as software will be described in Chap. 3. The focus is on detector components, which are relevant for this thesis.
- **How can a suited data sample be obtained?** The recorded data, taken with the COMPASS experiment are investigated and kinematical distributions are presented. The extraction of the desired final state is discussed. This can be found in Chap. 5.
- **Which methods can be used to analyse the data?** The technique of *amplitude analysis*, or equivalent *partial wave analysis*, will be explained in detail in Chap. 6 and in the first parts of the chapters 7 and 8.
- **What are the results?** The central part of this thesis is the discussion of the results, obtained by this analysis. The complexity of the analysis method requires the presentation of results at several places in that thesis. Kinematical distributions are shown in Chap. 5, while the decomposition of the final state into partial waves is discussed in Chap. 7. A first attempt to extract physical values, the goal of each partial wave analysis, will be explained in Chap. 8.
- **What can we learn from the experiment and what is still to be done?** Each finding opens the door for more and new questions. Both will be presented finally in Chap. 9.

Part I

Introduction

Chapter 1

Physics Motivation

> At present our level of understanding is about that of Mendeleyev, who discovered only that certain regularities in the properties of the elements existed. What we aim for is the kind of understanding achieved by Pauli, whose exclusion principle showed why these regularities were there, and by the inventors of quantum mechanics, who made possible exact and detailed predictions about atomic systems.
>
> M. Gell-Mann and E.P. Rosenbaum 1957 [GMR57]

The observation of Rutherford of dense compact atomic nuclei rises the question, which force holds the positively charged protons together. The discovery of the neutron by Chadwick did not solve the problem, but instead complicated the puzzle even more. Hideki Yukawa was the first to give a satisfactory explanation [Yuk35], by introducing the *U-particle* as mediator of this *strong force*. It took almost twelve years to find this particle in cosmic ray experiments. The *pion*[1], as it was named, was the first particle of a new family, called *mesons*[2]. Technical inventions during and after the second world war led to the development of particle accelerators. Hence the discovery of new particles was now taking place in labs instead of week long experiments on the top of mountains. With increasing energies of this machines more and more particles were discovered within the 1950'ies. This wealth of new particles, often called *particle zoo*, made a systematics ordering necessary. Soon after the introduction of a new quantum number, *Strangeness* $\mathscr{S}$, it was tried to find regularities in the production of hadrons using the Gell-Mann-Nishijima formula [NN53, GM56]:

$$Q = I_z + \frac{Y}{2} \qquad \text{with} \qquad Y = B + \mathscr{S} \tag{1.1}$$

Here Y denotes the *hypercharge*[3] which adds the *baryon number* B and the strangeness $\mathscr{S}$. This formula brings the charge Q and the third component of the *isospin* I_z of a particle in

[1] The name *pion* was chosen as the pion itself was not visible in the photo plates, used for the cosmic-ray experiments. But the decay of the pion into a *muon* and something (the neutrino could not be observed of course) at a *primary* vertex was visible.

[2] The name was derived from the Greek word *meson*, indicating that the expected mass should lie between the masses of particles known the at this time: the light electron and the heavy proton and neutron.

[3] Today six quark types are known and experimentally proven. With the introduction of additional quantum numbers for these quarks the hypercharge had to be extended by these numbers: $Y = B + \mathscr{S} + \mathscr{C} + \mathscr{B} + \mathscr{T}$.

relation. In the beginning of the sixties 25 light and strange hadrons were known and a first pattern could be found by Gell-Mann [GM61] and Ne'eman [Ne'61] based on the $SU(3)$ flavor symmetry. This scheme was called the *Eightfold Way* after the "Eightfold Path of Buddhism".

1.1 The Constituent Quark Model

The ordering scheme introduced by Gell-Mann and Ne'eman put a pattern to the observed baryons and mesons, but still it was unclear, what would be the underlying symmetry for this regularity. Inspired from the observation, that the new found $\phi(1020)$ meson dominantly decays into kaon pairs, George Zweig at CERN and Gell-Mann developed independently a theory of the fundamental building blocks of mesons and baryons [GM64, Zwe64a, Zwe64b]. Although the naming was different[4], both theories are based on the same assumptions.
The spectrum of observed hadrons could be explained by introducing point like fermions with non-integer charge. Three *quarks* (the name chosen by Gell-Mann became accepted) are needed to build up the $SU(3)$ flavor symmetry, which light hadrons follow. Two of them, the *up*- and the *down*-quark have almost same mass and can be represented in an isospin $I = 1/2$ doublet. The heavier *strange*-quark, which carries the strangeness quantum number, is an isospin-singlet $I = 0$. All quarks carry the additive Baryon-Number $\mathscr{B} = 1/3$ and positive parity $P = +1$. For each quark there exist an anti-quark, carrying the opposite flavor quantum numbers. Assigning these particles the spin $S = 1/2$ and an electric charge of $+2/3$ to the up-quark, $-1/3$ to the down quark and $-1/3$ to the strange quark, baryons can be built as combinations of three quarks ($qq'q''$) and mesons out of a quark anti-quark ($q\overline{q}'$) pair. The decay of a meson, for example, is seen as a dispartment of the quark pair into two single quarks and the creation of an additional $q\overline{q}'$ pair out of the vacuum. The dominant decay of the ϕ-meson into kaons can now be explained by its quark content being a pair of strange quark and anti-quark. The decay into pions is not allowed, as these mesons carry no strangeness.

1.1.1 Mesons in the Quark Model

Based on these assumptions a non-relativistic model for hadrons can be constructed. Herein mesons represent the simplest hadronic structure. A quark anti-quark pair is orbiting around each other. The spin $\hat{S}$ of the two components can couple to two different states of the total spin S.

$$\begin{aligned} |\uparrow\downarrow\rangle \quad & S=0 \\ |\uparrow\uparrow\rangle \quad & S=1 \end{aligned} \tag{1.2}$$

There can be relative orbital angular momentum L between the $q\overline{q}'$ pair and the total angular momentum results as

$$|L-S| \leq J \leq |L+S| \tag{1.3}$$

Taking the intrinsic parity of the two quarks into account, the parity of a meson is

$$P = (+1)(-1)(-1)^L = (-1)^{L+1} \tag{1.4}$$

[4] Zweig called the particles *aces*, as the key cards in a poker play, while Gell-Mann, inspired from a novel by James Joice, called them *quarks*. It is worth to mention, that Zweig saw the particles as physical objects from the beginning, while Gell-Mann saw them as mathematical constructs in order to explain the observed structures. Only after the experimental observation of a fourth quark, the *charm* quark, he changed his view [Zwe10].

Meson states fulfilling $P = (-1)^J$ belong to the natural spin-parity series and have *naturality* $\eta = +1$ with

$$\eta = P(-1)^J. \tag{1.5}$$

In case of a $q\overline{q}$ system, i.e. a neutral meson build up of a quark and its own antiparticle, the meson is in a C-parity eigenstate. This symmetry exchanges particles with their antiparticles.

$$C = (-1)^{L+S} \tag{1.6}$$

For charged systems, i.e. $q\overline{q}'$ pairs with non-zero isospin, this quantum number is not defined. The C-parity can be generalised to the G-parity [LY56], a multiplicative quantum number, which is defined for all states of a meson multiplet. It is a combination of charge conjugation followed by a rotation of 180° around the I_y-axis in the isospin space.

$$G = Ce^{i\pi I_y} = C(-1)^I \tag{1.7}$$

As the G-parity acts on the whole multiplet, the average charge $\overline{Q}$ must be equal to 0. Therefore only systems with $\overline{Q} = \overline{Y}$ (see Eq. (1.1)) are defined as G-parity eigenstates. This is valid for all light mesons. However, by convention the charged mesons got the same C-parity as their neutral isospin partner.

J^{PC}	$^{2S+1}L_J$	S	L	I	Exp. Representation	Family
0^{-+}	$^1S_0$	0	0	0	$\eta, \eta'(958)$, ...	Pseudo-scalar
				1	$\pi, \pi(1300), \pi(1800)$, ...	
0^{++}	$^0P_0$	1	1	0	$\sigma, f_0(980), f_0(1370), f_0(1500)$, ...	Scalar
				1	$a_0(980), a_0(1450)$, ...	
1^{--}	$^3S_1$	1	0	0	$\omega(782), \phi(1020), \omega(1429)$, ...	Vector
				1	$\rho(770), \rho(1450), \rho(1700)$, ...	
1^{+-}	$^1P_1$	0	1	0	$h_1(1170)$, ...	Pseudo Vector
				1	$b_1(1235)$, ...	
1^{++}	$^3P_1$	1	1	0	$f_1(1285), f_1(1420)$, ...	Axial-vector
				1	$a_1(1260), a_1(1640)$, ...	
2^{-+}	$^1D_2$	0	2	0	$\eta(1645)$, ...	
				1	$\pi_2(1670), \pi_2(1880)$, ...	
2^{++}	$^3P_2$	1	1	0	$f_2(1270), f_2'(1525)$, ...	Tensor
				1	$a_2(1320)$, ...	

Table 1.1 Allowed meson states within the quark model and experimental representations.

Based on these simple rules (more details can be found in every good text book, e.g. [Bop89]) meson states with certain quantum numbers J^{PC} can be constructed. Depending on their spin mesons of the natural spin-parity series are denoted as scalar or vector mesons, while other states are pseudo-scalar or pseudo-vector states. Table 1.1 gives an overview of allowed light meson states in the quark model. It is obvious from the aforementioned rules that certain spin-parity states cannot be constructed.

$$J^{PC} = 0^{--}, \text{odd}^{-+}, \text{even}^{+-} \tag{1.8}$$

These states are called *spin-exotic* mesons and are not allowed within the simple quark model. One challenge in the regime of meson spectroscopy is to clarify whether this model can explain the light-meson spectrum or whether experimental observations of spin-exotics can give a hint for hadronic states which cannot be explained within that framework.

1.2 Quantum Chromodynamics

The quark model introduced a classification scheme for hadrons, both mesons and baryons, but not all experimental observations could be explained by that model. Andrei Sakharov for example noticed the mass difference of the Λ and the Σ baryon although both having the same quark content. No free quarks could be observed in any experiment and it seemed that the Δ^{++} resonance (with quark content $|u\,u\,u\rangle$ and spin state $|\uparrow\uparrow\uparrow\rangle$) violates the Pauli Principle [5]. In addition the quark model does not clarify what is the binding force, holding quarks together in hadrons. It took almost one decade until a quantum field theory of the strong interaction was formulated [FGM72],[FGML73]: The Quantum Chromodynamics (QCD). A non-abelian gauge theory with quarks and gluons, the mediator of the color charge, as the degrees of freedom. As the gluons carry color charge too, the dynamics of QCD is very much different like e.g. the one of the QED. Quarks emit and absorb gluons. This is similar to Quantum Electrodynamics (QED) with photons the mediators of the electromagnetic force. But in addition gluons can emit or absorb gluons and can therefore interact. Both QCD and QED are renormaliseable theories, which leads to the fact that the coupling depends on the momentum transfer Q^2. Equation (1.9) describes the running coupling of the strong force, with β_0 a constant and the QCD scale $\Lambda = 220$ MeV (Fig. 1.1 shows the world average of α_s).

$$\alpha_s(Q^2) \approx \frac{1}{\beta_0 \ln(Q^2/\Lambda^2)} \tag{1.9}$$

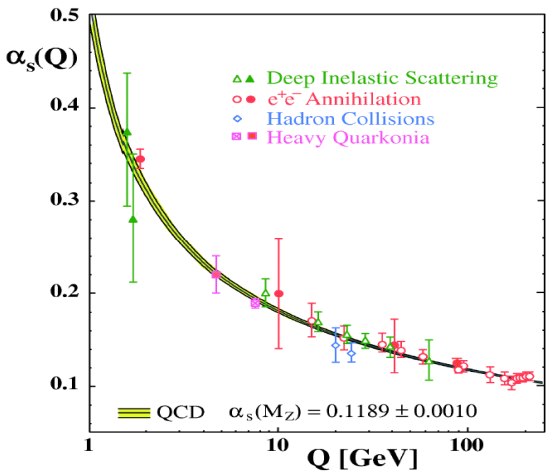

Figure 1.1 World average of α_S from [Bet07]

[5] To overcome this problem several theoretical physicists suggested to introduce an additional quantum number, the color charge (e.g. [Nam66])

The running coupling reveals two important features of QCD (a profound introduction can be found at [Bet07]). For a momentum transfer far above the QCD scale (or at small distances) the coupling of the strong force becomes extremely small. In this kinematic regime quarks can be seen as quasi-free or weakly bound particles. This is called the *Asymptotic Freedom* with quarks and gluons as the relevant degrees of freedom. Due to the small value of α_s perturbation theory can be applied in order to calculate the Lagrangian. The perturbative QCD (pQCD) shows very good agreement with experimental data.
On the opposite side of the momentum scale (small momentum transfer or large distances), close to or below Λ, the coupling becomes large and pQCD can not be applied anymore. This is the regime of *confinement*, with color-neutral objects, the hadrons, as the only degrees of freedom. Due to self-interactions and vacuum condensates, unavoidable consequences of the strong binding, the dynamics cannot be calculated in that regime.

1.3 QCD-inspired Models

The *November Revolution* in 1974 was a milestone in particle physics. With the discovery of the J/ψ and J/ψ' the final evidence for the quark model was given and quarks were accepted as fundamental real particles instead of a purely mathematical concept. As the charm quark being heavy and slow inside the Ψ it was now possible to calculate the charmonium spectrum and to predict not yet discovered resonances still the light meson spectrum persisted to be incalculable within the QCD. The quark model, however, was successful in describing along general lines the light meson sector but it does not take the color force and their mediators, the gluons, into account. QCD allows in addition to simple $|q\overline{q}'\rangle$ states, configurations where the gluon field contributes to the observed quantum numbers $|q\overline{q}' g\rangle$. These so-called *hybrids* can be realised with ordinary quark model quantum numbers or as a spin-exotics (see Eq. (1.8)). Due to the self-interaction of gluons pure gluonic bound states $|g\,g\rangle$, called *glueballs*, could also be possible. Taking these new states and their properties into account leads to new hadronic realisations. The first basic states of the Fock space expansion of an observed meson are shown below:

$$|\text{meson}\rangle = |q\overline{q}'\rangle + |q\overline{q}' g\rangle + |g\,g\rangle + ... \tag{1.10}$$

These additional states, brought in by QCD, go beyond the simple quark model and thus new models and concepts had to be invented in order to include some of the properties of QCD.

Bag and Flux Tube Models

The M.I.T. *bag model* (e.g. [CJJ+74, Joh75, FOW81]) describes hadrons as compound systems, consisting of quarks and gluon field variables . Although the same field components are used as implemented in QCD, they are only valid within the compound system, called *bag*, and zero outside. The lowest order states inside the bag are color-singlet basis states as seen in Eq. (1.10) and due to quark-gluon and gluon self interactions the physical realisations are linear combinations of these basis states just as for the meson Fock space. Even these early models predict pure gluonic states [JJ76] and hybrids [BCdV83]. Within these models the lowest quark mode has quantum numbers $J^P = 1/2^+$ and the lowest gluon mode has $J^P = 1^+$. The combination of both modes lead to the following hybrid states:

$$J^{PC} = (0^-, 1^-) \otimes 1^+ = 1^{--}, 0^{-+}, 1^{-+}, 2^{-+} \tag{1.11}$$

Except the $J^{PC} = 1^{-+}$ all are ordinary constituent quark model quantum numbers and could be experimentally hardly distinguished from $q\overline{q}$ states. The mass of the spin exotic hybrid is predicted to have mass in the range of 1.2 - 1.7 GeV/c^2

Early lattice simulations (see following section) showed a roughly cylindrical region of gluon fields between separated color sources [Bar00]. This observation inspired the formulation of *flux tube* models. Fixed endpoints are connected by a linear potential on which point-like masses are stringed. The simple quark model is recovered as a limit of these models [IP85]. A such defined system can be treated like a quantum oscillator with transverse excitation modes. The coupling of the orbital angular momentum of the excited string with the spin and orbital angular momentum of the $q\overline{q}$ system results in the following quantum numbers:

$$J^{PC} = 0^{\pm\mp}, 1^{\pm\mp}, 2^{\pm\mp}; 1^{\pm\pm} \tag{1.12}$$

The wealth of possible combinations leads to the prediction of two new 36-plets of meson states. In addition a rough estimation of the mass of these hybrids around 1.9 GeV/c^2 these models give an idea about the preferred decay modes of hybrids. According to them decays into two S-wave mesons, like $\rho\pi$ is suppressed in favor to a decay into a S-wave and a P-wave meson. Thus the dominant decay modes of the spin exotic 1^{-+} should be $b_1(1235)\pi$ and $f_1(1285)$ rather than $\rho\pi$, which is one of the accessible channels in the analysis presented in this thesis (see Sec. 1.4.2). However, recent studies showed that the flux-tube model cannot be applied to the light quark sector as the tube would brake down due to pion production out of the vacuum [Rob12].
For both kind of models, discussed here, a profound summary can be found in [Bar00].

Lattice QCD

The only first-principles approach to the light meson spectrum is to simulate QCD on a discretised four-dimensional space time lattice [Wil74]. The quark fields are localised on the nodes ('sites') of the lattice while the gluonic fields are defined at the connection lines ('links') between the nodes, separated by the lattice spacing a. In the limit of $a \to 0$ lattice QCD transforms to the continuum field theory. The ansatz of lattice approximation enables to evaluate numerical solutions of the non-perturbative regime of QCD. Short after its introduction it became clear that lattice calculations are extremely expensive. The computing costs can be roughly estimated by [Lep98]

$$\text{cost} \sim \left(\frac{L}{a}\right)^4 \frac{1}{a} \frac{1}{m_\pi^2 a} \tag{1.13}$$

where the first factor comes from the lattice while the others are representing the costs of the applied algorithms. When interpreting results calculated by lattice methods it has to be kept in mind that the outcome of these calculations are dimensionless, which have to be linked to physical values by setting a scale. Additionally the resulting masses are larger than the corresponding physical values as the quark masses, used in the calculations, are heavier than real quark masses in order to reduce the amount of vacuum loops, which are expensive to calculate. Finally the rotational symmetry is broken when calculating on a cubic lattice, thus the corresponding operators have to be matched with physical angular momenta.
In the last years huge progress has been made in this field. Modern computers are much faster

than in the beginning of LQCD and several new methods have been developed to optimize the calculations. In particular finer lattices could be introduced and the operator bases could be extended. These new calculations offer the possibility to identify higher excitations and access their gluonic content [Dud11]. Figure 1.2 shows the recently calculated isoscalar and isovector spectrum. Although shifted in mass due to the artificially larger pion mass of 396 MeV/c^2 most of the known resonances can be identified. In addition to pure $q\overline{q}$ states, hybrids with allowed and spin-exotic quantum numbers are resulting from this lattice calculations. A hybrid super multiplet with

$$J^{PC} = 0^{-+}, 1^{-+}, 2^{-+}; 1^{--} \tag{1.14}$$

is identified, as predicted before by the bag and flux-tube models. Modern lattice calculations can reproduce quite well the observed hadronic spectrum and corresponding findings should be taken seriously and taken into account for future experimental investigations.

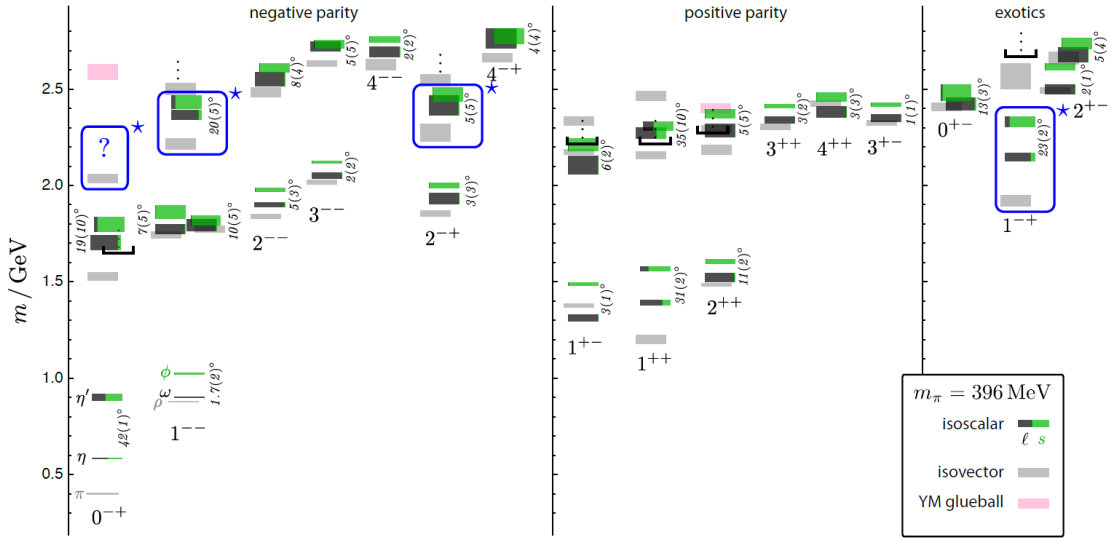

Figure 1.2 Spectrum of isoscalar and isovector mesons obtained by LQCD, plot from [Dud11].

1.4 Experimental Access to the Light Meson Sector

The evolution of models and theories, some of them introduced previously, are driven by experimental observations and tested against them. For instance lattice QCD and some models are predicting new states which are waiting for their experimental verification or falsification. In order to get access to the light meson sector, which is in the topic of this thesis, there exist two experimental methods. At *formation experiments* two reaction partners, either beam and target or two colliding particles, are forming a new state. The mass is determined by the center-of-mass energy and the possible quantum numbers like strangeness, charge or spin are defined by the two parent particles. This shows the biggest caveat of this method. Only certain states can be realised, dependent on the properties of the two reaction partners. Only the invariant mass and the orbital angular momentum L can be controlled by modifying the center-of-mass

energy of the reaction. Otherwise the initial state is known and thus phases between the initial state and the formed resonance can be accessed.
The data set used for the analysis presented here was obtained by the COMPASS experiment, which is a *production experiment*. Here high-energetic hadronic beams interacting with a target. Instead of investigating resonances in the cross-section, as done for formation experiments, the products of the reaction, or if they are short-lived, the final state is under study. The biggest advantage is the access to resonances where not all quantum numbers are the direct sum of the properties of the initial state. The number of accessible resonances is theoretically unlimited. The invariant mass is limited by the center-of-mass energy. The reaction is more complicated than a formation process as it is not only defined by the transition amplitude but also by the reaction properties. Thus phases can not be measured as the real initial state is not known.
The process exploited for this analysis is called *diffractive dissociation*, a peripheral high-energetic reaction via the strong interaction. The reaction, analysed in this thesis, can be described as follows. An incoming high-energetic negatively charged pion interacts with a target proton, gets excited to an intermediate state X^- and finally decays (dissociates) into a three-pion final state (see Eq. (1.15)).

$$\pi^- p \to \pi^- \pi^- \pi^+ p \tag{1.15}$$

The only interaction is the strong force, mediated by objects called *Reggeons* (the concept of Regge trajectories will be introduced in detail in Chap. 2). Due to the fact, that only strong interaction is taking place, charge, isospin and parity are conserved. From the two possible combinations of the final state the one with three charged pions is in the focus of this analysis (see Eq. (1.15)). Due to Pomeron interaction (see Sec. 2.1.1) only isovector states with negative G-parity can be produced by diffraction with a pion beam. These accessible mesons can be divided into two families, distinguished by their parity. Mesons with $I^G J^P = 1^- J^+$ belong to the a_J-mesons, while the π_J-mesons are associated to $1^- J^-$. Some of these known resonances are listed in Tab. 1.2.

1.4.1 Open Questions in the Isovector Regime of Light Mesons

The exploration of the three-pion spectrum began in the 1960ies with the discovery of the $a_1(1260)$ resonance and peaked about 10 years later with the investigations of non-resonant production processes like the Deck effect (see Sec. 2.2.3). Due to the fact that the light-meson spectrum could not be calculated within QCD, new models were still under development and, technical progress allowed to access charmed mesons, light-meson spectroscopy stagnated in the following decades, with some notable exceptions like the ACCMOR collaboration (e.g. [D$^+$81]) at the beginning of the 1980's. This kind of analysis had its renaissance 15 years later with observations of spin-exotic mesons by BNL852 e.g [CDH$^+$02], VES e.g. [Ame] and other experiments. In spite of decades of light meson spectroscopy a lot of questions are not yet answered satisfactorily. In the following some of these questions are introduced in order to illustrate the possibilities of a modern analysis with an unprecedented large data set, like the one used for this analysis.

particle	J^{PC}	mass [MeV/c^2]	width [MeV/c^2]
		"established" states	
$a_1(1260)$	1^{++}	1230 ± 40	$250 - 600$
$a_2(1320)$	2^{++}	$1318.3^{+0.5}_{-0.6}$	107 ± 5
$a_4(2040)$	4^{++}	1996^{+10}_{-9}	255^{+28}_{-24}
$\pi(1300)$	0^{-+}	1300 ± 100	$200 - 600$
$\pi_1(1400)$	1^{-+}	1354 ± 25	300 ± 35
$\pi_1(1600)$	1^{-+}	1662^{+8}_{-9}	241 ± 40
$\pi_2(1670)$	2^{-+}	1672.2 ± 3	260 ± 9
$\pi(1800)$	0^{-+}	1812 ± 12	208 ± 12
$\pi_2(1880)$	2^{-+}	1895 ± 16	235 ± 34
		"further" states	
$a_3(1875)$	3^{++}	$1874 \pm 43 \pm 96$	$385 \pm 121 \pm 114$
$a_1(1930)$	1^{++}	1930^{+30}_{-70}	155 ± 45
$a_2(1950)$	2^{++}	1950^{+30}_{-70}	180 ± 30
$a_2(1990)$	2^{++}	$2050 \pm 10 \pm 40$	$190 \pm 22 \pm 100$
		$2003 \pm 10 \pm 19$	$249 \pm 23 \pm 32$
$a_2(2030)$	2^{++}	2030 ± 20	205 ± 30
$a_3(2030)$	3^{++}	2031 ± 12	150 ± 18
$a_1(2095)$	1^{++}	$2096 \pm 17 \pm 121$	$451 \pm 41 \pm 81$
$\pi_2(2005)$	2^{-+}	$1974 \pm 14 \pm 83$	$341 \pm 61 \pm 139$
		2005 ± 15	200 ± 40
$\pi_1(2015)$	1^{-+}	$2014 \pm 20 \pm 16$	$230 \pm 32 \pm 73$
		$2001 \pm 30 \pm 92$	$333 \pm 52 \pm 49$
$\pi(2070)$	0^{-+}	2070 ± 35	310^{+100}_{-50}

Table 1.2 Isovector mesons of the a_J and π_J family in the mass range of 1-2.1 GeV/c^2 as taken from [B$^+$12].

Dynamics of Meson Production

It was mentioned before that the scattering of light mesons can be explained within the Regge framework. This theory describes diffractive dissociation as function of the the center-of-mass energy s, the invariant mass of the intermediate state m_X and the squared four-momentum transfer t (see Sec. 2.2.1). For fixed-target experiments s is fixed by the beam energy and only the latter two variables are of importance. While previous experiments investigated the mass dependence of the produced states, the t dependence is rather unexplored (except for some first studies by [D$^+$81] and [CDH$^+$02, DMS$^+$06]). It is known, that besides Regge exchange additional production mechanisms are contributing to the final state of interest (see Sec. 2.2.3, 2.2.2). The systematic analysis of t dependencies decomposed into partial waves must be the next logical step for a full understanding of the underlying production mechanisms.
In addition modern and future experiments offer the possibility to obtain much more data than previous ones so that the whole isovector spectrum can be studied in unprecedented detail and yet unresolved states could be observed for the first time.

Radial Excitations of the Pion

When investigating the three-pion sector with a pion beam it is obvious to explore the simplest excitation spectrum, the radial excitations of the pion. Two corresponding resonances are experimentally proven by several analyses, the $\pi(1300)$ and the $\pi(1800)$ (see Tab. 1.2). These observations fit well with some models which predict resonances in these mass ranges (e.g. [Kat04]) and additionally another one around 2.2 GeV/c^2. However, other calculations see additional not observed states between 1.1 and 1.7 GeV/c^2 (e.g. [CHS99]). In addition to other radial excitations, also the nature of the two observed resonances is not yet clarified. The $\pi(1300)$ has a large decay width ($\Gamma = 200 - 600$ MeV/c^2) and the coupling to the not well understood $(\pi\pi)_S$ wave is disputed. The $\pi(1800)$ is discussed as a possible hybrid candidate, i.e. this state might have a non-negligible gluon content [Pag98], [Dud11]). The experimentally observed suppression of decays to the $\rho\pi$ channel and the coupling to the $(\pi\pi)_S\pi$ channel support the idea that the $\pi(1800)$ is rather a hybrid than a $q\overline{q}'$ state [SS97]. The strength of the $f_0(980)\pi$ mode, which is in contrast to these models, is explained by a strong coupling to the $K\overline{K}$ channel [SS97]. In addition the observation of a decay to the $f_0(1500)$, which is a glueball candidate [IP85], and the decay width to the $f_2(1270)\pi$ channel could enlight the situation, The identification of the isospin partner η' and its corresponding decay channels meassured would clarify the picture further.

Understanding the $a_1(1260)$

The discovery of the $a_1(1260)$ [GBG$^+$64, CDH$^+$64] marks the beginning of the exploration of the isovector spectrum with negative G-parity. Being the dominantly produced resonance in processes like diffractive dissociation with pions, it is a standard candle for this kind of analyses. But its production strength and large decay width ($\Gamma = 250 - 600$ MeV/c^2 [B$^+$12]) could not be explained with the existing models. In addition the possibility of a competing production process resulting in a non-resonant three-pion final state was introduced by Deck [Dec64]. Later analyses [AJWW73, ACJ$^+$74] attributed some of the observed intensity of the $a_1(1260)$ to this process, named after his discoverer, the *Deck effect*. Further theories predicts a non-negligible effect of final-state interaction contributing to the observed decay channels of this resonance [Bre81]. After these findings and ideas, born in the 1970ies, no new insight was gained since then. Still its mass and width and the underlaying processes of its production are not well understood [Yao06].

$J^{PC} = 2^{-+}$ States

With improving techniques and resulting larger data sets resonances with higher spins could be observed. The $\pi_2(1670)$, formerly named as a_3 by its discoverer [D$^+$81], can be seen as another standard candle of the three-pion spectrum. A few years later a second resonance with the same quantum numbers was found, which was called the $\pi_2(1880)$ [ABB$^+$96, ABB$^+$01]. Its proximity in mass to the $\pi_2(1670)$ inspired various models to explain its nature. In [DS06] it was proposed that both π_2 states origin from the same 'true' resonance, both shifted to lower and higher masses by an additional Deck-like contribution. Some other models try to explain the $\pi_2(1880)$ as a hybrid (e.g. [LZ09], [Dud11]) which could explain its closeness to the $\pi_2(1670)$. In addition various other π_2 resonances are claimed by different experiments, but none is up to now verified by a second experiment.

1.4.2 The spin-exotic $J^{PC} = 1^{-+}$ Candidates

A convincing proof for meson states beyond the simple quark model would be the experimental observation of a spin-exotic state. Models and lattice QCD predict the $J^{PC} = 1^{-+}$ being the lightest hybrid [Bar00]. Its mass is predicted in the region of 1.3-2.2 GeV/c^2. There are three experimental candidates for a light 1^{-+} hybrid. The $\pi_1(1400)$ was observed by E852 [TAA97], VES [Ame][6] and by Crystal Barrel [Ams98]. The best experimentally investigated and established spin exotic is the $\pi_1(1600)$, decaying into $\rho\pi$ [CDH$^+$02, Zai00, AAA$^+$10], $\eta'\pi$ [B$^+$93, I$^+$01], $f_1(1285)\pi$ [Ame, K$^+$04] and $b_1(1235)\pi$ [Ame, Lu05]. A third spin-exotic candidate, the $\pi_1(2000)$, decaying to $f_1\pi$ and $b_1\pi$ was observed by only one collaboration [Lu05, K$^+$04].
Of particular interest for this analysis are decay channels accessible by the three pion-final state, which is only the before-mentioned $\rho\pi$ decay mode. While investigated by several experiments already the results are puzzling and create doubt about the experimental findings. While a clear $\pi_1(1600)$ peak was observed by [CDH$^+$02] (see Fig. 1.3a) the same collaboration, BNL E852, claimed, based on an extended data set, that no spin-exotic resonance can be observed in this mass region [DMS$^+$06](see the black curve in Fig. 1.3b). The VES group on the other hand confirmed a spin exotic around 1.6 GeV/c^2 [Zai00] but found a broad structure instead the narrow peak of the BNL analysis [CDH$^+$02]. Finally The COMPASS collaboration claimed to see a resonating structure around 1.66 GeV/c^2 [AAA$^+$10] in a three-pion analysis using data taken with a lead target in 2004. The search for a spin-exotic resonance is of course one of the topics of this thesis. Using COMPASS data a detailed investigation of these previous analyses will be carried out in order to clarify this confusing situation. A complete overview of experimental observations of hybrids, glueballs and multi-quark states including the corresponding models can be found in [KZ07] which also discuss the before-mentioned analyses.

[6]This publication summarises all experimental findings of the VES collaboration concerning the spin-exotic.

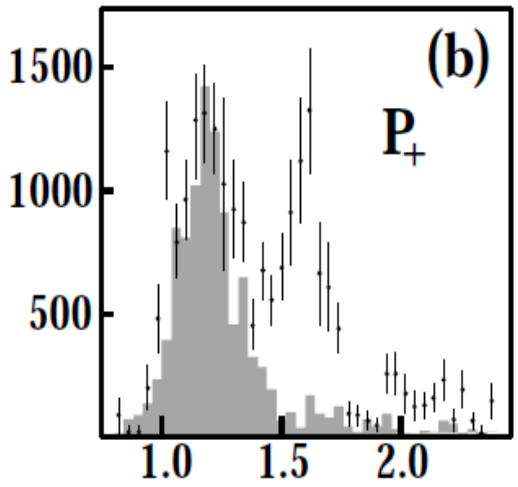

(a) BNL E852 [CDH+02]

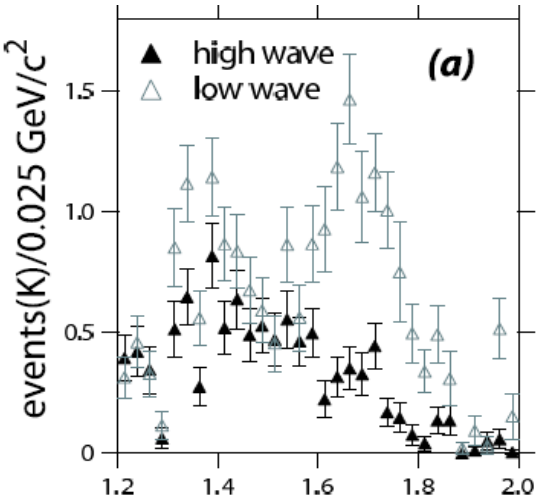

(b) BNL E852 [DMS+06]

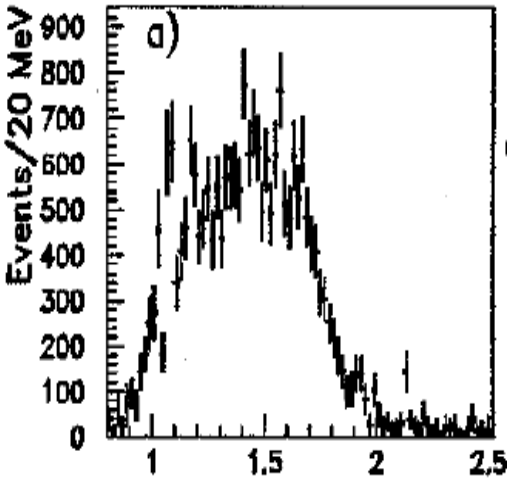

(c) VES [Zai00]

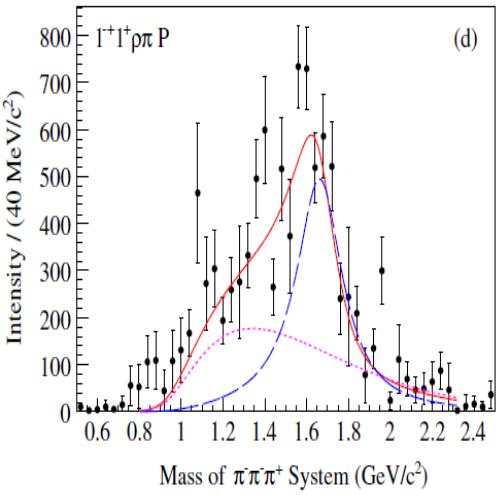

(d) COMPASS [AAA+10]

Figure 1.3 Overview of analyses investigating the spin-exotic 1^{-+} in the $\pi^-\pi^-\pi^+$ channel.

Chapter 2

Production Mechanisms

Strong interaction had been known decades before QCD was developed and accepted as theory of hadronic interaction. Despite the success of QCD in describing strong interaction at short distances or large momentum transfers, no satisfactory description could be established to describe hadronic dynamics in the non-perturbative region of QCD, as discussed in Sec. 1.2. In this region where hadrons are the degrees of freedom the pre-QCD theories of scattering, explained by the exchange of Reggeons, are still valid and are applicable to modern scattering experiments in the light-meson sector. Regge theory was developed by its eponym Tulio Regge for the case of non-relativistic scattering in the late 50ies of the previous century. The adaption to relativistic scattering was initiated a few years later by Mandelstam and others in the western hemisphere and by the Russian scientists Gribov and Pomerantschuk behind the iron curtain. For the analysis discussed in this thesis some level of understanding of the production mechanism is important in order to find selection rules for the data set (Sec. 5) and to set up a realistic and complete fit model (Sec. 6) in order to disentangle the various contributions to the observed intensity. However, a deep comprehension is not necessary for an amplitude analysis of a data set. Thus this chapter suggests a possibility to get an access to Regge theory as it is used for high-energy scattering in the relativistic case, omitting some mathematical details but preserving the motivation, which drove the original inventors to develop this framework. A fundamental mathematical derivation, which serves as guideline for this chapter, can be found in [BP10, DN09] and [SDN02].

2.1 Regge Theory and Pomeron Exchange

The S-matrix program, inaugurated in the late 1950ies of the last century, was an attempt to describe strong interaction processes alternatively to quantum field theories. At that time, many theorists believed, that any local quantum theory could explain strong interaction at short distances. A non-abelian gauge theory, with a decreasing coupling constant at short distances, was not yet known. QCD was developed 10 years later, introducing the running coupling constant α_s, and the logical consequences, asymptotic freedom and confinement. But nevertheless S-matrix theory showed a practical tool to explain hadronic interactions in the non-perturbative regime. An elaborate discussion of the development of S-Matrix theory can be found in [Whi08].
For the following discussion only two-body scattering (see Eq. (2.1)) is considered in order to

keep the derivation of the Regge concept straight forward.

$$a + b \to c + d \tag{2.1}$$

The scattering matrix S is the *linear* operator which transforms the initial state $|i\rangle$ of a scattering process into a final state $|f\rangle$.

$$S|i\rangle = |f\rangle \tag{2.2}$$

The linearity of the S-matrix simply reflects the superposition principle of quantum mechanics. In addition S has to be *Lorentzinvariand*. The S-matrix elements must depend on Lorentz invariant variables. In order to get the *transition matrix*, the identity operator has to be subtracted from S.

$$S = \mathbb{I} + iT \tag{2.3}$$

Thus the matrix elements of S are

$$S_{if} = \delta_{if} + iT_{if} \tag{2.4}$$

Separating from T the δ function, which corresponds to the four-momentum conservation $\hat{p}_i = \hat{p}_f$ gives

$$S_{if} = \delta_{if} + i(2\pi)^4 \delta^4(p_f - p_i) A_{i\to f}(s,t) \tag{2.5}$$

The relativistic scattering amplitude $A_{i\to f}(s,t)$ can be regarded as the real matrix element of S. The amplitude is a function of s and t, two representatives of the Lorentz-invariant set of kinematical variables, known as the *Mandelstam invariants*. In terms of Eq. (2.1) these variables are defined as

$$s = (\hat{p}_a + \hat{p}_b)^2 = (\hat{p}_c + \hat{p}_d)^2 \tag{2.6}$$

$$t = (\hat{p}_a - \hat{p}_c)^2 = (\hat{p}_b - \hat{p}_d)^2 \tag{2.7}$$

$$u = (\hat{p}_a - \hat{p}_d)^2 = (\hat{p}_b - \hat{p}_c)^2 \tag{2.8}$$

The most powerful consequence of S-matrix theory is the *optical theorem*, which is defined for relativistic scattering as follows

$$\sigma_{\text{tot}} = \frac{1}{s} \Im A_{\text{el}}(s, t = 0) \tag{2.9}$$

It allows to calculate the total cross section of any reaction by just taking the imaginary part of the cross section of the elastic fraction and the forward limit ($t = 0$) of this reaction into account. Thus the theoretically infinite summation over all possible inelastic terms can be avoided.
Relativistic scattering processes are usually investigated in reference systems, defined by the Mandelstam invariants:

$$s - \text{channel} = a + b = c + d \tag{2.10}$$

$$t - \text{channel} = a + \bar{c} = \bar{b} + d \tag{2.11}$$

$$u - \text{channel} = a + \bar{d} = \bar{b} + c \tag{2.12}$$

One feature of any relativistic field theory is that for a given reaction an incoming particle x with momentum p can be regarded as its outgoing antiparticle $\bar{x}$ with momentum $-p$. This symmetry is called *crossing* and one of the postulates of the relativistic S-matrix. As a consequence the same amplitude describes the process in the three different channels. Taking this

into account the amplitude is parametrised in the t-channel, following [BP10], which means that the square of the center-of-mass energy is t.
Thus the partial-wave expansion of the scattering amplitude $A(s,t)$ in the t-channel is defined as

$$A(s,t) \equiv A(s,\cos\vartheta_t) = \sum_{l=0}^{\infty}(2l+1)A_l(t)P_l(\cos\vartheta_t) \tag{2.13}$$

An intuitive way to describe the scattering amplitude is as a function of s and the cosine of the scattering angle in the respective channel (here t-channel) with

$$\cos\vartheta_t = 1 + \frac{2s}{t-4m^2} \tag{2.14}$$

The expansion is a sum of products of partial waves $A_l(t)$ and their respective Legendre polynomials $P_l(\cos\vartheta_t)$. Looking at one of the kinematical boundaries, i.e. t is fixed and s tends to infinity, which is called the *Regge limit*, and regarding Eq. (2.14) one can see that

$$P_l(\cos\vartheta_t) \underset{s\to\infty}{\sim} s^l \tag{2.15}$$

and thus the partial wave expansion diverges at high energies

$$A(s,t) \underset{s\to\infty}{\sim} \sum_l A_l(t)s^l \tag{2.16}$$

The equivalent problem in the non-relativistic case was the starting point for Regge to find a way in order to calculate the expansion at high energies. But before Regge's solution and its adaption to relativistic scattering will be introduced, it is worth to discuss another dilemma where Regge theory is a way out.
Since Yukawa introduced the pion as the mediator of the strong force it was an accepted concept to describe relativistic scattering by the exchange of a single meson. Regarding a single meson with defined spin, the scattering amplitude can be written as

$$A_{\text{meson}}(s,t) \sim A_J(t)P_J(\cos\vartheta_t) \tag{2.17}$$

with J being the spin of the meson. In order to determine the total cross section of this process it is convenient to find a formulation of the elastic scattering amplitude $A_{\text{el}}(s,t=0)$ of this process. Taking unitarity relations of the S-matrix and the fact that only one meson is exchanged into account, leads to the following form of the imaginary part of the elastic cross section in the high-energy limit:

$$\Im A_{\text{el}}(s,t=0) \underset{s\to\infty}{\sim} s^{2J-1} \tag{2.18}$$

Recalling the optical theorem (Eq. (2.9)) leads to the following proportionality

$$\sigma_{\text{tot}} \underset{s\to\infty}{\sim} s^{2(J-1)} \tag{2.19}$$

One consequence of the obtained cross section is that for exchanged mesons with spin J greater than one, this violates the *Froissart-Martin bound*. This theorem claims that in the high-energy limit the total cross section cannot grow faster than

$$\sigma_{\text{tot}} \leq \frac{\pi}{m_\pi^2}\ln^2 s, \qquad \text{with} s\to\infty \tag{2.20}$$

It is *Regge theory* in its relativistic advancement to show a way out of the previously described problems. The original idea of Regge was to describe bound states in the framework of non-relativistic quantum mechanics. Therein bound states can be sorted into families with increasing angular momentum l for attractive spherically potentials. They are realised as poles of the non-relativistic partial-wave amplitude $a_l(k)$ [1] for integer l. Inspired by Sommerfeld and its complex angular momentum formalism Regge continued $a_l(k)$ to complex values of l thus obtaining a smooth function $a(l,k)$ which reduces to $a_l(k)$ for integer l. For certain kind of potentials, like Yukawa-type ones for example, these poles are located at values following the relation

$$l = \alpha(k) \tag{2.21}$$

The function $\alpha(k)$ is called *Regge trajectory* with its poles named *Regge poles*.
Further developments by Mandelstam, Gribov et al. showed, under certain hypothesis and the consideration of properties of the S-matrix, that Regge's idea could be used for the relativistic case. The relativistic partial-wave amplitude $A_l(t)$ can be analytically continued to the complex plane by the function $A(l,t)$ which has simple poles at

$$l = \alpha(t) \tag{2.22}$$

Each of these poles contributes to the scattering amplitude by introducing a term like

$$A(s,t) \underset{s\to\infty}{\sim} s^{\alpha(t)} \tag{2.23}$$

under the constraint that t is fixed. The concept of Regge trajectories describes scattering by the exchange of a whole family of resonances, all on the same trajectory. Each trajectory can be described by a linear equation

$$\alpha(t) = \alpha(0) + \alpha' t \tag{2.24}$$

Using Regge trajectories in order to describe scattering processes it is possible to obey the Froissart-Martin bound (see Eq. (2.20)) under the constraint that

$$\alpha(0) < 1 \tag{2.25}$$

Otherwise unitarity is violated.
For simplicity more advanced properties of relativistic Regge theory, like *Regge cuts*, are omitted, as this brings no further enlightenment for the following discussion.
The scattering amplitude $A(s,t)$ can now be written for a single Regge exchange by

$$A(s,t) = \beta(t)\eta_\xi(t)s^{\alpha(t)} \tag{2.26}$$

with

$$\beta(t) = g_{ac}(t)g_{bd}(t) \tag{2.27}$$

$$\eta_\xi(t) = \begin{cases} -\frac{e^{-i\frac{\pi}{2}\alpha(t)}}{\sin\frac{\pi}{2}\alpha(t)} & \xi = +1 \\ -i\frac{e^{-i\frac{\pi}{2}\alpha(t)}}{\cos\frac{\pi}{2}\alpha(t)} & \xi = -1 \end{cases} \tag{2.28}$$

[1] The same convention is used in [BP10]. $a_l(k)$ denotes non-relativistic partial-wave amplitudes, while $A_l(s)$ or $A_l(t)$ describes these amplitudes for the relativistic case, see Eq. (2.13).

The *residue* $\beta(t)$ can be factorised into the couplings at the two vertices of a simple scattering process and $\eta(t)$ is the signature factor with ξ being the associated quantum number, called *signature* which is connected to the angular momentum l by

$$\xi = + \quad \text{for } l \text{ even} \tag{2.29}$$

$$\xi = - \quad \text{for } l \text{ odd} \tag{2.30}$$

Regarding Eq. 2.23 and the optical theorem (Eq. (2.9)) the total cross section for the scattering process with single Regge exchange behaves like

$$\sigma_{\text{tot}} \sim s^{\alpha(0)-1} \tag{2.31}$$

2.1.1 The Pomeron

All known meson Regge trajectories, some of them are plotted in Fig. 2.1a in the representation introduced by Chew and Frautschi, have intercepts $\alpha(0) \leq 0.6$. Thus the total cross section would decrease with higher energy. This contradicts experimental observations (since the beginning of the 60ies) as high-energy scattering data show a flat minimum of the total cross section at $\sqrt{s} \approx 10 - 20$ GeV, as shown in Fig. 2.1b. Thus Gribov introduced a new Regge trajectory with an intercept at one. The new trajectory was named *Pomeron* after his former student and brilliant theoretical physicist Isaac Pomeranchuk, who died in 1966. In contrast to all other meson trajectories there is no known resonance lying on it. Due to the fact that the Pomeron carries vacuum quantum numbers it is considered that realisations of the Pomeron must be glue rich states. A glueball candidate [A$^+$94] which would lie on this trajectory is plotted in Fig. 2.1a. The same plot shows that the Pomeron has a much flatter slope than the other trajectories. From fits on elastic scattering data the Pomeron can be parametrised as follows [SDN02]:

$$\alpha(t) \approx 1 + \epsilon_{\mathbb{P}} + 0.25\,(\text{GeV}/c)^{-2} t \tag{2.32}$$

Where $\epsilon_{\mathbb{P}} \approx 0.06 - 0.08$ is owed to the fact that the total cross section is slowly increasing at higher energy, in ful awareness that this is violating the Froissart-Martin bound (Eq. (2.20)). There is no explanation yet to describe this discrepancy between theoretical prediction and experimental observation. Due to its slope and intercept it is obvious that the Pomeron is the leading trajectory at large s. Its contribution to the total cross section of pion-proton scattering is shown in Fig. 2.1b. For large s the cross sections of $\pi^- p$ and $\pi^+ p$ become equal, following the Pomeranchuk theorem for total cross sections

$$\sigma_{\text{tot}}(ab) \underset{s\to\infty}{\sim} \sigma_{\text{tot}}(\bar{a}b) \tag{2.33}$$

and that the Pomeron contribution is almost one at $\sqrt{s} \approx 100$ GeV. The plot is calculated based on data from [CEG$^+$02]. The important input for the following analysis is the observation, that at COMPASS energies ($\sqrt{s} \approx 19$ GeV) the Pomeron contribution is larger than 95%.

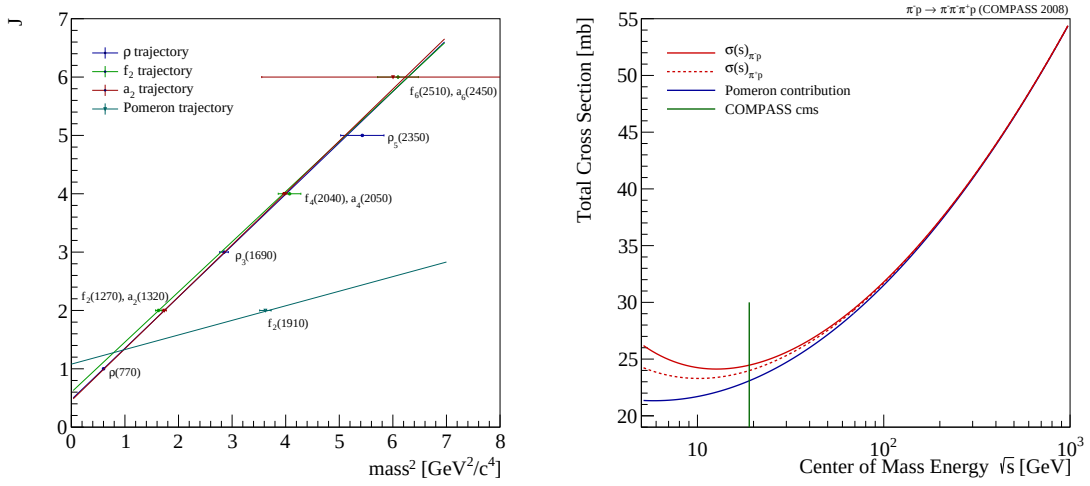

(a) **(b)**

Figure 2.1 Chew-Frautschi plot showing some Regge trajectories and the Pomeron trajectory (a). Comparison of $\pi^- p$ and $\pi^+ p$ elastic cross section with Pomeron contribution (b), plot based on data from [CEG+02].

2.2 Production Mechanisms

In the previous section a description of high-energy scattering processes mediated by the strong interaction was developed in the form of Regge theory. It is now possible to explain the process of interest in this analysis, *single diffractive dissociation* of negatively charged high energetic pions into the $\pi^-\pi^-\pi^+$ final state introduced in Sec. 1.4 within the Regge framework. It will be shown that competing mechanisms lead to the same final state. An understanding of these additional processes can help to disentangle their contribution to the final state and reduce the non-resonant background.

2.2.1 Diffractive Dissociation

A schematic drawing of single-diffractive dissociation is shown in Fig. 2.2. The incoming π^- interacts with the target proton via Regge exchange and gets excited to an intermediate state X^- which finally decays into a final state consisting of three charged pions. 'Single' diffratcion means that, for this case, the target proton stays intact. It was shown before that for the center-of-mass energy available at COMPASS, the leading trajectory is the Pomeron which results in the exchange of momenta and angular momenta but charge and flavour quantum numbers remain unchanged. In this sense diffractive dissociation can be explained as a process where all quantum numbers of the initial state stay intact except spin J and parity P of the intermediate state X^- which can be modified by the Pomeron.
Within the *Triple Regge Limit*

$$s \gg m_{3\pi}^2 \gg t \tag{2.34}$$

which can be regarded as fulfilled for the following analysis[2] with $t \leq 1.0$ GeV/$^2/c^2$, $m_{3\pi}^2 \geq 1.4$ GeV$^2/c^4$ and $s \approx 360$ GeV^2, the scattering amplitude of single-diffractive dissociation behaves

[2]The mass region where three-pion resoances begin to emerge is at 1.2 GeV/c^2

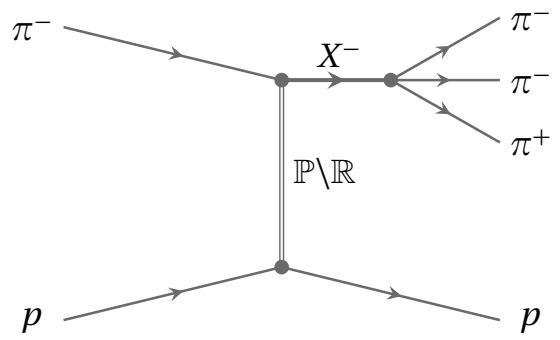

Figure 2.2 Schematic drawing of single-diffractive dissociation of π^- into $\pi^-\pi^-\pi^+$.

as

$$A(s,t) \underset{s\to\infty}{\sim} \sum_i g_{aX}(t) g_{bd}(t) \eta_i \left(\frac{s}{m_{3\pi}^2}\right)^{\alpha_i(t)} \tag{2.35}$$

$m_{3\pi}$ is the invariant mass of the intermediate state X^- and the sum over i denotes that besides the dominant contribution of the Pomeron additional trajectories are contributing to the process. It is clear from Eq. (2.35)that the scattering process depends on the center-of-mass energy s, the squared four-momentum transfer t and the mass $m_{3\pi}$ of the intermediate state. In the following analysis this has to be taken into account as well as the expected t dependence for diffractive processes

$$\frac{d\sigma}{dt} \sim \exp(-bt) \tag{2.36}$$

The relative cross section is exponential with a slope b which depends on the target radius. In this analysis, scattering on a pure proton target, a slope $b \approx 5$ GeV$^{-2}/c^{-2}$ can be expected.

2.2.2 Multi-Regge Exchange

Another exchange mechanism leading to the same final state is *central production* or multi-Regge exchange. For the case of this analysis the process is depicted in Fig. 2.3. The initial state is of course the same but the interaction between pion and proton happens here by the exchanges of two Reggeons. Thus the beam pion gets scattered by the exhange of one Reggeon and the target proton recoils via the exchange of a second Reggeon, therby creating an intermediate state which decays to a two-pion final state. Together with the scattered beam pion three charged pions are leaving the interaction and therefor central production resembles the process of interest.

However, the kinematic signature of this process differs from single diffraction and gives a handle to roughly separate both mechanisms on the level of event selection (see Sec. 5.1.7). The rapidity y (see Eq. (5.12)) of the fast scattered π^- is much larger than the rapidity of the centrally produced two pion system. For the same reason centrally produced systems dominates a mass region which overlaps with the upper limnit of the kinematic regime in the focus of this analysis, $0.5 \leq m_{3\pi} \leq 2.5$ GeV$/c^2$.

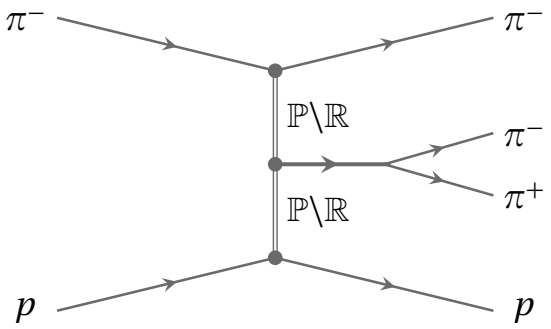

Figure 2.3 Schematic drawing of central production.

2.2.3 Non-Resonant Production - The Deck Effect

Short after the first experimental observation of the $a_1(1260)$ meson in the $\rho\pi S$ channel [GBG$^+$64, CDH$^+$64], an alternative explanation for the peak at the a_1 mass region was proposed [Dec64]. The so-called *Deck-Effect* describes a non-resonant production of the 3π final state. In this model an incident high energetic beam pion dissociates into a 2π resonance (in the original proposal this resonance was the $\rho(770)$ and an almost on-shell pion which scatters quasi-elastically from the proton. Both, the scattered pion and the two-pion resonance are forming the three-pion final state.

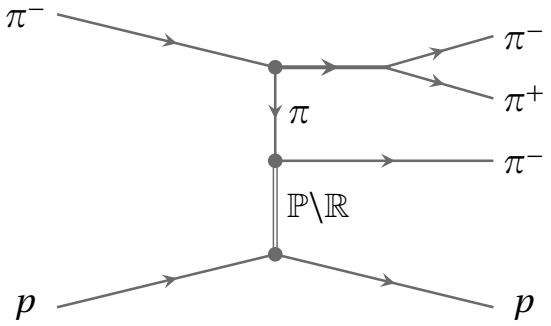

Figure 2.4 Schematic drawing of Deck mechanism (one possible solution is shown).

It is not possible to disentangle this process on the level of the event selection or the spin-parity analysis. Thus the applied method for this analysis is to develop a model of the Deck mechanism, based mainly on the work described in [D$^+$81]. Based on this a Deck Monte Carlo sample can be generated (see Sec. 5.4) and the same spin-parity analysis can be applied as to rhe real data. Thus a rough estimation of Deck-like contribution on the level of partial-waves can beobtained (see Sec. 7.3).

Part II

Instrumentation

Chapter 3

The COMPASS Experiment at CERN

The fixed-target experiment COMPASS is covering with its scientific program a wide range of physics objectives in the high-energy sector. Two collaborations proposed independently in 1996 a new multi-purpose experiment, with almost the same spectrometer setup but different physical goals. The *HMC* [HMC95] experiment proposed a successor of the very successful EMC experiment, whose observation that only a small fraction of the proton spin is carried by the quarks [ea88, ea89] lead to the so-called *EMC-* or *spin-crisis* [LA88]. The main goal of HMC was to determine the gluon polarisation in the nucleon, which was presumed to carry some fraction of the nuclear spin. The *CHEOPS*[ABB95] experiment, on the other side, proposed a third-generation experiment, dealing with open questions in the open charm sector and hadron spectroscopy. The requirements of both experiments, concerning infrastructure, beam facilities and spectrometer technology were almost identical and lead finally to a proposal for a joint experiment, the **Co**mmon **M**uon and **P**roton **A**pparatus for **S**tructure and **S**pectroscopy[BKT96]. Since 2002 the collaboration is taking data with this machine. A detailed and profound discussion about COMPASS concerning its physics program and the spectrometer layout can be found in [ea07] and [colb].

3.1 Science Program

Despite the fact, that COMPASS was initiated by two collaborations with different scientific intentions covering a physics topics, the overall scientific goal is to get a deeper insight into the structure of hadrons and the interplay of quarks and gluons in the region of non-perturbative QCD, i.e. the regime of large values of the strong coupling α_s (see Sec. 1.2). Both programs are presented briefly, further readings are [CER04, COMa]. In addition a complete list of COMPASS publications can be found at [COMb]

3.1.1 Muon Scattering

Observations by the EMC collaboration, later confirmed by other groups, showed that the quark spins only contribute a small fraction to the nucleon spin, which is in contrast to the description of hadrons by the quark model (see Sec. 1.1.1). Today it is assumed that also the gluon spin as well as the parton angular momentum contribute to the overall spin. Deep inelastic scattering with a muon beam offers the possibility to investigate, the longitudinal and

transverse, gluon polarisation, ΔG, which could be a key fragment to explain this riddle. The gluon polarisation is studied directly via photon-gluon fusion or by the indirect measurement of the Q^2 evolution of the spin-dependent structure functions.

3.1.2 Hadron Spectroscopy

Another ansatz to reveal the workings of QCD is the investigation of the hadronic spectrum in the regime of light mesons. COMPASS has the possibility to use hadronic beams of different types to achieve this goal. Different production mechanisms are exploited:

- In central production the production of gluonic states, glueballs, is expected to be enhanced via Pomeron-Pomeron fusion (see Sec. 2.2.2)
- In diffractive dissociation reactions (see Sec. 2.2.1) one may produce spin-exotic meson states and can investigate the light-meson spectrum unprecedented detail and precision (see Sec. 1.4)
- Photoproduction gives the chance to measure the electric and magnetic polarisability of pions and kaons and to learn about their internal dynamics. In addition measurements in the kinematical range of very small momentum transfer, $Q^2 < 1 \cdot 10^{-}3$ (GeV/c)^2 offers the possibility to learn more about chiral dynamics.

3.2 General Layout of the Spectrometer

As a consequence of merging two collaborations the final spectrometer layout has to cope with special requirements, in particular in the target region, of both physics programs. The technical solutions led to an extremely flexible experimental setup which makes COMPASS a real multi-purpose experiment. Both scientific programs demand large angular and momentum acceptance but in addition the capability of particles tracking at very small angles. High luminosity is a must and thus high-rate capabilities of all detectors, the possibility of coping with high trigger rates and the possibility to deal with very big data rates are the basic requirements. The experiment is located at the north area of the CERN complex, using the *M2 beam line*, fed by the SPS accelerator. The spectrometer can be split into three regions. Upstream of the target is the *beam telescope*, measuring the angular inclination of the incoming beam with extreme precision. In order to cope with the required kinematical acceptances, two similar spectrometer parts follow after the target. Right after the target the *large-angle spectrometer* and following the *small-angle spectrometer* for particles with high momenta. Both spectrometers parts are almost equipped identically with high-precision tracking detectors and calorimetry. In addition a Ring Imaging Cherenkov Counter *RICH1* for final-state particle identification of hadrons is installed at the large-angle spectrometer. In the following some components, which are relevant for this analysis, are discussed more in detail.

3.2.1 M2 Beam Line and Hadronic Beam

Primary protons with 400 GeV/c momentum are extracted from the *Super Proton Synchroton* (SPS) and guided to the beryllium production target (T6). By varying the thickness of this target (up to 500 mm), the intensity of the final beam can be modified. The reactions in the target

creates secondary particle, both hadronic and leptonic ones with both charges. Thus several types of beams are possible with this beam line. A positive muon beam is used for the spin physics program of COMPASS and a proton beam is used for observation of central production while a low-energetic and low-intensity electron beam is used for the calibration of the electromagnetic calorimeters. For this analysis a negativly charged hadronic beam with a beam momentum of 190 GeV/c was used. The average beam intensity was $5 \cdot 10^6 s^{-1}$. In order to achieve this intensity $9 \cdot 10^{12}$ primary protons per cycle were extracted, within a time of 9.6 seconds. The used beam consists of pions, kaons and anti-protons, the amount of electrons and muons can be ignored. The ratio of these particle species depends on the thickness of the target (this effects mainly the number of observed anti-protons, as this number decreases with increasing thickness) and the selected momentum of the secondary produced particles. Table 3.1 lists the dominant components for the 500 mm production target [bea, ea80]. The beam line has a length of 1.1 km and is equipped with beam optics for focusing and defocusing as well as bending magnets to sort out particles with wrong momentum. In order to be able to distinguish between different beam particles, two Cherenkov counters (CEDAR) can be installed right in front of the COMPASS target.
It is worth to note that no beam momentum measurement was possible, as the two *beam momentum stations* (BMS) had to be moved out of the beam, due to their big interaction length[1], which would have lead to hadronic showers inside the beam line. A calculation for the beam momentum, applicable to this analysis is presented in Sec. 5.1.5.

Particle	**Fraction at T6 Target**	**Fraction at COMPASS Target**
π^-	0.947	0.968
K^-	0.046	0.028
$\bar{p}$	0.007	0.008

Table 3.1 The main components of the negative hadron beam at the production target T6 and at the target region of COMPASS.

3.2.2 Tracking

In order to cover the required acceptance range a variety of different tracking detectors is installed in the spectrometer. Slow particles which are deflected by the analyzing magnets under large angles can be detected by the large-area tracking (LAT) system. This consists of multiwire proportional chambers (MWPC), straw-tube chambers and drift chambers. These detectors cover the whole geometrical acceptance, with their active areas up to several m^2. While the count rate is low in these regions, in particular for the high-energetic hadron beam, particle rates increases strongly with decreasing distance to the beam axis. High-rate capability and precise tracking is demanded in the vicinity of the beam. This is fulfilled by two types of micropattern gas detectors, both equipped with a strip readout: MicroMegas are placed between the

[1] The *nuclear interaction length* is defined as the mean distance traveled by a hadronic particle before undergoing an inelastic nuclear interaction. For charged leptonic particles one uses the term of *radiation length*, defined as the mean distance over which a high-energy electron loses all but $1/e$ of its energy by bremsstrahlung.

target and the first analysing magnet, while a set of 11 GEM detector stations [Haa04], with 2 detectors each, scattered across the spectrometer after the first analysing magnet. COMPASS was the first experiment where large-sized detectors of these types were used for data taking. Non-interacting beam particles are tracked by scintillating fiber detectors and in addition silicon micro-strip detectors are placed upstream of the target in order to measure the incoming beam particles and downstream for vertexing.

3.2.3 Final-State Particle Identification

Originally two *ring-imaging Cherenkov detectors* were foreseen for the spectrometer. Finally only the detector (RICH1) in the large angle spectrometer was realised, sensitive for hadrons with momenta between 5 and 50 GeV/c. The huge vessel of RICH1, covering the geometrical acceptance of COMPASS, both in horizontal and vertical direction, is filled with the radiator gas C_4F_{10}. The resolution of this detector allows to perform kaon-pion separation at 95% CL (confidence level) up to particle momenta of 45 GeV/c.

Neutral particles are detected with two sets of electromagnetic calorimeters. As this analysis focuses on a final state with only charged particles, a deeper discussion of the calorimeters is omitted here.

3.3 Data Acquisition

The COMPASS Data Acquisition System (*DAQ*) in conjunction with the Detector Control System (*DCS*) is constructed to monitor and control the spectrometer with its more than 250k electronic channels and to collect and handle the resulting data at trigger rates around 30 kHz, a typical value for the hadron data taking campaigns in 2008/2009. With an avergae event size of 40 kB the DAQ has to handle data rates of 1.2 GB/s during a 9.6 s long SPS spill. A global time signal, an unique event ID and the trigger signal is disributed by the COMPASS Trigger Control System (*TCS*). It synchronises the data merger modules, called *CATCH* and *GeSiCA* and connected front-end electronics (*FEE*). The FEE consists of analog readout electronics, located directly on the detector systems and digitizer modules, *ADCs* or *TDCs* close to the readout modules, converting the analog information into digital signals and applying a first-level data processing, e.g. filtering out empty or noisy channels (*zero-suppression*). The digital information is sent to the merger modules and together with additional information provided by the TCS, it is collected by buffer systems, called Local Data Collectors (*LDC*). During the off-spill time of a SPS supercycle (9.6 s on-spill, 32.4s off-spill) the last link of the DAQ chain, the Global Data Collectors (*GDCs*) have to merge the various detector information, buffered by the LDCs, into a common data block that belong to the same event.

3.4 Event Reconstruction and Analysis Framework

The reconstruction software package of COMPASS is called `CORAL` [Gob]. The package consists of algorithms for tracking, vertexing and due to its modular setup it can also process detector information from calorimeters and PID components of the spectrometer. The same software is used for the reconstruction of real data as well as for Monte Carlo simulations. The output

of CORAL is based on the ROOT tree format [ea] and stored in mDST(mini Data Storage Tape) files. These files can be handled most easily with PHAST [Ger], the physics analysis framework of COMPASS. For this analysis this framework was used for a first-level data skimming (see Sec. 5.1.1) in order to reduce the amount of data before processed by the final event selection (see Sec. 5.1.2 - 5.1.8). Important for this analysis is the track reconstruction and the vertexing, as calorimetry was not needed and most other detector information (CEDAR and Proton Recoil Detector) was transferred to the PHAST level as raw information, and thus will be discussed briefly in the following.
The track reconstruction combines the information (hits) of all tracking components with material maps of the spectrometer and detailed descriptions of the various magnetic fields. In a first step the spectrometer zones between the dipole magnets are scanned for straight tracks which are then connected through the magnetic fields or absorber layers with a procedure, called 'bridging'. Even between the dipole magnets the corresponding fringe fields must be taken into account. The track fitting is based on a Kalman filter [WH93]. After the reconstruction of tracks, downstream and upstream of the target it is possible to reconstruct vertices. In CORAL only primary vertices and secondary V^0s are in the focus. The latter are the decay vertices of neutral particles in two charged daughter particles and are not considered in this analysis. The primary vertex is defined by a reconstructed beam track and a multitude of spectrometer tracks. The vertex resolution for the hadron data taking campaigns is much better than the one for the muon setup, which is mostly due to the installation of additional silicon trackers around the target, which will be discussed in the next section. Values for the vertex resolution determined with Monte Carlo simulations for the final state of this analysis can be found in Tab. 5.3.

3.5 Upgrade of the Spectrometer - Key Components

For the hadron data taking campaign of COMPASS during 2008 and 2009 the spectrometer had to be upgraded extensively due to the different event topology in comparison to the spin physics program. Several detectors had to be replaced and new equipment, like an additional electromagnetic calorimeter, were installed. The following discussion concentrates on the description of detectors which were relevant for this analysis. A special place takes the discussion of a new kind of GEM detector, called PixelGEMs, which will be presented in Chap. 4. The development of this detector was part of this thesis. A detailed discussion of the complete spectrometer layout optimized for the hadron run can be found in [colb]. Figure 3.1 shows an isometric view of the spectrometer as it was set up for the hadron campaign.
Besides the installation of three PixelGEM stations along the spectrometer and an additional electromagnetic calorimeter most of the upgrade happened in front of and around the target region. Figure 3.2 shows the liquid hydrogen cell, which acts as a proton target, surrounded by the recoil proton detector (RPD). This main component of the diffractive trigger (DT0) consists of two rings of scintillating slabs around the target, measuring charged particles leaving the hydrogen cell. With the method of time-of-flight and calibrations, protons leaving the target could be disentangled from other particles. These signals were used in the trigger decision. Besides its function as trigger component the RPD information is used to reconstruct the four-momentum of the recoil particle. This information serves as important input for this analysis, in order to clean the data sample from non-exclusive background (see Sec. 5.1.3).

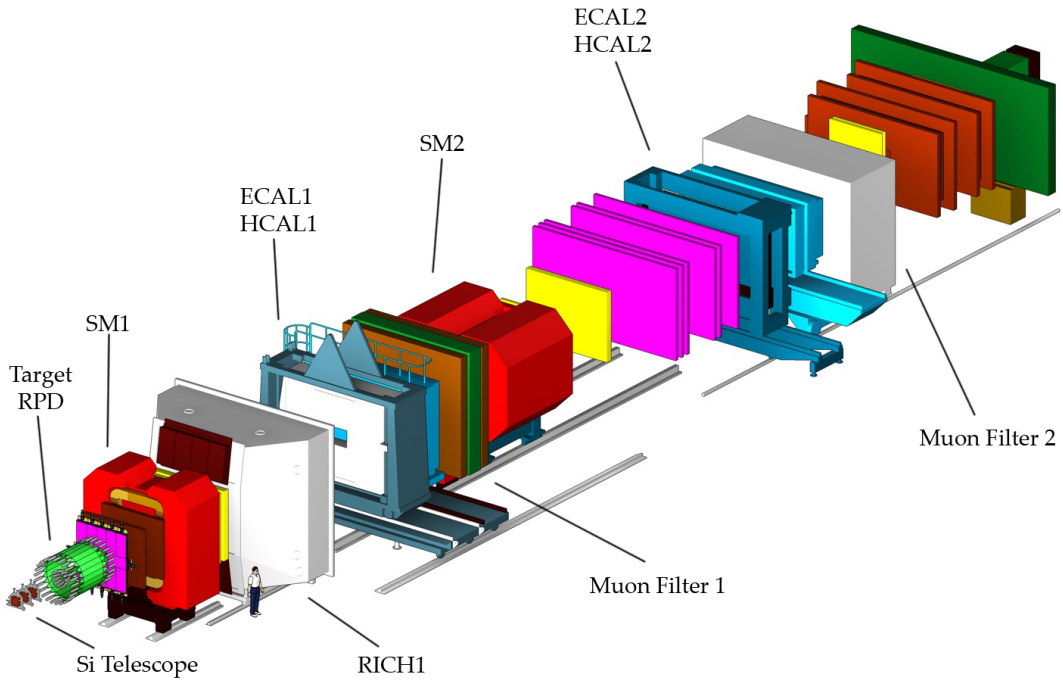

Figure 3.1 Schematic view of the COMPASS spectrometer layout of 2008.

In front of the target three silicon micro-strip stations were placed acting as a beam telescope. Due to their fine spatial and time resolution these detectors were able to measure the beam inclination of each beam particle and the reconstructed beam vector was used as one of the reference axes in the analysis(see Sec. 6.3). Diffractive events, produced with a 190 GeV/c beam have a forward characteristic, which means all resulting particles leaving the target under very small angles. Thus additional two silicon stations were placed right after the target in order to measure the trajectories of charged particles, leaving the target.
The veto system of the spectrometer was equipped with a new sandwich detector, vetoing on particles leaving the target outside of the geometrical acceptance of the spectrometer. In order to identify the different components of the incoming hadron beam two Cherenkov detectors (CEDARs) were installed in front of the spectrometer in the M2 beam line. During the 2008 data taking, these detectors were sensitive to pions and delivered important information for the diffractive trigger.

While the 2008 hadron campaign was mainly focused on data taking with a pion beam, in order to investigate pion diffraction in various final states, the following year was dedicated to several major topics in terms of the COMPASS hadron program, e.g. central production with a proton beam and determination of the pion polarisability using solid state targets. (Forward spectrometers and especially the COMPASS experiment offer the possibility to exchange spectrometer components without affecting the setup at all.) While the spectrometer was unchanged for central production data taking, new solid state targets were installed for the Primakoff campaign. First a segmented target, consisting of 16 discs of lead and tungsten, replaced the liquid hydrogen target inside the RPD (see Fig. 3.3) showing the target holder for the solid-state targets and

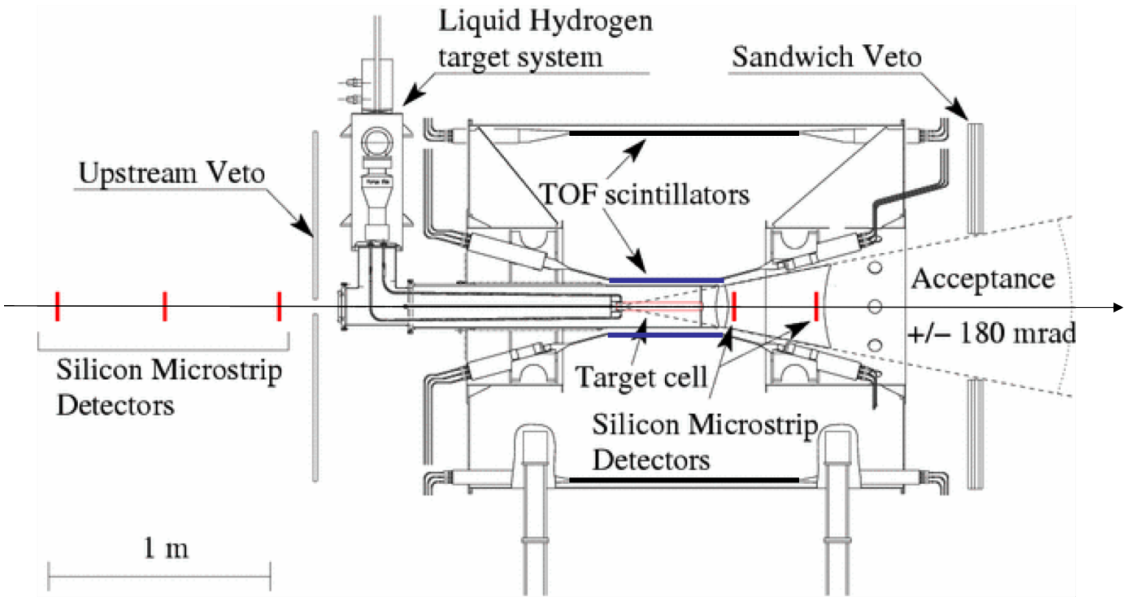

Figure 3.2 Target region of the 2008 layout of the COMPASS spectrometer.

Fig. 5.17a showin the distribution of the reconstructed primary vertices in the target region). In addition to a new target the biggest change of the setup was the installation of a new digital trigger attached to ECAL2. The commissioning of the digital trigger took some weeks but allowed a parallel data taking for charged tracks. Thus the switch over period to the Primakoff campaign was used to obtain a data sample of single diffraction events with a lead target. Analyses based on this sample should be compared with analyses of 2004 data. In order to have access to the whole kinematical range of t, like in 2004, an additional trigger component was installed. This multiplicity trigger[2], consisting of a scintillating disc, 36 mm in diameter and 3 mm thick, read out via photomultiplier tubes and an air guide, was able, in conjunction with the so-called MainzCounter [Wut07], to trigger on events of the low t region. Both trigger components are shown in Fig. 3.4.

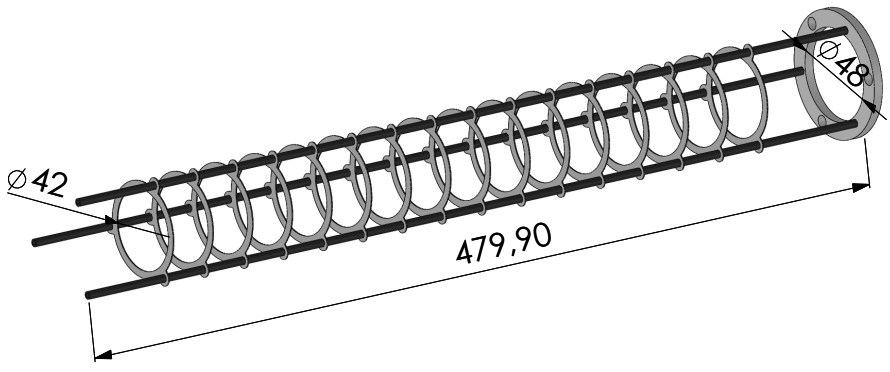

Figure 3.3 Stackholder of the combined lead and tungsten target.

[2]This trigger component was an additional part of this PHD work. But in order to keep this thesis straightforward, it was decided to omit a detailed discussion here.

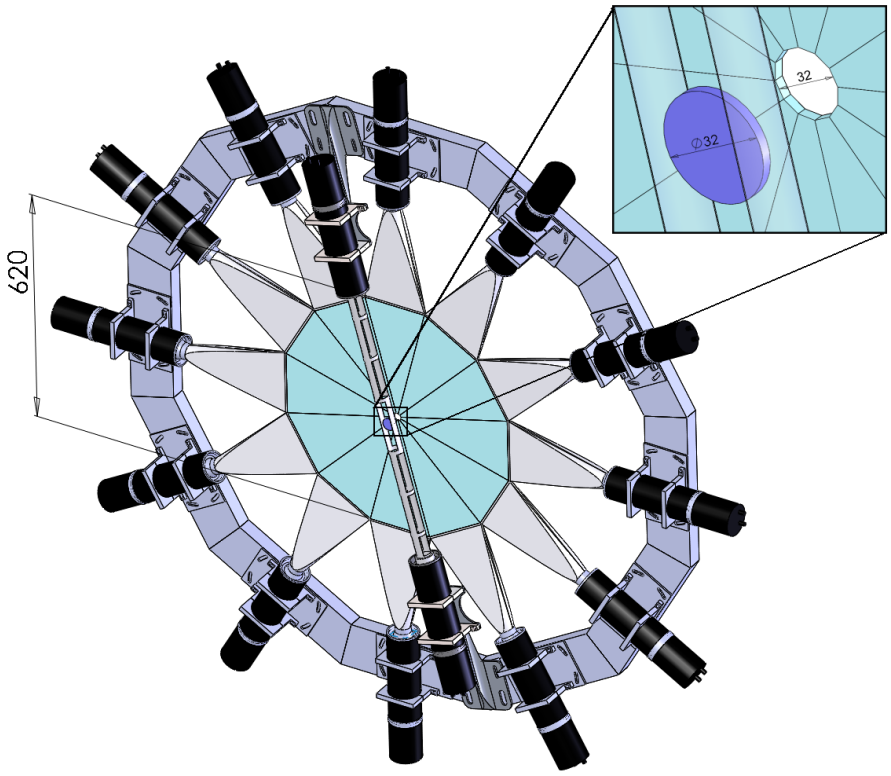

Figure 3.4 Setup of the multiplicity trigger. On top of the large-sized MainzCounter is the additional component, consisting of a scintillating disc placed by an airguide, which triggers on events with small and very small t

Chapter 4

A Gas Electron Multiplier Detector with Pixelised Readout

The first years of data taking at COMPASS, starting from 2002 and ranging to 2007, were dedicated to physics with muon beams. In order to prepare the hadron data taking campaign 2008/2009 a short pilot run with hadronic beams was undertaken during the beam time in 2004. The purpose of this run was to proof the ability of the spectrometer to cope with hadronic beams, and to detect weak points which should be removed while the scheduled spectrometer upgrade (see Sec. 3.5). During this pilot run it was found that the observed trigger rate was much larger than expected. The reason for this could be identified as the large number of secondary interactions downstream of the target. Especially the scintillating fiber (SciFi) stations contributed a lot. In Fig. 4.1 the distribution of secondary vertices downstream of the target region is plotted. Due to the correspondence of the interaction lengths of the detector material with the number of secondary interactions and thus the single detector stations could be identified. The number of secondary particles produced at the positions of detectors are clearly seen. In particular at the SciFi stations the number of secondary interactions is much larger than at the position of gas detectors (like e.g. MicroMegas (MM*), drift chambers (DC*) and GEMs (GEM1)).
SciFis were placed along the spectrometer being part of the very small angle tracker (VSAT) system. Due to their spatial and time resolutions (see Tab. 4.1) these kind of detectors are used to measure the beam and its vicinity. But because of its main detector material, Polystyrene [sci], this kind of detector acts as a big source for hadronic interactions. It was decided to replace at least some of the SciFi stations with another type of detector, similar in performance but with less relative length of interaction length x/λ_I. With their small material budget and spatial resolution (see Tab. 4.1) COMPASS triple GEM detectors [Sim01] seemed to be the best choice. They are the backbone of the small area tracking (SAT) system and showed a stable performance over the years [Wei03]. The fine time resolution of the SciFis allowed to reject non triggered beam events and thus reduced the amount of off-time tracks. The GEMs technology is known to in principle being able to stand the high beam rates expected for the hadron data taking periods in 2008 and 2009 and deliver the required time resolution [RKP+04]. But the two-dimensional strip readout of the COMPASS triple GEM detectors would make tracking impossible in the beam region due to too high occupancy on the strips and resulting ambiguities in the reconstruction of two-dimensional space-points from detector hits. The solution which

was finally found was to construct a GEM detector with pixelised readout for the center region and strip readout in the periphery, based on the experiences with and the concept of COMPASS triple GEMs.

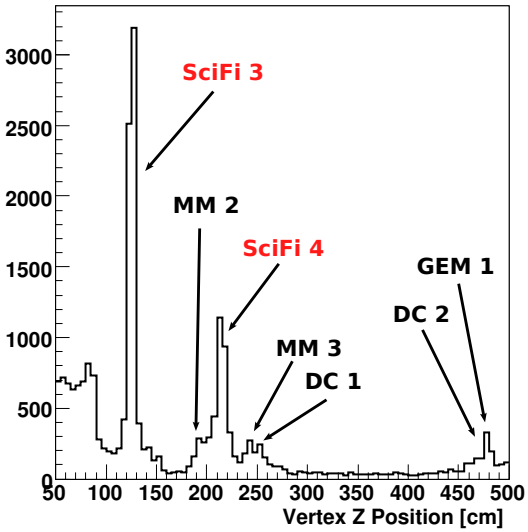

Figure 4.1 Distribution of secondary vertices downstream the target and the corresponding association with detector stations [Krä08].

Detector	x/X_0 **[‰]**	$\mathbf{x}/\lambda_\mathbf{I}$ **[‰]**	$\sigma_\mathbf{s}$ **[μm]**	$\sigma_\mathbf{t}$ **[ns]**
SciFi	16.4 - 27.9	$\sim$ 13 [sci]	130	0.4
Triple GEM (r $<$ 1.5 cm)	3.91	1.01	70	12
Triple GEM periphery	7.09	2.16		

Table 4.1 Key parameters of COMPASS SciFis and triple GEM detectors. All numbers are from [ea07], except other quoted.

4.1 Construction and Setup of a PixelGEM

Before the introduction of a PixelGEM detector it is necessary to explain the basic concept of the gas electron multiplier principal.

4.1.1 The Gaseous Electron Multiplier

In 1968 the introduction of the multi-wire proportional chamber (MWPC) revolutionised particle detectors. Invented and developed by Georges Charpak, Nobel prize laureate in 1992, its basic concept is simple: thin anode wires are stretched between two cathode foils at high voltage in a gas volume. Each wire acts as a proportional counter and amplifies the ionisation tracks, released by charged particles crossing the gas volume. In 1997 Fabio Sauli, inspired by

the work of Anton Oed on Micro-Strip-Gas-Chambers (MSCG) [Oed95], introduced the gaseous electron multiplier (GEM), by turning around the concept of MWPCs. Instead of anode wires, holes, etched in metal coated polyimide foils, are used for amplification in GEM detectors. [Sau04, F. 97]
To be more precise, the concept of a single GEM can be explained as follows: The centerpiece is the GEM foil, a polyimide foil with a thickness of 50 μm and covered by thin (1 μm to 5 μm) layers of copper on both sides. With photo-lithographic techniques holes with a diameter of usually 70 μm are etched into the foil with a hexagonal pattern. The pitch between two holes is in the order of 100 μm which results in $\sim 5 \cdot 10^3$ holes per cm^2. A microscopic view of a part of such a foil is shown in Fig. 4.2a. Placing this foil in a gas volume, consisting of at least a noble gas and an admixture of a quencher gas, between a drift cathode and a readout anode makes a single GEM detector. The gas volume between the surface of the GEM foil and the drift cathode is denoted as drift gap. Electrons resulting from ionisation of Argon atoms by high energetic particles traversing the drift gap[1] are guided to the GEM holes by an electric drift field applied between the cathode and the readout anode. An additional voltage applied between the top and bottom side of the GEM foil creates an electric field of $\sim$ 70 kV/cm [BBR$^+$99] within the holes. It should be noted that each hole acts as an individual region of amplification. The primary electrons, guided by the drift field towards the holes get accelerated and gain the possibility to ionise secondary electrons. Due to the field strength inside the holes several ionisations can take place and an avalanche of secondary electrons emerges from the bottom side of the hole. A Monte Carlo simulation [Van12] of this GEM amplification is shown for two primary electrons in Fig. 4.2b. The two primary electrons (yellow tracks top) enter the hole from the top side, resulting ionisations are denoted by green dots. The electron cloud (yellow tracks bottom) leaving the hole on the bottom side is clearly separated from the positive ions (red tracks) which are guided by the drift lines to the top side of the GEM foil.

The electron cloud emerging from the bottom side of the hole induces a signal on the readout anode. In order to obtain a measurable signal the effective gain of the GEM foil must be in the order of 1000. This can only be achieved by a GEM voltage so high that it would increase the discharge probability of the setup enormously [BBC$^+$02]. This can be circumvented by using a multi-GEM detector, where several foils are placed on top of each other, operated at moderate GEM voltages. For the COMPASS GEM detectors three foils and the drift foil form the GEM stack (see Fig. 4.3). At each amplification stage an effective gain of $\sim$20 is set which results in a total effective gain of a triple GEM detector of $\sim$ 8000, sufficient for the proper detection of a signal.
The principles of gas detectors were introduced in this section without going into detail. A well-grounded and detailed introduction into the operation of gas detectors can be found in [Sau77, Gru93].

One of the biggest advantages of GEM detectors is the fact that the amplification stage is completely decoupled from the readout in terms of construction. Thus the design of the readout structure is independent from the GEM stack. This was utilised in the development of the PixelGEM.

[1] Of course high energetic particles would ionise Argon atoms all over the detector, but due to the direction of the drift field only electrons from the drift gap are guided to the GEM foil

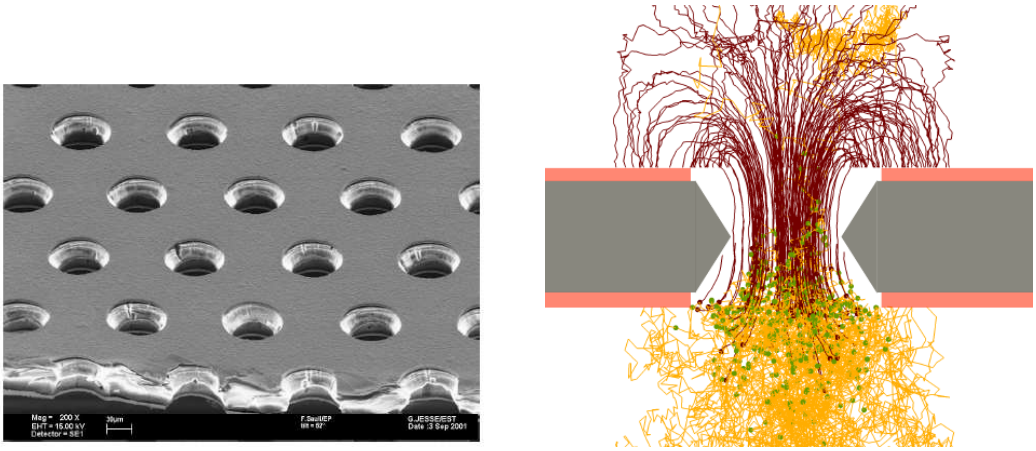

(a) **(b)**

Figure 4.2 Microscopic picture of a GEM foil (a). The copper layer on both sides is visible as well as the double-conical structure of the holes, a wanted side-effect of the etching process. Simulation of a GEM amplification (b) for two primary electrons (yellow tracks on the top side). The ionisation inside the holes is depicted by green dots. The resulting secondary electron avalanche (yellow tracks leaving the bottom side of the hole) are well separated from the positive ions (red tracks).

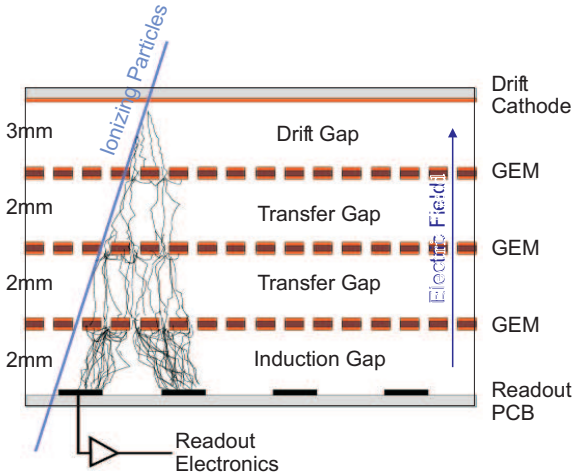

Figure 4.3 Schematic drawing of a triple GEM detector. The distances between the different stages agree with the dimensions used for the COMPASS GEM detectors.

4.1.2 Setup of a PixelGEM Detector for COMPASS

The realisation of the PixelGEM detectors happened in two steps. First a prototype was build, based on the experiences gained with the construction [KAD+02, Sim01, Haa04] and the operation of the COMPASS triple GEM detectors [Wei03, RKP+04]. This detector was implemented into the COMPASS spectrometer at the end of the data taking period of 2006. Placed in front of the beam telescope (see Sec. 3.2.2) various studies of spatial resolution and stability with high-intensity muon and hadron beams were done [Aus07]. Based on these investigations the concept of the detector was improved [Krä08] before the production of seven detectors [Uhl08] as essential part of the upgrade program of COMPASS (see Sec. 3.5). This final setup of the PixelGEM detectors, as they were used at COMPASS during data taking, is described in the following.

It was already mentioned that for GEM detectors the readout can be regarded decoupled from the amplification stage. Hence first the most important component of the PixelGEM, the readout foil, will be introduced. Like the GEM foils, the readout consists of polyimide foils coated with copper on both sides and the desired readout pattern is etched by photo-lithographic techniques. In Fig. 4.4 a photo of a readout foil is shown. Placed on a light table the different structure, explained below, can be seen in the picture. The central part of the readout, placed in the beam, is the 3.2×3.2 cm^2 pixel area. The pitch in this region is 1 mm with a pixel size of 0.95×0.95 mm^2 and thus the whole pixel part is covered by 1024 pixels. This inner part is surrounded by a two-dimensional strip readout, having the same parameters as the readout of the COMPASS triple GEM detectors. The strip readout consist of two layers of copper strips, separated by the insulating polyimide foil, and are read out independently. The pitch for both layers is 394 μm with a width of 80 μm for the top strips and 320μm for the bottom strips. These dimensions were chosen such that an equal charge-sharing for both strip layers can be achieved [Wei03]. The overall strip region has dimensions of 10×10 cm^2. For each direction the copper strips which are not ending at the pixel region are cut half in length in order to achieve that all strips have almost the same length. This results in equal capacitance on the strips and thus an electronic noise uniform for all strip channels [Sch18]. The signals of both parts, pixel and strips, are guided to the periphery of the readout foil out of the vicinity of the beam and region of high intensity where the front-end electronics can be connected.

The GEM stack, placed on top of the readout foil consists of three GEM foils, glued on fiber glass epoxy support structures and a drift foil, glued to a composite support plate, consisting of a papery honeycomb glued between two fiber glass epoxy plates. The whole support structure of the stack seals the gas volume of the detector. The dimension of stack and foils is 30×30 cm^2 although the readout area has only 10×10 cm^2. The reason is to avoid a huge accumulation of detector material in the proximity of the beam. The resulting large amount of hadronic interactions would be more than counterproductive. Although large in size the GEM foils have only an active area of 10×10 cm^2 in the center, thus only in this region GEM holes are etched in the foils. The standard compass parameters for GEMs are applied, i.e. a hole pitch of 140 μm with a hexagonal structure and a hole diameter of 70 μm. The etching process at CERN could be improved and the thickness of the copper layers could be reduced from 5 μm to 1-2 μm. Hence the material budget of a PixelGEM is even smaller than for a COMPASS triple GEM. The top copper side of each GEM foil is segmented in six areas. The active region consists of four segments covering the strip readout and one additional for the pixel area. In case of a discharge of a GEM foil the risk of damage could be minimised as only a relative small amount of charge is released to the bottom side. Each sector is electrically insulated against the others and powered separately by an external resistor chain, soldered on a high-voltage distribution board.

The non-active area of each foil is one large segment. Although there is no amplification, as no GEM holes but only few large holes for gas exchange are placed there, the same GEM voltage, distributed by the high-voltage board, is applied to this sector, in order to achieve a uniformity of electric field lines inside the detector. The GEM voltages applied to the foils are chosen such that a stable operation in a high-intensity environment is warranted, resulting in an effective gain of 6000 for the pixel area and 8000 for the strip readout, which is 4000 per strip layer. The segment of the third GEM foil, placed directly over the pixel readout, is powered independently

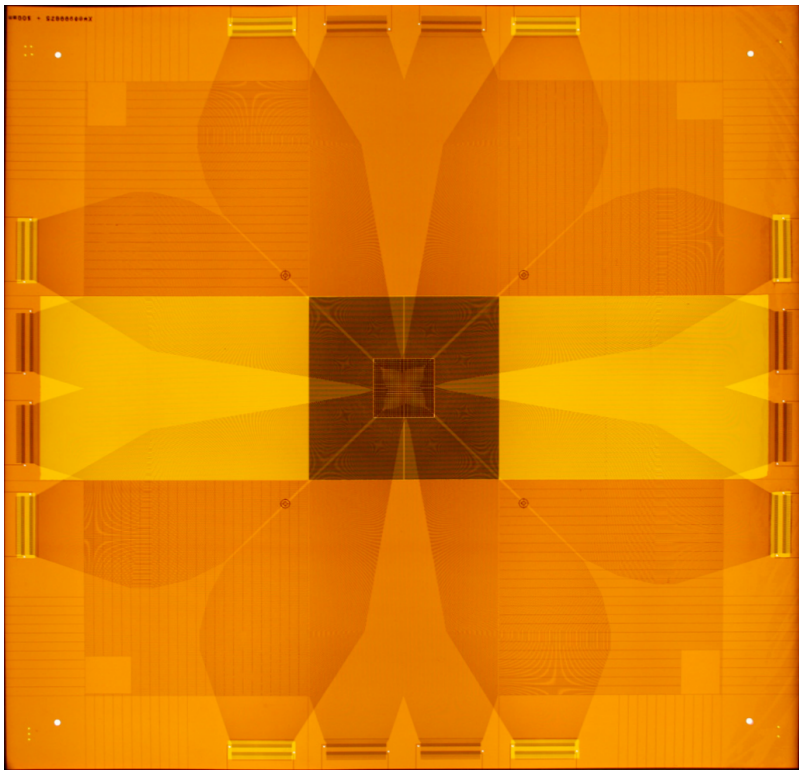

Figure 4.4 Photo of a readout foil for a PixelGEM, placed on a light table. In the center the pixel region is visible surrounded by the strip readout. The copper lines guiding the signals from the readout structures to the periphery can also be seen. A PixelGEM readout foil consists of two polyimide foils with at maximum three layers of copper on top of each other.

from the resistor chain, in order to adopt the effective gain of the pixel area in relation to the beam intensity. Due to the stable beam intensity at COMPASS and calibrations, done for each detector, the voltage needed not to be adapted during the data taking. A detailed description of the detector buildup can be found in [Sch07]. Figure 4.5 shows a commissioned detector, ready for the installation at the COMPASS spectrometer and already equipped with the front-end electronic.

In total 2048 channels have to be read out per PixelGEM by the front-end electronics. Because of the stable operation of COMPASS triple GEMs in regard of the electronic performance it was decided to use an improved front-end electronic system of the same kind. The analog part, including pre-amplification, buffering and multiplexing, is taken care by the APV[2] card. The main component is the APV25-S1 ASIC developed for the CMS tracker [FJM+01, RCF+00]. Each chip can handle 128 detector channels in parallel sampled with 40 MHz.

Its pipeline structure allows to store signals up to 4 μs before the serialised data is sent to the ADC. An important feature of the APV is the possibility to send three consecutive samples in case of a trigger. This allows to apply pulse shape analysis to the data which improves the detector timing and is used for the time reconstruction (see Sec. 4.2). In order to prevent damage

[2]Analog Pipeline Voltage

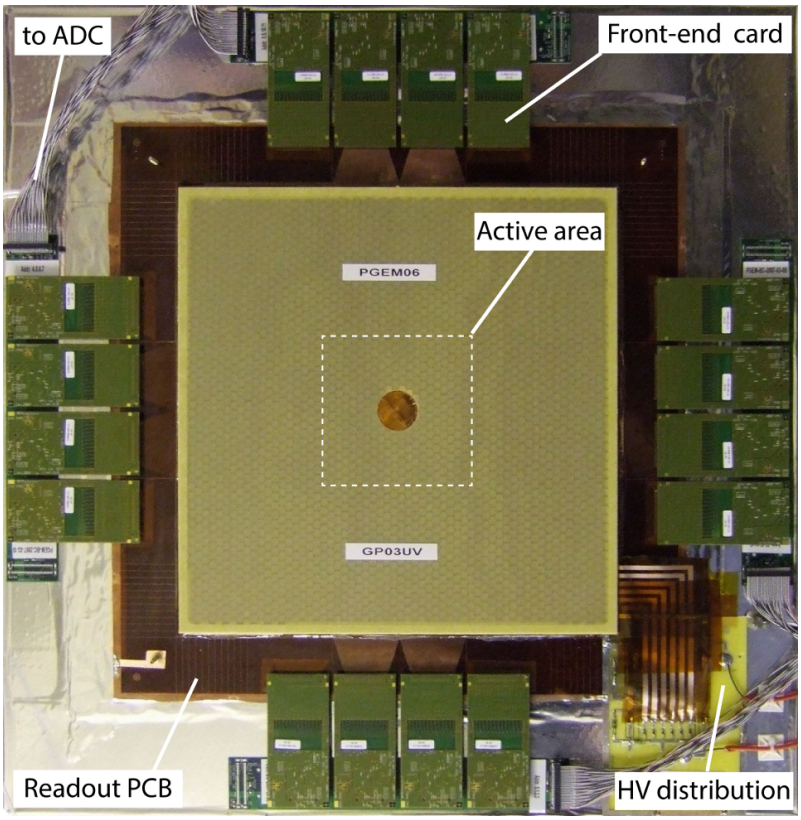

Figure 4.5 Commissioned PixelGEM detector, ready for the installation in the COMPASS spectrometer. At the bottom right corner the high-voltage distribution board is visible. The whole detector is already equipped with 16 APV front-end cards at the periphery of the detector. The composite support plate where the readout foil is glued on is wrapped in aluminised Mylar foil in order to shield the readout structure. In the center of the detector the support plates of the GEM stack as well as of the readout(not visible) have been removed in order to reduce the material placed into the beam.

from the APV, which could come from discharges inside the detector and transferred to the electronics, a diode protection circuit is placed on the APV card between the detector side and the APV (see Fig. 4.6a). In total 16 APV cards are needed to read out one PixelGEM, four cards are connected to one bus card, a passive electronic component, which transmits the analog data to the digitiser stage. The ADC card (see Fig. 4.6b) used for the PixelGEMs is a modified version of the electronics, developed at E18 in Munich and used for digitisation of the multi wire anode part of the RICH1 detector at COMPASS [ADD+06]. Two 10 bit ADC chips can handle the analog data of 16 APVs at once while the on-board FPGA performs on-line zero suppression and common mode correction. The prefiltered and digitised data of several ADC cards is sent to a concentrator module, GeSiCA, before it is transmitted to the Local Data Collectors (see Sec. 3.3). A schematic drawing [Tas11] of the complete PixelGEM DAQ chain can be seen in Fig. 4.7.

For the 2008 data taking period five PixelGEM detectors were installed in the spectrometer. A single detector (GP01) was placed in front of the first analysing magnet (SM1) replacing SciFi4. A set of two detectors (GP02), mounted back to back, was installed in front of the second analysing magnet (SM2) replacing SciFi6. In order to gain redundancy one of the detectors

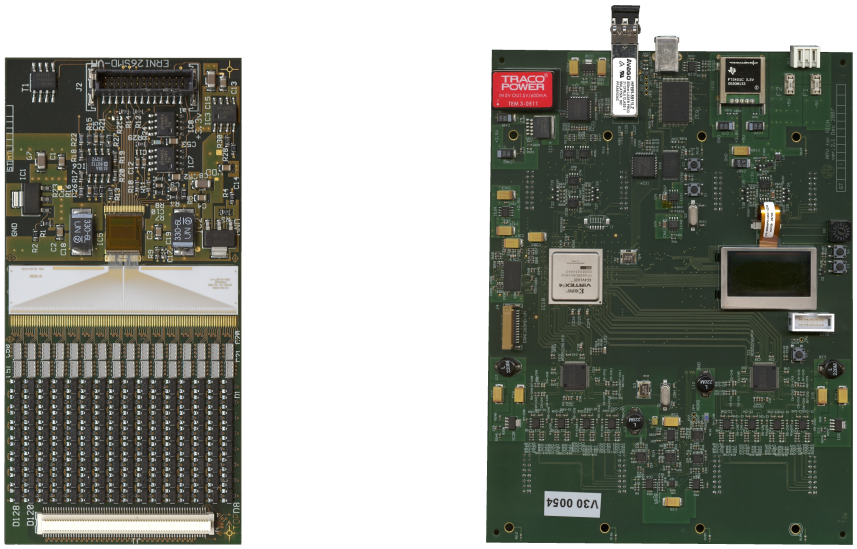

(a) (b)

Figure 4.6 Photo of an APV card as used for the COMPASS PixelGEMs(a). At the bottom the high density connector and the diode protection circuit is visible. In the center the APV25-S1 can be seen, handling the analog data, and on top the black connector which is used as power connector as well as for the transferring of the multiplexed data to the ADC. A modified version of the RICH ADC (b) is used for the digitisation of PixelGEM analog signals. Each card can handle the data of 16 APV cards at once and perform on-line common mode correction and zero-suppression.

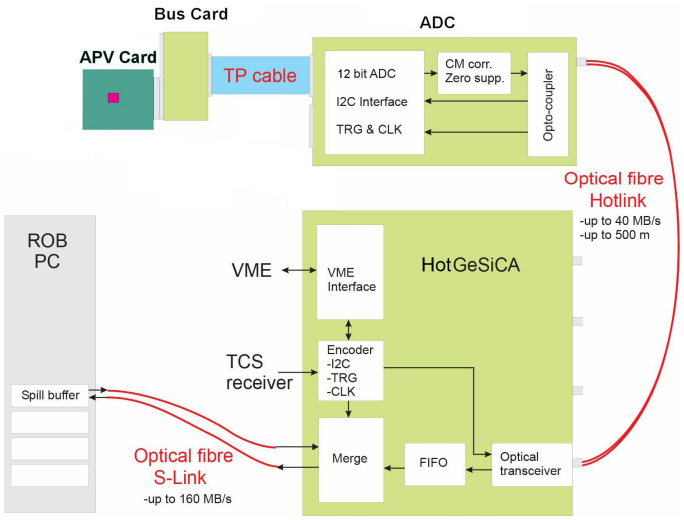

Figure 4.7 Schematic drawing [Tas11] of the complete PixelGEM DAQ chain, starting from the APV readout to the final buffering in the Local Data Collectors (see Sec. 3.3).

of GP02 is rotated by 45° with respect to the other. A third station (GP03) with the same setting was installed right after SM2 at the position of SciFi7. In 2012 GP01 was completed with a second detector.

4.2 Performance

With the gain, on which the PixelGEMs are set during data taking, the size of the electron clouds, emerging from the holes of the third GEM foil and inducing signals on the readout foil, is larger than individual strips and even larger than a single pixel. Hence clusterisation methods can be applied which improves the spatial resolution. For the strip readout with its strip widths and pitch equal to the COMPASS triple GEMs the same cluster algorithm based on a center-of-gravity method [Sim01] is applied. For the pixel region a dedicated cluster algorithm had to be developed [Krä08] due to non-uniformity of the induced charge on the pads. On the level of clusterisation cross-talk suppression algorithms are applied. Besides spatial cross-talk resulting from neighboring signal lines [Krä08] there exists cross talk in time, origin from the multiplexed signals, sent out by the APV and off-time sampling from the ADCs [Uhl08].
The feature of the APV to send three consecutive samples per channel and event allows an offline pulse shape analysis and a precise determination of the cluster time. This reduces the background of off-time clusters enormously and enhances the spatial resolution of the detector. If the detector is well timed in, i.e. the latency of the setup is determined correctly and the front-end electronics is adjusted to it, the three samples are lying on the rising edge of the detector signal, separated in time by 25 ns. In order to be independent from the amplitude height, the first two samples are normalised to the third one. The distribution of the obtained ratios r over the time can be parametrised by

$$r(t) = \frac{r_0}{\exp\left(\frac{t-t_0}{a}\right)+1} \tag{4.1}$$

with the three parameters r_0, t_0 and a (an explanation can be found in [Krä08, Uhl08]) which must be fitted to real data. By the inversion of Eq. (4.1) and respecting the TCS phase shift, i.e. the difference between the creation of a trigger signal and the discrete trigger time, a precise time information can be obtained for each cluster

$$t(r) = t_{\mathrm{TCS}} - \left(t_0 + a \cdot \ln\left(\frac{r_0}{r} - 1\right)\right) \tag{4.2}$$

The such obtained time residual, i.e the difference of cluster time and COMPASS track time, is shown in Fig. 4.8a for the pixel area and in Fig. 4.8b for the strip readout, respectively. Mean time resolutions of 10 ns can be achieved. For the investigation of the spatial resolution the corresponding detector has to be removed from the track reconstruction and the in this way obtained track is compared with the cluster position. The spatial resolution is defined as the difference between the cluster position and the track position. Typical values, after unfolding the track error, are plotted in Fig. 4.9, showing a mean resolution of 125 μm for the pixel part and 65 μm for the strip readout.
Besides time and spatial resolution the detector efficiency ϵ is another important performance parameter. Regarding the fact that these kind of detectors are placed in high intensity environments the problem of uncorrelated background hits must be considered. These hits can create a cluster and be linked with a certain probability b to a non-associated neighboring track. This would increase the efficiency and result in an apparent efficiency ϵ_{app}

$$\epsilon_{\mathrm{app}} = \epsilon + b(1-\epsilon) \tag{4.3}$$

The determination of the background probability is the most crucial point of this kind of analysis. The method used here is best described in [Uhl08].

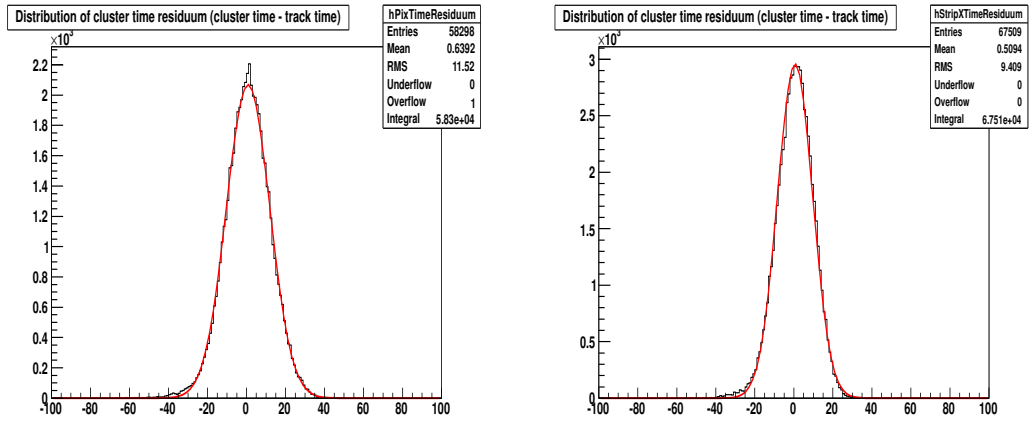

(a) **(b)**

Figure 4.8 Time residuals obtained with physics run 70118 (2008) for GP03XY, plots from [colb].

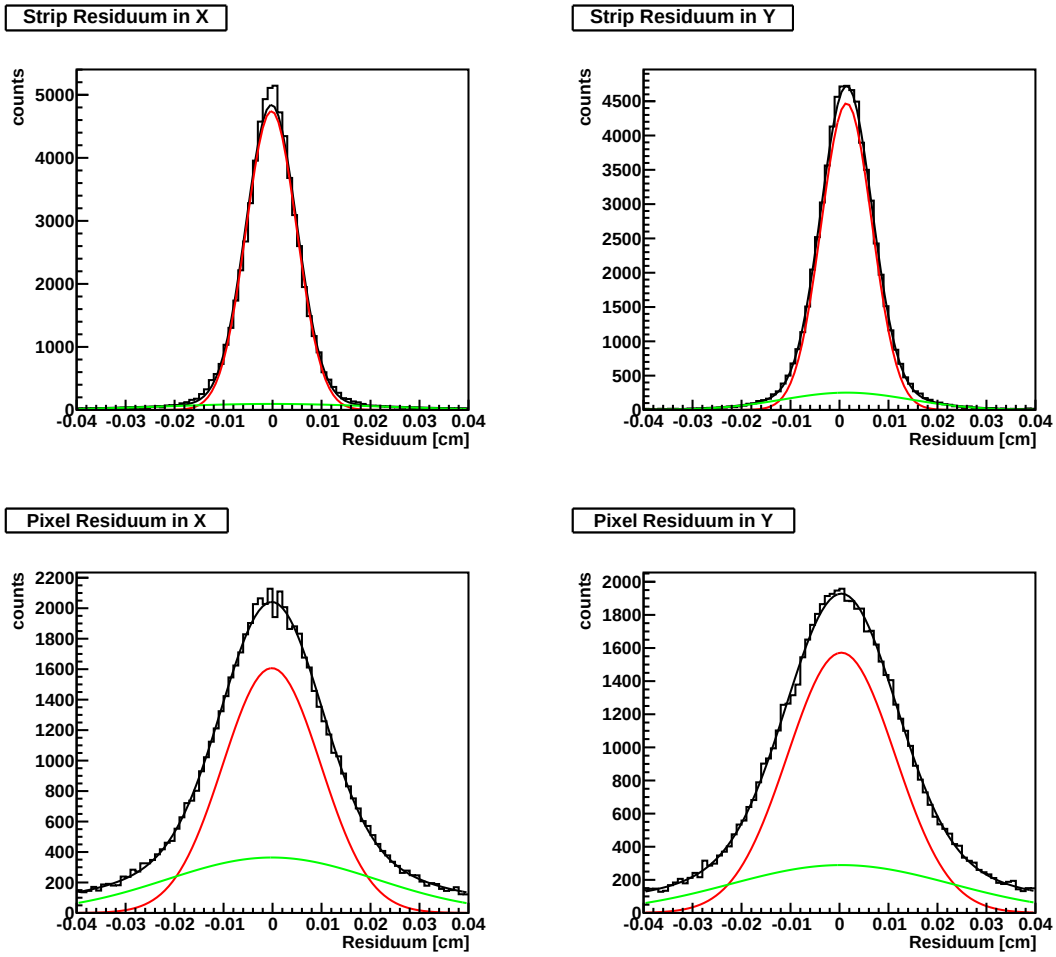

Figure 4.9 Spatial residuals obtained with physics run 70118 (2008) for GP03XY, plots from [Tas11].

With a known background probability the actual efficiency ϵ can be obtained. For the data taking period in 2008 it was found that all background corrected efficiencies of all PixelGEMs have values larger than 97% [Tas11]. In Fig. 4.11 the chronological evolution of the efficiency of GP03XY is plotted, starting from the middle of the 2008 beam time up to the last weeks of the 2010 data taking campain. A clear drop of the efficiency in the center, i.e. the pixel area, is visible at least since the end of the 2009 beam time. Several non-invasive studies (amplitude variation measurement and current measurement) were applied to the GP03XY detector but no new insight was gained by this. Finally it was decided to open the detector and investigate the components. Plots of the investigation are shown in Fig. 4.10. A contamination on the readout foil is visible which is similar to the beam spot, centered during he operation of this detector on the center of the PixelGEM. The distribution seen for the cluster amplitudes (see Fig. 4.12) can be correlated to contaminations on the bottom side of the third GEM foil. One reason for this fast aging of this detector could be a contamination of the inner part of the detector with Dow Corning Conormal Coating, which was used to seal the detector. The outgased products of this coating led to polymerisations on the detector components. A further explanation could be the high intensity of the hadron beam. Still the origin of the fast aging is not known and further studies have to be done. A detailed discussion of this problem can be found in [Tas11].

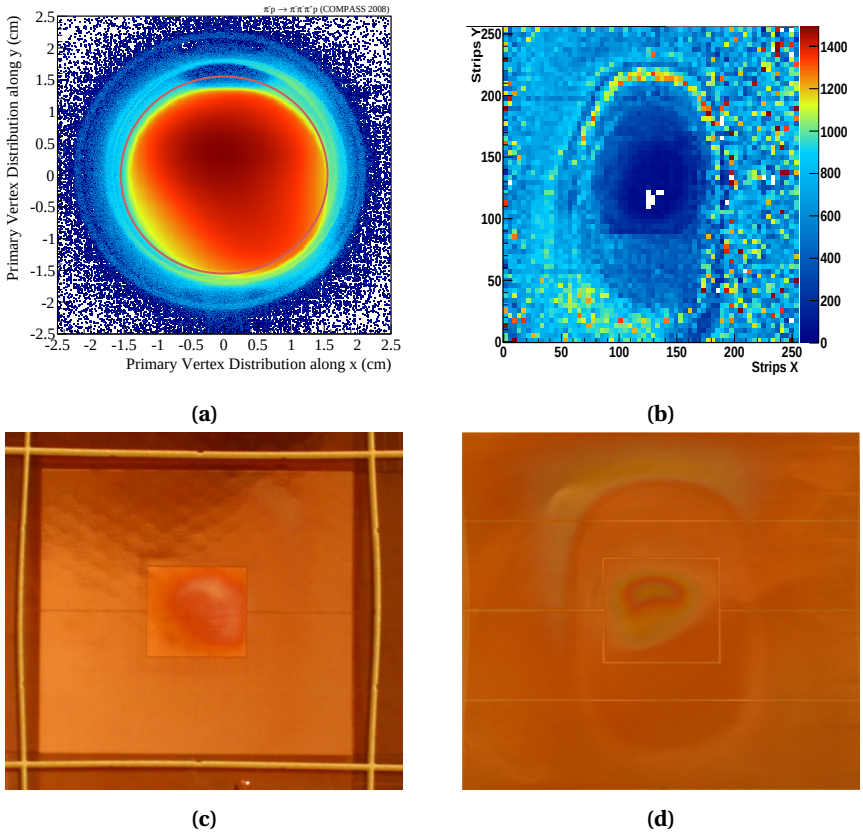

Figure 4.10 The beam shape seen in reconstructed 3π data (a), aging observed on the readout foil of P03XY (c). Cluster amplitude in arbitrary units (b) and aging observed on the bottom side of the third EM foil, both for GP03XY. Plots (b), (c) and (d) from [Tas11].

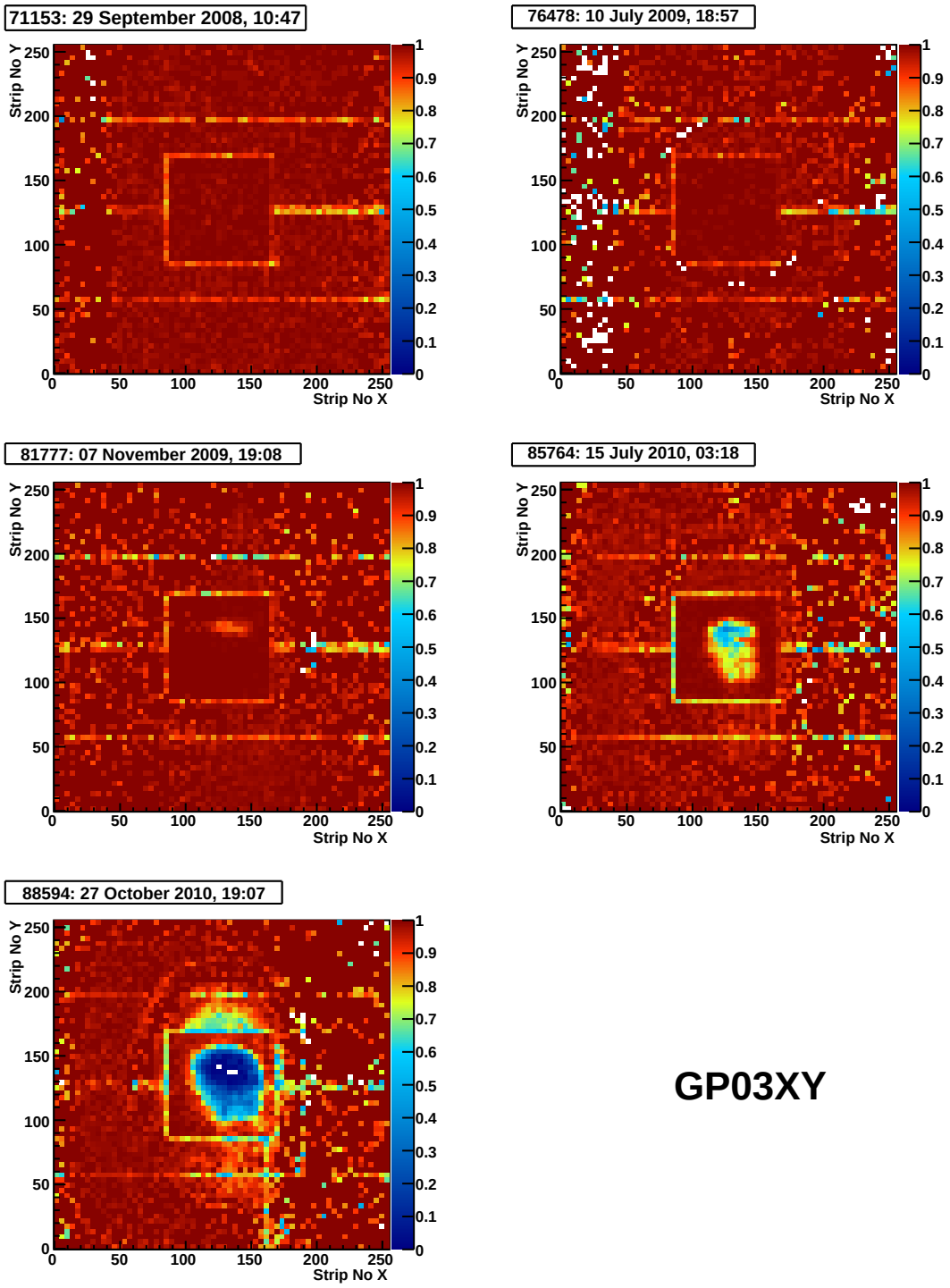

Figure 4.11 Chronological evolution of the efficiency of GP03XY for alignment runs (low intensity) recorded between 2008 and 2010, plots from [Tas11].

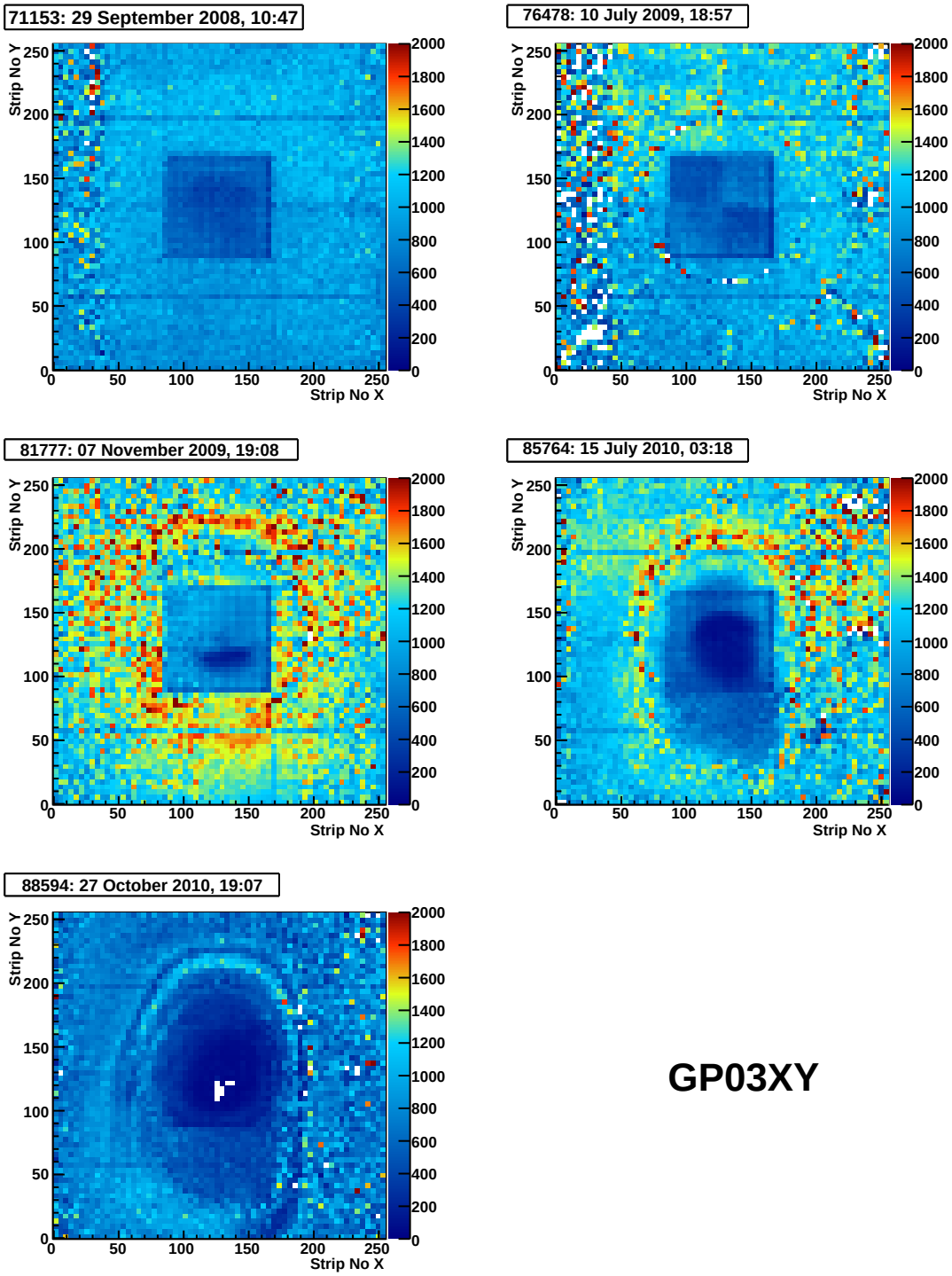

Figure 4.12 Chronological evolution of the cluster amplitudes of GP03XY for alignment runs (low intensity) recorded between 2008 and 2010, plots from [Tas11].

Part III

Analysis

Chapter 5

Kinematic Distributions

The focus of the following chapter lies on the event selection and the associated kinematic distributions of data taken in 2008 and 2009 during the main hadron campaign of COMPASS. The almost 7 weeks long data taking period in 2008 requires an investigation of the stability of this period with respect to beam properties and spectrometer performance. The large amount of data, especially the one collected in 2008, and the wide acceptance of the spectrometer, allows a variety of selection criteria in order to purify the sample. The amount of resulting distributions, necessary to explain the selection, is too large so as to show them all in this chapter. Further plots are presented in App. A. If necessary they will be referred in the following discussion.
In addition the MC simulation, which is crucial for a precise acceptance correction, will be discussed and compared to kinematical distribution of real data. Finally a Monte Carlo generated data sample of a Deck-model amplitude is presented which serves as input for systematic studies on the level of the partial-wave analysis.

5.1 Diffractive Dissociation on a Proton Target (2008 Data)

The process of interest of this analysis is pion diffraction into the three charged pion final state. The event kinematics is depicted in Fig. 5.1a, as it was introduced in Sec. 1.4. Beam pions with a momentum of ~ 190 GeV/c impinging on a proton target, a 40 cm long liquid hydrogen cell, get excited to an intermediate state X^- which decays to the $\pi^-\pi^-\pi^+$ final state. A Pomeron exchange is assumed as production process, which is a good approximation, concerning the center-of-mass energy at COMPASS (see Sec. 2.1.1). The lifetime of resonances, decaying via the strong interaction, is in the range of 10^{-24} s, thus the state X^- decays already in the target and only the decay fragments can be detected in the spectrometer. The recoiling target proton stays intact and leaves the target. The observed event topology, as detected by the spectrometer, is shown in Fig. 5.1b.

5.1.1 Preselection

The data selection is divided into several stages, applying tighter cuts each time, in order to get as clean a sample as possible. The cuts, applied at the first stage of the selection on the level of the `PHAST` framework (see Sec. 3.4), follow almost directly from the event topology. Exactly

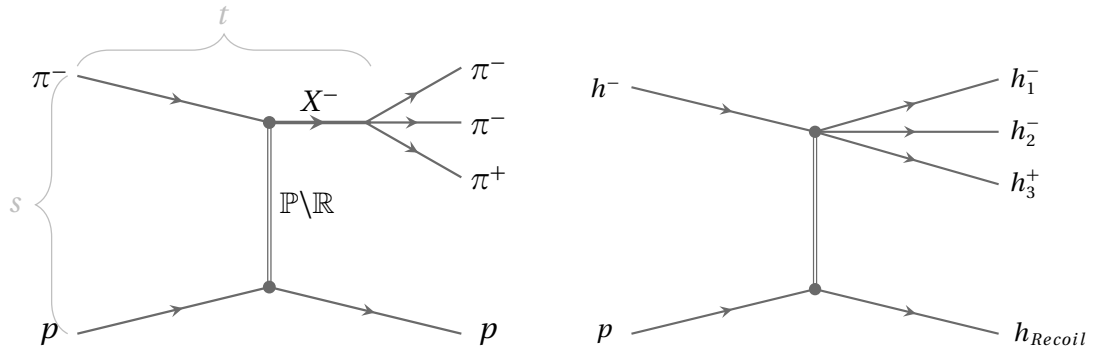

(a) Event Kinematics **(b)** Event Topology

Figure 5.1 Figure (a) shows the event kinematics, describing diffractive dissociation at COMPASS in three charged pions. The actually observed event topology is depicted in Fig. (b). An incoming negative charged beam particle interacts with a target proton and four charged particles leave the primary vertex. Three particles, forming the final state, can be detected with the forward spectrometer, while the recoiling target particle is detected in the Recoil Proton Detector (RPD).

one primary vertex (i.e. a vertex with an incoming beam and outgoing particles, see Sec. 3.4) ±2 m around the target region is required (this wide cut was intended in order to later will be able to investigate the target region). Three fast charged particles, i.e. reconstructed tracks in the spectrometer, are demanded to leave the primary vertex with a net charge sum equal to the negative charge of the beam particle. For each final-state particle, a set of reconstructed track parameters must be available. This preselection reduces the amount of events by a factor of ~ 14.7 while on the other hand it will allow to analyse different production processes with the same data set. For example the contribution of centrally produced systems, introduced in Sec. 2.2.2 can be investigated (see Sec. 5.1.7) as well as the background from processes, where one or more Kaons are involved (see Sec. 5.1.8). The individual selection criteria and their reduction factors are listed in the first part of Tab. 5.2.

5.1.2 Beam Time and Divergence

Unlike collider experiments, which require packets of beam particles (*bunched beam*) in order to increase the luminosity, fixed-target experiments demand a beam of single particles (*de-bunched beam*) entering one after the other the experiment. Additionally a precise time stamp of each beam particle is mandatory. The COMPASS beam telescope, set up with scintillating fibers and three silicon detector stations placed in front of the target, is able to measure time and position of each single beam particle with the required precision. Only a small fraction of the beam particles interacts with the target and fulfill the trigger requirements (see next section). Nevertheless it can happen that within the time window of one event additional beam interactions, not only in the target, take place and are recorded. One possibility to identify this so-called pileup is to investigate the beam time, adjusted with respect to the trigger time stamp. Only events around the trigger time $t_{\text{Trigger}} = 0$ can be regarded as pure events in the sense of consisting of only one triggered target interaction. Figure 5.2 shows the corrected beam time and the applied cut in order to clean the sample.
As previously discussed in Sec. 3.2.1, the hadronic beam for COMPASS is produced close to the SPS and transported via the 1.1 km long M2 beam line to the experiment. There is a certain

probability for beam kaons, to decay within the beam line, and part of the decay pions can arrive at the experiment. Most of them do not have the right energy. Figure 5.2b shows the beam spread, measured by the beam telescope, after all cuts applied and it is clearly visible that no further cut is needed to be applied in order to clean the sample.

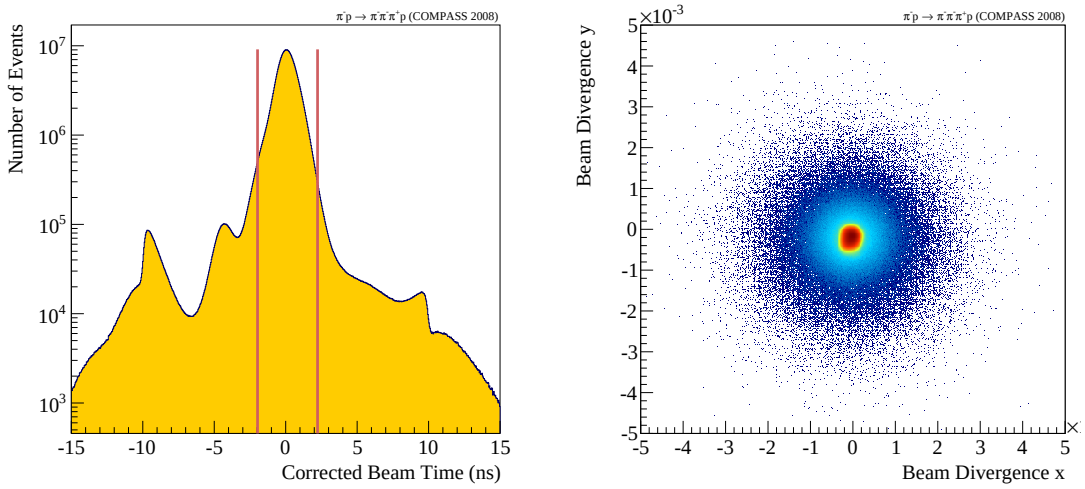

(a) Corrected Beam Time **(b)** Beam Divergence

Figure 5.2 Figure (a) shows the distribution of the corrected beam time (note that the y-axis is logarithmic in order to enhance small effects). Only the pre-selection criteria are applied. The red lines indicate the region of interest. Figure (b) shows the beam spread after all cuts applied (note that the z-axis is logarithmic in order to enhance small effects).

5.1.3 Trigger Condition and Recoil Particle

For the hadron campaigns in 2008 and 2009 a dedicated trigger system for diffractive physics was installed. The *DT0* trigger, used for this analysis, is a combination of three different trigger components, its schematics can be seen in Fig. 5.3:

- The so-called alternative beam trigger (*aBT*), requires a signal in a plane of scintillating fibers (*FI01X*) in coincidence with a hit in the beam counter (*BC01*), a scintillator disc with 30 mm diameter and 3 mm thickness, both located upstream of the target region. This trigger system is able to tag single beam particles.

- A clear signal for diffractive production, i.e. Pomeron exchange, in the t range of interest (see 5.1.6) is a slow charged particle, leaving the target under large angles. If a charged particle traversed both scintillator rings of the RPD (see Sec. 3.5), this trigger condition is fulfilled.

- The last trigger prerequisite is to get no signal from the veto system. It is a coincidence of the beam veto, detecting beam particles with trajectories far from the nominal one. The sandwich detector, right after the target, is sensitive to particles leaving the target area outside of the geometrical acceptance of the spectrometer. In addition two scintillator discs, equivalent to the beam counter, were positioned after the second analyzing magnet (*SM2*) and in front of the second electromagnetic calorimeter (*ECAL2*), in order to detect non-interacting beam particles.

Events tagged by the DT0 trigger can be regarded as good candidates for diffractive dissociation.

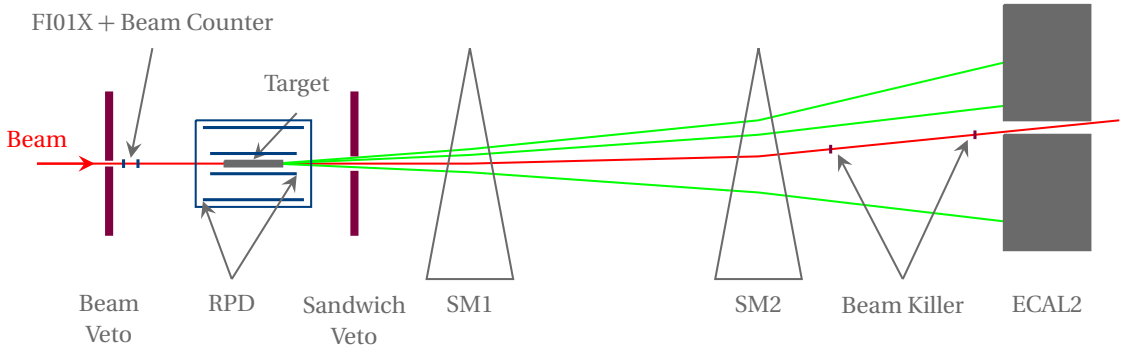

Figure 5.3 Trigger scheme of the DT0 trigger: The main component is the RPD detector (blue), triggering on slow charged particles leaving the target. In addition the alternative beam trigger (blue) is tagging single incoming beam particles. The veto system (violet), consisting of beam veto, sandwich and beam killer, is completing the DT0 trigger system.

The advantage of the RPD is to exploit its detector information on several ways. Besides the possibility to use this system as a trigger component, it is possible to reconstruct the three-vector of each recoil particle. Due to pile-up of RPD signals or bunched beam events (see Sec. 5.1.2), there can be several recoil particles per event. For some events the RPD algorithm also was not able to find any recoil particle. Thus it is required for this analysis, that exactly one recoil particle was detected by the RPD and successfully reconstructed.

5.1.4 Target and Primary Vertex Distributions

Precise tracking and vertexing demands as little material as possible in the path of the particles produced in the target. But the operation of a liquid hydrogen system is technically complicated and requires a lot of supporting infrastructure right around the target cell. Some of these components can be seen in Fig. 5.4a. At z-position -20 cm and -15 cm the two insulating exit windows of the target are visible, while at $z \sim$ -68 cm and $r \sim 1.6$ cm the cooling pipe acts as additional, but unwanted, target material. In addition the planes of the first silicon detector downstream of the target can be seen at $z \sim$ -11 cm. The red lines enclose the region of the target, which is considered for the analysis. The second plot, Fig. 5.4b, shows the vertex distribution transverse to the z-axis. The filling level and the target vessel are visible, additionally to the beam shape. Again the red circle illustrates the accepted target region.

5.1.5 Exclusivity and Co-Planarity

It is obvious that, due to conservation rules, the energy of the final state is equal to that of the initial state. Thus, only events, fulfilling this requirement, are accepted. A caveat of the experimental setup of COMPASS is the fact, that the beam momentum stations (*BMS*), placed along the beam line during the usage of the muon beam, are not suitable for hadron beams, due to their relatively large material budget ($X/X_0 = 1\%$) thus they had to be removed. Aside from the value of the average beam energy ($\sim$ 190 GeV) and the respective energy spread ($\sim$ 1% of the beam energy) [Gat] the exact value of the z-component of the momentum for each

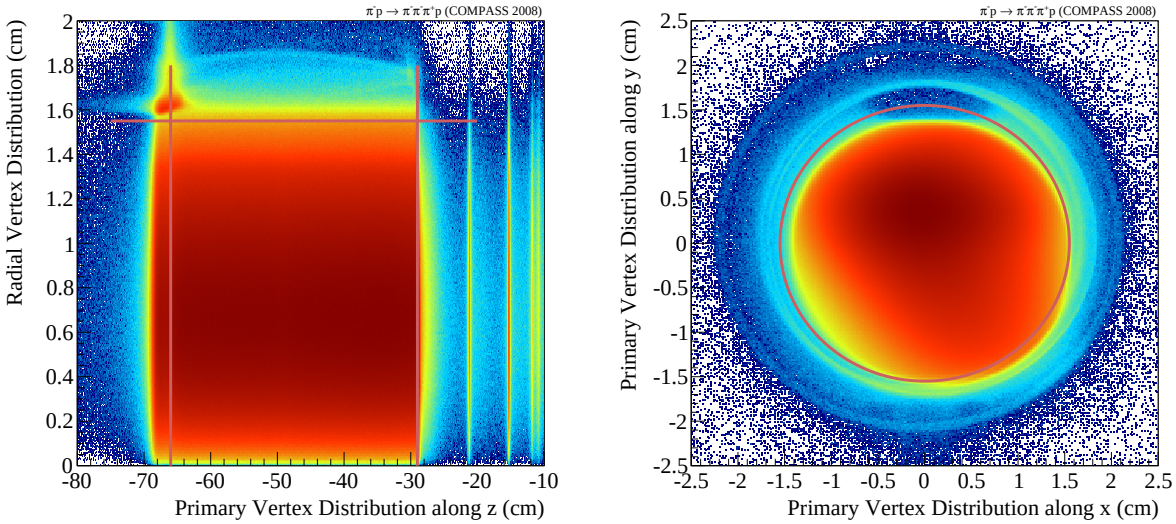

(a) **(b)**

Figure 5.4 Primary vertex distributions: (a) shows the radial vertex distribution along the z-axis in the target region. Target components, e.g. cooling pipes and entry windows, can be clearly seen. In (b) the vertex distribution perpendicular to the z-axis can be seen. In addition to the filling level of the target, the beam shape is visible.

beam particle is unknown. This lack of knowledge can be circumvented by a recalculation of the beam energy (a more detailed discussion can be found in [Wei08]) based on the following assumptions (Referring to Eq. (2.1) the index a corresponds to the beam, b to the target, c to the outoing system X^- and d to the recoil particle):

1. The target mass is equal to the mass of the recoil particle:
   $m_b = m_d = m_p$

2. The mass of the beam particle is much smaller than its energy
   $m_a = m_\pi \ll E_a$

Thus the absolute value of the beam momentum $|\vec{p}_a|$ can be expanded in terms of the beam energy E_a:

$$|\vec{p}_a| = \sqrt{E_a^2 - m_a^2} \approx E_a - \frac{m_a^2}{2E_a} \tag{5.1}$$

Using Eq. (5.1), the squared four-momentum transfer $t = (\hat{p}_a - \hat{p}_c)^2$ can be approximated as follows (with $\hat{p}_c$ being the four-momentum of the intermediate state X^-):

$$t \approx m_a^2 + m_c^2 - 2E_a(E_c - |\vec{p}_c|\cos\vartheta) - m_a^2\frac{|\vec{p}_c|}{E_a}\cos\vartheta \tag{5.2}$$

Recalling the Mandelstam variables (Eq. (2.8)) and using assumption (1), there is an alternative way to write t:

$$t = (\hat{p}_b - \hat{p}_d)^2 = 2m_p(E_c - E_a) \tag{5.3}$$

Equating (5.2) with (5.3) a quadratic equation in E_a is the result:

$$a_0 E_a^2 + a_1 E_a - a_2 = 0 \text{ with:} \tag{5.4}$$
$$a_0 = 2(m_p - E_c + |\vec{p}_c| \cos\vartheta)$$
$$a_1 = m_a^2 + m_c^2 - 2 m_p E_c$$
$$a_2 = |\vec{p}_c| \cos\vartheta$$

This equation can be solved analytically with the standard quadratic formula. The only physical solution is the positive one [Wei08]. The values of the beam energy, calculated with this method, are shown in the open histogram in Fig. 5.6a. A clear peak at 190 GeV is visible, but also a background shoulder reaching from low energies up to 200 GeV can be seen. This shoulder is caused by non-exclusive events, i.e. not all particles of the corresponding final state were taken into account for the energy calculation, for example neutral particles, which can be detected only by the calorimeters. Another explanation is that not all particles of the final state were reconstructed due to inefficiencies of detectors or the reconstruction framework or the particle got lost somewhere in the spectrometer due to hadronic or electromagnetic interactions. In order to remove these non-exclusive events more information about the scattering process must be exploit.
In the center-of-mass system of the reaction, the recoil proton and the intermediate state X^- are leaving the primary vertex back to back. In the lab system this translates into a correlation of the azimuthal angle φ around the beam axis. A cut on the difference $\Delta\varphi$ of the azimuthal angles φ of the outgoing system X^- and the recoil proton can be applied (see Fig. 5.5a). For

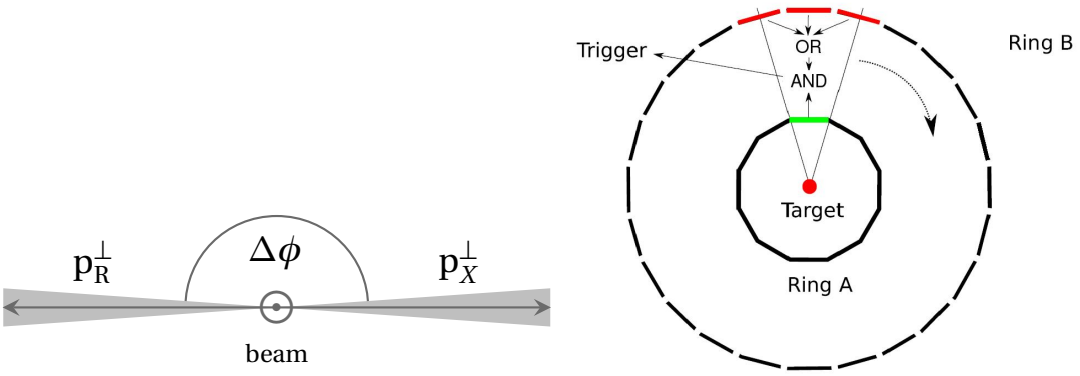

(a) **(b)**

Figure 5.5 The decay kinematics as seen transverse to the beam axis. The RPD trigger scheme based on the segmented scintillator rings.

this analysis no arbitrary value for this cut was chosen, taking into account the geometry of the RPD. At the present status the RPD software can only obtain discrete values of the φ angle of the recoiling particle. For the co-planarity cut, the same method was used:
In order to be detected the recoil particle has to traverse ring A and B of the RPD. Depending on the angle, a particle crossing ring segment A(n) can hit B($2n-1$), B($2n$) or B($2n+1$). If B($2n$) is hit, the particle is assumed to traverse at the center of this slat, leading to a resolution of $\pm 7.5°$, as each segment covers 15° of φ. While hitting B($2n-1$) or B($2n+1$), the resolution is double of it, $\pm 3.75°$. Using the information, whether the particle hit an even or odd slat in ring B, and

measuring the angle φ_X of the outgoing system X^-, one can cut on the co-planarity with respect to the geometrical resolution of the RPD. In addition the modification of the trajectory of the recoil particle by multiple scattering when traversing ring A has to be taken into account. Thus the resolutions are changed to $\pm 8.44°$ and $\pm 5.38°$, respectively. It is important to note, that for the co-planarity cut the azimuthal angles must be calculated with respect to the beam axis.
The effect of the co-planarity cut on the background can be seen in the filled histogram in Fig. 5.6a. The signal-to-background ratio could be enhanced from12.5 (open histogram) to 39.2 (filled histogram). Figure 5.6b shows the region around the exclusivity peak and the applied cut on the beam energy, in order to remove non-exclusive events.

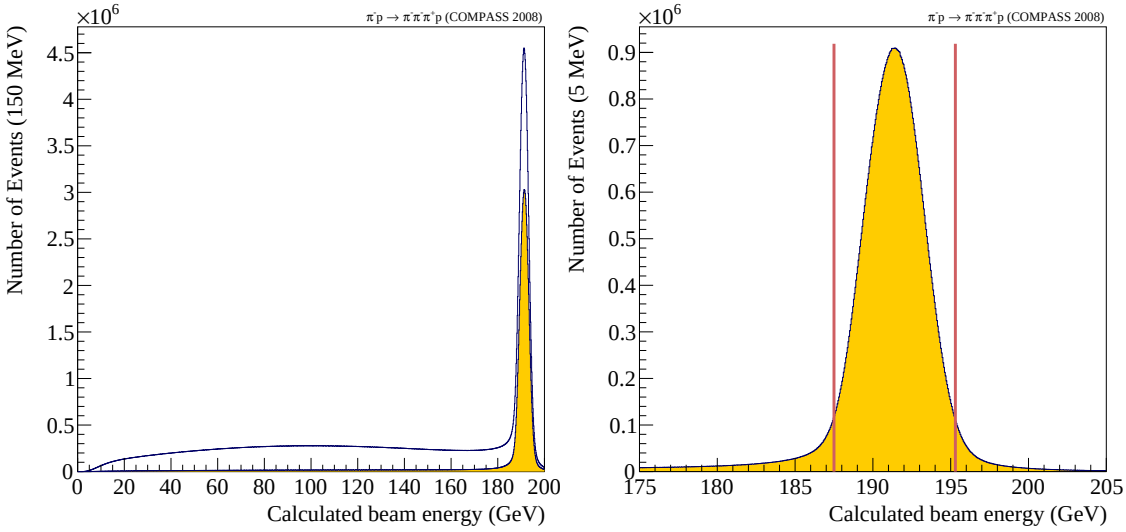

(a) **(b)**

Figure 5.6 Calculated beam energy, based on positive solution of Eq. (5.1.5). The filled histogram in Fig. 5.6a shows the beam energy with the co-planarity cut applied. The red lines in Fig. 5.6b illustrate the accepted range.

5.1.6 Squared Four-Momentum Transfer

As already discussed in Chap. 2, scattering and especially diffraction is described as function of t, the squared four-momentum transfer from the beam particle to the target. With the RPD it would be possible to measure t directly by detecting the recoil particle and reconstructing the three-momentum vector under a proton hypothesis . But in order to avoid systematic effects of the RPD reconstruction, e.g. calibrations needed to reconstruct the recoil particle, and to take into account the more precise tracking of charged particles in the forward spectrometer, another approach was chosen to obtain the value of t.
By definition t is negative in the physical region hence, following the notation introduced in Sec. 5.1.5, t can be written as:

$$\begin{aligned} -t &= -(\hat{p}_a - \hat{p}_c)^2 = -(E_a - E_c)^2 + (\vec{p}_a - \vec{p}_c)^2 \\ &= -(E_a - E_c)^2 + \vec{p}_a^{\,2} + \vec{p}_c^{\,2} - 2|\vec{p}_a||\vec{p}_c|\cos\vartheta \end{aligned} \tag{5.5}$$

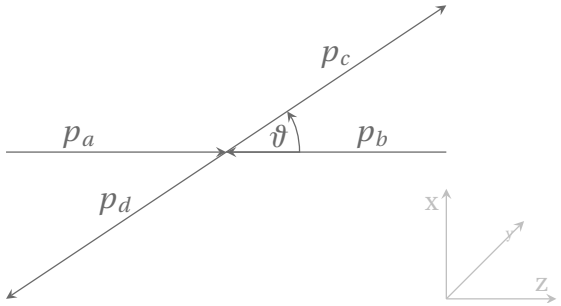

Figure 5.7 Scattering process described in the CMS reference system.

(see Fig. 5.7). In this analysis t is calculated using the four-momentum vectors of the beam and the intermediate state X^-. Taking into account the signature of the diffractive reactions under study — high beam energy, scattering at the target vertex, low momentum transfer to the target — the energy of the outgoing system is in good approximation equal to that of the beam energy

$$E_a \approx E_c, \qquad |\vec{p}_a| \approx E_c - \frac{m_a^2}{2E_c}, \qquad |\vec{p}_c| \approx E_c - \frac{m_c^2}{2E_c} \tag{5.6}$$

The Lorentz-invariant formula in Eq. (5.5) can now be expressed in the laboratory frame

$$-t = (|\vec{p}_a| - |\vec{p}_c|)^2 + 2\vec{p}_a\vec{p}_c(1-\cos\vartheta) \tag{5.7}$$

with ϑ being the scattering angle in the laboratory system. Since ϑ is very small for COMPASS, the following approximation is valid

$$\cos\vartheta \approx 1 - \frac{1}{2}\vartheta^2 \tag{5.8}$$

Finally t can be expressed for the COMPASS case as

$$-t \approx (E_c\vartheta)^2 + \left(\frac{m_c^2 - m_a^2}{2E_c}\right)^2 \tag{5.9}$$

It is obvious that $|t|$ has a minimum value $|t|_{\min}$

$$|t|_{\min} = \left(\frac{m_c^2 - m_a^2}{2E_c}\right)^2 \tag{5.10}$$

This minimal longitudinal momentum transfer is necessary to excite the pion into a higher mass state. Thus the observable of interest is t':

$$t' = |t| - |t|_{\min} \geq 0 \tag{5.11}$$

The resulting t' distribution is depicted in Fig. 5.8a as well as the effect of the co-planarity cut (see Sec. 5.1.5) on this observable. The open histogram shows the t' distribution without this cut. A reduction of the intensity below 0.08 GeV$^2/c^2$, the threshold of the RPD, of two orders of magnitude can be seen in the filled histogram, taking the co-planarity into account. Below the RPD threshold these events can be seen as pileup or noise. Regarding the decrease of the overall intensity by the application of the co-planarity cut leads to the assumption, that an overall

background is diminished.
The cleanest sample for single diffraction, that is reactions where the target stays intact, is expected in a t' region below 1.0 GeV^2/c^2. Above that region other processes start to contribute and it is very well possible, that the target proton gets excited. As a lower bound a cut at 0.1 GeV^2/c^2 is applied, right above the threshold of the RPD acceptance (see Fig. 5.8b, with the kinematical boundaries denoted as red lines.). This t' region was chosen in order to enrich the spin-exotic content in the data sample (further information can be found in Sec 6.3.1).

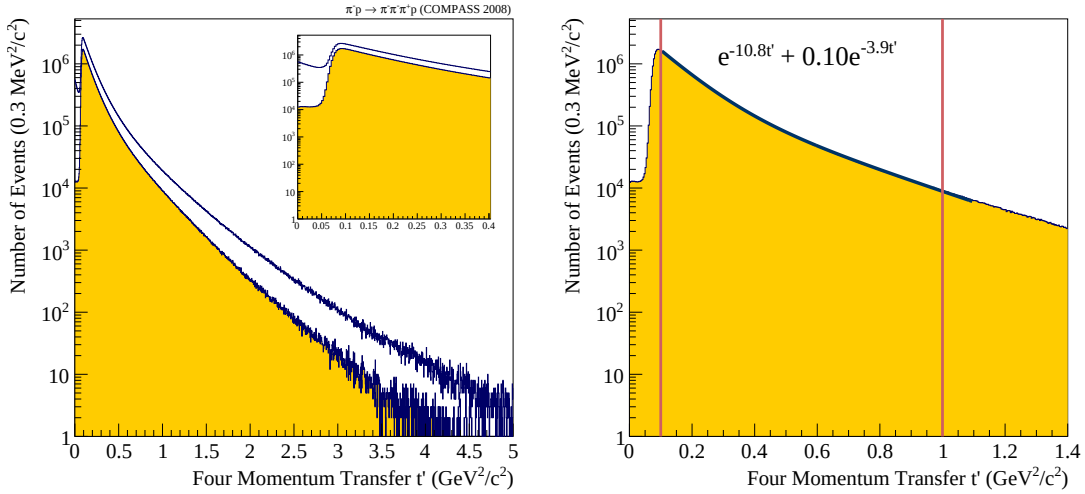

Figure 5.8 Figure (a) shows the t' distribution without (open histogram) and with (filled histogram) coplanar cut applied. The kinematic boundaries of the analysis are depicted in Fig. (b), denoted by red lines. All plots have logarithmic scale.

5.1.7 Background from Multi-Reggeon Processes

Different production mechanisms can contribute to the same final state. In particular for the $\pi^-\pi^-\pi^+p$ final state, there is a non-negligible contribution of centrally produced systems. This Pomeron-Pomeron exchange (see Sec. 2.2.2) is dominating in a mass region above 3 GeV/c^2 and thus above the region of interest. But the low-mass tail reaches down to 1 GeV/c^2. Deck-like production (see Sec 2.2.3) is assumed to peak at $\sim$ 1.5 GeV/c^2, as depicted in Fig. 5.20a, and thus contributes to the mass range under investigation.
Although the final state of these processes cannot be distinguished from diffractively produced systems, the kinematics of the corresponding subsystems differ. For central production a fast negatively charged final-state particle and a slow neutral subsystem is expected. A useful observable for this analysis is the rapidity , defined as:

$$y = \frac{1}{2} \ln \frac{E + p_z}{E - p_z} \tag{5.12}$$

with E and p_z being the energy and z-component of the three-momentum vector of a particle or system.

A second kinematic variable is Feynman's x, approximated in the center-of-mass frame by:

$$x_F \approx \frac{2p_{zcm}}{\sqrt{s}} \tag{5.13}$$

The correlation of the difference of the rapidity of the fast π^- and the rapidity of the $\pi^-\pi^+$ subsystem with the x_F of the fast π^- offers the possibility to tag events most likely produced centrally. The corresponding distribution (See Fig. A.4c) exhibits an accumulation of events with a rapidity gap larger than 4.5 and x_F of the fast pion larger than 0.9. The three-pion invariant mass distribution of these most likely centrally produced events can be seen in the red histogram overlaid to the overall invariant mass in Fig. 5.9a (the single distribution is plotted in Fig. A.4b), while the two-pion subsystem is shown in Fig. 5.9b. Comparing the latter with centrally produced systems discussed in [Aus13] shows a good agreement.

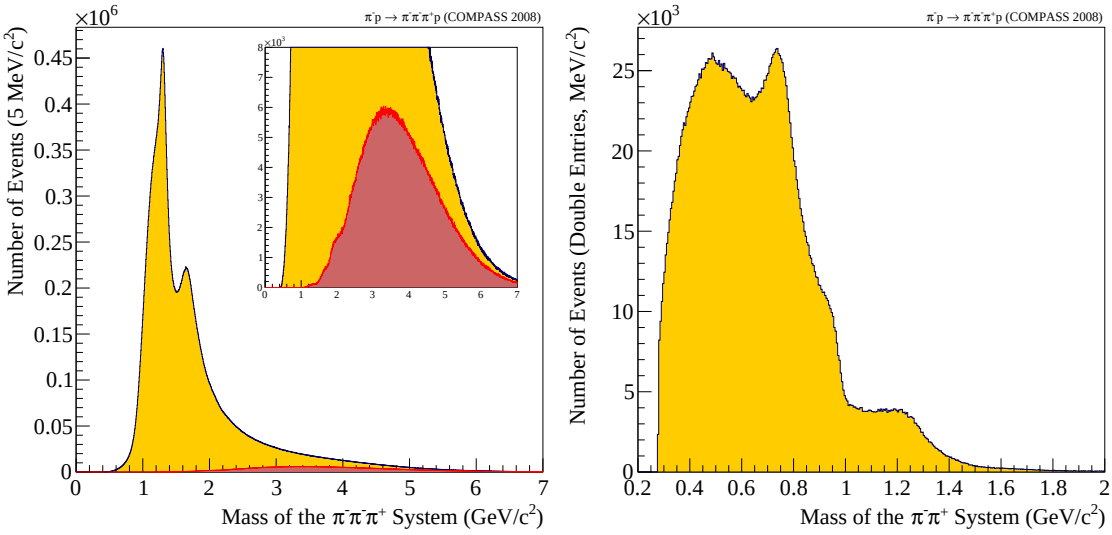

(a) **(b)**

Figure 5.9 Invariant mass distributions of the 3π system overlaid with the assumed centrally produced background (red). The inlay is a zoom in respect to the intensity of the red distribution (a). The $\pi^-\pi^+$ mass distribution associated to the assumed centrally produced background (b).

5.1.8 Background from Beam Kaons and Final-State Kaons

Up to now it was assumed that the three charged particles, detected by the spectrometer, can are pions (pion hypothesis). The validity of this hypothesis and possibilities to identify and remove non-pion particles from the data sample will be discussed. The most likely but still small contamination of the pion data sample is due to kaons. The COMPASS spectrometer offers various possibilities to identify decay particles and thus veto on events with kaons in the final-state.

- **Free kaon decay**: The hadron beam of COMPASS, transported by the M2 beam line (see Sec. 3.2.1) consists of a small contribution of negatively charged Kaons ($\sim$ 2.8%, see Tab. 3.1). With a momentum of $\sim$ 190 GeV/c and a $c\tau = 3.712$ m these particles can be regarded as stable within the spectrometer. Nevertheless there is a small probability

that beam kaons decay on their way through the beam line or the spectrometer (see. Sec 5.1.2). The branching fraction for kaons to decay into three charged pions is 5.59% (See Fig. 5.10a). Kaon decays far up- or donwstream of the target are not of importance, as these decay products will interact with the beam line walls or will be tagged by the veto system or will not traverse enough tracking detectors in order to be reconstructed. But non-interacting beam kaons, decaying close to the target can contribute to the three-pion final state. Normally, due to the applied selection criteria (i.e. primary vertex required, $t' > 0.1$ GeV$^2/c^2$, $m_{3\pi} > 0.5$ GeV$/c^2$) and the small fraction of these events surviving these cuts, this contribution can be ignored. This is illustrated in Fig. 5.10b. Looking at pileup events of the DT0 trigger and omiting the cuts on t' and $m_{3\pi}$ gives ~ 3000 reconstructed kaon 3π decays for the complete 2008 data set. Beam particle identification with the two CEDAR detectors (see Sec. 3.2.1) is an additional but not neccessary tool to minimize this contribution.

- **Diffractive kaon dissociation**: In the same way as pions, beam kaons can interact with target protons via Pomeron/Reggeon exchange with an intermediate negatively charged state decaying into three charged particles. The most likely final state for this reaction is $K^-\pi^-\pi^+$ (see Fig. 5.10c). Unlike for the free kaon decay, the beam particle identification helps to tag these events. In addition final-state particle identification can be performed using the RICH1 detector (see Sec.3.2.3). However, the RICH is only sensitive up to particle momenta of 50 GeV$/c$ (see Fig. 5.10f) while the kinematic range of the final-state particles reaches up to 190 GeV$/c$ (see Fig. A.3a). Nevertheless using the RICH information as a veto, i.e. vetoing only events where at least one of the two negative particles can be identified unambiguously as kaon, electron or background, does not modifiy heavily the phase-space distribution of the final state and the acceptance of this detecor does not need to be considered for performance studies (see Sec. 5.3). The invariant mass distribution of these tagged events can be seen in Fig. 5.10d, which is subtracted from the final data sample.

- **Kaon pair production**: It is an experimental fact that n-particle systems subsequently decay into a single particle and a (n-1)-particle subsytem (see Sec. 6.2). Applied to pion diffraction with a three-particle final-state (see Fig. 5.10e) and considering the two-pion subsystem invarinat mass distribution (see Fig. 5.11b) the most probable intermediate two-pion state above the $K\bar{K}$-threshold is the $f_2(1270)$ resonance (a detailed explanation about possible two-pion subsystems can be found in Sec. 6.5). The $f_2(1270)$ meson has a 4.5% branching fraction into a $K\bar{K}$ pair in comparison to 84.8 % probability into two pions [B$^+$12]. Other suitable subsystems like the $f_(980)$ or the $f_0(1500)$ have a larger probability for a kaon decay but their contribution to the overall two pion distribution is negligible. The easiest way to identify these events is to identify the positive particle as a kaon. Figure 5.10f shows the Cerenkov angle of the positive particle versus the z-component of its three-momentum. The vertical band close to zero momentum can be identified as noise, the dominant structure, starting almost at zero momentum is the pion band, followed by the kaon band, emerging at 10 GeV$/c$.

Summarising the combination of kinematical selection criteria and detector components of the COMPASS PID system (CEDAR, RICH) can help to reduce the kaonic background in the final data sample. Thus events, where the beam particle or one of the three decay particles are identified unambiguously as kaons are cut away in the event selection.

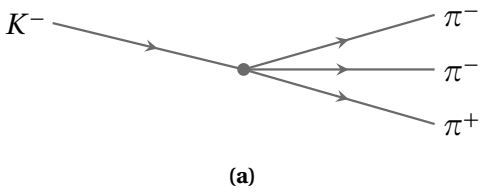

(a)

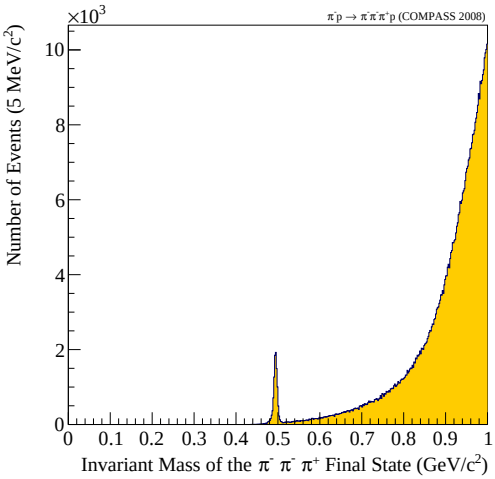

(b)

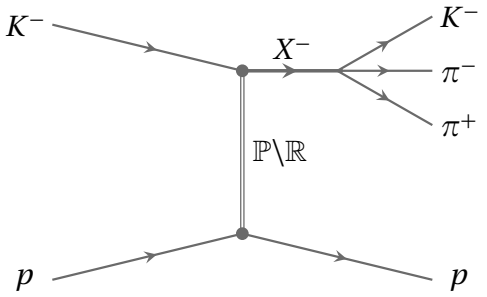

(c)

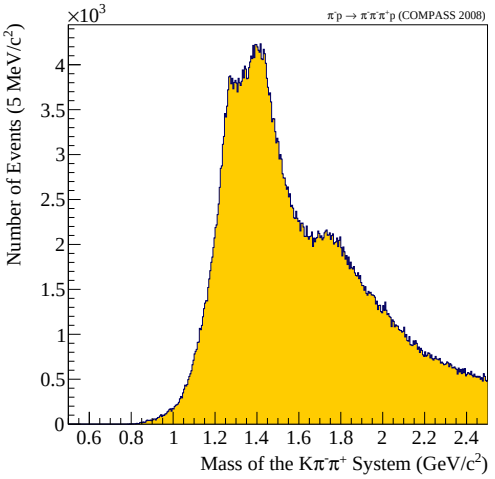

(d)

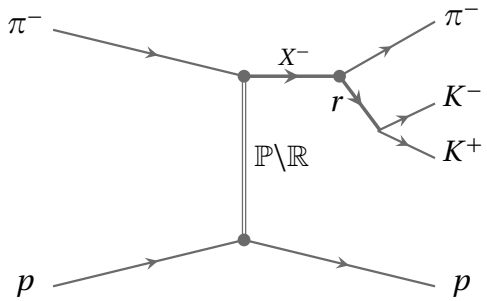

(e)

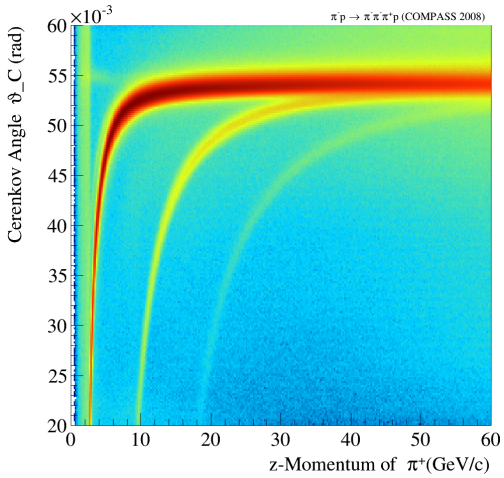

(f)

Figure 5.10 Overview of kaonic contributions. The contribution of the free kaon decay (a) is depicted in (b). The $K^-\pi^-\pi^+$ distribution (d) from K^- diffraction (c) is shown and the isobar decaying into kaon pairs (d) and its identification by the RICH (f).

5.1.9 Kinematic Distributions after Selection Cuts

Finally the data set is limited to the 3π mass range between 0.5 and 2.5 GeV/c^2 like in previous analyses. While the latter were limited in their statistics this data sample allows to increase the upper range. The aim is to analyse a known kinematic range with unpredecedented precision. Up to now the lightest 3π resonance is observed at ∼1.2 GeV/c^2. For a good understanding and parametrisation of the 3π non-resonant contribution, which is of importantance for the extraction of resonance parameters (see Sec. 8) the lower bound of the mass rane was chosen to be 0.5 GeV/c^2, far below the resonance region and close to the 3π threshold at ∼ 0.418 GeV/c^2. The three-pion invariant mass after all cuts is shown in Fig. 5.11a. Several structures are visible. A well pronounced peak at 1.3 GeV/c^2 can be attributed mostly to the $a_2(1320)$ resonance. A second peak at 1.7 GeV/c^2 can be identified as the contribution of the $\pi_2(1670)$. The shoulder at 1.2 GeV/c^2 is due to the $a_1(1260)$ meson. The corresponding $m_{\pi^+\pi^-}$ spectrum is plotted at Fig. 5.11b. Due to the indistinguishability of the two negative pions both possible combinations have are considered. Structures at 0.7 and 1.3 GeV/c^2 can be associated with the $\rho(770)$ and $f_2(1270)$ resonances, the two dominant mesons in the 3π decay. A shoulder at 1 GeV/c^2 reveals a non-negligible contribution of the $f_0(980)$. The small bump at 1.7 GeV/c^2 could be due to the $\rho(1700)$ or $\rho_3(1630)$ resonances.

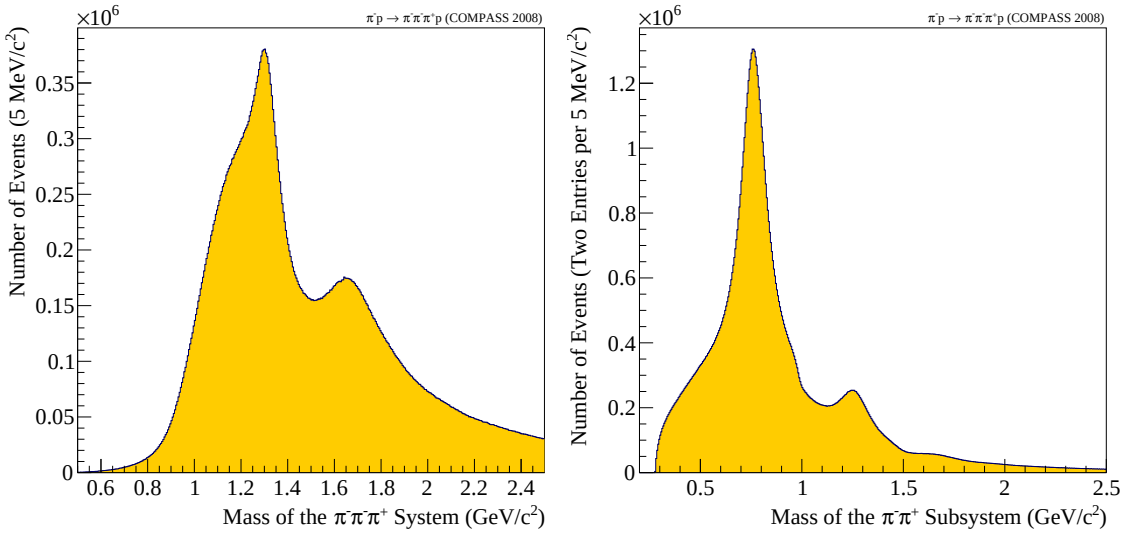

Figure 5.11 (a) shows the 3π invariant mass distribution after all kinematic cuts and within the mass range of interest. The corresponding two-pion invariant mass distribution is plotted in (b).

In order to illustarte the size of the data sample two Dalitz plots are shown. In Fig. 5.12a the squared invariant masses of the two $\pi^-\pi^+$ combinations are ploted in a 100 MeV/c^2 wide mass window around the $a_2(1320)$ at 1.32 GeV/c^2. The bands at 0.6 GeV^2/c^4 correspond to the $\rho(770)$ resonance, contributing most to the decays in this 3π mass region. The second distribution ±100 MeV/c^2 around the $\pi_2(1670)$ mass reveals several $\pi^-\pi^+$ contributions. Again a $\rho(770)$ band at 0.6 GeV^2/c^4 is visible in addition a second one at 1.6 GeV^2/c^4, attributed to the $f_2(1270)$ meson. The sharp lines at 1.0 GeV^2/c^4 can be associated to the $f_0(980)$ resonance.

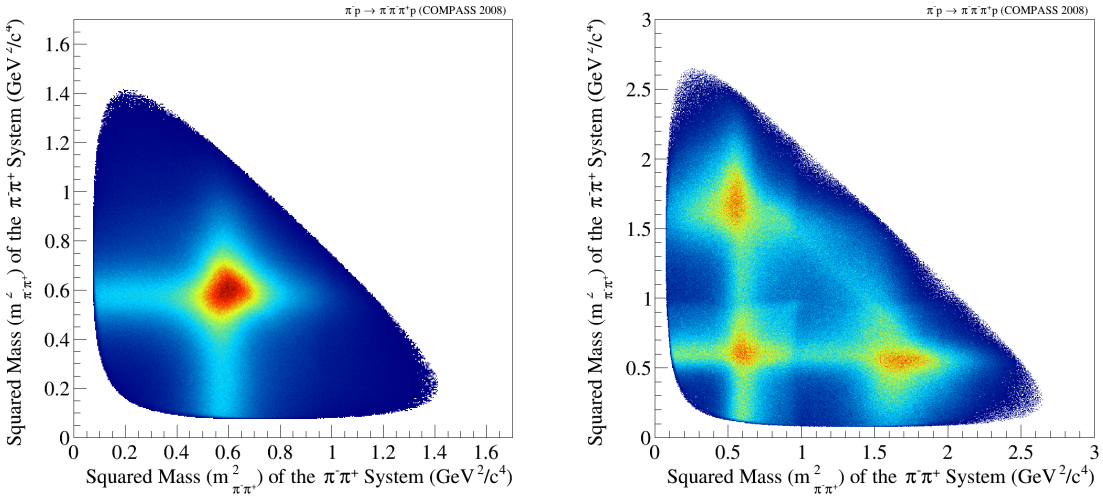

Figure 5.12 Dalitz plots for selected 3π mass ranges. Figure (a) shows a Dalitz plot for the mass region around the $a_2(1320)$, while Fig.(b) shows the distribution in the $\pi_2(1670)$ mass range.

5.1.10 Correlations Between the Squared Four-Momentum Transfer t' and the Invariant Mass $m_{3\pi}$

A description of diffractive dissociation within the Regge formalism was introduced in Sec. 2.2. It was shown that t' and $m_{3\pi}$ are parameters characterising this production process. Additionally these two kinematic variables are correltaed with each other.
Figures 5.13a and 5.13b show invariant mass distribution of the 3π system in certain ranes of t'. The observed mass spectrum at low t', between 0.1 and 0.115 GeV$^2/c^2$ is depicted in Fig. 5.13a. In comparison to the mass spectrum integrated over the whole t' region (Fig. 5.11a), the 'a_1 shoulder' at 1.2 GeV/c^2 and the a_2 peak at 1.3 GeV/c^2 are merged into a single structure. (Resonance parameters are independent of t', only the corresponding production strength, i.e. the resulting intensity, can depend on t'. Therefore only the ratio between the two peaks has changed). The peak at 1.6 GeV/c^2 is well pronounced, as observed in the overall mass distribution. The second plot, Fig. 5.13b, shows the the 3π invariant mass distribution in a region of larger t', $0.443 \leq t' \leq 1.0$ GeV$^2/c^2$. There the a_2 peak but the lower lying 'a_1 shoulder' seems to be vanished. The 'π_2 peak' is as pronounced as in the previous distribution, thus the relative t' dependence seems to be not as strong as in the a_1/a_2 region (Both t' ranges were selected such that the overall number of events is almost the same). The t' dependence of the various components in the spectrum has to be taken into account in for the following amplitude analysis.

This study can be done the other way round: investigating the t' dependence in different $m_{3\pi}$ ranges. Figure 5.14a shows the t' distribution in the 3π mass region around $m_{3\pi} \sim 0.8$ GeV/c^2, far below the resonances. The spectrum was fitted with two exponentials which describe the steep drop-off in the first part followed by a relatively flat second slope. Comparing this distribution with the one observed around $m_{3\pi} \sim 1.6$ GeV/c^2 shows a smoother slope in the latter. Still two exponentials are needed to fit the overall shape but the two slopes do not differ as much as in the first plot.

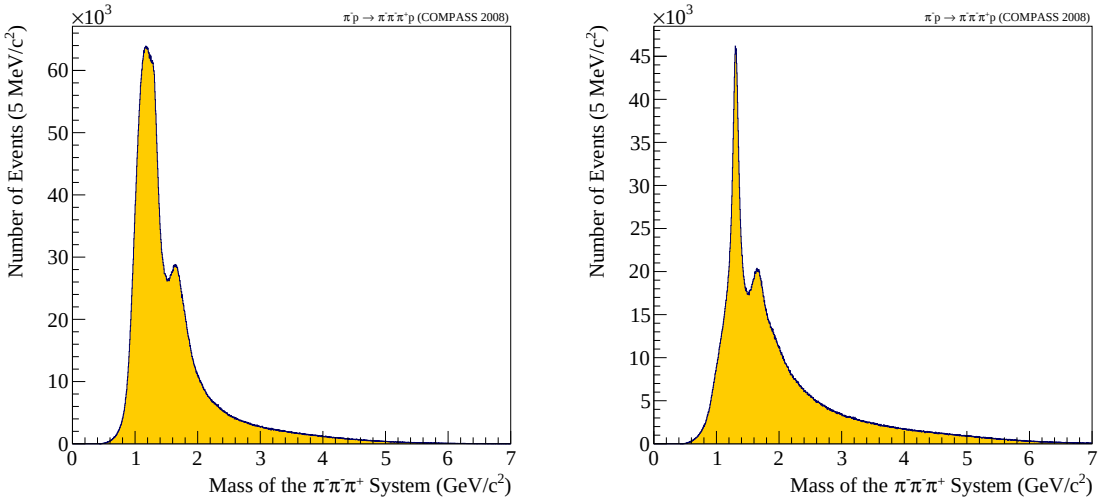

Figure 5.13 Invariant mass of the 3π system in the kinematic region of $0.1 \leq t' \leq 0.114$ GeV$^2/c^2$ (a) and $0.443 \leq t' \leq 1.0$ GeV$^2/c^2$ (b).

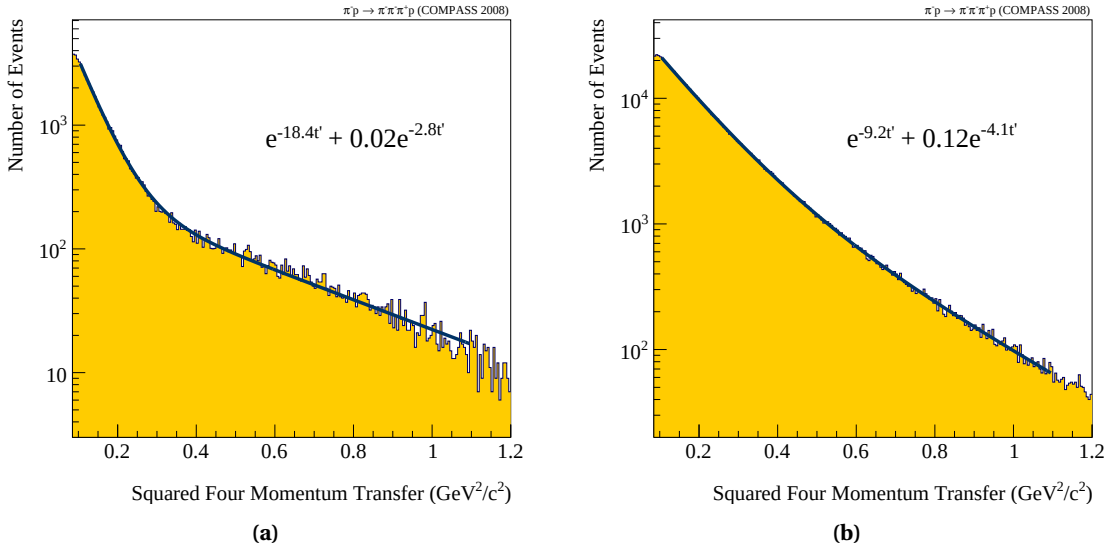

Figure 5.14 t' distribution in the kinematic range of $0.8 \leq m_{3\pi} \leq 0.81$ GeV$/c^2$ (a) and $1.6 \leq m_{3\pi} \leq 1.61$ GeV$/c^2$ (b).

It is worth to investigate the change of the slope parameters over the whole mass range, in order to learn more about the exchange mechansim. This study was performed first by the ACCMOR collaboration [D$^+$81]. The t' slopes were fitted for 50 MeV$/c^2$ wide mass bins, starting from 0.9 up to 1.9 GeV$/c^2$. The resulting slope parameter are plotted as a function of $m_{3\pi}$ seen at Fig. 5.15a. The same fit function, a sum of two exponentials, was used as here. Different models were tried, but yielded worse results. The COMPASS data set is 65 larger than the one of ACCMOR, thus a finer mass binning of 10 MeV$/c^2$ was chosen. The fitted slope parameter are plotted in Fig. 5.15b. Both plots look very similar within error bars. Below the resonace region at ~ 1.2GeV$/c^2$ the leading slope decreases fast, from ~ 20 GeV$^{-2}/c^{-2}$ down to 10 GeV$^{-2}/c^{-2}$. In the resonace region the leading slope decreases slowly starting around 9 GeV$^{-2}/c^{-2}$ while the

second slope stabilises at 5 GeV$^{-2}/c^{-2}$. The reason for this behavior is still unknown, but the new much more precise data could offer a starting point for future models of the production mechanism (see Sec. 7.4).

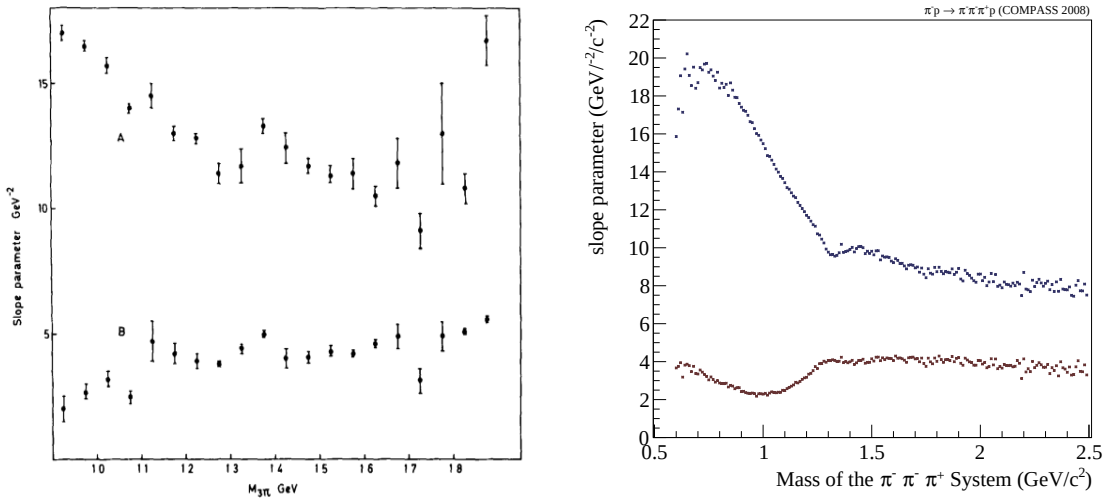

(a) **(b)**

Figure 5.15 Slope parameter from a fit of the t' distributions with two exponentials in mass bins of 50 MeV/c^2 [D$^+$81] (a) and in bins of 10 MeV/c^2 (b).

5.1.11 Hadron Campaign Stability Investigations

The quality of a data sample taken during a several weeks long campaign depends on numerous factors. Besides the preparatory works ahead the data taking, e.g. calibrating detectors, their positioning inside the spectrometer or the adjustment of the trigger system, several things can influence the data taking. The quality of the beam is affected by the stability of the accelerator complex, the production of the beam and the beam line stability, delivering the beam to the expermiment. Electronic components of the detectors can fail and have to be exchanged or even the quality of a shift crew, monitoring the data taking, can have influence on the data quality. It is not part of this thesis to analyse these factors into details as no absolute cross sections will be measured or are the topic of this analysis. But nevertheless some coarse investigations are done in oder to get a rough overview of the data quality and stability.
The data taking is organized in the followin scheme. The whole campaign is divided into two-weeks long periods (W33, W35, W37 and part of W39 for 2008 and W42 for the 2009 data, discussed in this thesis). The maximum size of a recorded run is 200 SPS spills (see Sec. 3.3). Only runs which fullfill some basic quality criteria are taken into account for reconstruction. These runs are flagged as 'good' by the shift crew in areement with the weekly coordinator and the run coordinator. The final choice which runs are worth to be reconstructed by the `CORAL` (see Sec. 3.4) framework is made by the analysis and the run coordinator. An overview of all reconstructed runs of 2008 and the respective number of events after the preselection (see Sec. 5.1.1) are plotted in Fig. 5.16a. The variations of the number of events per run corresponds mainly to the number of recorded spills (≤ 200) for theses runs. The ratio of these events over accepted events, normalised to the DT0 trigger, is depicted in Fig. 5.16b as a function of the run number.

Events are considered as accepted if they survive the major selection criteria after preselection, i.e. exclusive events inside the target and within the kinematic boundaries of t'. The ratio is rather flat over the whole 2008 campaign except for some single runs. This shows that the same fraction of data is selected for each run.

Period	First Run	Last Run	Runs	Spills	Events
W33	69561	69989	123	11607	$1.249814425 \cdot 10^9$
W35	70049	70488	128	12622	$1.959695710 \cdot 10^9$
W37	70450	70963	200	23319	$2.891751049 \cdot 10^9$
W39	70999	71018	13	1927	$2.66655633 \cdot 10^8$

Table 5.1 Overview of data taking periods of the 2008 campaign and the respective number of spills and events.

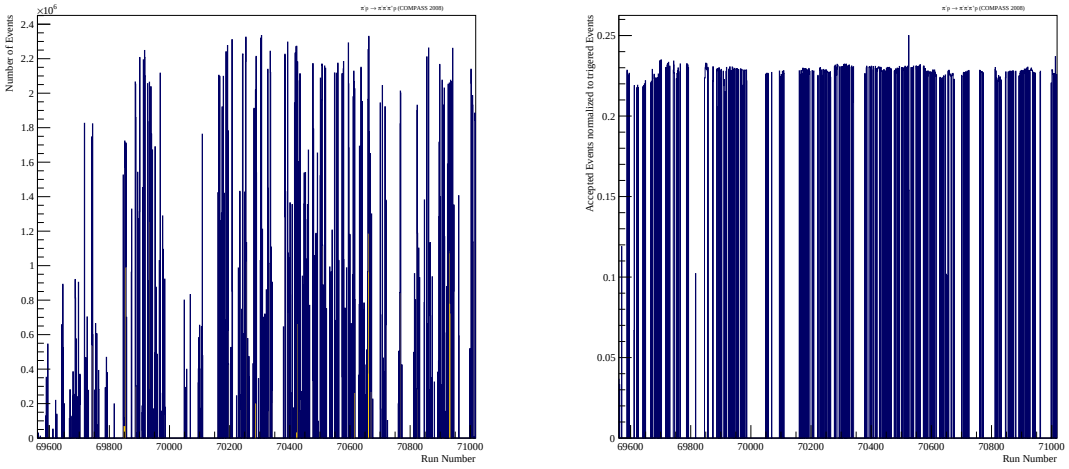

(a) **(b)**

Figure 5.16 Number of events as a function of the run number for the 2008 campaign. Fig. (a) shows the number of events after the preselection and in (b) the ratio of these events and the accepted events is depicted.

5.2 Diffractive Dissociation with Solid State Targets (2009 Data)

As already mentioned in Sec. 3.5 the switch-over period to the Primakoff campaign was used to obtain a data sample of single diffraction events with a lead target. The outcome of a spin-parity analysis based on this data should be compared with its predecessor analysis of 2004 data [AAA+10]. The amount of data of this 'parasitic' run is much less than for the 2008 data sample. In addition some peculiarities of the lead target and the modified trigger system have to be taken into account. Nearly all selection criteria, discussed in Sec .5.1 can be applied to the 2009 lead data as well, most of them even unchanged. For those which have to be adapted or ignored, a short discussion follows while a summary of all cuts applied to this data is listed in Tab. 5.2.

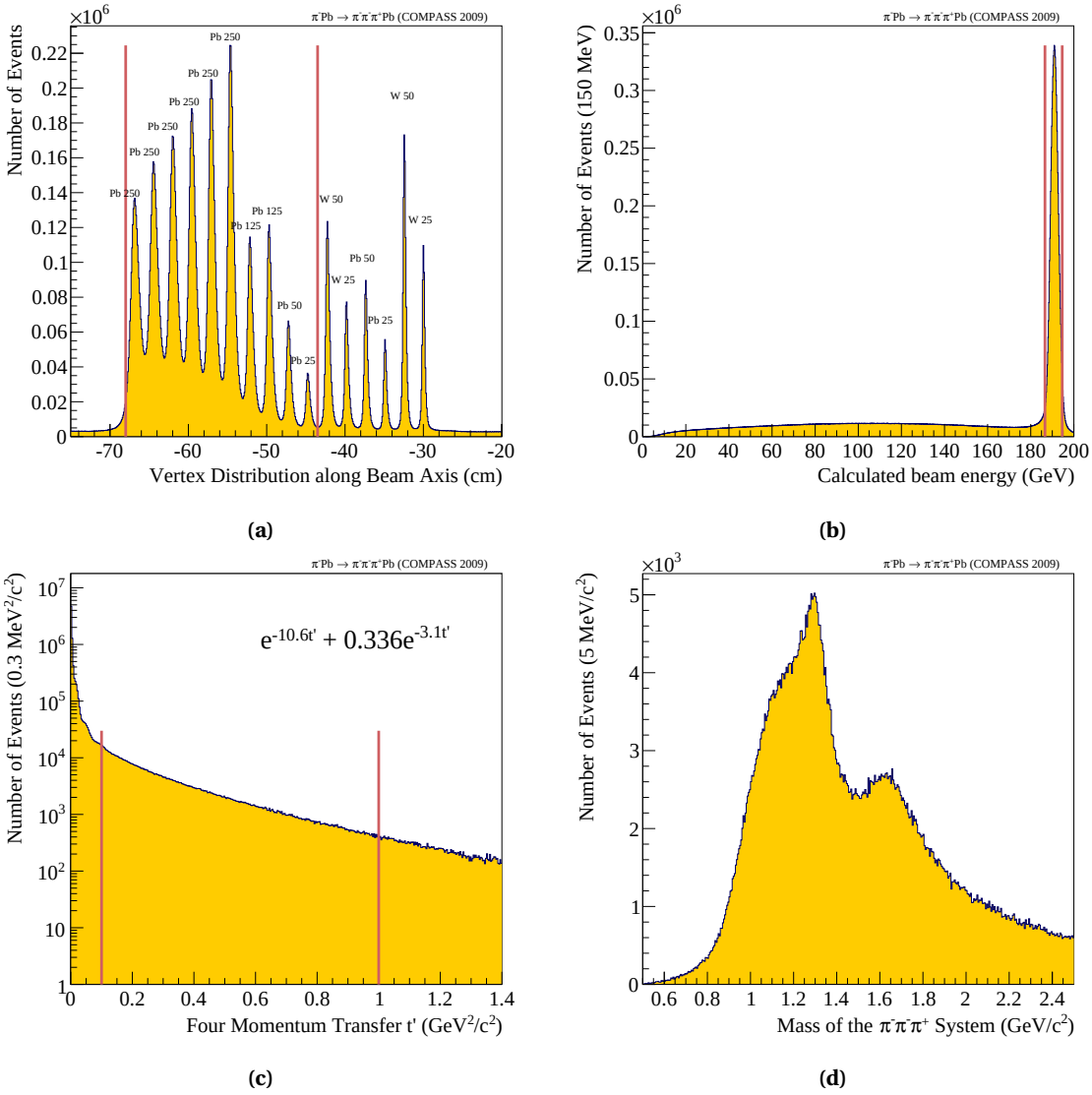

Figure 5.17 Characteristic kinematic distributions for the 2009 lead data. The vertex distribution along the z-axis is shown (a) as well as the calculate beam energy (b). In addition the squared four-momentum transfer distribution (c) and the final invariant mass distribution of the $\pi^-\pi^-\pi^+$ system (d) is plotted.

- **Vertex Cut**: The lead target (see Fig. 3.3) can be split in two sections. The upstream part corresponding to two third of the target consists only of lead disks with different thicknesses. Its dimension is used for the longitudinal cut along the z-axis. The second part is consisting of two lead disks in between tungsten disks and is not taken into account for the analysis. The primary vertex distribution along the z-axis is plotted in Fig. 5.17a and the selection criterium is indicated by red lines. Due to its lightweighted support structure of carbon fibre rods on the one hand and the weight of the target disks on the other hand a small skewness along the z-axis is observed. Thus, in order to consider only the target material and not part of the holding structure of the single discs, the radial cut is thightened by 0.5 mm.

- **Beam Time**: As introduced in the beginning of this section, the data were taken during the commissioning of the new ECAL digital trigger. As a consequence of this the trigger latency had to be increased and the mean of the measured beam time is shifted by 2 ns towards the positive times.
- **Trigger and Number of Recoil Particles**: The cut on the recoil protons can be used for the liquid hydrogen target, where the proton can be clearly detected and pileup events in the RPD can be rejected by demanding exactly one detected recoil proton in the RPD. For the lead target, this selection could not be applied, as the detection of protons, as it is implemented in the software, is highly disturbed by δ-electrons. This is also the reason why the DT0 was not considered as trigger. The multipilicity counter (see Sec. 3.5) was chosen in order to have an unbiased trigger.
- **Co-planarity**: This method can only applied to the 2008 data, while in 2009, multiple scattering of the recoil particle in the lead target and the low detection efficiency, lead to no enhancement of the signal to background of our final state.
- **Kaon and Multi-Regge Contributions**: The selection criteria would have no effect on the small data sample and are omitted thus.

5.3 Phase-Space Monte Carlo and Resolutions

It is eminent to understand the apparatus, used to obtain the data sample. A complex machinery like the COMPASS spectrometer consists of several thousands components of different materials, e.g. support structures, cables, detector gases. The hadronic and electromagnetic interaction of the traversing particles with these components needs to be known in order to correct for these effects in the analysis. In addition detector performance figures like energy or spatial resolution or detection efficiencies have to be estimated.
Therefore the whole spectrometer is simulated within the framework of `ComGEANT` [cola], a modified version of `GEANT3` [gea], adapted to the purpose of COMPASS. The quality of the simulation depends on the one hand on the attention to details, even thin layers of glue or single screws have to be considered. On the other hand the number of simulated events must be significantly larger than the number of events in the analysed data set. For the $5 \cdot 10^7$ data points analysed in this thesis, approximately $1.8 \cdot 10^8$ Monte Carlo events were generated within the kinematical limits of the initial beam and the measured t'-distribution. The decay particles are distributed isotropically over the phase space in order to illuminate the geometrical area of the spectrometer accessible to the physical process. These phase-space events are fed to `ComGEANT` and possible interactions between the reaction particles and the spectrometer are simulated with Monte Carlo methods. Finally the output of the simulation is fed to the reconstruction package of COMPASS. In order to investigate the effciency of the reconstruction, the same software version of `CORAL` is used than for the production of the real data. Details on the event generation, the simulation and reconstruction can be found in App. D.
One point of interest is the resolution of the spectromenter in these kinematic variables which play an important role in the analysis of the process of interest. Considering the exchange mechanism and the peculiarities of the COMPASS spectrometer, the resolutions of the following variables are investigated as a function of $m_{3\pi}$ and t'.

Applied Cut	**Ratio**	**Yield**
all events	–	$6.367916817 \cdot 10^9$
	–	*$2.691123210 \cdot 10^9$*
exactly one primary vertex (PV), Sec. 5.1.1	0.7089	$4.514188201 \cdot 10^9$
	0.7113	*$1.914295261 \cdot 10^9$*
$-256 < z_{\mathrm{PV}} < 123$ cm, Sec. 5.1.1	0.7002	$4.458972613 \cdot 10^9$
	0.5472	*$1.472594589 \cdot 10^9$*
3 fast particles leaving the PV, Sec. 5.1.1	0.0778	$4.95302499 \cdot 10^8$
	0.0478	*$1.28654554 \cdot 10^8$*
track parameters exists, Sec. 5.1.1	0.0778	$4.95302499 \cdot 10^8$
	0.0478	*$1.28654554 \cdot 10^8$*
$\sum_i^3 Q_i == -1$, Sec. 5.1.1	0.0680	$4.32710128 \cdot 10^8$
	0.0322	*$8.6750184 \cdot 10^7$*
beam time, Sec. 5.1.2	0.0642	$4.08529854 \cdot 10^8$
mean value shifted to +2 ns	*0.0313*	*$8.4217051 \cdot 10^7$*
DT0 triggered, Sec. 5.1.3	0.0629	$4.00843360 \cdot 10^8$
Multiplicity Trigger	*0.0261*	*$6.9200848 \cdot 10^7$*
exactly one reconstr. track in the RPD, Sec. 5.1.3	0.0493	$3.14114992 \cdot 10^8$
not applied for 2009 data	-	-
$-66 < z_{\mathrm{PV}} < -29$, $r_{\mathrm{PV}} < 1.55$ cm, Sec. 5.1.4	0.0461	$2.93315008 \cdot 10^8$
$-68 < z_{\mathrm{PV}} < -43.5$, $r_{\mathrm{PV}} < 1.50$ cm	*0.0071*	*$1.9111722 \cdot 10^7$*
$187.7 < E_{\mathrm{beam}} < 195.3$ GeV, Sec. 5.1.5	0.0158	$1.00592372 \cdot 10^8$
$186.6 < E_{\mathrm{beam}} < 194.6$ GeV	*0.0033*	*$8.786745 \cdot 10^6$*
Planarity, Sec. 5.1.5	0.0125	$7.9846179 \cdot 10^7$
not applied for 2009 data	-	-
$0.1 < t' < 1.0$ GeV$^2/c^2$, Sec. 5.1.6	0.0101	$6.4093914 \cdot 10^7$
	0.0003	*$8.29741 \cdot 10^5$*
CEDAR Veto, Sec. 5.1.8	0.0100	$6.3403707 \cdot 10^7$
not applied for 2009 data	-	-
RICH Veto, Sec. 5.1.8	0.0083	$5.3015789 \cdot 10^7$
not applied for 2009 data	-	-
CP Veto, Sec. 5.1.7	0.0080	$5.0672839 \cdot 10^7$
not applied for 2009 data	-	-
$0.5 \leq m_{3\pi} \leq 2.5$ GeV$/c^2$, Sec. 5.1.9	0.0072	$4.5927632 \cdot 10^7$
	0.0003	*$7.07488 \cdot 10^5$*

Table 5.2 Overview of selection criteria and corresponding yield for the 2008 and 2009 (italic font) data.

- **Invariant mass** $m_{3\pi}$: One of the two parameters that characterises diffractive dissociation. Figure 5.18a shows the mass resolution of the 2008 COMPASS spectrometer. It depends only on $m_{3\pi}$ not on t'. It ranges from 4 MeV/c^2 at masses near 0.5 GeV/c^2 up to 16 MeV/c^2 at the upper limit of 2.5 GeV/c^2 (see Tab. 5.3). The reason for this dependence can be explained by the kind of detectors used for the reconstruction. At low masses most of the three charged decay pions are detected by the small area tracking system (SAT, refer Sec. 3.2.2) having a much better spatial resolution than the detector components of the large area tracking system (LAT, refer Sec. 3.2.2) required to detect decay pions at large masses. At the boundaries of the plot some artifacts can be observed resulting from bin migrations at the edges of the MC sample.

- **Squared four-momentum transfer** t': The second variable characterising diffractive dissociation. As visible in Fig. 5.18b there is a clear t'-dependence of the t'-resolution. Decay particles emerging from the primary vertex with a small momentum transfer are dominantly detected at the SAT system while events with large t' are observed with the LAT system. Values of the resolution at the kinematic boundaries of $m_{3\pi}$ and t' are listed in Tab. 5.3.

- **Beam energy**: Previous in this chapter it was discussed, that the 2008/2009 spectrometer setup was not able to measure the beam momentum along the beam axis. Thus the beam energy has to be calculated (see Sec. 5.1.5) on the basis of the measured momenta of the final-state particles. The beam energy resolution gives a good measure of the precision of this method. Figure 5.18c shows these resolutions again as functions of t' and $m_{3\pi}$. The resolutions are well below 1 GeV, having a relatively small spread betweeen 0.6 and 0.9 GeV at the kinematical boundaries. These resolutions are significantly smaller than the energy spread of the beam itself.

- z**-Position of the primary vertex**: Finally the resolution of the z-position of the primary vertex is investigated. The position is important for the tracking of final-state particles through the spectrometer. As a part of the triggered events are poluted by pileup, it is eminent to reconstruct each vertex in order to identify the one related to the triggered event and associate it with its corresponding particle tracks. The z-resolution is shown in Fig. 5.18d. It mainly depends on the 3π mass. Events with small 3π masses leave the target under small angles which makes the reconstruction of the vertex position less precise.

Another important input to the analysis is the acceptances of the spectrometer for the final state under study. This will be discussed in Sec. 7.1.3, after the required variables are introduced and explained.

	small $m_{3\pi}$ small t'	large $m_{3\pi}$ small t'	small $m_{3\pi}$ large t'	large $m_{3\pi}$ large t'
$m_{3\pi}$ [GeV/c^2]	5.40 ± 0.01	14.85 ± 0.01	5.19 ± 0.01	15.47 ± 0.01
t' [10^{-3}GeV$^2/c^2$]	6.63 ± 0.01	8.44 ± 0.01	14.77 ± 0.01	19.25 ± 0.01
beam energy [GeV]	0.60 ± 0.01	0.80 ± 0.01	0.65 ± 0.01	0.87 ± 0.01
z_{PV} [mm]	6.04 ± 0.01	1.47 ± 0.01	5.7 ± 0.01	1.48 ± 0.01

Table 5.3 Exemplary resolutions of four important kinematic variables taken at the boundaries of $m_{3\pi}$ and t' (see Fig. 5.18).

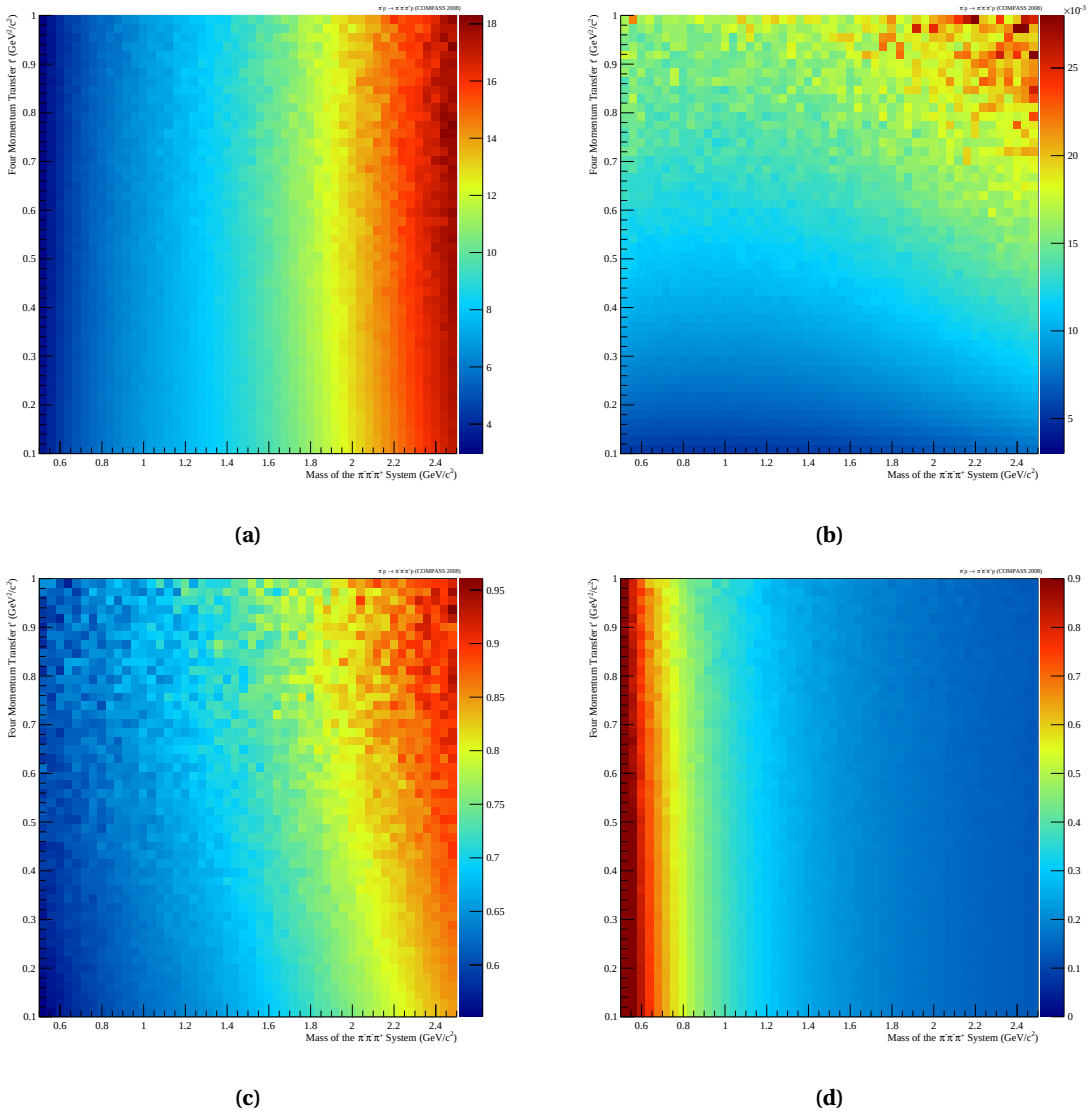

Figure 5.18 Resolutions of some kinematic variables as a function of t' and $m_{3\pi}$. Figure (a) shows the mass resolution for the 3π system, while the resolution of the squared four-momentum transfer t' is shown in (b), the energy resolution (c) and the vertex resolution along the z-axis in (d).

5.4 Deck Monte Carlo Simulation

The contribution of Deck-like processes is one of the major non-resonant contributions and has been studied in the last 45 years. But still there is up to now no satisfactory method to disentangle this kind of production from the resonant contribution of the observed intensity. The idea, followed in here is, to create a Deck Monte Carlo sample, where the kinematic distributions of the Monte Carlo events are defined by a Deck amplitude. This data sample is subject to the same spin-parity analysis with the identical fit model (see Sec. 7.2) as is applied to the real data. It is expected to learn more by the fit outcome about the single contributions of Deck processes on the level of partial waves. In the following the parametrisation of the Deck amplitude will be explained. There are several ways to model the Deck amplitude and the ansatz, how this amplitude is constructed for this analysis is based on the concept developed in [D+81]. The modelling of the Deck amplitude is based on experimental results of $\pi\pi$ and πN scattering. In some places of the description other values of the model parameters are used than in [D+81] in order to take more recent experimental findings into account. In these cases the originally values will be written in brackets.
The Deck process was already introduced in Sec. 2.2.3 as it was originally proposed by Deck [Dec64]. An incoming beam pion dissociates into a $\rho(770)$ and a virtual π, which scatters diffractively from the target proton into a real state. For this particular case the Deck amplitude can be described as

$$A(M_{\pi\pi}, t_\pi, t) = \frac{A_{\pi\pi}(M_{\pi\pi}, t_\pi) A_{\pi p}(s_{\pi p}, t)}{m_\pi^2 - t_\pi} \tag{5.14}$$

with $A_{\pi\pi}$ being the $\pi\pi$ scattering amplitude through the ρ meson and $A_{\pi p}$ the $\pi^- p$ scattering amplitude. The schematic drawing of this process is shown in Fig. 5.19 including all kinematical variables needed for the amplitude description. It is assumed that the virtual pion can be

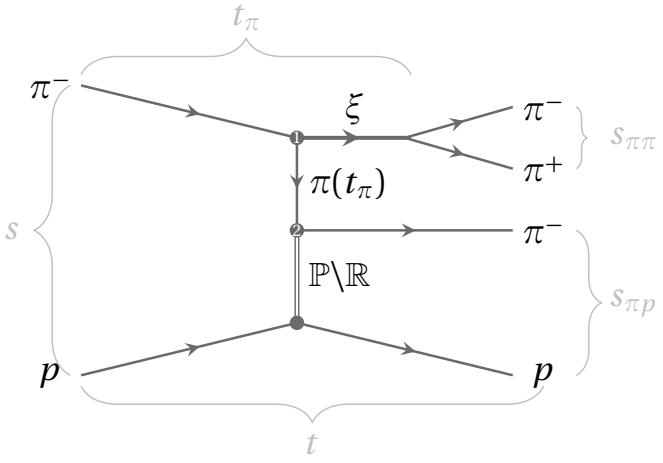

Figure 5.19 Schematic drawing of Deck mechanism with important Mandelstam variables of this process included..

treated as a real one and thus one can use elastic $\pi^- p$ scattering data for $A_{\pi p}$

$$A_{\pi p} = i s_{\pi p} \sigma_t e^{at} \tag{5.15}$$

where $\sigma_t = 64$ GeV^{-2} is the total $\pi^- p$ cross section and the slope parameter a is taken as $-8[-4.5]$ GeV$^{-2}/c^{-2}$. An additional form factor $e^{b(t_\pi - m_\pi^2)}$ with $b = 0.45[2]$ GeV^{-2} was introduced in order to reproduce the t dependence around 1 GeV/c^2 of the invariant three-pion mass. The model takes only pion scattering into account, other possible scattering processes, like the exchange of a virtual ρ, are not considered. For the description of the $\pi\pi$ scattering amplitude more recent data were used than in the original model [D$^+$81], which only took the ρ meson into account. For this Monte Carlo sample the $\pi\pi$ scattering is parametrised by data taken from [HJW$^+$73], including the $f_2(1270)$, the $f_0(980)$ and the $\rho_3(1690)$ in addition to the $\rho(770)$. Also a broad $(\pi\pi)_S$ component is included, based on [HJW$^+$73]
Finally 10^8 Deck-like Monte Carlo events were produced and being applied to the spin-parity analysis as third data sample (besides 2008 proton and 2009 lead data). The 3π invariant mass distribution of the Deck Monte Carlo is shown in Fig. 5.20a as the filled histogram. Accordingly the two-pion mass distribution is plotted in Fig. 5.20b. The different two-pion resonances, implemented in the Monte Carlo simulation, are clear seen in the spectrum.
In addition to the Monte Carlo sample described above a second one was produced, based on [ACJ$^+$74], as this parametrisation is widely used for three-pion partial wave analyses. The reason, why this Monte Carlo is not used for the following investigations is, that it is missing some two-pion resonances and that it is based on older experimental data. On the other hand this parametrisation is more advanced. It uses a Reggeised pion propagator and allows to take into account additional scattering processes, like ρ or f_2 scattering. For the future it is planned to merge both parametrisations in order to get a more realsitic model. The resulting three-pion mass is plotted in Fig. 5.20a as transparent histogram the corresponding two-pion mass in Fig. 5.20b.

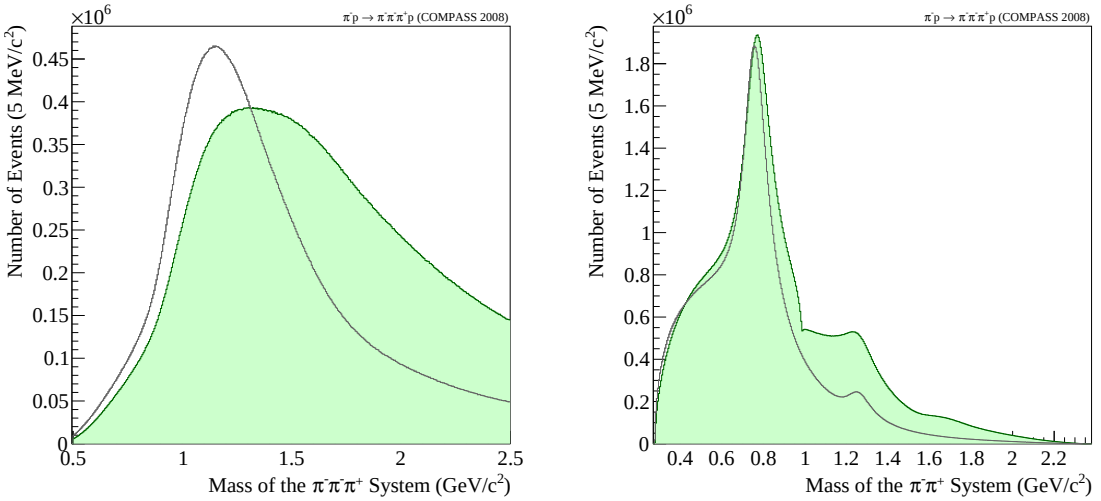

Figure 5.20 3π mass spectrum for Monte Carlo Deck events (a). The filled distribution represents the Deck model used for this analysis, the overlaid open spectrum is taken from the original approach. The same is shown for the 2π subsystem invariant mass (b).

Chapter 6

Amplitude Parametrisation

In the previous chapter the events, which fulfill kinematical criteria to originate from diffractive dissociation, are selected. Structures visible in the final three pion invariant mass distribution (Fig. 5.11a) indicate contributions of several resonances to the observed intensity. As already mentioned, the goal of an amplitude analysis is to disentangle the various contributions and extract the corresponding resonance parameters. For this purpose it is essential to develop a mathematical parametrisation of the contributing amplitudes. This chapter concentrates on the development of such a parametrisation which, together with the kinematical results of the previous chapter, serves as input for the analysis, discussed in the next chapters.

6.1 General Ansatz for the Amplitude

The observed intensity distribution $\mathscr{I}(m_{3\pi}, t', \tau)$ depends on the kinematical variables $m_{3\pi}$, t' and a set of additional observables τ, describing the three-body decay. It can be expanded in a basis of partial waves Ψ_i. As each partial wave leads to the same final state, they do interfere and thus are summed up coherently.

$$\mathscr{I}(m_{3\pi}, t', \tau) = \left| \sum_i \Psi_i(m_{3\pi}, t', \tau) \right|^2 \tag{6.1}$$

In peripheral reactions, like diffractive dissociation, the partial waves amplitudes are assumed to be factorized in a term describing the production of a particular intermediate state X and a term describing its decay into an n-particle final state. The intensity reads then

$$\mathscr{I}(m_{3\pi}, t', \tau) = \left| \sum_i \sum_k C_{ik} \mathscr{F}_k(m_{3\pi}; \zeta) f_i(m_{3\pi}, t') \psi_{ik}(\tau, m_{3\pi}) \right|^2 \tag{6.2}$$

The goal of an amplitude analysis is to obtain values for the unknown complex production amplitudes C_{ik}, which have no direct physical meaning, and the set of parameters ζ, which can be mass and widths of resonances (M_0, Γ_0) or parameters of non-resonant contributions. The complex decay amplitudes $\psi_{ik}(\tau, m_{3\pi})$ give a complete description of the final state. The index i introduced in Eq. (6.1) denotes all quantum numbers which are necessary to identify the state X, namely $I^G J^{PC} M$. As a consequence of the factorisation the production of a state is independent from its decay. Thus several decay channels can come from the same state X. This is taken

into account by the index k, summarising all possible decays for a certain state. In addition the dependence on t' can be parametrized by a set of real functions $f_i(m_{3\pi}, t')$. Coming to that point some questions arising which clarification is crucial for the whole analysis and will be discussed in this and the following sections.

- What quantum numbers $I^G J^{PC} M$ are possible for the intermediate state X?
  Diffractive dissociation of mesons is a process of strong interaction. At COMPASS energies the exchange is dominated by Pomeron exchange (see Sec. 2.1.1). Therefore some constraints regarding the production of possible states X must taken into account.
- How should the dynamics of production and decay be parametrised?
  This point is the focus of this chapter. Unrealistic parametrisations can bias the whole analysis. In addition it is important to find an ansatz which is as little model-dependent as possible. This is valid for parametrisations, the production, the t'-dependence and the decay. It will be shown that, although model dependencies are avoided as much as possible, a complete model-independent solution is not achievable yet, but in Sec. 9.1 further possibilities are discussed.

To give an answer to the first question, a discussion on relevant symmetries, which constrain the possibilities of quantum numbers, follows.

6.1.1 Isospin and G-Parity

For light mesons, consisting only of u and d quarks, isospin and G-parity are good quantum numbers in strong interaction processes. At COMPASS energies diffractive reactions can be viewed as scattering of the incoming beam pion ($I^G = 1^-$) and a Pomeron, the leading Regge trajectory with $I^G = 0^+$. Regarding the isospin it is obvious that the Pomeron carries no charge, thus the intermediate state X must have the same charge as the pion. Recalling the fact that the G-parity is multiplicative, the state X can only have the isospin and G-parity of the pion. For the $\pi^-\pi^-\pi^+$ final-state only negative G-parity is allowed, and the charge of the 3π system is equal its z-component of the isospin (see Eq. (1.1)). Thus only $I^G = 1^-$ is possible again [1]. From the relation between G- and C-parity (see Eq. (1.7)) it follows that $C = +1$ for X. As mentioned in Sec. 1.1.1 X is not an eigenstate of C, but the convention is to give the same C quantum number as for the neutral state.
Summarising it can be stated that for πN scattering at high energies only combinations with $2n+1$, $n = 0, 1, ...$ pions in the final state are allowed, i.e. the trivial case of elastic scattering, this analysis or for example 5π [Neu12].

6.1.2 Reflectivity and Parity

While isospin and G-parity are good quantum numbers only in strong interaction processes with light quarks, parity is a good symmetry regardless the meson content. This leads to further restrictions on the production of J^{PC} states. Recalling Eq. (1.3) and (1.4) reveals that scalar mesons with $J^{PC} = 0^{++}$, cannot be produced by diffractive pion dissociation via Pomeron exchange[2].

[1] The mathematical possibility of states with $I > 1$ is ignored as such states are not observed in nature
[2] There is no possible orbital angular momentum ell to conserve parity and total spin J.

Instead to account for the parity directly, it has been proven to be more useful to describe reactions of the type $A+B \to X+C$ under reflections through the production plane [CT75]. For any reference system as the rest frame of X and the y-axis perpendicular to the production plane, i.e. the reference axis of the spin lies in that plane, the reflection operator can be defined as

$$\Pi_y = P \exp(-i\pi J_y) \tag{6.3}$$

where P is the parity quantum number. This operator is related with the parity by a rotation by π through the y-axis of the system. The invariance under rotation implicates that the invariance under reflection is equivalent with an invariance under parity transformations. The eigenstates of Π_y are formed by linear combinations of states with opposite spin projection quantum number M

$$\psi^{\varepsilon}_{JM} = c(M)\left[\psi_{JM} - \varepsilon P(-1)^{J-M}\psi_{J(-M)}\right] \tag{6.4}$$

$$\text{with} \quad \varepsilon = \pm 1, \quad M \geq 0, \quad c(M>0) = \frac{1}{\sqrt{2}} \quad \text{and} \quad c(M=0) = \frac{1}{2} \tag{6.5}$$

An additional quantum number ε called *reflectivity* is introduced, defined such that the eigenvalues are given by

$$\Pi_y \psi^{\varepsilon}_{JM} = -\varepsilon \psi^{\varepsilon}_{JM} \tag{6.6}$$

For bosons the reflectivity can take on the values $\varepsilon = \pm 1$. There are several advantages in parametrising the different spin states in the reflectivity basis.
In the family of possible reference systems the Gottfried-Jackson frame is special (details will be discussed in Sec. 6.3). Within this frame and in the limit of high-energy scattering the reflectivity coincides with the naturality of the exchanged particle (a nice proof can be found at [Sch12]). Since the Pomeron is the leading Regge trajectory at COMPASS energies, amplitudes with positive reflectivity are the majority in the wave set, applied at this analysis. Nevertheless amplitudes with negative reflectivity are part of the wave sets, representing possible contributions from trajectories with negative naturality like the b_1 trajectory. Possible $J^{PC}M$ quantum numbers of the intermediate state X are summarised for given reflectivities in Tab. 6.1 up to spin $J = 2$.

reflectivity ε	**$J^{PC}M$ states**
$+1$	$0^{-+}0$, $1^{++}0$, $1^{++}1$, $1^{-+}1$, $2^{++}1$, $2^{++}2$, $2^{-+}0$, $2^{-+}1$, $2^{-+}2$, ...
-1	$1^{++}1$, $1^{-+}0$, $1^{-+}1$, $2^{++}0$, $2^{++}1$, $2^{++}2$, $2^{-+}1$, $2^{-+}2$

Table 6.1 $J^{PC}M$ states for given reflectivity ε.

The incoming beam is spinless and the spin configuration of neither the target proton nor the recoil proton is measured. Thus the spin state of X is not completely determined and therefore described by a *spin density matrix*. Parametrising the amplitudes in the reflectivity basis brings the density matrix in a block diagonal form [CT75]. This means that states with different reflectivities, i.e. produced by Regge trajectories with different naturality, do not interfere and must be add up incoherently.
The lack of knowledge of the spin state of the target proton leads to two non-interfering processes of the initial spin state [HJOR74]. This second source of incoherence, contributing to

the formulation of the spin-density matrix, is often called the *rank r* of the spin-density matrix. A detailed discussion about this parametrisation of the density matrix is in Sec. 7.1.2. The observed intensity can now be written as follows:

$$\mathscr{I}(m_{3\pi},t',\tau)=\sum_{\varepsilon}\sum_{r}\left|\sum_{i}\sum_{k}C^{\varepsilon}_{ir}\mathscr{F}_k(m_{3\pi},\zeta)f^{\varepsilon}_i(m_{3\pi},t')\psi^{\varepsilon}_{ik}(\tau,m_{3\pi})\right|^2 \tag{6.7}$$

6.2 The Isobar Model

The quality of this analysis depends on the correct and precise description of amplitudes in order to obtain the unknown variables of the system. In this analysis the dynamics of the intermediate state is unknown and in the focus while the decay into the final state is well measured. The first step of finding a proper parametrisation of the decay is to clarify how many independent variables are necessary for a complete description. Each final-state particle is represented by a four-vector. As already mentioned, it is appropriate to suppose that there is not final-state interaction between the recoil particle and the decay products of the state X in diffractive processes at high energies. That is for this analysis it is sufficient to consider only the decay vertex. A final state with three particles is described by 12 variables or three four-vectors. Final-state particles are measured physical entities, meaning on-shell particles, with well-defined masses, thus nine variables are still free. Energy and momentum conservation rules constrain one of the vectors and so finally a set of six variables gives a full description of the 3π final state.
Observations, since the beginning of accelerator physics, revealed that nature prefers two-body decays instead of spontaneous decays into several particles (one of the first observations is discussed in [LS57]). A description of this observations leads to the formulation of the *isobar resonance model*. In this model a n-body decay is seen as a subsequent decay into two daughter states under the assumption that each of this daughters form again a new resonance or is a final-state particle. The big advantage of this model is that multi-particle final states and their mathematical complicated treatment of the decay can be described by a chain of calculable two-body decays (see for example the description of the 5π final state in [Neu12]). Obviously the symmetries, discussed in Sec.6.1.1 and 6.1.2, are obeyed within that model. The decay topology of the 3π final state is depicted in Fig. 6.1. The intermediate state X with quantum numbers $J^{PC}M^{\varepsilon}$ decays at vertex 1 into another intermediate resonance ξ by the emission of a spectator pion π^-. The new resonance ξ is called the *isobar*. Spin is conserved through the orbital angular momentum L_1 between the spectator pion and the isobar. At vertex 2 the isobar finally decays into two pions of the final state with relative orbital angular momentum L_2. In order to describe the three-pion decay properly the following six variables are used: the decay of the state X is parametrised by its mass $m_{3\pi}$ and two angles describing the decay in a center of mass system of X. In order to consider the production mechanism (c.f. Sec 6.1.2), the Gottfried-Jackson frame is chosen with the azimuthal angle ϕ_{TY}, which is called the *Treiman-Yang* angle, and the cosine of the polar angle, $\cos\vartheta_{\mathrm{GJ}}$. The decay of the isobar is specified by its mass m_{ξ} and two angles describing the isobar decay in an appropriate center of mass system, here the *helicity frame*, with the respective angles ϕ_{HF} and $\cos\vartheta_{\mathrm{HF}}$. Exemplary the distributions of this set of variables, $\tau=\{\phi_{\mathrm{TY}},\cos\vartheta_{\mathrm{GJ}},m_{\xi},\phi_{\mathrm{HF}},\cos\vartheta_{\mathrm{HF}}\}$, for a fixed mass $m_{3\pi}$, is plotted in Fig. 6.3. Both reference frames will be discussed in the following section.

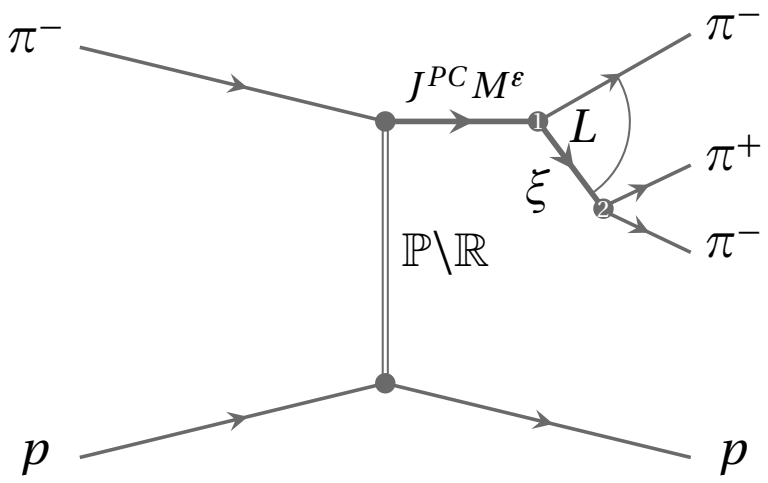

Figure 6.1 Schematic of the isobar model

6.3 Helicity Formalism

A complete parametrisation of the decay demands a description of the spin states of each final state particle. Applying the *spin-orbit formalism* requires a Lorentz-boost into the center of mass system of each of the particle in order to determine the spin state. In terms of the isobar model, however, it is possible to describe each two-body decay within the *helicity formalism* [JW59] which will be discussed in the following (details are discussed for example in [Per74], a tutorial for the application of this formalism to real data can be found in [Ric84]).
The determination of the spin state of a particle requires a rotation and boost into an appropriate reference system. The operator of an active rotation (i.e. the coordinate axes remain fixed, the physical system itself is rotated by the Euler angles α, β, γ), which is

$$R(\alpha,\beta\gamma) = e^{-i\alpha J_z} e^{-i\beta J_y} e^{-i\gamma J_z} \tag{6.8}$$

commutes with the angular momentum operator $\mathbf{J}^2$. The physical meaning is the invariance of the magnitude of the total angular momentum under rotations, thus the eigenvalues J of a spin state are invariant. The active rotation of a state $|JM\rangle$ can now be described as a linear combination of $|JM'\rangle$ states.

$$|JM\rangle \rightarrow R(\alpha\beta,\gamma)|JM\rangle = \sum_{M'=-J}^{+J} D^J_{M'M}(\alpha,\beta,\gamma)|JM'\rangle \tag{6.9}$$

The matrix elements $D^J_{M'M}(\alpha,\beta,\gamma)$ of the rotation operator describe the overlap of the states $|JM'\rangle$. These *D-functions*, trigonometric functions of α, β and γ, form the *D-matrix* describing the distribution of $|JM\rangle$ over the Jth multiplet.
The advantage of the description of a two-body decay within the helicity formalism can be seen best in the center of mass frame of the mother state. There the spin projection to a reference axis is equivalent to its helicity $\lambda = \vec{s}\vec{q}$. The helicity is invariant under rotations and can be used as identifier of the amplitude. The final state is described by $(2s_1+1)(2s_2+1)$ helicity states $|\vec{q}\lambda_1\lambda_2\rangle$ with λ_i the helicities of the particles and q their break-up momentum. The helicities

λ_1, λ_2 of the two daughter states couple to a total spin S with helicity $\lambda = \lambda_1 - \lambda_2$. The relative orbital angular momentum L between the two decay products couples to S in order to form the spin of the mother state with M. The two-body amplitude can be described as follows:

$$A(m, \phi, \vartheta = \sum_{\lambda} D^{J}_{\lambda M}(\phi, \vartheta, 0) f_{\lambda}(m, P_R, w_1, p_1, w_2, p_2) \tag{6.10}$$

The rotation of the system is described by the previously introduced D-functions. By conventions the third angle γ is set to zero, which has no physical implication. The dynamic part f_λ can be seen as follows

$$\begin{aligned} & f_{\lambda}(m_R, P_R, m_1, p_1, m_2, p_2) = \\ = & \underbrace{\sqrt{2l+1}}_{\text{normalization}} \underbrace{(l0s\lambda|J\lambda)(s_1\lambda_1 s_2 - \lambda_2|s\lambda)(I_1 I_2 I_{z1} I_{z2}|I_R I_{zR})}_{\text{Clebsch-Gordan coeff.}} \underbrace{F_l \Delta(m) \alpha_{ls}}_{\text{dynamics}} A_1 A_2 \end{aligned} \tag{6.11}$$

There are three couplings, arising in a two-body decay. The first term $(l0s\lambda|J\lambda)$ is needed to transform the l-s-coupling to the total spin J. As the orbital angular momentum l is perpendicular to the reference axis in the helicity formalism, the z-projection of l is 0. $(s_1\lambda_1 s_2 - \lambda_2|s\lambda)$ describes the s_1-s_2-coupling between the two daughter states. The third coefficient is needed to parametrise the isospin coupling. Parametrisations for the dynamics itself are discussed in Sec. 6.4. The two amplitudes A_1 and A_2 are describing the two daughter states. It is convenient to set the amplitude to 1 if this amplitude represents a stable or final state particle (For this analysis the pions of the final state can be regarded as stable). In the following the description of a final state as subsequent two-body decays formulated with the helicity parametrisation is discussed.

Description of the Intermediate State X^- in the Gottfried-Jackson System

The description of the decay of the intermediate state X into an isobar ξ and a spectator pion π^- is described in the Gottfried-Jackson reference system [GJ64]. It is the rest frame of the state X with the reference axis z_{GJ} along the beam direction in the rest frame. The y_{GJ}-axis is the normal to the production plane, spanned by the three-momenta of the target $\vec{p}_{\text{target,GJ}}$ and the recoil particle $\vec{p}_{\text{recoil,GJ}}$. Finally the x_{GJ}-axis is given by $y_{\text{GJ}} \times z_{\text{GJ}}$ (see Fig. B.1a). The advantage of the application of this frame was already mentioned in Sec. 6.1.2. At high energies the naturality of the exchanged Reggeon coincides with the reflectivity ε and thus the description of amplitudes in the reflectivity basis gives a connection to the production mechanism. At small angles and high energies (both fulfilled by the COMPASS kinematics) the reference axis of the Gottfried-Jackson system coincides with the reference axis of the common helicity frame, thus the amplitude can be parametrised based on the helicity formalism:

$$A_X(m_{3\pi}, \tau) = \sum_{\lambda} D^{J}_{\lambda M}(\vartheta_{\text{GJ}}, \phi_{\text{TY}}, 0) \sqrt{2L+1} (L0S\lambda|J\lambda)(S_\xi \lambda_\xi 00|S\lambda) \frac{1}{\sqrt{2}} F_L \Delta(m_{3\pi}) \alpha_{\pi\xi} A_\xi(m_\xi, \vartheta_{\text{HF}}, \phi_{\text{HF}}) \tag{6.12}$$

For a given spin state $|JM\rangle$ it is summed over the helicity difference $\lambda = \lambda_\xi - \lambda_{\pi^-}$ of the two daughter states. As the pion carries no spin the difference reduces to $\lambda = \lambda_\xi$. The rotation is defined by the two angles of the Gottfried-Jackson system. For the isospin coupling only one solution is possible. The isobar ξ can have isospin $I_\xi = 0, 1$, but the third component

is equal in both cases $I_{3_\xi} = 0$ as only neutral isobars are taken into account[3]. Considering the third component of the spectator pion $I_{3,\pi^-} = -1$ the Clebsch-Gordan coefficient is $1/\sqrt{2}$. The description of the dynamics $\Delta(m_X)$ is unknown, a circumvention for this problem will be discussed in Sec 6.5. By convention the decay amplitude of the π^- is set to 1, thus only the amplitude of the isobar A_ξ is contributing. Its parametrisation will be discussed in the following.

Description of the Isobar State ξ in the Helicity formalism

The description of the isobar amplitude A_ξ is again calculated in the helicity formalism. The center of mass frame of the isobar is chosen, but the reference axis z_{HF} is now the direction of motion of the isobar as seen in the Gottfried-Jackson system. The y_{HF}-axis is the normal to the production plane, spanned by the three-momentum vector of the two daughter states. The x_{HF}-axis follows by $y_{\mathrm{HF}} \times z_{\mathrm{HF}}$ (see Fig. B.1b). Finally the amplitude is

$$A_\xi(m_\xi, \vartheta_{\mathrm{HF}}, \phi_{\mathrm{HF}}) = D^{J_\xi}_{0M_\xi}(\vartheta_{\mathrm{HF}}, \phi_{\mathrm{HF}}, 0)\sqrt{2l_\xi + 1}(I_1 I_2 I_{z1} I_{z2} | I_\xi I_{z_\xi}) F_{l_\xi} \Delta(m_\xi) \alpha_{\pi\pi}. \tag{6.13}$$

As both decay particles carry no spin the helicity difference $\lambda = 0$, leading to the fact that there is no summation and the spin-spin-coupling as well as the s-l-coupling is set to one. Two Clebsch-Gordan coefficients are possible for the isospin coupling, depending on the isobar. The dynamics $\Delta(m_\xi)$ is parametrised by Breit-Wigner forms or based on the K-matrix formalism (See Sec. 6.4.1 and 6.4.3).

6.3.1 t' Dependence of the Amplitude

The description of diffractive dissociation in Sec. 2.2.1 reveals a t'-dependence of the amplitude of the form $\exp(-b/2t')$. The observation of helicity amplitudes at small but non-zero scattering angles exhibit an additional dependency, namely $t'^{\lambda/2}$ for each two-body decay. The difference between the two helicities $\lambda = \lambda_1 - \lambda_2$ leads to a suppression of the resulting amplitude. For the 3π decay, parametrised by two decay amplitudes, this results in a total 'penalty' of $t'^{M/2}$, as the isobaric decay into two pions, both carrying no spin, does not contribute to this dependency. Summarising the t'-dependency of the 3π amplitude is

$$f_i(t') \sim t'^{M/2} \exp(-b\,t'/2) \tag{6.14}$$

which is the function $f(t')$, introduced in Sec. 6.1.
Figure 6.2 shows the behavior of this t' dependence in a kinematical range of $0 \geq t' \geq 1.5$ GeV$^2/c^2$ for $M = 0, 1, 2$ and a slope parameter of 9 which is a typical value for Pomeron mediated scattering on a proton. One of the goals of the COMPASS hadron campaign is the investigation of possible hybrid meson states. As seen in Tab. 6.1, a spin-exotic state with $J^{PC} = 1^{-+}$ and positive reflectivity can only be realised with spin projection $M = 1$. In order to increase the fraction of spin states with $M \geq 1$ in the data sample, the acceptance of the main trigger component, the RPD, was set to $t' > 0.08$ GeV$^2/c^2$, denoted by the green lines in the plots. Under the assumption that most of the amplitudes follow the just described t' dependence, a relative fraction of 83% of $M = 1$ states is within the t' range of 0.08 and 1.0 GeV$^2/c^2$ in contrast to 48% of $M = 0$ states.

[3]The possibility of double negative charged isobars was investigated, but not resonance structure was found

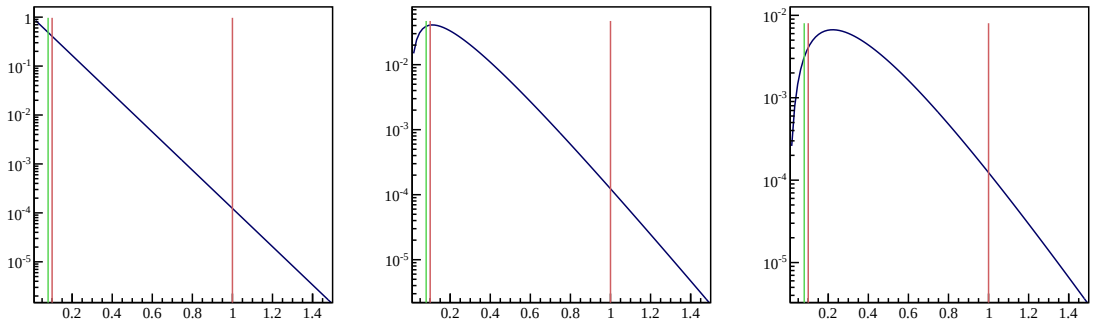

Figure 6.2 t' distributions for increasing spin projections M, starting left with $M = 0$. The green lines denote the acceptance of the RPD, the red lines corresponds to the kinematic region, focused in that analysis.

6.4 Parametrisation of the Isobar Dynamics

The formalism and parameters describing the isobar dynamic are of eminent importance for n-particle decays parametrised within the isobar model. In this section several formalisms are discussed and an overview of isobars used in the analysis is given.

6.4.1 Breit-Wigner Formalism

The mass-dependence of resonances, i.e. short-lived particles, is commonly described by the Breit-Wigner formalism [BW36]

$$A_{\mathrm{BW}}(m, m_0, \Gamma_0) = \frac{m_0 \Gamma_0}{m_0^2 - m^2 - i\, m_0 \Gamma_{\mathrm{tot}}(m)} \tag{6.15}$$

where m_0 and Γ_0 are the mass and the width of the resonance. The mass-dependent width $\Gamma_{\mathrm{tot}}(m)$ is

$$\Gamma_{\mathrm{tot}}(m) = \Gamma_0 \frac{m_0}{m} \frac{q}{q_0} \frac{F_l^2(q)}{F_l^2(q_0)}. \tag{6.16}$$

Here q denotes the break-up momentum of the resonance at mass m and $q_0 = q(m_0)$. The maximum orbital angular momentum, which can be obtained in a strong decay, is limited by the momentum q. If the break-up momentum is small, the two decay particles have difficulties to generate sufficient orbital angular momentum in order to conserve the spin [Asn03]. This is taken into account by the Blatt-Weisskopf centrifugal-barrier factors $F_l(q)$ [BW52] in the parametrisation of von Hippel and Quigg [VHQ72]. Instead of the original normalisation of the barrier factors such that $F_l(q) \to 1$ for $q \to \infty$, von Hippel and Quigg modified the normalisation in a way that $F_l(q) = 1$ for $z = 1$, where $z = (q/q_R)^2$ and $q_R = 0.1973$ GeV/c corresponding to 1 Fermi. Now the amplitude behaves like $A_{\mathrm{BW}} \sim p^l$ for small q. A list of the parametrisations of these barrier factors can be found in [Chu96].
The mass-dependent width $\Gamma_{\mathrm{tot}}(m)$ is the sum over the mass-dependent partial width of the different decay channels, Breit-Wigner parametrisations are best in use for non-overlapping, single narrow resonances far from the threshold of additional decay channels. In this analysis the above described formulation is used to describe some of the isobars, see Sec. 6.5 and to parametrise the dynamics of resonances, obtained by a fit of the 3π amplitudes, see Sec. 8.

6.4.2 Flatté Formalism

If a second decay channel opens close to the resonance, the Flatté formulation [F+76], in contrast to the Breit-Wigner form, gives a better description, as it takes the two decay modes into account:

$$A_{\text{Flatté}} = \frac{1}{m_0^2 - m^2 - i(\Phi_1 g_1^2 + \Phi_2 g_2^2)} \tag{6.17}$$

with $g_1^2 + g_2^2 = m_0 \Gamma_{\text{tot}}$. In this analysis the Flatté formula is used to parametrise the $f_0(980)$, as this resonance is right at the $K\bar{K}$ threshold. The two contributing couplings, determined by a partial wave analysis of J/ψ decaying into $\phi\pi^-\pi^+$ and ϕK^+K^- [ea05], are $g_{\pi\pi} = 0.165$ GeV/c^2 and $g_{KK}/g_{\pi\pi} = 4.21$.

6.4.3 K-Matrix Formalism

For heavily overlapping resonances, regarding the decay as well as the state itself, the K-matrix formulation is used. The previously introduced transition matrix T (see Sec. 2), can be written as

$$\mathbb{T} = (\mathbb{I} - i\mathbb{K}\Phi)^{-1}\mathbb{K} \tag{6.18}$$

where $\mathbb{K}$ is the Lorentz-invariant K-matrix and ρ the corresponding phase-space. This ansatz is used for the $(\pi\pi)_S$-wave, a combined parametrisation for scalar mesons below 1.5 GeV/c^2. Two solutions of a fit to $\pi\pi$ scattering data [AMP87] are applied to the analysis. The matrix elements of the K_1 solution are chosen in the form

$$K_{ij} = \frac{s - s_0}{4m_K^2} \sum_p \frac{f_i^p f_j^p}{(s_p - s)(s_p - s)} + \sum_{n=0}^{4} c_{ij}^n \left(\frac{s}{4m_K} - 1 \right)^n \tag{6.19}$$

The K_1 solution has one pole. The $f_0(980)$ is treated as a single isobar resonance in the analysis, but it is part of the K_1 fit, besides the $f_0(600)$ and the $f_0(1370)$, resulting as a dip, due to destructive interference in the $(\pi\pi)_S$ intensity. Thus the $f_0(980)$ amplitude, modeled in form of a relativistic Breit-Wigner, is subtracted from the $(\pi\pi)_S$ line-shape (see Fig. C.2):

$$A_{\pi\pi} \rightarrow A_{\pi\pi} - c \cdot A_{f_0(980)} \tag{6.20}$$

with $c = (-0.3878, 0.2991)$, $m_0 = 0.9855$ GeV/c^2 and $\Gamma_0 = 0.0449$ GeV/c^2. This Breit-Wigner parametrisation of the $f_0(980)$ is used for systematics studies, instead of the Flatté formalism. The $M-$fit, the second solution is based on the M-matrix, the inverse of the K-matrix

$$T = (\mathbb{M} - i\Phi)^{-1} \tag{6.21}$$

with its matrix elements

$$M_{ij} = \frac{a_{ij}}{s - s_0} + \sum_p \frac{f_i^{`p} f_j^{`p}}{s_p{`} - s} + \sum_{n=0}^{4} c_{ij}^{`n} \left(\frac{s}{4m_K^2} - 1 \right)^n \tag{6.22}$$

As the K_1 solution, the $M-$ansatz has one pole, but in contrast the $f_0(980)$ is not part of the resulting $(\pi\pi)_S$ amplitude by construction (see Fig. C.3).
Besides the $\rho(770)$, the PDG lists two additional resonances with $J^{PC} = 1^{--}$, the $\rho(1450)$ and

the $\rho(1700)$. A recent K-matrix fit to the reaction $J/\psi \to K^+K^-\pi^0$ [GMSS12] involves in a $\pi\pi_P$ wave, including only the $\rho(1700)$ in addition to the $\rho(770)$. The two channel K-matrix representation follows

$$\left[\mathbb{T}^{-1}(s)\right]_{\alpha\beta} = \left[\mathbb{K}^{-1}(s)\right]_{\alpha\beta} + \delta_{\alpha\beta}(s - s_\alpha)I_\alpha(s) \tag{6.23}$$

with the dispersion integral

$$I_\alpha(s) = I_\alpha(0) - \frac{s}{\pi}\int_{s_\alpha}^{\infty} ds' \sqrt{1 - \frac{s_\alpha}{s'}}\frac{1}{(s'-s)s'} \tag{6.24}$$

and $\alpha, \beta = \pi, K$ corresponding to the two channels $\pi\pi$ and KK. The subtraction constant $I_\alpha(0)$ is defined such, that $\Re I_\alpha(m_\rho^2) = 0$. Details for K-matrix elements and the fit parameters can be found in Fig. C.7 and [GMSS12].

Finally the constraints, which resonances can be used as isobars for this analysis, will be discussed. G-parity is multiplicative thus only resonances with $G = +1$ are allowed. The fact that only resonances decaying into two charged pions come into consideration causes in isospin singlets ($I = 0$) and triplets ($I = 1$). The rules, introduced in Sec. 6.1.1, are the basis for the construction of possible J^{PC} states, decaying into two pions ($J^{PC} = 0^{-+}$). Concluding the following $I^G J^{PC}$ quantum numbers are allowed for potential isobar candidates: $I^G J^{PC} = 0^+0^{++}, 1^+1^{--}, 0^+2^{++}, 1^+3^{--}, 0^+4^{++}, \ldots$ Table 6.2 gives an overview of all isobars ans their parametrisation, which are used in the different fits, discussed in the next chapters.

6.5 Amplitude Parametrisation for Fixed Three-Body Mass $m_{3\pi}$ and Fixed Four-Momentum Transfer t'

It is now possible to construct amplitudes with a complete description of the decay into three pions. Each partial wave is identified by a unique set of quantum numbers $I^G J^{PC} M^\varepsilon$ for the intermediate state X and $I^G_\xi J^{PC}_\xi L$, tagging the isobar ξ and the orbital angular momentum between the isobar and the spectator pion. It is convenient to abbreviate this nomenclature to a more handsome formulation of partial waves: $J^{PC} M^\varepsilon <$ isobar $> \pi L$.
As discussed at the beginning, it is favored to have the parametrisation as little model dependent as possible and to avoid assumptions where it is feasible. Therefore the amplitude parametrisation has to be modified.

- The mass dependence, described by Δ_X, can be set to 1, if the data are split in narrow bins of the invariant mass $m_{3\pi}$
- The t' dependence, parametrised by $f_i(t')$, can be set to 1, if the data are split in narrow t' bins
- The production amplitudes $C_i k$ are replaced by transition amplitudes T_i which absorb all unknown parameters. For the 3π final state this is the production amplitude, and coupling constants of the isobar decay vertex, $\alpha_{\pi\pi}$ and the coupling constant at the X decay vertex, $\alpha_{\pi\xi}$. The index i denotes individual partial waves, as introduced at the beginning of this section..

Isobar	**Parameter**	**Formalism**
$(\pi\pi)_S$ Wave	available at [AMP87]	"K_1-Solution" including $f_0(600)$ and $f_0(1370)$, $f_0(980)$ subtracted from amplitude, Details see Fig. C.2
$(\pi\pi)_S$ Wave	available at [AMP87]	"M-Solution" including $f_0(600)$ and $f_0(1370)$ Details see Fig. C.3
$f_0(980)$	$M_0 = 0.965$ GeV/c^2 $g_1 = 0.165$ GeV/c^2, $g_1/g_2 = 4.21$	Flatté formalism Details see Fig. C.5
$f_0(980)$	$M_0 = 0.98$ GeV/c^2 $\Gamma_0 = 0.04$ GeV/c^2	Breit-Wigner Details see Fig. C.4
$f_0(1500)$	$M_0 = 1.507$ GeV/c^2 $\Gamma_0 = 0.109$ GeV/c^2	Breit-Wigner Details see Fig. C.6
$(\pi\pi)_P$ Wave	available at [GMSS12]	K-Matrix including $\rho(770)$ and $\rho(1700)$ Details see Fig. C.7
$\rho(770)$	$M_0 = 0.770$ GeV/c^2 $\Gamma_0 = 0.161$ GeV/c^2	Breit-Wigner Details see Fig. C.8 and Fig. C.9
$\rho_3(1690)$	$M_0 = 1.688$ GeV/c^2 $\Gamma_0 = 0.161$ GeV/c^2	Breit-Wigner Details see Fig. C.11 and C.12
$f_2(1270)$	$M_0 = 1.275$ GeV/c^2 $\Gamma_0 = 0.185$ GeV/c^2	Breit-Wigner Details see Fig. C.10
$f_4(2050)$	$M_0 = 2.05$ GeV/c^2 $\Gamma_0 = 0.185$ GeV/c^2	Breit-Wigner Details see Fig. C.10

Table 6.2 Overview of the isobar parametrisations, applied to the analysis.

$$
\begin{aligned}
\psi_i^{\varepsilon}(\tau) = c(M)\Bigg[& \sum_{1,2}\sum_{\lambda} D^{J}_{\lambda M}(\vartheta_{\mathrm{GJ}},\phi_{\mathrm{TY}},0)\sqrt{L+1}(L0S\lambda|J\lambda)(S_\xi\lambda_\xi 00|S\lambda)\frac{1}{\sqrt{2}}F_L\cdot \\
& D^{I_\xi}_{0M_\xi}(\vartheta_{\mathrm{HF}},\phi_{\mathrm{HF}},0)\sqrt{2l_\xi+1}(I_1I_2I_{z1}I_{z2}|I_\xi I_{z_\xi})F_{l_\xi}\Delta(m_\xi) \\
-\varepsilon P(-1)^{J-M}\Bigg(& \sum_{1,2}\sum_{\lambda} D^{J}_{\lambda(-M)}(\vartheta_{\mathrm{GJ}},\phi_{\mathrm{TY}},0)\sqrt{L+1}(L0S\lambda|J\lambda)(S_\xi\lambda_\xi 00|S\lambda)\frac{1}{\sqrt{2}}F_L\cdot \\
& D^{I_\xi}_{0M_\xi}(\vartheta_{\mathrm{HF}},\phi_{\mathrm{HF}},0)\sqrt{2l_\xi+1}(I_1I_2I_{z1}I_{z2}|I_\xi I_{z_\xi})F_{l_\xi}\Delta(m_\xi)\Bigg)\Bigg]
\end{aligned}
\tag{6.25}
$$

Summarising the observed intensity for each mass and t' bin can be set up as

$$\mathscr{I}(\tau) = \sum_{r=1}^{N_r} \sum_{\varepsilon=\pm 1} \left| \sum_i T_{ir}^{\varepsilon} \psi_i^{\varepsilon}(\tau) \right|^2 \tag{6.26}$$

And the corresponding cross section is

$$\sigma(\tau) = \sigma_0 \cdot \mathscr{I}(\tau) \tag{6.27}$$

with an unknown constant factor σ_0.

Quantum Numbers $I^G J^{PC} M^{\varepsilon}$ of the state X	**Quantum Numbers $I^G J^{PC}$ of the isobar ξ**	**Orbital Angular Momentum L**
$1^-0^{-+}0^+$	0^+0^{++}	S
	1^+1^{--}	P
	0^+2^{++}	D
	1^+3^{--}	F
$1^-1^{++}0^+, 1^-1^{++}1^+$	0^+0^{++}	P
	1^+1^{--}	S, D
	0^+2^{++}	P, F
	1^+3^{--}	D, G
$1^-1^{-+}1^+$	1^+1^{--}	P
	0^+2^{++}	D
	1^+3^{--}	F
$1^-2^{++}1^+, 1^-2^{++}2^+$	1^+1^{--}	D
	0^+2^{++}	P, F
	1^+3^{--}	D, G
$1^-2^{-+}0^+, 1^-2^{-+}1^+, 1^-2^{-+}2^+$	0^+0^{++}	D
	1^+1^{--}	P, F
	0^+2^{++}	S, D, G
	1^+3^{--}	P, F, H

Table 6.3 Possible $J^{PC} M^{\varepsilon} \xi \pi L$ partial waves.

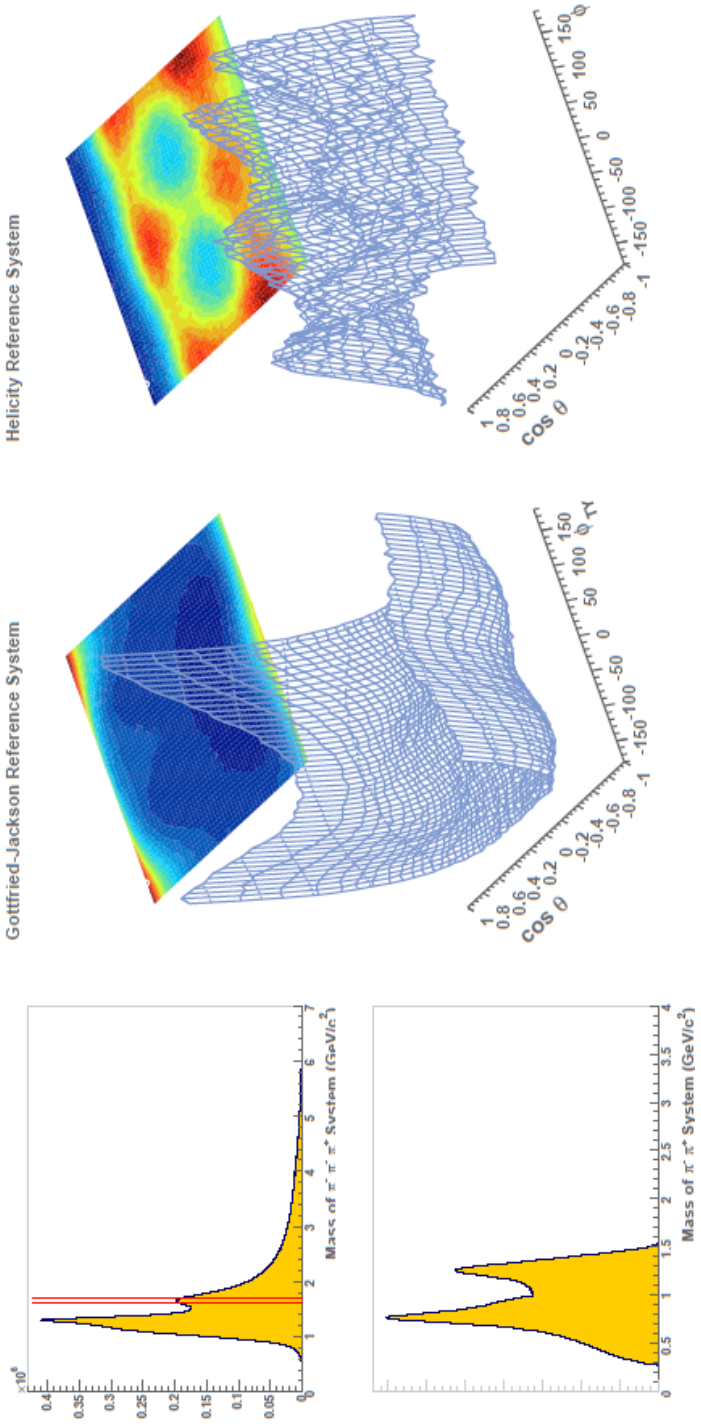

Figure 6.3 Overview of the kinematical variables τ, used to describe the 3π final state for a given mass $m_{3\pi}$. As an example m_X was chosen to be at 1.6 Gev/c^2, as seen in the top left histogram. The corresponding 2π mass is shown below. Several structures are visible, indicating the possibility of decays into the $(\pi\pi)_S$ wave, the $\rho(770)$ and the $f_2(1270)$. The shoulder at 1 GeV/c^2 gives hint for a possible decay into the $f_0(980)$. The two right plots present the angular distributions for this mass bin. The first plots shows the two angles, describing the decay of the intermediate state X into an isobar and a bachelor pion in the Gottfried-Jackson frame, while the right plot shows the angular distributions of the 2π state.

Chapter 7

Decomposition in Amplitudes for Fixed Mass $m_{3\pi}$ and Squared Four-Momentum Transfer t'

Once a proper data sample is selected and the mathematical framework is set up, the next logical step follows: The decomposition of the data set into partial-wave amplitudes, in order to identify the contributions to the overall intensity distribution. First of all an appropriate fit method and an associated complete model has to be constructed. The completeness of the fit model assures an objective and realistic description of the data. This is from very importance for the following discussion of the fit results and will be explained in detail. The major part is the presentation of the outcome of the fit. The unique amount of data and the resulting high degrees of fineness of the amplitude distributions offers unprecedented details of the reaction of interest. This will be complemented by comparative analyses with the 2009 data and results of an amplitude analyses with the Deck Monte Carlo data set. Finally, different systematic studies will be discussed in order to give an overview of the reliability of the model and its unavoidable bias.

7.1 Spin-Parity Analysis in Bins of Mass and t'

The mathematical foundation (a profound derivation can be found in [Bar90]) and the concept of a amplitude decomposition is presented. This includes acceptance studies and the determination of a realistic model, in order to describe the overall intensity distribution.

7.1.1 The Principle of an Extended Maximum Likelihood Estimation

An observed data set of an experiment in particle physics can be described as a sample of N_{obs} independent and identically distributed (iid[1]) random variables $\{x_1, ..., x_{N_{\text{obs}}}\}$, distributed according to a probability density function (pdf) $\hat{f}(x_i|a_1, ..., a_k)$. This function which belongs to a family of distributions, called the finite-dimensional model, can be described by a finite set

[1] a set of random variables is independent and identically distributed if each random variable has the same probability distribution and all are correlative independent

of unknown, constant parameters $\{a_1,...,a_k\}$ and depends on the set of variables $\{x_1,...,x_{N_{\text{obs}}}\}$. The *pdf* is normalized, so that the integral over the whole range x is entity.

$$\int dx\, \hat{f}(x|a_1,...,a_k) = 1 \tag{7.1}$$

The overall probability of the entire set of data points is given by the joint probability distribution, which can be calculated for iid variables as

$$\hat{f}(x_1,...,x_{N_{\text{obs}}}|a_1,...,a_k) = \prod_{i=1}^{N_{\text{obs}}} \hat{f}(x_i|a_1,...,a_k) \tag{7.2}$$

The fact that the measured values x_i are known, but the set of parameters a_j are not, brings up the concept of *likelihood*. In contrast to *pdf*s, likelihood functions depend on the unknown parameters a_j and are characterised by the observed and thus constant set of data points x_i.

$$\hat{\mathcal{L}}(a_1,...,a_k|x_1,...,x_{N_{\text{obs}}}) = \prod_{i=1}^{N_{\text{obs}}} \hat{f}(x_i|a_1,...,a_k) \tag{7.3}$$

The parameters can be estimated by maximizing the likelihood function resulting in a set of k solutions for the equation set

$$\frac{\partial\, \hat{\mathcal{L}}(a_1,...,a_k|x_1,...,x_{N_{\text{obs}}})}{\partial\, a_j} = 0, \qquad \forall j \tag{7.4}$$

An Extended Likelihood Function

Breaking up the normalisation of $\hat{f}$ leads to the unnormalised probability density function f and Eq. (7.1) can now be written as

$$\int dx\, f(x|a_1,...,a_k) = N_{\text{exp}}(a_i,...,a_k) \tag{7.5}$$

With N_{exp} the total number of expected events. This number must not be mixed with N_{obs}, the number of actual observed events, introduced in the beginning. If the events occur randomly, as it it the case for diffractive events in phase space, they are distributed according to the Poisson distribution. For that case the probability of the occurrence of m events in the interval w, and taking into account the average number of occurrences per unit interval g, is

$$P_w(m) = \frac{(g\cdot w)^m}{m!} e^{-g\cdot w} \tag{7.6}$$

Applying the Poisson probability function to the specific problem discussed here gives

$$P_{N_{\text{exp}}}(N_{\text{obs}}) = \frac{N_{\text{exp}}^{N_{\text{obs}}}}{N_{\text{obs}}!} e^{-N_{\text{exp}}} \tag{7.7}$$

The possibility of fluctuations of events in phase space is considered by multiplying the Poisson probability[2] to the likelihood function (7.3) resulting in the extended likelihood $\mathcal{L}$

$$\mathcal{L} = P_{N_{\text{exp}}}(N_{\text{obs}})\cdot \hat{\mathcal{L}} = \frac{N_{\text{exp}}^{N_{\text{obs}}}}{N_{\text{obs}}!} e^{-N_{\text{exp}}} \prod_{i=1}^{N_{\text{obs}}} \hat{f}(x_i|a_1,...,a_k) \tag{7.8}$$

[2]For the huge amount of events, analysed in the 2008 data set, the Poisson distribution converges to a Gaussian one.

Regarding Eq. (7.1) and Eq. (7.5) offers the feasibility to connect the normalised density function $\hat{f}$ with the unnormalised one f

$$f(x|a_1,...,a_k) = N_{\text{exp}} \hat{f}(x|a_1,...,a_k) \tag{7.9}$$

Finally the *extended likelihood* can be written

$$\mathcal{L}(a_1,...,a_k|x_1,...,x_{N_{\text{obs}}}) = \frac{e^{-N_{\text{exp}}}}{N_{\text{obs}}!} \prod_{i=1}^{N_{\text{obs}}} f(x_i|a_1,...,a_k) \tag{7.10}$$

Equation (7.10) is the stencil which will be used to construct a fit function in order to disentangle the various amplitude contributions to the overall intensity.

7.1.2 An Extended Log-Likelihood Fit Formalism

Based on the mathematical concept, introduced in the previous section, it is now possible to develop a fit formalism for the amplitude analysis, discussed in this thesis. The starting point is the formula (see Eq. (6.26)) for the observed intensity $\mathscr{I}$ in a bin of $m_{3\pi}$ and t' with the parametrisation, proposed by Chung and Truemann [CT75]:

$$\mathscr{I}(\tau|T) = \sum_{r=1}^{N_r^\varepsilon} \sum_{\varepsilon=\pm 1} \left| \sum_a T_{ar}^\varepsilon \psi_a^\varepsilon(\tau) \right|^2 \tag{7.11}$$

The summation over the rank allows the fit to take the corresponding partial waves (equivalent in this thesis is the notion 'amplitude') several times into account, every time with different non-interfering complex transition amplitudes. From the physical point of view this can be seen as the consideration of several non-interfering production processes. The introduction of the reflectivity ε as additional quantum number (see Sec. 6.1.2) takes the parity conservation into account and thus the naturality of the Regge trajectory. Final state amplitudes with different reflectivities cannot interfere and are added incoherently, taken into account by the summation outside the square.
Previously discussed in Chap. 6, it is obvious for practical reasons that in contrast to theory, the number of amplitudes, building up the wave set, is limited. Even for an unique large wave set, as applied to this analysis (see Sec. 7.2) it is possible, that the fit will not be able to identify the contributions of some events to the overall intensity. In addition not all three-pion final-state events originate from diffractive dissociation due to miss-identification of tracks during reconstruction (see Sec. 7.1.3) or events decay directly into three pions, without the intermediate step of a decay into an isobar and bachelor pion. For these kind of events an extra amplitude is introduced. The *Flat* amplitude is isotropic in phase space and added incoherently to the observed intensity

$$\mathscr{I}(\tau|T) = \sum_{r=1}^{N_r^\varepsilon} \sum_{\varepsilon=\pm 1} \left| \sum_a T_{ar}^\varepsilon \psi_a^\varepsilon(\tau) \right|^2 + A_{\text{Flat}}^2 \tag{7.12}$$

Technically it makes no difference to treat this special amplitude like the incoherent sum of different reflectivities. Hence for simplicity the Flat wave is considered for the following discussion as an amplitude with an additional reflectivity value and is implemented in the corresponding sum

$$\mathscr{I}(\tau|T) = \sum_{r=1}^{N_r^\varepsilon} \sum_{\varepsilon} \left| \sum_a T_{ar}^\varepsilon \psi_a^\varepsilon(\tau) \right|^2 \tag{7.13}$$

At this point of the discussion it is necessary to introduce the concept of an *anchor wave*. The biggest caveat of production experiments is the ignorance of the initial state. Thus it is not possible to measure absolute phases only relative phase motions between two amplitudes can be investigated. The fit must be constrained in a way that the interference between two waves can be compared, i.e. the interferences must be aligned to a common zero phase. A solution is to select an arbitrary wave of the fit model which is known to have a relative large intensity over the complete mass range. The corresponding complex transition amplitude T_i is then forced to be real which accord to zero phase in the complex plane. The transition amplitudes of all other waves are now defined relative to this wave.

The total number of expected events N_{exp} is determined by the integral of Eq. (7.13) over the full three-body phase space (the number of dimensions here is only valid for a three particle decay, see Sec. 6.2), with $d\Phi_{3\pi}(\tau)$ the phase space differential

$$N_{\text{exp}}(T) = \int d\Phi_{3\pi}(\tau)\mathscr{I}(\tau|T) \tag{7.14}$$

But again the reality has to be taken into account and this formula is only valid for a perfect system, i.e. full efficient detector systems, covering the complete phase space and an absolute perfect reconstruction framework. In order to consider inefficiencies and 'blind spots' of the complete data taking, the *acceptance* $\eta(\tau)$ is introduced, as a function of the set of decay variables τ. Thus Eq. eq7.14 reads as follows

$$N_{\text{exp}}(T) = \int d\Phi_{3\pi}(\tau)\mathscr{I}(\tau|T)\eta(\tau) \tag{7.15}$$

Recalling Eq. (7.5) the product $\mathscr{I}(\tau|T)\eta(\tau)$ can be identified as an unnormalised probability density function $f(x|a_1,...,a_k)$. With (7.10) the according likelihood function can now be written as

$$\mathcal{L}(T|\tau_1,...,\tau_{N_{\text{obs}}}) = \frac{e^{-N_{\text{exp}}}}{N_{\text{obs}}!}\prod_{i=1}^{N_{\text{obs}}}\mathscr{I}(\tau_i|T)\eta(\tau_i) \tag{7.16}$$

The technical goal of an amplitude analysis is the determination of a set of transition amplitudes T which satisfies the density function. As mentioned in the previous section the method of choice is to maximize the likelihood. In order to find the maximum for each transition amplitude first and second derivatives have to be calculated. Hence and due to the fact that N_{obs} and N_{exp} are large, it is more convenient for the computation to use the natural logarithm of the likelihood instead of the pure likelihood itself. The logarithm is a monotonically increasing function thus the maxima remain unchanged. Summarising the fit procedure is called *extended maximum likelihood estimation*. Resuming the logarithm laws and dropping the factor $1/N_{\text{obs}}$, as it is constant and irrelevant for the evaluation of derivatives, Eq. (7.16) transforms to

$$\ln\mathcal{L} = \sum_{i=1}^{N_{\text{obs}}}\ln\eta(\tau_i) + \sum_{i=1}^{N_{\text{obs}}}\ln\mathscr{I}(\tau_i|T) - N_{\text{exp}} \tag{7.17}$$

The sum over the acceptance is again a constant and can be dropped. Inserting Eq. (7.13) and (7.15) gives

$$\ln\mathcal{L} = \sum_{i=1}^{N_{\text{obs}}}\ln\left[\sum_{r=1}^{N_r^\varepsilon}\sum_{\varepsilon}\left|\sum_a T_{ar}^\varepsilon\psi_a^\varepsilon(\tau_i)\right|^2\right] - \int d\Phi_{3\pi}(\tau)\eta(\tau)\sum_{r=1}^{N_r^\varepsilon}\sum_{\varepsilon}\left|\sum_a T_{ar}^\varepsilon\psi_a^\varepsilon(\tau)\right|^2 \tag{7.18}$$

Expanding both squares of the absolute values and reshuffling the components in terms of known and unknown fraction brings Eq.7.18 in the following form

$$\ln \mathcal{L} = \sum_{i=1}^{N_{\text{obs}}} \ln \left[\sum_{\varepsilon} \sum_{ab} \psi_a^{\varepsilon}(\tau_i) \psi_b^{\varepsilon *}(\tau_i) \sum_{r=1}^{N_r^{\varepsilon}} T_{ar}^{\varepsilon} T_{br}^{\varepsilon *} \right] - \sum_{\varepsilon} \sum_{ab} \int d\Phi_{3\pi}(\tau) \eta(\tau) \psi_a^{\varepsilon}(\tau) \psi_b^{\varepsilon *}(\tau) \sum_{r=1}^{N_r^{\varepsilon}} T_{ar}^{\varepsilon} T_{br}^{\varepsilon *} \tag{7.19}$$

The sum over all events in the first term is computationally very expensive, regarding the large number of events of modern spectroscopy data sets. In addition several fit attempts are usually necessary in order to determine the global maximum of the fit function. Therefore it is an advantage that the complete information for the calculation of decay amplitudes $\psi_q^{\varepsilon}(\tau_i)\psi_s^{\varepsilon *}(\tau_i)$ for each event is in the data and these products can be pre-calculated before the maximisation. The same is true for the integral in the second term. Its purpose is to illuminate the whole phase space of the reaction and and to take the acceptance into account, leading to the notion of *normalisation integrals*. For the calculation of the integral the same Monte Carlo events are used, as introduced in Sec. 5.3. The integral is approximated by a sum over the Monte Carlo events, whose number must be significantly larger than the number of real events, in order to ensure coverage of almost the whole phase space volume V.

$$\int d\Phi_{3\pi}(\tau) \eta(\tau) \psi_a^{\varepsilon}(\tau) \psi_b^{\varepsilon *}(\tau) \equiv I A_{ab}^{\varepsilon} \approx \frac{V}{N_{\text{MC}}} \sum_{j=1}^{N_{\text{MC}}} \eta(\tau_j) \psi_a^{\varepsilon}(\tau_j) \psi_b^{\varepsilon *}(\tau_j) \tag{7.20}$$

As mentioned before the calculation of the integrals can be carried out in advance of the fit.

Normalisations and Spin-Density Matrices

The individual contribution of the amplitudes to the overall intensity ranges from $\mathcal{O}(10)\%$ to $\mathcal{O}(0.1)\%$ as one will see later in the discussion of the fit results. In order to stabilize the fit and in particular the calculation of the error matrix, the decay amplitudes are normalised such that a common scale is established. For this purpose *phase space integrals* are calculated similar as in Eq. (7.20), but without taking the acceptance into account and only the diagonal terms are relevant.

$$I_{aa}^{\varepsilon} = \frac{V}{N_{\text{MC}}} \sum_{j=1}^{N_{\text{MC}}} \psi_a^{\varepsilon}(\tau_j) \psi_a^{\varepsilon *}(\tau_j) \tag{7.21}$$

The normalisation of a decay amplitude is then

$$\overline{\psi}_a^{\varepsilon}(\tau) \equiv \frac{\psi_a^{\varepsilon}(\tau)}{\sqrt{I_{aa}^{\varepsilon}}} \tag{7.22}$$

and accordingly the normalisation integrals are transformed

$$\overline{IA}_{ab}^{\varepsilon} = \frac{I A_{ab}^{\varepsilon}}{\sqrt{I_{aa}^{\varepsilon} I_{bb}^{\varepsilon}}} \tag{7.23}$$

The introduction of this normalisation implicates that the products of the transition amplitudes $T_a^{\varepsilon} T_b^{\varepsilon *}$ have now a straight forward interpretation. These product terms, taking into account the summation over their respective ranks, build up the *spin-density matrix*

$$\rho_{ab}^{\varepsilon} = \sum_{r}^{N_r^{\varepsilon}} T_a^{r\varepsilon} T_b^{r\varepsilon *} \tag{7.24}$$

The introduction of the reflectivity ε leads to an enormous simplification of the spin-density matrix. As mentioned earlier amplitudes with different reflectivities cannot interfere by construction. The matrix for a particular reflectivity is constructed such

$$\rho^{\varepsilon} = \begin{pmatrix} T_1^{\varepsilon} T_1^{\varepsilon *} & T_1^{\varepsilon} T_2^{\varepsilon *} & \dots \\ & T_2^{\varepsilon} T_2^{\varepsilon *} & \dots \\ & \dots & \dots \end{pmatrix} \tag{7.25}$$

Therefore the overall spin-density matrix has a block-diagonal form and reads adopted for this analysis as

$$\rho = \begin{pmatrix} \text{Flat} & 0 & 0 \\ 0 & \rho^{+1} & 0 \\ 0 & 0 & \rho^{-1} \end{pmatrix} \tag{7.26}$$

Summarising the fit function (Eq. (7.19)) for each individual bin of m_x and t' can now be simplified

$$\ln \mathcal{L} = \sum_{i=1}^{N_{\text{obs}}} \ln \left[\sum_{\varepsilon} \sum_{ab} \overline{\psi}_a^{\varepsilon}(\tau_i) \overline{\psi}_b^{\varepsilon *}(\tau_i) \rho_{ab}^{\varepsilon} \right] - \sum_{\varepsilon} \sum_{ab} \rho_{ab}^{\varepsilon} \overline{IA}_{ab}^{\varepsilon} \tag{7.27}$$

It is important to recall that this function does not incorporate any model assumption about the dependence on $m_{3\pi}$ and t' as anticipated (see Chap.6).

For the maximisation of the log-likelihood a modified version of the `MINUIT` program [Jam] is used. This software package contains several algorithms to minimise a given function, thus the negative of the log-likelihood is computed. It is worth mentioning, that the resulting absolute value of the likelihood has no interpretation, only the comparison between two fit iterations based on the same model and the same data set, gives a handle to identify the best of both fits. One feature of a maximum likelihood estimation is that the fit can give no goodness of fit measure. It is likely that during the minimizing process a local minimum of the fit function is determined and assumed to be the best likelihood but does not describe the data at all. In order to circumvent that problem several fit attempts with random start parameters are performed to each bin (of $m_{3\pi}$ and t'). For the final analysis 30 individual fits were undertaken per bin.

Error Propagation

The correct way to calculate the statistical errors of the resulting transition amplitudes T_{ar}^{ε} is to determine the inverse of the Fisher information matrix evaluated at the *maximum likelihood estimators*, i.e. the points where the fit function $\ln \mathcal{L}$ is supposed to have its global maximum. The Fisher information matrix element is

$$\mathscr{F}_{ab}(T) = -E \left[\frac{\partial^2 \ln L}{\partial T_a \partial T_b} \right] \tag{7.28}$$

Eq. (7.28) can be interpreted as the negative of the expectation value of the Hessian matrix, determined at the maximum likelihood. In [EH78] it is argued that the observed information (obtained by the Hessian matrix) should be used in favor to the expected information. This is only valid when the maximum likelihood estimates are assumed to be distributed asymptotically normal, which is the case for a large data sample like the ones discussed in this thesis.

Thus the inverse of the negative Hessian matrix results in the covariance matrix of the fit function with the transition amplitudes as its variables

$$\mathrm{Cov}(T) = -\begin{pmatrix} \frac{\partial^2 \ln L}{\partial T_1 \partial T_1} & \frac{\partial^2 \ln L}{\partial T_1 \partial T_2} & \dots \\ \dots & \frac{\partial^2 \ln L}{\partial T_2 \partial T_2} & \dots \\ & \dots & \dots \end{pmatrix}^{-1} \tag{7.29}$$

The 1σ statistical error for a single amplitude T_a is the square root of the respective diagonal element of the covariance matrix

$$\sigma_a = \sqrt{\mathrm{Cov}(T_a, T_a)} \tag{7.30}$$

The spin-density matrix consists not only of diagonal elements and thus the error calculation of the mixing terms and the error propagation of the observables (see Sec.7.1.4) has to be considered. A nice introduction to this topic can be found in [Neu12].

7.1.3 Acceptances

Unavoidable imperfections have to be taken into account, by the construction of a mathematical tool to investigate the data sample (see Eq. (7.15)). The size of the data set reduces the statistical errors such that systematic and acceptance are dominating, in contrast to previous analyses. It is eminent to control the systematics (see Sec. 7.6) as well as to understand acceptance effects occurring in different fields of the analysis. The main source of deficiencies coming from the spectrometer, precisely from the contributions of the respective detector components. A realistic Monte Carlo setup of the whole spectrometer, as it was used for the data taking is an indispensable basis. With this model characteristics of the spectrometer and its components can be investigated. Parts of the results of these studies were already discussed in Sec. 5.3, namely resolutions of the setup for specific kinematic variables as a function of $m_{3\pi}$ and t'. The acceptance of the spectrometer is the other important outcome of these studies. Another possible source of loss is the reconstruction software and its contribution to the overall acceptance must be taken into account. Thus the Monte-Carlo generated events are guided through the simulation of the spectrometer and reconstructed with the same software revision used for the real-data production (details can be found in App. D).
In order to obtain the acceptance, the reconstructed Monte Carlo events are passed through the event selection, discussed in Sec. 5.1, with two exceptions: the selection on the invariant three-pion mass $m_{3\pi}$ and the squared four-momentum transfer t' is ignored. In this way the bin migration, which comes from the finite resolutions of the spectrometer, is circumvented for the two kinematic variables, which are divided into bins for this analysis. The final acceptance is then the ratio of accepted Monte Carlo truth events over all generated events. As well as the investigation of resolutions and the final decomposition of the intensity distribution, the acceptance has to be surveyed as a function of $m_{3\pi}$ and t'. A striking property of the COMPASS acceptance is the almost flat distribution indicating an uniform detector coverage of the observed kinematic range for the three-pion channel. This regularity is unprecedented in respect to former experiments studying this reaction.

Figure 7.1 shows the two-dimensional acceptance of the both characterising variables $m_{3\pi}$ and t'. A small drop of the acceptance at small masses and independent from t' can be observed. It could be identified as a feature of the track reconstruction right after the target. Events with small masses correspond to low breakup momenta and thus leaving the target under small angles. The only capable detectors after the target region and in front of the first bending magnet are the two silicon stations and with a worse resolution the first PixelGEM. It was found that the track reconstruction merges two hits in the silicon detectors, which are close together and thus reconstructs only one instead of two tracks. As visible in Fig. 7.1 this happens only at small masses, below the resonance region, starting at ~ 1 GeV/c^2.

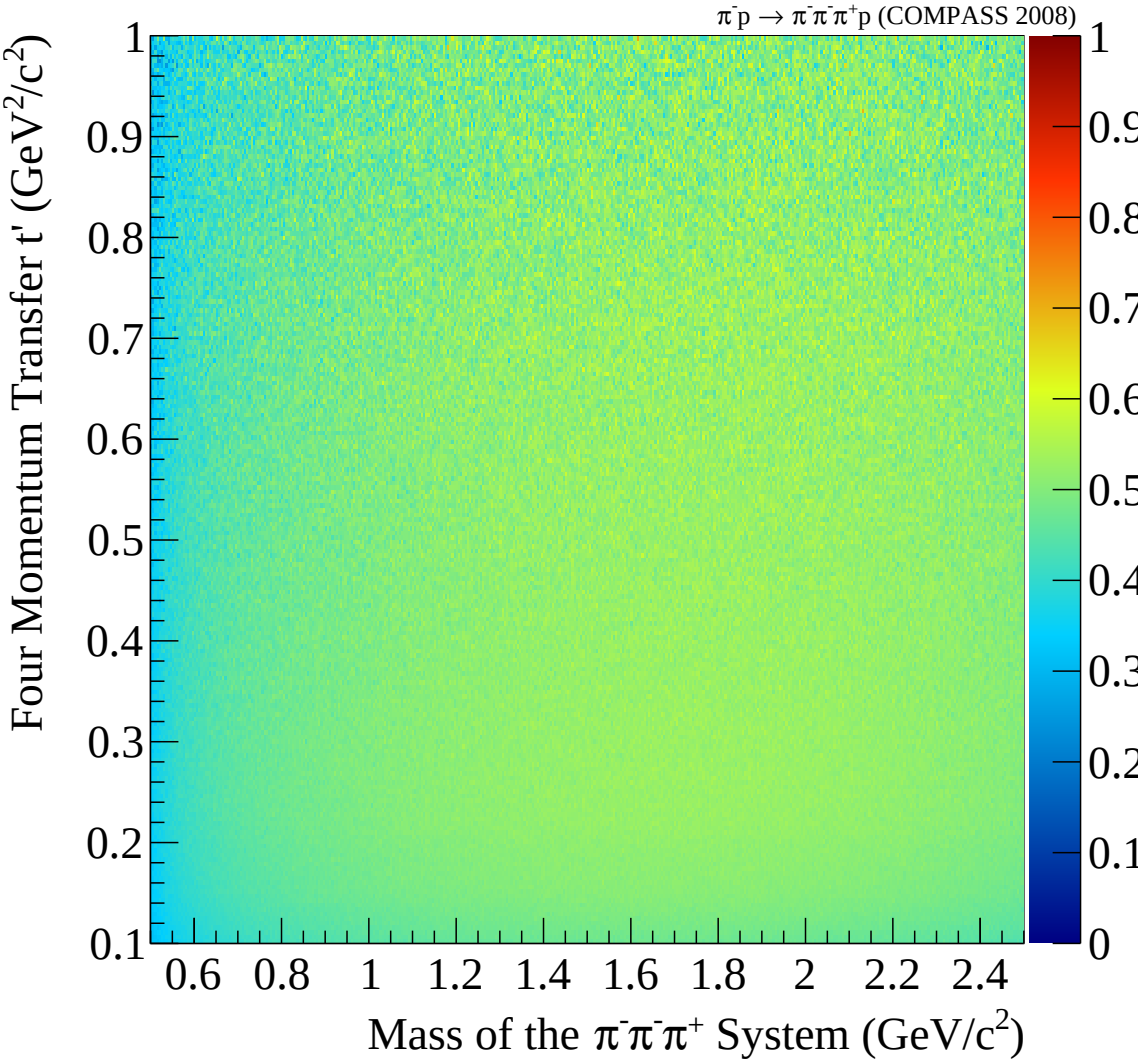

Figure 7.1 Two-dimensional acceptance as a function of the invariant mass $m_{3\pi}$ and the squared four-momentum transfer t'.

The acceptance in the two-pion mass is depicted in Fig. 7.2 as a function of $m_{3\pi}$ and t'. The available phase space is getting larger with increasing mass $m_{3\pi}$, thus the upper limit of the two-pion mass spectra is dependent on $m_{3\pi}$. The distributions are flat and show no significant structures. The small spike visible in the plot at high $m_{3\pi}$ and small t' is an artifact of the event selection for a single event and does not harm the overall acceptances. The shoulder in all four plots at smallest $m_{3\pi}$ are an indirect result of the three-pion acceptance (see Fig. 7.1). The decreasing acceptance at the upper limit of each $m_{3\pi}$ spectrum is an direct result of the track reconstruction.

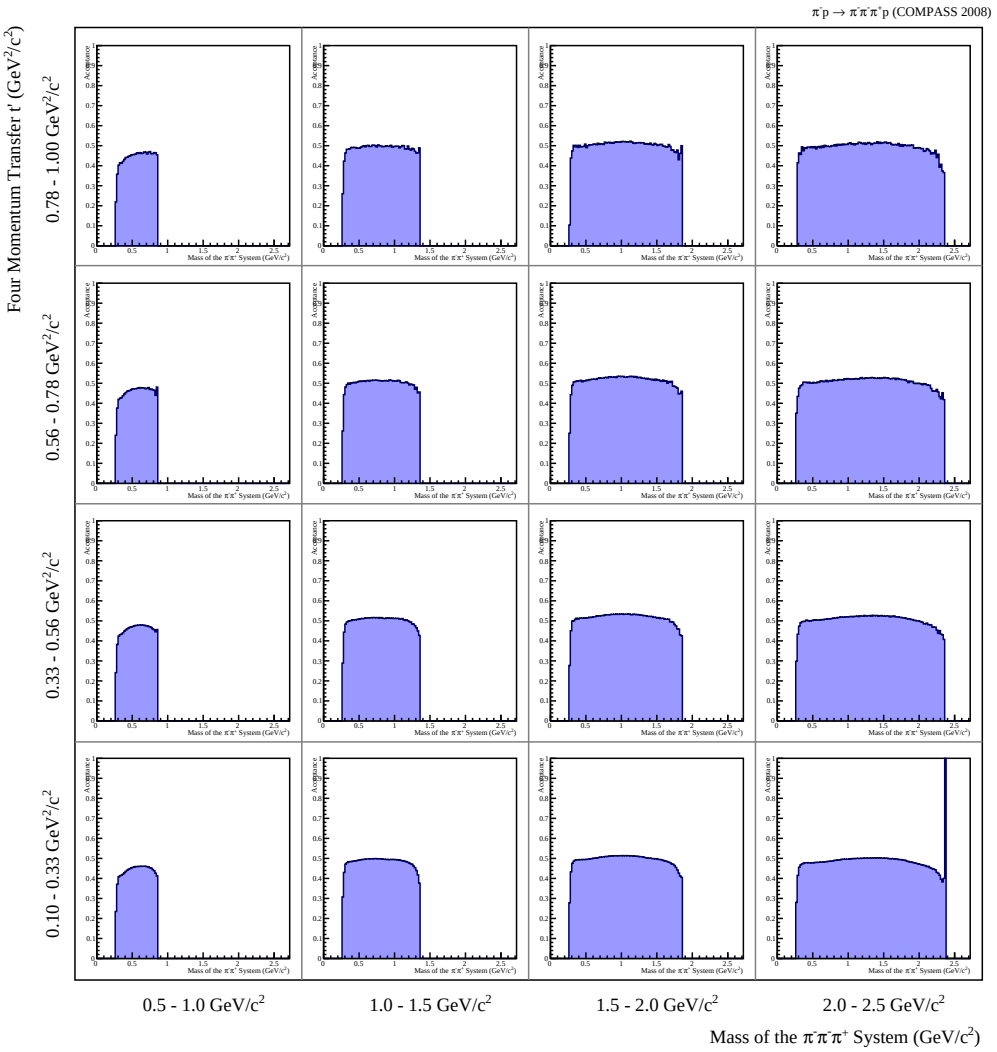

Figure 7.2 Acceptances of the two-pion mass as a function of $m_{3\pi}$ and t'.

The two-dimensional acceptance of the angular variables describing the isobar orientation in the Gottfried-Jackson reference frame as a function of $m_{3\pi}$ and t' is plotted in Fig. 7.3. As far as known this kind of representation was never used before for previous analyses. It allows to investigate the acceptance of the decay distribution in four dimensions. Each plot represents the acceptance of $\cos\vartheta_{\mathrm{GJ}}$ (x-axis) against the corresponding Treiman-Young angle ϕ_{TY} for a certain region of $m_{3\pi}$ and t'. Due to the indistinguishability of the two negative pions, both $\pi^-\pi^+$ combinations are taken into account. A small but nevertheless visible drop of the acceptance can be observed in all 16 plots for $\phi_{\mathrm{TY}} \approx 0$. While it is distributed like an ellipse for low masses it moves towards the upper limit of $\cos\vartheta_{\mathrm{GJ}}$ for large masses. In addition the position of the dip varies with t'. It is difficult to identify the origin of such effects, observed in a certain center-of-mass reference system, in the laboratory frame. The position of this drop, mostly at the limits of $\cos\vartheta_{\mathrm{GJ}}$ and around zero for ϕ_{TY}, suggests that the bachelor pion could be lost by the reconstruction. However, the modulation of the acceptance is small and looking at one-dimensional projections, integrated over t' and $m_{3\pi}$, the usual way of representation, the acceptance can be regarded as flat.

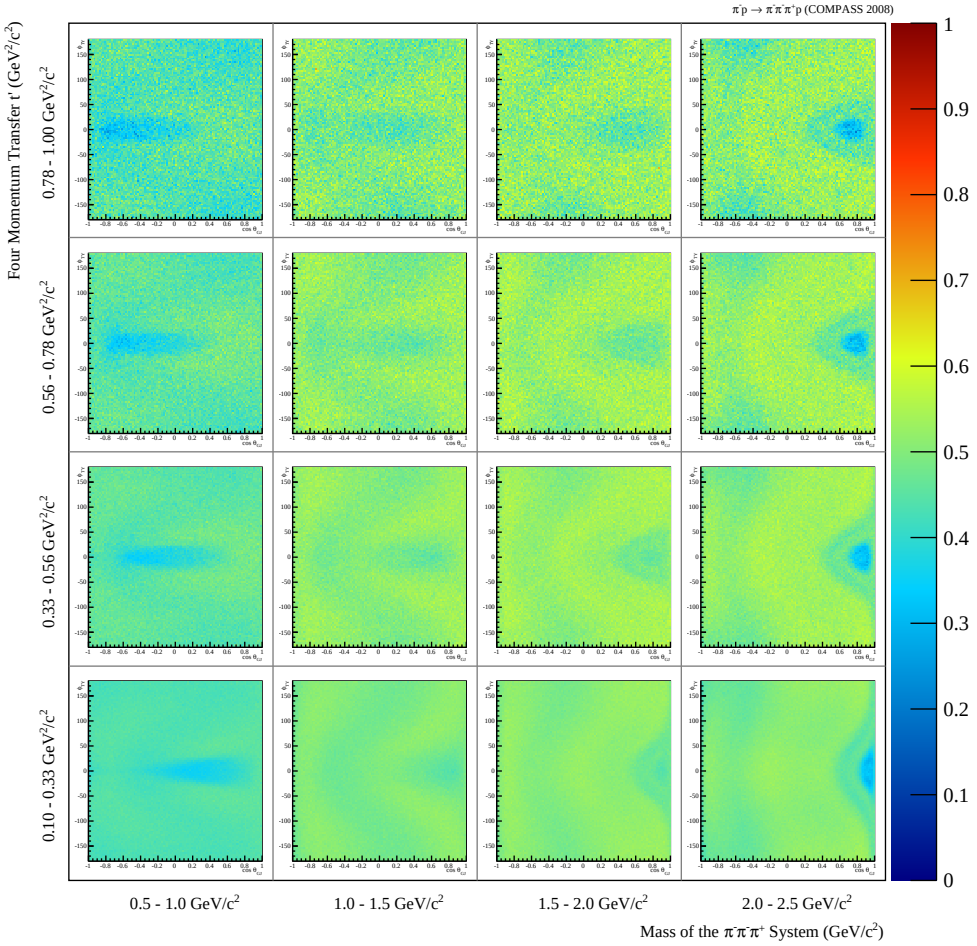

Figure 7.3 Two-dimensional acceptances of the two decay angles observed in the Gottfried-Jackson reference frame as a function of $m_{3\pi}$ and t'.

The same kind of representation is used for the variables, describing the decay of the isobar in the helicity reference frame. The two-dimensional acceptance, with $\cos\vartheta_{\mathrm{HF}}$ on the x-axis and ϕ_{HF} on the y-axis are plotted for 16 different regions of $m_{3\pi}$ and t'. Only little variations, independent from both variables, can be observed as symmetry of the ϕ_{HF}-angle, clustering at large values of ϕ_{HF}. Just like the previous representation both $\pi^-\pi^+$ combinations are taken into account.

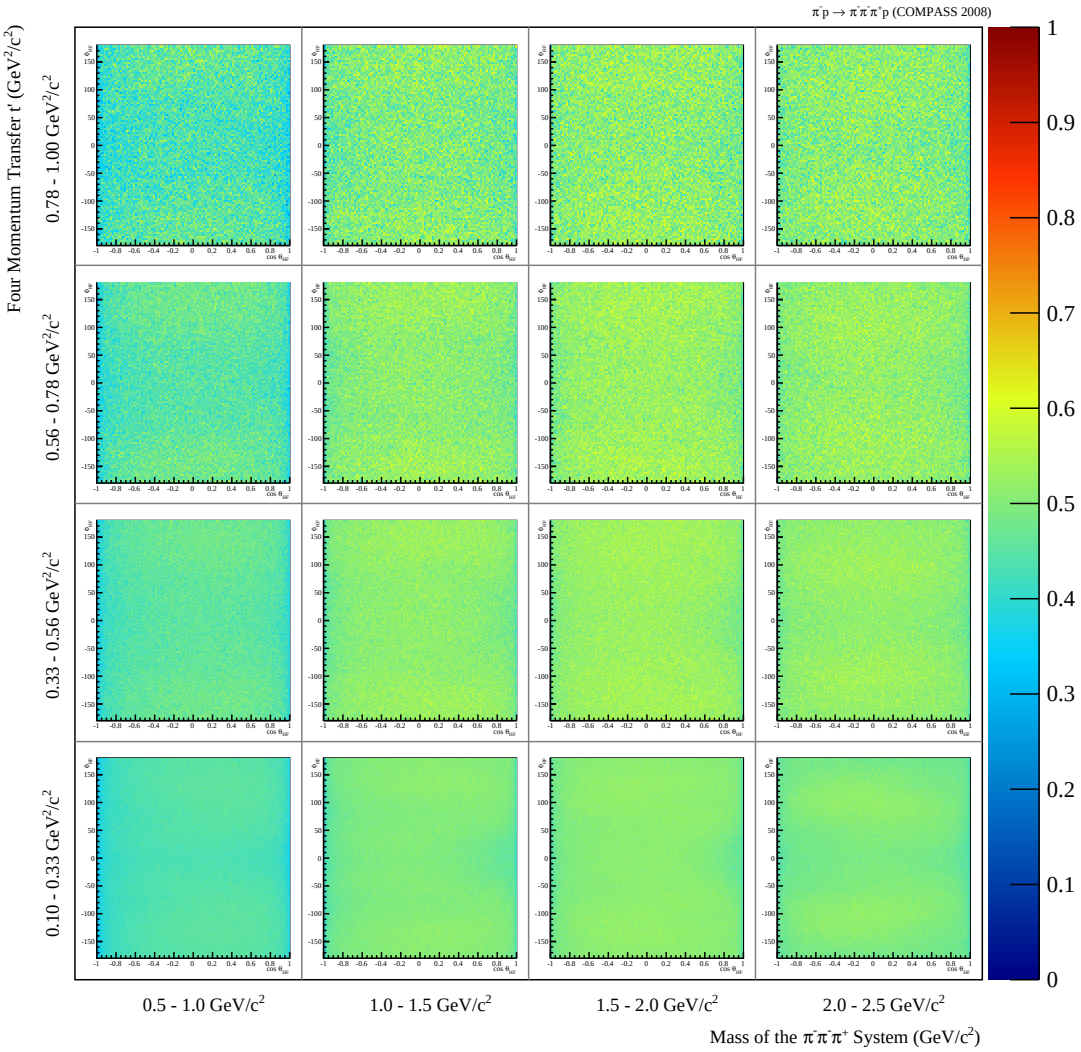

Figure 7.4 Two-dimensional acceptances of the two decay angles observed in the helicity reference system as a function of $m_{3\pi}$ and t'.

7.1.4 Observables

The outcome of the fit is a set of complex-valued transition amplitudes $T_a^\varepsilon(m_{3\pi}, t')$ which do not have direct physical interpretation. Thus observables based on these amplitudes, must be introduced in order to obtain information about the process of interest.

Number of Expected Events, Intensity and Overlap of Amplitudes

The starting point is again the overall intensity distribution with normalised decay amplitudes $\overline{\psi}_i$ (see Sec. 7.1.2) in the most general form for a single bin of $m_{3\pi}$ and t':

$$\mathscr{I}(\tau) = \sum_r \sum_\varepsilon \left| \sum_a T_{ar}^\varepsilon \overline{\psi}_a^\varepsilon(\tau) \right|^2 = \sum_\varepsilon \sum_{ab} \rho_{ab}^\varepsilon \overline{\psi}_a^\varepsilon(\tau) \overline{\psi}_b^{\varepsilon *}(\tau) \tag{7.31}$$

The second term shows the expansion of the square of the absolute value and in terms of the spin-density matrix elementρ_{ab}^ε (see Sec. 7.1.2). Another way to define the intensity distribution is the number of expected (i.e. acceptance corrected) events per unit of phase space:

$$\mathscr{I}(\tau) = \frac{dN_{\text{exp}}}{d\Phi_{3\pi}(\tau)} \tag{7.32}$$

Solving Eq. (7.32) for N_{exp} results in

$$N_{\text{exp}} = \int \mathscr{I}(\tau) d\Phi_{3\pi}(\tau) = \sum_\varepsilon \sum_{ab} \rho_{ab}^\varepsilon I_{ab}^\varepsilon \tag{7.33}$$

with

$$I_{ab}^\varepsilon = \int \overline{\psi}_a^\varepsilon(\tau) \overline{\psi}_b^{\varepsilon *}(\tau) d\Phi_{3\pi}(\tau) \tag{7.34}$$

Unlike the integrals used in Eq. (7.23), these do not take the acceptance into account.
The sum in Eq. (7.34) can be split in two terms. For the first case, where $a = b$ the terms in the sum reduce to the spin-density matrix elements ρ_{aa}^ε. The integrals I^ε are unity on all diagonal terms due to the normalisation chosen for the amplitudes $\overline{\psi}_a$. Thus the *intensity* for a particular amplitude a and reflectivity ε can be written as follows:

$$Intens_a^\varepsilon = \rho_{aa}^\varepsilon \tag{7.35}$$

For the case where $a \neq b$ the notion *overlap* between two amplitudes is introduced and the sum term can be expressed as:

$$Overlap_{ab}^\varepsilon = 2\Re\left(\rho_{ab}^\varepsilon I_{ab}^\varepsilon\right) \tag{7.36}$$

taking into account that $\rho_{ab}^\varepsilon = \rho_{ba}^{\varepsilon *}$ and $z + z^* = 2\Re(z)$ for $z \in \mathbb{C}$. For non-acceptance corrected integrals (i.e. acceptance = 1) non-diagonal elements are equal to zero unless the amplitudes a and b have the same quantum numbers J^{PC}. This is a consequence of the orthogonality of the description of the decay amplitudes in terms of D-functions (see Sec. 6.3). The overlap must not be mixed up with the concept of interference, that will be introduced in the following section.

Interference, Coherence and Phase Motion

In contrast to the overlap of two amplitudes the *interference* is defined by the non-diagonal term of the spin-density matrix only. As its elements, the transition amplitudes T_a^ε, are obtained in consideration of the acceptance, interference is taking place between all amplitudes of a particular reflectivity ε. The interference consists of two real numbers, being $\Re(\rho_{ij}^\varepsilon)$ and $\Im(\rho_{ij}^\varepsilon)$. Rather than the intensity of a single amplitude the investigation of interferences gives a handle whether one observes a resonance or something different.
In common the *relative phase* $\Delta\varphi_{ab}$ instead of the pure interference is used for the analysis of the spectrum. It is defined as

$$\Delta\varphi_{ab} = \arg(\rho_{ab}^\varepsilon) \tag{7.37}$$

with $\arg(z)$ the argument of the spin density matrix element.
Talking about interference implicates the introduction of another observable. Analogous to the complex degree of spectral coherence, known from optics, the *coherence* between two amplitudes is defined as:

$$Coh_{ab}^\varepsilon = \frac{r_{ab}^\varepsilon}{\sqrt{\rho_{aa}^\varepsilon \rho_{bb}^\varepsilon}} = \sqrt{\frac{\Re(\rho_{ab}^\varepsilon)^2 + \Im(\rho_{ab}^\varepsilon)^2}{Intens_a^\varepsilon \, Intens_b^\varepsilon}} \tag{7.38}$$

with r_{ab}^ε the absolute value of ρ_{ab}^ε. The coherence ranges from zero, absolute no coherence between two amplitudes, to unity, both amplitudes are complete coherent. Using only rank-1 for the fit model the coherence is always one per definition and the observable brings no information. In general both, phase motions and coherence, are tools to identify structures in the intensity distributions of waves as resonances even in the presence of large non-resonant contributions.

The size of this data sample offers the opportunity to exploit the information of an additional observable. The slope of the *t'-dependence* for each single wave. The strength of this parameter can help to disentangle different production mechanisms contributing to the observed intensity. A detailed discussion can be found in Sec. 7.4.

7.1.5 Thresholds in the Three-Body Decay

The fact that a set of only five kinematic variables is necessary to describe a three-body decay leads to unavoidable ambiguities, when the decay is parametrised within the isobar model. This has to be taken into account, when setting a up the fit model. It is important to understand the origins of these ambiguities in order find solutions to overcome them. In the following some examples are discussed were these kind of effects can happen in the model:

- The main source for ambiguities results from cross talk between amplitudes with the same quantum numbers J^{PC}, where the spin of the isobar and the orbital angular momentum can be permuted. A nice example is the cross talk between the $1^{++}1^+\rho\pi D$ (see Fig. 7.27b) wave and $1^{++}1^+ f_2\pi P$ (see Fig. 7.27f). The bump below the resonance region, i.e. below 1 GeV/c^2, can be avoided by switching off one of these two waves in the model. But both waves are known to contribute to the a_1 resonances and thus are kept in the model. The normal procedure would be to apply a mass threshold on the three body mass $m_{3\pi}$ for one of these two amplitudes which offers the fit then only one possibility in the low-mass region. But the aim during the construction of the fit model was to use

as less thresholds as possible, and as the effect is localised on a small mass region below 1 GeV/c^2 it was decided to not apply any threshold for these two waves.

- Using isobars with identical quantum numbers can distort the fit. One example is the usage of several ρ isobars. Some studies were undertaken to implement in addition to the well-established $\rho(770)$ two additional ρ resonances, $\rho(1450)$ and $\rho(1700)$, described by relativistic Breit-Wigners (see Sec. 7.6.2). Other than the dominant isobar $\rho(770)$ a possible contribution of these new two-pion resonances can be regarded as very small (see Fig. 7.56). In addition they both overlap as they are not well separated, resulting in an unstable fit, having difficulties to disentangle amplitudes parametrised by these two ρ resonances. To overcome these problems particular thresholds can be applied to amplitudes with $\rho(1450)$ and $\rho(1700)$ isobars. But this is contradictory to the aim to reduce the number of thresholds of the fit model to a minimum. A more profound ansatz was chosen by the K-matrix fit of the $\rho(770)$ and $\rho(1700)$ (see Sec. 7.6.1). In contrast to the ρ parametrisations the implementation of a $(\pi\pi)_S$ and a $f_0(980)$ isobar, both having quantum numbers $J^{PC} = 0^{++}$, leads to no distortion of the fit, as the $f_0(980)$ has a small width of ~ 100 MeV/c^2 in contrast to the very broad $(\pi\pi)_S$ isobar.

- The orthogonality of different J^{PC} states is broken open as the acceptance has to be considered. An imperfect acceptance correction can lead to cross talk between amplitudes with different quantum numbers J^{PC} due to over- or under-corrections of some of the decay variables in certain kinematic regions. This effect was mainly observed for amplitudes with large spin J or some very weak waves. It will be discussed in the following sections for some waves if it is important for their interpretation.

- Depending on the isobar and the quantum numbers the phase-space integral of the partial waves begins to rise in different regions of the three-pion mass. In some extreme cases the phase space is almost vanishing over a wide range of $m_{3\pi}$ and opens only at rather high masses. This is the case for example for the amplitude with $J^{PC} M^{\varepsilon} \zeta \pi L = 0^{-+}0^{+} f_0(980)\pi S$, where the phase space begins to increase at 1.2 GeV/c^2. Dropping the corresponding thresholds leads to instabilities in the fit, resulting in unphysical large intensities for lower masses, affecting other amplitudes.

A complete non-isobaric description of a three-body decay is yet not available and thus the implementation of thresholds for the three-body mass $m_{3\pi}$ are essential in order to circumvent these ambiguities. These thresholds acts like switches in order to include certain partial waves of the model only above the thresholds. The usage of thresholds is a trade off between fit stability and a smooth model. The presence of too much thresholds at one mass acts like a second fit model. Thus the reduction of the number of thresholds above 1 GeV/c^2 was one aim for this analysis and possible due to the huge amount of events of the data sample. Only 27 out of 88 waves are limited by a threshold at the lower bound of the invariant mass $m_{3\pi}$. In addition the thresholds are spread over $m_{3\pi}$ in order to avoid an accumulation of them at a certain point of $m_{3\pi}$. An overview of all applied thresholds can be found in Tab. 7.2.

7.1.6 Weighted Monte Carlo

The last step of each iteration of an amplitude analysis is an objective quality assurance. In common the likelihood of fits of different models are compared and finally the fit with the best

likelihood is assumed to be the best representation of the real intensity distribution. From the mathematical point of view this is correct, but it gives only a handle on the quality of one fit against one other as the pure numeric likelihood value has no meaning. Changing the model, parametrisations or even the event selection makes it difficult to interpret different likelihood values. As the fit is done in bins of $m_{3\pi}$ and t' even the degree of change of the likelihood of a particular bin can have different impact.
A more sophisticated way in order to determine how well the whole analysis is able to reproduce the intensity distribution is *weighted Monte Carlo*. Even when the comparison of likelihoods was used in some particular cases the procedure of weighted Monte Carlo is the method of choice used for this analysis and thus will be introduced in the following. The input for this kind of investigation are the phase-space distributed Monte Carlo truth events (i.e. without simulation and reconstruction) and the resulting spin-density matrices estimated from fitting real data. For each event the weight is calculated based on the model function.

$$weight = \mathscr{I}(\tau_{\mathrm{MC}}) = \sum_{\varepsilon} \sum_{ab} \rho^{\varepsilon}_{ab} \overline{\psi}^{\varepsilon}_{a}(\tau_{\mathrm{MC}}) \overline{\psi}^{\varepsilon *}_{b}(\tau_{\mathrm{MC}}) \tag{7.39}$$

The weighted events are now distributed in phase space like predicted by the model. The obtained MC data set can be exploit in several ways. On the one hand the quality of the Monte Carlo simulation can be checked against the real data by comparing hit distributions or detector responses of the simulation with recorded detector information. On the other hand the set of variables τ, describing the decay, can be probed in order to review the fit model, in particular isobar parametrisations and wave sets. In the same manner like all other issues of this analysis the weighted Monte Carlo distributions have to be studied as a function of $m_{3\pi}$ and t'. Here 11 t' bins and 10 mass bins are used for this study, resulting in 110 plots which have to be checked in order to identify effective discrepancies between model and real data. Two kinematical regions representing characteristic aspects of the intensity distribution are plotted for the final fit, discussed in the next section. Figure 7.5 shows the overlap of the weighted Monte Carlo sample with real data in the kinematic regime close to the lower bound of the t' region and a cutout around the $\pi_2(1670)$ mass. The ratio of the overall mass spectrum (Fig. 7.5a)shows a good agreement by definition, while in Fig. 7.5b some deviations in the isobar mass are visible. It seems that the $f_0(980)$ is over pronounced a bit in the model in contrast to the real data and the $f_2(1270)$ is shifted slightly to higher masses. Nevertheless, taking the angular distributions (Fig. 7.5c - 7.5h) into account, the degree of agreement between real data and the respective weighted Monte Carlo distributions is excellent for all decay variables. In Fig. 7.6 the same distributions for the kinematic range nearby the upper limit of the analysed t' range and around the $a_1(1260)/a_2(1320)$ mass are presented. Both the angular distributions and the isobar spectrum are dominated by the $\rho(770)$, the major isobar in the $a_1(1260)/a_2(1320)$ region. The weighted Monte Carlo agrees well with the data no larger deviations are observed.

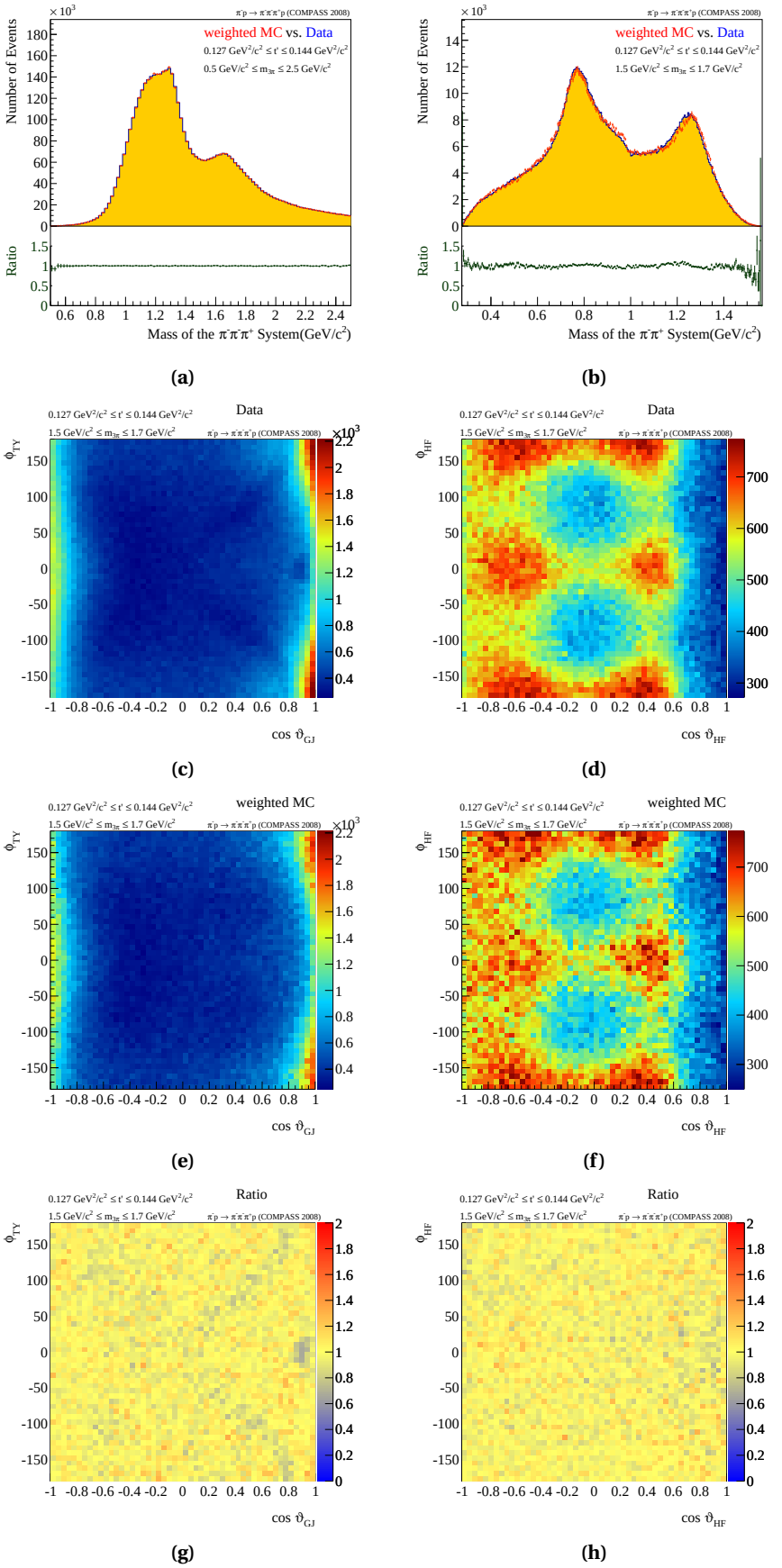

Figure 7.5 Comparison of a weighted Monte Carlo sample to real data in the kinematic regime close to the lower bound of the t' region and a cutout around the $\pi_2(1670)$ mass (except plot (a), where the complete range of $m_{3\pi}$ is shown). The comparison of the invariant mass $m_{3\pi}$ (a) and the two pion mass (b) are shown. The comparison of distributions in the Gottfried-Jackson frame for real data (c) and weighted Monte Carlo (e) ant its ratio (g) is plotted. The same for the respective distributions in the helicity frame (d), (f) and (h).

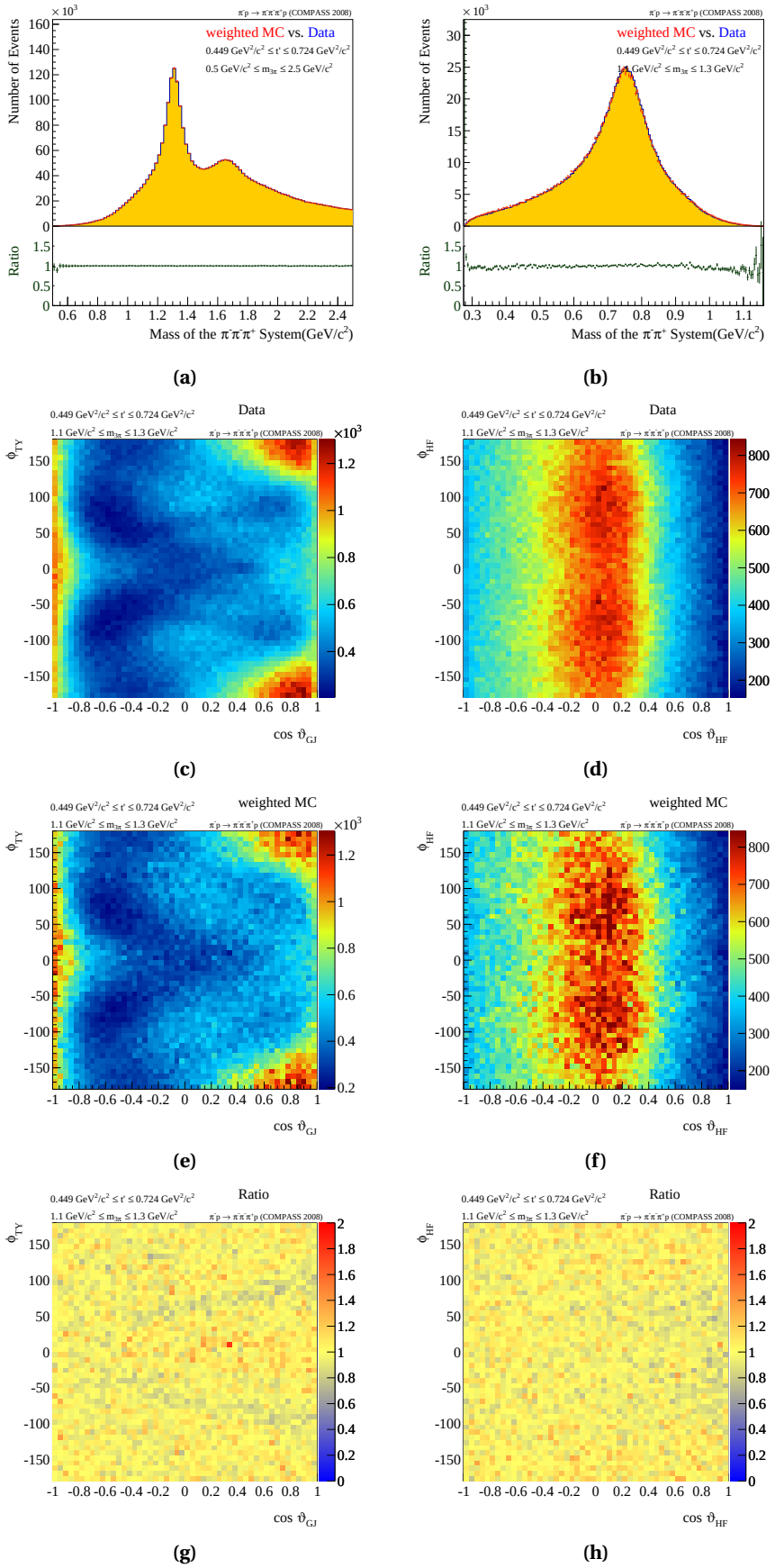

Figure 7.6 Comparison of a weighted Monte Carlo sample to real data in the kinematic regime close to the upper bound of the t' region and a cutout around the $a_1(1260)/a_2(1320)$ mass (except plot (a), where the complete range of $m_{3\pi}$ is shown). The comparison of the invariant mass $m_{3\pi}$ (a) and the two pion mass (b) are shown. The comparison of distributions in the Gottfried-Jackson frame for real data (c) and weighted Monte Carlo (e) ant its ratio (g) is plotted. The same for the respective distributions in the helicity frame (d), (f) and (h).

7.2 Determination of the Fit Model

The objective determination of a fit model is as long-disputed issue as this kind of analysis exists. There is no generally accepted road map, which defines a proper way, how to get a physical correct and complete model. This section summarises briefly the different steps performed in this analysis, as discussed up to now, in order to explain the way how this fit model was defined. Before the discussion of finding a model and its objectivity it is important to define the notion *model* in the course of this analysis. Herein model stands for a holistic ansatz including even the event selection and finishes with a wave set, consisting of a specific number of amplitudes with a certain parametrisation.

1. **Event Selection**: The event selection cannot be seen decoupled from the rest of the analysis. It is eminent to purifying the data sample without biasing the analysis result. By applying too tight cuts it can happen that parts of the phase space are cut away which could lead, especially for spin-parity analyses, to artificial angular distributions or their modification. On the other hand the cleaner the sample is the more stable is the fit and the more robust is the fit result. Thus different event selections were tried in order to find the most unbiased but cleanest data sample. Fit results with different event selections are part of the systematic error and will be discussed in Sec.7.6.

2. **Amplitude Parametrisation and Implementation**: Since the first observation of resonances there exists a pool of mathematical descriptions. These parametrisations can have significant influence on the fit result, as they are a major component of the construction of the decay amplitudes (see. Sec.6.3) which are the basis of the fit. Hence different parametrisations for the two major isobars, the $\rho(770)$ and the $(\pi\pi)_S$ wave were tested and the respective fit results are part of the systematic error (see Sec.7.6 for more details).

3. **Wave Set Generation**: The finding of a proper set of amplitudes is the most disputed part for this kind of spin-parity analysis. The usual way of determination is to start with a basic wave set, consisting of amplitudes which are expected to be observed for this kind of reaction and final state. Some of them are so dominant that their contributions can be seen in the overall intensity distribution. From that point the model can be developed further based on previous analyses and investigations. Limitations originate mainly from the amount of data, the geometrical acceptance of the spectrometer and the kinematical region of interest. This method has the big disadvantage that it is biased by the person or group developing the model, based on their experiences or findings. This unwanted effect can modify the fit results in different ways. A worse resolution and a too extended wave set can lead to an *over-fitting* of the data sample which 'washes out' the fit result. On the other hand a too simple model forces the fit algorithm to put intensity in amplitudes which have similar angular distributions as the one, which would fit best, but is not part of the model. One example is discussed in Sec.7.5.4.
   The large data set and the high resolution of the spectrometer (see next point) result in a fine granulation of the data as a function of $m_{3\pi}$ and t'. This finally allowed to apply a very simple and for this case largely unbiased method to determine the wave set. All possible amplitudes (~ 140) with spin projection $M = 0$ and 1 up to a total spin $J = 6$ and positive reflectivity $\varepsilon = +1$ are taken into account. After several iterations of adjusting

thresholds, where needed (see Sec. 7.1.5), the fit result was very clear: Almost half of the given amplitudes showed a flat intensity compatible with zero over the whole mass region. All other waves exhibit structures which raise clearly from the background. In addition seven waves with $M = 2$, motivated by the amount of data, were added to the model as well as seven waves with negative reflectivity, considering the contribution of Regge trajectories with negative naturality (see Sec. 6.1.2). Finally a single partial wave with the $f_0(1500)$ isobar and inspired by [N+04] is implemented.

4. **Resolution and Acceptance Studies**: With increasing number of events and the subsequent decrease of the statistical error the validity of the Monte Carlo model comes into the focus. A poor understanding of the spectrometer and its characteristic can lead to artificial or wrong distributions of the decay variables τ and thus influence the fit result. The achievement of an high level of accuracy of the spectrometer simulation is one of the most important preparatory works for high-statistic spin-parity analyses.
   An analysis in bins of $m_{3\pi}$ and t' must consider the given spectrometer resolutions, which limits the granularity of the kinematics. Thus the investigation, discussed in Sec. 5.3 have a direct influence on the binning of the data, which can be seen as part of the model.

5. **Fit in Bins of $\mathbf{m_{3\pi}}$ and $\mathbf{t'}$**: The method of fitting the data was extensively discussed in the first part of this chapter. A correct mathematical fitting routine can not influence the result, but constraints to the fit can bias the result. The common way in order to describe the mass dependence is not to describe the mass dependence, as done for this analysis. The fine granulation of the data avoids the problem to find a model of the mass dependence which pushes the fit in some direction. The same approach was chosen for the t' dependence in order to resign a mathematical description of this yet unknown dependence (One goal of this analysis is to enlight this situation). Besides the two ways of handling the t' dependence another tool is called the 'infinite rank' [Ame].
   Finally, another influence for this analysis was the size of the rank. Usually a rank-2 fit is assumed to take incoherent effects, e.g. spin flips, into account by construction. But the binning of the data, both in $m_{3\pi}$ and t' shows no justification for a fit with more than one rank. Nevertheless a fit with rank 2 was tested and the result is discussed in Sec.7.6.2.

6. **Weighted Monte Carlo**: This technique, introduced in the previous section, is of course not part of the model. But it is the most objective measure to compare the outcome of the spin-parity analysis with the actual distributions. Thus it is the last step in the iterative process of finding a complete model. For this analysis it was the best tool to specify certain kinematic cuts like the identification of possible centrally produced events, to improve the amplitude parametrisation or the detection of artifacts in the acceptance.

Finally the model consists of 88 waves, 80 amplitudes with positive reflectivity, seven with negative plus an incoherent Flat wave. The wave set is listed in Tab. 7.2, including the applied necessary mass thresholds. Regarding the investigations of the spectrometer resolutions 20 MeV/c^2 wide 3π mass bins were chosen. The granulation in t' was a trade off between as narrow bins with equal statistics as possible, in order to be less sensitive to the t' dependence, and enough statistics in each t' bin in order to be able to extract resonance parameters (see Chap. 8). Therefore the data were split in 11 non-equidistant t' bins, with almost equal amount of

events. The discussion of the fit results and the further analysis is based on this binning. The resulting fragmentation of the data is shown in Fig. 7.7a. On the other hand, as mentioned before, less is known about the t' dependence, thus for that purpose each of the 11 t' bins is split in the middle. Thereby 22 data points per amplitude are available in order to learn more about the production and the contribution of non-resonant processes. It will be shown that the difference between the fit results obtained by these two binnings can be seen as equal (see Sec. 7.6.2). It is important to mention that for each bin of mass and t' an independent individual fit is performed. By construction, there is no guarantee that the extended maximum log-likelihood fit finds the global maximum. It can happen that the fit finds a local maximum and converges far from the real maximum. Therefore for each bin 30 fit attempts with random start values were applied.
For the lead data the same wave set has been applied having the advantage of a simple comparison of this fit with the main analysis. The binning of the data has been adapted for the smaller amount of data with 40 MeV/c^2 mass bins and 8 bins in t' (see Fig. 7.7b). The fit of the lead data has one caveat. Due to practical reasons, the lead data sample is not part of the main analysis, no valid Monte Carlo simulation could be developed and thus this data is fit without any acceptance correction.

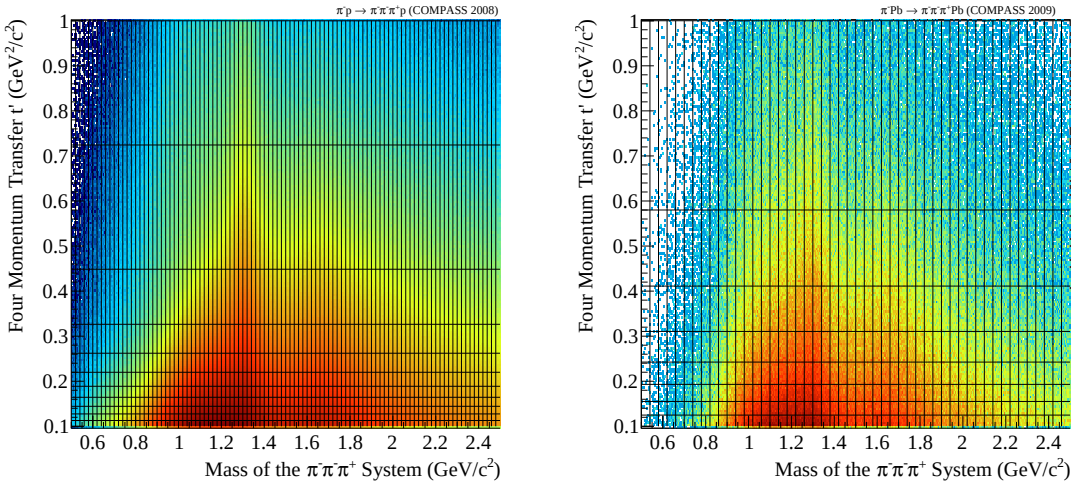

(a) **(b)**

Figure 7.7 Binning of the kinematic range of the invariant mass $m_{3\pi}$ and the squared four-momentum transfer t'. Equidistant mass bins are chosen (20 MeV/c^2) with 11 t' bins (a) or (40 MeV/c^2) with 8 t' bins (lead data) (b).

11 t′ bins [GeV²/c²]	**22 t′ bins [GeV²/c²]**	**8 t′ bins [GeV²/c²]**
0.100000-0.112853	0.100000-0.106427	0.100000-0.124894
	0.106427-0.112853	
0.112853-0.127471	0.112853-0.120162	0.124894-0.155140
	0.120162-0.127471	
0.127471-0.144385	0.127471-0.135928	0.155140-0.193053
	0.135928-0.144385	
0.144385-0.164401	0.144385-0.154399	0.193053-0.242515
	0.154399-0.164401	
0.164401-0.188816	0.164401-0.176609	0.242515-0.310531
	0.176609-0.188816	
0.188816-0.219907	0.188816-0.204362	0.310531-0.411179
	0.204362-0.219907	
0.219907-0.262177	0.219907-0.241042	0.411179-0.580026
	0.241042-0.262177	
0.262177-0.326380	0.262177-0.294228	0.580026-1.000000
	0.294228-0.326380	
0.326380-0.448588	0.326380-0.387484	
	0.387484-0.448588	
0.448588-0.724294	0.448588-0.586441	
	0.586441-0.724294	
0.724294-1.000000	0.724294-0.862147	
	0.862147-1.000000	

Table 7.1 Overview of all three binnings of the t' spectrum used for the analysis.

$J^{PC}M^{\varepsilon}$	Isobar	L	Threshold (GeV/c^2)
FLAT			-
$0^{-+}0^{+}$	$(\pi\pi)_S$	S	-
$0^{-+}0^{+}$	$f_0(980)$	S	1.20
$0^{-+}0^{+}$	$\rho(770)$	P	-
$0^{-+}0^{+}$	$f_0(1500)$	S	1.70
$0^{-+}0^{+}$	$f_2(1270)$	S	-
$1^{++}0^{+}$	$\rho(770)$	S	-
$1^{++}1^{+}$	$\rho(770)$	S	-
$1^{++}0^{+}$	$\rho(770)$	D	-
$1^{++}1^{+}$	$\rho(770)$	D	-
$1^{++}0^{+}$	$(\pi\pi)_S$	P	-
$1^{++}1^{+}$	$(\pi\pi)_S$	P	1.1
$1^{++}0^{+}$	$f_2(1270)$	P	1.22
$1^{++}1^{+}$	$f_2(1270)$	P	-
$1^{++}0^{+}$	$f_2(1270)$	F	-
$1^{++}0^{+}$	$f_0(980)$	P	1.18
$1^{++}1^{+}$	$f_0(980)$	P	1.14
$1^{++}0^{+}$	$\rho_3(1690)$	D	-
$1^{++}0^{+}$	$\rho_3(1690)$	G	-
$1^{-+}1^{+}$	$\rho(770)$	P	-
$2^{++}1^{+}$	$\rho(770)$	D	-
$2^{++}2^{+}$	$\rho(770)$	D	-
$2^{++}1^{+}$	$f_2(1270)$	P	1.00
$2^{++}2^{+}$	$f_2(1270)$	P	1.40
$2^{++}1^{+}$	$\rho_3(1690)$	D	0.80
$2^{-+}0^{+}$	$f_2(1270)$	S	-
$2^{-+}1^{+}$	$f_2(1270)$	S	1.1
$2^{-+}2^{+}$	$f_2(1270)$	S	-
$2^{-+}0^{+}$	$f_2(1270)$	D	-
$2^{-+}1^{+}$	$f_2(1270)$	D	-
$2^{-+}2^{+}$	$f_2(1270)$	D	-
$2^{-+}0^{+}$	$f_2(1270)$	G	-
$2^{-+}0^{+}$	$\rho(770)$	P	-
$2^{-+}1^{+}$	$\rho(770)$	P	-
$2^{-+}2^{+}$	$\rho(770)$	P	-
$2^{-+}0^{+}$	$\rho(770)$	F	-
$2^{-+}1^{+}$	$\rho(770)$	F	-
$2^{-+}0^{+}$	$\rho_3(1690)$	F	1.00
$2^{-+}1^{+}$	$\rho_3(1690)$	F	1.30
$2^{-+}0^{+}$	$(\pi\pi)_S$	D	-
$2^{-+}1^{+}$	$(\pi\pi)_S$	D	-
$2^{-+}0^{+}$	$f_0(980)$	D	1.16
$3^{-+}1^{+}$	$\rho(770)$	F	-
$3^{-+}1^{+}$	$f_2(1270)$	D	1.34
$3^{++}0^{+}$	$\rho(770)$	D	-
$3^{++}1^{+}$	$\rho(770)$	D	-
$3^{++}0^{+}$	$\rho(770)$	G	-
$3^{++}1^{+}$	$\rho(770)$	G	-
$3^{++}0^{+}$	$f_2(1270)$	P	0.96
$3^{++}1^{+}$	$f_2(1270)$	P	1.14
$3^{++}0^{+}$	$\rho_3(1690)$	S	1.38
$3^{++}1^{+}$	$\rho_3(1690)$	S	1.38
$3^{++}0^{+}$	$\rho_3(1690)$	6	-
$3^{++}0^{+}$	$(\pi\pi)_S$	F	1.38
$3^{++}1^{+}$	$(\pi\pi)_S$	F	1.38
$4^{-+}0^{+}$	$\rho(770)$	F	-
$4^{-+}1^{+}$	$\rho(770)$	F	-
$4^{-+}0^{+}$	$f_2(1270)$	D	-
$4^{-+}1^{+}$	$f_2(1270)$	D	-
$4^{-+}0^{+}$	$f_2(1270)$	G	1.6
$4^{-+}0^{+}$	$(\pi\pi)_S$	G	1.4
$4^{++}1^{+}$	$\rho(770)$	G	-
$4^{++}2^{+}$	$\rho(770)$	G	-
$4^{++}1^{+}$	$\rho_3(1690)$	D	1.7
$4^{++}1^{+}$	$f_2(1270)$	F	-
$4^{++}2^{+}$	$f_2(1270)$	F	-
$5^{++}0^{+}$	$\rho(770)$	G	-
$5^{++}0^{+}$	$\rho_3(1690)$	D	1.36
$5^{++}0^{+}$	$f_2(1270)$	F	0.98
$5^{++}1^{+}$	$f_2(1270)$	F	-
$5^{++}0^{+}$	$f_2(1270)$	H	-
$5^{++}0^{+}$	$(\pi\pi)_S$	H	-
$5^{++}1^{+}$	$(\pi\pi)_S$	H	-
$6^{-+}0^{+}$	$(\pi\pi)_S$	6	-
$6^{-+}1^{+}$	$(\pi\pi)_S$	6	-
$6^{-+}0^{+}$	$\rho(770)$	H	-
$6^{-+}1^{+}$	$\rho(770)$	H	-
$6^{-+}0^{+}$	$\rho_3(1690)$	F	-
$6^{-+}0^{+}$	$f_2(1270)$	G	-
$6^{++}1^{+}$	$\rho(770)$	6	-
$6^{++}1^{+}$	$f_2(1270)$	H	-
$1^{++}1^{-}$	$\rho(770)$	S	-
$1^{-+}0^{-}$	$\rho(770)$	P	-
$1^{-+}1^{-}$	$\rho(770)$	P	-
$2^{++}0^{-}$	$\rho(770)$	D	-
$2^{++}0^{-}$	$f_2(1270)$	P	1.18
$2^{++}1^{-}$	$f_2(1270)$	P	1.3
$2^{-+}1^{-}$	$f_2(1270)$	S	-

Table 7.2 Wave-set used both for proton and lead data. 80 amplitudes with positive reflectivity, 7 with negative.

7.3 Fit Results - An Overview

Each single fit consists of 1100 spin-density matrices with more than $4.2 \cdot 10^6$ elements in total. In order to be able to interpret the fit the data points are plotted as a function of $m_{3\pi}$ which results in 88 **intensity** plots and 3916 **interference** patterns per t' bin. Regarding Eq. 7.35 and taking into account that each fit result represents a certain t' bin offers the possibility to simply add up the intensities. This **incoherent sum** or **integrated intensity** is often sufficient to show and thus this kind of presentation is preferred for this thesis unless peculiarities in certain regions of t' arise. The two-dimensional representation of the result as a function of both $m_{3\pi}$ and t', as applied to some kinematic resolution or acceptance plots, was tried but found to be less convenient. There is no better way to interpret the results than looking at each plot by eye. The dynamics as function of t' can be observed best by the **t′ dependence**, i.e. the integral of an amplitude in a certain mass range as a function of t'. This dependence is almost unexplored and poorly settled with experimental data. The wealth of the data set offers the possibility to get for the first time a precise measurement of this dependence for each single partial wave in order to gain insight in the different production processes and to have a handle to disentangle resonant and non-resonant contributions by their different t' dependence. Thus a detailed discussion follows in Sec. 7.4.
As mentioned in the previous section, the model plays an important role for the evaluation of the data, thus several fit models were applied to the data and their influence was investigated. These additional fits are the main part of the **systematic studies** (see Sec. 7.6) and their deviation from the best fit can be plotted as band of uncertainty if necessary for the interpretation. In addition the usage of **thresholds** influences the fit, as discussed in Sec. 7.1.5. Thus the position of the thresholds applied are overlaid to the fit results, if necessary.
It was stated in the Chap. 2 that additional production mechanisms can lead to the same final state and in particular Deck-like processes must be considered. Several mathematical models are on the market, to describe Deck-like processes (see Sec. 5.4) and it is currently not possible to disentangle the Deck contribution from diffraction on this level of the analysis. Some attempts will be undertaken in the following Chap. 8. The best way at the moment is to create a Monte Carlo data set (see Sec. 5.4), comparable with the real data in terms of number of events, and apply the same fit model. This exercise was done and the fit results of the **Deck Monte Carlo** data can be compared with the fit outcome of the real data. It is important to note that the outcome of this investigation has only limited informative value. The fit results of the Deck Monte Carlo sample are overlaid to the fit of the real data, but the possible interference between diffraction and Deck is not taken into account by construction. Nevertheless this part of the analysis is important in order to understand the dynamics, especially of the background, and insights can lead to enhanced fit models.
Representative for the different plotting options, discussed above, the integrated intensity of the amplitude with $J^{PC}M^{\varepsilon}\xi\pi L = 6^{-+}0^{+}\rho(770)\pi H$ is shown in Fig. 7.8a. The fit result is plotted as dark blue markers with the statistical error as determined by the fit. It is assumed that this wave is dominated by Deck-produced final states and thus it has been decided to use this wave to normalise the real data fit results with the ones obtained by the Deck Monte Carlo, see Fig. 7.8b. The yellow band in Fig. 7.8a shows the maximum spread of the intensity with respect to the systematic studies performed as discussed in Sec. 7.6, while the blue lines corresponds to the thresholds applied to some waves of that fit model.
Finally the influence of different target materials can be investigated by comparing the fit out-

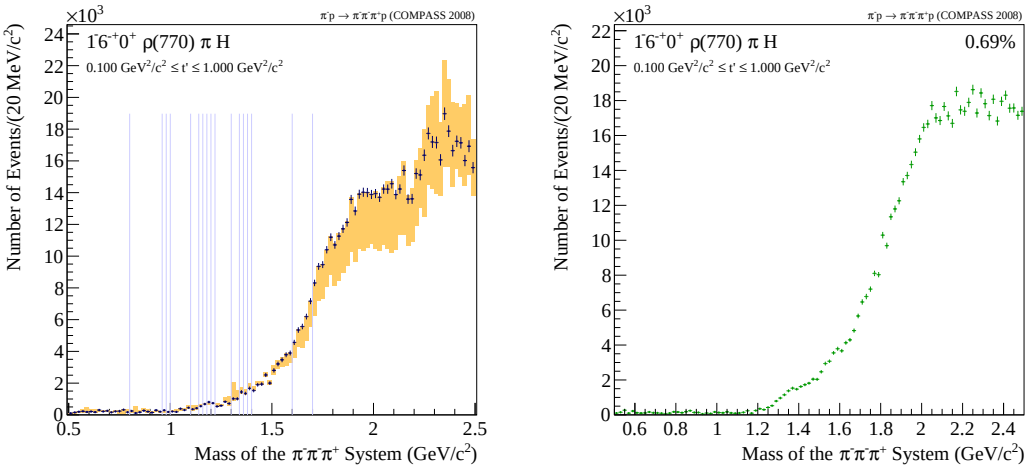

(a) **(b)**

Figure 7.8 Integrated intensity of the partial wave with $J^{PC}M^{\varepsilon}\xi\pi L = 6^{-+}0^{+}\rho(770)\pi H$ (a). This amplitudes is assumed to be dominated by Deck-produced final states and thus is taken as normalisation for the fit results of the Deck Monte Carlo data sample (b). The yellow band in plot (a) shows the maximum spread of the intensity with respect to the systematic studies, discussed in Sec. 7.6. The blue lines corresponds to thresholds applied to some amplitudes.

come of the 2008 data set, obtained with a proton target with the 2009 data set, taken with a **lead target**. Although magnitudes smaller in size, the 2009 data set offers the possibility to cross check the 2004 COMPASS analysis [AAA+10] and to investigate the influence of the target material on the final state.

7.3.1 Flat Wave and Negative Reflectivity

Before discussing details of the fit it is important to understand the general properties of the analysis result. The model consists of two non-interfering blocks of amplitudes with different reflectivities (see Sec. 7.1.2) plus the incoherent Flat wave and thus their respective contribution to the overall intensity will be investigated.
The purpose of the Flat wave is to absorb intensity of uncorrelated 3π events which cannot be attributed to the amplitudes of the fit model. For a complete model, i.e. all contributing amplitudes are taken into account, the only intensity, which should go to the Flat wave corresponds to phase-space events, i.e. events, which decay to the final state, without producing an intermediate isobar and also no 3π resonance. This would result in isotropic angular distributions (that's why the Flat wave is called like this). The Flat wave intensity is plotted in Fig. 7.9a. The integrated intensity does not have the expected phase-space line shape but two dips at 1.2 and 1.65 GeV/c^2. The structure of this wave is independent of the number of amplitudes in the fit model. Fit results of models with 53 and 151 waves, show the same intensity structure. The origin of the dips is still unclear. One possible explanation is that intensity which should be associated to the Flat wave is put to the dominant waves with quantum number $J^{PC} = 1^{++}$ and 2^{-+} having their maximum in the mass ranges of 1.2 and 1.7 GeV/c^2. As this wave contributes only $\sim 3\%$ to the overall intensity, as shown in Fig. 7.9b, this effect was not further investigated.
The fit model contains seven ampliutdes with negative reflectivity. It was discussed in Sec. 2.1.1

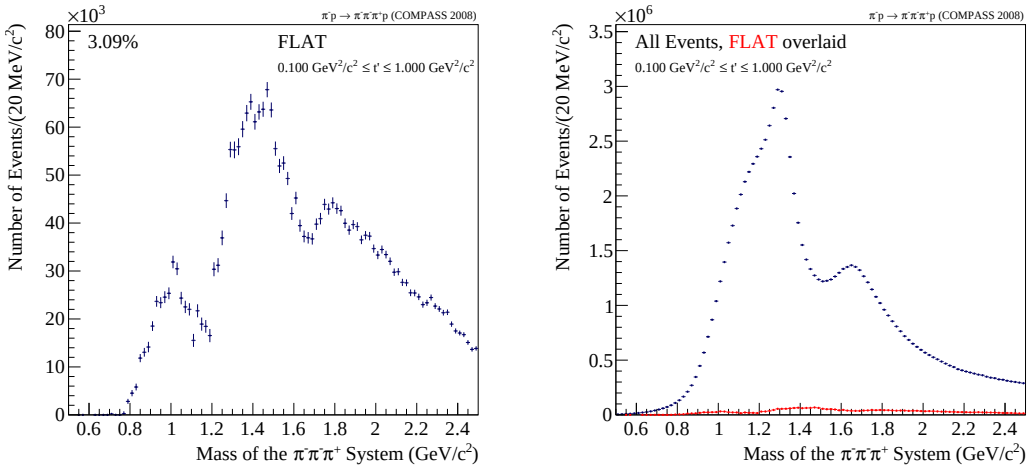

(a) **(b)**

Figure 7.9 Integrated intensity of the FLAT amplitude (a) and total intensity with FLAT wave overlaid in red (b).

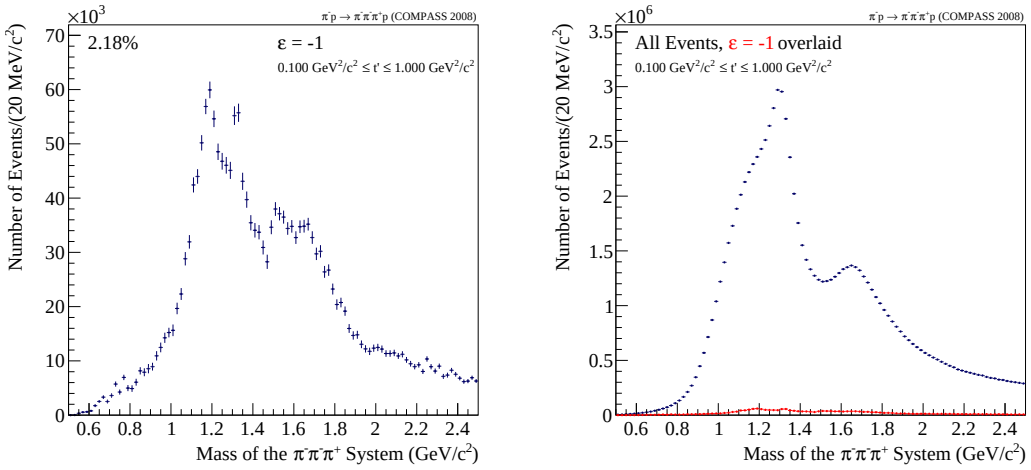

(a) **(b)**

Figure 7.10 Coherent sum of all seven amplitudes with negative reflectivity (a) and total intensity with coherent sum overlaid in red (b).

that the non-Pomeron production of events should contribute approximately 5% to the observed intensity. In Fig. 7.10a the coherent sum, i.e. the intensities plus overlaps (see Sec. 7.1.4), of this seven waves is plotted. The relative contribution to the overall intensity is $\sim 2\%$ which is an good agreement with the predicted value. Figure 7.10b shows the coherent sum of all negative waves overlaid with the total intensity.

The corresponding plots for the lead target data are shown in Fig. 7.11. Although the intensities of the Flat wave and the coherent sum of the negative-reflectivity waves seems to be more pronounced, still their contribution to the overall intensity is small in the order of 10%. One possible explanation for the small difference to the respective plots of the proton target analysis (Fig. 7.9b and Fig. 7.10b) could be the relatively coarse event selection (see Sec. 5.2) applied

to the lead target data.

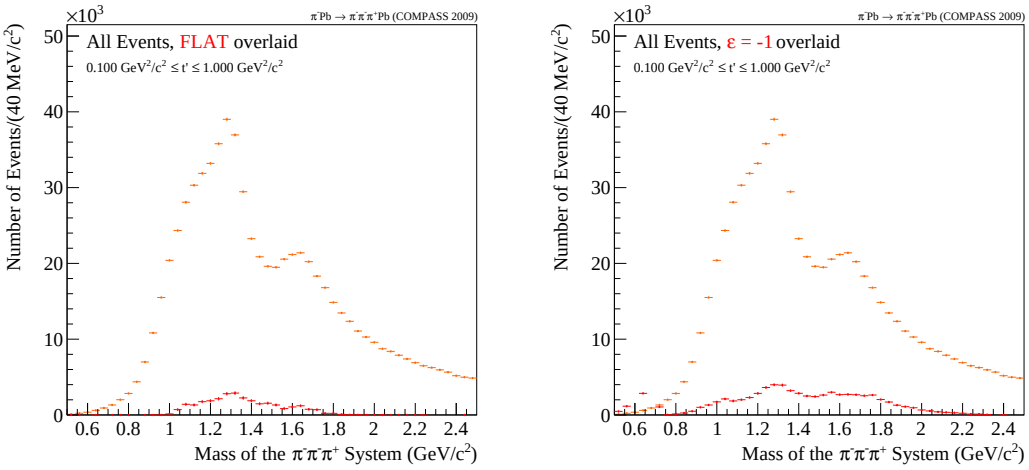

Figure 7.11 Integrated total intensity with FLAT wave overlaid (a) and total intensity with coherent sum of the negative-reflectivity waves overlaid (b), 2009 data

7.3.2 Characteristic Amplitudes

The dominant block in the model with 88 amplitudes is the one with positive reflectivity, motivated by the idea that Pomeron production is the leading mechanism at COMPASS energies and predicted in the model, discussed in Sec. 2.1.1. In the following a subset of these 80 waves will be discussed. The selection is based on the observations of previous analyses, therefore well established and investigated partial waves are shown as a kind of standard candles. In addition this extended model and the large data set allows to discuss waves, never shown before, which could also help to gain insight into the dynamics of the meson spectrum.

Amplitudes with $J^{PC} = 0^{-+}$

Partial waves with quantum numbers $J^{PC} = 0^{-+}$ have in common that they correspond to rather flat angular distributions. Especially the wave with $J^{PC} M^{\varepsilon} \xi \pi L = 0^{-+} 0^{+} (\pi\pi)_S \pi S$ can be seen as the coherent twin of the incoherent Flat wave. The integrated intensity of this wave is depicted in Fig. 7.12a. The fit outcome of the Deck Monte Carlo data sample is overlaid in green. In addition to the normalisation of the Deck intensity, discussed in the introduction of this section, an additioanal scaling had to be applied, as the used Deck model is known to overshoot for some waves [ACJ+74]. In this plot the shortcomings of this kind of comparison became apparent. But the absolute or normalised intensity of the Deck fit is not the important input to the analysis, it is the mass-dependence of the intensity which could give a hint on how to parametrise non-resonant contributions in the the real data. In that spirit the Deck intensity looks like the three-pion damped phase space while the intensity of the real data reveals two peaks at 1.3 and 1.8 GeV/c^2 which were identified as $\pi(1300)$ and $\pi(1800)$ in previous analyses. Whether this is still valid, based on informations obtained by this analysis, will be discussed in Chap. 8. The large amount of data leads to almost vanising statistical error bars and

hence jumps in the intensity distributions cannot be explained by statistical uncertainities as in previous analyses. Therefore the thresholds of the model (see Sec. 7.1.5), an inevitable part of three-pion analyses, are drawn as blue lines. Most of the discontinuities in the real data or Deck Monte Carlo fit results can be associated with these thresholds. As discussed in Sec. 7.1.5 one important part of this thesis was to reduce the amount of thresholds in the model and to spread the necessary ones along the three-pion mass range as good as possible. But nevertheless discontinuities cannot be avoided completely, they are part of this kind of analysis. The $\pi(1800)$ is also clearly visible in the partial wave with the $f_0(980)$ isobar (Fig. 7.12b), where a mass threshold at 1.2 GeV/c^2 was necessary.

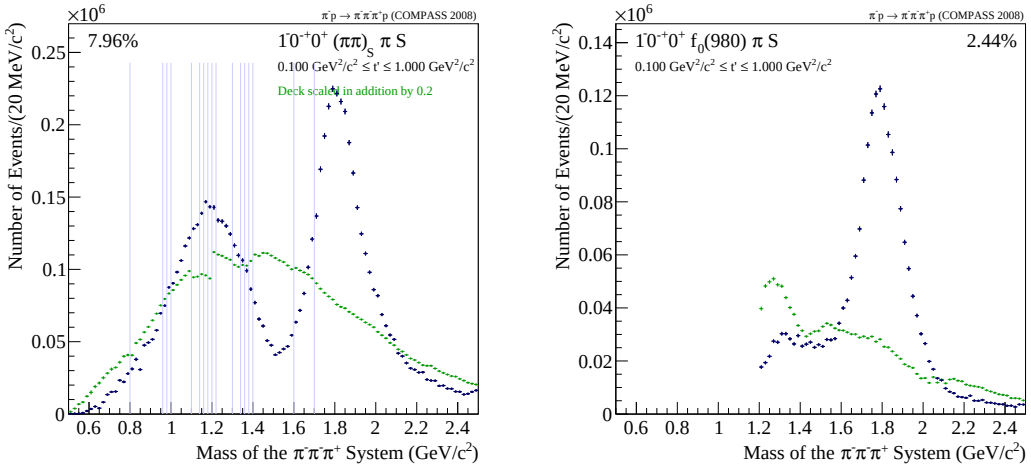

(a) **(b)**

Figure 7.12 Integrated intensity of partial waves with $J^{PC} = 0^{-+}$ decaying into the $(\pi\pi)_S$ wave (a) and the $f_0(980)$ isobar (b).

Finally the 0^{-+} wave with the $\rho(770)$ (Fig. 7.13a) as isobar is known to contribute to the $\pi(1300)$. The shoulder at 1.8 GeV/c^2 cannot be identified with the $\pi(1800)$, the relative phase motion can shed light on this issue. Unlike the intensities it is not possible to obtain a kind of integrated phase motion of all t' bins. A weighted phase, averaged over all t' bins could be one option but it was decided to plot phase differences of four t' bins representing the observed kinematic range. In this way variation of the phase motions with increasing t' (from light red to dark blue) can be investigated. The relative phase motion (see Fig. 7.13b) between the $\rho\pi$ amplitude and the wave with the $f_0(980)$ isobar (Fig. 7.12b), where the $\pi(1800)$ could be clearly identified, shows a clear phase motion. The falling phase differences at 1.8 GeV/c^2 indicate a resonance in the amplitude, decaying into the $f_0(980)$ and no resonance contribution in the amplitude with the $\rho(770)$ isobar. Further partial waves with $J^{PC} = 0^{-+}$ will be discussed in Sec. 7.5.2.

Amplitudes with $J^{PC} = 1^{++}$

The $J^{PC} = 1^{++}$ sector is covered by 13 partial waves with positive reflectivity in the fit model. These amplitudes represent the decay modes of the a_1 resonances, especially of the long-known but still vague $a_1(1260)$ (see Sec. 1.4.1). The PDG [B+12] lists nine of these waves as observed decay channels. Nevertheless only the two dominating waves will be presented here in order to gain an first overview of the overall analysis. Most of these other amplitudes will be

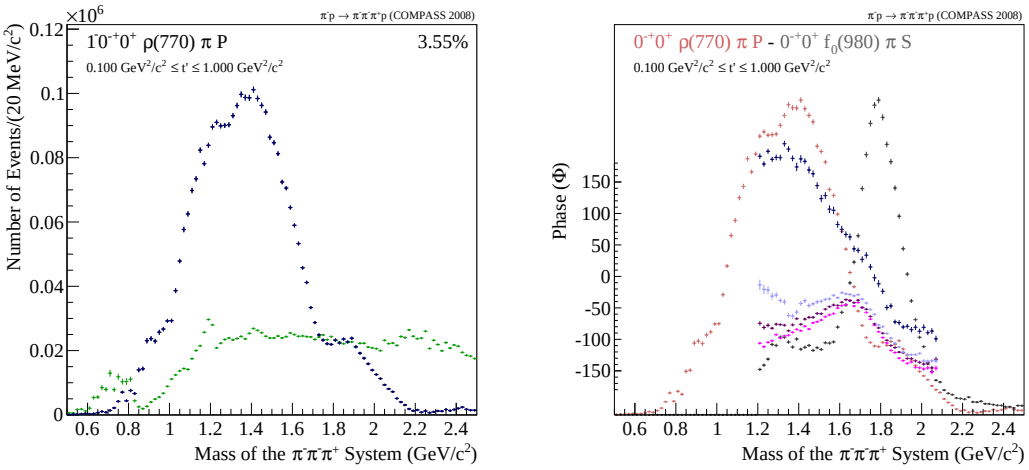

(a) **(b)**

Figure 7.13 Integrated intensity of the partial wave with $J^{PC} = 0^{-+}$ decaying into the $\rho(770)$ isobar and a P-wave. The relative phase motion (from light red to dark blue with increasing t') between this wave (a) and the one shown in Fig. 7.12b is depicted in (b).

discussed in Sec. 7.5.1 and Sec. 7.5.5.
The wave which contributes most, with more than 30%, to the observed intensity has quantum numbers $1^{++}0^{+}\rho(770)\pi S$, depicted in Fig. 7.14a. Its huge intensity and broad shape makes it to a natural choice for the anchor wave (see Sec. 7.1.2). This amplitude is used since decades to obtain resonance parameters for the $a_1(1260)$ resonance. The small statistical error bars reveal discontinuities in the mass depenence which can be again linked to the presence of thresholds. The possible Deck contribution is plotted in green. The first published Deck model by Ascoli [ACJ+74] assumed a peak of Deck produced final states at the $a_1(1260)$ mass and a contribution of more than 40% to the observed intensity in that particular amplitude. Although a more modern and extended Deck model was used for the studies in this thesis (see Sec. 5.4) the assumed Deck contribution peaks at the same mass as the real data and its contribution is not neligible. This plot illustrates the difficulties of the community to settle the resonance parameters: the understanding of non-resonant contributions is poor up to now but essential to understand the $a_1(1260)$. The highly granualted data set in bins of $m_{3\pi}$ and t' offers the possibility to learn more about this. Regarding the PDG at least one aditional resonance is observed to decay into this wave, the $a_1(1640)$. Clarity can bring only the next step of this analysis, discussed in Chap. 8. The $M = 1$ partner wave of the major amplitude is shown in Fig. 7.14b. The triangular shape of the peak is an artefact of thresholds but not so relevant for the analysis. More interesting is the shoulder at 1 GeV/c^2, a mass region below the first three pion resonances which, can be correlated to the complicated t' dependence of this amplitude (see Sec. 7.4 for more details). Striking is the influence of the mass thresholds to the Deck intensity, regaridng the jump at 1.1 GeV/c^2. This shows that for each data set a particular adjustment of the thresholds has to be performed. In this analysis, however, the same mass thresholds are applied to the Deck Monte Carlo as used for the real data.

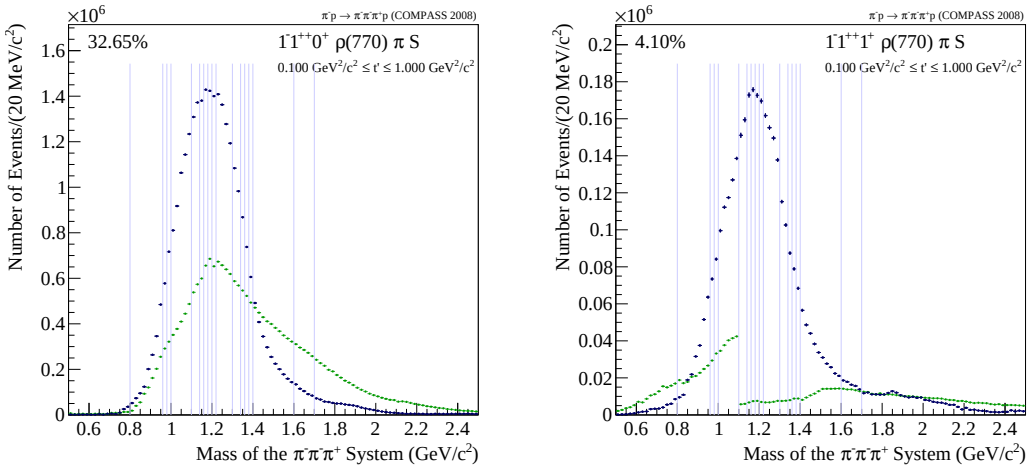

(a) **(b)**

Figure 7.14 Integrated intensity of the partial waves with $J^{PC} = 1^{++}$ decaying into the $\rho(770)$ isobar, with spin projection $M^{\varepsilon} = 0^{+}$ (a) and $M^{\varepsilon} = 1^{+}$ (b) and orbital angular momentum $L = 1$.

Amplitudes with $J^{PC} = 2^{++}$

The $2^{++}1^{+}\rho(770)\pi D$ partial wave is one of the standard candels of the three-pion spin-parity analysis (see Fig. 7.15a). It is the dominant decay mode of the $a_2(1320)$ resonance and almost background free. Its huge peak structure is even visible in the raw three pion mass spectrum (see Fig. 5.11a). Besides the $a_2(1320)$ another resonance, the $a_2(1700)$, is observed to decay into this channel, but its contribution is not visible at this level of the analysis. It will be considered for the extraction of resonance parameters, discussed in Chap. 8. It is known from basic quantum mechanics that for a total spin $J = 2$ all spin projections up to 2 are allowed. On the other hand it was predicted in Sec. 6.3.1 and will be shown in the following section about t' dependencies that amplitudes with spin projection $M = 2$ are highly suppressed in comparison to waves with $M = 1$ or even more with respect to $M = 0$ (which is not allowed for partial waves with $J^{PC} = 2^{++}$, see Sec. 6.1). Nevertheless the large data set allows to investigate the corresponding amplitude with $M = 2$, shown in Fig. 7.15b. It is clearly separated from the background and the known '$a_2(1320)$ peak' is seen. In contrast to its dominant $M = 1$ partner the falling edge is rather sharp which could be a hint of destructive interference between the $a_2(1320)$ and the $a_2(1700)$. The almost identical shape of both waves and the fact they seem not to be visibly dominated by non-resonant contributions (the projected Deck contribution can be regarded negligible in comparison to the overall intensity) allows a first esimate of the suppression between $M = 2$ with respect to $M = 1$ states. Integrating both intensities between 1.2 and 1.4 GeV/c^2 and taking the ratio results in a supression of ~ 24 of the $M = 2$ wave. This explains why this amplitude was hardly visible in previous experiments. Finally the amplitude decaying into $f_2(1270)$ is shown in Fig. 7.15c, with a peak at 1.3 GeV/c^2 which is known to be associated with the $a_2(1320)$. In addition a clear structure at 1.6 GeV/c^2 sticks out. Recalling the PDG tables, a possible decay mode of the second a_2. The spin projection partner of this wave with $M = 2$ is part of the model, but the large suppression factor reduces its contribution to $\sim 0.01\%$.

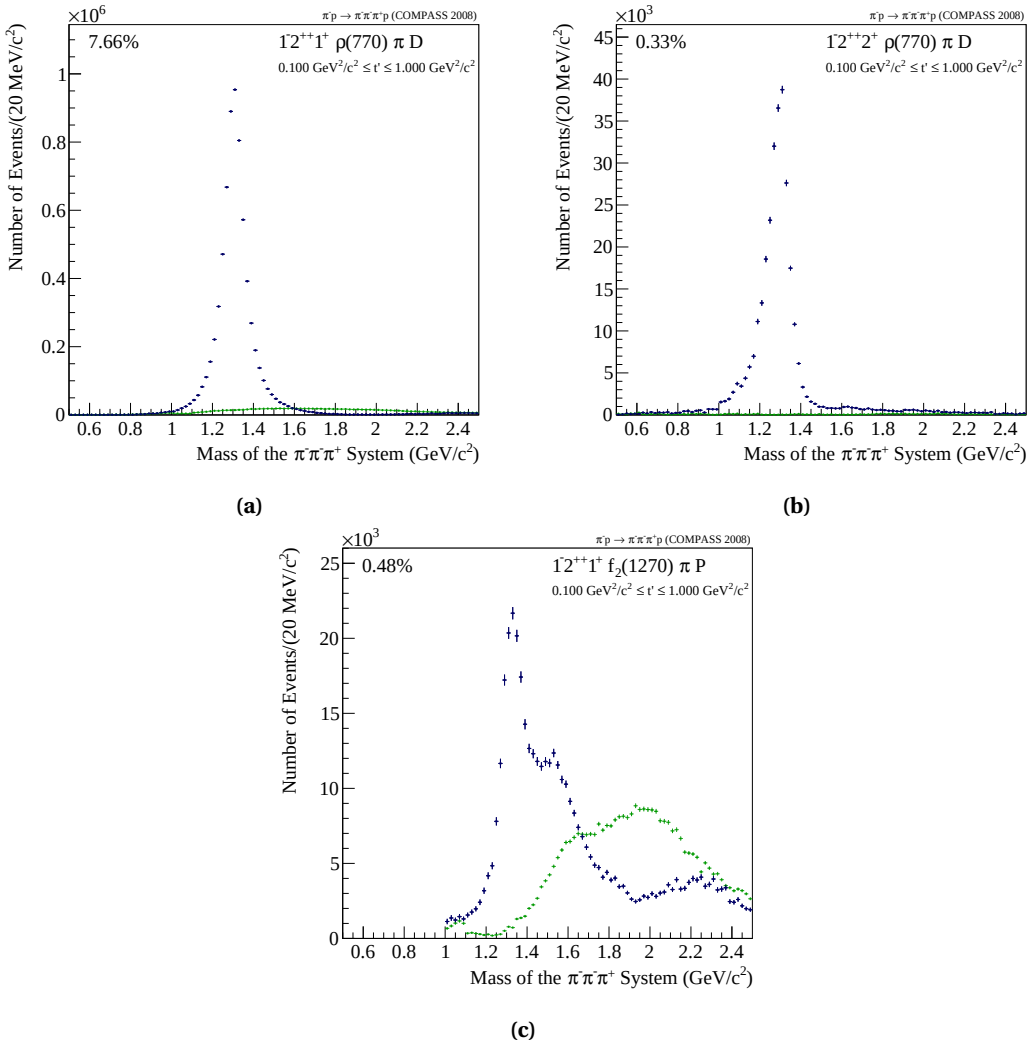

Figure 7.15 Integrated intensity of partial waves with $J^{PC} = 2^{++}$ decaying into the $\rho(770)$ isobar, with spin projection $M^{\varepsilon} = 1^{+}$ (a) and $M^{\varepsilon} = 2^{+}$ (b) and decaying into $f_2(1270)$ shown in (c).

Amplitudes with $J^{PC} = 2^{-+}$

Partial waves with quantum numbers $J^{PC} = 2^{-+}$ and positive reflectivity contribute the biggest fraction of the model. They correspond to the possible decay channels of π_2 resonances with the $\pi_2(1670)$ and the $\pi_2(1880)$ being the most prominent representatives. As discussed in Sec. 1.4.1 the $\pi_2(1670)$ is well measured since decades but with the discovery of the $\pi_2(1880)$ and the close distance of both resonances there came the idea that both resonaces are the same object [DS06].

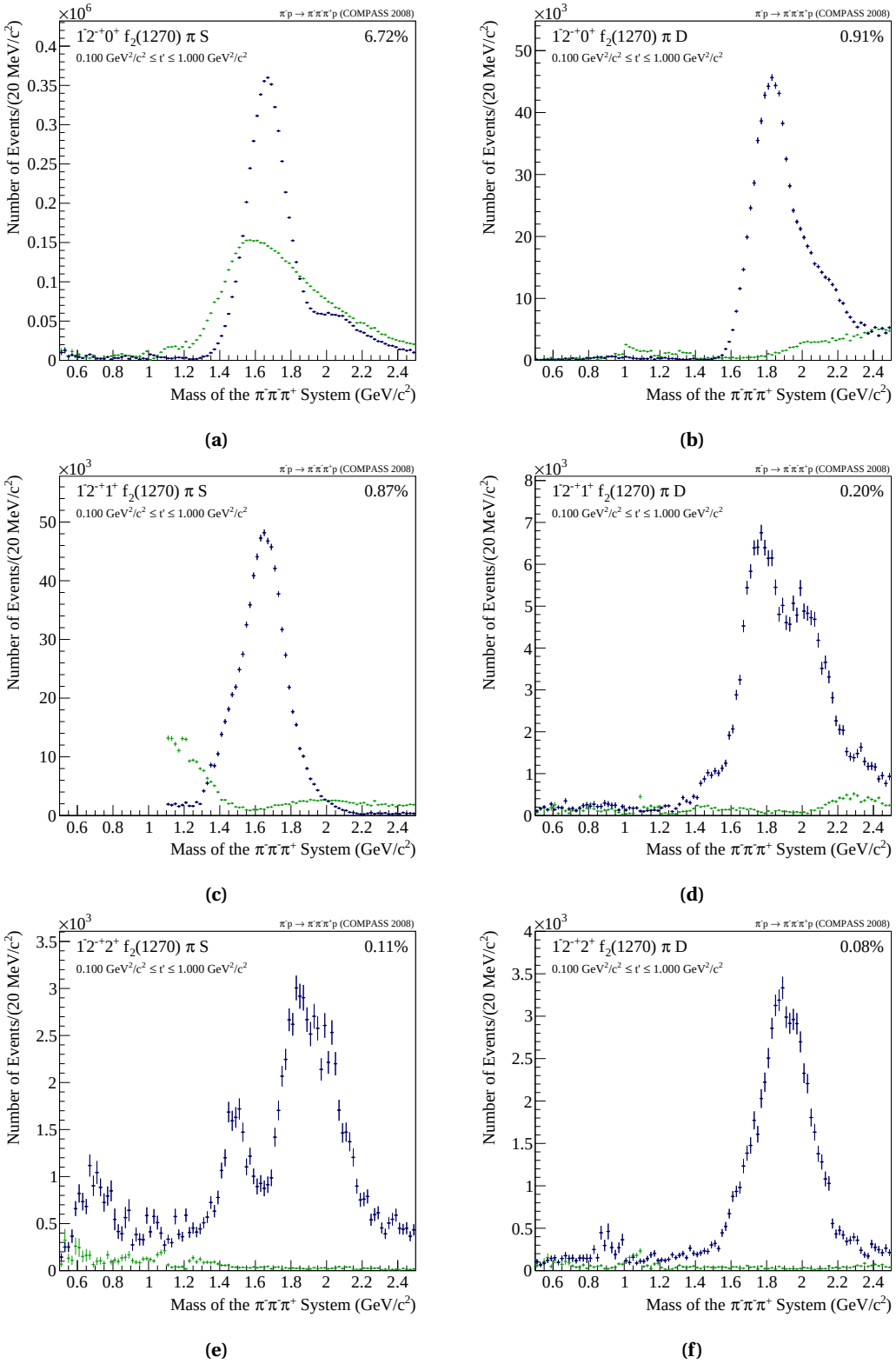

Figure 7.16 Integrated intensity of partial waves with $J^{PC} = 2^{-+}$ decaying into the $f_2(1270)$ isobar, with spin projection from $M^{\varepsilon} = 0^+$ up to $M^{\varepsilon} = 2^+$ and orbital angular momentum $L = 1$ and $L = 2$.

The two π_2 mesons are then the the result of this mezanine meson, shifted by Deck background. The main decay channel of the $\pi_2(1670)$ is depicted in Fig. 7.16a and for the $\pi_2(1880)$ in Fig. 7.16b. In both cases the Deck projection is plotted which helps to understand the idea of a possible single π_2 resonance. The Deck intensity shown in Fig. 7.16a peaks at ~ 1.4 GeV/c^2, supporting the idea of a genuine resonance shifted to lower masses in that decay channel, while the Deck in Fig. 7.16b shows a continous rising edge, indicating a possible shift to slightly higher masses in that channel. This model explanation is based on fit results of the ACMOR collaboration [D+81] and was waiting to be proven with more recent data. The analysis presented here offers the possibility by regarding more amplitudes with a much higher precision. An overview of both decay channels sorted in columns, $f_2(1270)\pi S$ on the left versus $f_2(1270)\pi D$ in the right column, is shown in Fig. 7.16 up to spin projection $M = 2$. The partial wave $2^{-+}2^+ f_2(1270)\pi S$ (Fig. 7.16e) is observed for the first time and shows an unexpected behavior. In contrast to its spin projection partners witn $M = 0$ and $M = 1$ it peaks at 1.9 GeV/c^2 and reveals an additional bump at 1.4 GeV/c^2. While relative phase motions between this wave and known resonances at 1.9 GeV/c^2 can be observed, which give a hint for the $\pi_2(1880)$, the bump at lower masses shows no phase. Its origin is unknown but its peak at 1.4 GeV/c^2, which is the sum of the pion mass and the f_2 isobar, could be explained by dynamical processes at the threshold of the $f_2\pi$-system. Regarding the partial wave with $M = 1$, plotted in Fig. 7.16c a shoulder at the same mass position at 1.4 GeV/c^2 can be seen.
The most striking finding for the three partial waves decaying into a D-wave is shown in Fig. 7.16d, the amplitude with $M = 1$. A double-peak structure and corresponding phase motions could reveal, as well as the previous observation in Fig. 7.16e, a hint for the $\pi_2(1670)$ and the $\pi_2(1880)$ being two distinct resonances. An answer can only be given by a further extraction of resonance parameters (see Chap. 8). The wave with spin projection $M = 2$, depicted in Fig. 7.16f, is observed for the first time, too. This amplitude shows an almost background-free peak at the $\pi_2(1880)$ position.
Only six waves of the rich set of 2^{-+} amplitudes were introduced at that place of the thesis. Further discussions deserve their own section (see Sec. 7.5.3).

Amplitudes with $J^{PC} = 3^{++}$

Partial waves with $J^{PC} = 3^{++}$ are quite unexplored. A possible resonance, the $a_3(1875)$, was claimed to be observed in several 3^{++} decay channels [CDH+02], namely waves decaying through $\rho(770)$, $\rho_3(1690)$ and $f_2(1270)$ isobars, all with spin projection $M = 0$. In order to take these facts into account 11 partial waves with $J^{PC} = 3^{++}$ are part of the model. In contrast to previous analyses waves with $M = 1$ are considered. Representative for these amplitudes both spin projections, $M = 0$ and $M = 1$, with the $\rho_3(1690)$ isobar involved are depicted in Fig. 7.17. If there exists an a_3 resonance, this would be its preferred decay channel. Analogous to the main decay of the $a_1(1260)$ into the $\rho(770)\pi$ and a S wave, the isobar would carry the spin and the orbital angular momentum L would be again the S wave.

Amplitudes with $J^{PC} = 4^{++}$

In contrast to the previous, partial waves with 4^{++} are under investigation since more than 30 years. The reason is the existence of the $a_4(2040)$ meson, which can be clearly seen in two decay channels. The one decaying through the $\rho(770)$ isobar is depicted in Fig. 7.18a while the

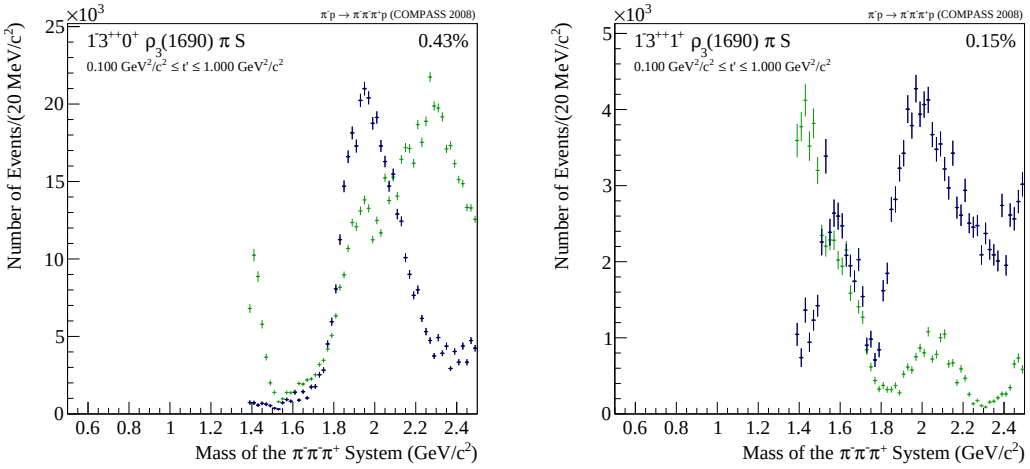

(a) **(b)**

Figure 7.17 Integrated intensity of amplitudes with $J^{PC} = 3^{++}$ decaying into the $\rho_3(1690)$ isobar, with spin projection $M^{\varepsilon} = 0^+$ and $M^{\varepsilon} = 1^+$.

second decay involving the $f_2(1270)$ is plotted in Fig7.18b. Both channels show a clear peak. The projection of the Deck contribution follows the corresponding phase space without any peak structure around the a_4 mass. The distinct structure is the reason, why this high-spin resonance could be observed with comparatively small number of events. Consistent with the most recent analyses [AAA+10, Neu12, Sch12] the observed peak reveals a mass around 1.9 GeV/c^2, contrary to the official naming. For both amplitudes, discussed in this section, the spin projection partners with $M = 2$ are considered in the model. While the $\rho(770)\pi$ channel with $M = 2$ (Fig. 7.18c) shows the same structure, the partial wave with the $f_2(1270)$ and $M = 2$ (Fig. 7.18d) reveals a dip at the a_4 mass region, which could be generated by destructive interference.

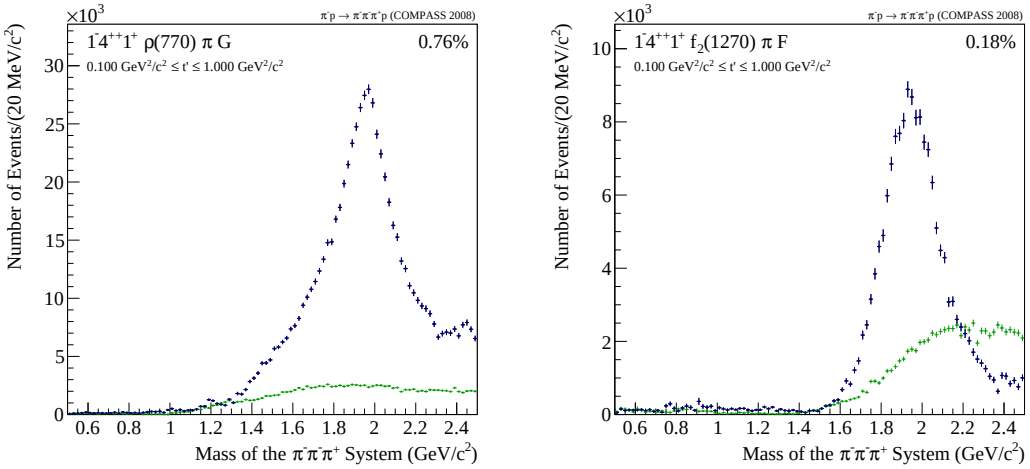

(a) **(b)**

Figure 7.18 Integrated intensity of amplitudes with $J^{PC} = 4^{++}$ decaying into the $\rho(770)$ (a) and $f_2(1270)$ (b) isobar, both with spin projection $M^{\varepsilon} = 1^+$.

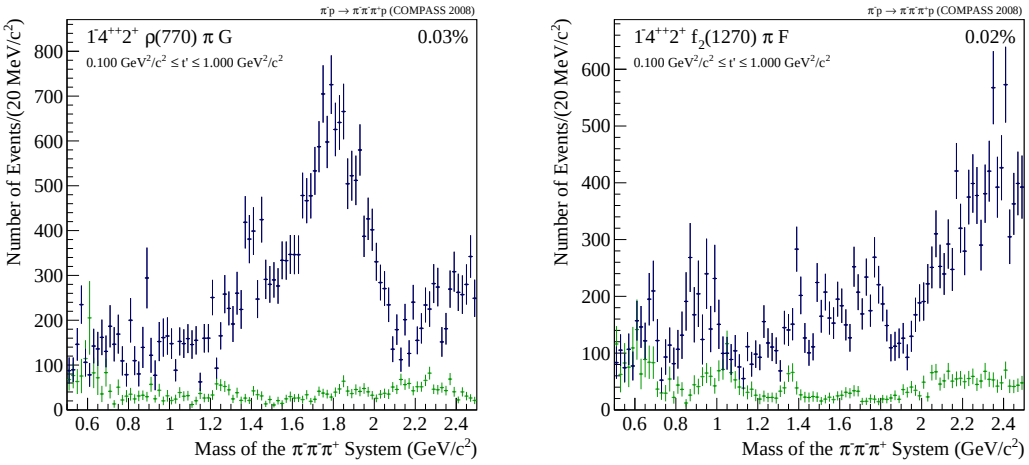

(c) **(d)**

Figure 7.18 Integrated intensity of amplitudes with $J^{PC} = 4^{++}$ decaying into the $\rho(770)$ (a) and $f_2(1270)$ (b) isobar, both with spin projection $M^{\varepsilon} = 2^+$.

Major Waves in the Lead Data Set

Comparing the total intensities of the three pion-mass spectrum taken with the proton target (Fig. 7.9b) and the lead target (Fig. 7.11a) shows no obvious discrepancies, as expected. For a fist survey the major waves of the lead target data set are observed and its production strengths and shapes with the corresponding results of the main analysis with a proton data are compared. For the lead target the four dominat amplitudes, also visible as characteristic bumps at the mass spectrum, are depicted in Fig. 7.19.
Analogous to the proton data the most dominant wave is the $1^{++}0^+\rho\pi S$ wave (Fig. 7.19a), followed by the $2^{++}1^+\rho\pi D$ (Fig. 7.19b) and the $2^{-+}0^+ f_2\pi S$ waves, shown in Fig. 7.19c. Despite the fact that for this analysis a more coarse binning in $m_{3\pi}$ and t' is used, the overall shape of these three amplitudes is comparable to the fit result of the proton data set. A striking feature are the different relative intensities. While, for example, the $1^{++}0^+\rho\pi S$ wave is observed with a relative intensity of $\sim 33\%$ in the proton data the same wave has only $\sim 19\%$ for the lead data set. This is valid for all waves discussed in this section and more waves not shown here.
The $0^{-+}0^+(\pi\pi)_S\pi S$ wave (Fig. 7.19d) differs significantly from the corresponding intensity observed for the proton data (see Fig. 7.12a). The best agreement can be find when comparing Fig. 7.19d with the proton result for a certain kinematic regime of t' (see Fig. 7.19e). The reason for this is not understood completely. It could be linked to the complicated t' dependence of this particular wave (see Sec. 7.4.2) or with the interference of resonances and Deck-like contributions which also effects the line shapes. A further discussion on this can be found in Sec. 7.5.4.

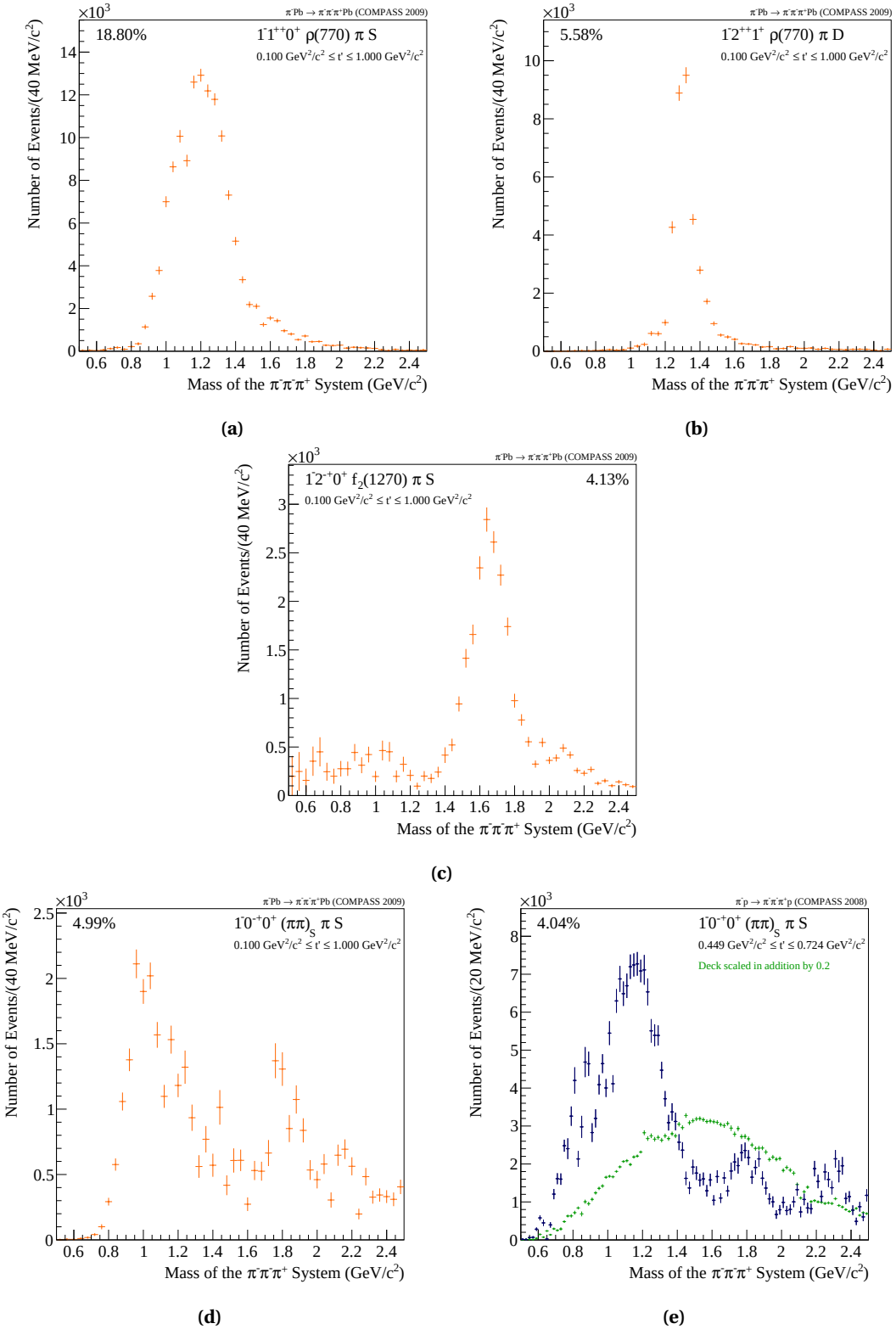

Figure 7.19 Characteristic partial waves in the 2009 lead data sample, 2009 data.

7.4 Dependence on the Squared Four-Momentum Transfer t'

Up to now only the variance of the amplitudes as a function of $m_{3\pi}$ was discussed, while the depence on t' was taken out by summing incoherently over all 11 independent fit results, for each t' bin, of one amplitude. As a first approximation in order to get an overview of the structures observed for every partial wave, this is sufficient. But the fact, that this data sample is split in bins of $m_{3\pi}$ and t' offers the possibility to investigate the behaviour of each amplitude not only as a function of the invariant mass but additionaly the realisation of each amplitude for different kinemtaic regions of t'. As an example the intensity of the partial wave with quantum numbers $1^{++}1^{+}\rho\pi S$ for every second t' bin, starting from the first bin, is plotted in Fig. 7.21. In contrast to Fig. 7.14b, where the integrated intensity is plotted for this amplitude, the individual intensities reveal details which are washed out by the summation. The most striking observation is the shift of the peak, located at ~ 1.2 GeV/c^2 in the low t' region and at ~ 1.0 GeV/c^2 for the upper limit of t'. This partial wave is known to contribute to the $a_1(1260)$ thus the peak structure corresponds to this resonance. Since resonances are independent from the squared four-momentum t' a possible interference between the $a_1(1260)$ and non-resonant background, e.g origin from the Deck effect, could be an explanation. From the description of the different production mechanisms (see Chap. 2) it is obvious that they are connected to different t' dependencies. The questions is how to visualise this dependence.
The fact that the data sample is binned in t' allows to apply a similar plotting scheme than the one used in the previous section. This concept is not new, it was shown by e.g. [CDH^{+}02, DMS^{+}06], but due to their limited data sample this study was done for only one amplitude of their models. The large size of the sample studied here enables to extract the t' dependence for each maplitude of the model. The approach of this investigation is to sum up the resulting intensity of an amplitude in a certain mass region for each t' bin and plot the sums as a function of t'. The focus is on the possible resonant realm of an amplitude. For example the partial wave with $1^{++}0^{+}\rho\pi S$ is known to contribute to the $a_1(1260)$ meson. In order to learn more about the t' dependence of the $a_1(1260)$ meson in that certain decay channel the corresponding intensities of all 11 t' bins in the mass range of 1.2 ± 0.1 GeV/c^2 is plotted as a function of t' (see Fig. 7.22a). As a second example serves the partial wave with quantum numbers $2^{++}1^{+}\rho\pi D$ which is one possible realisation of the $a_2(1320)$. The intensities are summed in the intervall of 1.32 ± 0.1 GeV/c^2 (see Fig. 7.22b). It has to be stated that each bin of these kind of plots is normalised by its corresponding bin width and the y-axis has a logarithmic scale. These actions should help to guide the eye. While the first plot shows a clear exponential behaviour the latter seems to reveal a mixture of quadratic and exponential components. Therefore the next step in the study of t' dependencies is to define a fit function, which is able to describe these data.

7.4.1 Derivation of t' Dependence Formulation

The exponential behaviour is motivated by Regge exchange. The amplitude is proportional to an exponential function (see Sec. 2.2.1):

$$A(s,t,M) \sim \exp(-bt'/2) \tag{7.40}$$

Without loss of generality it seems that the second element couples to the spin projection M, as it is not seen for the amplitude with $M = 0$, shown in Fig. 7.22a. In order to derive the

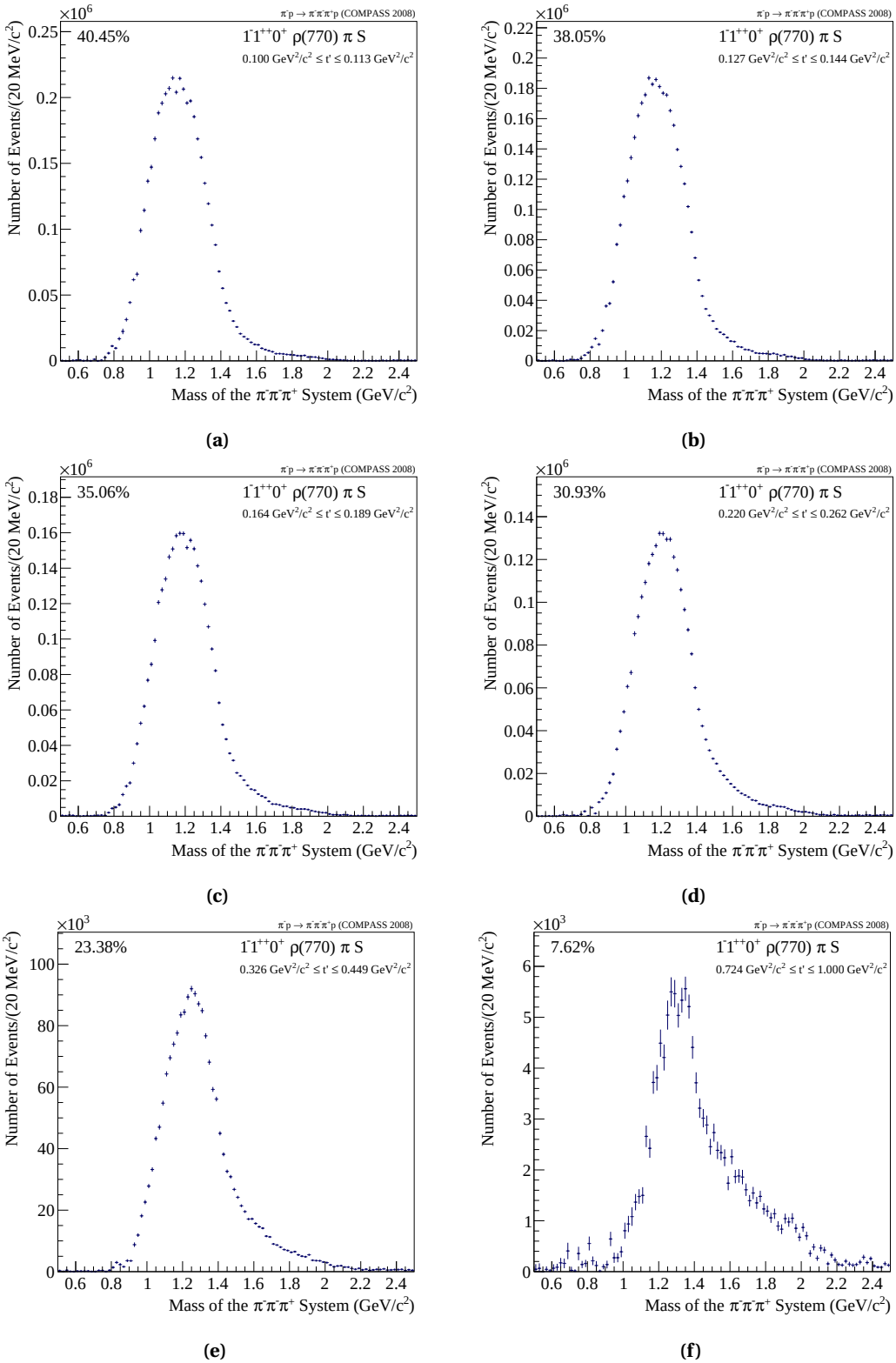

Figure 7.20 Intensity of the amplitude with $J^{PC}M^{\varepsilon}\xi\pi L = 1^{++}0^{+}\rho\pi S$ for different t' bins.

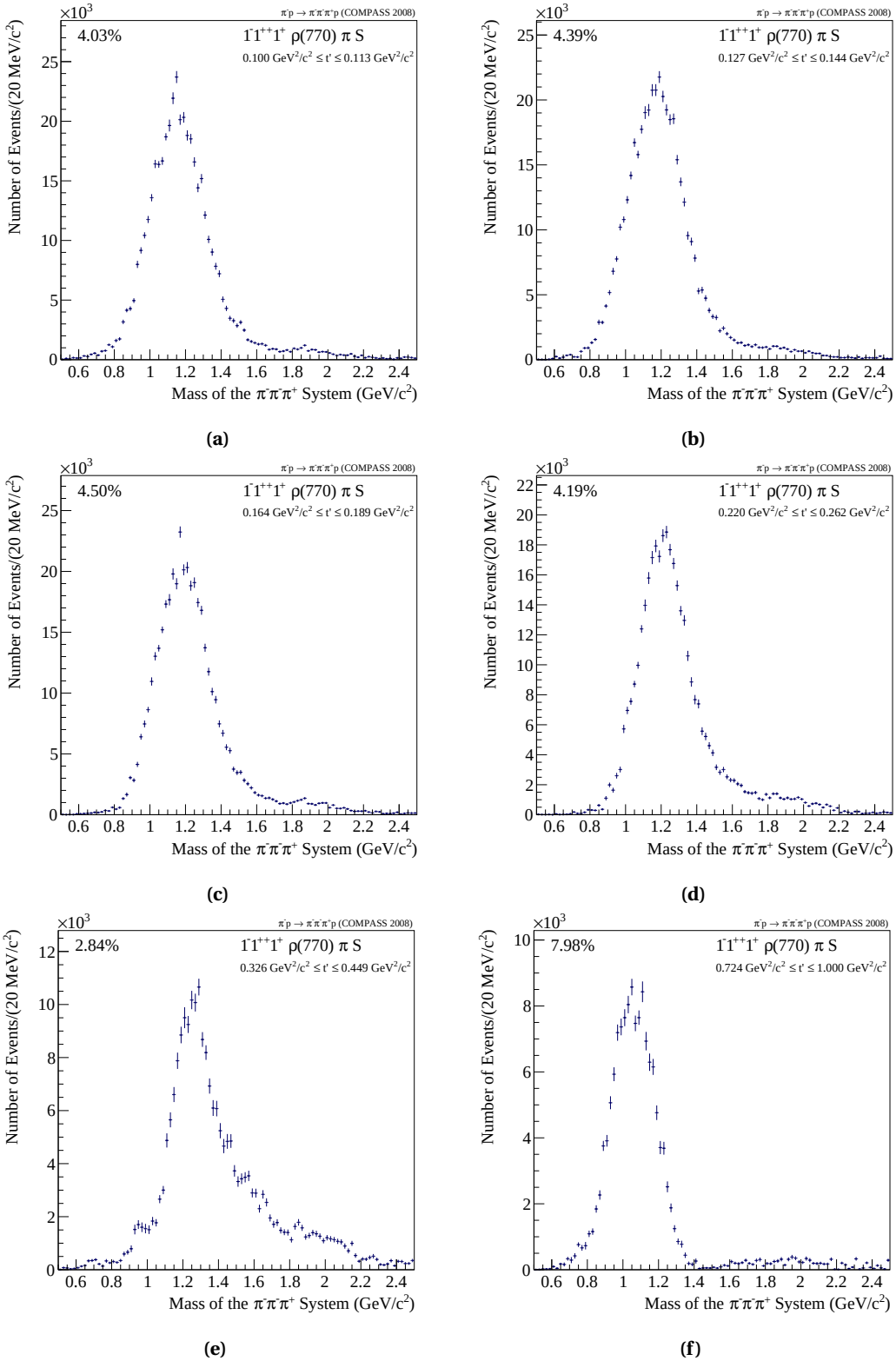

Figure 7.21 Intensity of the amplitude with $J^{PC}M^{\varepsilon}\xi\pi L = 1^{++}1^{+}\rho\pi S$ for different t' bins.

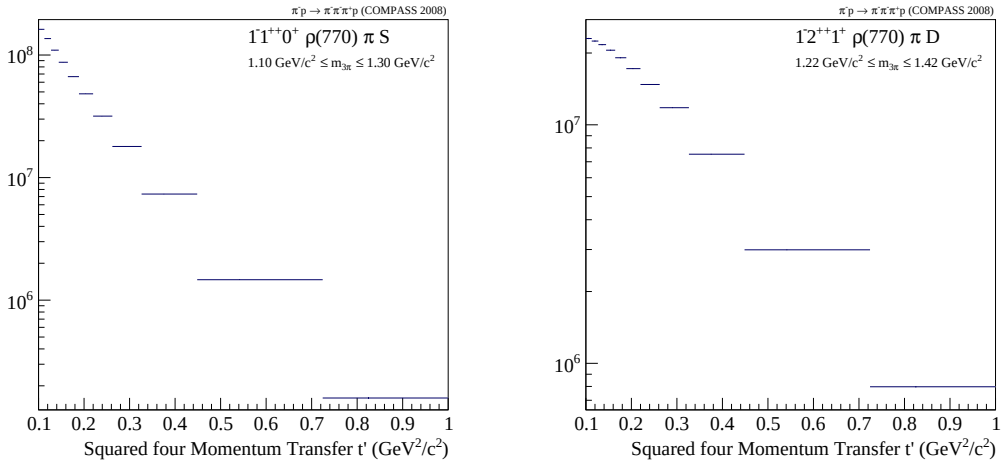

(a) **(b)**

Figure 7.22 t' dependence for the amplitude $1^{++}0^{+}\rho\pi S$ in the mass range of 1.2 ± 0.1 GeV/c^2 (a) and for the amplitude $2^{++}1^{+}\rho\pi D$ in the mass range of 1.32 ± 0.1 GeV/c^2(b).

correct spin dependence it is convenient to start with an investigation of the diffractive production as a simple two-particle scattering process. The initial and final state can be described as a plane-wave helicity states with $|\vartheta\phi\mu_1\mu_2\rangle$, with ϑ and ϕ describing the orientation of the two interacting particles while μ_1 and μ_2 are the corresponding helicities. These states are not eigenstates of $\mathbf{J}^2$ and J_z therefore have to be transformed in order to be so.

$$|\vartheta\phi\mu_1\mu_2\rangle = \sum_{JM}\left(\frac{2J+1}{4\pi}\right)^{1/2} D^{J}_{M\mu}(\phi,\vartheta,-\phi)|JM\mu_1\mu_2\rangle \tag{7.41}$$

With the D-functions introduced in Sec. 6.3. Thus the helicity states can be constructed by an infinite sum of two-particle angular momentum helicity states. The amplitude A of the scattering process (see Fig. 2.2), described with plane-wave helicity waves and the transition matrix T is

$$A \sim \langle\vartheta\phi\mu_c\mu_d|T|00\mu_a\mu_b\rangle \tag{7.42}$$

and can be transformed to

$$A \sim \sum_{J_fM_f}\sum_{J_iM_i}\left[\left(\frac{(2J_f+1)(2J_i+1)}{16\pi^2}\right) D^{J_f*}_{M_f\mu_f}(\phi,\vartheta,-\phi) D^{J_i}_{M_i\mu_i}(0,0,0)\langle J_fM_f\mu_c\mu_d|T|J_iM_i\mu_a\mu_b\rangle\right] \tag{7.43}$$

With the conservation of the total angular momentum, i.e. $J_f = J_i = J$ and $M_f = M_i = M$ and assuming that the S-matrix (see Sec. 2.1) is rotationally invariant, Eq. (7.43) can be simplified to

$$A \sim \sum_{J}\left[(2J+1)\langle JM\mu_c\mu_d|T|JM\mu_a\mu_b\rangle e^{i(\mu_i-\mu_f)\phi} d^{J}_{\mu_i\mu_f}(\vartheta)\right] \tag{7.44}$$

In the limit of small angles the d-function can be simplified and Eq. (7.44) reduces to

$$A \sim (\sin\frac{1}{2}\vartheta)^{|\mu_i-\mu_f|} e^{i(\mu_i-\mu_f)\phi}, \qquad \vartheta \to 0 \tag{7.45}$$

Taking into account the equivalence $\sin(x/2) = \sqrt{(1-\cos(x)/2)}$ and regarding the calculations of the squared four-momentum transfer in Sec. 5.1.6, Eq. (7.45) can be rewritten as

$$A \sim |t - t_{\min}|^{|\mu_i - \mu_f|/2} e^{i(\mu_i - \mu_f)\phi} \tag{7.46}$$

Recalling the fact that the helicity of pions is zero and of the intermediate state X always integer, simplifies $|\mu_i - \mu_f|$ to M (see Sec. 6.3), and thus the transition amplitudes T_i are proportional to

$$T_i \sim t'^{M/2} e^{i(\mu_i - \mu_f)\phi} \exp(-bt'/2) \tag{7.47}$$

The observable of interest is the intensity $\mathscr{I}$ and with Equ. (7.35) the intensity of a partial wave as a function of t' is proportional to

$$Intens(t') \sim t'^{M} e^{-bt'} \tag{7.48}$$

whith the squared phase factor $e^{i(\mu_i - \mu_f)\phi}$ being one. A complete and detailed derivation of the t' dependence can be found in [Per74].

7.4.2 Fit Model and Results

With the derivation of a formulation of the t' dependence it is now possible to construct fit models which can be applied to the data. As noted at the beginning of this section only possible resonant regions of the amplitudes are investigated where a t' dependence as described in Eq. (7.48) can be regarded as valid. On the other hand a non-resonant backgrounds are contributing in these regions although their strength cannot be evaluated on the level of a spin-parity analysis. Two fit functions are taken into account. A single exponential function, motivated by the assumption that only one production process significantly contributes to the observed intensity (see Eq. (7.49)). The incoherent sum of two exponentials should reflect the possibilty of two production processes involved (see Eq. (7.50)). A coherent sum was tried but the fit was not able to take the interference into account. In addition no complete coherent description of amplitudes with two contributing mechanisms could be derived.

$$f_{\text{single}} = t'^{M} \cdot G \cdot e^{-bt'} \tag{7.49}$$

$$f_{\text{double}} = t'^{M}(G_1 \cdot e^{-b_1 t'} + G_2 \cdot e^{-b_2 t'}) \tag{7.50}$$

Both fit functions were applied to the data. For each partial wave of the study a dedicated mass range was chosen, as noted before. Based on the resulting χ^2/ndf it was decided, which fit functions can be regarded as the best description of the data. In order to stabilise the fit the number of data points has been doubled (11 data points face four parameters for the double-exponential function) by halving each t' bin (see Sec. 7.2) and thus 22 data points are now available for the study. The qualitative equivalence of both spin-parity analyses (11 versus 22 t' bins) is shown in Sec. 7.6.2. The fit itself has to be defined such that for each t' bin its center-of-gravity has to be considered and not the bin center as the t' binning follows the common t' spectrum which has an exponential behaviour and therefore shifts the real bin center away from the middle towards the lower edge. Finally it has to be beared in mind that the summation over a certain mass region results in large numbers of the intensity and thus small statistical errors. This means that even small deviations of fit result from the data points lead to relatively large values of χ^2/ndf.

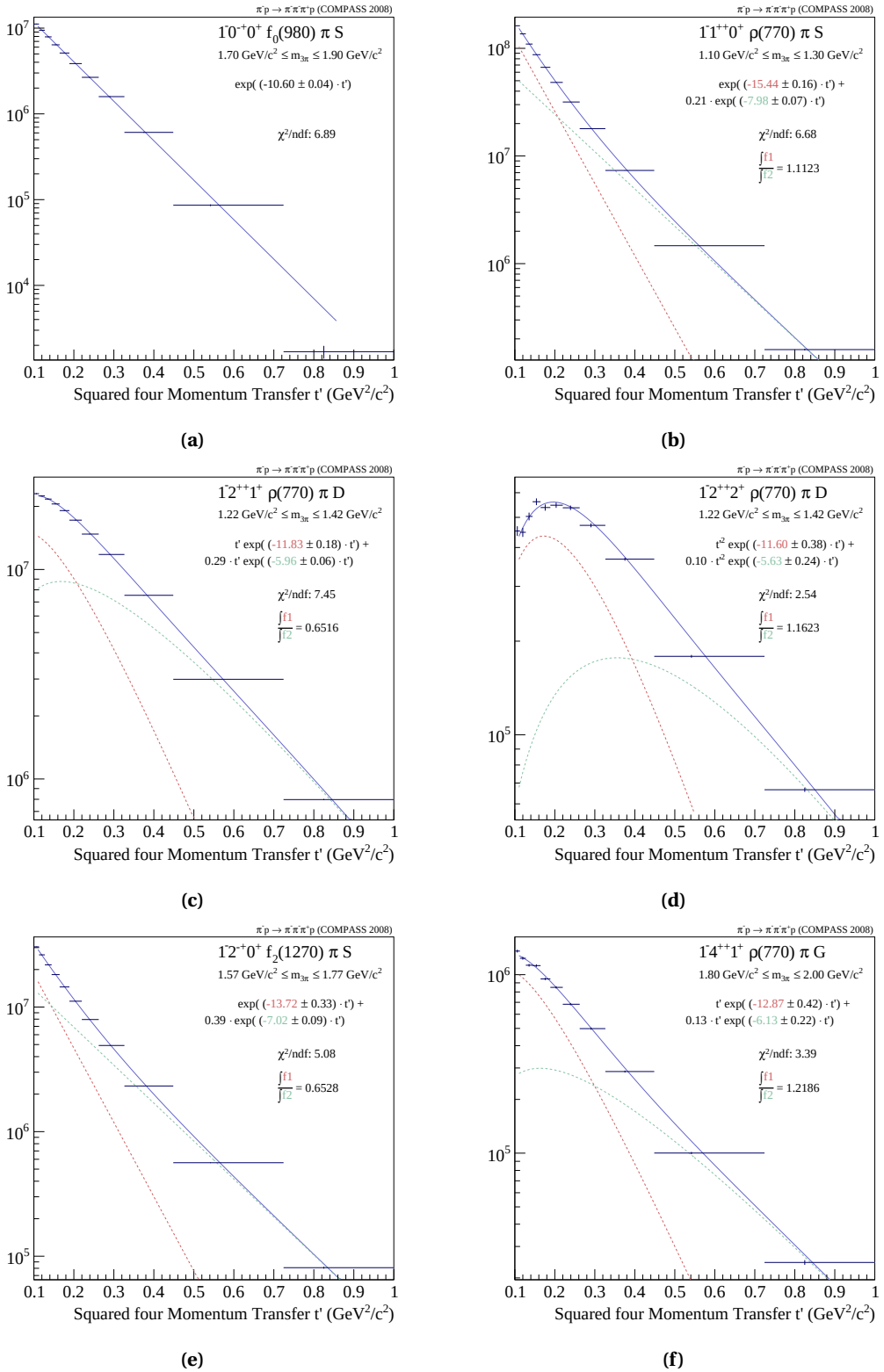

Figure 7.23 Fitted t' dependencies of selected partial wave intensities.

Exemplary some fit results of amplitudes discussed in the previous section are shown in Fig. 7.23. Generally the fit functions can describe the data quite well. The intensity of the $0^{-+}0^{+}f_0(980)\pi S$ partial wave (Fig. 7.23a) is summed in the mass region of the $\pi(1800)$ for all 22 t' bins. The best fit can be achieved with a single exponential function. Both fit models are not able to describe the behaviour seen for the last two t' bins, especially the jump at the last bin cannot be reproduced by the fit. That this leap of the last t' bin is not an artefact is discussed later together with more pronounced similar effects observed in other waves (Fig. 7.24). The t' dependence of the most dominant amplitude, the $1^{++}0^{+}\rho\pi S$, can be described best with a double exponential fit function (Fig. 7.23b). The exponential with the more steep slope dominates the low-t' region while the second with a slope, expected for Pomeron exchange on a proton target, emerges with increasing t'. This pattern can be seen for all other waves shown in Fig. 7.23 except the first plot. Both spin projections of the 2^{++} wave decaying via the ρ isobar can be described by the double exponential fit function (Fig. 7.23cand 7.23d). In addition the resulting slope parameter agree well for both ampitudes. The t' dependence of the main partial wave contributing to the $\pi_2(1670)$, the $2^{-+}0^{+}f_2\pi S$ wave, is depicted in Fig. 7.23e. Like for the $2^{++}1^{+}\rho\pi D$ (Fig. 7.23c), the exponential with the more shallower slope, which can be asociated to Pomeron exchange, dominates the overall t' dependence, regarding the integral ratio of both exponential functions. This could give a hint that a possible non-resonant background is relatively small. Finally the dependence of a high-spin amplitude, the $4^{++}1^{+}\rho\pi G$, is presented in Fig. 7.23f. Similar to the $2^{++}2^{+}\rho\pi D$ amplitude (Fig. 7.23d) this partial wave shows bin by bin fluctuations in the low-t' regime which cannot be described quite good by the fit functions. Nevertheless the general behaviour is reproduced by two exponentials, one having a slope greater 10 $(\mathrm{GeV}/c)^{-2}$ and the second with a value, predicted by Regge theory.
It was mentioned before, in the discussion of the $0^{-+}0^{+}f_0(980)\pi S$ partial wave (Fig. 7.23a), that the t' dependence of some amplitudes exhibits a behaviour which cannot be described by the fit functions. Some striking examples are shown in Fig. 7.24.

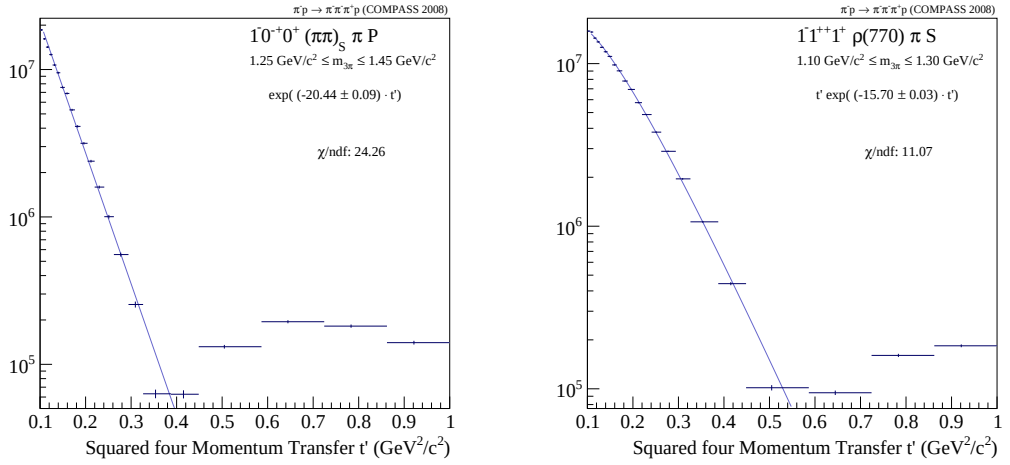

(a) **(b)**

Figure 7.24 Fitted t' dependence of the $0^{-+}0^{+}(\pi\pi)_S\pi S$ wave in the mass range of 1.35 ± 0.1 GeV/c^2 (a) and for the $1^{++}1^{+}\rho\pi S$ wave in the mass range of 1.2 ± 0.1 GeV/c^2(b).

Only the low-t' region can be explained by the fit while at $t'\sim0.5$ GeV$^2/c^2$ a kind of diffrac-

tion dip appears followed by shoulder in the high t' region. One possible explanation of this effect could be that at the dip the Pomeron and other production processes interfere destructively and the resulting intensity is minimal in this t' region. The kinematic regime of t' where this dip occurs could give a handle to determine the phase between Regge production and non-resonant contributions. For a better understanding the intensity of certain t' regions are plotted for both waves in Fig. 7.25. The left colunm shows the evolution of $0^{-+}0^{+}(\pi\pi)_S\pi S$ with increasing t'. At the lower boundary of t' the usual intensity distribution is shown while for medium t' region the peak at 1.3 GeV/c^2 vanishes completely. It recovers for the upper boundary of t' while there hte second peak at 1.8 GeV/c^2 disappears. At the right column the evolution of $1^{++}1^{+}\rho\pi S$ is shown again. It is not only that the peak shifts with increasing t' but the whole line shape is changing. This behaviour can only be explained by inerferences between the resonance contribution of this wave with non-resonant contributions. More insight can be gained by the determination of resonance and background parameters (see Chap. 8).
As input for future development of models decribing the t' dependence selected slope parameters b are listed for different data sets and partial waves in Tab. 7.3.

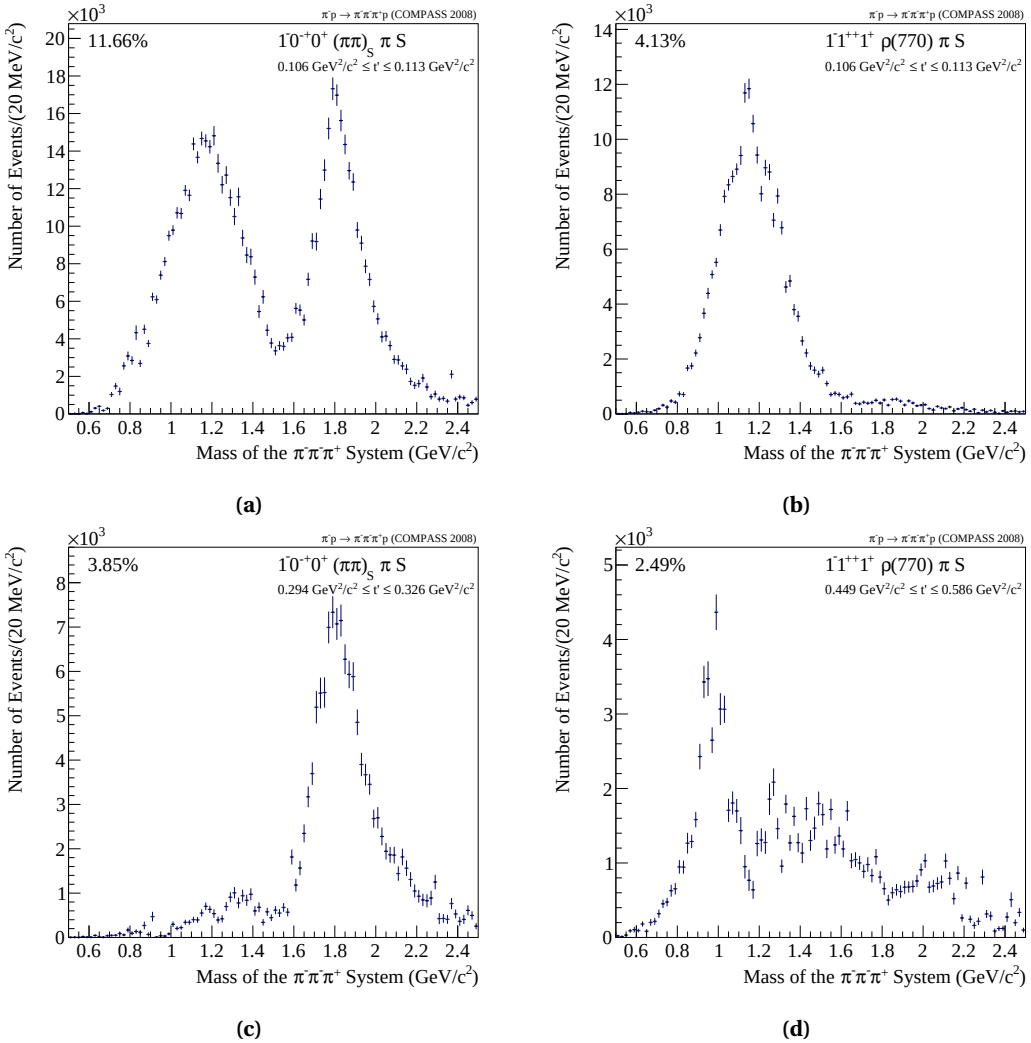

Figure 7.25

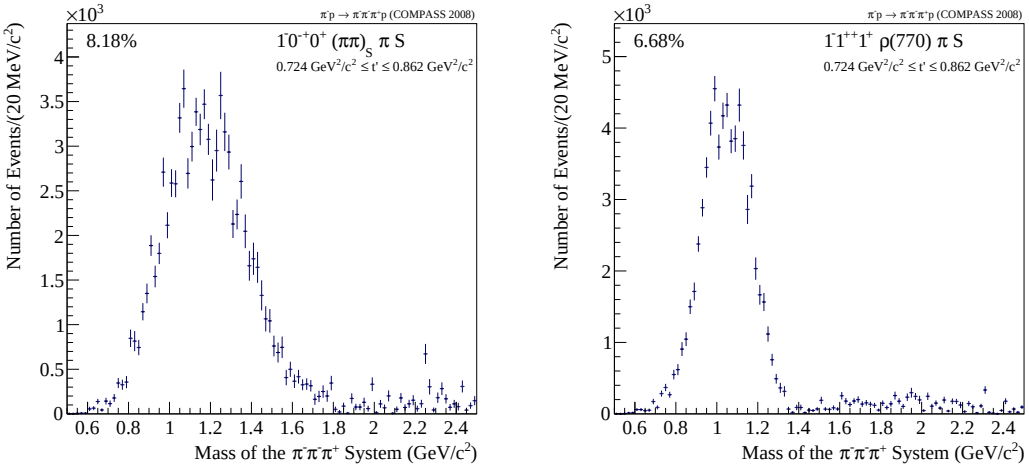

Figure 7.25 Intensity of the $0^{-+}0^{+}(\pi\pi)_S\pi S$ wave for increasing t' regions (a), (c) and (e) and accordingly for the $1^{++}1^{+}\rho\pi S$ wave (b), (d) and (f).

		Proton Data		*Deck MC*		*Lead Data*	
Partial Wave	**$m_{3\pi}$Range (GeV/c²)**	**b_1, b_2 $(GeV/c)^{-2}$**	**Ratio**	**b_1, b2 $(GeV/c)^{-2}$**	**Ratio**	**b_1, b2 $(GeV/c)^2$**	**Ratio**
$0^{-+}0^{+}(\pi\pi)_S\pi S$	[1.25, 1.45]	†20.44 ± 0.09	1	9.82 ± 0.02	1	11.87 ± 1.83	1
$0^{-+}0^{+}(\pi\pi)_S\pi S$	[1.70, 1.90]	†12.14 ± 0.04	1	8.99 ± 0.01	1	15.86 ± 1.15	1
$0^{-+}0^{+}\rho\pi P$	[1.25, 1.45]	†18.49 ± 0.06	1	15.15 ± 0.07	1	41.62 ± 7.46 2.28 ± 0.21	0.15
$0^{-+}0^{+}f_0(980)\pi S$	[1.70, 1.90]	10.67 ± 0.03	1	9.66 ± 0.05	1	†111.00 ± 1.65	1
$1^{++}0^{+}\rho\pi S$	[1.10, 1.30]	15.01 ± 0.16, 7.88 ± 0.08	1.25	10.26 ± 0.01	1	20.11 ± 3.47, 6.36 ± 0.24	0.20
$1^{++}1^{+}\rho\pi S$	[1.10, 1.30]	†15.70 ± 0.03	1	11.52 ± 0.09	1	13.54 ± 2.92, 3.84 ± 0.28	0.19
$2^{++}1^{+}\rho\pi S$	[1.22, 1.42]	11.58 ± 0.06, 5.94 ± 0.06	0.69	12.17 ± 0.06	1	9.27 ± 2.68, 3.95 ± 1.51	0.95
$2^{++}2^{+}\rho\pi S$	[1.22, 1.42]	11.38 ± 0.30, 5.40 ± 0.21	1.33	13.94 ± 1.42	1	⋆ -	-
$2^{-+}0^{+}f_2\pi S$	[1.57, 1.77]	13.76 ± 0.34, 7.05 ± 0.09	0.63	10.46 ± 0.02	1	4.84 ± 0.13	1
$2^{-+}0^{+}f_2\pi D$	[1.78, 1.98]	11.08 ± 0.75, 6.16 ± 0.40	1.54	7.48 ± 0.12	1	⋆ -	-
$4^{++}1^{+}\rho\pi G$	[1.80, 2.00]	12.14 ± 0.38, 5.62 ± 0.27	1.72	11.00 ± 0.09	1	⋆ -	-

Table 7.3 Overview of fitted t' dependencies for different data sets. For each wave one or two slopes and the integral ratio are listed. (†*: limited fit range,*⋆ *fit does not converge)*

7.5 Further Details of the 3π Spectrum

In Sec. 1.4.1 several longstanding open questions related to the three pion spectrum were introduced. Concepts were discussed how to attack these problems by the investigation of amplitudes and corresponding branching ratios between them. These ratios cannot be determined at this level of the analyis but a first estimation can be achieved by the discussion of observables.

7.5.1 The $a_1(1260)$ and its Possible Excitations

The complicated structure of the $a_1(1260)$ was introdcued in Sec. 1.4.1 and one excitation, the $a_1(1640)$ is listed in the PDG [B+12] as an established state. In addition four more possible a_1 resonances are listed under further states. In Fig. 7.27a and Fig. 7.27b both spin projections of the partial waves with the $\rho(770)$ isobar and a D wave are shown. In order to undertsand the influence of (neccessary and unavoidable) thresholds in the model the corresponding positions are drawn with blue lines. The instability seen in Fig. 7.27a at 1.1 GeV/c^2 both in the real data and the Deck Monte Carlo shows the effect. The more interesting findings are the structures around 1.6 GeV/c^2. The peak below 1 GeV/c^2 in Fig. 7.27b can be correlated to cross talk, explained in Sec. 7.1.5.
Both spin projections of 1^{++} partial waves decaying through the $(\pi\pi)_S$ are plotted in Fig. 7.27c and Fig. 7.27d. This decay channel is known to be affected by rescattering in combination with the $\rho\pi$ channels. In Fig. 7.26 exemplary one possible process is sketched. The positive pion, coming from the decay of the isobar ξ interacts, in this example, with the bachelor pion to a new two-pion state ξ' which then decays. Together with the negative pion from the decay of the first isobar they form the observed final state. This effect was investigated [Bre81] and applied to the data [AW75]. Later analyses found the result too large and new calculations predict a possible contribution of rescattering to this channel by $\sim 10-20\%$ [GP76]. As already discussed, the Deck model overshoots in amplitudes with a $(\pi\pi)_S$ isobar.

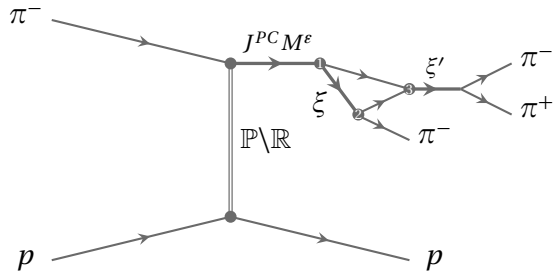

Figure 7.26 Schematic drawing of rescattering of the final state.

Finally two 1^{++} decay modes with a $f_2(1270)$ isobar are shown in Fig. 7.27e and Fig. 7.27f. The focus here is on the region around 1.6 - 1.8 GeV/c^2 which reveal structures in both amplitudes. The peak at 0.8 in Fig. 7.27f is cross talk with the partial wave shown in Fig. 7.27b.

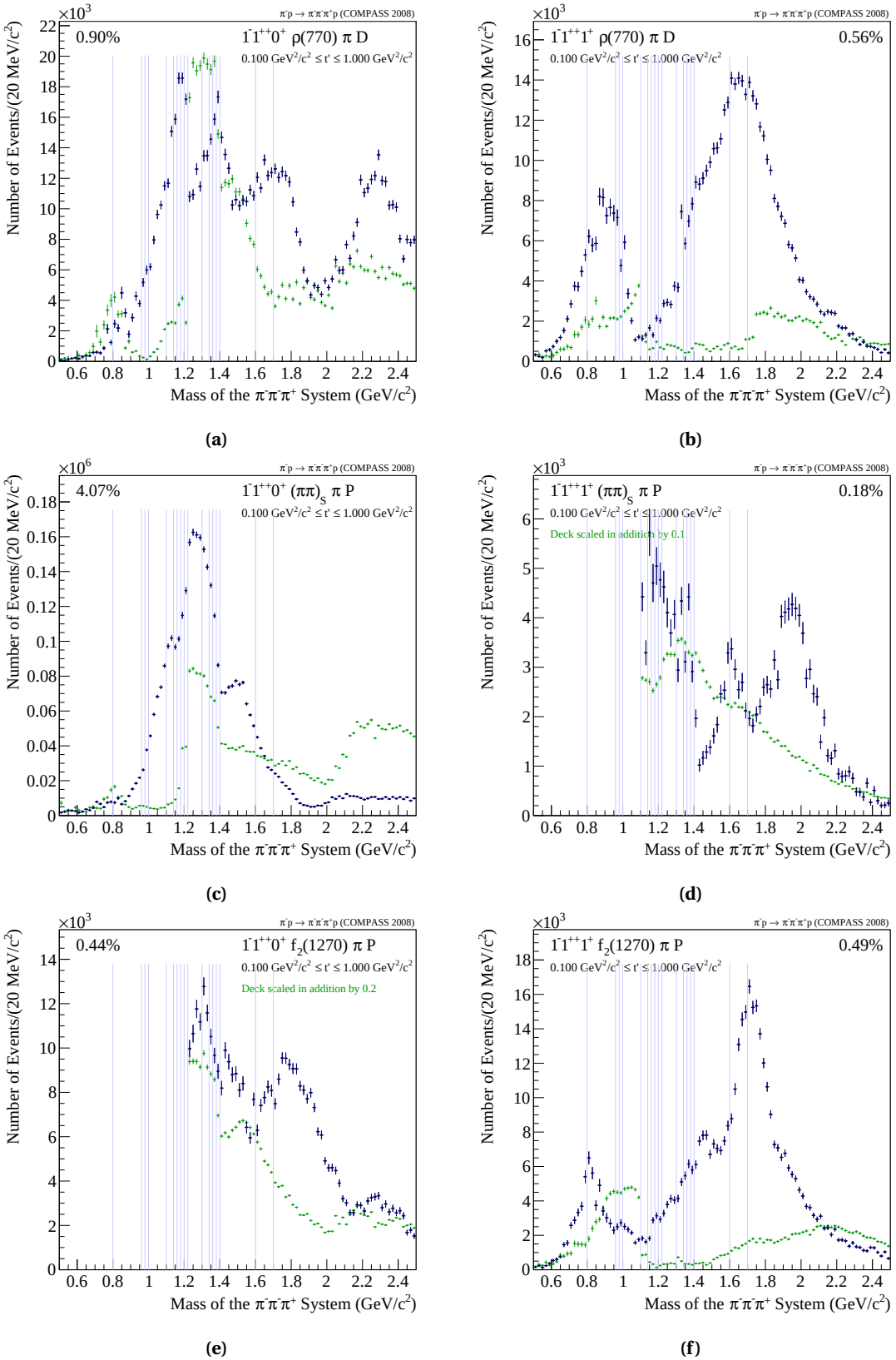

Figure 7.27 Integrated intensity of further waves with $J^{PC} = 1^{++}$.

7.5.2 On the Nature of the $\pi(1800)$

A detailed introduction about the radial excitations of the pion was given in Sec. 1.4.1 and the main decay channels of the two settled resonances, $\pi(1300)$ and $\pi(1800)$, were shown in Sec. 7.3.2. The suppressed decay into the ρ isobar would give a hint for a hybrid structure as in QCD-inspired models the decay of hybrids into two S-wave particles (e.qg pion and ρ is heavily quenched [IP85, CP97]. Another clue could be the observed decay into the $f_0(1500)$ isobar, shown in Fig. 7.28a, as this isobar is a strong candidate for a glueball with non-exotic quantum numbers. The nature of the $f_0(1500)$ could be associated to a hybrid nature of the $\pi(1800)$ [Zai00]. It must be stated that this partial wave is the only one in the model with the $f_0(1500)$ as isobar. For all other J^{PC} quantum numbers the introduction of this isobar leads to instabilities of the fit.
Some calculations [CHS99] pedict additional π states between 1.1 and 1.7 GeV/c^2. This brought up the idea to look at further decay channels. The decay into the $f_2(1270)$ isobar is suppressed for hybrids and structures observed in this channel could be a hint for an additional resonance at 1.7 GeV/c^2 [CP97]. Indeed the observed intensity in this channel reveals a drop to almost zero around 1.8 GeV/c^2 which could be the result of destructive interference. The question then arises which components interfere against each other. One possibility is a resonance at 1.8 GeV/c^2 and a non-resonant contribution; an alternative is the interference between two resonances. The investigation of the mass dependence (see Chap. 8) can shed some light on this.

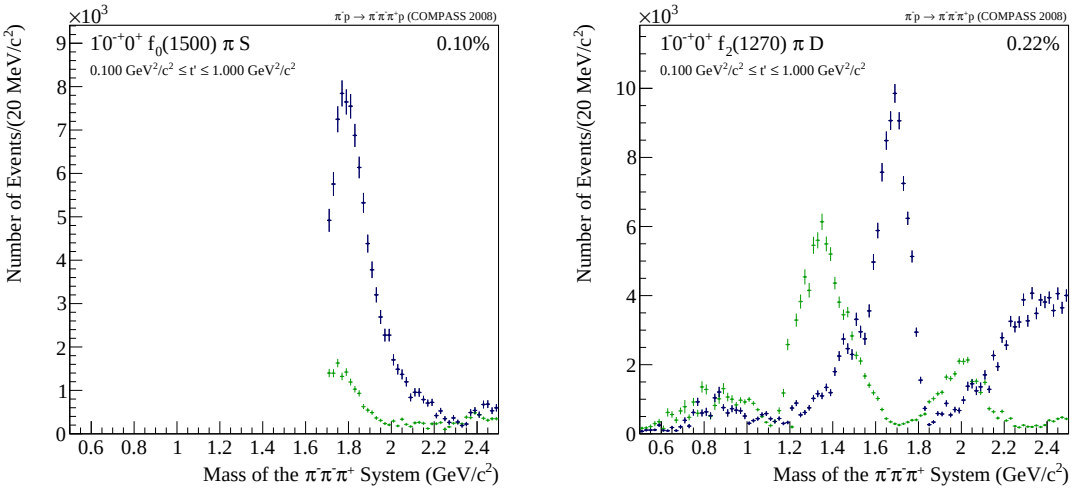

(a) **(b)**

Figure 7.28 Integrated intensity of the $0^{-+}0^+ f_0(1500)\pi S$ (a) and the $0^{-+}0^+ f_2(1270)\pi D$ (b) wave.

7.5.3 Understanding the $J^{PC} = 2^{-+}$ Sector Below 2 GeV/c^2

Looking at Tab. 7.2 one can see that the 2^{-+} sector is represented in this model with 17 partial waves. This abundance of amplitudes should help to clarify some of the open questions dealing with π_2 resonances (see Sec. 1.4.1). In addition to these questions there was an experimental

observation in the $\rho\pi P$ decay channel [D+81] which up to now could not be explained. In the corresponding intensity plots a double peak structure was seen. While the second peak could be associated to the $\pi_2(1670)$ resonance the first peak at 1.2 GeV/c^2 couldn't be explained and was stated as an artefact. The same intensity plots from this analysis are shown in Fig. 7.29a and Fig. 7.29b. The peak in Fig. 7.29a was seen for this analysis, too. But with the optimisation of the thresholds this stucture at 1.2 GeV/c^2 vanishes almost completey and only the peak at 1.6 GeV/c^2 is visible. Fot the wave with spin projection $M = 1$ parts of this artefacts are still seen. The fact that the strength of this peak is correlated with some thresholds and that almost all three-pion analyses in the last 40 years faced instabilities in partial waves with a decay to $\rho\pi P$ brings up the assumption that due to their angular distributions the fit has problems to disentangle these waves from others. A possible way out is a less model-biased description of the ρ isobar which will be discussed in Sec. 9.1.
Another question was whether the $\pi_2(1670)$ and the $\pi_2(1880)$ are in fact one resonance, shifted by some coherent background to different mass positions. Looking at Fig. 7.30c and Fig. 7.30d the concept of one resonance seems to be not valid as the observed interference patter for these two plots can be explained best with at least two resonances. A final answer for the three-pion case can give the modelling of the mass dependence (see Chap. 8).
Finally several models predict that there is a π_2 resonance above the $\pi_2(1670)$ which is part of a hybrid multiplet [Dud11]. The $\pi_2(1880)$, if it is a single resonance, is a natural candidate. The different possibilities, hybrid or $q\overline{q}'$, were investigated with certain models and some prediction was given about the decay properties dependent on the nature of the $\pi_2(1880)$ [LZ09]. Regarding the discussion in the previous section some models predict a supression of the ρ decay for hybrids. While at this level of the analyis a clear observation of the decay into the $\rho\pi P$ channel cannot be stated, some hints for a possible decay can be found in both spin projections of the $\rho\pi F$ channel (Fig. 7.30a and Fig. 7.30b). In addition the observed intensity in the channel of $f_2(1270)\pi G$ must not be zero if the $\pi_2(1880)$ is a $q\overline{q}'$ candidate [LZ09]. The corresponding plot is shown in Fig. 7.30e. Summarising there are some signs that the $\pi_2(1880)$ has a dominant $q\overline{q}'$ content although a possible fraction of a hybrid contibution cannot be excluded.

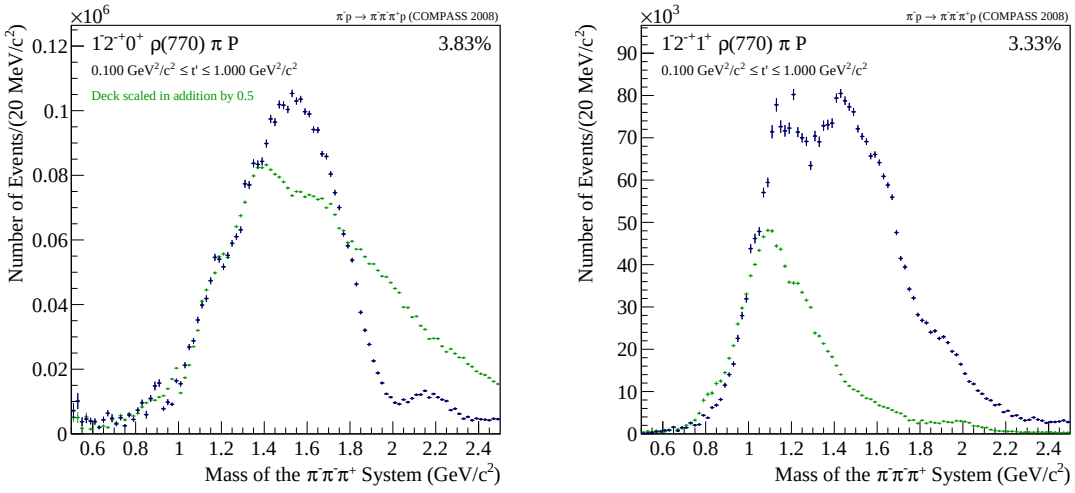

Figure 7.29 Integrated intensity of further waves with $J^{PC} = 2^{-+}$.

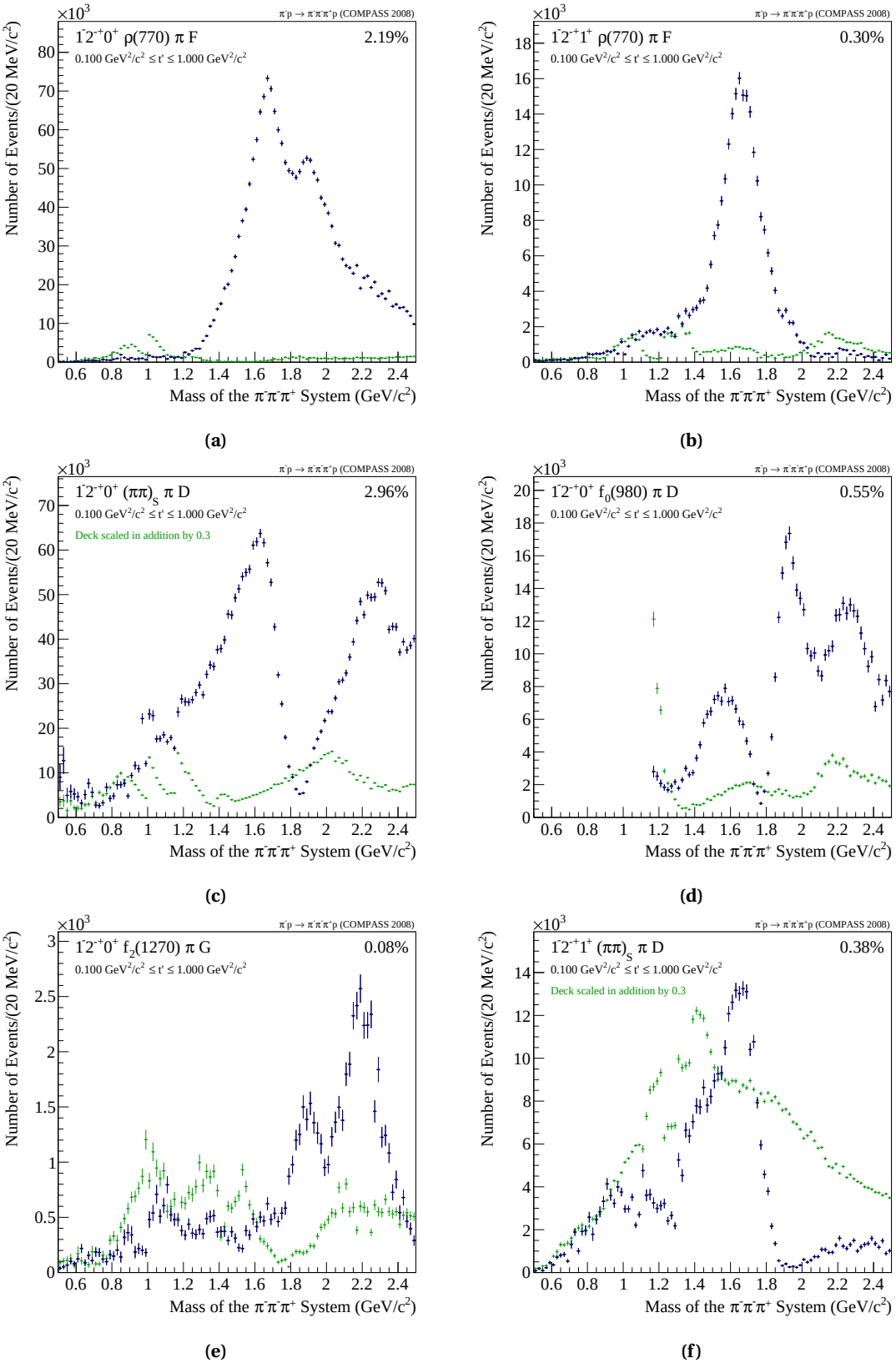

Figure 7.30 Integrated intensity of further waves with $J^{PC} = 2^{-+}$.

7.5.4 Spin-Exotic Contribution with $J^{PC} = 1^{-+}$

There is one partial wave with spin-exotic quantum numbers $J^{PC} = 1^{-+}$ part of the model. All possible isobars were considered, but intensity was only seen in the amplitude with quantum numbers $1^{-+}1^{+}\rho\pi P$, the same channel which was investigated before by other analyses. Its integrated intensity is plotted in Fig. 7.31a. It shows a broad enhancement between 1.0 and 1.8 GeV/c^2. This plot has no similarity with the findings of [CDH+02] (see Fig. 7.36a) but resembles the one made by VES [Zai00] (see Fig. 7.36e). The source of the peak at 1.1 GeV/c^2 can be identified as a threshold effect, which cannot be avoided, however, as mentioned before, instabilities of partial waves decaying via $\rho\pi P$ are known and being part of three-pion analyses since decades (e.g see Fig. 7.36e). The assumed Deck contribution is plotted but is scaled by a factor of five in order to show the line shape. As already discussed before, the actual intensity of the Deck Monte Carlo is of minor importance, as intereferences between Deck data sample and real data is not taken into account for this simulation. Looking at the shape of the Deck contribution it shows an almost identical shape in comparison to the real data. The t' dependence for a mass region around 1.6 GeV/c^2 is shown in Fig. 7.31b. This dependence can be fitted best by two exponentials. The bigger slope of $b \sim 15.25$ (GeV/c)$^{-2}$ is dominating the low t' region while the second slope $b \sim 6.04$ (GeV/c)$^{-2}$ is describing mostly the high t' regime.

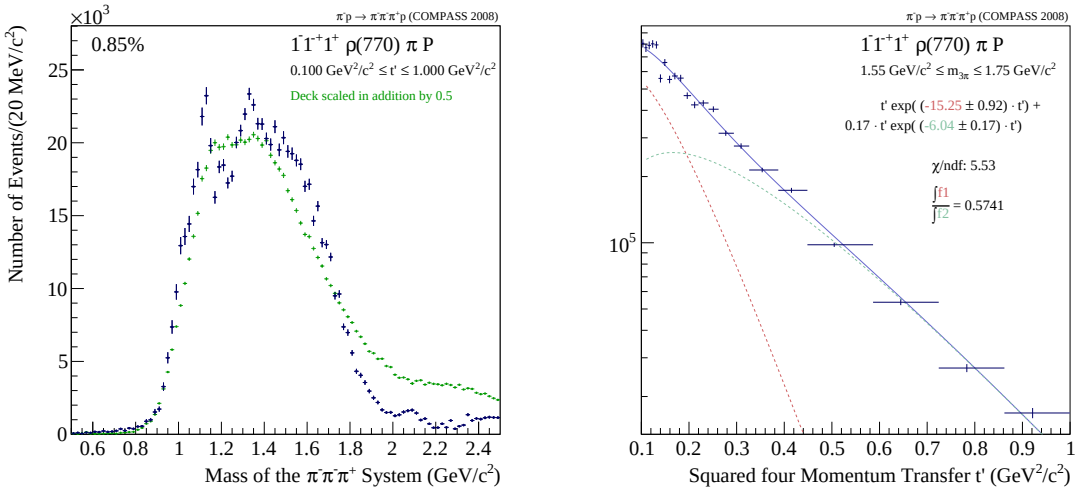

(a) **(b)**

Figure 7.31 Integrated intensity of the $1^{-+}1^{+}\rho\pi P$ wave, Deck Monte Carlo with an additional scaling overlaid (a), t' dependence in the mass region of 1.6 GeV/c^2 (b).

In order to look for a possible resonance in this amplitude one has to look at the relative phases. In previous analyses it was shown that a phase motion can be observed around the mass region of 1.6 GeV/c^2, however, the phases showed a very flat motion in contrast to an expected phase shift of 180°. Exemplary two phase shifts are shown, both were presented in previous publications. In Fig. 7.32a the relative phase w.r.t. the $1^{++}0^{+}\rho\pi S$ wave is plotted which shows a rising phase at 1.6 GeV/c^2, however, the phase shift is less than 100°. The phase motion w.r.t. the $2^{-+}0^{+}f_2(1270)\pi S$ wave is even smaller (see Fig. 7.32b). Only $\sim 15°$ can be observed. This observation was one of the biggest arguments against a spin-exotic resonance at 1.6 GeV/c^2. Assuming a resonance for this amplitude at this mass there are some explanations for this

small phase motions. First the corresponding mass region is crowded with resonances, besides the well measured $\pi_2(1670)$ first excitations of the $a_1(1260)$, namely the $a_1(1640)$, and of the $a_2(1320)$, the $a_2(1700)$, are expected and observed. Second the interference with the non-neglibible Deck contribution can damp the phase motions and the width of a resonance does influence the phase shifts. If a spin exotic resonance can be fit to the data (see Chap. 8), its width must be considerably broader than the published ones.

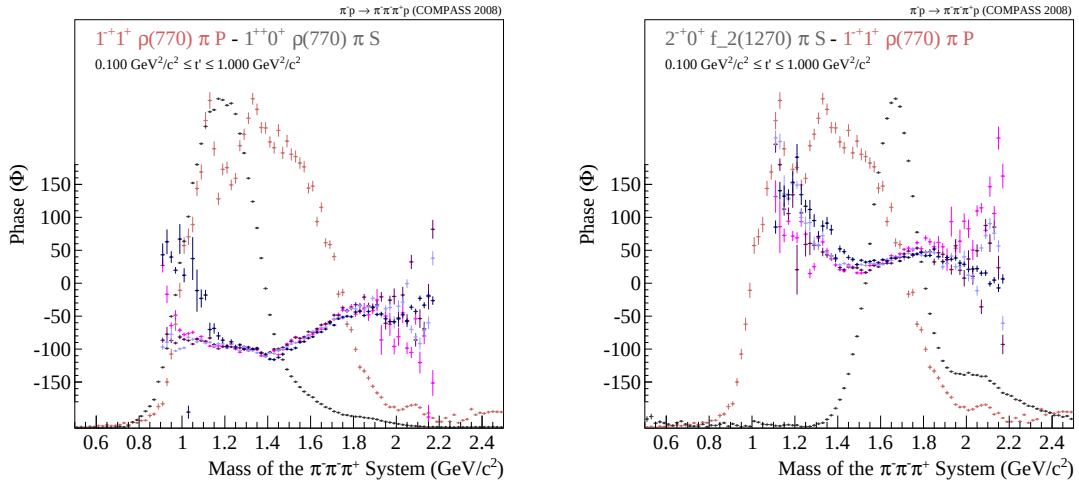

Figure 7.32 Phase motion of the spin-exotic amplitude w.r.t. the $1^{++}0^+\rho\pi S$ (a) and $2^{-+}0^+ f_2(1270)\pi S$(b) wave.

In order to obtain a deeper understanding of the underlying production processes and their contributions it is the best to investigate the intensity plots for different regions of t'.

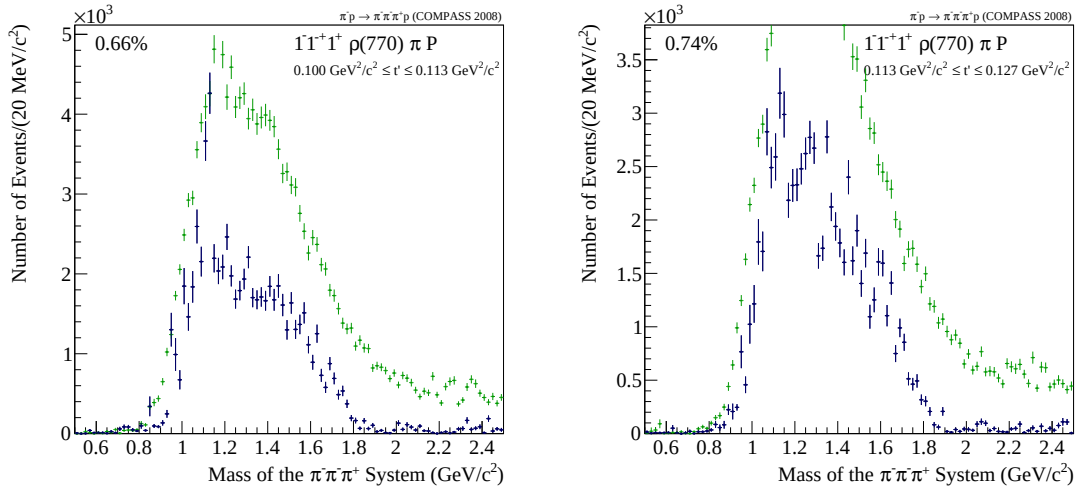

Figure 7.33 Intensity of the spin-exotic wave at low t'.

The intensities observed in the two lowest t' bins is shown in Fig. 7.33a and Fig. 7.33b. The outcome of the spin-parity analysis with Deck Monte Carlo is overlaid. Common for both figures is the dominant instability around 1.1 GeV/c^2, both for real data and Monte Carlo. Again a hint that these fluctuations possibly originate from the isobar parametrisation or the similarity of the angular distributions of $\rho\pi P$ decays with other decay channels. An artefact of the acceptance can be excluded as the Deck Monte Carlo was generated and fitted without any acceptance correction. No peak or shoulder is visible around 1.6 GeV/c^2.
Looking at the upper t' region the observed intensity (Fig. 7.34a and Fig. 7.34b) looks quite different than the previous ones. It has to be mentioned that the same scaling for the Deck Monte Carlo is applied. It can be seen that in contrast to the low t' region the assumed Deck intensity is smaller and a peak at 1.6 GeV/c^2 emerges. The instability at 1.1 GeV/c^2 is completely gone.

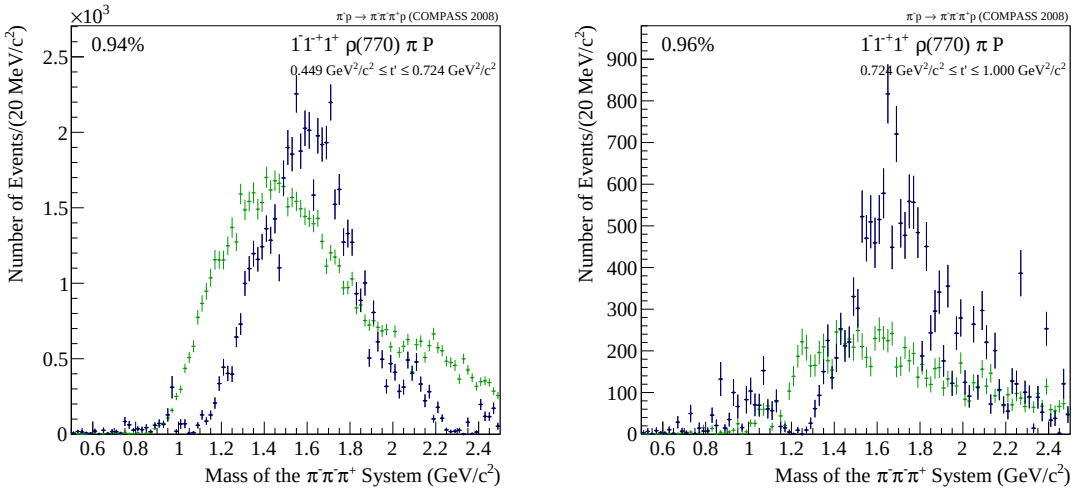

(a) **(b)**

Figure 7.34 Intensity of the spin-exotic wave at high t'.

Comparing the fit result seen in Fig. 7.34b with the published result of the COMPASS analysis with 2004 data and a lead target [AAA+10] in Fig. 7.35a shows a quite good agreement. It seems that the lead target acts as a background filter, in particular for Deck-like mechanisms. It was supposed since decades that in the t' regime between 0.1 and 1.0 GeV$^2/c^2$ an incoming beam particle interacts with the nuclei of a solid-state target instead of the nucleus. This cannot be taken as valid regarding the two analyses. In adition the spin-exotic intensity in the 2009 lead data (see Fig. 7.35b) again matches with both previous plots. The accordance between 2004 and 2009 data implies that in both cases the spin-paritxy analysis, based on acceptance corrections and fit models, come to the same result, whereupon the 2004 COMPASS spectrometer cannot be compared with the one of 2009. The modifications of the spectrometer between 2008 and 2009, concerning this analysis, are only the different trigger and target. The same fit model is applied to the 2008 and 2009 data sets and the accordance between Fig. 7.34b and Fig. 7.35b allows the conclusion that the observed difference depend on the target.

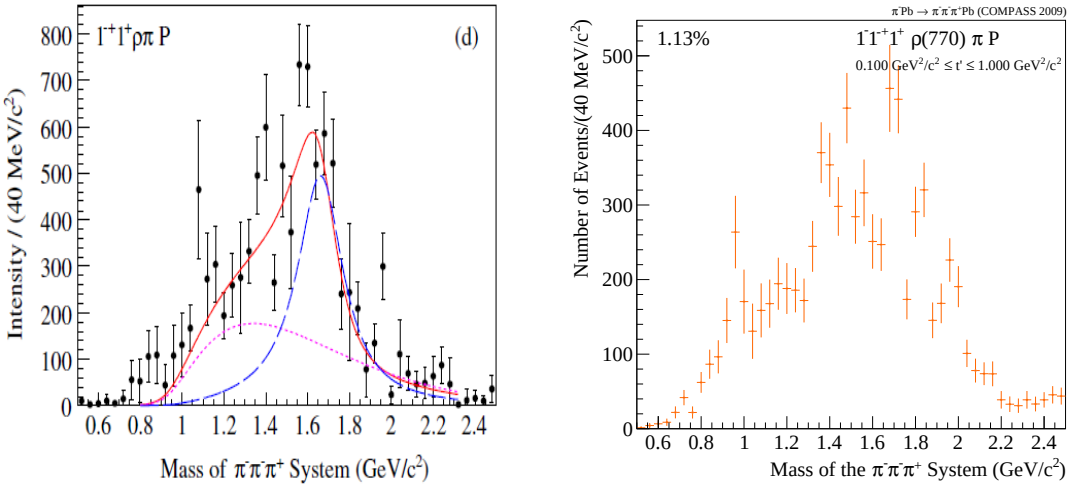

(a) **(b)**

Figure 7.35 Intensity of the spin-exotic partial wave observed in the 2004 data (a) and in the 2009 data (b).

Understanding Previous Analyses

It was discussed in Sec. 1.4.2 that three-pion analyses in the last two decades, investigating a possible realisation of a spin-exotic at 1.6 GeV/c^2, came to complete different observations in that channel although they all quite agree for the study of standard candles, e.g. $a_1(1260)$, $a_2(1320)$, $\pi_2(1670)$, ... This circumstence is more than annoying as it distract from the actual scientific discussion, if there can be a spin-exotic resonance experimentaly proven or not. With the large data set at hand it was decided to apply the fit models of the previous analyses to this data and learn from the outcome the origin of the puzzle. In Tab. 7.4 all analyses of interest and their corresponding models are listed.
The COMPASS 2004 analyses was already discussed previously and a good agreement was seen with the 2009 data, both taken with a lead target. It was found that the target material has an influence on the result. Thus both analyses can only be compared to each other, as they are the only one, discussed here, based on the same target material.
The remaining three analyses investigated data taken with liquid hydrogen targets, like this analysis, or a beryllium target. Starting chronological the first analysis to be discussed is 'BNL-1' [CDH$^+$02] ,named after the experiment *BNL E52* and the first of two BNL analyses examined. It was the only publication presenting a clear and narrow peak around 1.6 GeV/c^2 (see Fig. 7.36a). Assuming no big influence whether one is using a valid t' parametrisation like for the BNL-1 case or whether on splits the data into t' bins, the BNL-1 wave set was set up and the fit was carried out in 11 t' bins. The observed intensity in the $1^{-+}1^+\rho\pi P$ wave, based on a model with 21 waves is plotted in Fig. 7.36b. The agreement between both analyses is very good. Both, the peak around 1.3 GeV/c^2 as well as the presumably exotic peak could be reproduced. In the publication a second wave set, consisting of 27 waves, was presented, used for various studies. Applying this extended model to the data both peaks vanish and a broad component is visible. Nevertheless a phase motion against other waves, like the $1^{++}0^+\rho\pi S$ is still there. Investigating this futher revealed model leakage, due to the too small wave set. For this case, the leakage originates from the missing partial waves $2^{-+}0^+/1^+\rho\pi F$ and $2^{-+}0^+\rho\pi P$.

On this argument based a second BNL analysis, here denoted as 'BNL-2' [DMS+06]. In this analysis the full data set was used and instead of a t' parametrisation a binnin in t' was used. The 21 wave set was extended to 36 partial waves and as a result only a broad component was found for the partial wave with $1^{-+}1^{+}\rho\pi P$ (see Fig. 7.36c, black curve). Instead of investigating all 15 t' bins in terms of the exotic, the authors focused on only on t' bin. Applying the 36 waves model to the 2008 COMPASS data and plotting the fit result for a similar t' bin only (see Fig. 7.36d, the red curve) the result looks almost the same. The argumentation of the non-existence of a spin-exotic in the $\rho\pi P$ channel is mainly based on that single plot for a certain t' bin, although the authors showed a phase motion of the exotic wave against the $1^{++}0^{+}\rho\pi S$. The analysis taken with the VES spectrometer, named after its publication 'VES 2000' [Zai00] show an observed intensity for the spin-exotic wave (see Fig. 7.36e) very similar to the analysis presented here (see. Fig. 7.36f. The VES study is based on 44 waves and used an infinite rank fitting method.
After all the discrepancies between the different analyses can be explained. While BNL-1 applied an insufficient model, BNL-2 focused on a too small region of t' for their argumentation. VES and COMPASS analyses both agree in the observation of a broad distribution with instabilities around 1.1 GeV/c^2.

Experiment	**Fit Model**	**Setup**
BNL-1 [CDH+02]	21 waves t' parametrisation $0.1 \leq t' \leq 1.0$ GeV$^2/c^2$	250 k events 18 GeV/c pion beam proton target
BNL-2 [DMS+06]	36 waves fit in t' bins $0.1 \leq t' \leq 0.5$ GeV$^2/c^2$	2.6 M events 18 GeV/c pion beam proton target
VES 2000 [Zai00]	44 waves infinite rank $0.1 \leq t' \leq 1.0$ GeV$^2/c^2$	9.0 M events 36.6 GeV/c pion beam Be target
COMPASS 2004 [AAA+10]	42 waves t' parametrisation $0.1 \leq t' \leq 1.0$ GeV$^2/c^2$	440 k events 190 GeV/c pion beam proton target

Table 7.4 Overview of fit models used for different three pion analyses investigating a possible realisation of a spin-exotic at 1.6 GeV/c^2.

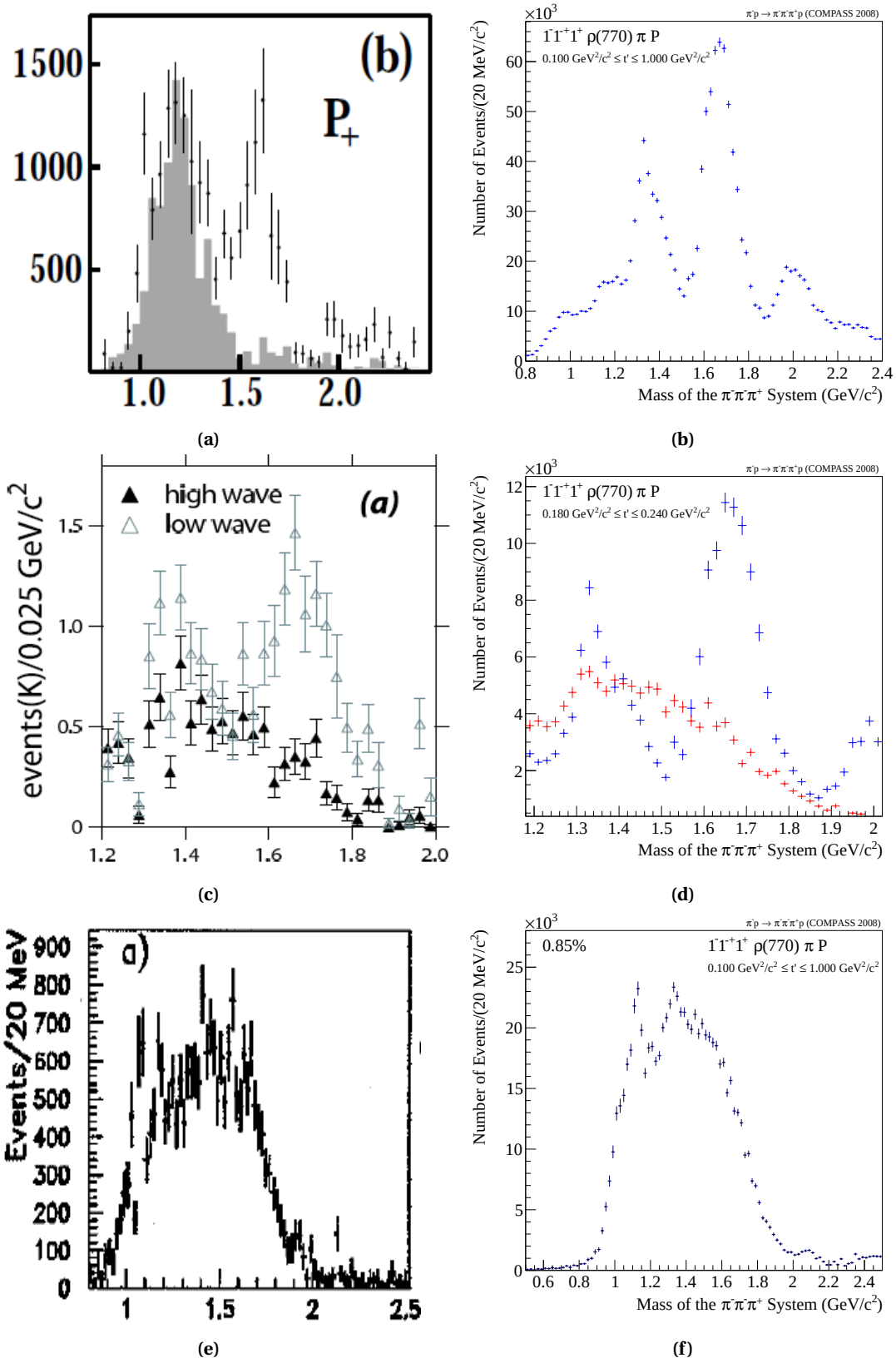

Figure 7.36 Overview of analyses investigating the spin-exotic 1^{-+} in the $\pi^-\pi^-\pi^+$ channel at 1.6 GeV/c^2.

7.5.5 A New Axial-Vector Resonance $a_1(14xx)$?

A completely new finding is the observed peak structure at 1.4 GeV/c^2 in the partial wave wit quantum numbers $1^{++}0^+ f_0(980)\pi P$ (see Fig. 7.37a) and the corresponding wave with spin projection $M = 1$ (see Fig. 7.37b). The t' dependence of both amplitudes in the mass region around 1.4 GeV/c^2 is shown in Fig. 7.38a and Fig. 7.38b.

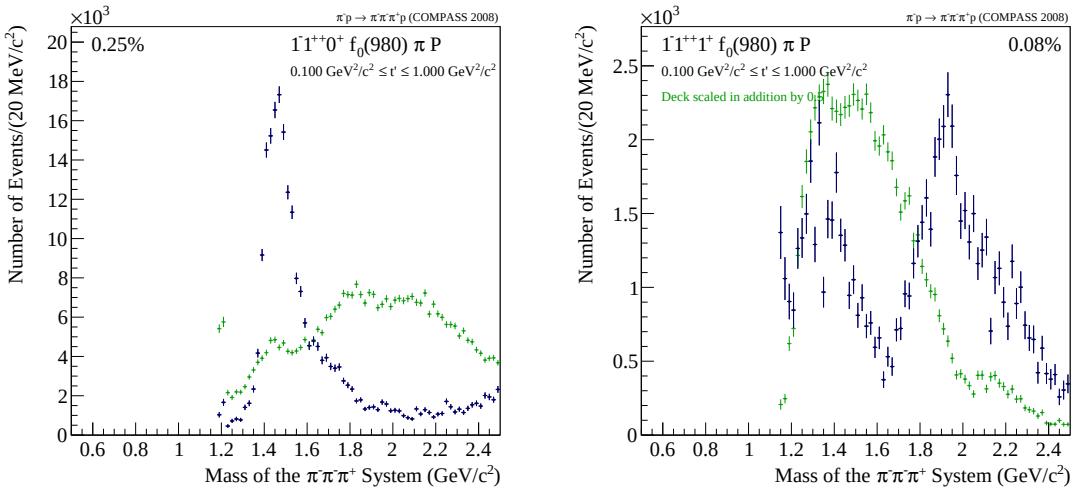

(a) **(b)**

Figure 7.37 Integrated intensity of the $1^{++}0^+ f_0(980)\pi P$ (a) and $1^+1^+ f_0(980)\pi P$ (b) partial waves.

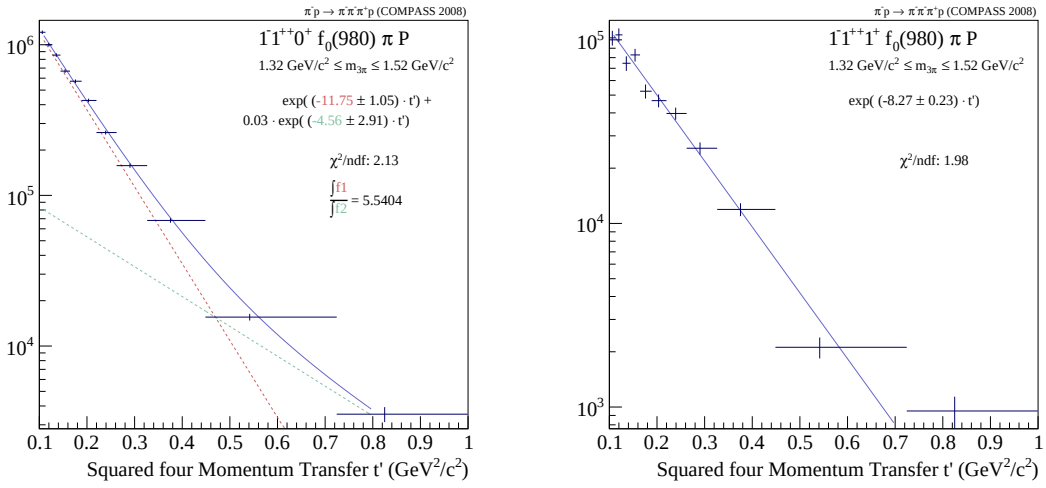

(a) **(b)**

Figure 7.38 t' dependence of the $1^{++}0^+ f_0(980)\pi P$ (a) and $1^+1^+ f_0(980)\pi P$ (b) wave.

As already mentioned due to this new kind of investigations there is a lack of models or theories in order to explain the fitted t' slopes. Thus it can only be said that the wave with $M = 0$ can be described well be two exponetials following the already observed behaviour that the one with the steep slope ($b \sim 11.56$ (GeV/c)$^{-2}$ is dominating the low t' region while the upper kinematic

region is following an exponential with $b \sim 4.11$ (GeV/c)$^{-2}$. The t' dependence of the second partial wave can be decribed by a single exponential with $b \sim 8.22$ (GeV/c)$^{-2}$.
The question arises whether this peak is related to a new resonance or whether it is an artefact of the analysis. Both cases were investigated. In Fig. 7.39 relative phases of the amplitude with $M = 0$ against standard candles of the three-pion spectrum are plotted. The most interesting is the phase shift against the dominant $1^{++}0^+\rho\pi S$ wave seen in Fig. 7.39a which gives a strong hint that the peak observed at 1.4 GeV/c^2 in the $f_0(980)\pi P$ decay cannot be correlated to the $a_1(1260)$. But also the other phase motions shown indicates a resonating behaviour of the structure at 1.4 GeV/c^2.

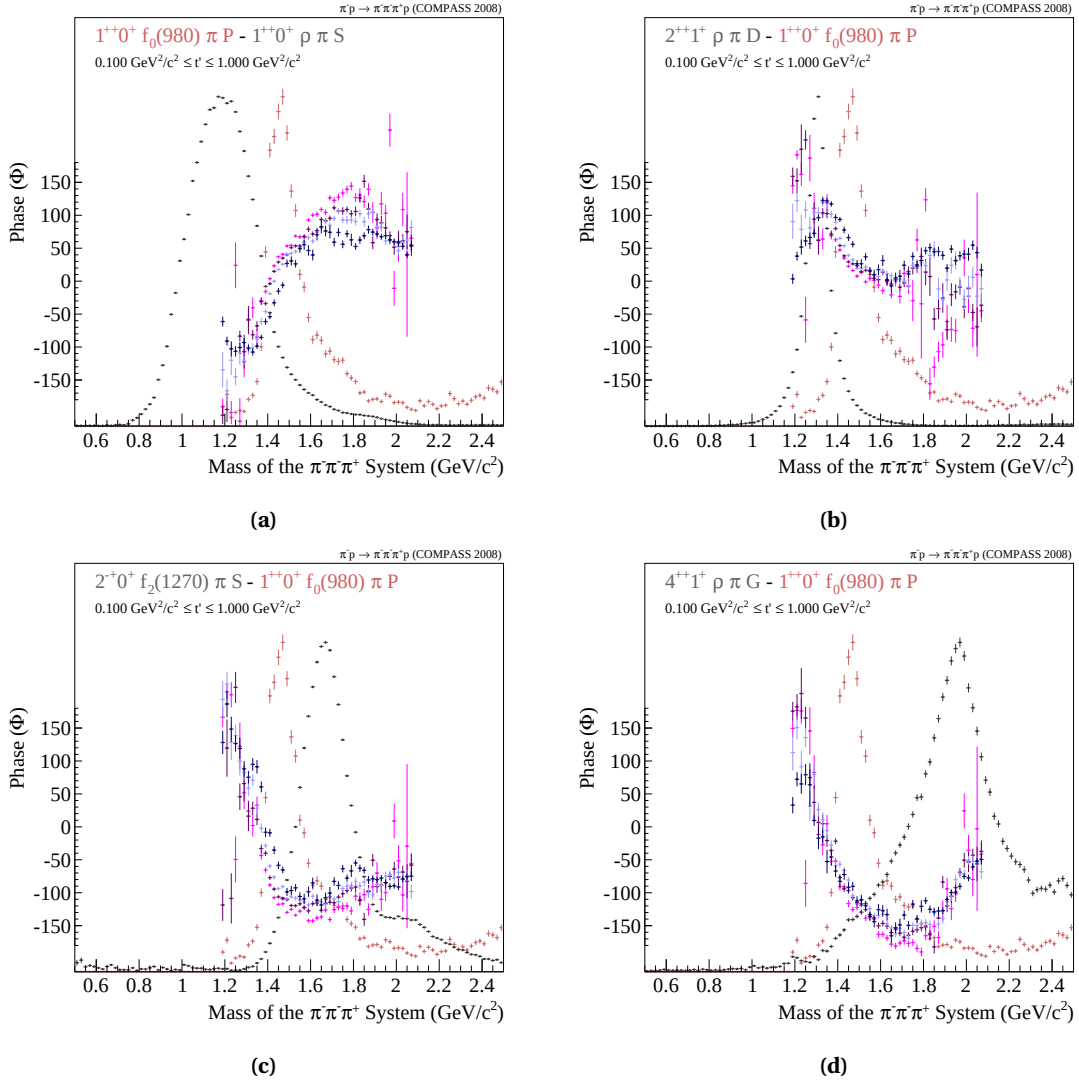

Figure 7.39 Relative phase motions of the $1^{++}0^+ f_0(980)\pi P$ wave w.r.t. standard candles.

Although the phase motions give a clear hint for a single object in this channel still other possible influences must be discussed. Regarding the PDG [B$^+$12] there is no experimental proof for a decay of the $a_1(1260)$ into $f_0(980)\pi$, marked as *not seen*. The possibility of leakage was consid-

ered but dedicated studies showed an assumed contribution, originating from the $1^{++}0^{+}\rho\pi S$ wave, is below 2-3 % (see Sec. 7.6.3). Influences from the model were taken into account by systematic studies of the event selection or isobar parametrisations (see Sec. 7.6.1), but no impact on the observed intensity could be seen except the fact that the whole peak structure decrease in intensity but keeping its shape, when changing the parametrisation of the $f_0(980)$ isobar.
Assuming a resonance $a_1(14xx)$ it seems that it couples only to the $f_0(980)$ channel, as it cannot be seen in any other 1^{++} amplitude of the model. It was already mentioned that the $f_0(980)$ has a complicated structure and its dynamics is not understood yet thus the nature of this possible resonance is unclear, too. Based on the hypothesis that there is a resonance with a strong *strange* quark content, due to its decay channel, some attempts to explain a possible $a_1(14xx)$ resonance are discussed in the following.
The simplest answer is that this object is the isospin partner of the $f_1(1420)$ which has its dominant decay to $K\overline{K}\pi$. Thus the new object would be a single resonance with a dominant decy to $f_0(980)\pi$ the only isobar of the three pion final state with a large strangeness contribution.
Another explanation is to describe this object as a meson molecule with a $K\overline{K}$ nucleus with a pion orbiting around [Chu]. The Kaon nucleus rescatters to the observed $f_0(980)$ isobar forming with the orbiting pion the final state.
Another possible explanation is to take coupled-channel effects into account [BB77]. The $a_1(1260)$ is known to decay into the $K\overline{K}^*(892)$ final state [B$^+$12] and regarding the decay of $\overline{K}^*(892)$ into a Kaon and a pion the following decay chain is possible

$$a_1(1260) \rightarrow K\overline{K}^*(892) \rightarrow K\overline{K}\pi \rightarrow f_0(980)\pi \tag{7.51}$$

Regardless of its possible nature the line shape observed in the intensity plots and the corresponding phase motions indicates a new a_1 resonance. The next step is to verify its resonant nature and if applicable to determine its resonance parameters (see Chap. 8).

7.6 Systematic Studies

It was discussed in Sec.7.2 that a complete analysis model consists of more than a wave set. Additionally the statistical errors of most of the waves are so small that systematic effects become dominant. It is therefore eminent for this analysis to investigate the impacts of the event selection, the amplitude parametrisations and different wave sets, on the fit result.

7.6.1 Variations of the Model

For the following studies the analysis model was changed in certain areas, from the event selection to the final fit. Based on this modified model, the same partial-wave analysis is applied to the data sample. An overlay of this fit outcome with the main analysis, in terms of intensities and t' dependencies of some partial waves showcases, to which degree the analysis is biased by certain model variations. The resulting studies of the various spin-parity analyses are the basis for further investigations on the level of resonance extraction (see Chap8).

Influence of the Event Selection

The purpose of this study is to investigate the influence of potentially centrally produced events (see Sec.5.1.7) or kaonic contributions to the fit result, originating from the beam (see Sec.5.1.8) or kaon pairs in the final state (see Sec.5.1.8). Additionally the cut on the correct beam time was omitted. All these events, normally cut away by the event selection, are now part of the data sample, on which the same spin-parity analysis was applied. The data sample obtained by the new event selection with looser cuts consists of $\sim 25\%$ more events which results in a common scaling of the intensity distributions. In order to compare directly both results the fit result was normalised to the reference fit, on basis of the number of input events.
Despite of the applied normalisation the Flat wave (Fig7.40a) shows a larger intensity by a factor of ~ 1.5 in the mass range between 0.8 and 2.2 GeV/c^2. The coherent isotropic amplitude $0^{-+}0^{+}(\pi\pi)_S\pi S$ (Fig.7.40b), however, can be regarded as almost identical. The most interesting effect is shown for the $1^{++}0^{+}\rho\pi S$ wave (Fig.7.41a). While the general shape of the intensity distribution and the corresponding t'-dependence (Fig.7.41b) is quite similar, more intensity can be observed around the $a_1(1260)$ mass region for the reference fit. The new 1^{++} state (Fig.7.41c and Fig.7.41d) seems to be unaffected from the modified event selection, the biggest discrepancy can be seen at the high mass region above 2.2 GeV/c^2. Finally another characteristic wave, the $2^{++}1^{+}\rho\pi S$ is investigated. Both, intensity (Fig.7.41e) and t'-dependence (Fig.7.41f), show no difference in shape but in terms of the fitted intensity. Like for the $1^{++}0^{+}\rho\pi S$ amplitude the intensity obtained for the reference fit is larger than for the modified event selection.

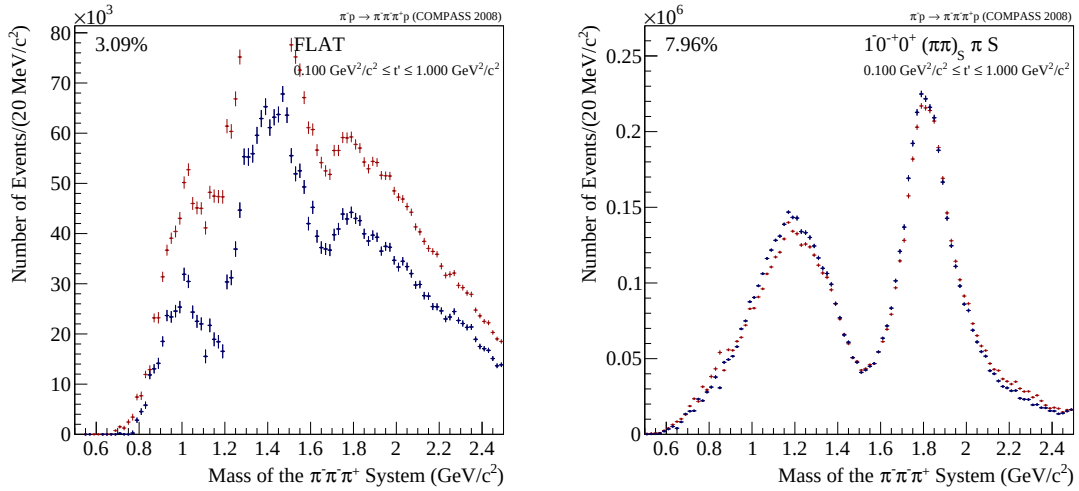

(a) **(b)**

Figure 7.40 Integrated intensity of the Flat wave obtained from the main fit (blue) overlaid by the normalised fit result based on a data sample with looser cuts (red) (a), the corresponding plot for the $0^{-+}0^{+}(\pi\pi)_S\pi S$ wave (b).

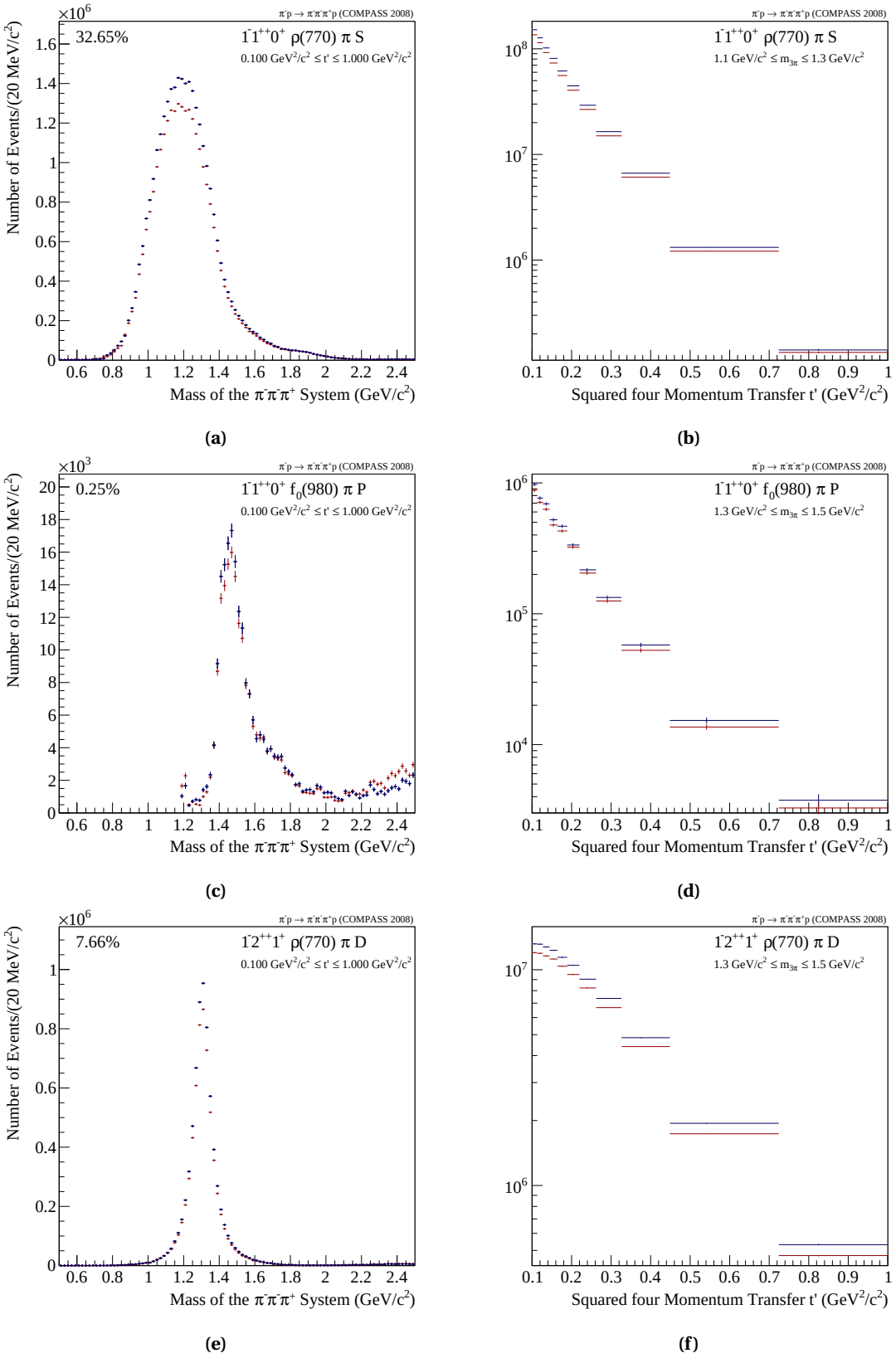

Figure 7.41 Integrated intensity of the $1^{++}0^{+}\rho\pi S$ wave obtained from the main fit (blue) overlaid by the normalised fit result based on a data sample with looser cuts (red) (a), the corresponding t' dependence (b). The same plot for the new a_1 state (c) and (d) and the $2^{++}1^{+}\rho\pi D$ wave (e) and (f).

The VES/K1 Parametrisation

The biggest challenge in terms of isobar parametrisations is to find a proper description for the f_0 mesons. In the last decades most analyses used the fit of $\pi\pi$ scattering data [AMP87] as basis for the description of the f_0 isobars. This analysis makes use of these parametrisations, too. In [AMP87] several fits are discussed and the so-called *M-solution* was found to be the best way to describe the f_0 states. It offers the possibility to handle the $f_0(980)$ as an extra isobar, as it is not part of the M-solution (see Sec.6.4.3). Another possible parametrisation of the scalar mesons is based on the *K1-solution* which takes the $f_0(980)$ explicitly into account which results in a dip in the intensity distribution. For this analysis, in order to be able to use the $f_0(980)$ as a separate resonance, it has to be subtracted from the K1 amplitude. A caveat of this method is that the description of the $f_0(980)$ is constraint by the subtraction term and other parametrisations, like the here used Flatté form used here, are not possible.
The Flat wave (Fig.7.42a) shows no difference to the reference fit, it is interesting to observe that the $0^{-+}0^{+}(\pi\pi)_S\pi S$ wave varies in intensity only around the $\pi(1800)$ mass region (Fig.7.42b). It is expected to also see a difference for the $0^{-+}0^{+}f_0(980)\pi S$ (Fig.7.43a), which is true, but the modified intensity in both waves leads to the conclusion that the two f_0 isobars are less disentangled than expected. The larger intensity for the reference fit comes from the fact that the sharper $f_0(980)$ Flatté form helps the fit to distinguish between broad $(\pi\pi)_S$ and $f_0(980)$ contributions. The same is true for the new a_1 state (Fig.7.43c and Fig.7.43d) where the overall shape and t' dependence seems to be similar only the intensity is larger in case of the reference fit. Finally two 2^{-+} amplitudes are discussed which shows interesting structures in the intensity distributions which are assumed to be due to a destructive interference of two π_2 resonances (see Sec.7.5.3). Both, the $2^{-+}0^{+}(\pi\pi)_S\pi D$ as well as the $2^{-+}0^{f}_{0}(980)\pi D$ wave, seem to conserve their structure although variations of form and intensity are visible. This gives a strong hint that the observed structures are not an artifact of the various isobar parametrisations.

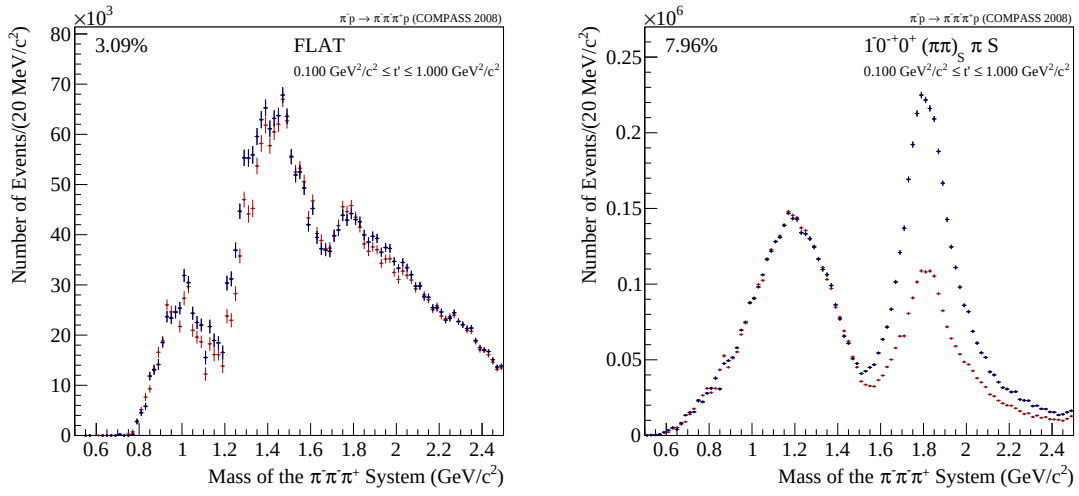

(a) **(b)**

Figure 7.42 Integrated intensity of the Flat wave obtained from the main fit (blue) overlaid by the fit result based on a model with the VES/K1 $(\pi\pi)_S$ and $f_0(980)$ parametrisation (red) (a), the corresponding plot for the $0^{-+}0^{+}(\pi\pi)_S\pi S$ wave (b).

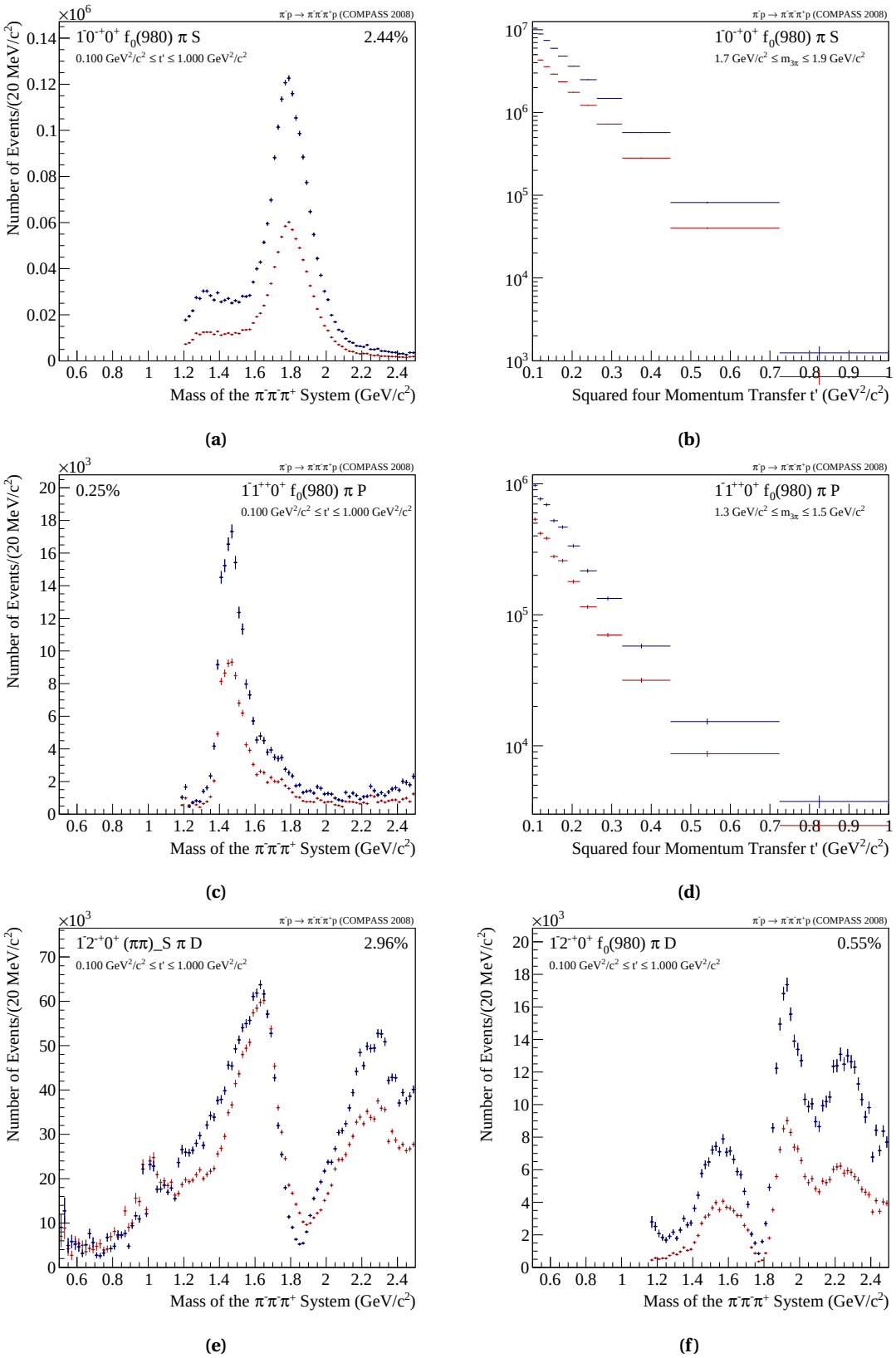

Figure 7.43 Integrated intensity of the $0^{-+}0^{+}f_0(980)\pi S$ wave obtained from the main fit (blue) overlaid by the fit result based on model with the VES/K1 $(\pi\pi)_S$ and $f_0(980)$ parametrisation (red) (a), the corresponding t' dependence (b). The same plot for the new a_1 state (c) and (d) and integrated intensity of the $2^{-+}0^{+}(\pi\pi)_S\pi D$ (e) and the $2^{-+}0^{+}f_0(980)\pi D$ wave (f)

M-Solution with Breit-Wigner Form for the $f_0(980)$ Isobar

The previous exercise modified the model for two cases, the $(\pi\pi)_S$ and the $f_0(980)$. Now it is interesting to see how the modification of the $f_0(980)$ isobar while leaving the $(\pi\pi)_S$ unmodified, affects the fit result. The M-solution of the reference fit was used together with a simple Breit-Wigner parametrisation for the $f_0(980)$ isobar.
Like for the previous study, there is no difference visible in the Flat wave (Fig.7.44a) but the same difference in the $0^{-+}0^{+}(\pi\pi)_S\pi S$ wave (Fig.7.44b) is seen. The bump at 1.3 GeV/c^2 is identical but the intensity around the $\pi(1800)$ mass region is smaller than for the reference fit. The same is observed to the 0^{-+} wave with the $f_0(980)$ isobar (Fig.7.45a). The same behavior is observed for the new a_1 state in terms of intensity (Fig.7.45b). The same two 2^{-+} amplitudes, discussed in the previous study are shown again and exhibit the same characteristics. Exemplary for amplitudes not associated with a 0^{++} isobar the $2^{++}2^{+}\rho\pi D$ (Fig.7.45e) and the $4^{++}1^{+}\rho\pi G$ wave (Fig.7.45f) are presented, both having a relative intensity below 1%. They seems to be not affected by the different f_0 isobar parametrisations. Finally the conclusion can be drawn, regarding this and the previous study, that the deviations come from $f_0(980)$ parametrisation than from the different parametrisations of the $(\pi\pi)_S$ wave.

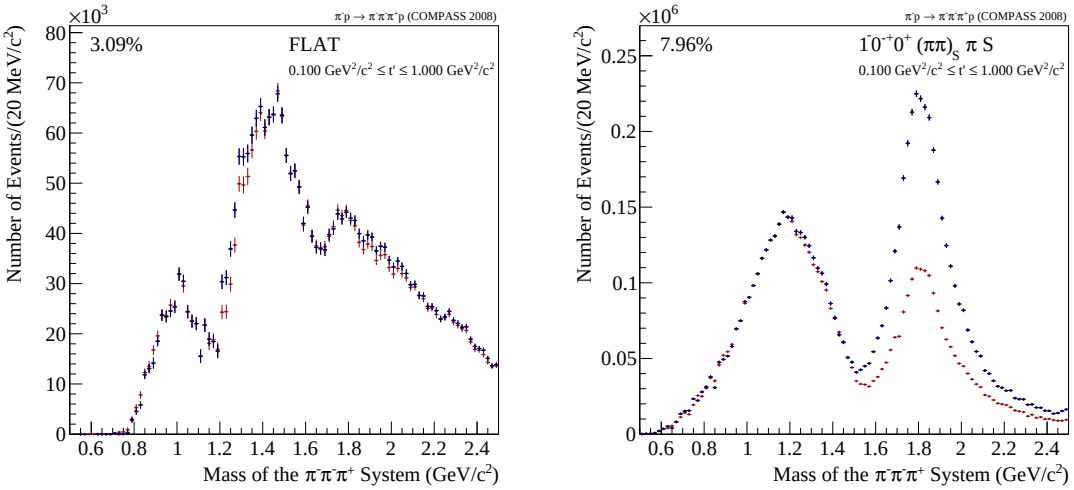

(a) **(b)**

Figure 7.44 Integrated intensity of the Flat wave obtained from the main fit (blue) overlaid by the fit result based on a model with a Breit-Wigner form for the $f_0(980)$ (red) (a), the corresponding plot for the $0^{-+}0^{+}(\pi\pi)_S\pi S$ wave (b).

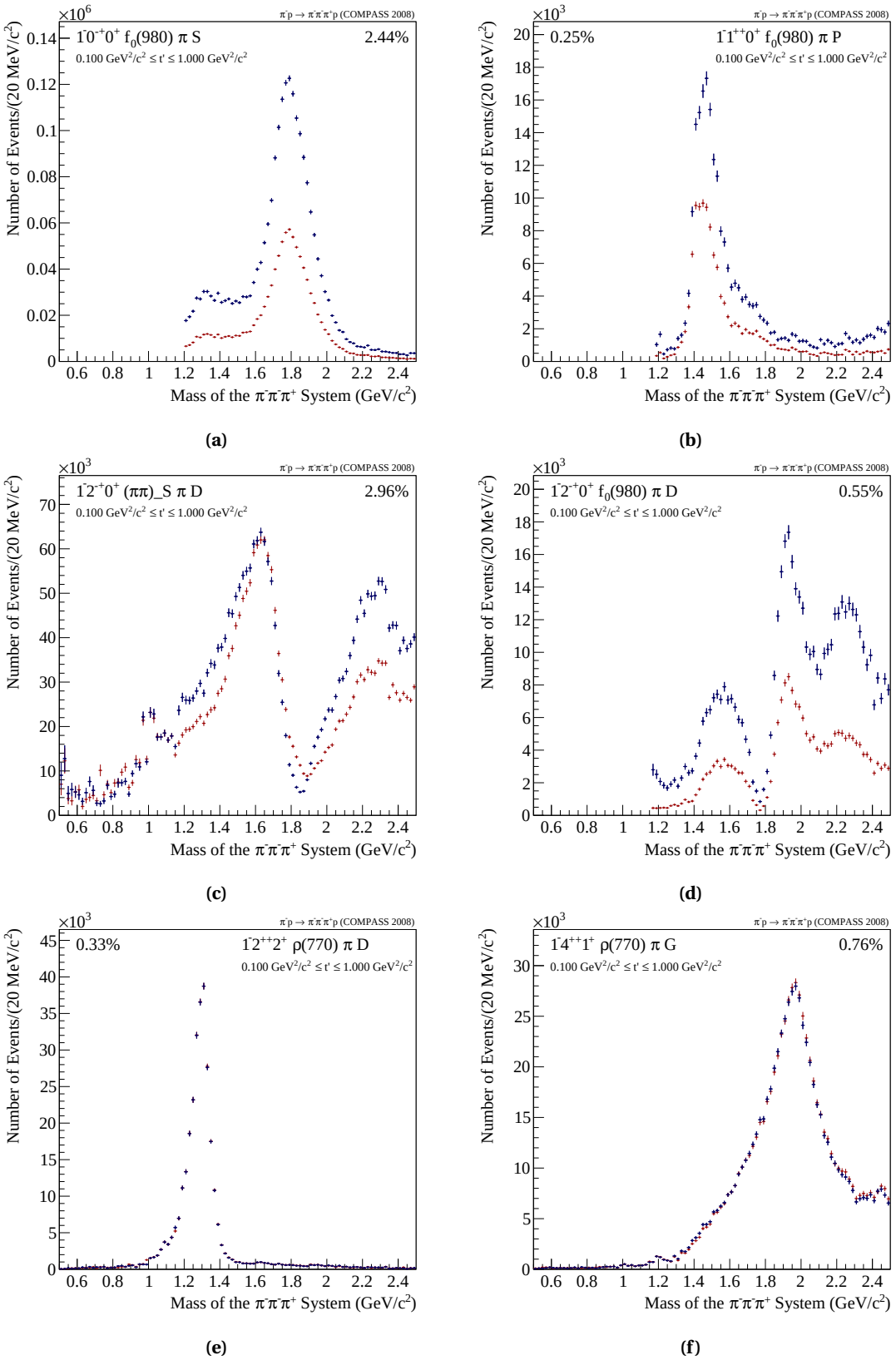

Figure 7.45 Integrated intensity of the $0^{-+}0^{+}f_0(980)\pi S$ wave obtained from the main fit (blue) overlaid by the fit result based on a model with a Breit-Wigner form for the $f_0(980)$ (red) (a), the corresponding plot for the $1^{++}0^{+}f_0(980)\pi P$ (b), the $2^{-+}0^{+}(\pi\pi)_S\pi D$ (c), the $2^{-+}0^{+}f_0(980)\pi D$ (d), the $2^{++}2^{+}\rho\pi D$ (e) and the $4^{++}1^{+}\rho\pi G$ wave (f).

A $\pi\pi_P$ Wave Instead of the $\rho(770)$

The dominant isobar in the 3π data is the $\rho(770)$ resonance. Major partial waves, contributing to the $a_1(1260)$ or the $a_2(1320)$, or spin-exotic waves like the one being part of this wave set appear in the $\rho\pi$ decay channel. Nevertheless the precise line shape if the $\rho(770)$ is still not understood completely. Additional resonances with $J^{PC} = 1^{--}$ are found and the question arises, whether these excited ρ states should or can be taken into account (see Sec.7.6.2) or if a more sophisticated ansatz, similar to the $(\pi\pi)_S$ wave, can be found. This concept of a $(\pi\pi)_P$ isobar was used to describe one possible decay of the J/ψ [GMSS12]. The wave includes in addition to the ground-state $\rho(770)$ the excited state $\rho(1700)$, both part of a K-matrix fit to the J/ψ decay data.
Using this $(\pi\pi)_P$ parametrisation the Flat (Fig.7.46a) wave shows a significant increase of intensity around the $a_2(1320)$ mass region while above there is no visible difference. The coherent isotropic wave $0^{-+}0^+(\pi\pi)_S$ (Fig.7.46b) differs in both peaks of the intensity distribution, the one at 1.3 GeV/c^2 and the second at 1.8 GeV/c^2. The biggest amplitude of the wave set, the $1^{++}0^+\rho\pi S$ wave (Fig.7.47a), exhibits a slight shift of the rising edge of about 20 MeV/c^2 towards higher masses. But no difference on the corresponding t'-dependence (Fig.7.47b) is observed. The new a_1 (Fig.7.47c) shows a similar behavior with a mass shift of the complete wave intensity of one mass bin here towards lighter masses. Nevertheless the corresponding t' dependence (Fig.7.47d) differs in terms of the intensity but not slope. The most striking effect can be seen for the 2^{++} waves, where the $2^{++}1^+\rho\pi D$ wave (Fig.7.47e) has a lower intensity which seems to be distributed to the Flat wave and the $2^{++}1^+ f_2\pi P$ wave (Fig.7.47f).

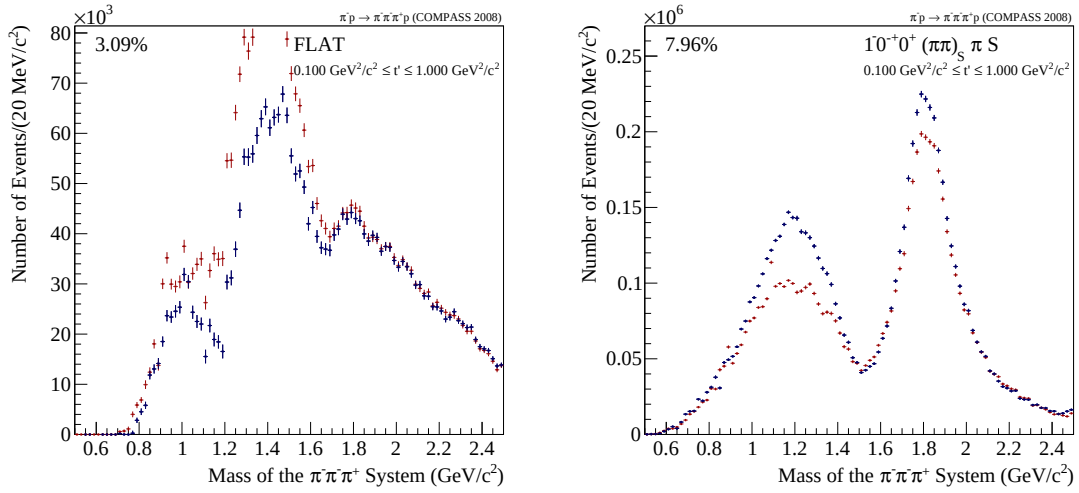

(a) **(b)**

Figure 7.46 Integrated intensity of the Flat wave obtained from the main fit (blue) overlaid by the fit result based on a model with the $(\pi\pi)_P$ parametrisation (red) (a), the corresponding plot for the $0^{-+}0^+(\pi\pi)_S\pi S$ wave (b).

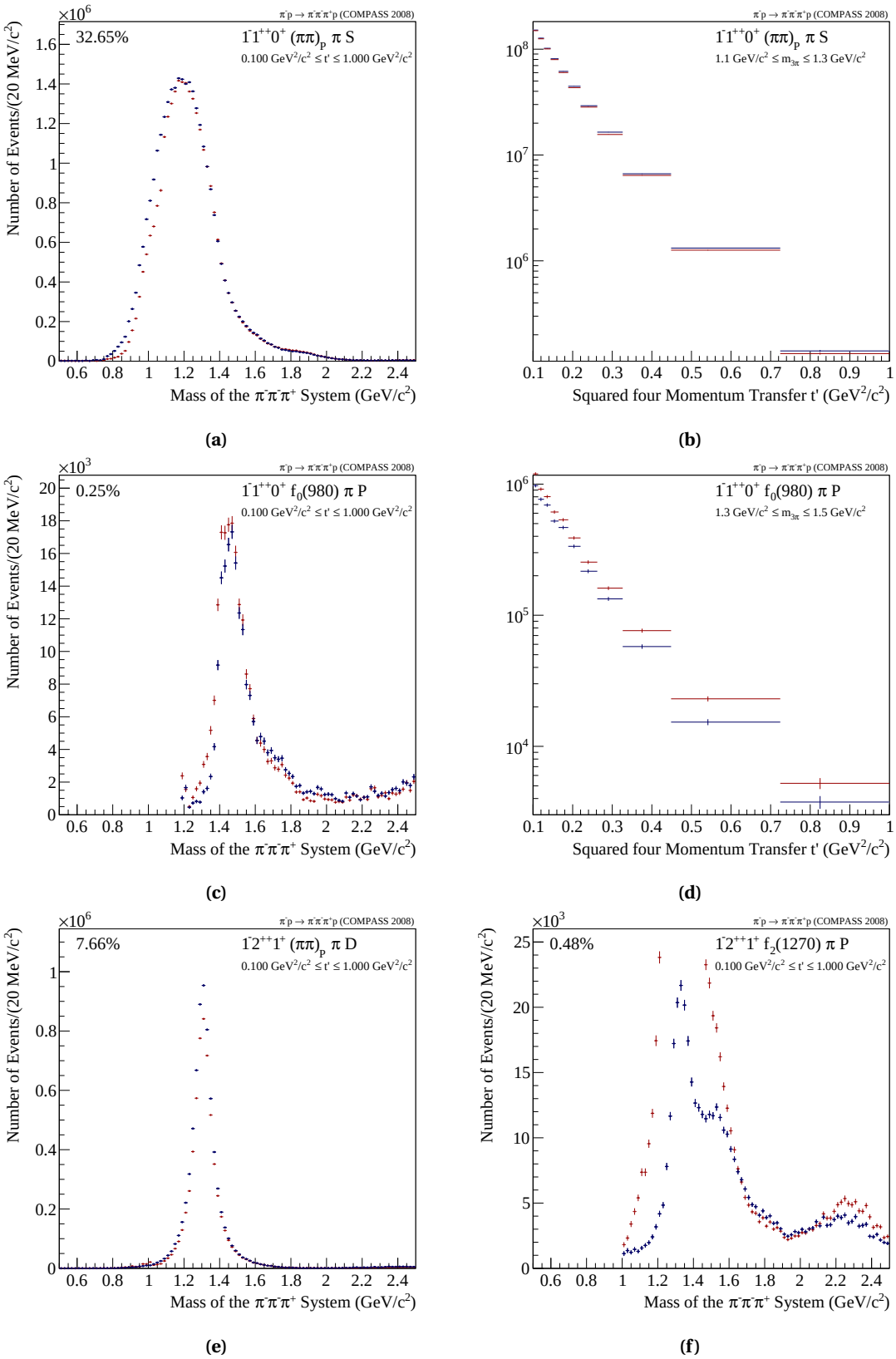

Figure 7.47 Integrated intensity of the $1^{++}0^{+}\rho\pi S$ wave obtained from the main fit (blue) overlaid by the fit result based on model with the $(\pi\pi)_P$ parametrisation (red) (a), the corresponding t' dependencies (b). The same plot for the new a_1 state (c) and (d) and the integrated intensity of the $2^{++}1^{+}\rho\pi D$ (e) and the $2^{++}1^{+}f_2(1270)\pi P$ wave (f).

A Wave Set Without Negative-Reflectivity Waves

It was discussed in Sec.7.2 that for the center-of-mass energy, obtained at COMPASS, it can be assumed that the Pomeron trajectory contributes more than 90% to the scattering process. Nevertheless a small fraction remains which offers the possibility for other trajectories like the f_2 trajectory (positive naturality) or the b_1 trajectory (negative naturality). 80 waves of the model are representing exchange trajectories with positive naturality/reflectivity. In order to regard the trajectories with negative naturality seven waves with $\varepsilon = -1$ are part of the waveset. Partial waves with different reflectivities do not interfere by definition (see Sec.6.1.2) and have different angular distributions. Thus they should be well distinguishable. A waveset without these seven negative waves was applied to the data.
The Flat wave (Fig.7.48a) increases by a factor of $\sim$ 1.5 while all 80 waves with positive reflectivity show no difference. Exemplary for the positive-reflectivity waves the $0^{-+}0^{+}(\pi\pi)_S$ wave (Fig.7.48b) is shown as well as the $1^{++}0^{+}\rho\pi S$ (Fig.7.49a), the new a_1 state in the $1^{++}0^{+}f_0(980)\pi P$ wave (Fig.7.49c) and the $2^{-+}0^{+}f_2\pi S$ wave (Fig.7.49e), for the last three amplitudes the corresponding t' dependencies are plotted, too.

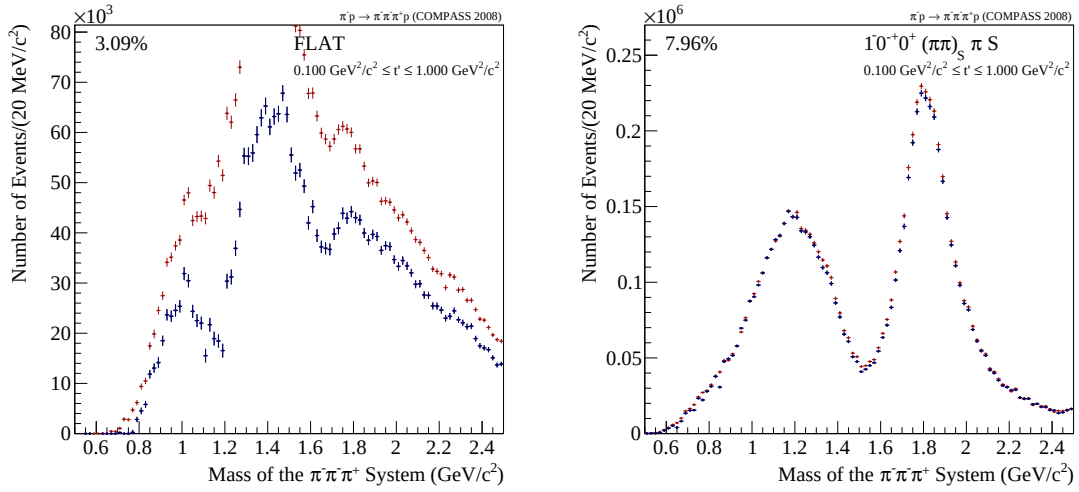

(a) **(b)**

Figure 7.48 Integrated intensity of the Flat wave obtained from the main fit (blue) overlaid by the fit result based on a model without waves with negative reflectivity (red) (a), the corresponding plot for the $0^{-+}0^{+}(\pi\pi)_S\pi S$ wave (b).

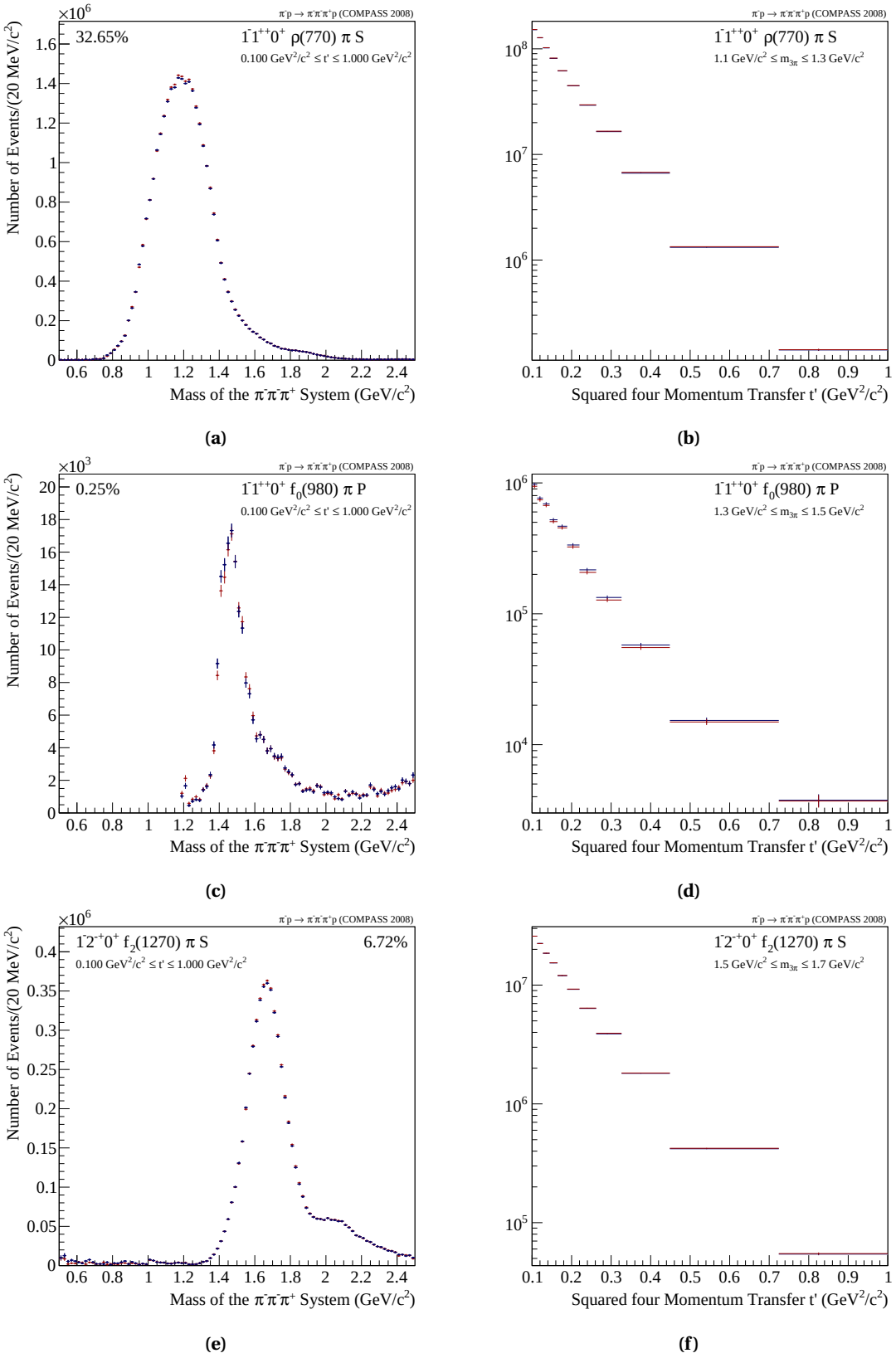

Figure 7.49 Integrated intensity of the $1^{++}0^{+}\rho\pi S$ wave obtained from the main fit (blue) overlaid by the fit result based on a model without waves with negative reflectivity (red) (a), the corresponding t' dependencies (b). The same plot for the $1^{++}0+f_0(980)\pi P$ (c) and (d) and the $2^{-+}0^{+}f_2(1270)\pi S$ wave in (e) and (f)

Summary

Summarising the investigations in the previous section results in a band of uncertainty which illustrates the effect of model changes for each mass bin on the partial-wave amplitude. As noted at the beginning these systematic modifications are taken into account for the resonance extraction, discussed in the next chapter.
The Flat wave (Fig.7.50a) has only deviations in the positive direction. This can be interpreted that no systematic study improved the fit, which would result in a decrease of the intensity. This statement is true for rank-1 fits. The Flat wave vanishes completely if the rank is increased to 2 (see Sec.7.6.2). The $0^{-+}0^{+}(\pi\pi)_S\pi S$ wave (Fig.7.50b) shows the opposite behavior. Except for a few mass bins the observed intensity is smaller for all systematic studies. The behavior below 1.5 GeV/c^2 is mostly driven by the different $(\pi\pi)_S$ isobar parametrisations and above the $f_0(980)$ parametrisations influences the intensity. The variations observed for the $1^{++}0^{+}\rho\pi S$ wave (Fig. 7.51a) are mainly triggered by the $(\pi\pi)_P$ parametrisation used instead of a single Breit-Wigner form for the $\rho(770)$. The same is true for the $2^{++}1^{+}\rho\pi D$ wave (Fig. 7.51b). The two dominant waves in the $J^{PC} = 2^{-+}$ sector are mainly influenced by the $(\pi\pi)_P$ parametrisation (Fig. 7.51c) and the usage of different isoscalar isobars, more precisely the $(\pi\pi)_S$ and $f_0(980)$ forms (Fig. 7.51d). The new 1^{++} state (Fig. 7.51e) is biased by the $(\pi\pi)_S$ and the $f_0(980)$ form, while the spin-exotic amplitude (Fig. 7.51f) shows variation at 1.1 GeV/c^2 caused by the K_1 parametrisation while the overall intensity is slightly affected again by the $(\pi\pi)_P$ isobar.
In general the dominant variations origins from the various isobar parametrisations.

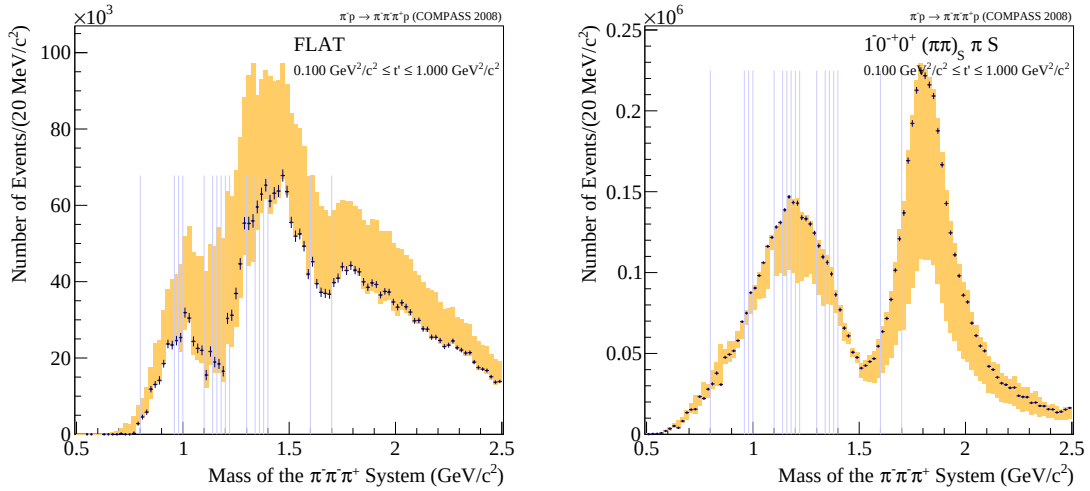

Figure 7.50 Integrated intensity of the Flat wave obtained from the main fit (blue) overlaid by the band of uncertainty resulting from model studies (yellow) (a), the corresponding plot for the $0^{-+}0^{+}(\pi\pi)_S\pi S$ wave (b).

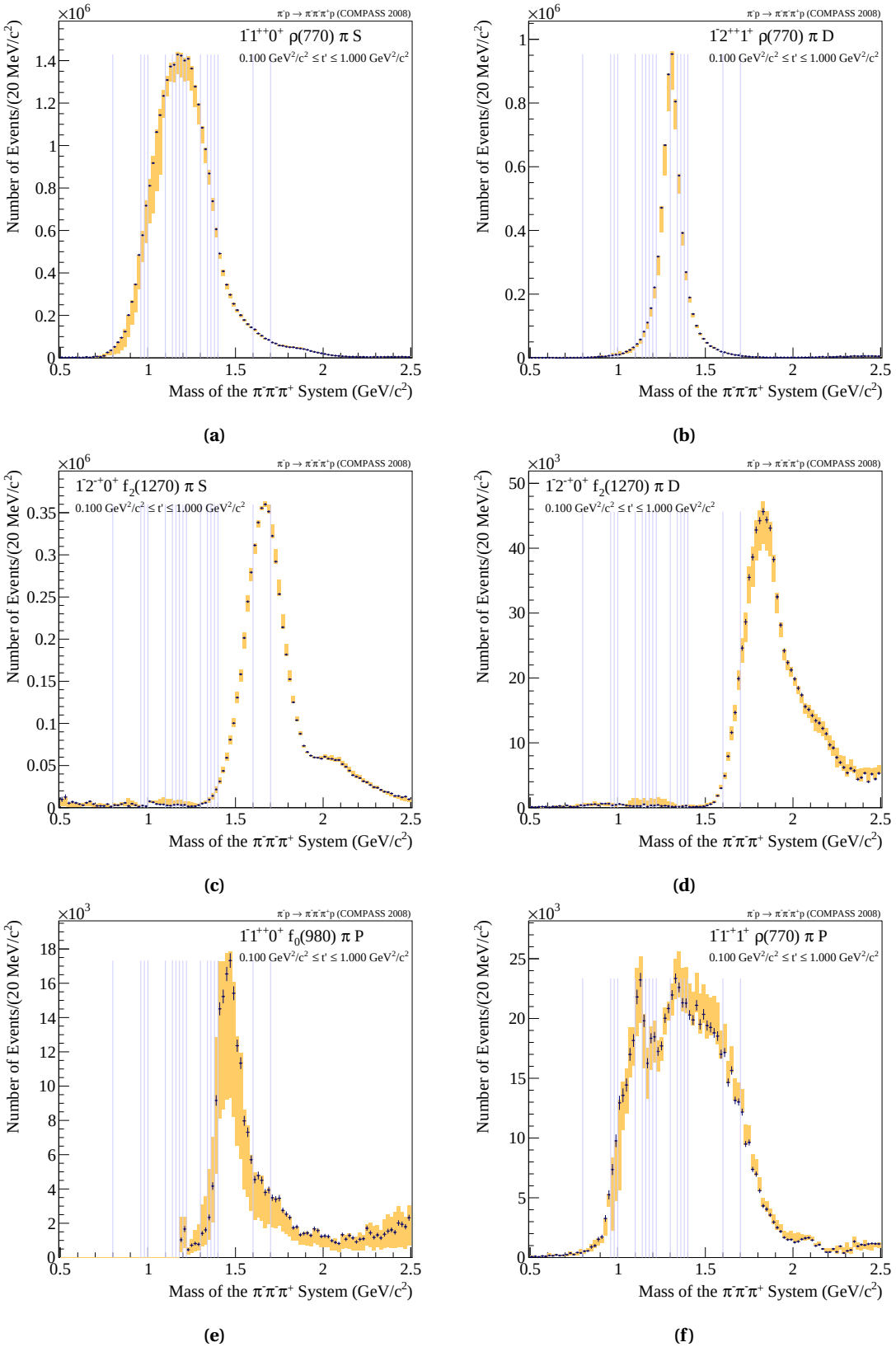

Figure 7.51 Integrated intensity of the $1^{++}0^{+}\rho\pi S$ wave obtained from the main fit (blue) overlaid by the band of uncertainty resulting from model studies (yellow) (a), the corresponding plot for the $2^{++}1^{+}\rho\pi D$ (b), the $2^{-+}0^{+}f_2(1270)\pi S$ (c), the $2^{-+}0^{+}f_2(1270)\pi D$ (d), the $1^{++}1^{+}f_0(980)\pi P$ (e) and the $1^{-+}1^{+}\rho\pi P$ wave (f).

7.6.2 Further Studies

In addition to the variations of the fit model in the previous section some more studies were undertaken. They are not part of the main uncertainty, as their impact is negligible or cannot be compared easily with the reference fit.

Rank-2 Fit

From the mathematical point of view a rank-2 fit consists of two incoherent sets of transition amplitudes. As a result the coherence of these waves ranges between zero and one (see Sec.7.1.4). This means physically that different non-interfering production processes are taken into account. For this study the 80 waves with positive reflectivity are now fitted with rank 2.
The most striking effect is observed for the Flat wave (Fig. 7.54a) which vanishes almost completely. This could be interpreted that by the doubling of the fit parameters (what a rank-2 fit means practically) almost all events can be associated to any partial wave. But this would imply that no events without any angular correlation are part of the data set which is rather unlikely. For most of the other waves the increase of the rank is reflected in an increase of intensity in the various peaks (e.g. Fig. 7.54b - Fig. 7.53b). Modifications of the general shape can be observed for the spin-exotic amplitude (Fig. 7.53c), resulting in an doubling of the intensity around 1.1 GeV/c^2, and for the $2^{-+}0^+\rho\pi P$ wave (Fig. 7.53d). The interference pattern observed for the $2^{-+}0^+ f_0(980)\pi D$ wave at 1.8 GeV/c^2 vanishes while additional peak structure rises for other waves (Fig. 7.53f). As already mentioned there is no justification at the moment to use a rank-2 fit for binned data in $m_{3\pi}$ and t' taken with a pure proton target.

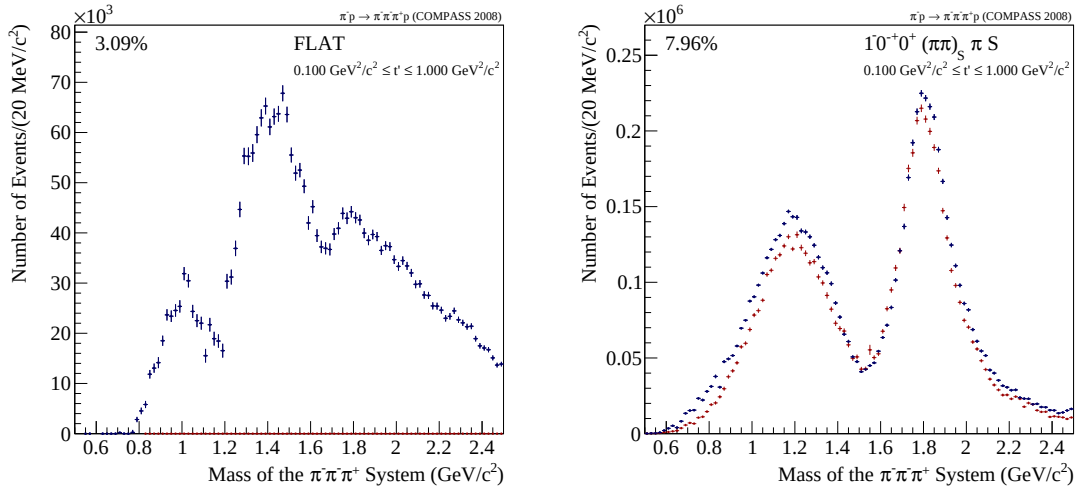

(a) **(b)**

Figure 7.52 Integrated intensity of the Flat wave obtained from the main fit (blue) overlaid by the rank-2 fit result (red) (a), the corresponding plot for the $0^{-+}0^+(\pi\pi)_S\pi S$ wave (b).

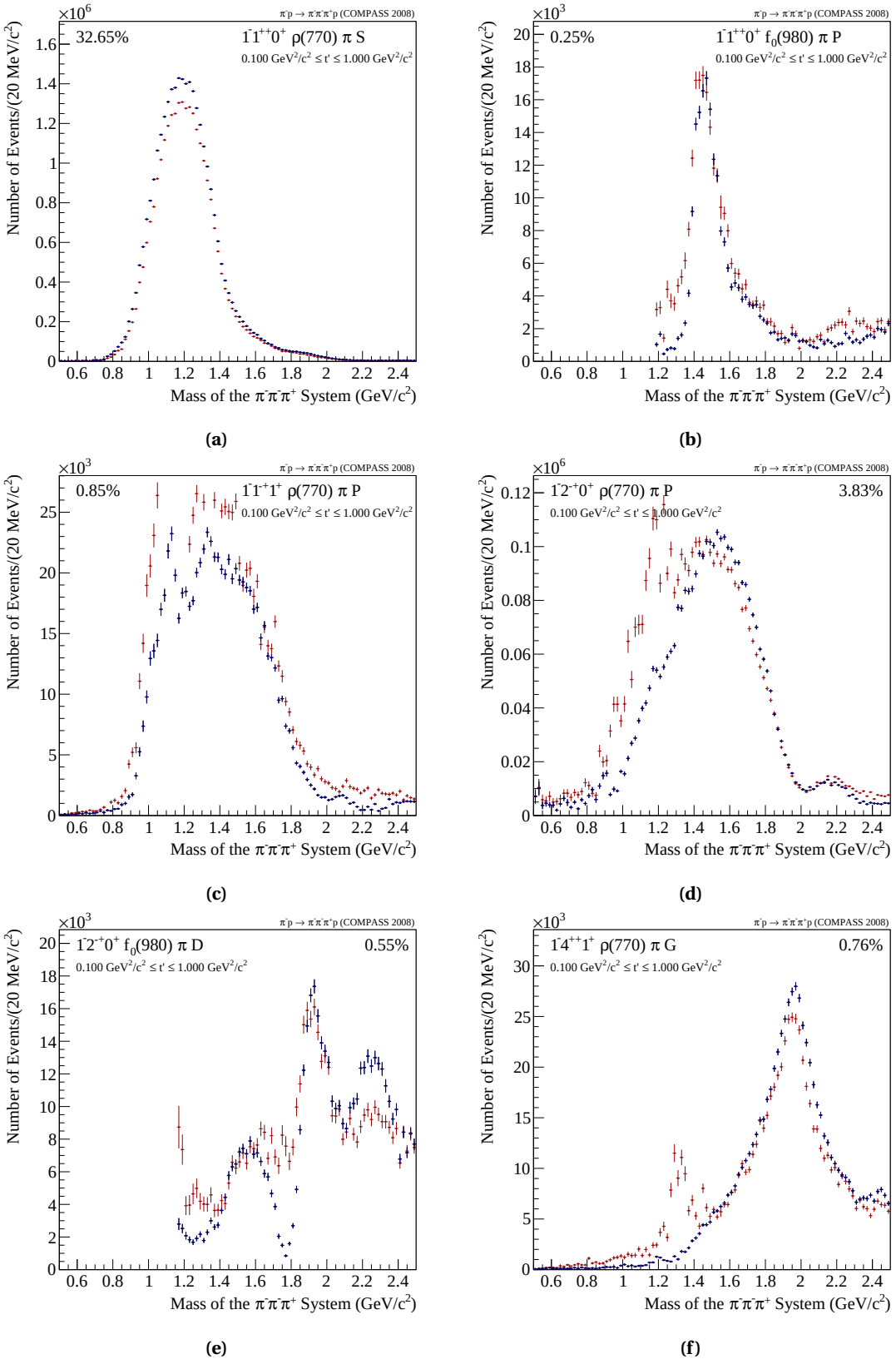

Figure 7.53 Integrated intensity of the $1^{++}0^+\rho\pi S$ wave obtained from the main fit (blue) overlaid by the rank-2 fit result (red) (a), the corresponding plot for the $1^{++}0^+ f_0(980)\pi P$ (b), the $1^{-+}1^+\rho\pi P$ (c), the $2^{-+}0^+\rho\pi P$ (d), the $2^{-+}0^+ f_0(980)\pi D$ (e) and the $4^{++}1^+\rho\pi G$ wave (f)

11 Versus 22 t' Bins

It was mentioned in Sec.7.2 that the binning of the data in 11 t' bins is the best compromise between a necessary fine granulation, in order to assume no t' dependence, and the possibility to investigate the intensity distributions of each partial wave even for single t' bins (see Chap.8). On the other hand a finer binning could help to investigate details of the t' dependence and the participating production processes. Both fits are discussed in this thesis and thus the purpose of this study is to show the equivalence of both fits in terms of intensity distributions.
Besides some small effects in the overall intensity distribution of the Flat wave (Fig. 7.54a) no variations of the amplitudes can be observed, so that both fits can be regarded as equivalent. Thus for the study of the t' dependence on the level of partial waves the fit with 22 t' bins is used while for the extraction of resonance parameters (see Chap. 8) the fit with 11 t' is used.

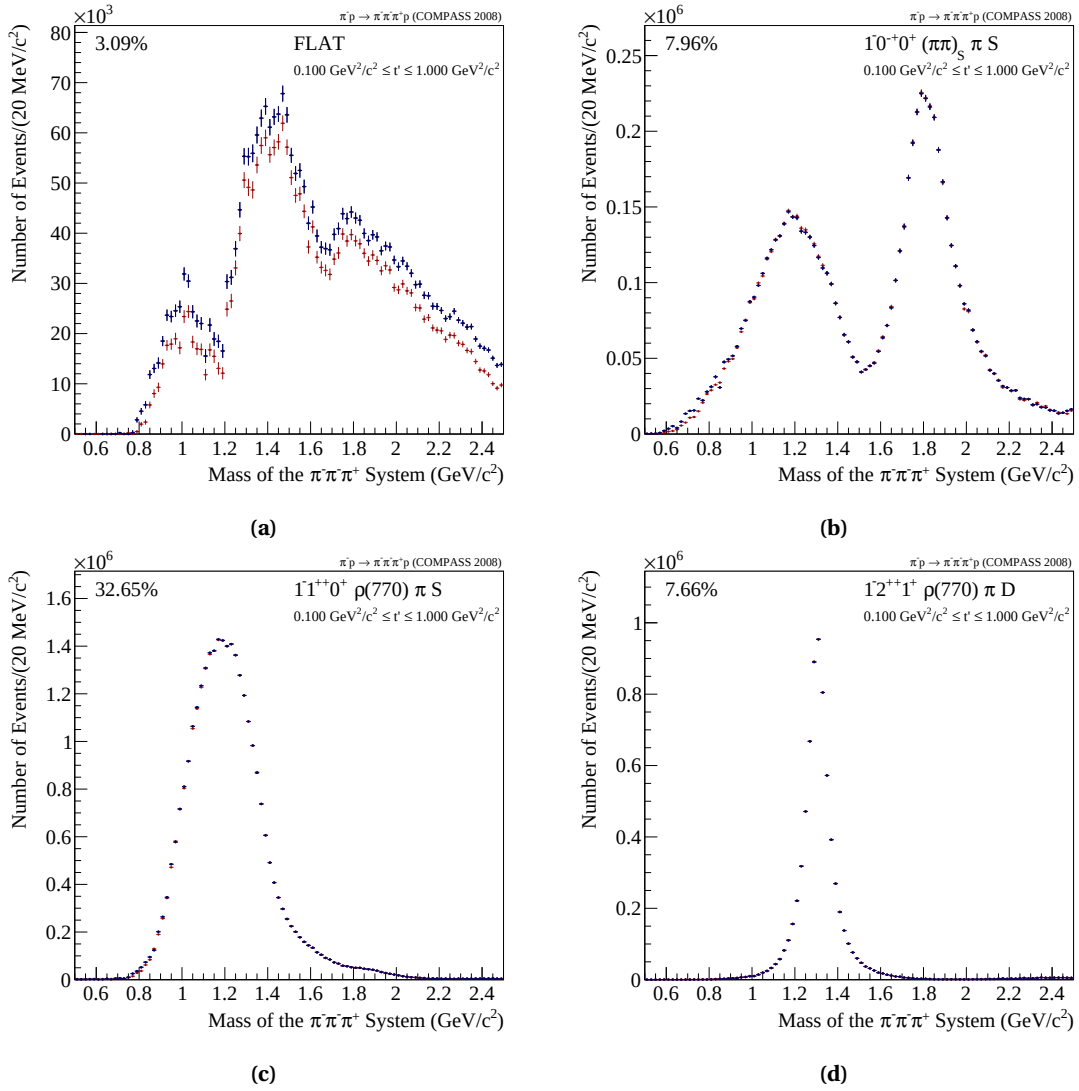

Figure 7.54 Integrated intensity of the Flat wave obtained from the main fit (blue) overlaid by the fit result based on a data set split in 22 t' bins (red) (a), the corresponding plot for the $0^{-+}0^{+}(\pi\pi)_S\pi S$ (b), the $1^{++}0^{+}\rho\pi S$ (c) and the the $2^{++}1^{+}\rho\pi D$ wave (d).

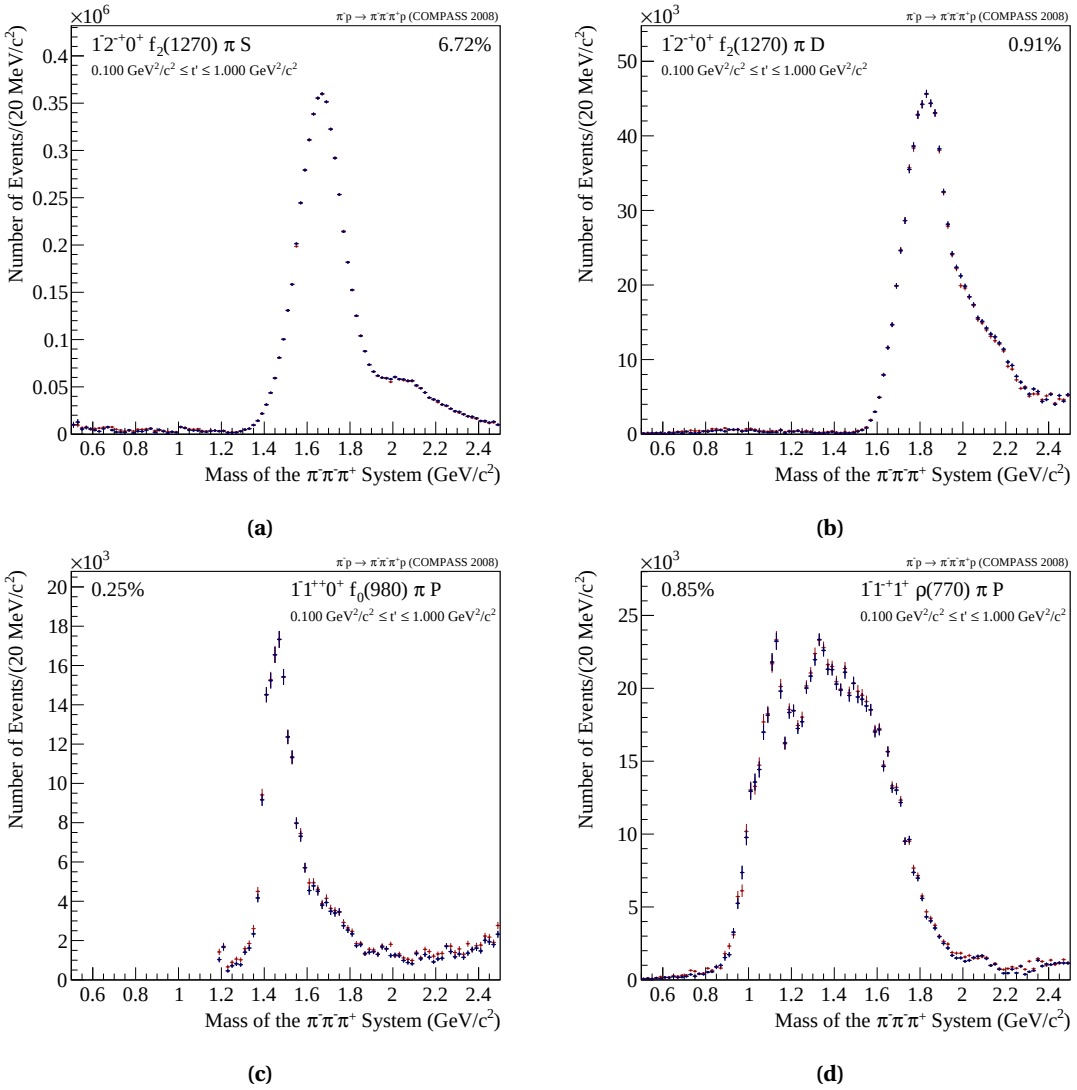

Figure 7.55 Integrated intensity of the $2^{-+}0^+ f_2(1270)\pi S$ (a), the $2^{-+}0^+ f_2(1270)\pi D$ (b), the $1^{++}0^+ f_0(980)\pi P$ (c) and the $1^{-+}1^+ \rho\pi P$ wave (d).

Additional studies were undertaken to investigate the influence of different anchor waves.

- For this purpose the $1^{++}0^+\rho\pi S$ wave was replaced by other dominant waves like the $0^{-+}0^+(\pi\pi)_S\pi S$ or the $2^{++}1^+\rho\pi D$. As expected there was no effect observed.

- Another possible isobar the $f_4(2050)$ was implemented but no partial wave associated with this isobar showed any intensity so it was omitted from the final model.

- Additional isobars with $J^{PC} = 1^{--}$, the $\rho(1430)$ and the $\rho(1700)$, were introduced in addition to the dominant $\rho(770)$. The fit was not able to disentangle the two additional ρ isobars which results in very similar and unstable intensity distributions for partial waves with the same J^{PC} decaying into these two isobars (e.g. see Fig. 7.56).

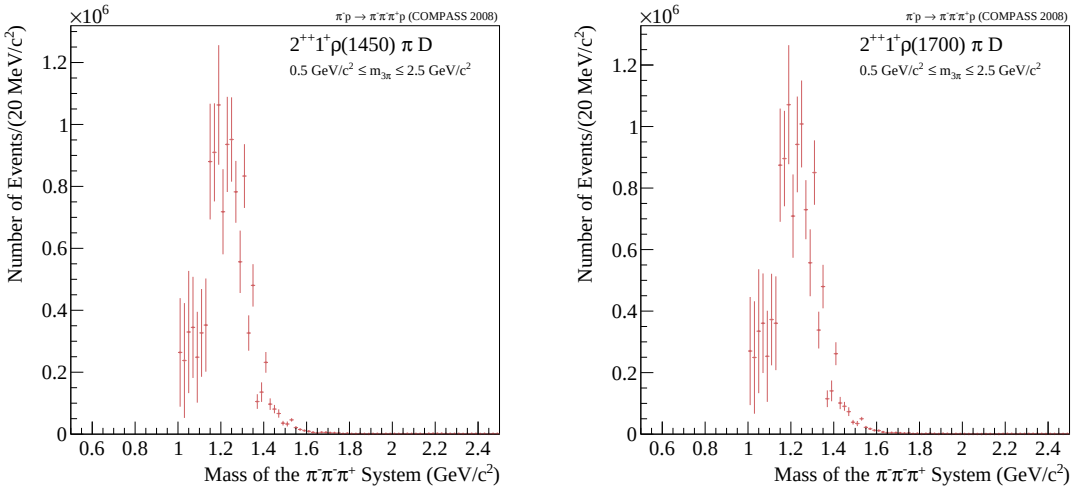

Figure 7.56 Integrated intensity of the $2^{++}1^{+}\rho(1450)\pi D$ (a) and the $2^{++}1^{+}\rho(1700)\pi D$ wave (b).

7.6.3 Leakage Studies

The spin-parity analysis method used here is prone to various kinds of leakage, that is some intensity can be wrongly associated to a certain partial wave due to imperfections of the model. Model leakage originating from a simplified wave set was discussed in Sec. 7.5.4 and can be excluded with a set based on 88 waves. Another source of leakage can be deficiencies of the acceptance correction or the data reconstruction or the neglecting of resolution effects in the analysing procedure. This topic is investigated in the following.
First a data sample with known angular distributions, i.e. a well-defined set of partial waves, is created via the method of weighted Monte Carlo (see Sec. 7.1.6). The data is fed through the Monte Carlo chain, consisting of a simulation of the spectrometer and subsequent reconstruction of the Monte Carlo information (see Sec. 5.3 and App. D). The outcome is analysed with the same event selection and partial wave analysis, applied to the real data. By omitting certain amplitudes in the input Monte Carlo data set, one can determine what fraction of the resulting intensity leaks to this partial wave, which should be small if the method is working correctly. Two extreme scenarios were investigated. In the first kind of study all amplitudes except one were used to generate the input data. The consequential partial-wave analysis reveals the leakage of all the 87 waves into the amplitude that was left out. This was done in two bins of t' for the spin-exotic $1^{-+}1^{+}\rho\pi P$ partial wave (Fig. 7.57a and 7.57b) and the new a_1 state observed in the $1^{++}0^{+}f_0(980)\pi P$ wave (Fig. 7.58a and 7.58b). Common for all four studies is the small amount of leakage origin from the 87 amplitudes, which is in the range of 2-3% of the intensity spread homogeneously in the $m_{3\pi}$ of the respective wave, observed in real data.
For another series of studies the input wave set consists only of one partial wave. The three dominating amplitudes, which together represent more than 50% of the overall observed intensity, were taken for this survey. The individual leakage of the three amplitudes to the remaining 87 waves was investigated. Again this study was undertaken in the same two bins of t'. The resulting plots can be seen in Fig. 7.59, showing the observed intensity as a function of $m_{3\pi}$ for all partial waves. The z-axis is limited to the range between 0 and 800 events in order to make even small leakages visible. The study of the $1^{++}0^{+}\rho\pi S$ (Fig. 7.59a and 7.59b) reveals

significant leakage only to some negative-reflectivity waves in the mass region of the $a_1(1260)$. Almost the same is true for the $2^{++}1^+\rho\pi D$ wave (Fig. 7.59c and 7.59d), while the study for the $2^{-+}0^+ f_2(1270)\pi S$ wave (Fig. 7.59e and 7.59f) shows detects leakage only below 0.8 GeV/c^2 for waves with the same quantum numbers $J^{PC} = 2^{-+}$. All these identified leakages do not influence the region of interest, i.e. positive-reflectivity waves in a mass region above 1 GeV/c^2. Furhter details can be found in [Lie13].

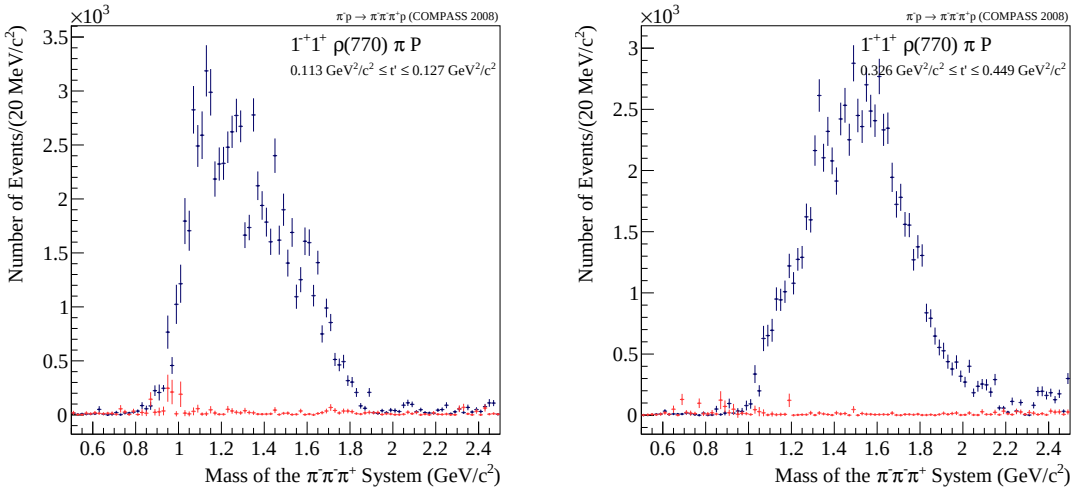

(a) **(b)**

Figure 7.57 Leakage study for the $1^{-+}1^+\rho\pi P$ wave for two kinematic regions of t', $0.113 \leq t' \leq 0.127$ GeV$^2/c^2$ (a) and $0.326 \leq t' \leq 0.449$ GeV$^2/c^2$ (b). The leakage is depicted in red while the blue data points represent the result from real data.

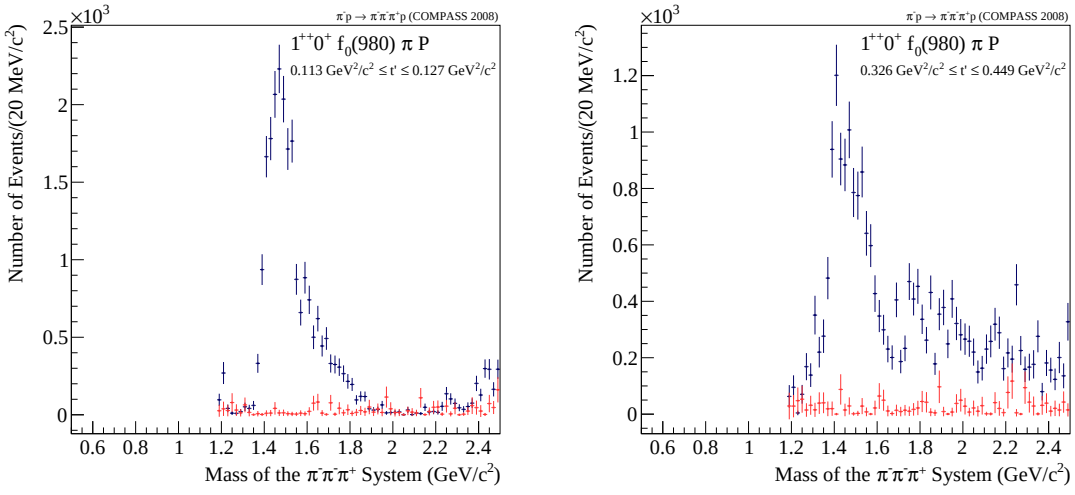

(a) **(b)**

Figure 7.58 Leakage study for the $1^{++}0^+ f_0(980)\pi P$ wave for two kinematic regions of t', $0.113 \leq t' \leq 0.127$ GeV$^2/c^2$ (a) and $0.326 \leq t' \leq 0.449$ GeV$^2/c^2$ (b). The leakage is depicted in red while the blue data points represent result from real data.

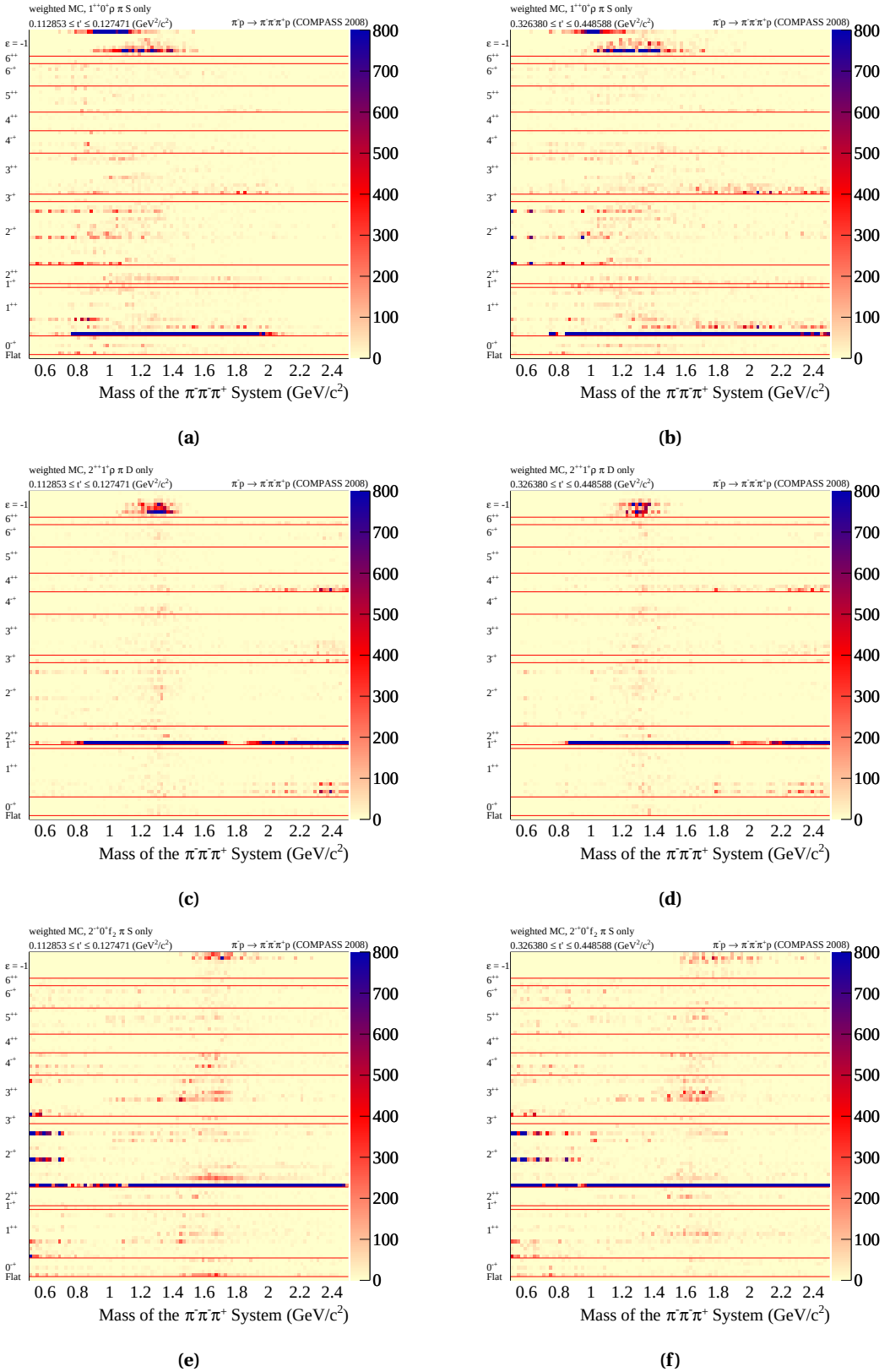

Figure 7.59 Leakage study of dominant waves and their contribution to all other waves. For each wave the invariant mass is plotted against the partial waves. The z-axis ranges from 0 t0 800 events in order to make even small leakages visible. In (a) and (b) the leakage from $1^{++}0^+\rho\pi S$ to all other waves is visible. The corresponding plots are shown for the $2^{++}1^+\rho\pi D$ (c) and (d) and for the $2^{-+}0^+ f_2(1270)\pi S$ (e) and (f).

Chapter 8

Extraction of Resonance Parameters

The partial-wave analysis scheme, applied in this thesis work, is a two-step approach. The first step, discussed in detail in Chap. 7, is a spin-parity analysis that does not assume any particular 3π resonances. The decomposition of the data into partial waves allows to identify the potential of the data by studying intensities and phase motions. Although these observables give hints for possible resonating structures in the data, concrete physical conclusions cannot be drawn at this level. The extracted spin-density matrices serves as basis for the second step of the partial wave analysis, the modeling of the $m_{3\pi}$ dependence of the partial waves and the consequential extraction of resonance parameters. In the following $m_{3\pi}$ is replaced by m_X in order to stress that the study of resonances in the 3π spectrum is the mission of this part of the analysis. The implementation of the model and the corresponding results, the extracted resonance parameters, are the focus of this chapter.

8.1 Model for the m_X Dependence

The starting point for modeling the mass dependence is the outcome of the previous step, the spin-parity analysis, which is the spin-density matrix, introduced in Eq. (7.24). The definition of the matrix is written in Eq. (8.1) with the left lower indices indicating that the matrix is valid only for a certain bin in m_X and t'.

$$ {}_{m_X,t'}\rho^{\varepsilon}_{ab} = \sum_{r}^{N^{\varepsilon}_{r}} {}_{m_X,t'}T^{r\varepsilon}_{a}\,{}_{m_X,t'}T^{r\varepsilon *}_{b} \tag{8.1} $$

The spin-density matrix is a compact representation of the basic results of the spin-parity analysis, the complex transition amplitudes T_a. These amplitudes absorb by definition (see Sec. 6.5) all unknown couplings of the production and decay vertices and possible dynamics in the corresponding regions of m_X and t'. The aim of this part of the analysis is to model the real and imaginary parts of a spin density sub matrix, i.e. the full information of each matrix in terms of intensities and phase motions, is exploited. A possible parametrisation of the spin-density matrix describing the m_X dependence is shown in Eq. (8.2). Due to the fact that for the following analysis only rank-1 and partial-waves with positive reflectivity are considered, the corresponding summation will be omitted for simplicity as well as the index ε.

$$\rho_{ab}(m_X,t') = \sum_{k,l} {}_{t'}C_{ak}\mathscr{F}_{ak}(m_x;\zeta_k)\sqrt{\Phi^a_{3\pi}(m_X)}\left[{}_{t'}C_{bl}\mathscr{F}_{bl}(m_x;\zeta_l)\sqrt{\Phi^b_{3\pi}(m_X)}\right]^* \tag{8.2}$$

The continuous amplitudes $\mathscr{F}_{ak}(m_x;\zeta_k)$, that have a set of parameters ζ_k, describe the mass dependence. Several of these components and the corresponding couplings ${}_{t'}C_{ak}$, both labeled by the index k, are taken into account, in order to parametrise a certain partial wave a. The amplitudes, used for this analysis, is listed in Tab. 8.1, including Breit-Wigner formulations for resonances and various terms for the non-resonant contributions.

Relativistic Breit-Wigner with mass-dependent width for one decay channel

$$\mathscr{F}(m) = \frac{m_0\Gamma_0}{m_0^2 - m^2 - i m_0\Gamma(m)} \quad \text{with} \quad \Gamma(m) = \Gamma_0\frac{m_0}{m}\frac{p F_L^2(p)}{p_0 F_L^2(p_0)} \tag{8.3}$$

Relativistic Breit-Wigner with mass-dependent width for two decay channels

$$\mathscr{F}(m) = \frac{m_0\Gamma_0}{m_0^2 - m^2 - i m_0\Gamma(m)} \quad \text{with} \quad \Gamma(m) = \Gamma_0\frac{m_0}{m}\left[(1-x)\frac{p_1 F_L^2(p_1)}{p_{1,0} F_L^2(p_{1,0}} + x\frac{p_2 F_L^2(p_2)}{p_{2,0} F_L^2(p_{2,0})}\right] \tag{8.4}$$

Relativistic Breit-Wigner with mass-dependent width taking finite width of the $\rho(770)$ isobar into account [Bow86]

$$\mathscr{F}(m) = \frac{\sqrt{m_0\Gamma_0}}{m_0^2 - m^2 - i m_0\Gamma_B(m)} \quad \text{with} \quad \Gamma_B(m) = \Gamma_0\frac{m_0}{m}\frac{\Phi_{\rho\pi}(m)}{\Phi_{\rho\pi}(m_0)} \tag{8.5}$$

Non-resonant contribution

$$\mathscr{F}(m) = e^{c_1 p^2} \tag{8.6}$$

Non-resonant contribution including simple t' dependence

$$\mathscr{F}(m,t') = (m - m_0)^{c_0} e^{(c_1 + c_2 t' + c_3 t'^2)p^2} \tag{8.7}$$

Table 8.1 Amplitudes $\mathscr{F}(m_x;\zeta_k)$ used for the fit models in order to describe the m_X dependence.

Most of the amplitudes $\mathscr{F}^{\varepsilon}_{ak}(m_x;\zeta_k)$ are independent of t' while the associated couplings ${}_{t'}C^{\varepsilon}_{ak}$ maybe different for each t' bin. The reason is that the resonance parameters mass and width do not depend on t' while the according production strength and phase, represented by the couplings, maybe change with t'. Non-resonant terms, however, can be t'-dependent and a possible parametrisation (see Eq. (8.7)) is used in parts of this analysis (see Sec. 8.2). The bulk of partial waves is described by Breit-Wigner amplitudes with a mass-dependent width that takes into account decay channel (Eq. (8.3)) with $F_L(p)$ being the Blatt-Weisskopf centrifugal-barrier

factors, introduced in Sec. 6.4.1 and p the break-up momentum. One of the exceptions is the description of the $a_2(1320)$ resonance which also has a non-negligible branching to the $\eta\pi$ final state [B$^+$12]. This is taken into account by a Breit-Wigner with mass-dependent width for two decay channels (see Eq. (8.4)) with fraction $x = 0.2$ for the $\eta\pi$ final state. Another exception is the description of the $a_1(1260)$ resonance which is known to have non-resonant contribution comparable to the resonance itself. This fact is accommodate by the parametrisation[Bow86] of the $a_1(1260)$ as shown in Eq. (8.5). With the implementation of the dynamical factor $\Phi_{\rho\pi}(m)$, the three-body phase-space of the $\rho\pi S$ wave, the finite width of the $\rho(770)$ isobar is considered. The last ingredient for the model are the factors $\sqrt{\Phi^a_{3\pi}(m_X)}$ which are taking into account the available phase space for each partial-wave. They are the same phase space integrals as introduced in Eq. (7.21). Finally for each partial-wave a non-resonant contribution term (Eqs. (8.6)(8.7)) is implemented.
The fit of the model spin-density matrix ${}_{t'}\rho_{ab}(m_X)$ to the set of matrices obtained by the spin-parity analysis $\sum_m^{\text{bins}} {}_{m_X,t'}\rho^{\varepsilon}_{ab}$ is performed via the minimisation of a χ^2-function (see Eq. (8.8)). The 2×2 covariance matrix Cov^{-1}_{ab} corresponds to the real and imaginary parts of the spin-density matrix elements.

$$\chi^2 = \sum_{t'}^{\text{bins}} \sum_{m}^{\text{bins}} \sum_{a,b}^{\text{waves}} \left({}_{m_X,t'}\rho_{ab} - \rho_{ab}(m_x,t')\right)^T \text{Cov}^{-1}_{ab} \left({}_{m_X,t'}\rho_{ab} - \rho_{ab}(m_x,t')\right) \tag{8.8}$$

Like for the spin-parity analysis in $m_{3\pi}$ and t' bins an anchor wave (see Sec. 7.1.2) is defined for each model. In this case it means that the complex coupling ${}_{t'}C_{ak}$ of a certain amplitude $\mathscr{F}_{ak}(m_x;\zeta_k)$ is chosen to be real in order to accommodate for the unmeasurable absolute phase. For all fit models discussed in this chapter the $a_1(1260)$ resonance, in the $1^{++}0^+\rho\pi S$ partial wave, is taken as the anchor wave. Thus the coupling ${}_{t'}C_{1^{++}0^+\rho\pi S,a_1(1260)}$ is real valued. The corresponding Breit-Wigner amplitude shows a large and stable intensity in all fits and the production phase $\Delta\varphi^{\text{Prod}}_{ak}$ of the other model components is defined as

$$\Delta\varphi^{\text{Prod}}_{ak} = \arg({}_{t'}C_{ak} \cdot {}_{t'}C_{1^{++}0^+\rho\pi S,a_1(1260)}) \tag{8.9}$$

It is now possible to study the relative phases of the model components in dependence on t', and thereby gaining more information about the production process.

The fit model is crucial for this analysis. The naive idea to fit the complete spin-density matrix with 88 waves is unfortunately impractical due to limited computing power and lack of knowledge. Hence a spin-density sub matrix ${}_{m_X,t'}\rho_{ab}$ is formed consisting of a subjective selection of partial waves. The selection criteria are driven by the catalog of questions of the corresponding analysis (see Sec. 8.2) and the quality of the signal of a partial wave of interest.
A challenge for this analysis is to model the strong t' dependence of the peaks observed in some partial waves. Prime examples are both dominant partial waves of the $a_1(1260)$ (see Fig. 7.20 and Fig. 7.21) decaying via ρpi and a S wave. The shift of the peak cannot be caused by the resonating component thus a valid description of the non-resonant contribution has to be developed. This makes it necessary to take the t' dependence of background contributions into account besides the dependence on the mass. The consequences of ignoring the t' information is illustrated in Fig. 8.1. It shows the variation of the fitted mass parameter for some selected resonances based on a fit model with 21 partial waves and 65 model components (i.e.

Breit-Wigner forms or simple non-resonant terms (Eq. 8.6)) applied independently to each t' bin (see Sec 9.1). In order to illustrate the fit quality the statistical errors are scaled by a factor 100 otherwise they would not be visible in the plot. The fit converged for all t' bins but without the simultaneous information of all t' bins the fit adjusts resonance parameters and non-resonance contributions independently for each t' bin. This results in variations of the fitted mass, albeit small for some resonances like the $a_2(1320)$ the overall variation of the mass of the $a_1(1260)$, for example, is out of the actual statistical error.

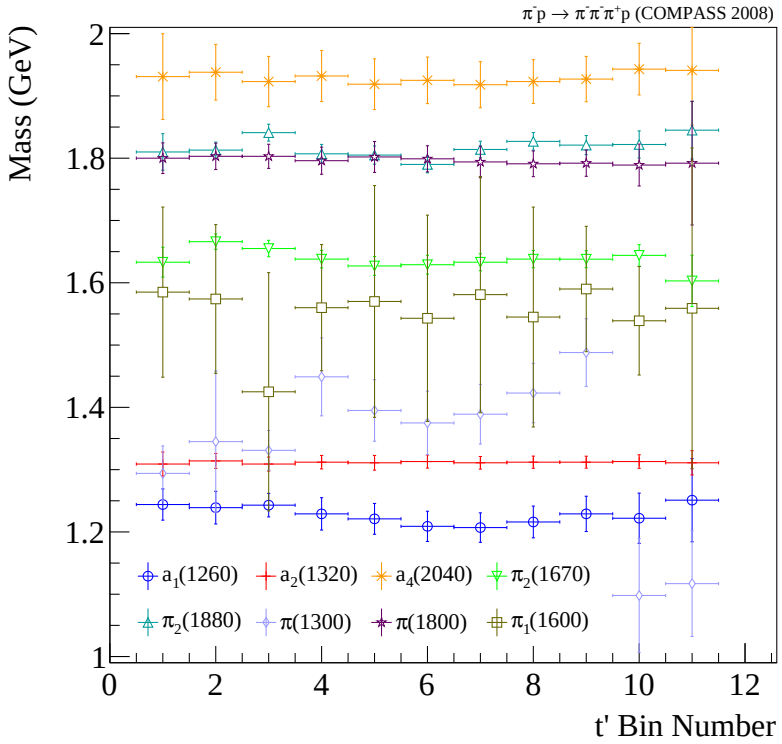

Figure 8.1 Variation of the fitted mass parameter for some selected resonances obtained by independent fits in the 11 t' bins. The statistical errors are scaled by a factor 100.

Thus the fit can be improved significantly by including the information of the t' dependence. The simultaneous fit of t' bins leads to a better separation of resonant and non-resonant contributions. This, however, leads to a larger number of fit parameters as shown in Eq. (8.10). For each amplitude $\mathscr{F}_{ak}(m_x;\zeta_k)$ in each partial wave a complex coupling ${}_{t'}C_{ak}$ must be taken into account for each t' bin plus two parameters (mass and width) of resonances and one or four parameters for the description of the background.

$$N_{\text{param}} = \underbrace{N_{t'\text{bins}} \cdot (2 \cdot N_{\mathscr{F}} - 1)}_{\text{couplings}} + \underbrace{2 \cdot N_{\text{Breit-Wigner}} + N_{\text{simple BG}} + 4 \cdot N_{t'\text{dep BG}}}_{\text{amplitudes}} \tag{8.10}$$

$$N_{\text{data points}} = N^2_{\text{waves}} \cdot N_{m_{3\pi}\text{bins}} \cdot N_{t'\text{bins}} \tag{8.11}$$

The fit algorithm used for the analysis treats every spin-density matrix element as independent neglecting existing correlations, hence the number of available data points for a certain model

cannot be calculated with Eq. (8.11) because real and imaginary parts of each wave are considered.
At the moment computational and software related constraints limit the number of parameters. This is why the information exploitation of all 11 t' bins limits the number of partial waves that can be included in one fit. In these analyses typically seven waves are included. This is comparable with former analyses which, however, did not perform the analysis in t' bins.

For the sake of clarity a certain presentation pattern will be used in the following discussion of various fit models. In order to illustrate the fit quality the fitted spin-density sub matrix in a certain t' bin is plotted. Intensities, if not otherwise stated, will be presented in the form of incoherent sums of all t' bins. In addition the focus is on the presentation of t' dependencies of different amplitudes $\mathscr{F}_{ak}(m_x;\zeta_k)$ and corresponding production phases.
At the moment only statistical errors are available for the fits presented in the next section. As discussed before correlations between the spin-density sub matrix elements are not taken into account. This and the large number of events shrinks all statistical errors in the order of 100 keV/c^2. Hence it was decided to not state errors for the obtained resonance parameters. For the analysis of a data sample with such a statistical precision like the 2008 COMPASS data extensive systematic studies are eminent in order to obtain systematic errors for the resonance parameters. Due to the time constraints of the thesis work it was not possible to undergo this kind of studies but are planned for the near future (see Sec. 9.1).

8.2 Coupled Fit in 11 t' Bins

As mentioned above taking into account the information of all 11 t' bins limits the number of partial waves which could be incorporated to the model but gives a better handle on separations of resonant and non-resonant contributions. Dedicated models are developed, driven by certain physical problems, introduced in Sec. 1.4.1 and motivated by the investigation of partial waves on the level of the spin-parity analysis (see Sec. 7.3.2 and Sec. 7.5). Thus four different topics will be discussed in this section, based on four different fit models.

8.2.1 The $a_1(1260)$ and First Observation of the $a_1(1420)$

The focus for this study is the $a_1(1260)$ and the investigation of the newly observed structure in the $1^{++}0^+ f_0(980)\pi P$ (see Sec. 7.5.5) partial wave. In addition this fit model was driven by the idea to consider major amplitudes from different mass regions and with various quantum numbers in order to get a broad profile from the accessible spectrum. Three partial waves with quantum numbers $J^{PC} = 1^{++}$ are part of the model. The dominant amplitude which contributes most to the $a_1(1260)$, having quantum numbers $1^{++}0^+\rho\pi S$ is modeled by two Breit-Wigner amplitudes. The $a_1(1260)$ is modeled by a modified Breit-Wigner (see Eq. (8.5)). In addition a second resonance the $a_1(1930)$ is included into the model. The $a_1(1640)$ was tried but the fit did not find a solution for it. A t'-dependent non-resonant contribution is added as third component. The same wave with spin-projection $M = 1$ is considered as well including both a_1 resonances. The non-resonant term is again modeled with explicit t' dependence (Eq. (8.7)). The third 1^{++} wave, the aforementioned $1^{++}0^+ f_0(980)\pi P$ wave is assumed to consist of a resonance at 1.4 GeV/c^2, modeled by a Breit-Wigner of the type Eq. (8.3) and a simple exponential non-resonant term (Eq. (8.6). The dominant $2^{++}1^+\rho\pi D$ wave is taken into account with two

resonances, the $a_2(1320)$, modeled by a modified Breit-Wigner, that takes into account different decay branchings (see Eq. (8.4)), and the first excitation of the a_2, the $a_2(1950)$. The large intensity of this wave in all t' bins makes it possible to apply a t'-dependent non-resonant term for this amplitude, too. The same is true for the biggest wave with $J^{PC} = 2^{-+}$, the $2^{-+}0^+ f_2(1270)\pi S$ wave. A t'-dependent non-resonant term and two Breit-Wigners for the $\pi_2(1670)$ and the $\pi_2(1880)$ are assumed to describe the observed intensity and interference pattern. The 4^{++} sector is represented by the $4^{++}1^+\rho\pi G$ wave with one Breit-Wigner for the $a_4(2040)$ and a simple exponential non-resonant. Finally the $\pi(1800)$ is considered in the $0^{-+}0^+ f_0(980)\pi S$ wave in addition to an exponential non-resonant contribution. Thus the whole model consists of 16 amplitudes in 7 partial waves resulting in 422 parameters fitted to 4900 data points. The model is listed in Tab. 8.2. Note that the model does not cover the whole mass range for each wave. Below the resonance region which starts around 1.0 GeV/c^2 the underlying production processes are not well understood and thus could not described by the model. Above 2.2 GeV/c^2 it seems that the region is overcrowded with resonances and the investigation of this regime, where also central production begins to contribute significantly, is the task of future analyses. The fit ranges for each partial wave are listed in Tab. 8.2.

Partial Wave	**Fit Range (GeV/c²)**	**Model**
$0^{-+}0^+ f_0(980)\pi S$,	[1.2, 2.3]	Breit-Wigner for $\pi(1800)$, Eq. (8.3) non-resonant contribution, Eq. (8.6)
$1^{++}0^+\rho(770)\pi S$,	[0.9, 2.3]	Breit-Wigner for $a_1(1260)$, Eq. (8.5) Breit-Wigner for $a_1(1930)$, Eq. (8.3) t' dep. non-resonant contribution, Eq. (8.7)
$1^{++}1^+\rho(770)\pi S$,	[0.9, 2.3]	Breit-Wigner for $a_1(1260)$, Eq. (8.5) Breit-Wigner for $a_1(1930)$, Eq. (8.3) t' dep. non-resonant contribution, Eq. (8.7)
$1^{++}0^+ f_0(980)\pi P$,	[1.3, 1.6]	Breit-Wigner for peak at 1.4 GeV/c^2, Eq. (8.3) non-resonant contribution, Eq. (8.6)
$2^{++}1^+\rho(770)\pi D$,	[0.9, 2.1]	Breit-Wigner for $a_2(1320)$, Eq. (8.4) Breit-Wigner for $a_2(1950)$, Eq. (8.3) t' dep. non-resonant contribution, Eq. (8.7)
$2^{-+}0^+ f_2(1270)\pi S$,	[1.4, 2.3]	Breit-Wigner for $\pi_2(1670)$, Eq. (8.3) Breit-Wigner for $\pi_2(1880)$, Eq. (8.3) t' dep. non-resonant contribution, Eq. (8.7)
$4^{++}1^+\rho(770)\pi G$,	[1.25, 2.3]	Breit-Wigner for $a_4(2040)$, Eq. (8.3) non-resonant contribution, Eq. (8.6)

Table 8.2 Model consisting of 7 partial waves and 9 resonances.

In order to illustrate the quality of the fit the spin-density matrix of the bin of $0.144 \leq t' \leq 0.164$ GeV$^2/c^2$ is plotted in Fig. 8.2. Of course the fit uses the information of all 11 t' bins and thus the complete result consists of 11 spin-density matrices which were fitted as a whole. However, the

presentation of 11 matrices per fit would go beyond the scope of this thesis. On the diagonal the intensities are plotted and the off-diagonal elements show the corresponding phases. The result of the spin-parity analysis is plotted with blue markers in the mass ranges where the data is included into the fit is considered. The outcome of this model is overlaid in red. The gray markers represents mass regions not taken into account by the fit. The fit is able to describe the distributions quite well and even outside of the fit range, where the red curve is plotted as a dashed line, the description follows the data in many cases, which means the fit outcome has a certain validity even outside its boundaries. While there is no obvious discrepancy found for the intensities minor differences can be seen for some phase motions. In particular for phases that include the $1^{++}0^{+}f_0(980)\pi P$ wave the model deviates in the light mass region. It was tried to extend the rather narrow fit range for this partial wave but no successful fit result could be found for the moment.

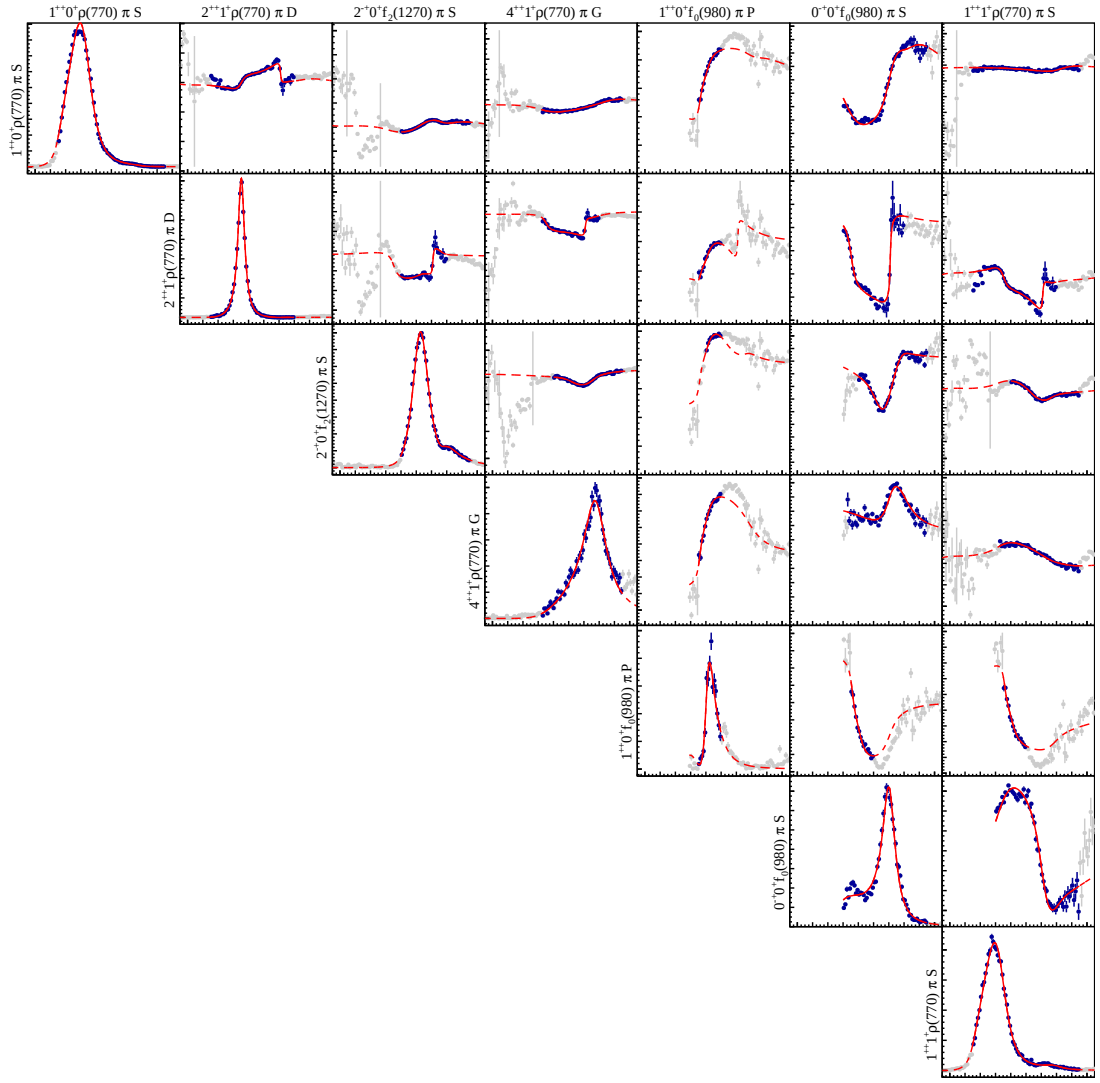

Figure 8.2 Spin-density matrix $\rho(m_x, t')$ with the fit result of the model listed in Tab. 8.2 in the bin of $0.144 \leq t' \leq 0.164$ GeV$^2/c^2$.

In the following the fit result of selected partial waves is discussed.

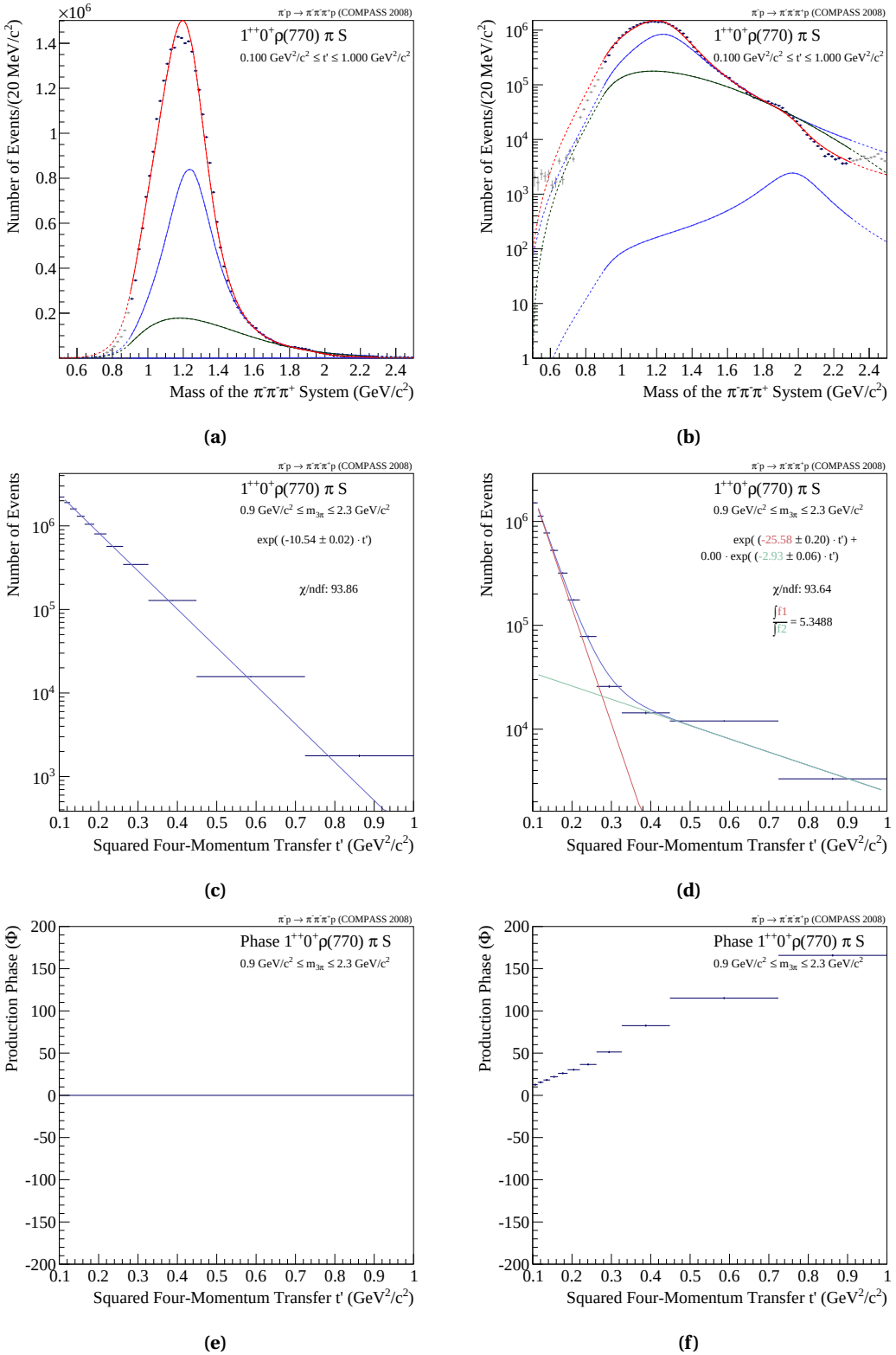

Figure 8.3 Fit result for the $1^{++}0^{+}\rho\pi S$ partial wave based on the model listed in Tab. 8.2. The t'-integrated intensity is shown in (a) with the blue markers being the data points of the spin-parity analysis fit. The red curve shows the overall fit result, the blue curves the Breit-Wigner components and the green line the non-resonant contribution. The same plot in logarithmic scale where the second Breit-Wigner is visible (b). The t' dependence of the $a_1(1260)$ is plotted in (c) and that of non-resonant contribution in (d). The corresponding production phases are shown in (e) and (f).

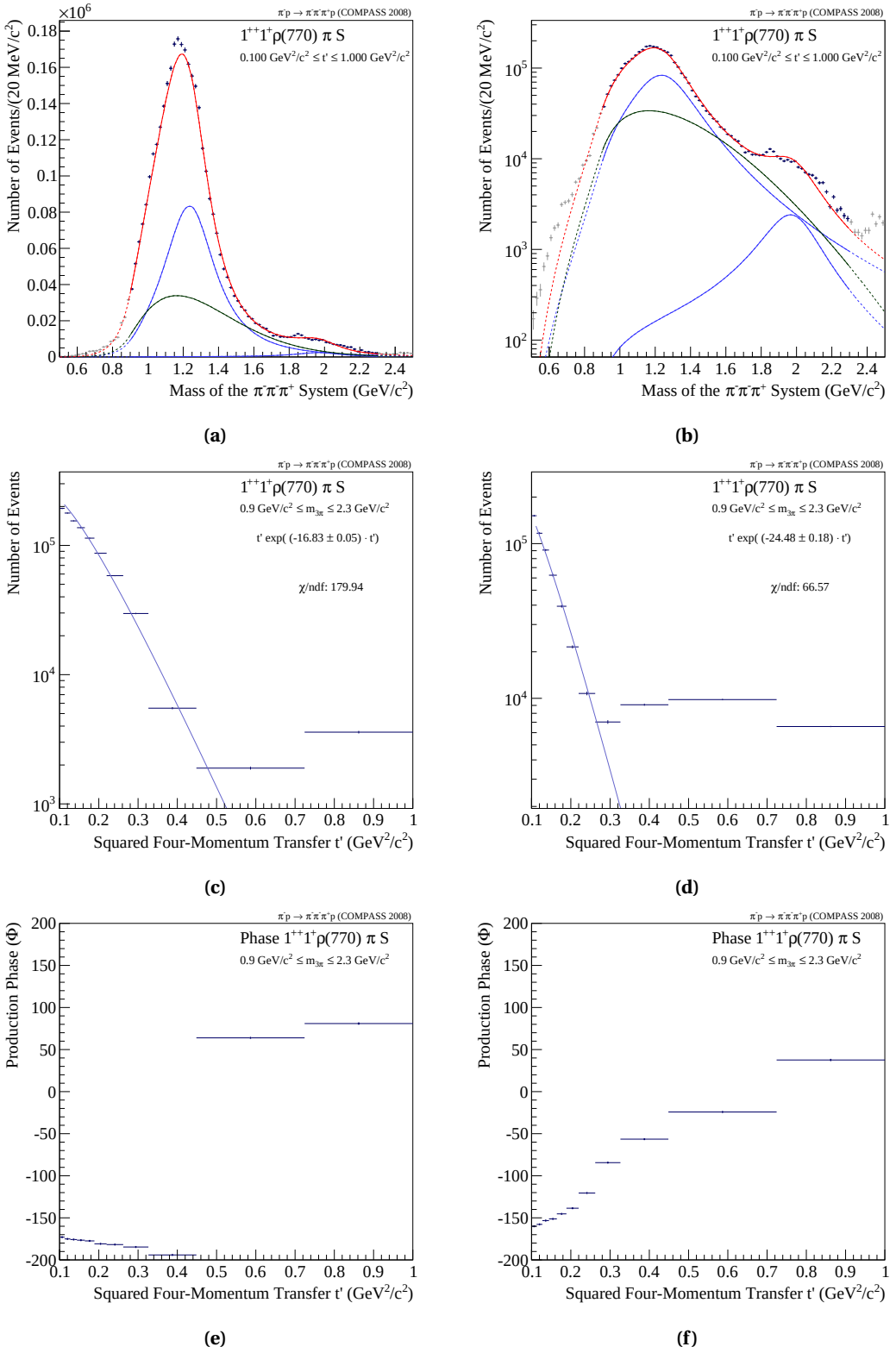

Figure 8.4 Fit result for the $1^{++}1^+\rho\pi S$ partial wave based on the model listed in Tab. 8.2. The t'-integrated intensity is shown in (a) with the blue markers being the data points of the spin-parity analysis fit. The red curve shows the overall fit result, the blue curves the Breit-Wigner components and the green line the non-resonant contribution. The same plot in logarithmic scale where the second Breit-Wigner is visible (b). The t' dependence of the $a_1(1260)$ is plotted in (c) and that of non-resonant contribution in (d). The corresponding production phases are shown in (e) and (f).

In Fig. 8.3 the fit result for the $1^{++}1^{+}\rho\pi S$ partial wave is shown. The t'-integrated intensity is plotted in 8.3a with the blue markers being the data points of the spin-parity analysis fit. The red curve is showing the overall fit result, the blue curves the Breit-Wigner components of the $a_1(1260)$ and the $a_1(1930)$. The green curve finally shows the t'-dependent non-resonant contribution. The $a_1(1930)$ is hardly visible in the figure, hence the same plot is shown in Fig. 8.3b in logarithmic scale. The intensity of the $a_1(1930)$ is three orders of magnitude smaller than that of the $a_1(1260)$ and the question arises whether this second Breit-Wigner is really needed to describe the data. For this model the impact of the excited a_1 is rather negligible and does not influence the fit result significantly. Further studies with this resonance are shown in [Sch14]. For completeness the corresponding t' distribution and production phase is shown in App. F in Fig. F.1a and Fig. F.1b.
The combination of the t'-dependent non-resonant contribution and the particular parametrisation of the $a_1(1260)$ gives a good description of the intensity. This is true for the whole t' range (Fig. F.3). The non-resonant contribution, visible in Fig. 8.3a, has a much smaller intensity than predicted by Deck models e.g. [ACJ+74] and the projected Deck intensity used for this analysis (Fig. 7.14a). An explanation could be that on the one hand the models overshoot due to lack of knowledge for a realistic description of the Deck amplitude, on the other hand the t'-dependent non-resonant contribution implemented here is describing the data phenomenologically. For the future it is aimed to use the information obtained by this analysis and define a proper model for the description of the non-resonant contribution.
The t' dependence of the $a_1(1260)$ (Fig. 8.3c) can be fitted best with a single exponential while the non-resonant contribution (Fig. 8.3d) needs two exponentials to follow the data. The t' dependence of the resonance contribution differs from the one obtained for the same partial wave in the spin-parity analysis (Fig. 7.23b), which can only be explained by two exponentials. No conclusion can be drawn yet due to the fact that the systematic analysis of the t' dependence on the level of partial waves is done here for the first time and hence no valid model descriptions are available.
The production phase of the $a_1(1260)$ (Fig. 8.3e) is zero by definition. More interesting is the production phase of the non-resonant contribution with respect to the $a_1(1260)$. With increasing t' the phase is rising and reaching finally 180°. This observation is important for a future description of a Deck-like background as it shows the relative phase relation between the $a_1(1260)$ and additional mechanisms and explains the shift of the peak in that particular partial wave.
The shift of the peak position observed for the $1^{++}0^{+}\rho\pi S$ and $1^{++}1^{+}\rho\pi S$ partial waves as a function of t' was one motivation to take the t' dependence into account for this part of the analysis. The t' integrated intensity of the latter one is plotted in Fig. 8.4a and shows a nice description of the data. The fit result is even more impressive when looking at particular t' regions (Fig. F.4) which shows a very good agreement to the data and gives a satisfactory explanation for the shift of the peak position as an interference of resonance and non-resonant contribution. Again the contribution of the $a_1(1930)$ is negligible small (Fig. 8.4b). While the intensity and the moving peak is explained well, the t' distribution of the $a_1(1260)$ in this wave is puzzling. Even after the separation of non-resonant contribution and resonant contribution the t' dependence of the $a_1(1260)$ shows a diffractive pattern (Fig. 8.4c). The corresponding production phase is almost constant except for the last two t' bins, where a shift of the phase of about 50° can be observed in the same t' region where the diffraction pattern appears.

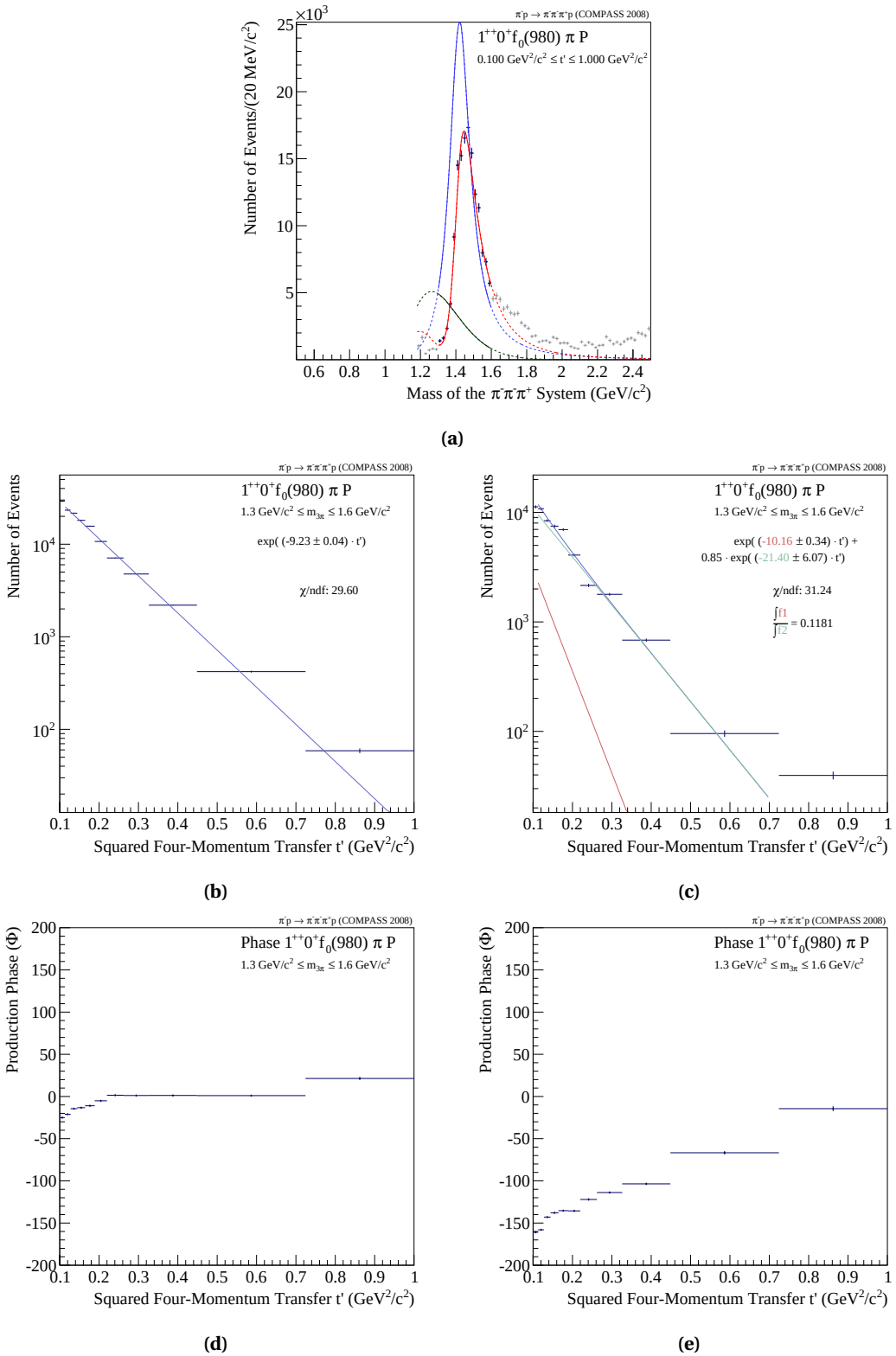

Figure 8.5 Fit result for the $1^{++}0^+ f_0(980)\pi P$ partial wave based on the model listed in Tab. 8.2. The t'-integrated intensity is shown in (a) with the blue markers being the data points of the spin-parity analysis. The red curve shows the overall fit result, the blue curves the Breit-Wigner components and the green line the non-resonant contribution. The t' dependence of the $a_1(1420)$ is plotted in (b) and that of the non-resonant contribution in (c). The corresponding production phases are shown in (d) and (e).

The new structure observed in the partial wave $1^{++}0^+ f_0(980)\pi P$ can be fitted by a Breit-Wigner amplitude and a non-resonant term. The result is plotted in Fig. 8.5a and shows a good agreement with the data. The t' dependence of the resonant component is depicted in Fig. 8.5b. It exhibits a roughly exponential behavior with a slope comparable to other resonances. On the other hand this behavior of the t' dependence can be observed for almost all resonances that decay into the $f_0(980)$ isobar. Astonishing is the production phase (Fig. 8.5d) which is almost flat. This behavior is expected for a resonance but an alternative explanation exists for this case. As discussed in Sec. 7.5.5 the observed resonance-like structure could be the result of coupled-channel effects [BB77] in the decay of the $a_1(1260)$.
The facts that this structure can be fitted in various models [Sch14], shows a stable intensity in all systematic studies (Sec. 7.6), an exhibits a large relative phase motion with respect to other partial waves, as seen in the spin-density matrix (Fig. 8.2), supports the resonance interpretation corresponding to a $\mathbf{a_1(1420)}$ state.

An overview of the fit result, including resonance parameter and t' dependencies is listed in Tab. 8.3.

Resonance	**Parameters (MeV/c^2)**	**t′ Slopes (GeV^{-2}/c^{-2})**	**Intensity Ratio**
$\pi(1800)$	$m = 1805,\quad \Gamma = 207$	9.74 ± 0.01	-
$a_1(1260)$	$m = 1267,\quad \Gamma = 357$	10.54 ± 0.02 ($1^{++}0^+\rho\pi S$) $^{\dagger}16.83 \pm 0.05$ ($1^{++}1^+\rho\pi S$)	- -
$a_1(1930)$	$m = 1970,\quad \Gamma = 320$	$^{\dagger}11.54 \pm 0.13$ ($1^{++}0^+\rho\pi S$) $18.81 \pm 0.34,\ 3.06 \pm 0.16$ ($1^{++}1^+\rho\pi S$)	- 1.76
$a_1(1420)$	$m = 1416,\quad \Gamma = 145$	9.23 ± 0.04	-
$a_2(1320)$	$m = 1313,\quad \Gamma = 107$	$10.13 \pm 0.16,\ 5.85 \pm 0.10$	1.00
$a_2(1950)$	$m = 1767,\quad \Gamma = 325$	$^{\dagger}10.78 \pm 0.10$	-
$\pi_2(1670)$	$m = 1643,\quad \Gamma = 281$	9.52 ± 0.04	-
$\pi_2(1880)$	$m = 1946,\quad \Gamma = 271$	6.11 ± 0.05	-
$a_4(2040)$	$m = 1946,\quad \Gamma = 375$	$11.10 \pm 0.14,\ 4.80 \pm 0.26$	4.42

Table 8.3 Resonance parameters obtained by a coupled fit in 11 t' bins based on the model shown in Tab. 8.2.
† *limited fit range for the t′ dependence.*

8.2.2 The Spin-Exotic $\pi_1(1600)$

The aim of this study is to investigate the mass dependence of the $1^{-+}1^{+}\rho\pi P$ spin-exotic partial wave included in the model used for the spin-parity analysis. Following the same motivation than in the previous model six other waves representing the dominant parts of the available 3π spectrum are included in the mass-dependent fit. Thus several waves discussed in Sec. 8.2.1 used here as well. This is true for the $0^{-+}0^{+}f_0(980)\pi S$, $1^{++}0^{+}\rho\pi S$, $2^{++}1^{+}\rho\pi D$, $2^{-+}0^{+}f_2(1270)\pi S$ and the $4^{++}1^{+}\rho\pi G$ waves. In addition the $2^{-+}0^{+}f_2(1270)\pi D$ partial wave, being modeled exactly like the $2^{-+}0^{+}f_2(1270)\pi S$ wave, is part of the model and of course the wave of interest, the $1^{-+}1^{+}\rho\pi P$ wave described by a Breit-Wigner and a t'-dependent non-resonant term. The complete model, including the mass ranges for the fit, is listed in Tab. 8.4.

Partial Wave	**Fit Range (GeV/c^2)**	**Model**
$0^{-+}0^{+}f_0(980)\pi S$,	[1.2, 2.3]	Breit-Wigner for $\pi(1800)$, Eq. (8.3) non-resonant contribution, Eq. (8.6)
$1^{++}0^{+}\rho(770)\pi S$,	[0.9, 2.3]	Breit-Wigner for $a_1(1260)$, Eq. (8.5) Breit-Wigner for $a_1(1930)$, Eq. (8.3) t' dep. non-resonant contribution, Eq. (8.7)
$1^{-+}1^{+}\rho(770)\pi P$,	[0.9, 2.3]	Breit-Wigner for $\pi_1(1600)$, Eq. (8.3) t' dep. non-resonant contribution, Eq. (8.7)
$2^{++}1^{+}\rho(770)\pi D$,	[0.9, 2.0]	Breit-Wigner for $a_2(1320)$, Eq. (8.4) Breit-Wigner for $a_2(1950)$, Eq. (8.3) t' dep. non-resonant contribution, Eq. (8.7)
$2^{-+}0^{+}f_2(1270)\pi S$,	[1.4, 2.3]	Breit-Wigner for $\pi_2(1670)$, Eq. (8.3) Breit-Wigner for $\pi_2(1880)$, Eq. (8.3) t' dep. non-resonant contribution, Eq. (8.7)
$2^{-+}0^{+}f_2(1270)\pi D$,	[1.5, 2.3]	Breit-Wigner for $\pi_2(1670)$, Eq. (8.3) Breit-Wigner for $\pi_2(1880)$, Eq. (8.3) t' dep. non-resonant contribution, Eq. (8.7)
$4^{++}1^{+}\rho(770)\pi G$,	[1.25, 2.3]	Breit-Wigner for $a_4(2040)$, Eq. (8.3) non-resonant contribution, Eq. (8.6)

Table 8.4 Model consisting of 7 partial waves and 9 resonances.

In order to show the quality of the fit the resulting spin-density matrix of the t' bin $0.144 \leq t' \leq 0.164$ GeV$^2/c^2$ is plotted in Fig. 8.6. The description of the data, especially the off-diagonal elements, is better than for the previous model. Most of the curves follow the data even outside of the fit range indicating a valid model description.
Before discussing the spin-exotic wave two other partial waves should be presented as these two are being part of almost all models discussed in this chapter but there is no dedicated section for their introduction.
The $2^{++}1^{+}\rho\pi D$ wave is the dominant partial wave associated to the $a_2(1320)$ resonance. The

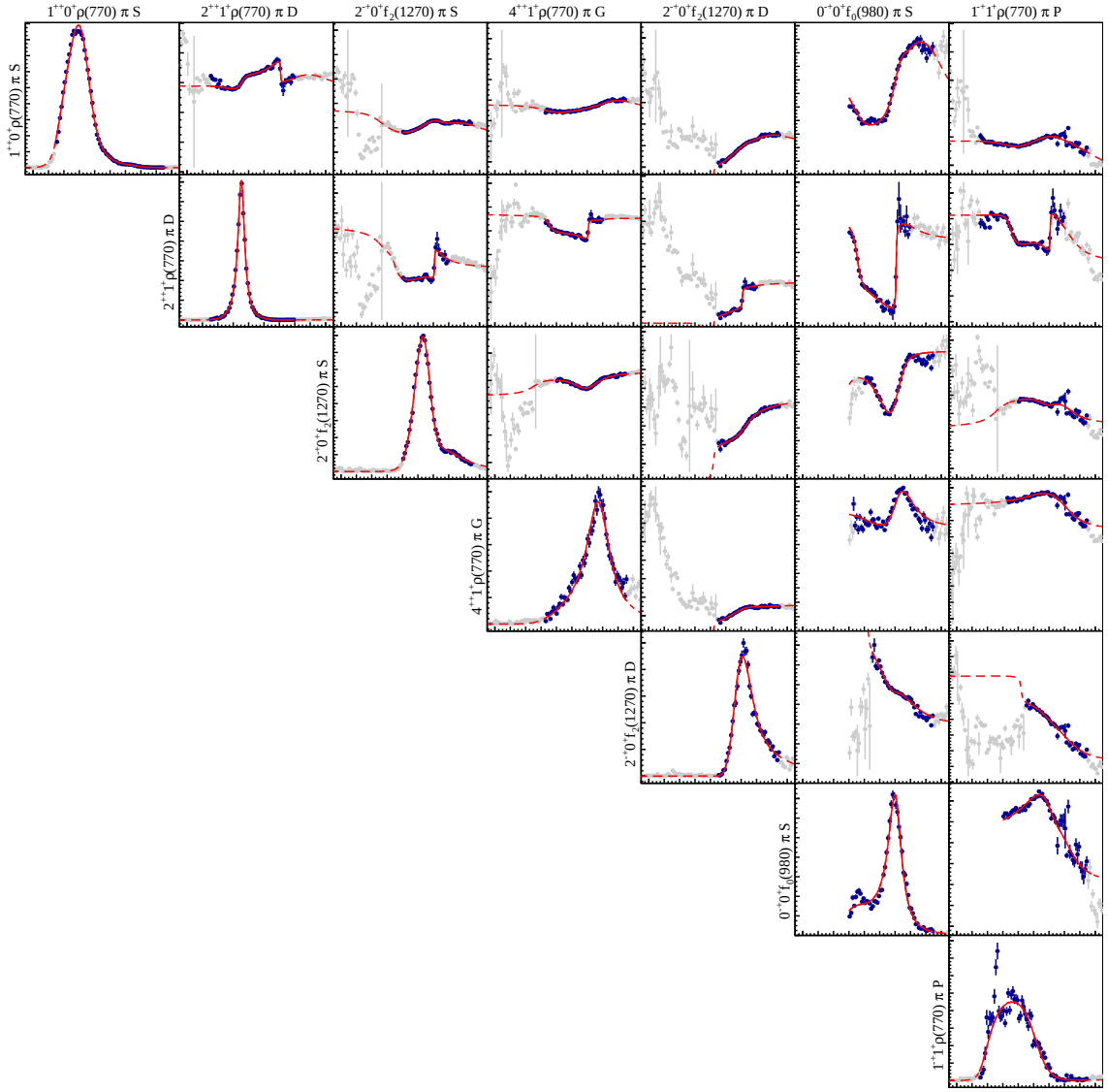

Figure 8.6 Spin-density matrix $\rho(m_x, t')$ of the model listed in Tab. 8.4 in the t' bin of $0.144 \leq t' \leq 0.164$ GeV$^2/c^2$.

t'-integrated intensity is depicted in Fig. 9.2a. As expected the non-resonant contribution is rather small and its distribution can be better seen in the logarithmic presentation (Fig. 9.2b). This figure shows also the necessity for a second resonance, the $a_2(1950)$, in order to describe the shoulder and dip at the falling edge around 1.8 GeV/c^2. This becomes even more clearer if one looks at intensity plots of certain t' regions, depicted in Fig. F.5. For the fit of the t' dependence two exponential must be taken into account for both, the resonance contribution (Fig. 8.7c) and the non-resonant contribution term (Fig. 8.7d). The corresponding production phases are rather constant expected for a resonance (Fig, 8.7e) but also the non-resonant contribution shows almost no phase variation (Fig. 8.7f). Phases and t' dependencies of the $a_2(1950)$ are plotted in Fig. F.6.

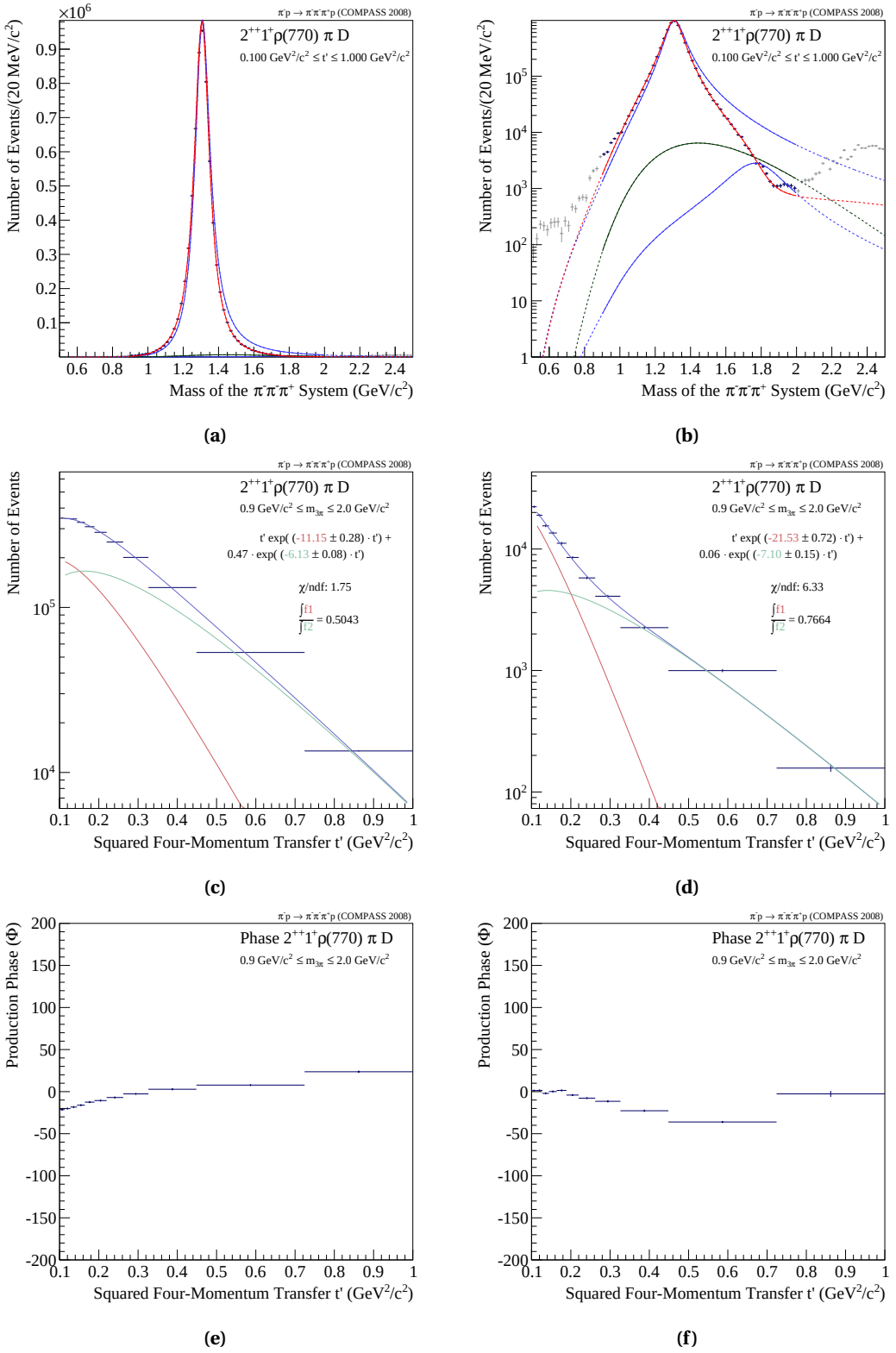

Figure 8.7 Fit result for the $2^{++}1^{+}\rho\pi D$ partial wave based on the model listed in Tab. 8.4. The t'-integrated intensity is shown in (a) with the blue markers being the data points of the spin-parity analysis fit. The red curve is showing the overall fit result, the blue curves the Breit-Wigner components and the green line shows the non-resonant contribution. The same plot in logarithmic scale where the second Breit-Wigner is visible (b). The t' dependence of the $a_2(1320)$ is plotted in (c) and that of non-resonant contribution in (d). The corresponding production phases are shown in (e) and (f).

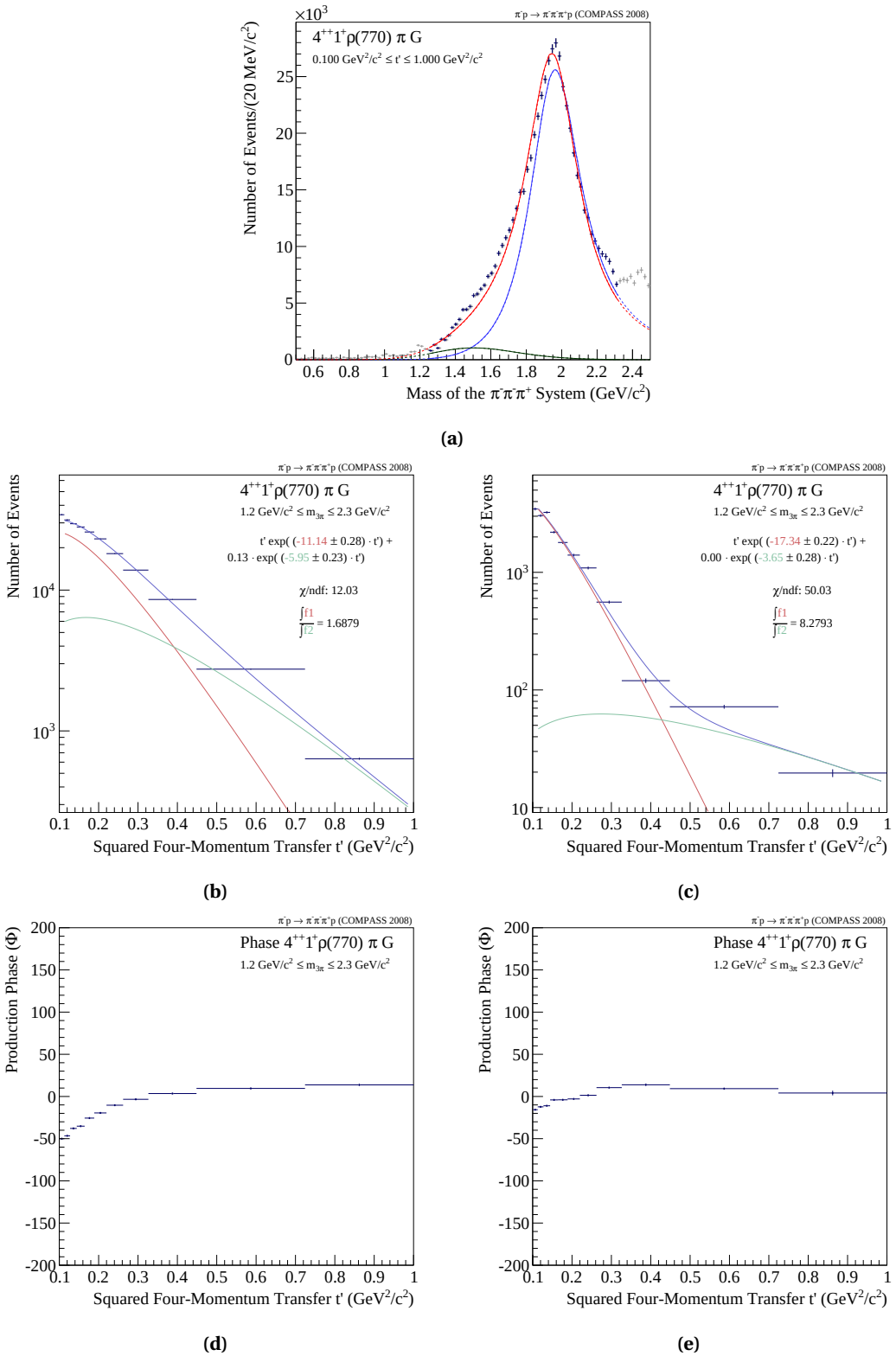

Figure 8.8 Fit result for the $4^{++}1^{+}\rho\pi G$ partial wave based on the model listed in Tab. 8.4. The t'-integrated intensity is shown in (a) with the blue markers being the data points of the spin-parity analysis. The red curve shows the overall fit result, the blue curves the Breit-Wigner components and the green line the non-resonant contribution. The t' dependence of the $a_4(2040)$ is plotted in (b) and that of the non-resonant contribution in (c). The corresponding production phases are shown in (d) and (e).

A similar behavior in terms of non-resonant contribution, t' dependencies and production phases as seen for the $2^{++}1^{+}\rho\pi D$ wave is observed in the $4^{++}1^{+}\rho\pi G$ wave with the $a_4(2040)$ resonance.

The fit result for the spin-exotic $1^{-+}1^{+}\rho\pi P$ wave is depicted in Fig. 8.10. The description of the t'-integrated intensity (Fig. 8.10a) is quite poor for the rising edge. The two peak structures at 1.1 and 1.3 GeV/c^2 are most probably not of resonant origin. They seem to be model artifacts most visible in this wave, but, as mentioned before, it seems that most of the $\rho\pi P$ waves show these instabilities. Even former analyses faced this problem [D+81]. Also for this case more information can be gained by looking at certain kinematic regions of t'. The corresponding plots can be found in Fig. 8.9.

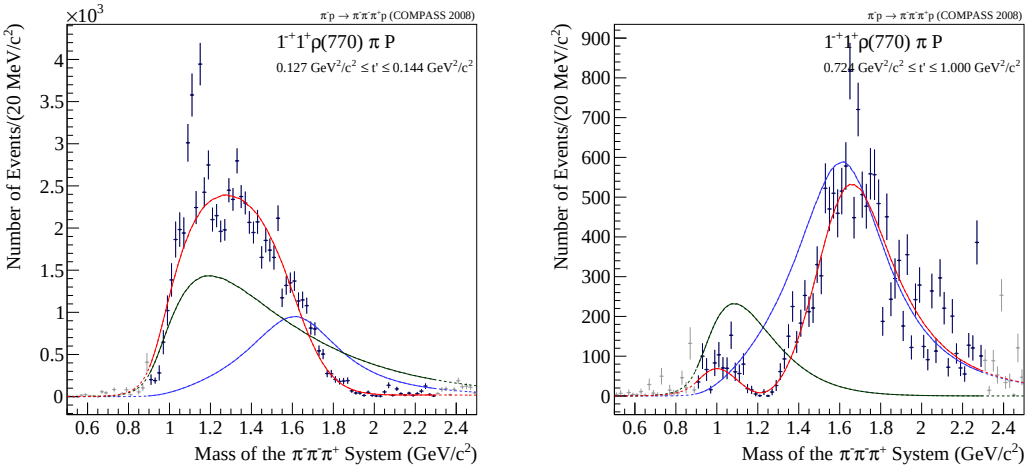

(a) **(b)**

Figure 8.9 Fit result for the $1^{-+}1^{+}\rho\pi P$ partial wave based on the model listed in Tab. 8.4 for selected t' bins.

The plot shows that the Deck-like non-resonant contribution is dominant at low t' while it almost vanishes for high t'. The fitted mass of the $\pi_1(1600)$ of $m = 1.597$ MeV/c^2 is lower than published results of former analyses. The width of $\Gamma = 579$ MeV/c^2 is on the other hand significantly broader than in previous publications. However, the parameters are in good agreement with another recent COMPASS analysis investigating the $\eta\pi$ and $\eta'\pi$ final state [Sch12]. The t' dependence (Fig. 8.10c) cannot be fitted completely. At low t' the fit overshoots the data but the obtained slope parameter shows a reasonable value. Quite astonishing is the stable phase motion with an offset of 50° (Fig. 8.10d). Both, the t' dependence and the phase motions indicate a resonance in this channel. The behavior of the non-resonant t' dependence (Fig. 8.10c) correlates again with the corresponding phase motion (Fig. 8.10e) observed in the last two t' bins.
An overview of the complete fit result can be found in Tab. 8.5.

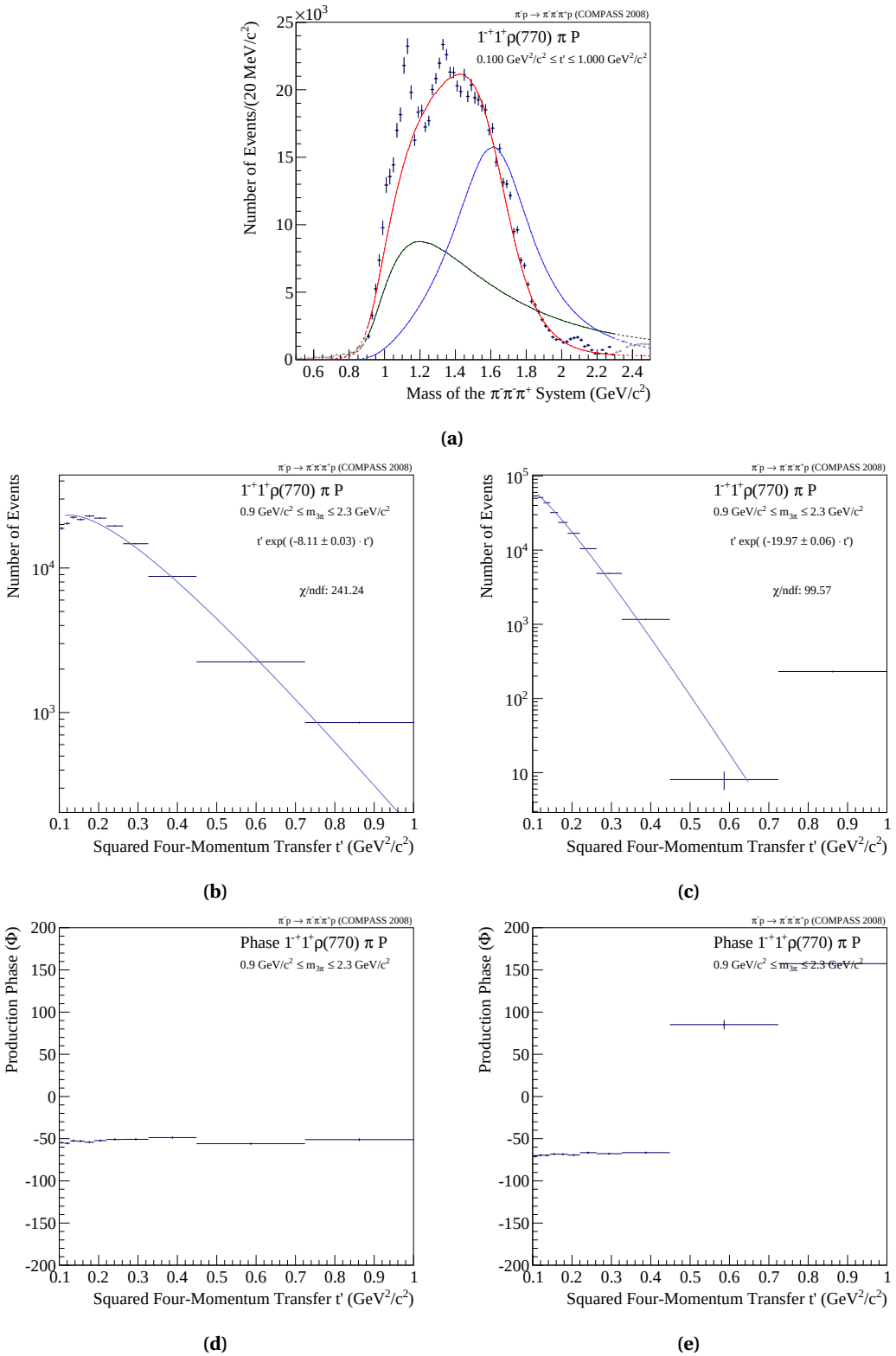

Figure 8.10 Fit result for the partial wave $1^{-+}1^{+}\rho\pi P$ based on the model listed in Tab. 8.4. The t' integrated intensity is shown in (a) with the blue markers being the data points of the spin-parity analysis. The red curve is showing the overall fit result, the blue curves the implemented Breit-Wigner components and the green line shows the non-resonant contribution. The t' dependence of the $\pi_1(1600)$ is plotted in (b) and the t' dependence of the non-resonant contribution in (c). The corresponding production phases are shown in (d) and (e).

Resonance	**Parameters (MeV/c^2)**	**t′ Slopes (GeV^{-2}/c^{-2})**	**Intensity Ratio**
$\pi(1800)$	$m = 1804,\quad \Gamma = 213$	9.17 ± 0.02	-
$a_1(1260)$	$m = 1290,\quad \Gamma = 379$	$28.35 \pm 1.89,\ 9.88 \pm 0.06$	0.16
$a_1(1930)$	$m = 1948,\quad \Gamma = 154$	$^{\dagger}6.38 \pm 0.18$	-
$\pi_1(1600)$	$m = 1597,\quad \Gamma = 579$	8.11 ± 0.03	-
$a_2(1320)$	$m = 1315,\quad \Gamma = 108$	$11.15 \pm 0.28,\ 6.13 \pm 0.08$	0.50
$a_2(1950)$	$m = 1763,\quad \Gamma = 322$	$^{\dagger}11.88 \pm 0.19$	-
$\pi_2(1670)$	$m = 1667,\quad \Gamma = 385$	7.93 ± 0.07 $(2^{-+}0^+ f_2(1270)\pi S)$ 8.62 ± 0.11 $(2^{-+}0^+ f_2(1270)\pi D)$	- -
$\pi_2(1880)$	$m = 1783,\quad \Gamma = 410$	7.42 ± 0.11 $(2^{-+}0^+ f_2(1270)\pi S)$ 8.78 ± 0.08 $(2^{-+}0^+ f_2(1270)\pi D)$	- -
$a_4(2040)$	$m = 1940,\quad \Gamma = 366$	$11.14 \pm 0.28,\ 5.95 \pm 0.23$	1.69

Table 8.5 Resonance parameters obtained by a coupled fit in 11 t' bins based on the model shown in Tab. 8.4.
† *limited fit range for the t′ dependence.*

8.2.3 The 0^{-+} Sector and the Nature of the $\pi(1800)$

As was discussed in Sec. 1.4.1 a study of the three-pion spectrum should also investigate the 0^{-+} sector, where radial excitations of the pion can be identified. The two known resonances, the $\pi(1300)$ and the $\pi(1800)$, the latter being a hybrid candidate, are in the focus. For the mass-dependent analysis all 0^{-+} partial waves that were included in the the spin-parity analysis are taken into account. In addition two standard resonances are implemented to stabilise the fit. The $0^{-+}0^{+}f_0(980)\pi S$, $2^{++}1^{+}\rho(770)\pi D$ and $2^{-+}0^{+}f_2(1270)\pi S$ waves were already introduced in the previous section and are modeled with the same parametrisations. The $0^{-+}0^{+}(\pi\pi)_S\pi S$ and $0^{-+}0^{+}\rho(770)\pi P$ waves are described by the two resonances, $\pi(1300)$ and the $\pi(1800)$, and an additional t'-dependent non-resonant contribution. The $0^{-+}0^{+}f_0(1500)\pi S$ wave is incorporated with one Breit-Wigner for the $\pi(1800)$ and a simple non-resonant contribution. Finally the $0^{-+}0^{+}f_2(1270)\pi D$ wave is described by a Breit-Wigner for the $\pi(1800)$ and a t'-dependent non-resonant contribution. The complete model is listed in Tab. 8.6.

Partial Wave	**Fit Range (GeV/c^2)**	**Model**
$0^{-+}0^{+}(\pi\pi)_S\pi S$,	[0.9, 2.3]	Breit-Wigner for $\pi(1300)$, Eq. (8.3) Breit-Wigner for $\pi(1800)$, Eq. (8.3) t' dep. non-resonant contribution, Eq. (8.7)
$0^{-+}0^{+}f_0(980)\pi S$,	[1.2, 2.3]	Breit-Wigner for $\pi(1800)$, Eq. (8.3) non-resonant contribution, Eq. (8.6)
$0^{-+}0^{+}\rho(770)\pi P$,	[0.9, 2.3]	Breit-Wigner for $\pi(1300)$, Eq. (8.3) Breit-Wigner for $\pi(1800)$, Eq. (8.3) t' dep. non-resonant contribution, Eq. (8.7)
$0^{-+}0^{+}f_2(1270)\pi D$,	[0.9, 2.3]	Breit-Wigner for $\pi(1800)$, Eq. (8.3) t' dep. non-resonant contribution, Eq. (8.7)
$0^{-+}0^{+}f_0(1500)\pi S$,	[1.7, 2.3]	Breit-Wigner for $\pi(1800)$, Eq. (8.3) non-resonant contribution, Eq. (8.6)
$2^{++}1^{+}\rho(770)\pi D$,	[0.9, 2.0]	Breit-Wigner for $a_2(1320)$, Eq. (8.4) Breit-Wigner for $a_2(1950)$, Eq. (8.3) t' dep. non-resonant contribution, Eq. (8.7)
$2^{-+}0^{+}f_2(1270)\pi S$,	[1.4, 2.3]	Breit-Wigner for $\pi_2(1670)$, Eq. (8.3) Breit-Wigner for $\pi_2(1880)$, Eq. (8.3) t' dep. non-resonant contribution, Eq. (8.7)

Table 8.6 Model consisting of 7 partial waves and 6 resonances.

As for the previous studies the resulting spin-density matrix of the t' bin $0.144 \leq t' \leq 0.164$ GeV$^2/c^2$ is plotted in Fig. 8.11. One can see that the model cannot describe well the intensity of the $0^{-+}0^{+}f_2(1270)\pi D$ wave. In addition, the relative phases of this wave with respect to the other waves show deviations between the model and the data in the mass region below 1.4 GeV/c^2 irrespective of whether this mass range was included in the fit range or not. A further discussion of the fit of this wave follows later in this section. The modelled intensity of the

$0^{-+}0^{+}f_0(1500)\pi S$ wave agrees well with the data, however, for the corresponding phases the model is not able to describe the high-mass part even inside the fit ranges. In all interference plots of the $0^{-+}0^{+}f_0(1500)\pi S$ wave with respect to the other waves a rising phase is observed above 2 GeV/c^2 which would indicate a second resonance in this wave. It was tried to implement a second Breit-Wigner amplitude but the fit was not successful. As the available fit range of this wave is quite narrow, due to the threshold applied to it, and its intensity is small the fit with two resonances becomes complicated and unstable.

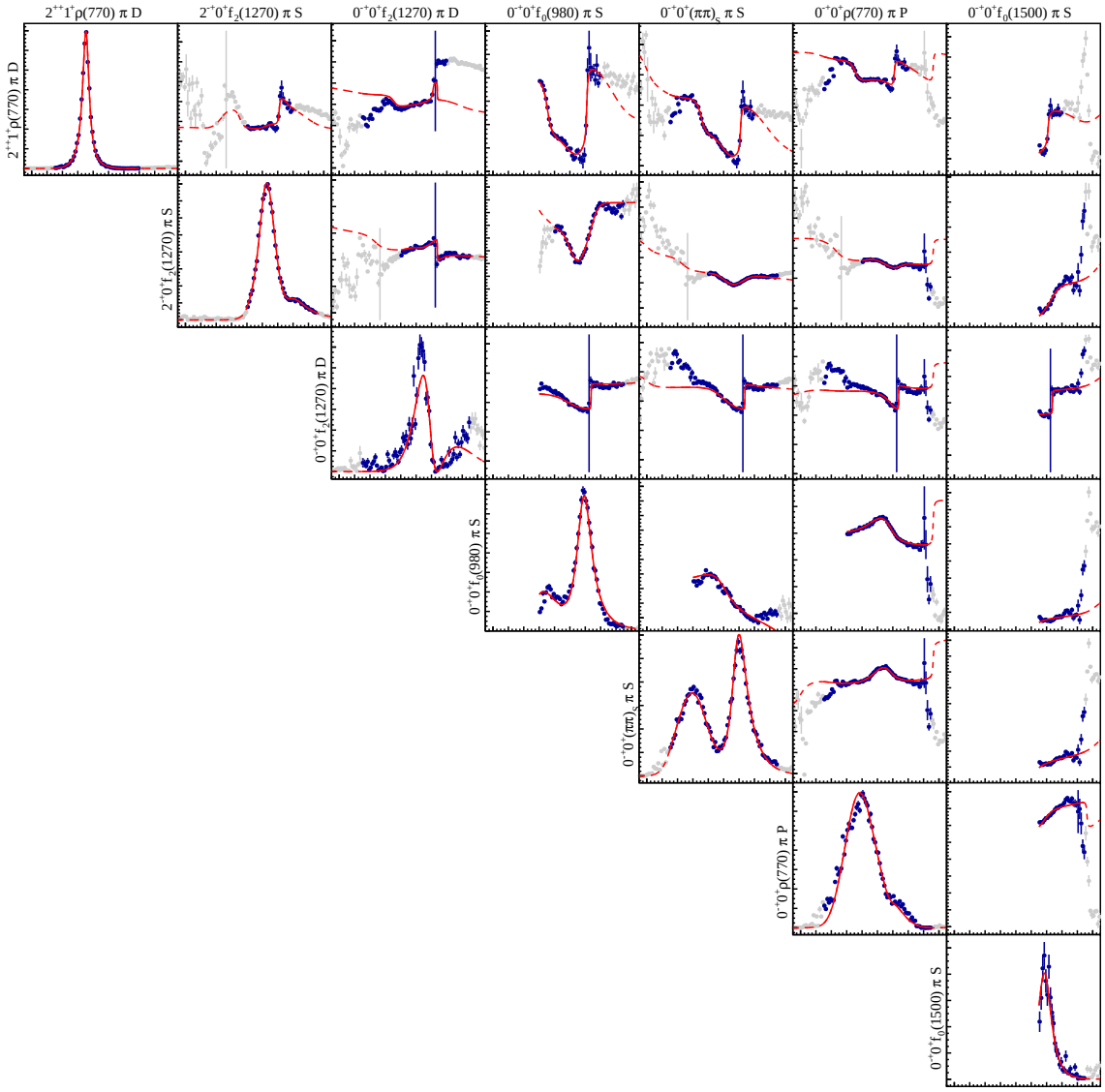

Figure 8.11 Spin-density matrix $\rho(m_x, t')$ of the model listed in Tab. 8.6 in the kinematic region of $0.144 \leq t' \leq 0.164$ GeV$^2/c^2$.

In the following the fit result of selected partial waves is discussed.

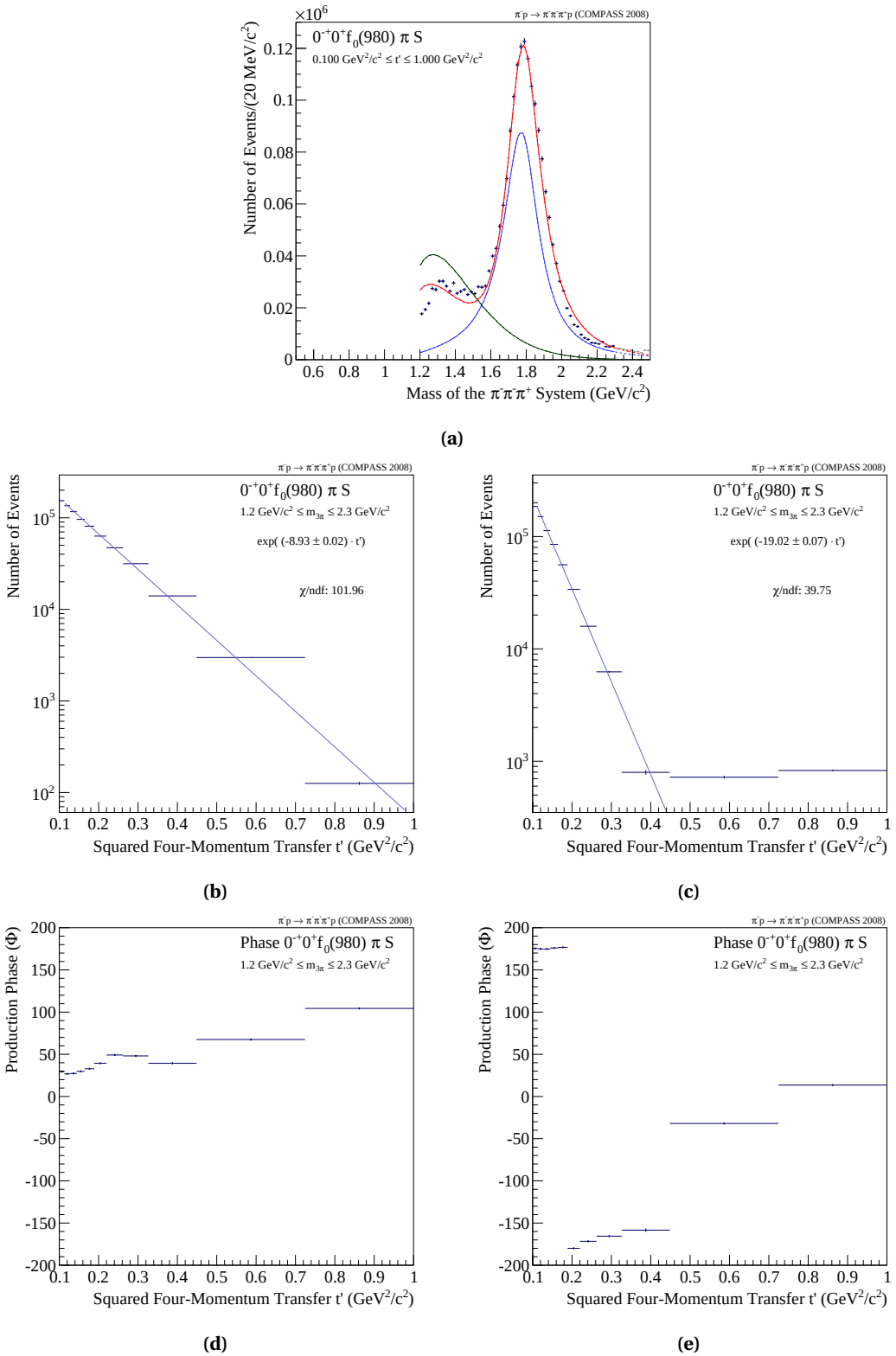

Figure 8.12 Fit result for the $0^{-+}0^{+}f_0(980)\pi S$ partial wave based on the model listed in Tab. 8.6. The t'-integrated intensity is shown in (a) with the blue markers being the data points of the spin-parity analysis. The red curve shows the overall fit result, the blue curves the Breit-Wigner components and the green line the non-resonant contribution. The t' dependence of the $\pi(1800)$ is plotted in (b) and that of the non-resonant contribution in (c). The corresponding production phases are shown in (d) and (e).

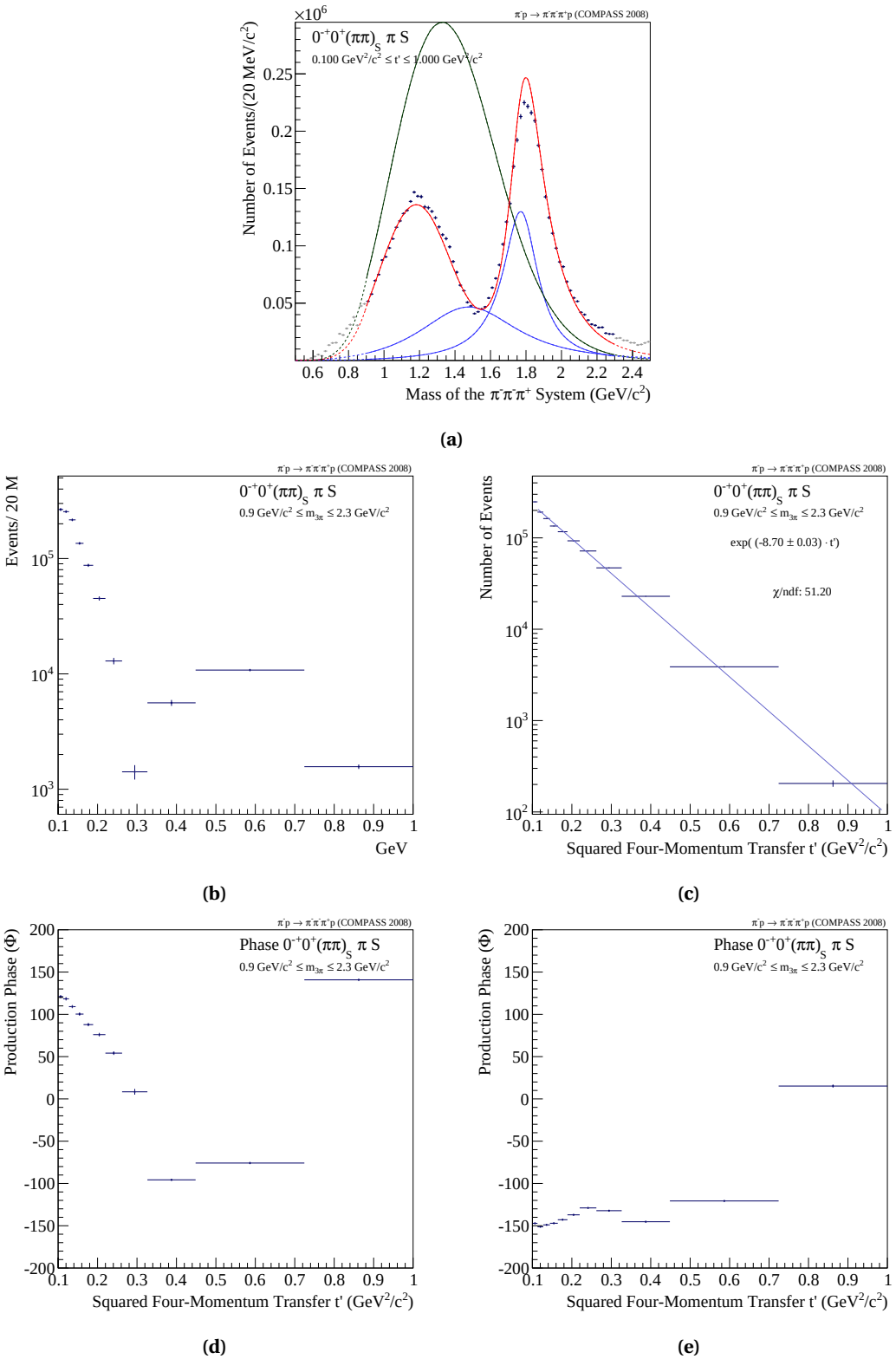

Figure 8.13 Fit result for the $0^{-+}0^{+}(\pi\pi)_S\pi S$ partial wave based on the model listed in Tab. 8.6. The t'-integrated intensity is shown in (a) with the blue markers being the data points of the spin-parity analysis. The red curve shows the overall fit result, the blue curves the Breit-Wigner components and the green line the non-resonant contribution. The t' dependence of the $\pi(1300)$ is plotted in (b) and that of the $\pi(1800)$ in (c). The corresponding production phases are shown in (d) and (e).

In Fig. 8.12 the fit result for the $0^{-+}0^{+}f_0(980)\pi S$ partial wave is plotted. The model can describe the data in the peak (see Fig. 8.12a) but shows minor deviations above 2 GeV/c^2 and in the low-mass shoulder around 1.3 GeV/c^2. This shoulder is explained in the model by a destructive interference of the falling edge of the t'-dependent non-resonant component and the rising Breit-Wigner amplitude. The t' dependence of the $\pi(1800)$ (see Fig. 8.12b) is fitted best with a single exponential with a value for the slope parameter expected for resonating components. The t' dependence of the non-resonant contribution reveals a diffractive pattern with a minimum in the next-to-last t' bin (see Fig. 8.12c). Thus only the low t' region can be fitted, also with a single exponential. The production phase of the $\pi(1800)$, depicted in Fig. 8.12d shows a complicated structure. The overall phase motion is about 70° with a phase motion of 30° in the low t' region, a constant phase in the medium range and again a phase motion of about 30° in the last two t' bins. The production phase of the non-resonant contribution is constant at low t' (see Fig. 8.12e) and shows an overall phase motion of 180° for the t' range between 0.2 and 1.0 GeV^2/c^2.

The dominant component in the model description of the intensity of the $0^{-+}0^{+}(\pi\pi)_S\pi S$ wave (see Fig. 8.13a) is the t'-dependent non-resonant contribution which peaks at 1.3 GeV/c^2. In order to describe the broad component at 1.2 GeV/c^2 in the data the Breit-Wigner amplitude of the $\pi(1300)$, peaking around 1.4 GeV/c^2, interferes destructively with the non-resonant contribution. The width the $\pi(1300)$ of 783 MeV/c^2 that is extracted from the data is rather large. The non-resonant term reaches over the complete fit range, so that the peak at 1.8 GeV/c^2 is described as the coherent sum of all three model components, the $\pi(1300)$, the $\pi(1800)$ and the non-resonant contribution. The t' dependence of the $\pi(1300)$ (see Fig. 8.13b) shows a diffractive pattern with a minimum around 0.3 GeV^2/c^2. Even the low-t' region cannot be fitted satisfactorily and thus the plot is shown without a fit to the data. The t' dependence of the $\pi(1800)$ (Fig. 8.13c) on the other hand can be fitted with a single exponential and a value for slope parameter which is expected for resonating components. The production phase of the $\pi(1300)$ (see Fig. 8.13d) starts with an offset of 120° shows a falling phase motion of about 220° up to 0.4 GeV^2/c^2 and a rapidly increasing phase in the last two t' bins ending at 140°. In contrast to this the phase motion of the $\pi(1800)$ (Fig. 8.13e) can be regarded as almost constant in the low-t' region with a phase motion of about 30°. But again in the last two t' bins a phase motion of about 130° is observed. The corresponding plots for the t' dependence and the production phase of the non-resonant term can be seen in Fig. F.7.

In Fig. 8.14a the t'-integrated intensity of the $0^{-+}0^{+}\rho\pi P$ wave is depicted. The dominant component is again the non-resonant contribution, describing the broad bump at 1.3 GeV/c^2. But in contrast to the $0^{-+}0^{+}(\pi\pi)_S\pi S$ wave, the contribution of the $\pi(1300)$ is significant. The most striking finding is the fact that the bump at 1.8 GeV/c^2 cannot be described by the $\pi(1800)$ which is hardly visible in Fig. 8.14a. The same plot in logarithmic scale (see Fig. 8.14b) reveals the negligible intensity of the $\pi(1800)$ comparable with the strength of the $a_1(1930)$ observed in the $1^{++}0^{+}\rho\pi s$ wave (see Fig. 8.3b).

The $0^{-+}0^{+}f_2(1270)\pi D$ wave (Fig. 8.14c) cannot be described completely by the model, as mentioned earlier in this section. The sharp falling edge of the intensity with the dip at 1.8 GeV/c^2 and the corresponding phase motions motivated to describe this wave with the $\pi(1800)$. The overall fit follows the data only the full intensity of the rising edge at 1.7 GeV/c^2 cannot be ex-

plained sufficiently. As proposed by [CP97] an additional resonance at 1.7 GeV/c^2 was tried but the fit interpreted this component as a very broad component acting like a second non-resonant contribution. What could be tried in the future is to implement the $\pi(1300)$ as second resonance contribution, which maybe could also explain the phase motions, observed in the low-mass region. In addition an improved parametrisation of the non-resonant term could enhance the fit, but such a description is not yet available.

Finally the t'-integrated intensity of the $0^{-+}0^{+}f_0(1500)\pi S$ wave (see Fig. 8.14d) can be explained almost completely by the $\pi(1800)$. In the peak around 1.8 GeV/c^2 the line-shape of the overall fit result and the Breit-Wigner of the $\pi(1800)$ overlaps entirely only in the high-mass region is the contribution of the non-resonant contribution visible.

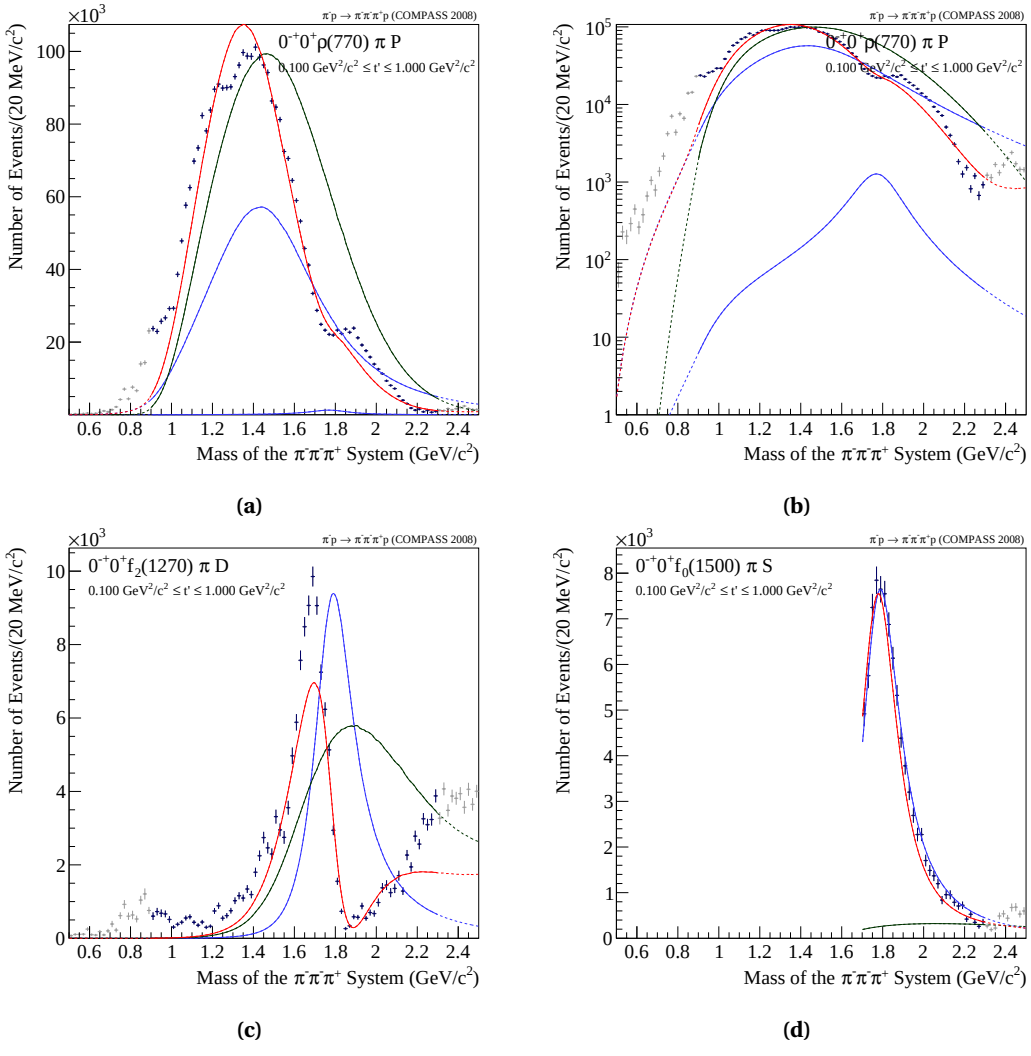

Figure 8.14 Additional fit results for $0^{-+}0^{+}$ partial waves based on the model listed in Tab. 8.6. The t'-integrated intensity of the $0^{-+}0^{+}\rho\pi P$ wave is shown in (a) with the blue markers being the data points of the spin-parity analysis. The red curve is showing the overall fit result, the blue curves the Breit-Wigner components and the green line shows the non-resonant contribution. The same plot in a logarithmic scale where the second Breit-Wigner is visible (b). The t'-integrated intensity of $0^{-+}0^{+}f_2(1270)\pi D$ wave is shown in (c) and that of the $0^{-+}0^{+}f_0(1500)\pi S$ wave in (d)

The observation of the $\pi(1800)$ in the $0^{-+}0^{+}f_0(980)\pi S$ and $0^{-+}0^{+}f_0(1500)\pi S$ waves and the additional suppression of the the $\pi(1800)$ in the $0^{-+}0^{+}\rho\pi P$ wave is a strong hint for the hybrid nature of this resonance, following [IP85, CP97]. On the other hand a possible hybrid $\pi(1800)$ should be suppressed in the $0^{-+}0^{+}f_2(1270)\pi D$ wave [CP97] which is not observed in this analysis, however, the description of this wave is incomplete. In summary the data seem to suggest a dominant hybrid nature of the $\pi(1800)$.

For the $\pi(1300)$ no statement can be made. In both waves, where this resonance was included, the broad structures in the data are explained by dominant non-resonant components. The $\pi(1300)$ is known to be a very broad state [B^{+}12] and maybe the fit has difficulties to distinguish between the non-resonant term and the $\pi(1300)$ here as well. A more realistic description of the non-resonant contribution could improve the fit.

An overview of the complete fit result can be found in Tab. 8.7.

Resonance	**Parameters (MeV/c^2)**	**t′ Slopes (GeV^{-2}/c^{-2})**	**Intensity Ratio**
$\pi(1300)$	$m = 1405,\quad \Gamma = 783$	* – $(0^{-+}0^{+}(\pi\pi)_S\pi S)$	-
		47.42 ± 0.71 $(0^{-+}0^{+}\rho\pi P)$	-
$\pi(1800)$	$m = 1770,\quad \Gamma = 240$	8.93 ± 0.02 $(0^{-+}0^{+}f_0(980))$	-
		16.14 ± 0.25, 4.78 ± 0.20 $(0^{-+}0^{+}f_2\pi D)$	3.63
		8.70 ± 0.03 $(0^{-+}0^{+}(\pi\pi)_S\pi S)$	-
		* – $(0^{-+}0^{+}\rho\pi P)$	-
		10.22 ± 0.10 $(0^{-+}0^{+}f_0(1500))$	-
$a_2(1320)$	$m = 1315,\quad \Gamma = 107$	9.94 ± 0.10, 3.76 ± 0.15	3.06
$a_2(1950)$	$m = 1840,\quad \Gamma = 470$	$^{\dagger}13.24 \pm 0.11$	-
$\pi_2(1670)$	$m = 1620,\quad \Gamma = 312$	7.71 ± 0.06	-
$\pi_2(1880)$	$m = 1899,\quad \Gamma = 397$	8.32 ± 0.08	-

Table 8.7 Resonance parameters obtained by a coupled fit in 11 t' bins based on the model shown in Tab. 8.6.
† *limited fit range for the t′ dependence.** *fit does not describe the data*

8.2.4 The 2^{-+} Sector and the Nature of the $\pi_2(1880)$

The last model discussed in this chapter concentrates on the 2^{-+} sector. The selection of partial waves is mainly motivated by a recent discussion about the possible hybrid nature of the $\pi_2(1880)$, based on the flux-tube and the $^3P_0$ model [LZ09]. In this paper the $2^{-+}0^+ f_2(1270)\pi S$, $2^{-+}0^+ f_2(1270)\pi D$, $2^{-+}0^+\rho(770)\pi F$ and $2^{-+}0^+ f_2(1270)\pi G$ waves are used as benchmark waves, in addition to other waves, not accessible in the $\pi^-\pi^-\pi^+$ final state, in order to test the hybrid hypothesis. Hence these waves are part of the model. In addition the $2^{-+}0^+\rho(770)\pi P$ wave is taken into account, being one of the dominant 2^{-+} waves as well as the $2^{-+}0^+ f_0(980)\pi D$ wave, which reveals an interesting interference structure in its intensity. All these waves are modeled using $\pi_2(1670)$ and $\pi_2(1880)$ resonances. The respective parametrisations of the non-resonant contributions are listed in Tab. 8.8. Finally the $2^{++}1^+\rho(770)\pi D$ wave is implemented, described as in the previous models, in order to stabilise the fit.

Partial Wave	**Fit Range (GeV/c^2)**	**Model**
$2^{++}1^+\rho(770)\pi D$,	[0.9, 2.12]	Breit-Wigner for $a_2(1320)$, Eq. (8.4) Breit-Wigner for $a_2(1950)$, Eq. (8.3) t' dep. non-resonant contribution, Eq. (8.7)
$2^{-+}0^+ f_2(1270)\pi S$,	[1.4, 2.3]	Breit-Wigner for $\pi_2(1670)$, Eq. (8.3) Breit-Wigner for $\pi_2(1880)$, Eq. (8.3) t' dep. non-resonant contribution, Eq. (8.7)
$2^{-+}0^+ f_2(1270)\pi D$,	[1.4, 2.3]	Breit-Wigner for $\pi_2(1670)$, Eq. (8.3) Breit-Wigner for $\pi_2(1880)$, Eq. (8.3) t' dep. non-resonant contribution, Eq. (8.7)
$2^{-+}0^+ f_0(980)\pi D$,	[1.2, 2.5]	Breit-Wigner for $\pi_2(1670)$, Eq. (8.3) Breit-Wigner for $\pi_2(1880)$, Eq. (8.3) non-resonant contribution, Eq. (8.6)
$2^{-+}0^+\rho(770)\pi P$,	[0.9, 2.3]	Breit-Wigner for $\pi_2(1670)$, Eq. (8.3) Breit-Wigner for $\pi_2(1880)$, Eq. (8.3) t' dep. non-resonant contribution, Eq. (8.7)
$2^{-+}0^+\rho(770)\pi F$,	[1.4, 2.3]	Breit-Wigner for $\pi_2(1670)$, Eq. (8.3) Breit-Wigner for $\pi_2(1880)$, Eq. (8.3) non-resonant contribution, Eq. (8.6)
$2^{-+}0^+ f_2(1270)\pi G$,	[1.3, 2.3]	Breit-Wigner for $\pi_2(1670)$, Eq. (8.3) Breit-Wigner for $\pi_2(1880)$, Eq. (8.3) non-resonant contribution, Eq. (8.6)

Table 8.8 Model consisting of 7 partial waves and 4 resonances.

The resulting spin-density matrix of the t' bin $0.144 \leq t' \leq 0.164$ GeV$^2/c^2$ is plotted in Fig. 8.15. The major discrepancies between model and data can be found in some intensity distributions. The largest deviations is seen for the $2^{-+}0^+ f_2(1270)\pi G$ wave, where the intensity cannot

be explained at all by the model (see also Fig. 8.19c). The fit is mainly driven by the corresponding phase motions, which are, however, well described. In addition the model cannot describe completely the $2^{-+}0^{+}\rho(770)\pi F$ in the peak region around 1.7 GeV/c^2. For the $2^{-+}0^{+}f_0(980)\pi D$ wave the model agrees around 1.8 GeV/c^2 with the data, however, the low-mass shoulder and the high-mass part cannot be described. This wave is of particular interest as its model description could give a strong hint for the $\pi_2(1880)$ being a single resonance, separate from the $\pi_2(1670)$.

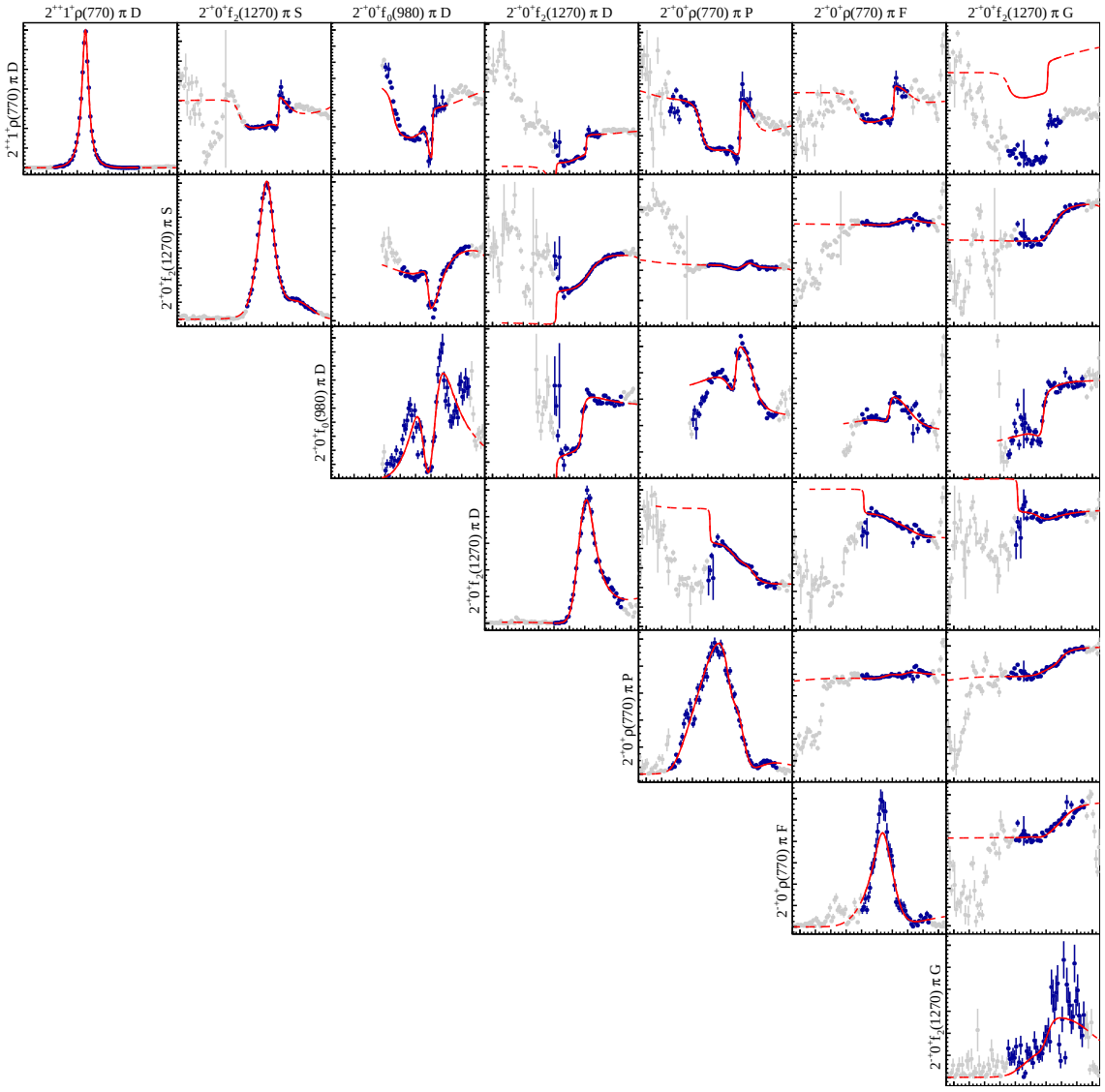

Figure 8.15 Spin-density matrix $\rho(m_x, t')$ of the model listed in Tab. 8.2 in the kinematic region of $0.144 \leq t' \leq 0.164$ GeV$^2/c^2$.

In the following the fit result of selected partial waves is discussed.

The t'-integrated intensity of the $2^{-+}0^{+}f_2(1270)\pi S$ partial wave is depicted in Fig. 8.16a. Striking is the observation of a large non-resonant term, peaking at 2 GeV/c^2 and the correspond-

ing almost negligible contribution of the $\pi_2(1880)$. This can be seen as an artifact of this model. This assumption is supported by the comparison of the obtained t' dependence of the $\pi_2(1880)$ (see Fig. 8.16c) and the one of the non-resonant term (see Fig. F.8a). The t' dependence of the $\pi_2(1880)$ is rather unstable, a behavior not observed for any other resonating structure investigated in this analysis, while t' dependence of the non-resonant component resembles more the distribution one would expect for a resonance in this partial wave. Also the production phase of the $\pi_2(1880)$ exhibits an unusual behavior. A phase motion of 180° cannot be explained by a resonance (see Fig. 8.16e). The phase motion of the non-resonant contribution (Fig. F.8b), however, is about 70° over the whole t' region, except the last t' bin. Otherwise the extracted mass and width of the $\pi_2(1880)$ have reasonable values, dominated by other waves (see Tab. 8.9), expected for the $\pi_2(1880)$. Thus it seems that the fit has difficulties to disentangle the $\pi_2(1880)$ and the non-resonant contributions in this partial wave. Systematic studies with this wave and both resonances, the $\pi_2(1670)$ and the $\pi_2(1880)$, were performed [Sch14] and revealed difficulties in getting a stable fit for this wave. The peak at 1.7 GeV/c^2 in the $2^{-+}0^+ f_2(1270)\pi S$ wave is mainly described by the $\pi_2(1670)$. Its t' dependence is plotted in Fig. 8.16b and the associated production phase in Fig. 8.16d which is constant over the whole t' region except the last t' bin.

A good agreement between model and data is found for the $2^{-+}0^+ f_2(1270)\pi D$ wave. The t'-integrated intensity is depicted in Fig. 8.17a. Both resonances, the $\pi_2(1670)$ and the $\pi_2(1880)$, are needed with equal strength in order to describe the intensity. The non-resonant contribution is rather small. Deviations between model and data emerge in a mass region above 2 GeV/c^2 which could be an indication for a missing resonance in the model. A third Breit-Wigner amplitude for the $\pi_2(2005)$ was tested for this wave and the $2^{-+}0^+ f_2(1270)\pi S$ wave but the fit result was not satisfactory. The resulting width of the $\pi_2(2005)$ had values around 1 GeV/c^2 and the intensity was almost negligible. The mass region above 2 GeV/c^2 is crowded with resonances and the development of a suited model for this mass range is not within the scope of this thesis. The t' dependence of the $\pi_2(1670)$ is depicted in Fig. 8.17b and the one for the $\pi_2(1880)$ in Fig. 8.17c. The respective slope parameters are in the expected range for resonances. Noticeable is the almost constant production phase for both resonances, shown in Fig. 8.17d and Fig. 8.17e. The t' dependence and corresponding production phase of the non-resonant term are depicted in Fig. F.9.

The most interesting wave in the model is the $2^{-+}0^+ f_0(980)\pi D$ wave, depicted in Fig. 8.18a. Its complicated structure is explained in the model by destructive interference between the $\pi_2(1670)$ and the $\pi_2(1880)$. While the interference region around 1.8 GeV/c^2 is described quite well by the model, deviations can be seen below 1.6 GeV/c^2 and above 1.9 GeV/c^2. Nevertheless the description of this wave supports the need of two separate resonances, $\pi_2(1670)$ and $\pi_2(1880)$. The t' dependencies of the $\pi_2(1670)$ (see Fig. 8.18b) and the $\pi_2(1880)$ (see Fig. 8.18c) are both fitted with a single exponential and slope parameters expected for resonant components. The production phases of both resonances (Figs. 8.18d and 8.18e) can be regarded as constant, again, except the highest t' bin. The t' dependence and corresponding production phase of the non-resonant term are depicted in Fig. F.10.

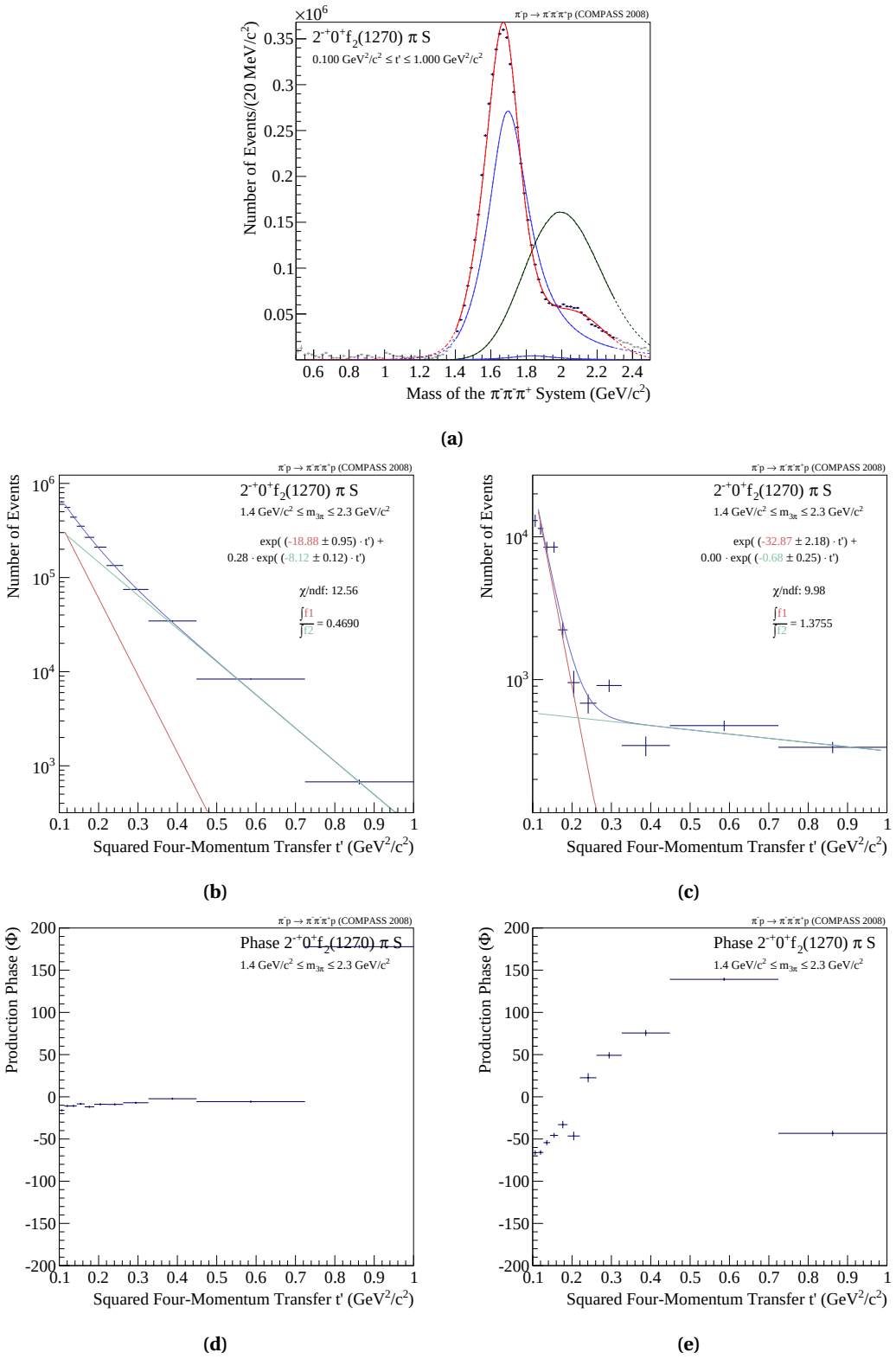

Figure 8.16 Fit result for the $2^{-+}0^{+}f_2(1270)\pi S$ partial wave based on the model listed in Tab. 8.8. The t'-integrated intensity is shown in (a) with the blue markers being the data points of the spin parity analysis. The red curve shows the overall fit result, the blue curves the Breit-Wigner components and the green line the non-resonant contribution. The t' dependence of the $\pi_2(1670)$ is plotted in (b) and that of the $\pi_2(1880)$ in (c). The corresponding production phases are shown in (d) and (e).

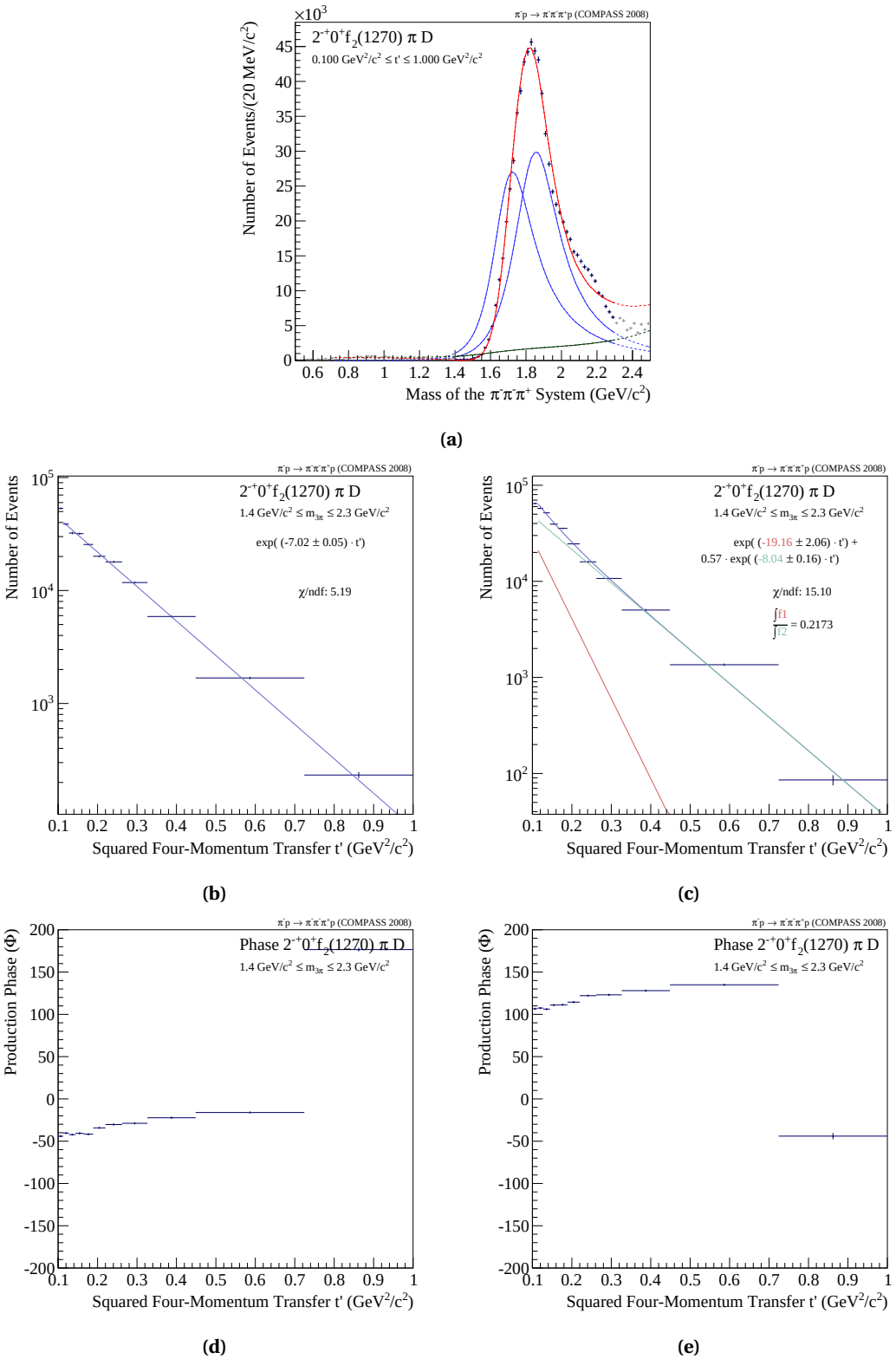

Figure 8.17 Fit result for the $2^{-+}0^+ f_2(1270)\pi D$ partial wave based on the model listed in Tab. 8.8. The t'-integrated intensity is shown in (a) with the blue markers being the data points of the spin parity analysis. The red curve shows the overall fit result, the blue curves the Breit-Wigner components and the green line the non-resonant contribution. The t' dependence of the $\pi_2(1670)$ is plotted in (b) and that of the $\pi_2(1880)$ in (c). The corresponding production phases are shown in (d) and (e).

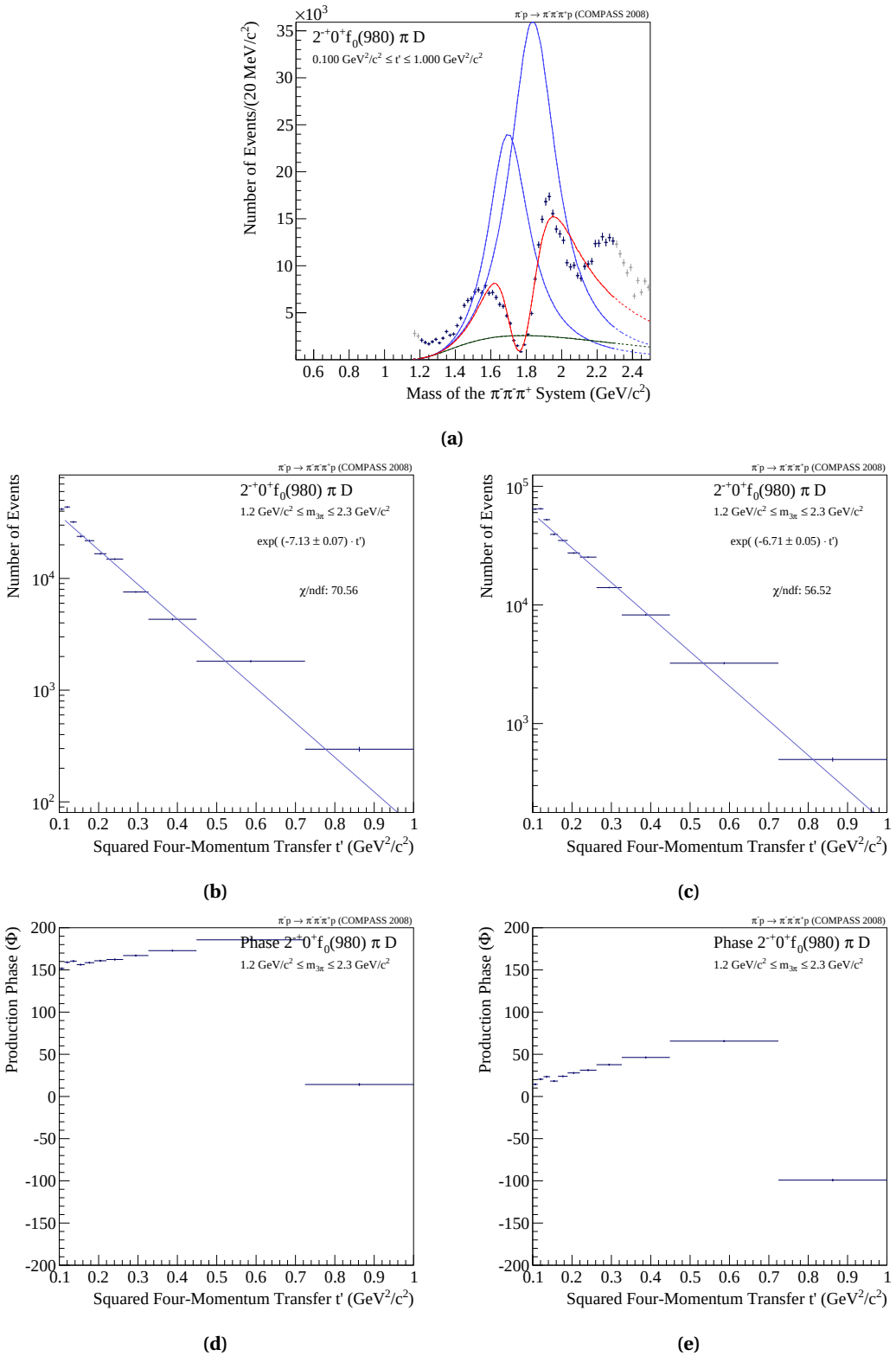

Figure 8.18 Fit result for the $2^{-+}0^+ f_0(980)\pi D$ partial wave based on the model listed in Tab. 8.8. The t'-integrated intensity is shown in (a) with the blue markers being the data points of the spin parity analysis. The red curve shows the overall fit result, the blue curves the Breit-Wigner components and the green line the non-resonant contribution. The t' dependence of the $\pi_2(1670)$ is plotted in (b) and that of the $\pi_2(1880)$ in (c). The corresponding production phases are shown in (d) and (e).

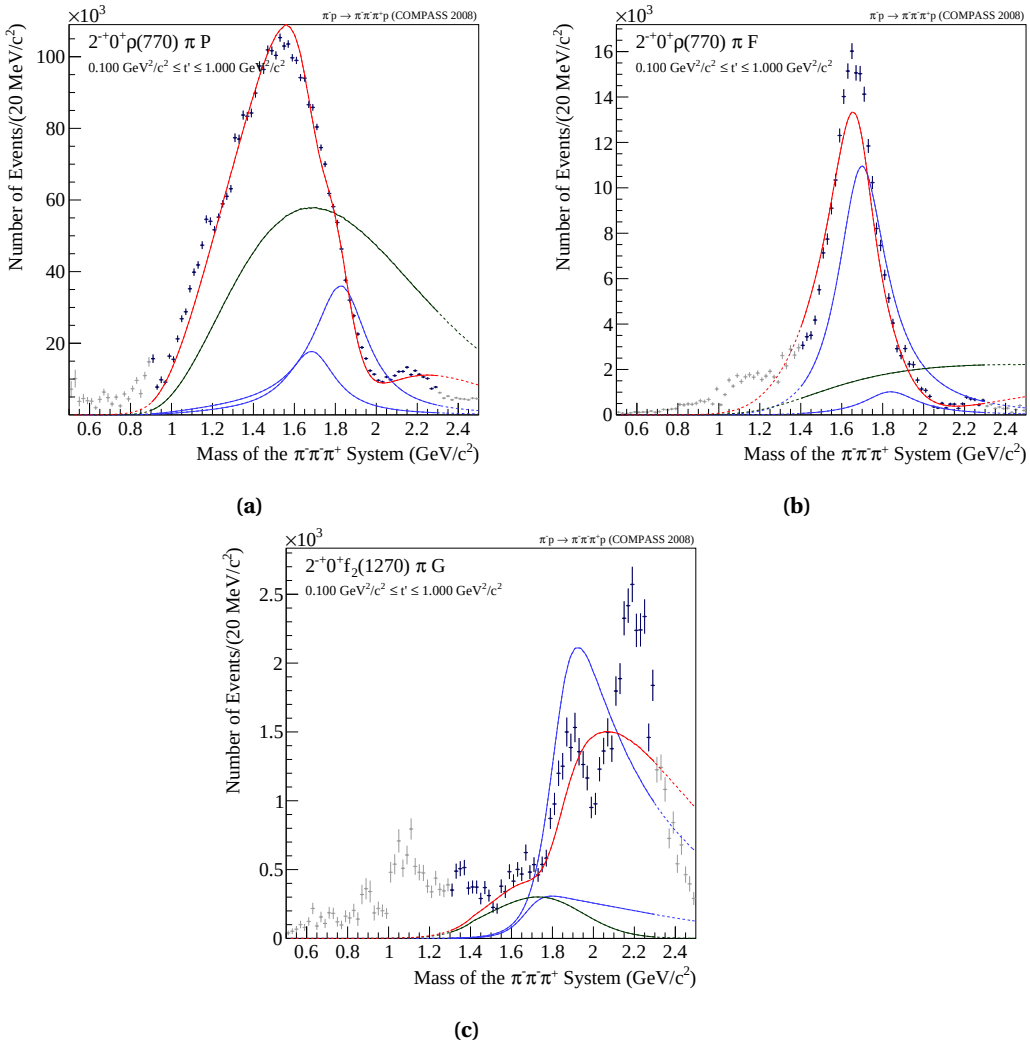

Figure 8.19 Additional fit results for $2^{-+}0^+$ partial waves based on the model listed in Tab. 8.8. The t'-integrated intensity of the $2^{-+}0^+\rho\pi P$ wave is shown in (a) with the blue markers being the data points of the spin parity analysis. The red curve showings the overall fit result, the blue curves the Breit-Wigner components and the green line the non-resonant contribution. The t'-integrated intensity of $2^{-+}0^+\rho\pi F$ wave is shown in (b) and of the $2^{-+}0^+ f_2(1270)\pi G$ wave in (c)

In Fig. 8.19 the remaining 2^{-+} waves are shown. The $2^{-+}0^+\rho(770)\pi P$ (see Fig. 8.19a) is known to be dominated by non-resonant contributions [D+81]. Noticeable is that this model agrees well with the data. In particular the low-mass region up to 1.4 GeV/c^2 is explained almost solely by the non-resonant contribution. The shoulder at 1.8 GeV/c^2, however, is described by the coherent sum of both resonances, $\pi_2(1670)$ and $\pi_2(1880)$, and the non-resonant term.

The description of the $2^{-+}0^+\rho(770)\pi F$ wave (see Fig. 8.19b) is based mainly on the $\pi_2(1670)$ and a small but non-negligible contribution of the $\pi_2(1880)$ albeit smaller in intensity than the non-resonant term. The model cannot describe the complete peak structure, maybe an enhanced model for the non-resonant contribution can improve the fit.

As mentioned earlier, the intensity of the $2^{-+}0^+ f_2(1270)\pi G$ wave cannot be explained at all

by the model. The Breit-Wigner parameters are driven by the associated interference distributions. The dominant amplitude for this wave is the $\pi_2(1880)$.

The model discussed here shows explicitly that the $\pi_2(1880)$ is a resonance distinct from the $\pi_2(1670)$ in contrast to some models explaining the $\pi_2(1670)$ and $\pi_2(1880)$ as one resonance, shifted by Deck-like background to lower and higher masses, respectively [DS06].

With the status of the $\pi_2(1880)$ clarified now, what can be said about its possible hybrid nature, which is predicted by [Dud11]? Referring to the discussion in [LZ09] and under the assumption that the $\pi_2(1880)$ is a hybrid, its contribution to the $2^{-+}0^+ f_2(1270)\pi S$ wave should be dominant. As the fit of this wave showed an unusual behavior using the fit model of Tab. 8.8 the fit results of models, discussed previously in sections 8.2.1 and 8.2.2, are used for this study. The fit result of the $2^{-+}0^+ f_2(1270)\pi S$ wave, based on the model listed in Tab. 8.2 is shown in Fig. 8.20a,that for the model, listed in Tab. 8.4 is depicted in Fig. 8.20b. It can be seen that the fit result for this partial wave depends strong on the fit model. In both cases the fit can describe the data but while in Fig. 8.20a the dominant peak is described almost only by the $\pi_2(1670)$, the contribution of the $\pi_2(1880)$ is more significant in Fig. 8.20b. In both models the $\pi_2(1880)$ is not the major component.

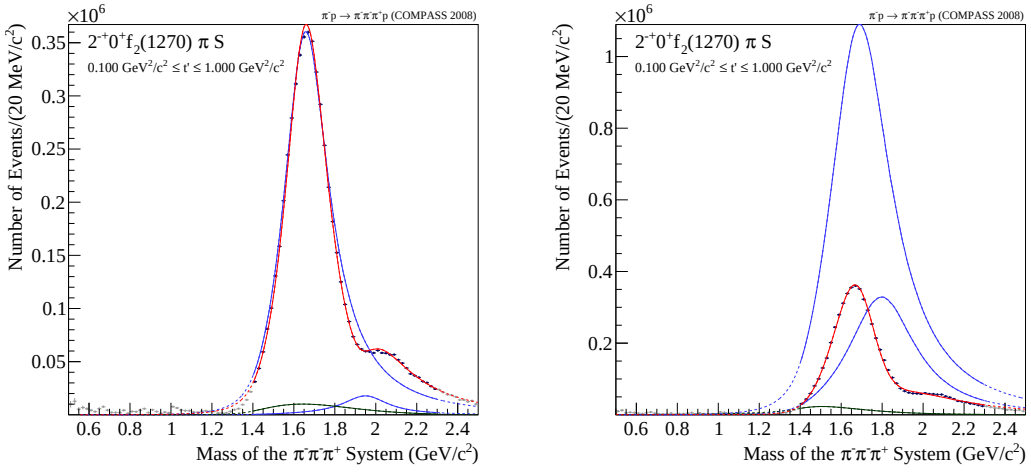

Figure 8.20 Fit result for the $2^{-+}0^+ f_2(1270)\pi S$ partial wave based on the model listed in Tab. 8.2. The t'-integrated intensity is shown in (a). The corresponding plot of the fit result based on the model listed in Tab. 8.4 is depicted in (b).

A hybrid $\pi_2(1880)$ is expected to be suppressed in the $2^{-+}0^+ f_2(1270)\pi D$ wave which is not observed either. In addition the obtained width of $\Gamma = 327$ MeV/c^2 contradicts the model predictions for the width of a hybrid $\pi_2(1880)$ which should be in the mass range of about 100 MeV/c^2 [LZ09].
Furthermore flux-tube models predict a suppression of hybrid decays into the $\rho\pi$ channel [IP85], as observed for instance for the $\pi(1800)$ in this analysis (see Fig. 8.14a). However, the contribution of the $\pi_2(1880)$ to the $2^{-+}0^+ \rho\pi P$ wave and the $2^{-+}0^+ \rho\pi F$ wave is small but not

negligible.
Finally the branching into the $2^{-+}0^{+}f_2(1270)\pi G$ wave indicates a non-hybrid nature for the $\pi_2(1880)$. Summarising based on the observations made with the models discussed in this section it is more likely that the $\pi_2(1880)$ is not a hybrid.

An overview of the complete fit result can be found in Tab. 8.9.

Resonance	**Parameters (MeV/c^2)**	**t′ Slopes (GeV^{-2}/c^{-2})**	**Intensity Ratio**
$a_2(1320)$	$m = 1314$, $\Gamma = 108$	12.36 ± 0.23, 5.98 ± 0.06	0.51
$a_2(1950)$	$m = 1844$, $\Gamma = 324$	11.64 ± 0.27	-
$\pi_2(1670)$	$m = 1685$, $\Gamma = 292$	18.88 ± 0.95, 8.12 ± 0.12 ($2^{-+}0^{+}f_2\pi S$)	0.47
		7.13 ± 0.07 ($2^{-+}0^{+}f_0(980)\pi D$)	-
		7.02 ± 0.05 ($2^{-+}0^{+}f_2\pi D$)	-
		9.08 ± 0.17 ($2^{-+}0^{+}\rho(770)\pi P$)	-
		* ($2^{-+}0^{+}\rho(770)\pi F$)	-
		* ($2^{-+}0^{+}f_2\pi G$)	-
$\pi_2(1880)$	$m = 1829$, $\Gamma = 327$	32.87 ± 2.18, 0.68 ± 0.25 ($2^{-+}0^{+}f_2\pi S$	1.38
		6.71 ± 0.05 ($2^{-+}0^{+}f_0(980)\pi D$)	-
		19.16 ± 2.06, 8.04 ± 0.16 ($2^{-+}0^{+}f_2\pi D$)	0.22
		8.63 ± 0.06 ($2^{-+}0^{+}\rho(770)\pi P$)	-
		* ($2^{-+}0^{+}\rho(770)\pi F$)	-
		5.15 ± 0.25 ($2^{-+}0^{+}f_2\pi G$)	-

Table 8.9 Resonance parameters obtained by a coupled fit in 11 t' bins based on the model shown in Tab. 8.8.
† *limited fit range for the t' dependence.*$\star$ *fit does not describe the data*

Chapter 9

Conclusions and Future Prospects

> A story has no beginning or end: arbitrarily one chooses that moment of experience from which to look back or from which to look ahead.
>
> Graham Greene, The End of the Affair

In 2008 the by far world's largest data set of diffractive dissociation of pions into the $\pi^-\pi^-\pi^+$ final states was recorded with the upgraded COMPASS spectrometer using a 190 GeV/c π^- beam on a proton target. The large data set leads to an unprecedented statistical precision that demands to go beyond the traditional methods of a partial-wave analysis. On the level of the event selection the full information of the spectrometer was exploit in order to obtain an exclusive 3π data sample and to separate contributions other reactions. A simultaneous spin-parity analysis in bins of the invariant 3π mass and the squared four-momentum transfer t' was applied to the data set, consisting of about $\sim 4.2 \cdot 10^7$ exclusive events based on a model of 88 partial waves up to an angular momentum of 6. Based varying the analysis model the bias of the spin-parity analysis was studied. A two-dimensional method was developed to extract the resonance parameters which for the first time takes into account the complete information of the underlying spin-density matrices as a function of $m_{3\pi}$ and t'. Thereby it is possible to better disentangle non-resonant contributions from the resonance part. This final stage, the extraction of resonance parameters, cannot be seen as completed. The future road map for this analysis is sketched in the next section. Based on the partial-waves analysis, discussed in this thesis, the following conclusions can be drawn.

The most remarkable finding is a new a_1 state in the 3π mass region of about 1.4 GeV/c^2 observed in the $J^{PC}M^{\varepsilon} = 1^{++}0^+$ partial wave decaying into $f_0(980)\pi$. The signal is small, with a relative strength of only 0.25% of the full 3π sample, but the corresponding structure in the $1^{++}0^+ f_0(980)\pi P$ wave is stable with respect to model variations. This new resonance is not seen in other decay channels of 1^{++} partial waves, neither in $f_2(1270)\pi$ nor in $(\pi\pi)_S\pi$. The decay to the $\rho\pi$ channel can also be excluded because of the large phase motions between the $1^{++}0^+ f_0(980)\pi P$ and the $1^{++}0^+\rho\pi S$ waves. This supports the interpretation of the signal as a single resonance which couples exclusively to the $f_0(980)\pi$ channel. In turn the $a_1(1260)$ is not seen to decay into this channel which is consistent with [B$^+$12]. Leakage studies were performed in order to investigate intensity migrations of other partial waves into the

$1^{++}0^+ f_0(980)\pi P$ wave, but this effect was found to be negligible. A mass of $m = 1416$ MeV/c^2 and a width of $\Gamma = 145$ MeV/c^2 was extracted. The production phase of this resonance with respect to the $a_1(1260)$ resonance is independent of t'. The new axial-vector meson state was dubbed $a_1(1420)$.
An explanation why this state was not observed by previous experiments is the small relative strength of 0.25%. The nature of the $a_1(1420)$ is still unclear. Neither models e.g. [IP85] nor lattice-QCD calculations [Dud11] predict a resonance in this mass region with this spin-parity configuration and negative G-parity. Regarding the small relative intensity of 0.25%, its phase motion against dominant partial waves associated to the $a_1(1260)$ resonance and its exclusive coupling to the $f_0(980)$, which is known to have a large $s\overline{s}$ component [Ach00], the $a_1(1420)$ is more likely a non-$q\overline{q}'$ meson which couples to the strangeness content of the $f_0(980)$. It could be interpreted as the isospin partner of the $f_1(1420)$ meson which decays dominantly into the $K\overline{K}\pi$ channel. Another possible explanation for this state could be coupled-channel effects. The $a_1(1260)$ can decay into the $K\overline{K}^*(892)$ channel which could rescatter via $K\overline{K}\pi$ into the $f_0(980)$ [BB77]. An alternative idea is that the $a_1(1420)$ is a meson molecule with a $K\overline{K}$ nucleus and a pion orbiting around it [Chu]. Common to all models is the fact that the strangeness content of this new state plays a major role.

The spin-exotic $\pi_1(1600)$ resonance was found in the $1^{-+}1^+\rho\pi P$ partial wave. In contrast to a previous analysis [CDH+02] the intensity is dominated by a broad component, consistent with observations of [Zai00]. In order to better understand possible non-resonant contributions a Monte Carlo sample, based on a Deck-like scattering amplitude was generated, and the same spin-parity analysis was applied to this sample as to the real data. This study shows that the intensity of the spin-exotic $1^{-+}1^+\rho\pi P$ wave at low t' around 0.1 GeV$^2/c^2$ is dominated by non-resonant contributions which vanish almost completely at high t' around 1.0 GeV$^2/c^2$, leaving a structure at 1.6 GeV/c^2. From the two-dimensional extraction a mass of $m = 1597$ MeV/c^2 and a width of $\Gamma = 579$ MeV/c^2 is obtained. The large width can be explained by the phase motions of the spin-exotic $1^{-+}1^+\rho\pi P$ wave with respect to other waves, which are only in the range of 70°. The reason for this is yet unclear, a possible explanation could be interferences between the resonance and the non-resonant component. On the other hand this finding is consistent with another recent COMPASS analysis of the $\eta\pi$ and $\eta'\pi$ final states [Sch12].
The data analysed in this thesis also offer the possibility to investigate the apparent discrepancies between previous 3π analyses, in particular their different findings for the spin-exotic $1^{-+}1^+\rho\pi P$ wave. The models of these analyses were applied to the 2008 COMPASS data yielding similar results as the original analyses. Therefore the experimental data are actually consistent and the differences are explained by model artifacts or the constraint to certain kinematical ranges.

The two experimentally known radial excitations of the pion, the $\pi(1300)$ and the $\pi(1800)$, were studied and in addition the possible hybrid nature of the latter one was investigated. The $\pi(1300)$ was found in the $0^{-+}0^+(\pi\pi)_S$ and the $0^{-+}0^+\rho\pi P$ waves but the extracted resonance parameters of $m = 1405$ MeV/c^2 and $\Gamma = 783$ MeV/c^2, cannot describe well the intensity structures observed in the mass region around 1.3 GeV/c^2 in both waves. The two-dimensional fit in $m_{3\pi}$ and t' reveals that these structures are dominated by non-resonant components.
The $\pi(1800)$ was found in all 0^{-+} partial waves that were included into the model except in the $0^{-+}0^+\rho\pi P$ wave. This finding and the dominant decay into the $f_0(980)\pi$ and $f_0(1500)\pi$ chan-

nels supports the hypothesis that the $\pi(1800)$ has a dominant hybrid component.
In order to describe the interference structure seen in the $0^{-+}0^{+}f_2(1270)\pi P$ wave it was tried to include an additional 0^{-+} resonance at 1.7 GeV/c^2, as proposed by [CP97]. This could indicate the coexistence of a $q\overline{q}'$ meson and a hybrid state. The fit, however, was not successful only the $\pi(1800)$ could be found in this wave.

The central question of this analysis regarding the 2^{-+} sector is, whether the $\pi_2(1880)$ is a separate resonance and, if this is the case, what is its nature. All 2^{-+} partial waves implemented in the four analysis models are described best by two Breit-Wigner amplitudes, for the $\pi_2(1670)$ and the $\pi_2(1880)$. Striking is the explanation of the interference structure, observed in the $2^{-+}0^{+}f_0(980)\pi S$ wave, by these two resonances. Thus the $\pi_2(1880)$ is very likely a separate resonance, albeit close in mass to the $\pi_2(1670)$.
Following the discussion in [LZ09] a dedicated model was developed in order to clarify the nature of the $\pi_2(1880)$. Although this model has difficulties to disentangle the $\pi_2(1880)$ and non-resonant contributions in the $2^{-+}0^{+}f_2(1270)\pi S$ wave, however, the resulting description was not useless. Based on the fit result the $\pi_2(1880)$ is more likely a $q\overline{q}'$ meson than a hybrid. A hybrid contribution to this state cannot be excluded but it seems to be small.

In this thesis for the first time a systematic study of the t' dependence on the level of partial waves was performed. It is found that the t' dependence of most of the resonances can be parametrised by a leading slope with values between 5 - 10 (GeV/c)$^{-2}$, expected for resonant scattering on a proton. In most cases the low-t' region must be described by a second steeper slope. The t' dependence of the non-resonant terms reveals a diffractive pattern with a minimum at around $t' = 0.35$ GeV$^2/c^2$ and can therefore often not be described by a single exponential. Up to now no model exists in order to explain the observed t' spectra. It is anticipated that the obtained t' dependencies serve as input for the development of future models of the underlying production process.

With the new method of performing the analysis in bins of $m_{3\pi}$ and t' it was possible to better describe some resonance peaks that moved as a function of t'. In particular the $a_1(1260)$ could be described in the analysed t' range in the $1^{++}0^{+}\rho\pi S$ and the $1^{++}1^{+}\rho\pi S$ waves. The non-resonant component in both waves is known to contribute significantly to the intensity. The model is able to explain the t' dependence of the non-resonant contribution and thus gives an improved description of the $a_1(1260)$.

Despite all progress the extraction of the resonance parameters is still work in progress. The two-dimensional analysis in $m_{3\pi}$ and t' is still developed further and it was shown how sensitive the fit is to various model descriptions. The present status of the analysis is illustrated in Tab. 9.1, which lists the resonance parameters obtained in the four fits discussed in this thesis and compares them to PDG values [B$^+$12]. As some resonances were part of several fits a parameter range is given for them instead of a single number. As explained in Chap. 8 no errors can be stated at the current stage of the analysis. The extracted parameters roughly agree with PDG values, but some of the extracted resonance parameter deviates from the PDG values by several standard deviations. But it must be taken into account that the analysis models were constructed for dedicated studies. Taking this and the computational limitations into account it is clear that the models were too simplistic (by the implementation of Breit-Wigner forms)

and the used sub-matrices were too small. Thus the fit had difficulties to find the global minimum of the fit function. Strategies how to improve the resonance extraction are discussed in the following section.

Resonance	**Mass (Range) (MeV/c²)**	**Width (Range) (MeV/c^{-2})**	**PDG Mass (MeV/c²)**	**PDG Width (MeV/c²)**
$\pi(1300)$	1405	783	1300 ± 100	200-600
$\pi(1800)$	1770 - 1805	207 - 240	1816 ± 14	208 ± 12
$a_1(1260)$	1267 - 1290	357 - 379	1230 ± 40	250 - 600
$a_1(1910)$	1948 - 1970	154 - 320	1930^{+30}_{-70}	155 ± 45
$a_2(1320)$	1313 - 1315	107 - 108	1318.3 ± 0.6	107 ± 5
$a_2(1950)$	1763 - 1844	322 - 470	1950^{+30}_{-70}	180^{+30}_{-70}
$\pi_1(1600)$	1597	579	1602^{+15}_{-11}	234 ± 50
$\pi_2(1670)$	1620 - 1685	281 - 385	1672 ± 3.2	259 ± 9
$\pi_2(1880)$	1783 - 1946	271 - 410	1895 ± 16	235 ± 34
$a_4(2040)$	1940 - 1944	366 - 375	2001 ± 10	235 ± 29

Table 9.1 Resonance parameters obtained from the various fits discussed in this thesis and the comparison with the respective PDG values [B$^+$12]. Parameter ranges are given for resonances that were included in several fits.

9.1 Future Prospects

The epigraph at the beginning of this section describes well the present status and the outlook of the partial-wave analysis of the 3π data. Even with the improved analysis methods developed for this data sample, which constitute the main part of this thesis work, the potential of the data cannot be revealed completely. In the following a possible road map of the future analysis of the 3π data will be introduced.

One general topic of the future analysis can be labeled with extension. More data, taken in 2009 with the exact same setup, is on tape which, if analysed, will enhance the precision of the COMPASS 3π data significantly. In addition it will be possible to extend the kinematical reach of the analysis. The idea is to shift the upper bound of the 3π mass to 3 GeV/c^2 in order to learn more about the transition of diffractive production to central production. It was shown that centrally produced events already start to appear at 1.2 GeV/c^2 and the analysis of an extended mass range could help to describe the contribution of centrally produced events in the low-mass region

By extending the upper bound of the t' region the diffractive data could be cleaned from non-resonant components. On the other side the excitation of target protons become more likely and double diffraction starts to contribute. Nevertheless a spin-parity analysis in bins of $m_{3\pi}$ and t' could bring new insights to the diffractive production.

On the level of the spin-parity analysis the final-state interactions must be taken into account as proposed by [Bre81]. A promising candidate is the $1^{++}0^+(\pi\pi)_S\pi P$ wave where it is assumed that rescattered events of the $\rho\pi$ decay channel contribute to the observed intensity.
The analysis of the $\pi^-\pi^0\pi^0$ final state of the 2008 data sample progressed significantly in the last month [Uhl14]. The same spin-parity analysis in bins of $m_{3\pi}$ and t' and the same model, developed for the analysis presented, was applied to the $\pi^-\pi^0\pi^0$ data. Although the number of events recorded for this final-state is smaller by a factor of 10, the fit result is similar to the one discussed in this thesis. Even the new $a_1(1420)$ resonance can be seen in the intensity distribution of the $1^{++}0^+ f_0(980)\pi P$ wave. An overlay of both fit results is shown in Fig. 9.1, with the intensity of the charged channel scaled to the intensity of the neutral channel in order to compare the line shape.

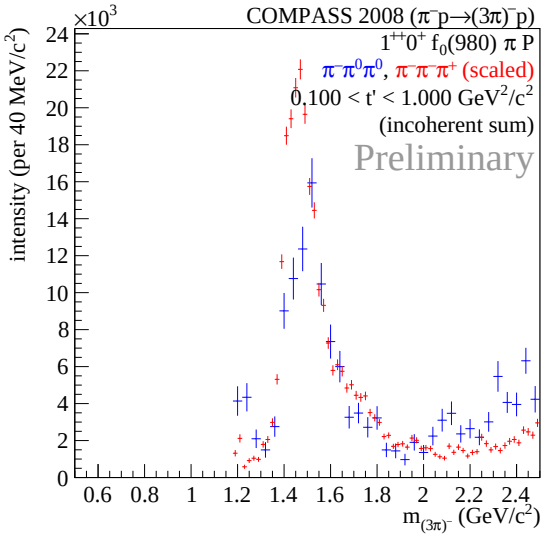

Figure 9.1 Intensity of the $1^{++}0^+ f_0(980)\pi P$ wave for the charged and neutral final state overlaid. The intensity of the charged channel is scaled to the intensity of the neural channel in order to compare the line shape. Plot from [Uhl14].

The VES experiment has recently taken data for both 3π final-states, comparable with the 2008 COMPASS data [Rya], using a Be target and in a slightly different kinematical region. Thus a combination of both data sets and both final-states may enhance the 3π analysis enormously.

The influence of isobar parametrisations on the result of the spin-parity analysis was shown in several systematic studies. In order to be more model-independent a new analysis method is developed. The concept of a spin-parity analysis in bins of $m_{3\pi}$ has the advantage that no description of the $m_{3\pi}$ is required. Instead the $m_{3\pi}$ dependence is extracted from the data at the expense of an increased number of fit parameters. This idea is now extended to the description

of the two-pion isobar states. Each $m_{3\pi}$ mass bin is again divided into several bins of the $\pi^-\pi^+$ mass and thus the description of the isobar (see Sec. 6.4) can be circumvented by setting the dynamic part Δ_ξ (see Eq. (6.3)) to one:

$$\Delta_\xi(m_\xi; m_\pi, m_\pi) = \begin{cases} 1 & m_\xi \in [m_\alpha, m_\alpha + \delta m_\xi] \\ 0 & \text{else} \end{cases} \tag{9.1}$$

Each $m_{2\pi}$ mass slide, $[m_\alpha, m_\alpha + \delta m_\xi]$ acts as separate partial wave. Thus the fit result is driven by the data and not by the isobar parametrisation. In Fig. 9.2 an exemplary snapshot of the recent analysis [Kri17] using this method is shown. The two partial waves with $J^{PC} = 1^{++}$ and spin-projection $M = 0$ decaying to the $(\pi\pi)_S\pi$ and $f_0(980)\pi$ decay channel are replaced by a set of new partial waves, $1^{++}0^+[\pi\pi]^*_S\pi P$, where the isobar description is free and the corresponding contribution of the two-pion system to the decay amplitude is extracted by the spin-parity analysis. The correlation of the $m_{3\pi}$ and $m_{2\pi}$ dependence of the intensity is plotted for two regions of t' in Fig. 9.2. In both plots an accumulation at $m_{3\pi} = 1.4$ GeV/c^2 and $m_{2\pi} = 1$ GeV/c^2 is visible which corresponds to the decay of the new $a_1(1420)$ into the $f_0(980)\pi$ channel.

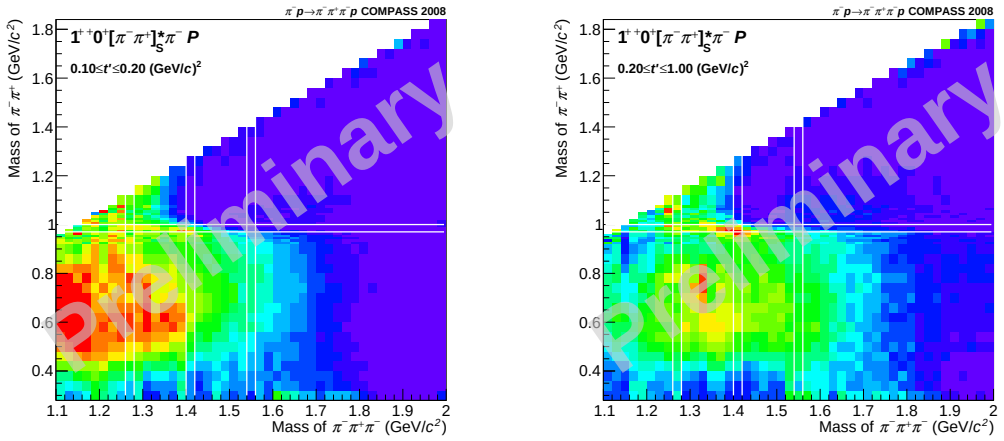

(a) **(b)**

Figure 9.2 Partial wave and $[\pi\pi]^*_S$-isobar correlation for the $1^{++}0^+[\pi\pi]^*_S\pi P$ wave for low t' (a) and high t' (b).

The biggest challenge is the further enhancement of the extraction of resonance parameters: In the analysis presented here four different fit models have been studied. The goal is to have one model including all the relevant information. In the course of the thesis work it was tried to enhance the fit model within the limitations defined by the software and the computing resources. The result is a model consisting of 21 partial waves which could be fitted simultaneously in two bins of t' as shown in Fig. 9.3. This model can seen as balanced such that it contains partial waves over a wide range of quantum numbers and at least two waves per resonance. The goal for the near future is to extend this model to 11 t' bins. In the last days of this thesis a number of software limitations were overcome but the establishment of a stable convergence of the fit based on this model is difficult.
In addition resonances in the mass region above 2 GeV/c^2 must be considered, which up to

now were not included in the fit. This is a challenging task since this mass region is crowded by resonances, so that there are generally no striking phase motions observable.
After having a satisfactory fit model it has to undergo an extended series of systematic studies as the systematic error is dominant in comparison to the negligible statistical error obtained for the 2008 data set.
Since the introduction of the Deck effect a working parametrisation is developed which could describe the data. In the last decades different approaches were pursued, from analytical descriptions of the Deck amplitude up to phenomenological parametrisations. The 2008 data set with its statistical precision and the development of the two-dimensional analysis method could help to refine the existing models.
Finally a point to consider is the fact that the description of the data by a sum of Breit-Wigner amplitudes violates unitarity and analyticity. In previous analyses the large statistical error bars shadowed this fact but with the large data sets available now this must be taken into account. A correct ansatz would be the usage of dispersion relations [SKN12] which describe the partial-wave amplitudes in the complex scattering plane. The fit to the data would determine the pole positions of the resonances in this plane. This approach is from the computation point of view difficult as for every partial wave the corresponding dispersion relation has to be developed and implemented in the fit model. The computing costs are also extremely high. A more practical ansatz would be the usage of Pietarinen functions [Pie72] where the partial-wave amplitudes are expanded in a fast converging power series which determines also the poles in the complex scattering plane. A fit method based on these functions will be developed and tested with the data in the near future.

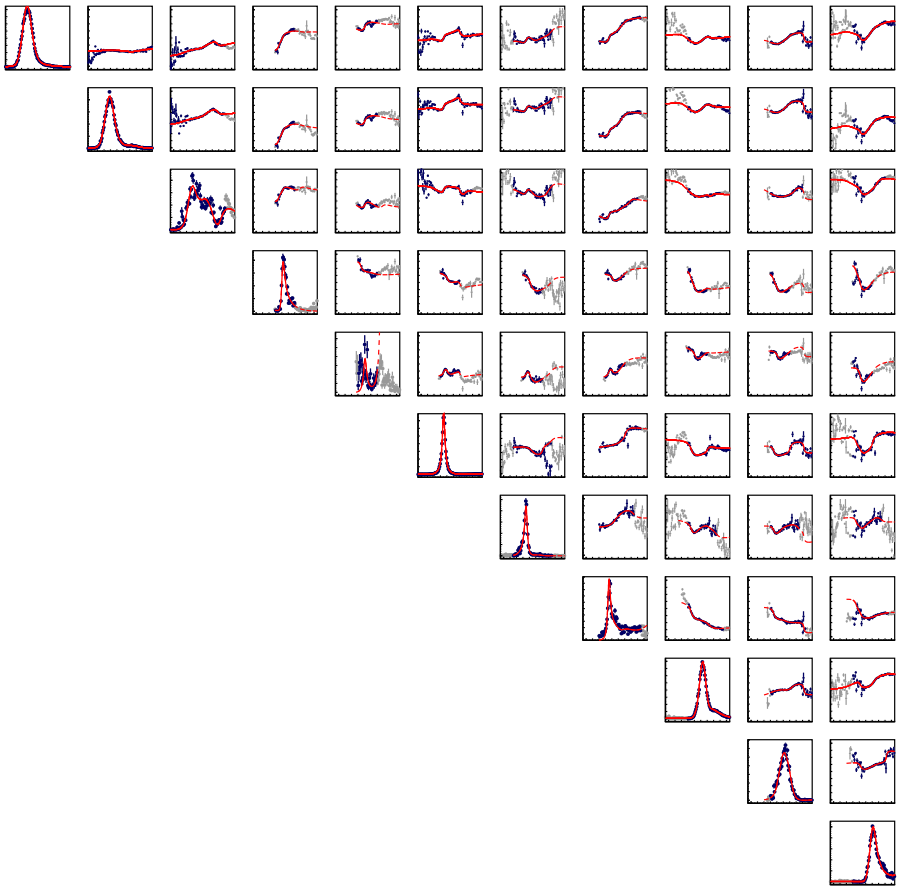

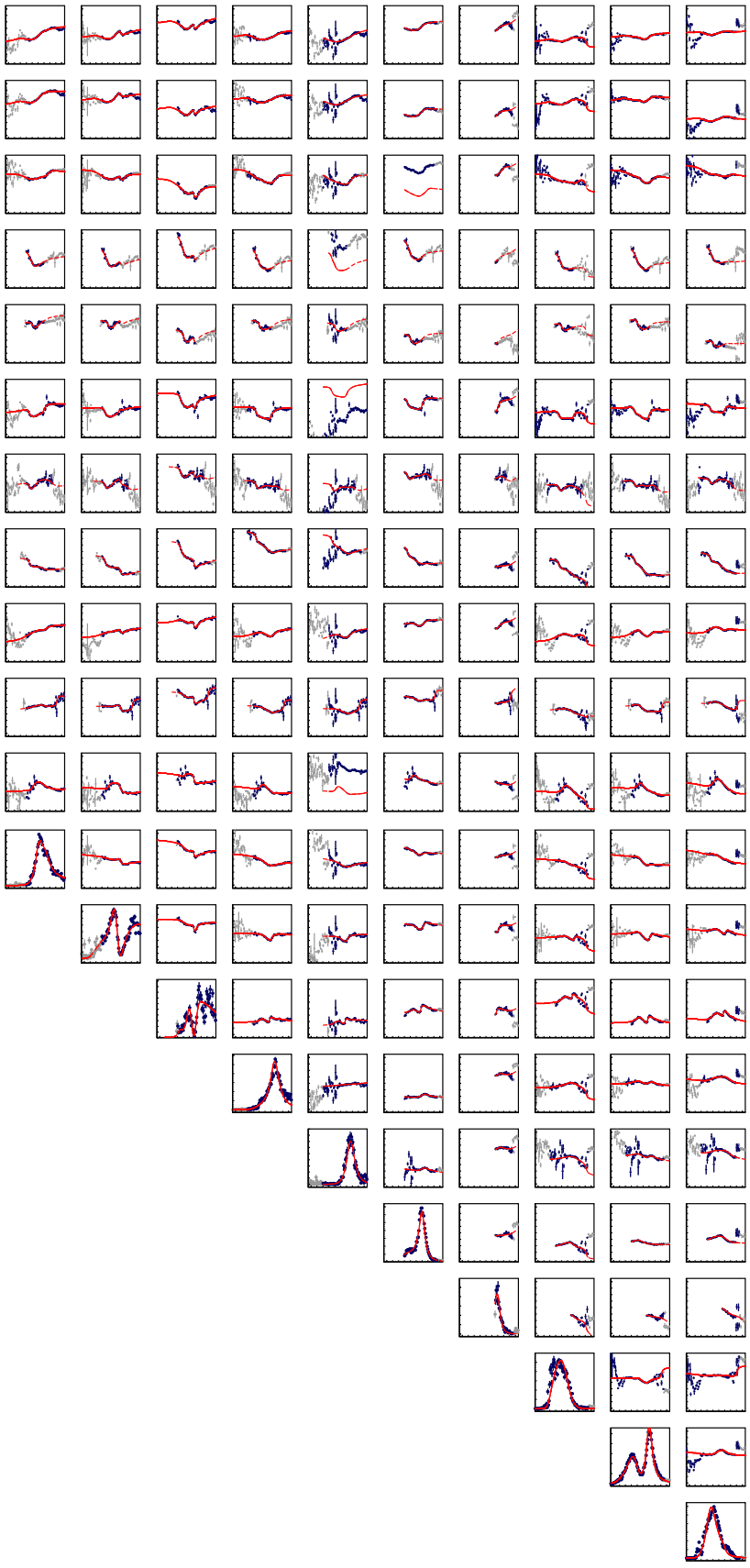

Figure 9.3 Spin-density matrix ${}_{t'}\rho(m_x)$ of a model consisting of 21 partial waves in the kinematic region of $0.164 \leq t' \leq 0.189$ GeV$^2/c^2$.

Appendix A

Additional Kinematic Distributions

Additional kinematic distributions are plotted in the following. These figures provide additional information about the three-pion final state.

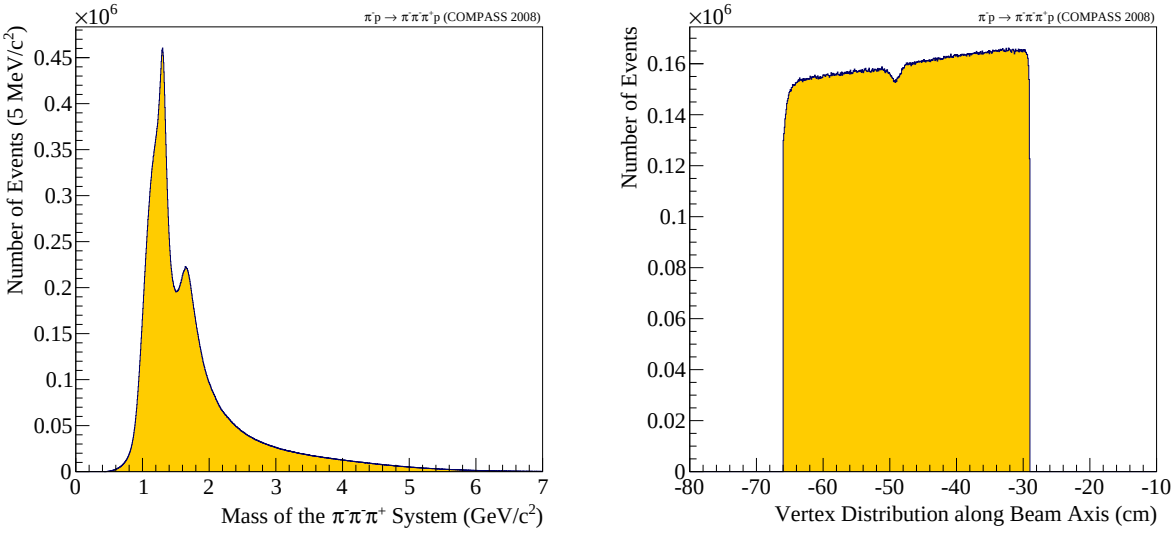

(a) **(b)**

Figure A.1 Invariant mass of the three pion final state (a) and primary vertex distribution along the z-axis (b).

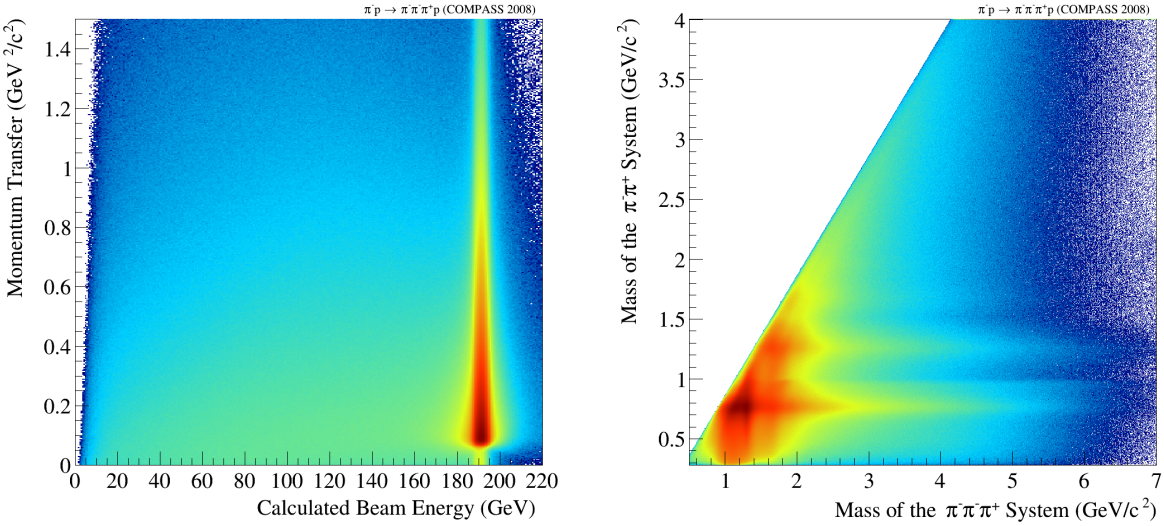

(a) **(b)**

Figure A.2 Calculated beam energy versus t' (a) and two pion mass versus invariant mass of the three pion final state (b).

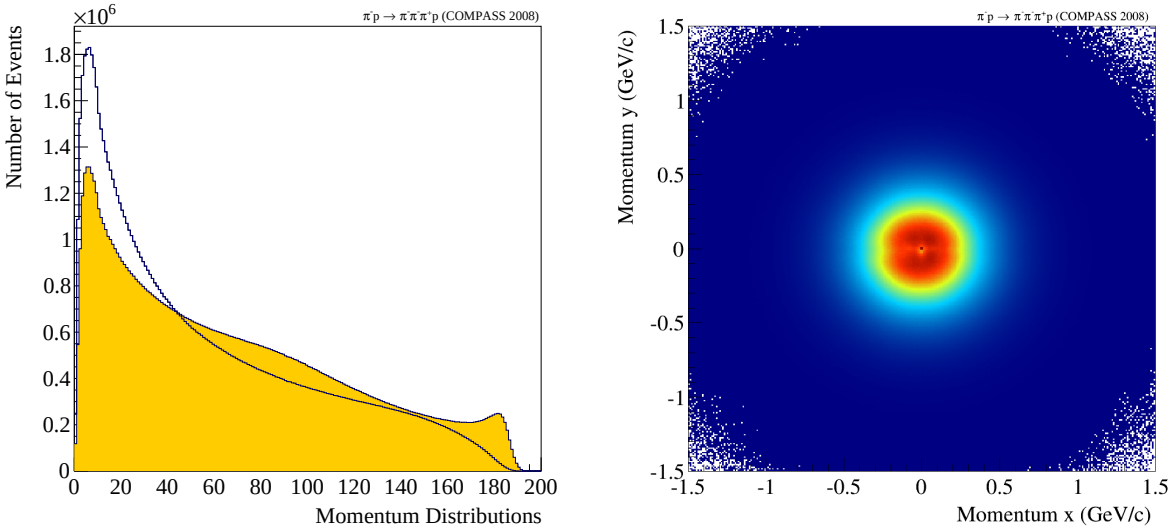

(a) **(b)**

Figure A.3 Momentum distributions, z component of the positive pion (yellow) and of the two negative pions (overlaid) (a), and xy momentum distribution of all three particles (b).

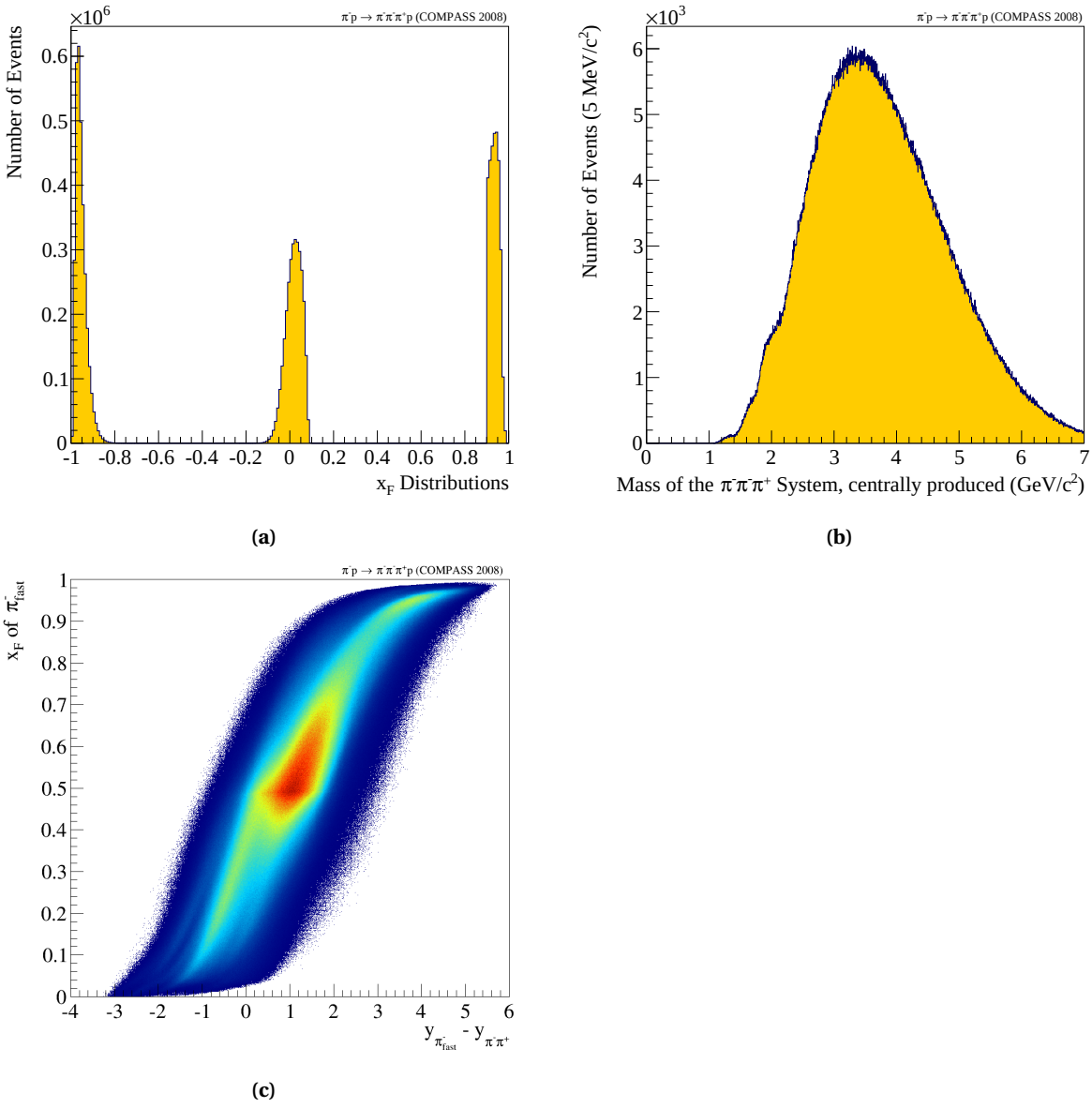

Figure A.4 Feynman x_F of the recoil particle, the fast π^- and the slow two pion system (a), invariant mass of the three pion final state in the CP reion (b), rapidity gap of the fast π^- and the twopion system against Feynman x_F of the fast π^- (c).

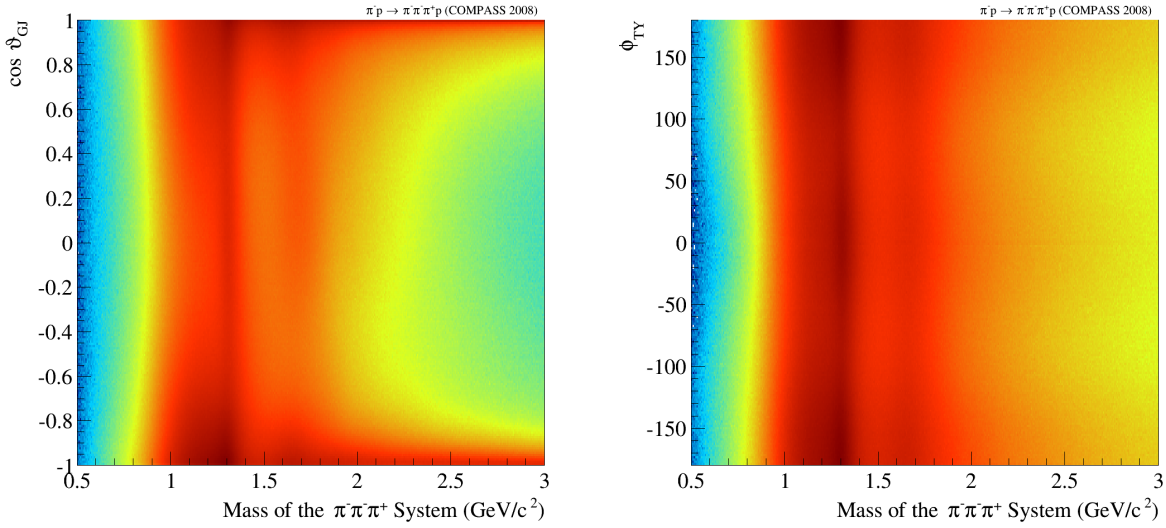

(a) **(b)**

Figure A.5 Integrated angular distributions in the Gottfried-Jackson reference system.

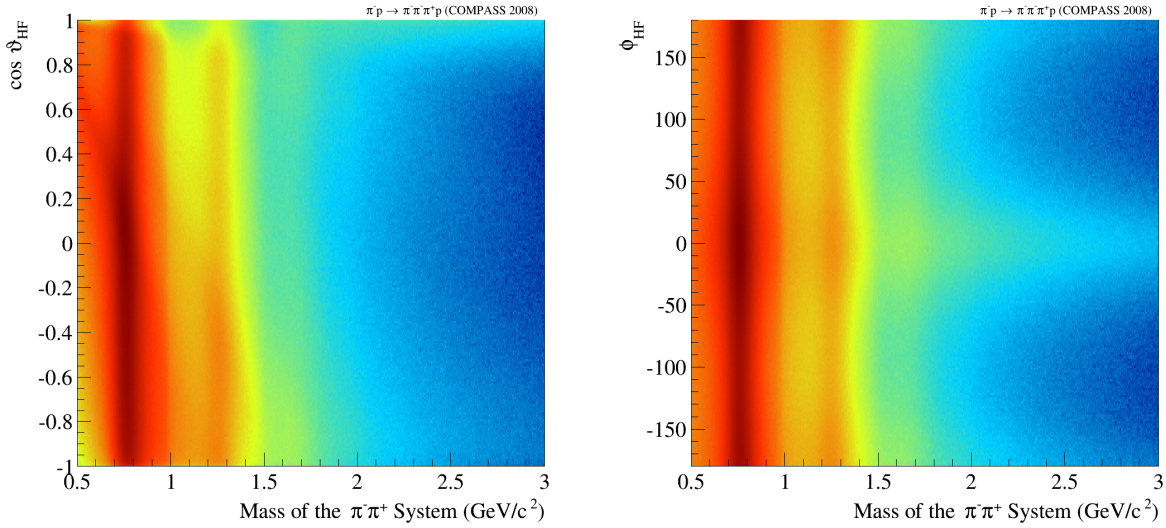

(a) **(b)**

Figure A.6 Integrated angular distributions in the two pion helicity reference system.

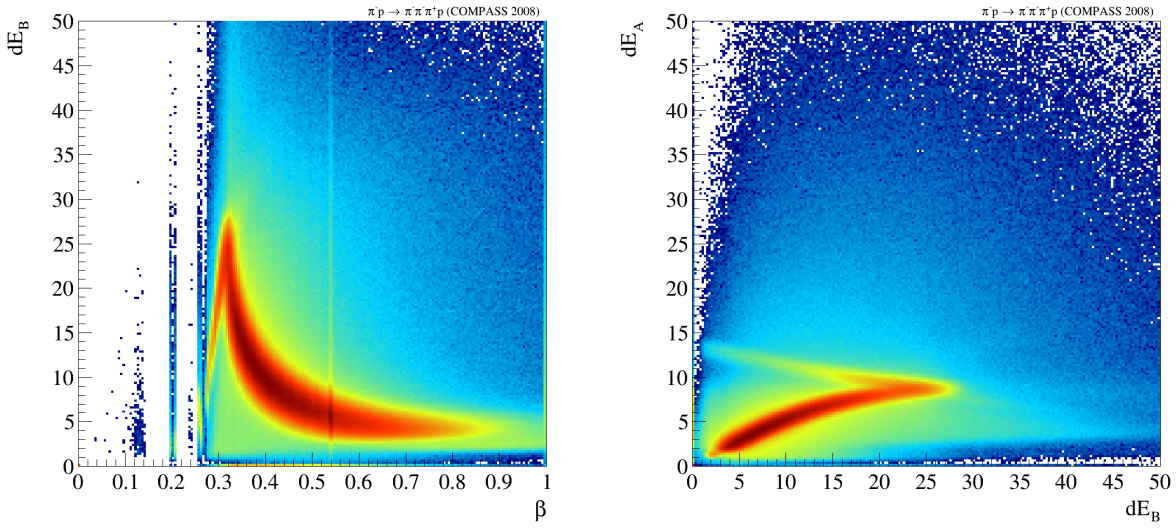

(a) **(b)**

Figure A.7 Energy loss in the RPD.

Appendix B

Reference Systems

Reference systems used to describe the decay of an intermediate state X^- within the isobar model.

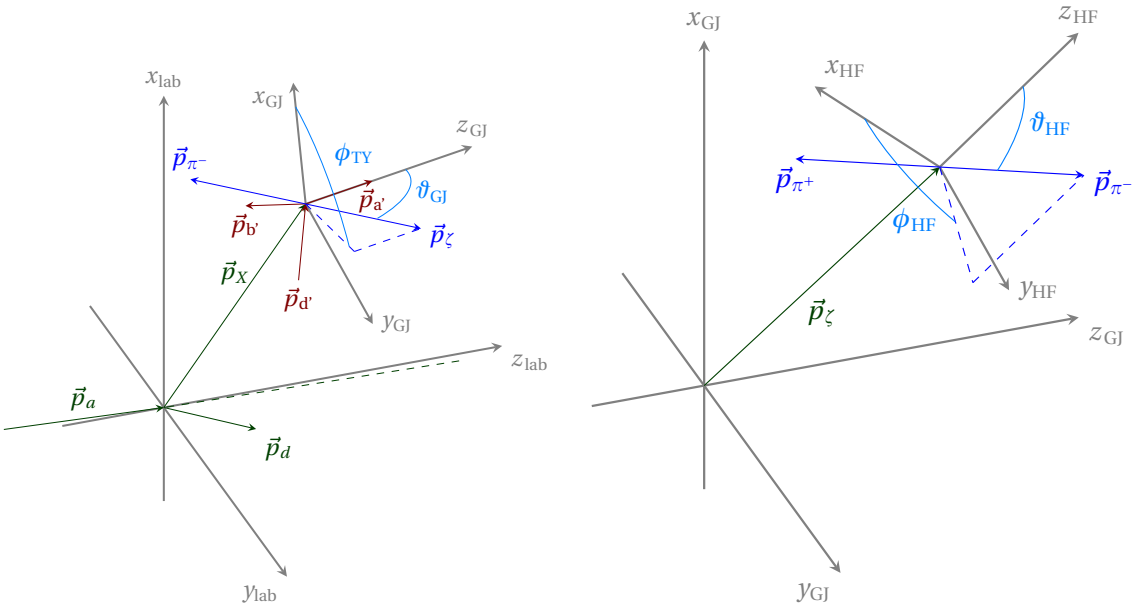

Figure B.1 Reference systems used to describe the decay of an intermediate state X^- within the isobar model. Gottfried Jackson reference system (a) and helicity reference system (b).

Appendix C

Isobar Parametrisations

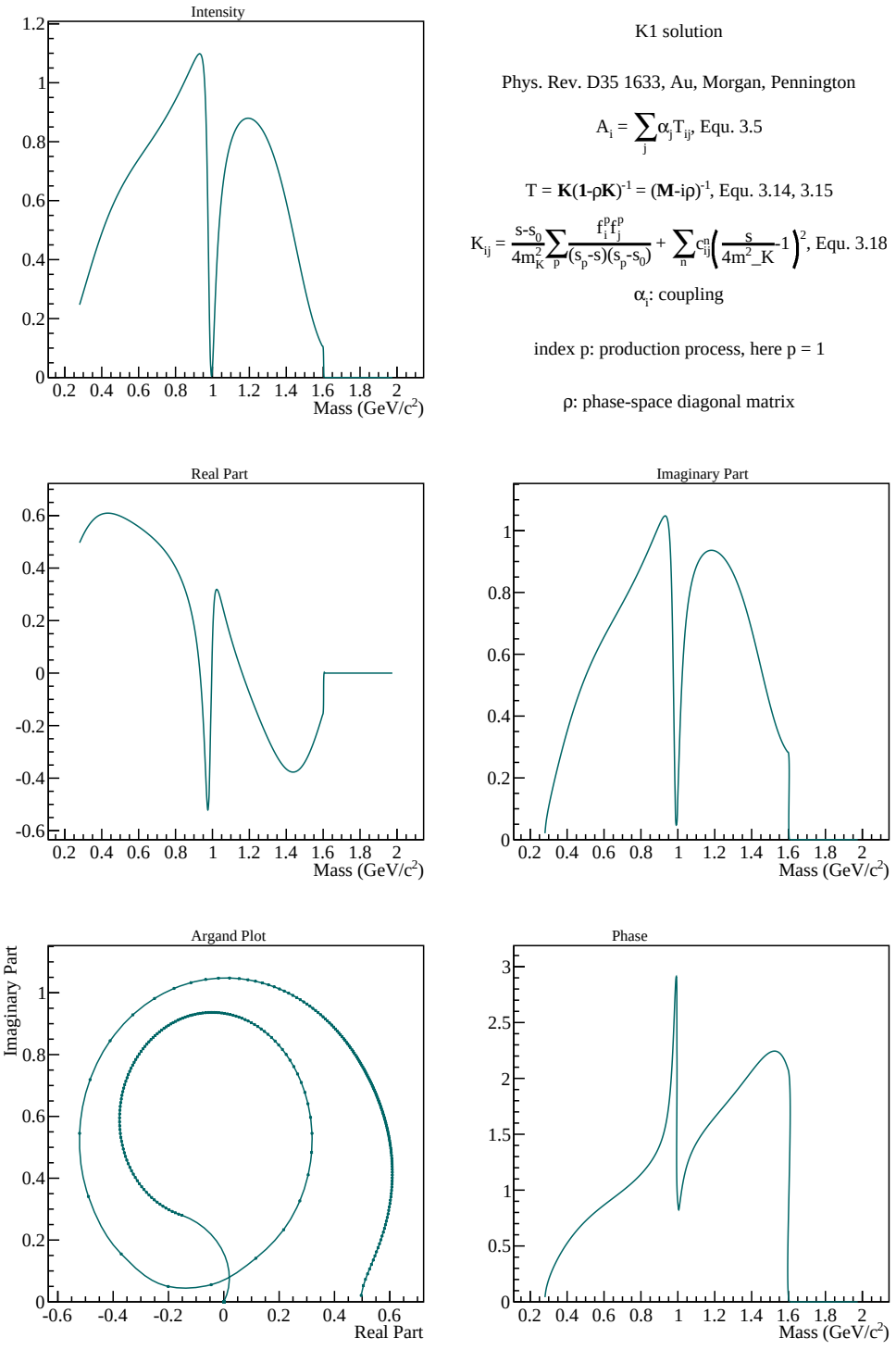

Figure C.1 $(\pi\pi)_S$ wave parametrisation. Based on the 'K1'-solution, described in [AMP87].

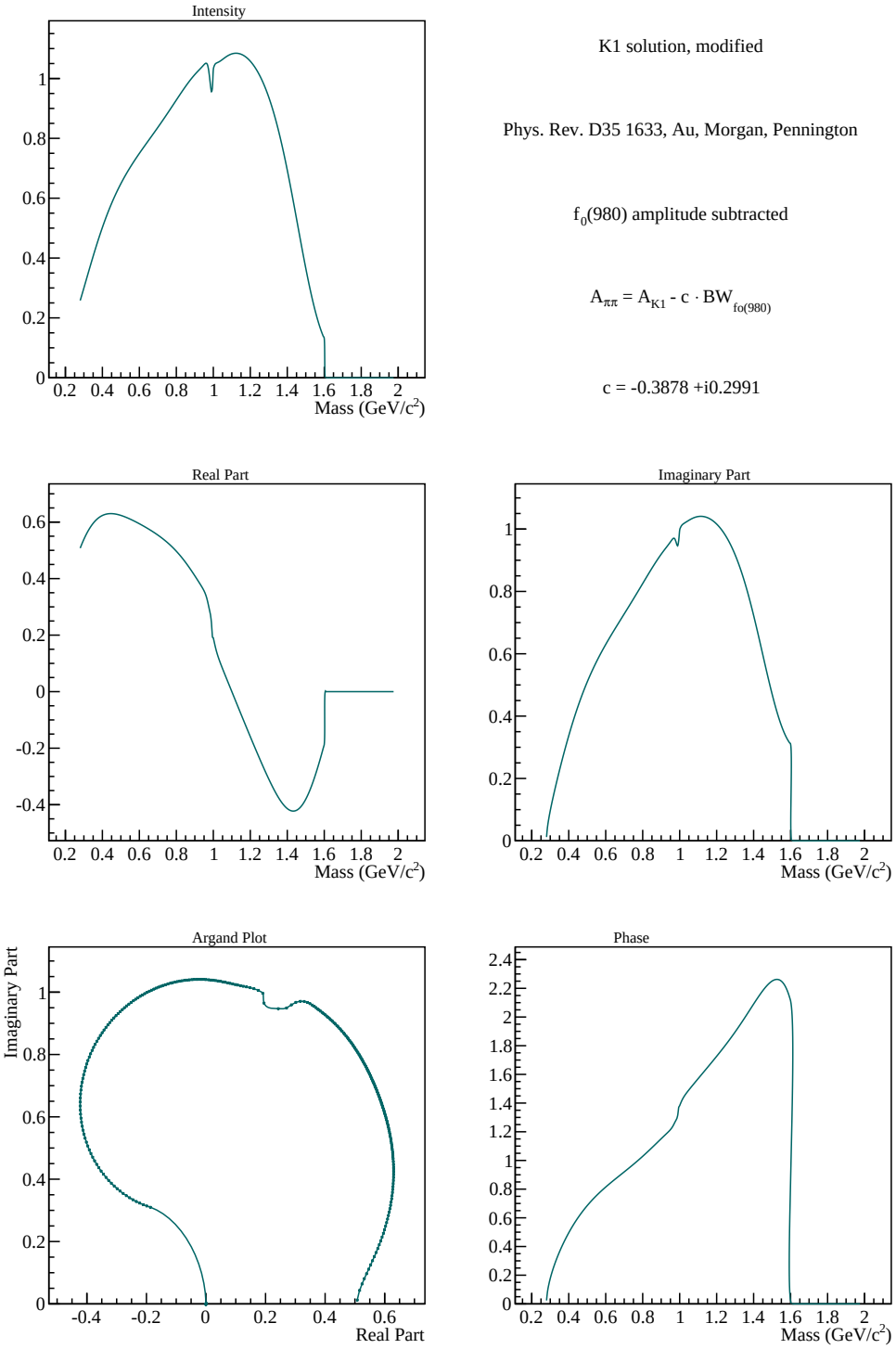

Figure C.2 $(\pi\pi)_S$ wave parametrisation. Based on the 'K1'-solution, described in [AMP87]. The $f_0(980)$ amplitude is subtracted from the K1 amplitude.

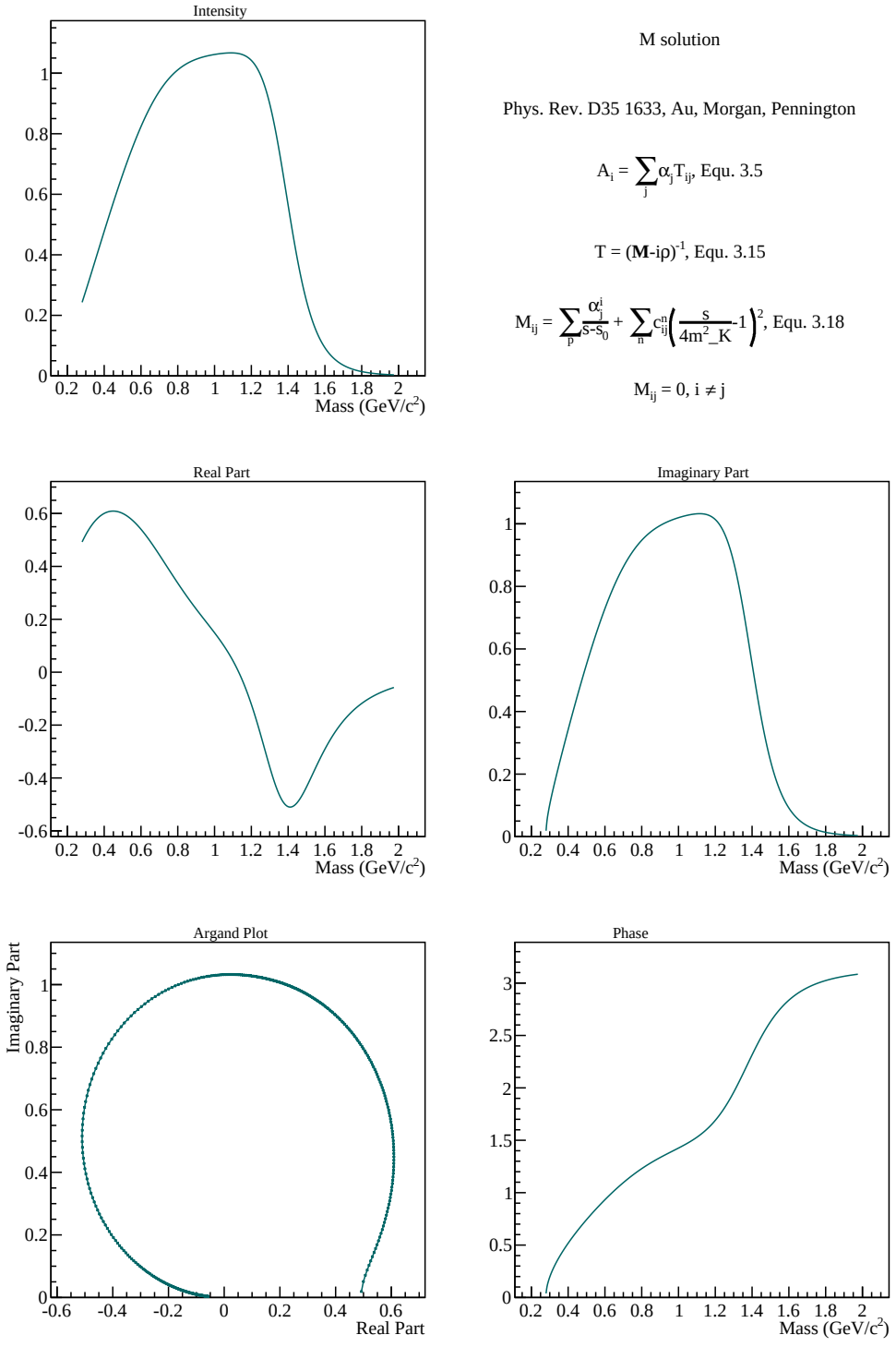

Figure C.3 $(\pi\pi)_S$ wave parametrisation. Based on the 'M'-solution, described in [AMP87]. The $f_0(980)$ amplitude was not incorporated into the M-fit.

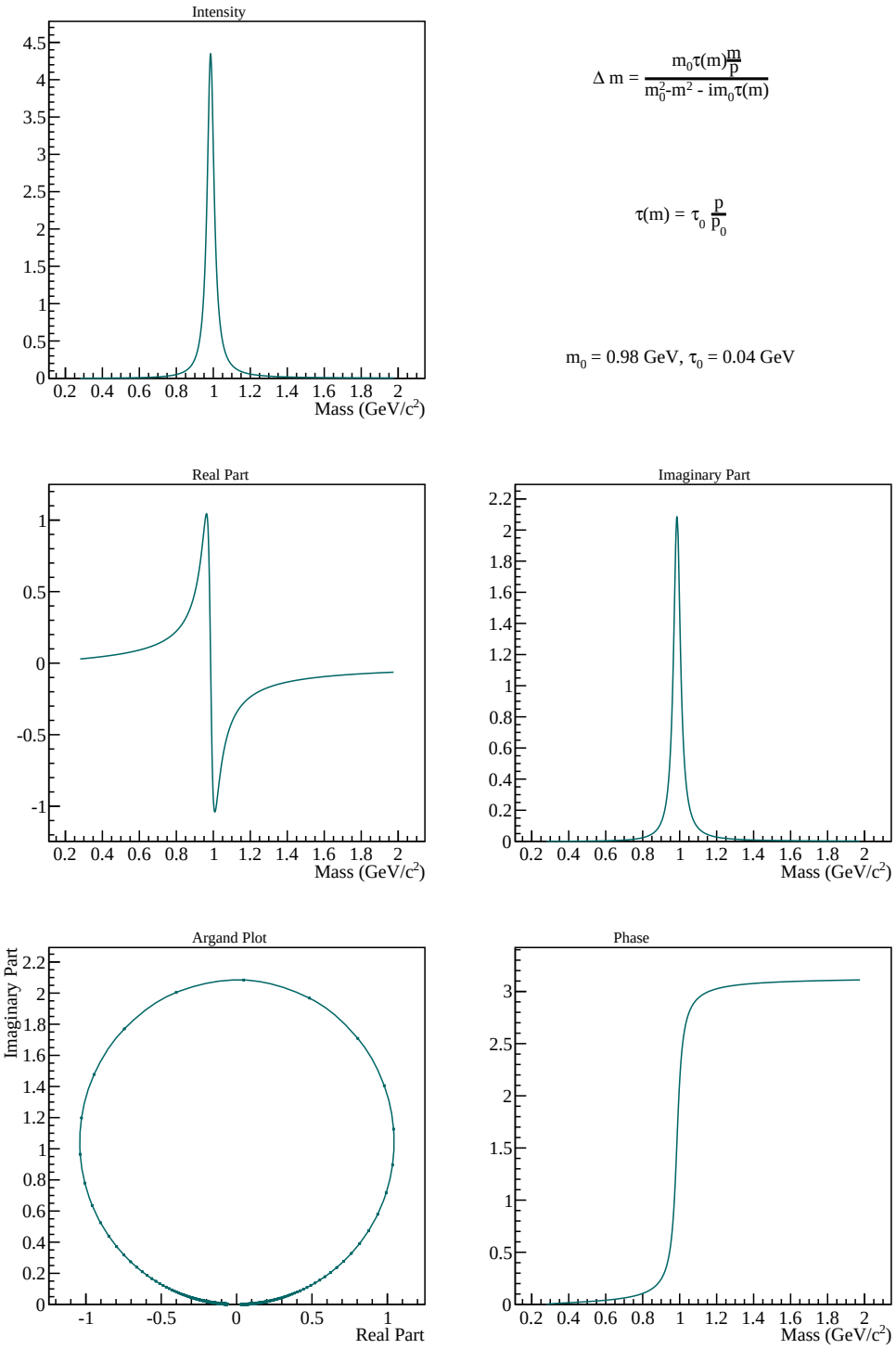

Figure C.4 Breit-Wigner Parametrisation of the $f_0(980)$ amplitude.

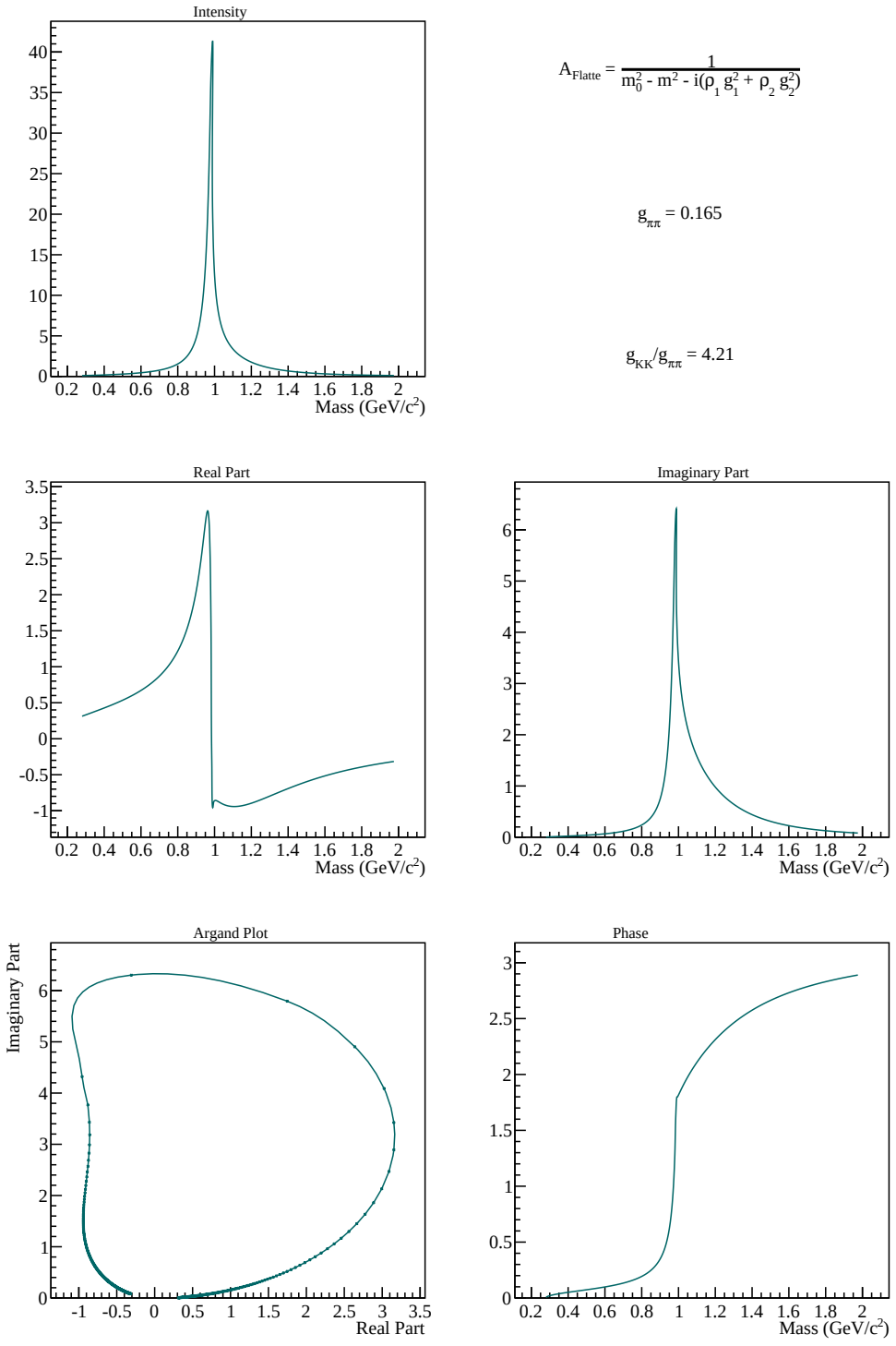

Figure C.5 Flatté Parametrisation of the $f_0(980)$ amplitude [ea05].

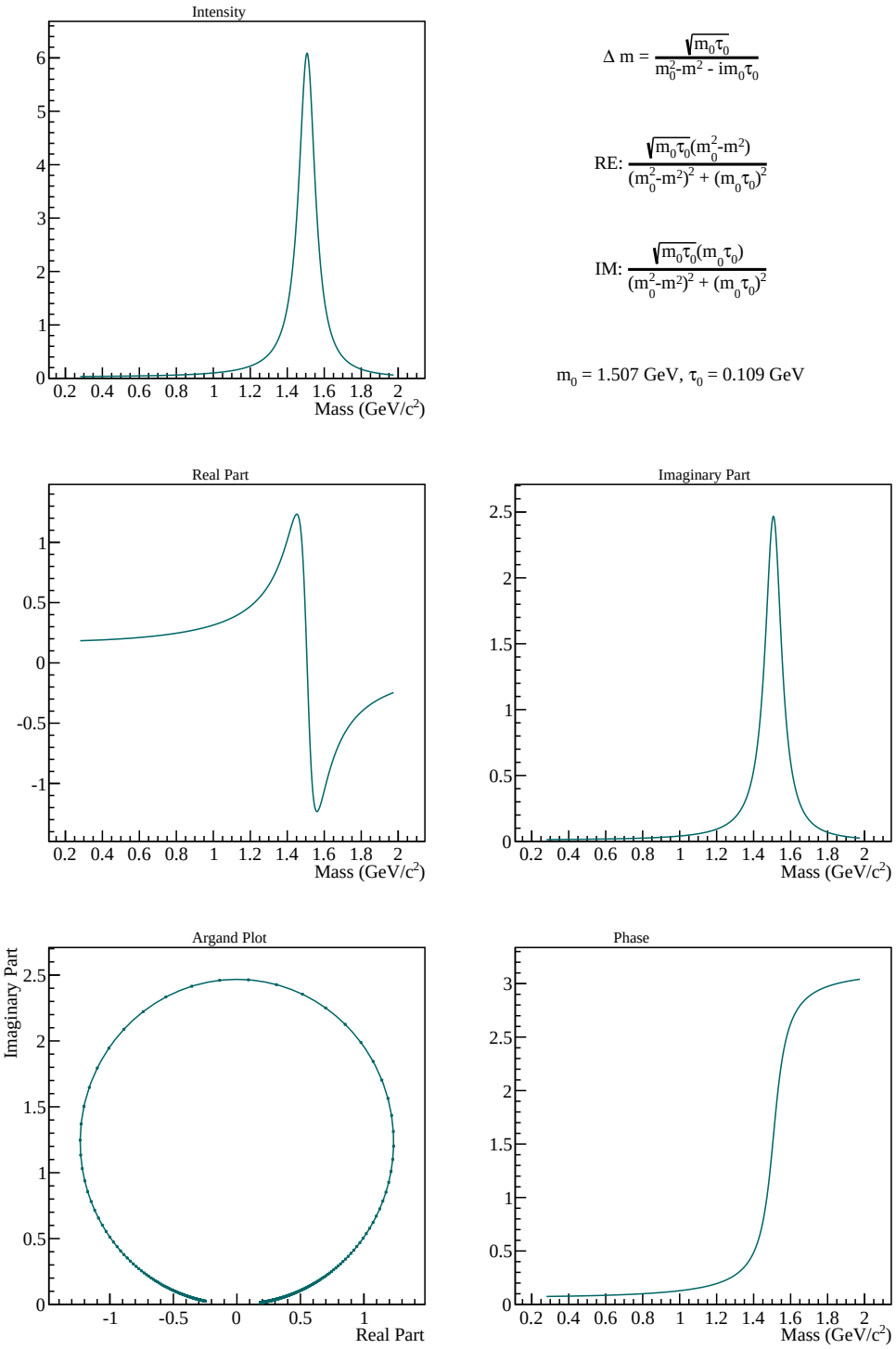

Figure C.6 Parametrisation of the $f_0(1500)$ amplitude.

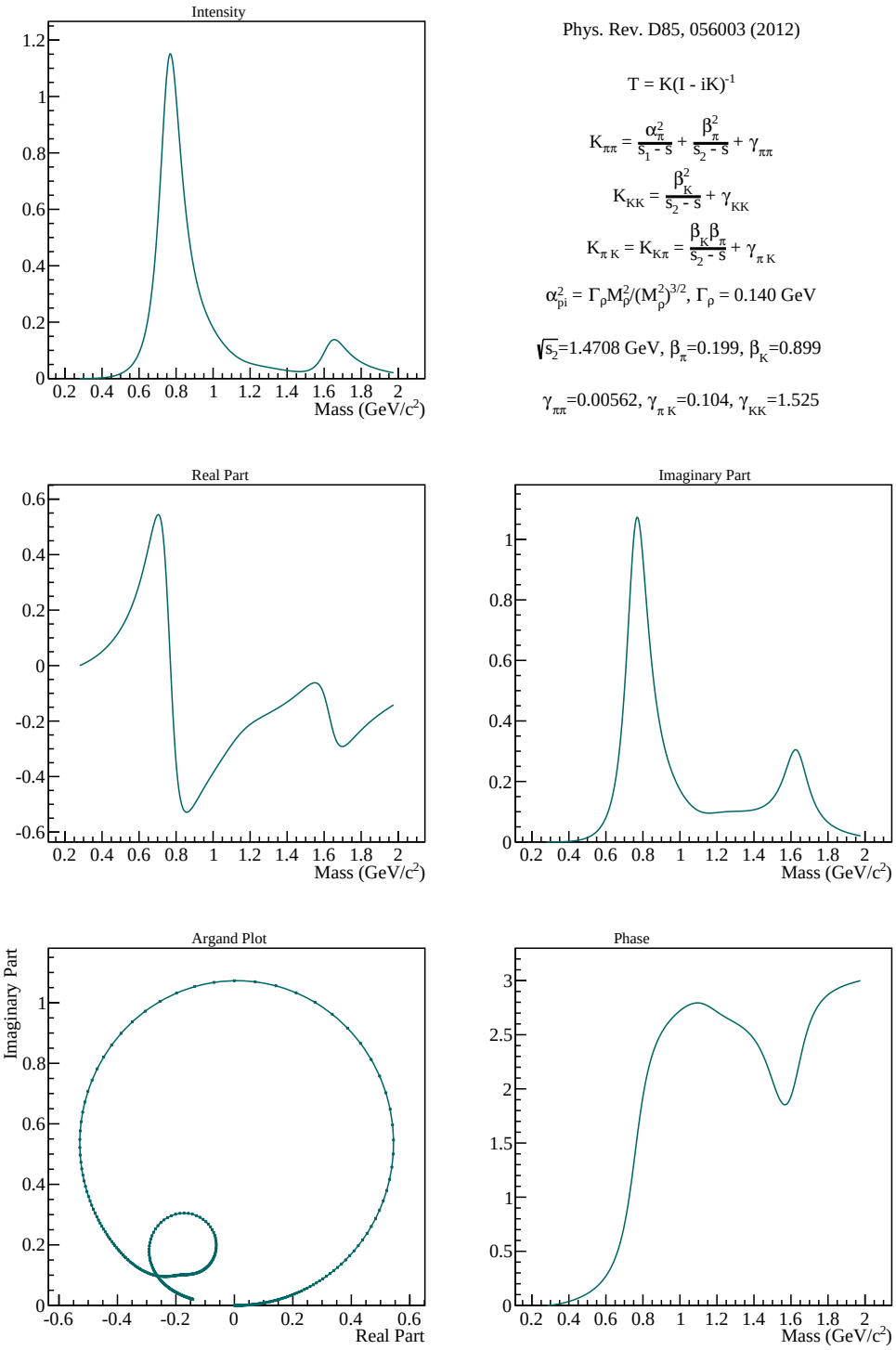

Figure C.7 $(\pi\pi)_P$ wave parametrisation. Based on the K-matrix fit, described in [GMSS12].

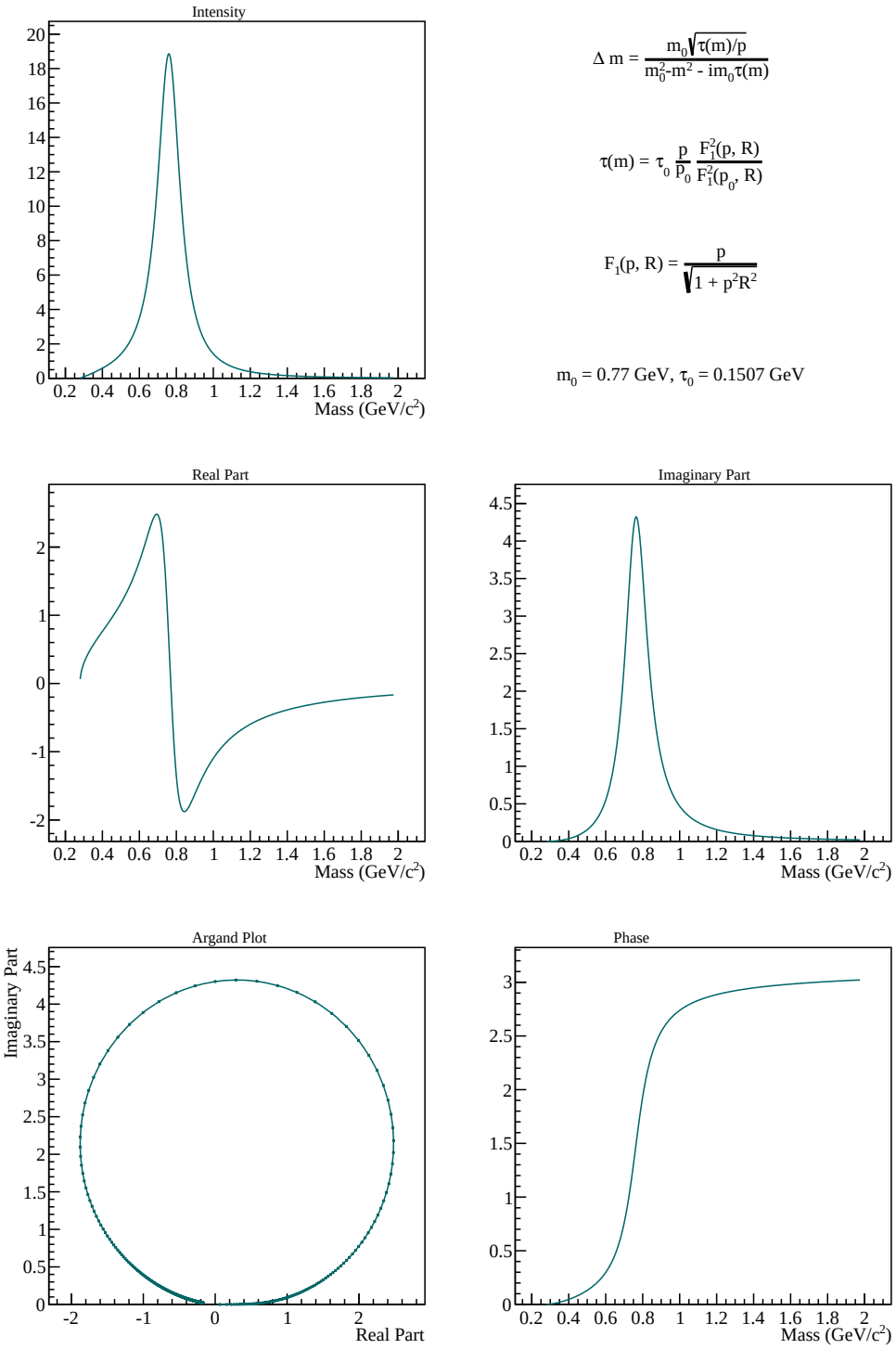

Figure C.8 Parametrisation of the $\rho(770)$ amplitude with reduced phase space.

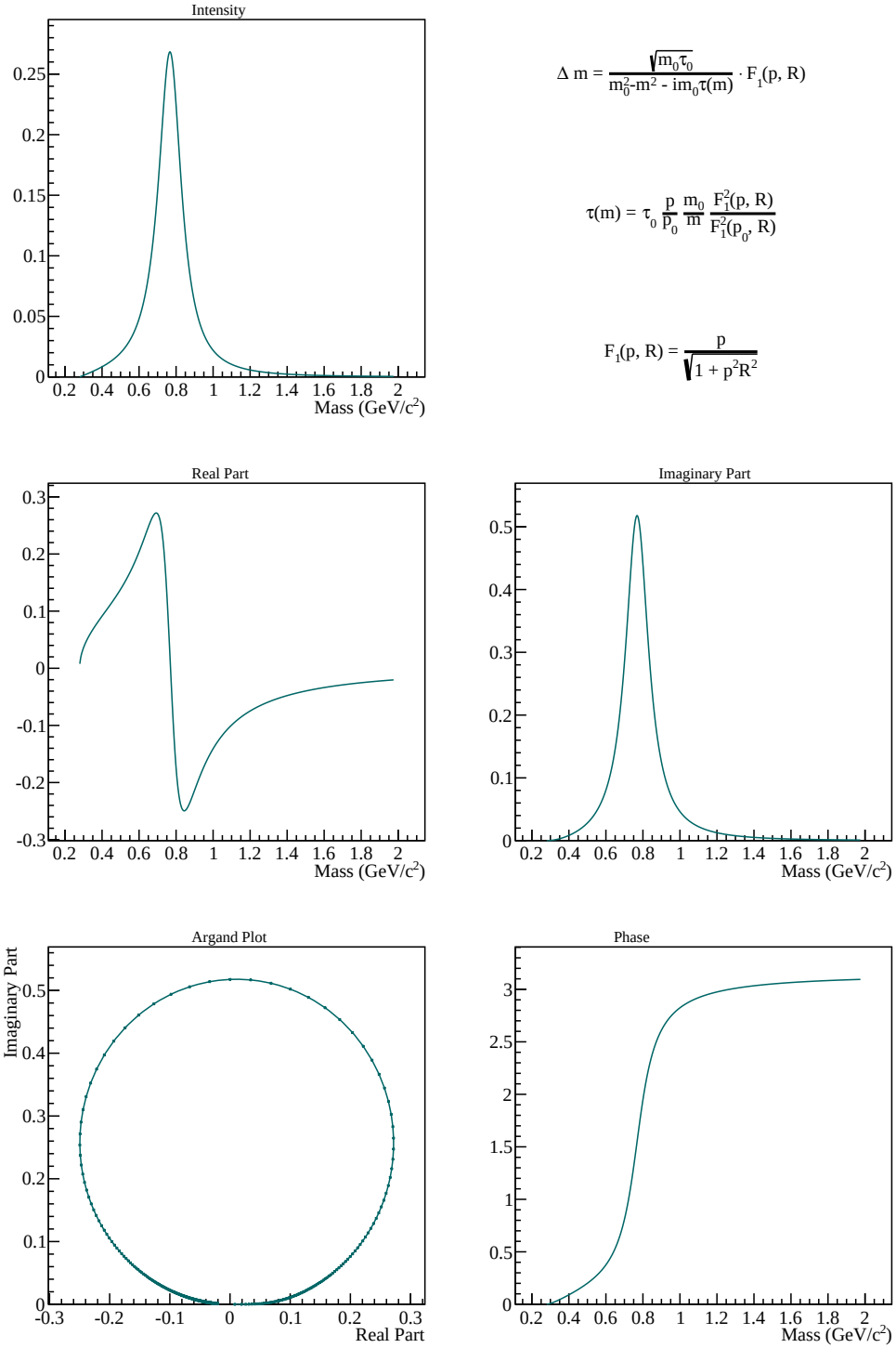

$$\Delta m = \frac{\sqrt{m_0 \tau_0}}{m_0^2 - m^2 - i m_0 \tau(m)} \cdot F_1(p, R)$$

$$\tau(m) = \tau_0 \frac{p}{p_0} \frac{m_0}{m} \frac{F_1^2(p, R)}{F_1^2(p_0, R)}$$

$$F_1(p, R) = \frac{p}{\sqrt{1 + p^2 R^2}}$$

Figure C.9 Parametrisation of the $\rho(770)$.

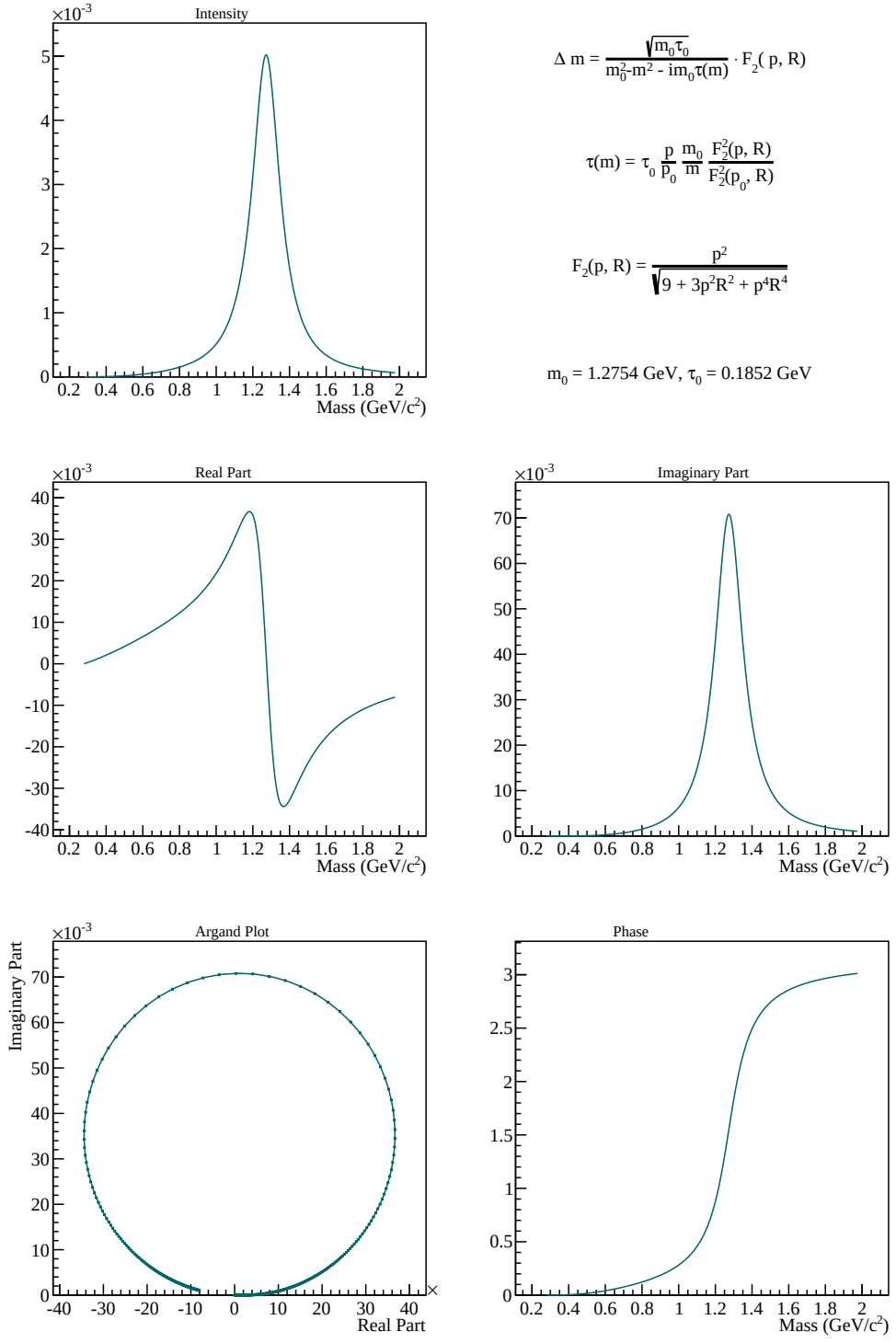

Figure C.10 Parametrisation of the $f_2(1270)$ amplitude.

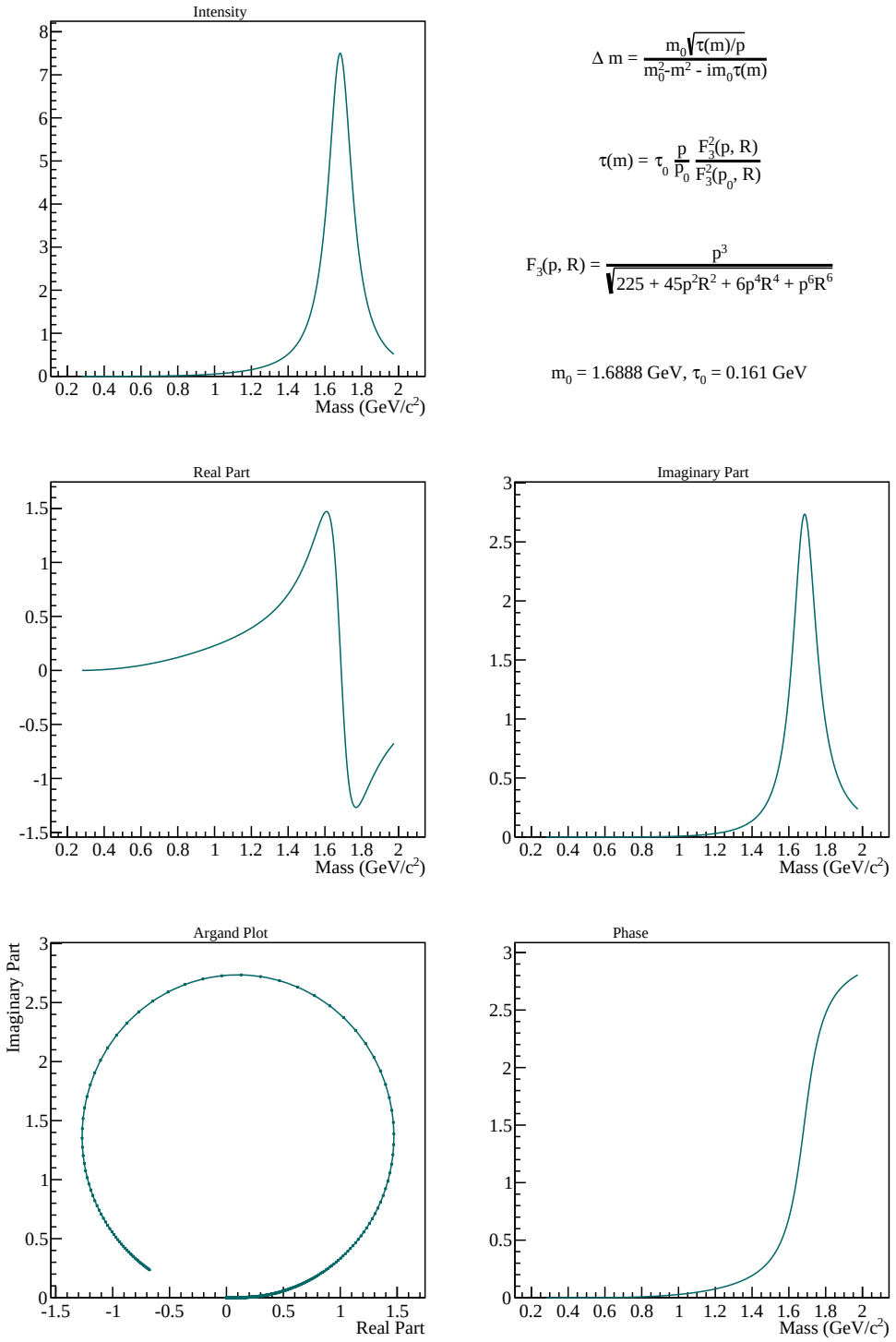

Figure C.11 Parametrisation of the $\rho_3(1690)$ amplitude with reduced phase space.

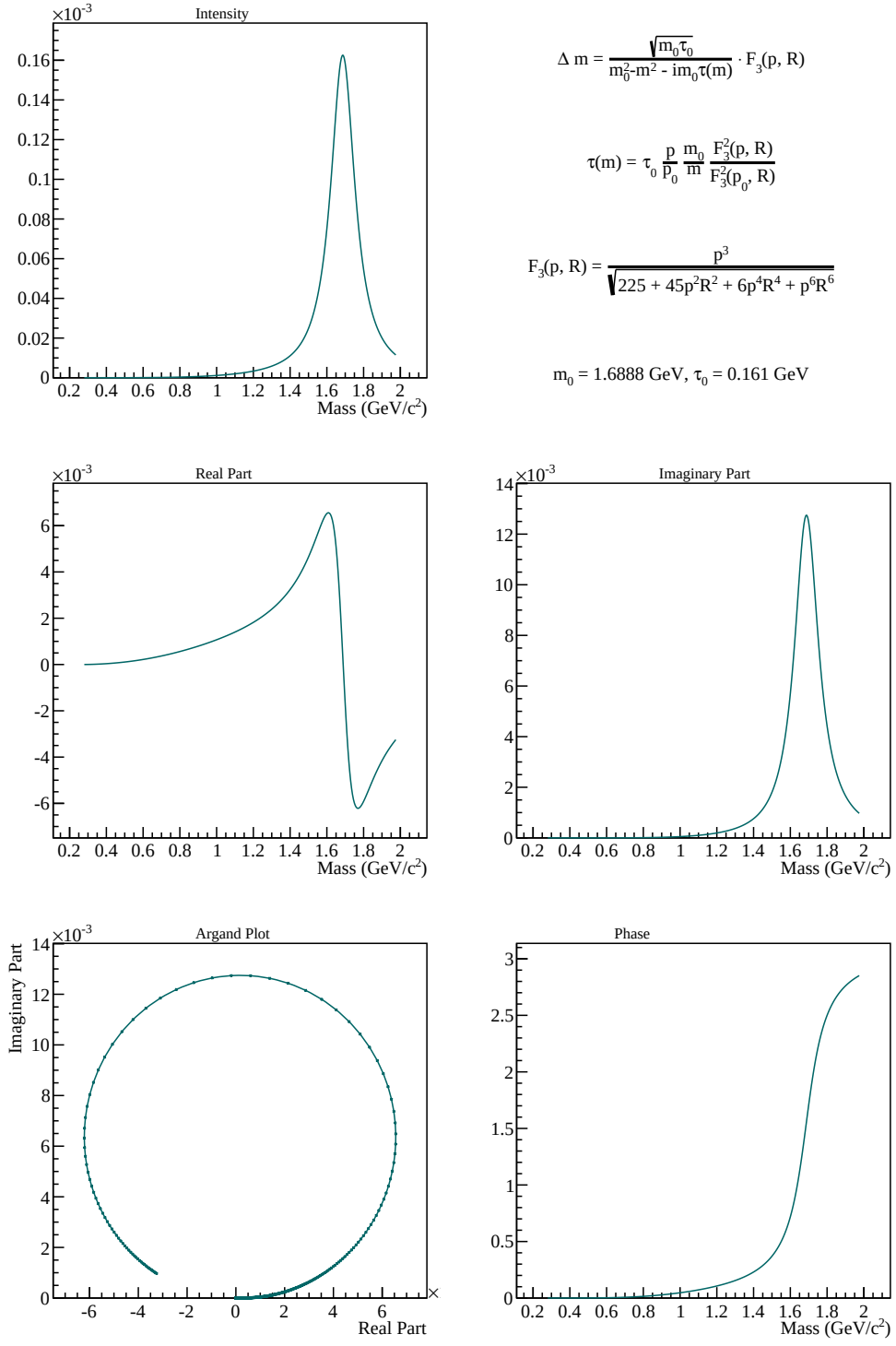

Figure C.12 Parametrisation of the $\rho_3(1690)$ amplitude.

Appendix D

Phase Space and Reconstruction

In the following there is a short instruction how the phase space events for the sudy of the geometrical acceptance were created.

- Use the corresponding beam file (`ROOT` tree with beam and vertex information)
  - Smear beam mmomentum and vertex, without destroying correlation
- Create mass of particle X randomly in the desired mass range
- Create lab angles ϕ and ϑ of X
  - For ϕ: Create ϕ randomly and isotropic between 0 and π
  - For ϑ: Use fit function of the data t'-spectrum as input
  - For small angles: $\vartheta \sim \sqrt{\frac{t-(\frac{m_X^2-m_a^2}{2E_{\text{beam}}})^2}{{E_{\text{beam}}}^2}}$
- Get recoil energy and energy of particle X
  - $E_{\text{recoil}} = \frac{t+m_{\text{recoil}}^2+m_{\text{target}}^2}{2m_{\text{target}}}$
  - $E_X = E_{\text{beam}} + E_{\text{target}} - E_{\text{recoil}}$
- Based on this information create LV_X and rotate the LorentzVector into the production plane (ϕ is symmetric to the beam axis not to the z-axis)
- Put LV_X to `GenBod` and create phase-space decay into n particles

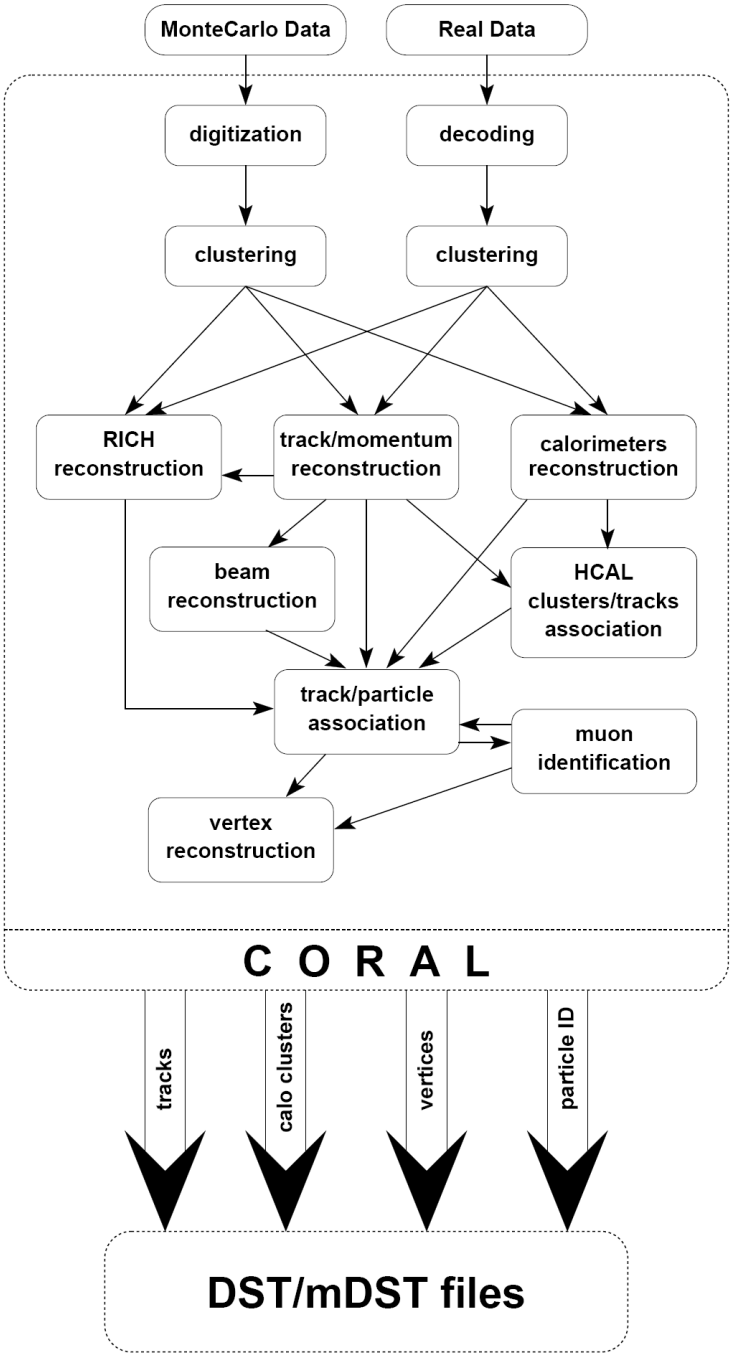

Figure D.1 Schematics of the CORAL reconstruction process.

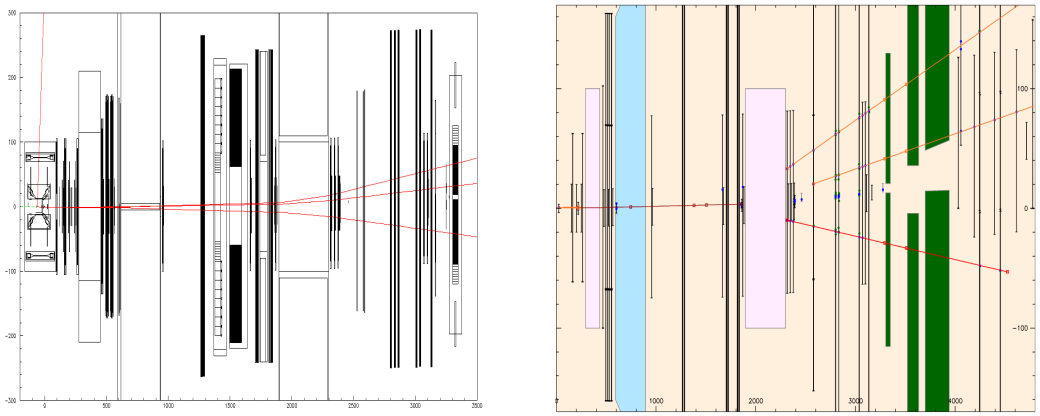

(a) **(b)**

Figure D.2 comGEANT output of a phase space generated three pion event without any physical interactions traversing the spectrometer (a), CORAL reconstruction of the corresponding event (b).

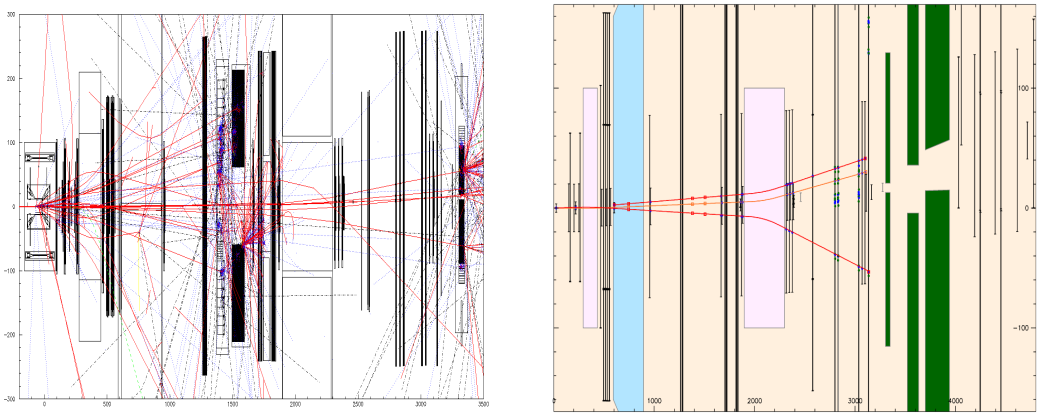

(a) **(b)**

Figure D.3 comGEANT output of a phase space generated three pion event with all relevant physical interactions traversing the spectrometer (a), CORAL reconstruction of the corresponding event (b)

Appendix E

Intensities of Further Partial Waves

E.1 Spin Totals

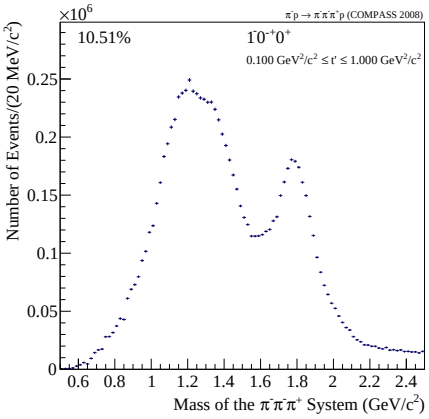

(a)

Figure E.1 Coherent sum of all amplitudes with $J^{PC}M^{\varepsilon} = 0^{-+}0^{+}$ (a).

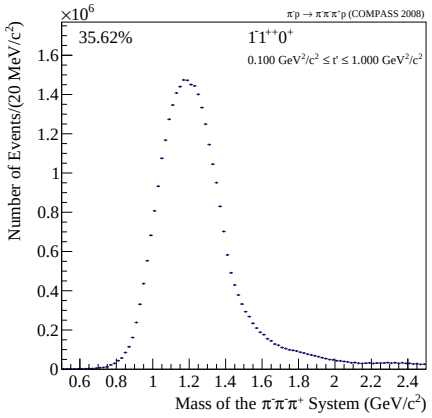

(a)

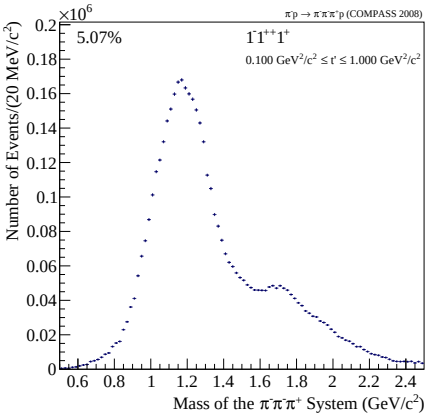

(b)

Figure E.2 Coherent sum of all amplitudes with $J^{PC}M^{\varepsilon} = 1^{++}0^+$ (a) and $1^{++}1^+$ (b).

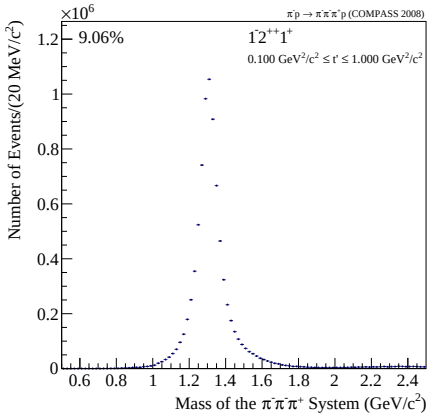

(a)

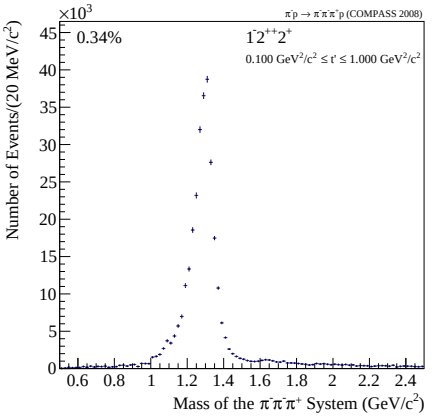

(b)

Figure E.3 Coherent sum of all amplitudes with $J^{PC}M^{\varepsilon} = 2^{++}1^+$ (a) and $2^{++}2^+$ (b).

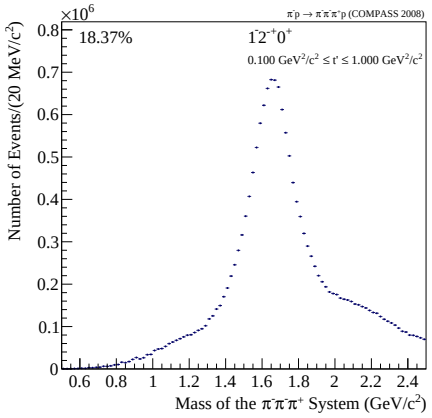

(a)

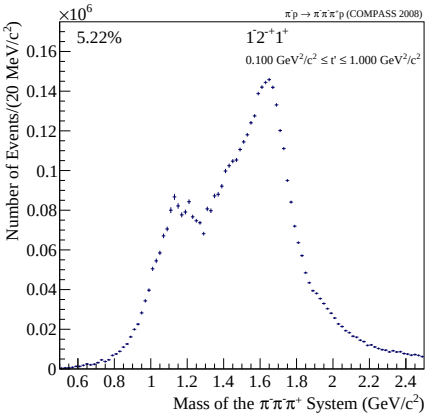

(b)

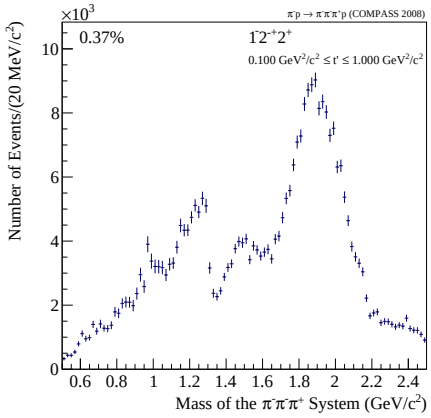

(a)

Figure E.3 Coherent sum of all amplitudes with $J^{PC}M^{\varepsilon} = 2^{-+}0^{+}$ (a), $2^{-+}1^{+}$ (b) and $2^{-+}2^{+}$ (c).

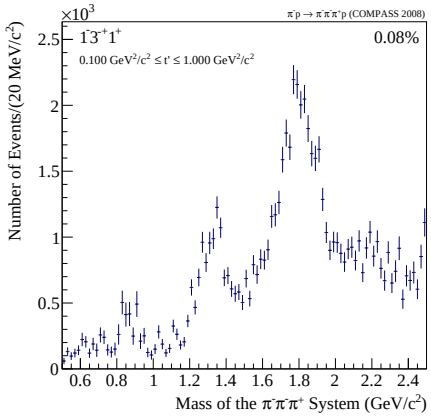

(b)

Figure E.3 Coherent sum of all amplitudes with $J^{PC}M^{\varepsilon} = 3^{-+}1^{+}$ (a).

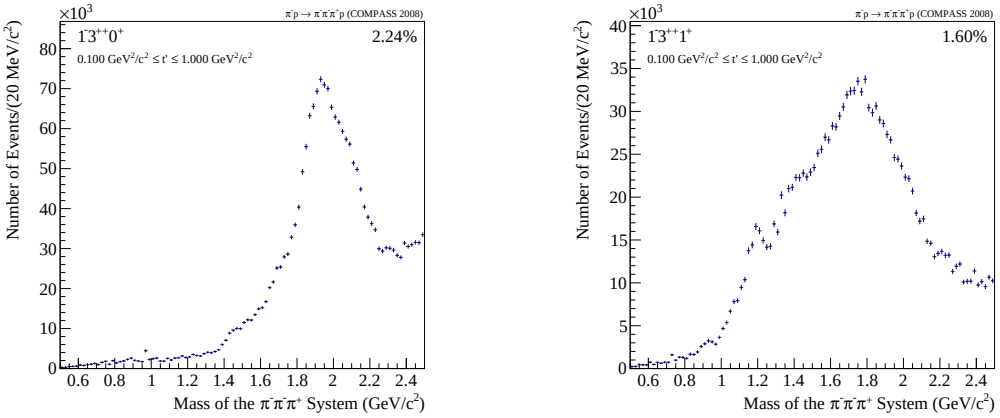

(a) **(b)**

Figure E.4 Coherent sum of all amplitudes with $J^{PC}M^{\varepsilon} = 3^{++}0^{+}$ (a) and $3^{++}1^{+}$ (b).

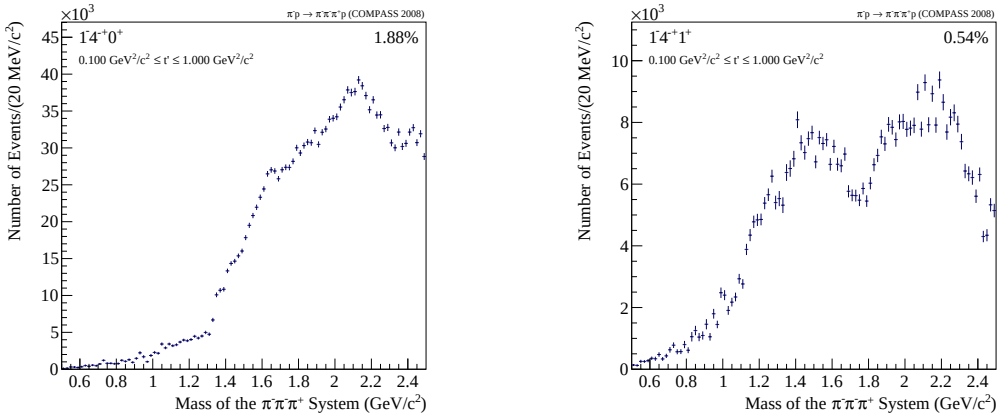

(a) **(b)**

Figure E.5 Coherent sum of all amplitudes with $J^{PC}M^{\varepsilon} = 4^{-+}0^+$ (a) and $4^{-+}1^+$ (b).

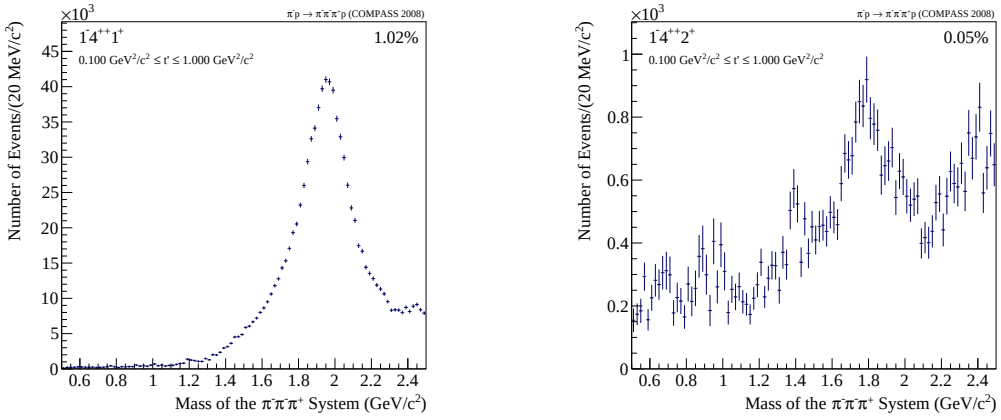

(a) **(b)**

Figure E.6 Coherent sum of all amplitudes with $J^{PC}M^{\varepsilon} = 4^{++}1^+$ (a) and $4^{++}2^+$ (b).

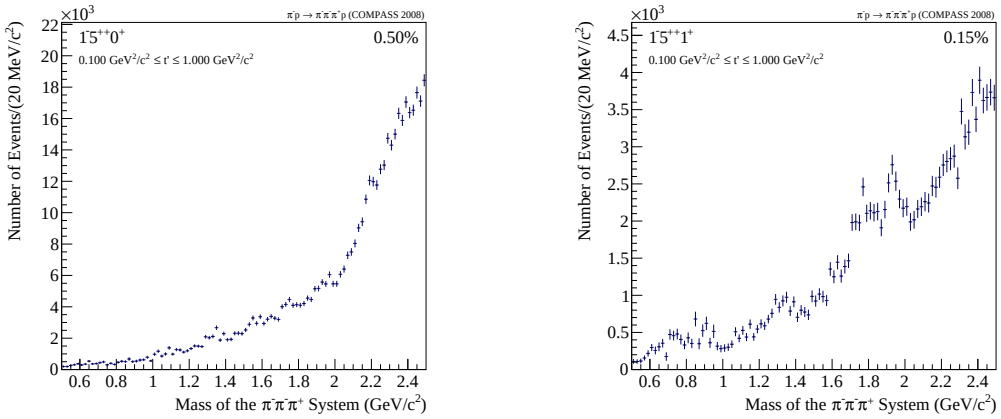

(a) **(b)**

Figure E.7 Coherent sum of all amplitudes with $J^{PC}M^{\varepsilon} = 5^{++}0^+$ (a) and $5^{++}1^+$ (b).

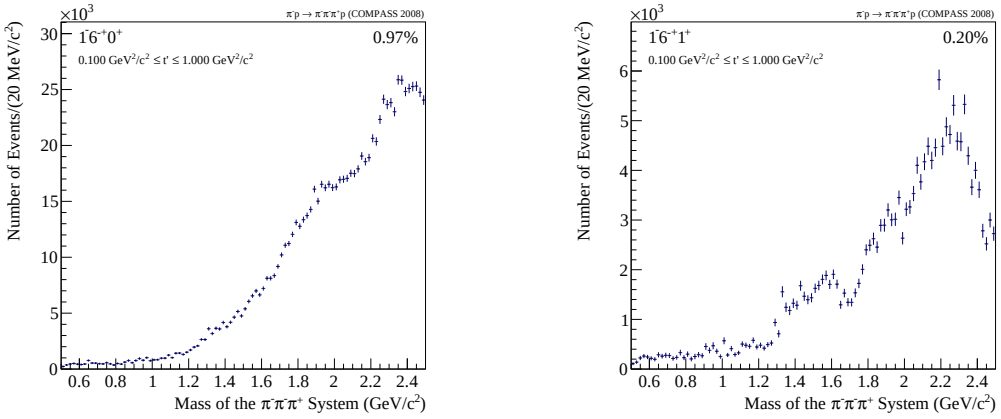

(a) **(b)**

Figure E.8 Coherent sum of all amplitudes with $J^{PC}M^{\varepsilon} = 6^{-+}0^{+}$ (a) and $6^{-+}1^{+}$ (b).

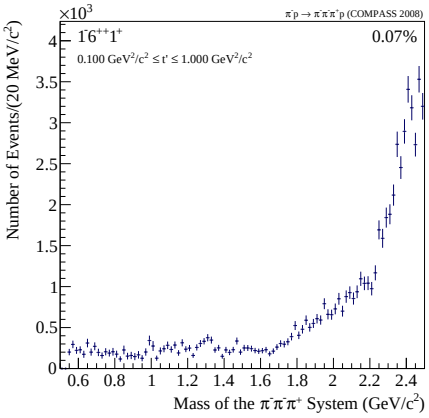

(a)

Figure E.9 Coherent sum of all amplitudes with $J^{PC}M^{\varepsilon} = 6^{++}1^{+}$ (a).

Appendix F

Further Fit Results of the Amplitude Dependence on $m_{3\pi}$

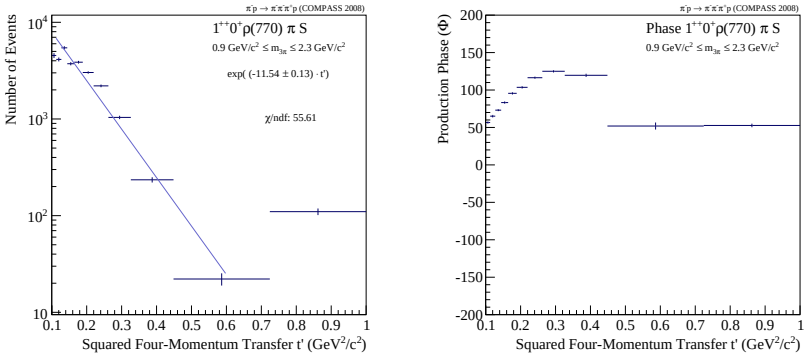

(a) **(b)**

Figure F.1 Fit result for the $1^{++}0^{+}\rho\pi S$ partial wave based on the model listed in Tab. 8.2. The t' dependence of tha $a_1(1910)$ is shown in (a) and the corresponding production phase (b).

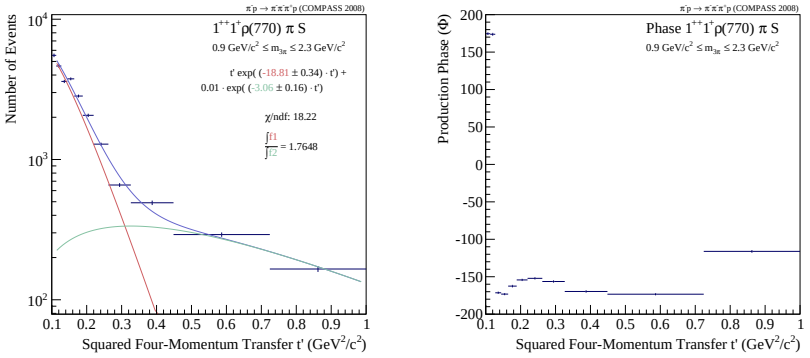

(a) **(b)**

Figure F.2 Fit result for the $1^{++}1^{+}\rho\pi S$ partial wave based on the model listed in Tab. 8.2. The t' dependence of the $a_1(1910)$ is shown in (a) and the corresponding production phase (b).

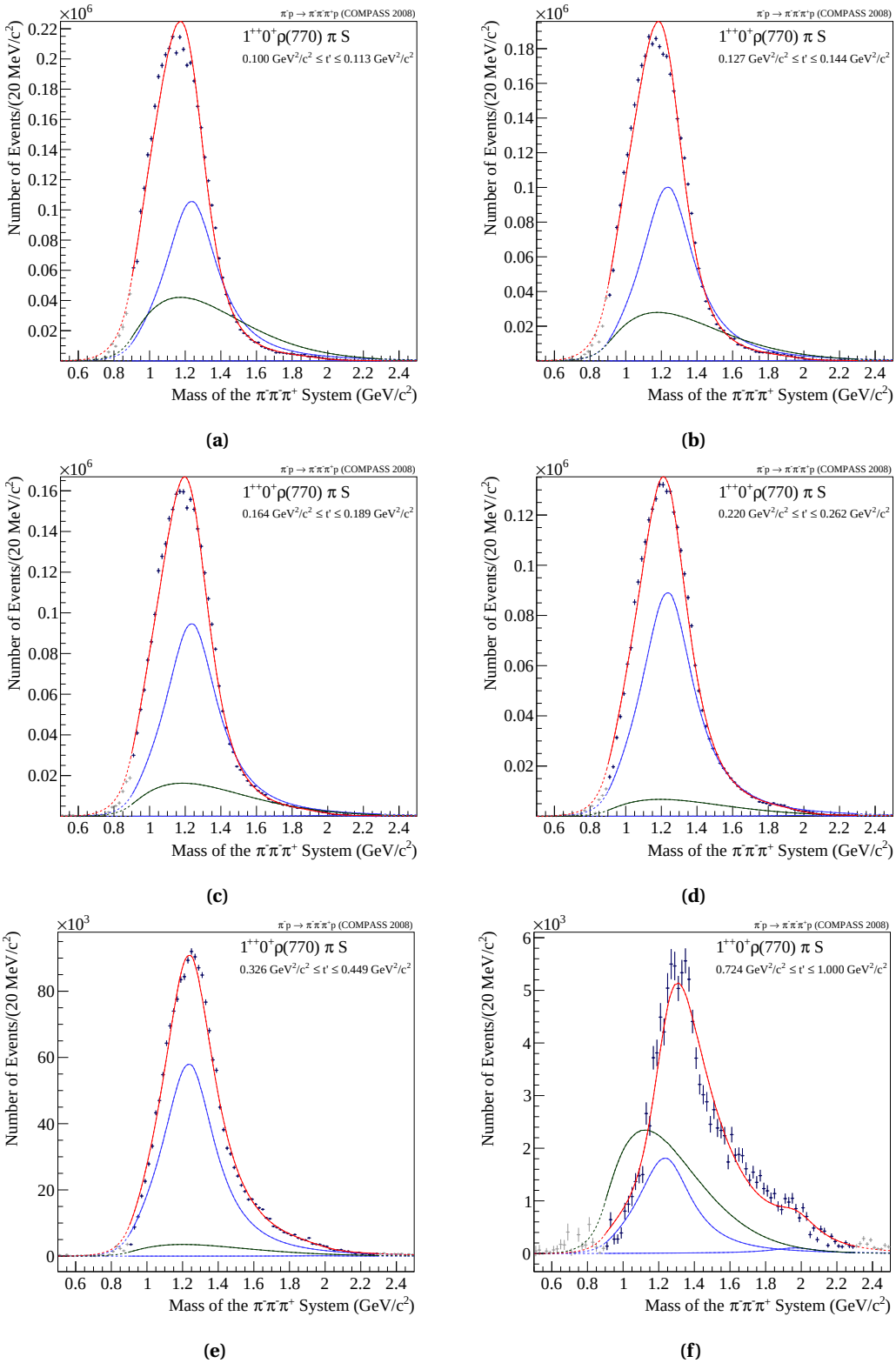

Figure F.3 Fit result for the $1^{++}0^+\rho\pi S$ partial wave based on the model listed in Tab. 8.2 for certain t' bins.

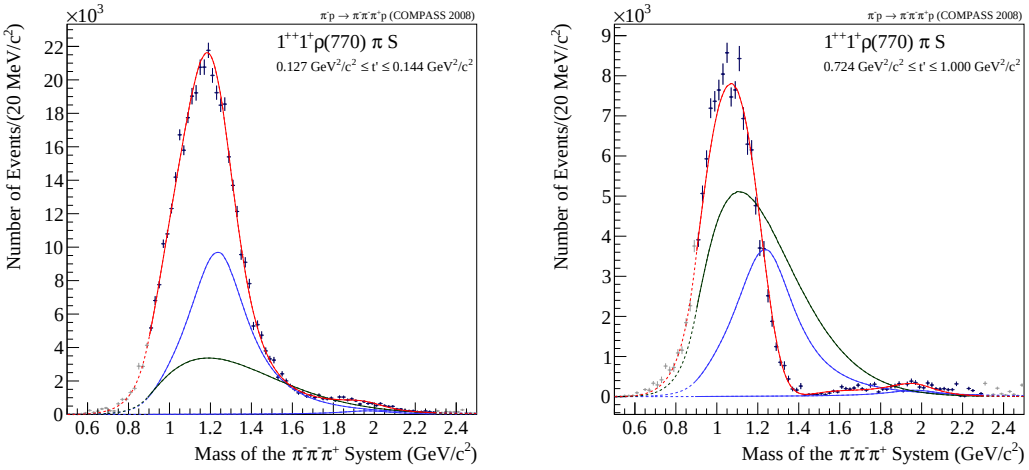

(a) **(b)**

Figure F.4 Fit result for the $1^{++}1^+\rho\pi S$ partial wave based on the model listed in Tab. 8.2 for selected t' bins.

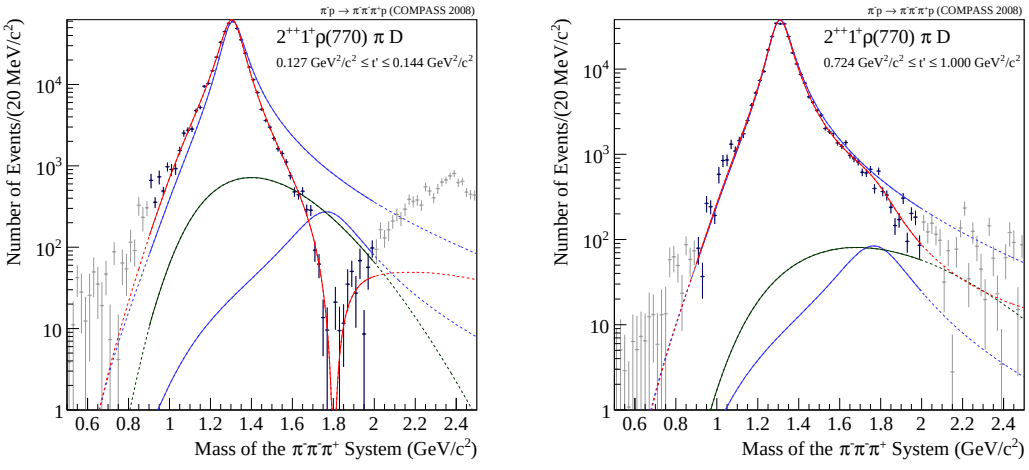

(a) **(b)**

Figure F.5 Fit result for the $2^{++}1^+\rho\pi D$ partial wave based on the model listed in Tab. 8.4 for selected t' bins.

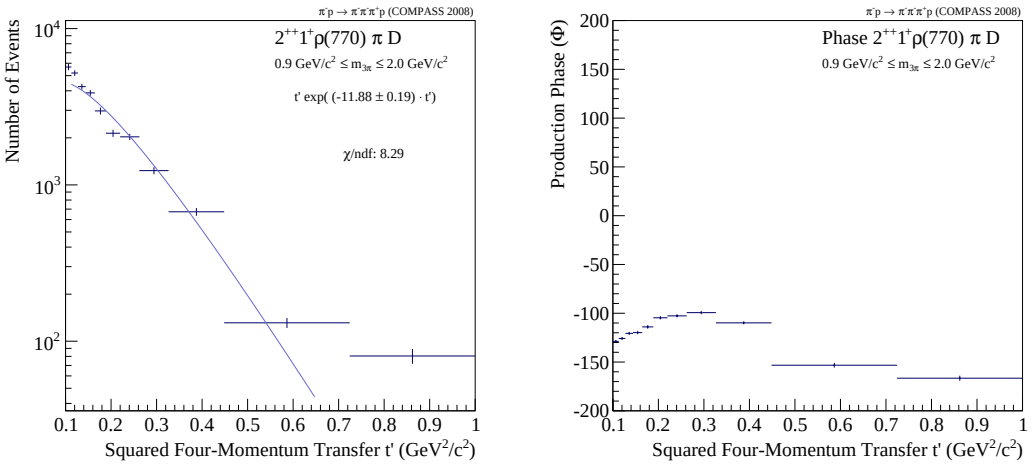

(a) **(b)**

Figure F.6 Fit result for the $2^{++}1^{+}\rho\pi D$ partial wave based on the model listed in Tab. 8.4. The t' dependence of the $a_2(1700)$ is shown in (a) and the corresponding production phase (b).

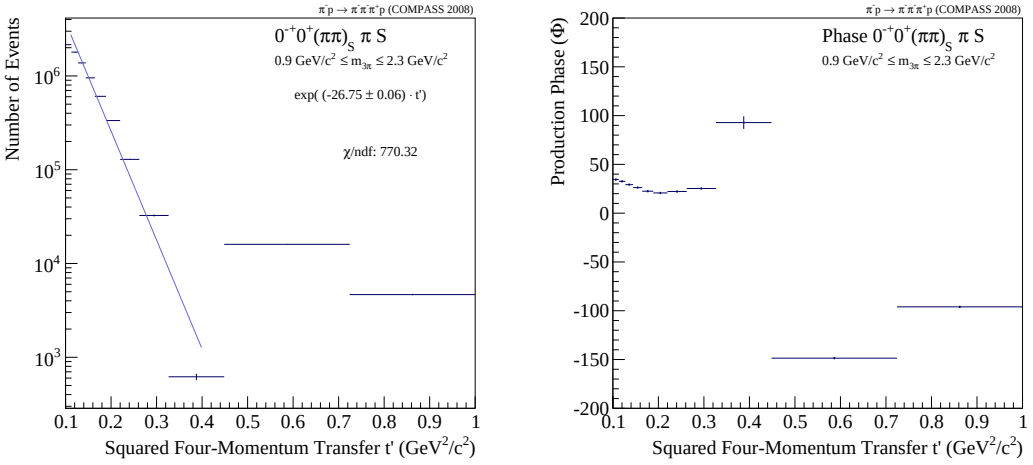

(a) **(b)**

Figure F.7 Fit result for the $0^{-+}0^{+}(\pi\pi)_S\pi S$ partial wave based on the model listed in Tab. 8.6. The t' dependence of the non-resonant contribution is shown in (a) and the corresponding production phase (b).

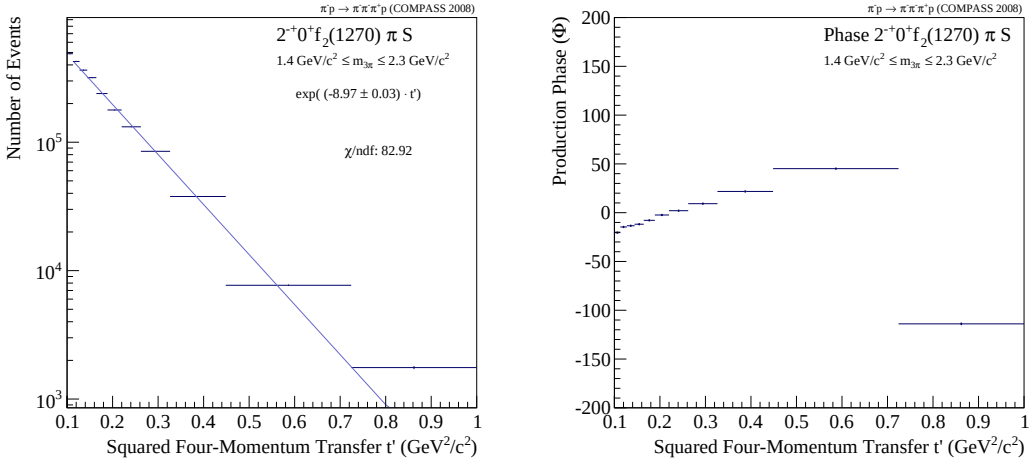

(a) **(b)**

Figure F.8 Fit result for the $2^{-+}0^{+}f_2(1270)\pi S$ partial wave based on the model listed in Tab. 8.8. The t' dependence of the non-resonant is shown in (a) and the corresponding production phase (b).

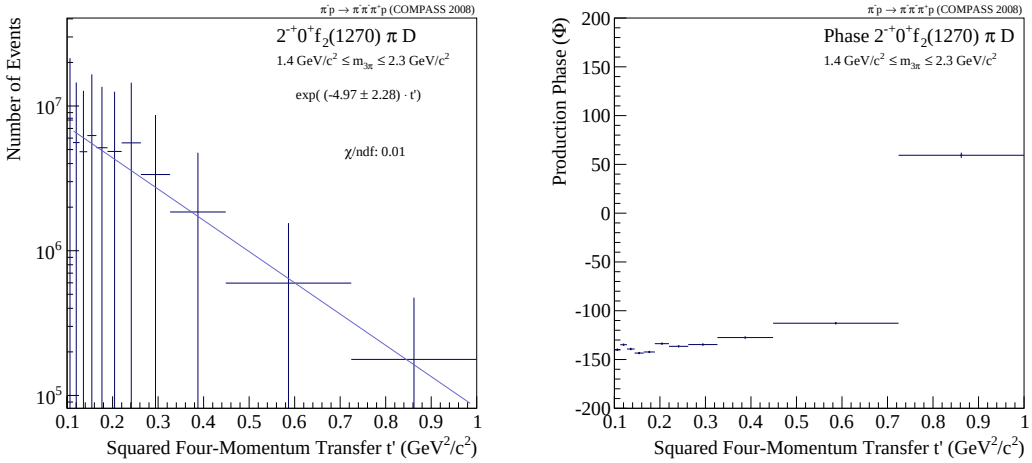

(a) **(b)**

Figure F.9 Fit result for the $2^{-+}0^{+}f_2(1270)\pi D$ partial wave based on the model listed in Tab. 8.8. The t' dependence of the non-resonant is shown in (a) and the corresponding production phase (b).

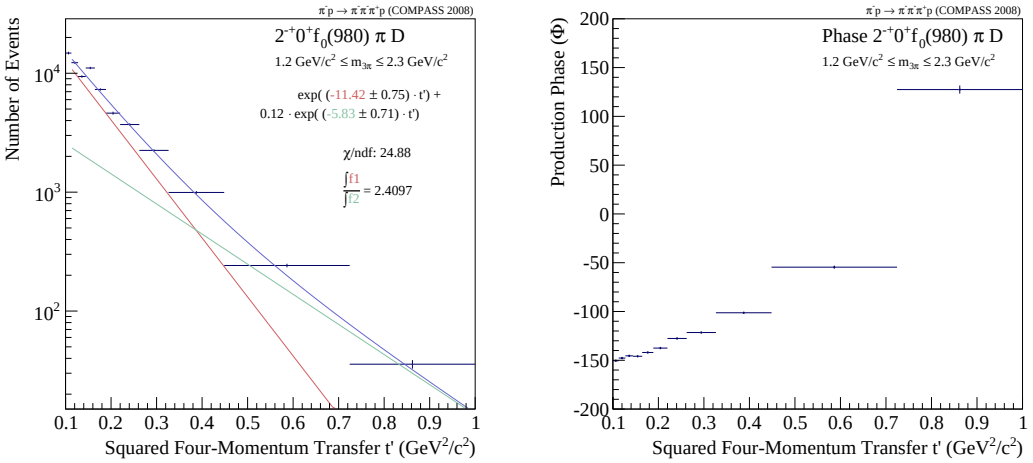

(a) **(b)**

Figure F.10 Fit result for the $2^{-+}0^{+}f_0(980)\pi D$ partial wave based on the model listed in Tab. 8.8. The t' dependence of the non-resonant is shown in (a) and the corresponding production phase (b).

List of Figures

List of Tables

Bibliography

[A+94] S. Abatzis et al. Observation of a narrow scalar meson at 1450-MeV in the reaction p p → p(f) (pi+ pi- pi+ pi-) p(s) at 450-GeV/c using the CERN Omega Spectrometer. *Phys.Lett.*, B324:509–514, 1994. *cited in 2.1.1 (p. 21)*

[AAA+10] M. G. Alekseev, V. Yu. Alexakhin, Yu. Alexandrov, G. D. Alexeev, A. Amoroso, A. Austregesilo, B. Badełek, F. Balestra, and ... Ball. Observation of a $J^{PC} = 1^{-+}$ exotic resonance in diffractive dissociation of 190 gev/c π^- into $\pi^-\pi^-\pi^+$. *Phys. Rev. Lett.*, 104:241803, Jun 2010. *cited in 1.4.2 (p. 15), 1.3d (p. 16), 5.2 (p. 66), 7.3 (p. 110), 7.3.2 (p. 119), 7.5.4 (p. 138),* **??** *(p. 140)*

[ABB95] Yu A Alexandrov, F Balestra, and M Beck. Cheops: charm experiment with omnipurpose setup. Technical Report CERN-SPSLC-95-22. SPSLC-I-202, CERN, Geneva, 1995. *cited in 3 (p. 27)*

[ABB+96] D.V. Amelin, E.B. Berdnikov, S.I. Bityukov, G.V. Borisov, Yu.P. Gouz, et al. Study of diffractive reaction pi- A -> eta eta pi- A at the momentum P(pi-) = 37-GeV/c. *Phys.Atom.Nucl.*, 59:976–981, 1996. *cited in 1.4.1 (p. 14)*

[ABB+01] A.V. Anisovich, C.A. Baker, C.J. Batty, D.V. Bugg, V.A. Nikonov, A.V. Sarantsev, V.V. Sarantsev, and B.S. Zou. Study of $\bar{p}p \to \eta\eta\pi^0\pi^0$ in flight. *Physics Letters B*, 500(3–4):222 – 231, 2001. *cited in 1.4.1 (p. 14)*

[Ach00] N.N. Achasov. On nature of scalar a(0)(980) and f(0)(980) mesons. *Nucl.Phys.*, A675:279C–284C, 2000. *cited in 9 (p. 200)*

[ACJ+74] G. Ascoli, R. Cutler, L.M. Jones, U. Kruse, T. Roberts, et al. Deck-model calculation of pi- p -> pi- pi+ pi- p. *Phys.Rev.*, D9:1963–1979, 1974. *cited in 1.4.1 (p. 14), 5.4 (p. 73), 7.3.2 (p. 112), 7.3.2 (p. 114), 8.2.1 (p. 173)*

[ADD+06] P. Abbon, E. Delagnes, H. Deschamps, F. Kunne, S. Gerasimov, B. Ketzer, I. Konorov, N. Kravtchuk, A. Magnon, D. Neyret, S. Panebianco, S. Paul, P. Rebourgeard, and F. Tessaroto. Fast readout of the compass rich csi-mwpc photon chambers. *Nuclear Instruments and Methods in Physics Research, Section A: Accelerators, Spectrometers, Detectors and Associated Equipment*, 567(1 SPEC. ISS.):104–106, 2006. Cited By (since 1996):10. *cited in 4.1.2 (p. 41)*

[AJWW73] G. Ascoli, L.M. Jones, B. Weinstein, and H.W. Wyld. Partial-wave analysis of the deck amplitude for pi n -> pi pi pi n. *Phys.Rev.*, D8:3894–3919, 1973. *cited in 1.4.1 (p. 14)*

[Ame] D.V. et all Amelin. Investigation of hybrid states in the ves experiment at the institute for high energy physics (protvino). *Physics of Atomic Nuclei*, 68(3):359–371. *cited in 1.4.1 (p. 12), 1.4.2 (p. 15), 5 (p. 105)*

[AMP87] K. L. Au, D. Morgan, and M. R. Pennington. Meson dynamics beyond the quark model: Study of final-state interactions. *Phys. Rev. D*, 35:1633–1664, Mar 1987. *cited in 6.4.3 (p. 82),* **??** *(p. 84),* **??** *(p. 84), 7.6.1 (p. 147), C.1 (p. 216), C.2 (p. 217), C.3 (p. 218), 9.1 (p. 246)*

[Ams98] Claude Amsler. Proton - anti-proton annihilation and meson spectroscopy with the crystal barrel. *Rev.Mod.Phys.*, 70:1293–1340, 1998. *cited in 1.4.2 (p. 15)*

[Asn03] D. Asner. Charm Dalitz plot analysis formalism and results: Expanded RPP-2004 version. 2003. *cited in 6.4.1 (p. 81)*

[Aus07] Alexander Austregesilo. Commissioning and performance of a prototype pixelgem detector for compass. Master's thesis, Technische Universität München, 2007. *cited in 4.1.2 (p. 38), 9.1 (p. 261)*

[Aus13] Alexander Austregesilo. Central Production of Two-Pseudoscalar Final States at COMPASS. 2013. *cited in 5.1.7 (p. 59)*

[AW75] G. Ascoli and H. W. Wyld. Unitary states for three pions. *Phys. Rev. D*, 12:43–58, Jul 1975. *cited in 7.5.1 (p. 131)*

[B+93] G.M. Beladidze et al. Study of pi- N -> eta pi- N and pi- N -> eta-prime pi- N reactions at 37-GeV/c. *Phys.Lett.*, B313:276–282, 1993. *cited in 1.4.2 (p. 15)*

[B+12] J. Beringer et al. Review of Particle Physics (RPP). *Phys.Rev.*, D86:010001, 2012. *cited in 1.2 (p. 13), 1.4.1 (p. 14), 5.1.8 (p. 60), 7.3.2 (p. 113), 7.5.1 (p. 131), 7.5.5 (p. 143), 7.5.5 (p. 144), 8.1 (p. 166), 8.2.3 (p. 189), 9 (p. 199), 9 (p. 201), 9.1 (p. 202), 9.1 (p. 248), 9.1 (p. 249)*

[Bar90] Roger J. Barlow. Extended maximum likelihood. *Nucl.Instrum.Meth.*, A297:496–506, 1990. *cited in 7.1 (p. 87)*

[Bar00] Ted Barnes. Exotic mesons, theory and experiment. *Acta Phys.Polon.*, B31:2545–2556, 2000. *cited in 1.3 (p. 10), 1.3 (p. 10), 1.4.2 (p. 15)*

[BB77] J.L. Basdevant and Edmond L. Berger. Unitary Coupled-Channel Analysis of Diffractive Production of the a1 Resonance. *Phys.Rev.*, D16:657, 1977. *cited in 7.5.5 (p. 144), 8.2.1 (p. 175), 9 (p. 200)*

[BBC+02] S. Bachmann, A. Bressan, M. Capeans, M. Deutel, S. Kappler, et al. Discharge mechanisms and their prevention in the gas electron multiplier (GEM). *Nucl.Instrum.Meth.*, A479:294–308, 2002. *cited in 4.1.1 (p. 37)*

[BBR+99] S. Bachmann, A. Bressan, L. Ropelewski, F. Sauli, A. Sharma, et al. Charge amplification and transfer processes in the gas electron multiplier. *Nucl.Instrum.Meth.*, A438:376–408, 1999. *cited in 4.1.1 (p. 37)*

[BCdV83] T. Barnes, F.E. Close, and F. de Viron. {QQG} hybrid mesons in the {MIT} bag model. *Nuclear Physics B*, 224(2):241–264, 1983. *cited in 1.3 (p. 9)*

[bea] Table with ratio of produced beam particles at the t6 target. `http://gatignon.web.cern.ch/gatignon/M2compo.txt`. *cited in 3.2.1 (p. 29)*

[Bet07] S. Bethke. Experimental tests of asymptotic freedom. *Progress in Particle and Nuclear Physics*, 58(2):351 – 386, 2007. *cited in 1.1 (p. 8), 1.2 (p. 9)*

[BKT96] G Baum, J Kyynäräinen, and A Tripet. Compass: a proposal for a common muon and proton apparatus for structure and spectroscopy. Technical Report CERN-SPSLC-96-14. SPSLC-P-297, CERN, Geneva, 1996. *cited in 3 (p. 27)*

[Bop89] F. W. Bopp. *Kerne, Hadronen und Elementarteilchen*. Teubner Studienbuecher, 1989. ISBN 3-519-03068-3. *cited in 1.1.1 (p. 7)*

[Bow86] M.G. Bowler. The {A1} revisited. *Physics Letters B*, 182(3–4):400–404, 1986. *cited in ?? (p. 165), 8.1 (p. 166)*

[BP10] V. Barone and E. Predazzi. *High-Energy Particle Diffraction*. Springer Verlag, 2010. ISBN 978-642-07567-4. *cited in 2 (p. 17), 2.1 (p. 19), 1 (p. 20)*

[Bre81] J. J. Brehm. Final-state interactions in a system of three pions. *Phys. Rev. D*, 23:1194–1206, Mar 1981. *cited in 1.4.1 (p. 14), 7.5.1 (p. 131), 9.1 (p. 203)*

[BW36] G. Breit and E. Wigner. Capture of slow neutrons. *Phys. Rev.*, 49:519–531, Apr 1936. *cited in 6.4.1 (p. 81)*

[BW52] J.M. Blatt and V.F. Weisskopf. *Theoretical nuclear physics*. Wiley, 1952. *cited in 6.4.1 (p. 81)*

[CDH+64] Suh Urk Chung, Orin I. Dahl, Lyndon M. Hardy, Richard I. Hess, George R. Kalbfleisch, Janos Kirz, Donald H. Miller, and Gerald A. Smith. Analysis of the 1.0- to 1.4-bev π-ρ enhancement. *Phys. Rev. Lett.*, 12:621–625, Jun 1964. *cited in 1.4.1 (p. 14), 2.2.3 (p. 24)*

[CDH+02] S.U. Chung, K. Danyo, R.W. Hackenburg, C. Olchanski, J.S. Suh, et al. Exotic and q anti-q resonances in the pi+ pi- pi- system produced in pi- p collisions at 18-GeV/c. *Phys.Rev.*, D65:072001, 2002. *cited in 1.4.1 (p. 12), 1.4.1 (p. 13), 1.4.2 (p. 15), 1.3a (p. 16), 7.3.2 (p. 118), 7.4 (p. 122), 7.5.4 (p. 136), 7.5.4 (p. 139), ?? (p. 140), 9 (p. 200)*

[CEG+02] J. R. Cudell, V. V. Ezhela, P. Gauron, K. Kang, Yu. V. Kuyanov, S. B. Lugovsky, B. Nicolescu, and N. P. Tkachenko. Hadronic scattering amplitudes: Medium-energy constraints on asymptotic behavior. *Phys. Rev. D*, 65:074024, Mar 2002. *cited in 2.1.1 (p. 21), 2.1 (p. 22)*

[CER04] CERN. *oai:cds.cern.ch:585520. Workshop on Future Physics at COMPASS*, Geneva, 2004. CERN. distribution. *cited in 3.1 (p. 27)*

[CHS99] L. S. Celenza, Bo Huang, and C. M. Shakin. Covariant confinement model for the calculation of radial excitations of the pion. *Phys. Rev. C*, 59:1041–1058, Feb 1999. *cited in 1.4.1 (p. 14), 7.5.2 (p. 133)*

[Chu] Suh Urk Chung. private communication. *cited in 7.5.5 (p. 144), 9 (p. 200)*

[Chu96] S. U. Chung. Formulas for partial-wave analysis - version ii. Technical report, Brookhaven National Laboratory, 1996. BNL-QGS-93-05. *cited in 6.4.1 (p. 81)*

[CJJ+74] A. Chodos, R.L. Jaffe, K. Johnson, Charles B. Thorn, and V.F. Weisskopf. A New Extended Model of Hadrons. *Phys.Rev.*, D9:3471–3495, 1974. *cited in 1.3 (p. 9)*

[cola] COMPASS collaboration. Comgeant. `http://wwwcompass.cern.ch/compass/software/offline_old/comgeant/comgeant/`. *cited in 5.3 (p. 68)*

[colb] COMPASS collaboration. The compass setup for physics with hadron beams. to be published. *cited in 3 (p. 27), 3.5 (p. 31), 4.8 (p. 44), 9.1 (p. 242)*

[COMa] Official website of the compass experiment. `http://wwwcompass.cern.ch`. *cited in 3.1 (p. 27)*

[COMb] Overview of compass publications. `http://wwwcompass.cern.ch/compass/publications/papers`. *cited in 3.1 (p. 27)*

[CP97] Frank E. Close and Philip R. Page. Distinguishing hybrids from radial quarkonia. *Phys. Rev. D*, 56:1584–1588, Aug 1997. *cited in 7.5.2 (p. 133), 8.2.3 (p. 188), 8.2.3 (p. 189), 9 (p. 201)*

[CT75] S. U. Chung and T. L. Trueman. Positivity conditions on the spin density matrix: A simple parametrization. *Phys. Rev. D*, 11:633–646, Feb 1975. *cited in 6.1.2 (p. 76), 6.1.2 (p. 76), 7.1.2 (p. 89)*

[D+81] C. Daum et al. DIFFRACTIVE PRODUCTION OF 3 pi STATES AT 63-GeV AND 94-GeV. *Nucl.Phys.*, B182:269, 1981. *cited in 1.4.1 (p. 12), 1.4.1 (p. 13), 1.4.1 (p. 14), 2.2.3 (p. 24), 5.1.10 (p. 64), 5.15 (p. 65), 5.4 (p. 72), 5.4 (p. 73), 7.3.2 (p. 118), 7.5.3 (p. 134), 8.2.2 (p. 180), 8.2.4 (p. 196)*

[Dec64] Robert T. Deck. Kinematical interpretation of the first pi - rho resonance. *Phys.Rev.Lett.*, 13:169–173, 1964. *cited in 1.4.1 (p. 14), 2.2.3 (p. 24), 5.4 (p. 72)*

[DMS+06] A.R. Dzierba, R. Mitchell, E. Scott, P. Smith, M. Swat, et al. A Partial wave analysis of the pi- pi- pi+ and pi- pi0 pi0 systems and the search for a J**PC = 1-+ meson. *Phys.Rev.*, D73:072001, 2006. *cited in 1.4.1 (p. 13), 1.4.2 (p. 15), 1.3b (p. 16), 7.4 (p. 122), 7.5.4 (p. 140), ?? (p. 140)*

[DN09] Y.L. Dokshitzer and J. Nyiri. *Strong Interactions of Hadrons at High Energies - Gribov Lectures on Theoretical Physics.* Cambridge University Press, 2009. ISBN 978-0-521-85609-6. *cited in 2 (p. 17)*

[Dre14] Christian Dreisbach. Analysis of elastic scattering processes with hadron beams at compass. in preparation, Technische Universität München, 2014. *cited in 9.1 (p. 261)*

[DS06] Jozef Dudek and Adam Szczepaniak. The deck effect in pi n –> pi pi pi n. *AIP Conference Proceedings*, 814(1):587–591, 2006. *cited in 1.4.1 (p. 14), 7.3.2 (p. 116), 8.2.4 (p. 197)*

[Dud11] Jozef J. Dudek. The lightest hybrid meson supermultiplet in QCD. *Phys.Rev.*, D84:074023, 2011. *cited in 1.3 (p. 11), 1.2 (p. 11), 1.4.1 (p. 14), 1.4.1 (p. 14), 7.5.3 (p. 134), 8.2.4 (p. 197), 9 (p. 200)*

[ea] Rene Brun et al. Root | a data analysis framework. http://root.cern.ch/. *cited in 3.4 (p. 31)*

[ea80] Atherton H. W. et al. Precise measurements of particle production by 400 gev/c protons on beryllium targets. Technical Report Yellow Report 80-07, CERN, 1980. *cited in 3.2.1 (p. 29)*

[ea88] J. Ashman et al. A measurement of the spin asymmetry and determination of the structure function g1 in deep inelastic muon-proton scattering. *Physics Letters B*, 206(2):364 – 370, 1988. *cited in 3 (p. 27)*

[ea89] J. Ashman et al. An investigation of the spin structure of the proton in deep inelastic scattering of polarised muons on polarised protons. *Nuclear Physics B*, 328(1):1 – 35, 1989. *cited in 3 (p. 27)*

[ea05] M. Ablikim et al. Resonances in $j/\psi \to \phi\pi^-\pi^+$ and ϕk^+k^-. *Physics Letters B*, 607(3–4):243 – 253, 2005. *cited in 6.4.2 (p. 82), C.5 (p. 220), 9.1 (p. 246)*

[ea07] P. Abbon et al. The compass experiment at cern. *Nuclear Instruments and Methods in Physics Research Section A: Accelerators, Spectrometers, Detectors and Associated Equipment*, 577(3):455 – 518, 2007. *cited in 3 (p. 27), 4.1 (p. 36)*

[EH78] BRADLEY EFRON and DAVID V. HINKLEY. Assessing the accuracy of the maximum likelihood estimator: Observed versus expected fisher information. *Biometrika*, 65(3):457–483, 1978. *cited in 7.1.2 (p. 92)*

[F. 97] F. Sauli. A new concept for electron amplification in gas detectors. *Nucl. Inst. Methods*, A386, 1997. *cited in 4.1.1 (p. 37)*

[F+76] Stanley M. Flatte et al. Observation of the B Meson in K- p Interactions at 4.2-GeV/c. *Phys.Lett.*, B64:225, 1976. *cited in 6.4.2 (p. 82)*

[FGM72] Harald Fritzsch and Murray Gell-Mann. Current algebra: Quarks and what else? *eConf*, C720906V2:135–165, 1972. *cited in 1.2 (p. 8)*

[FGML73] H. Fritzsch, M. Gell-Mann, and H. Leutwyler. Advantages of the color octet gluon picture. *Physics Letters B*, 47(4):365 – 368, 1973. *cited in 1.2 (p. 8)*

[FJM+01] M.J. French, L.L. Jones, Q. Morrissey, A. Neviani, R. Turchetta, et al. Design and results from the APV25, a deep sub-micron CMOS front-end chip for the CMS tracker. *Nucl.Instrum.Meth.*, A466:359–365, 2001. *cited in 4.1.2 (p. 40)*

[FOW81] Mariana Frank, PatrickJ. O'Donnell, and Brenden Wong. Mesons in the bag model. *Zeitschrift für Physik C Particles and Fields*, 7(3):277–281, 1981. *cited in 1.3 (p. 9)*

[Gat] Lau Gatignon. private communication. M2 beam line liason physicist. *cited in 5.1.5 (p. 53)*

[GBG+64] Gerson Goldhaber, John L. Brown, Sulamith Goldhaber, John A. Kadyk, Benjamin C. Shen, and George H. Trilling. Evidence for a π-ρ interaction produced in the $\pi^+ p$ reaction at 3. 65 bev/*c*. *Phys. Rev. Lett.*, 12:336–340, Mar 1964. *cited in 1.4.1 (p. 14), 2.2.3 (p. 24)*

[gea] Geant3. `http://wwwasd.web.cern.ch/wwwasd/geant/`. *cited in 5.3 (p. 68)*

[Ger] S. Gerassimov. Phast, physics analysis tools for compass. `http://ges.home.cern.ch/ges/phast/index.html`. *cited in 3.4 (p. 31)*

[GJ64] K. Gottfried and John David Jackson. On the Connection between production mechanism and decay of resonances at high-energies. *Nuovo Cim.*, 33:309–330, 1964. *cited in 6.3 (p. 79)*

[GM56] M. Gell-Mann. The interpretation of the new particles as displaced charge multiplets. *Il Nuovo Cimento (1955-1965)*, 4:848–866, 1956. 10.1007/BF02748000. *cited in 1 (p. 5)*

[GM61] M. Gell-Mann. The eightfold way: A theory of strong interaction symmetry. California Institute of Technology Report CTSL-20, 1961. *cited in 1 (p. 6)*

[GM64] M. Gell-Mann. A schematic model of baryons and mesons. *Physics Letters*, 8(3):214 – 215, 1964. *cited in 1.1 (p. 6)*

[GMR57] M. Gell-Mann and E.P. Rosenbaum. Elementary Particles. *Scientific American*, July:72–86, 1957. *cited in 1 (p. 5)*

[GMSS12] Peng Guo, Ryan Mitchell, Matthew Shepherd, and Adam P. Szczepaniak. Amplitudes for the analysis of the decay $j/\psi \to K^+K^-\pi^0$. *Phys. Rev. D*, 85:056003, Mar 2012. *cited in 6.4.3 (p. 83), 6.4.3 (p. 83), ?? (p. 84), 7.6.1 (p. 151), C.7 (p. 222), 9.1 (p. 246)*

[Gob] B. Gobbo. Coral, the compass reconstruction program. `http://coral.web.cern.ch/coral/`. *cited in 3.4 (p. 30)*

[GP76] Gösta Gustafson and Carsten Peterson. Rescattering effects in the decay of the $a1$. *Nuclear Physics B*, 116(2):301 – 316, 1976. *cited in 7.5.1 (p. 131)*

[Gru93] C. Grupen. *Teilchendetektoren*. BI Wissenschafts-Verlag, 1993. *cited in 4.1.1 (p. 37)*

[Haa04] Florian Haas. Design and commissioning of a general purpose triple gem and installation of a gem tracking detector at compass. Master's thesis, Technische Universität München, 2004. *cited in 3.2.2 (p. 30), 4.1.2 (p. 38)*

[HJOR74] J.D. Hansen, G.T. Jones, G. Otter, and G. Rudolph. FORMALISM AND ASSUMPTIONS INVOLVED IN PARTIAL WAVE ANALYSIS OF THREE - MESON SYSTEMS. *Nucl.Phys.*, B81:403, 1974. *cited in 6.1.2 (p. 76)*

[HJW+73] B. Hyams, C. Jones, P. Weilhammer, W. Blum, H. Dietl, et al. $\pi\pi$ Phase Shift Analysis from 600-MeV to 1900-MeV. *Nucl.Phys.*, B64:134–162, 1973. *cited in 5.4 (p. 73)*

[HMC95] Letter of intent: semi-inclusive muon scattering from a polarised target. Technical Report CERN-SPSLC-95-27. SPSLC-I-204, CERN, Geneva, 1995. *cited in 3 (p. 27)*

[I+01] E.I. Ivanov et al. Observation of exotic meson production in the reaction pi- p -> eta-prime pi- p at 18-GeV / c. *Phys.Rev.Lett.*, 86:3977–3980, 2001. *cited in 1.4.2 (p. 15)*

[IP85] Nathan Isgur and Jack Paton. Flux-tube model for hadrons in qcd. *Phys. Rev. D*, 31:2910–2929, Jun 1985. *cited in 1.3 (p. 10), 1.4.1 (p. 14), 7.5.2 (p. 133), 8.2.3 (p. 189), 8.2.4 (p. 197), 9 (p. 200)*

[Jam] F. James. Minuit2 minimization package. *cited in 7.1.2 (p. 92)*

[JJ76] R.L. Jaffe and K. Johnson. Unconventional States of Confined Quarks and Gluons. *Phys.Lett.*, B60:201, 1976. *cited in 1.3 (p. 9)*

[Joh75] K. Johnson. The M.I.T. Bag Model. *Acta Phys.Polon.*, B6:865, 1975. *cited in 1.3 (p. 9)*

[JW59] M. Jacob and G.C. Wick. On the general theory of collisions for particles with spin. *Annals of Physics*, 7:404–428, 1959. *cited in 6.3 (p. 78)*

[K+04] Joachim Kuhn et al. Exotic meson production in the f(1)(1285) pi- system observed in the reaction pi- p -> eta pi+ pi- pi- p at 18-GeV/c. *Phys.Lett.*, B595:109–117, 2004. *cited in 1.4.2 (p. 15)*

[KAD+02] B. Ketzer, M.C. Altunbas, K. Dehmelt, J. Ehlers, J. Friedrich, et al. Triple GEM tracking detectors for COMPASS. *IEEE Trans.Nucl.Sci.*, 49:2403–2410, 2002. *cited in 4.1.2 (p. 38)*

[Kat04] A L Kataev. Qcd sum rules and radial excitaions of light pseudoscalar and scalar mesons. Technical Report hep-ph/0406305, 2004. *cited in 1.4.1 (p. 14)*

[Krä08] Markus Krämer. Performance optimization of a gem detector with pixel readout fot beam tracking in compass. Master's thesis, Technische Universität München, 2008. *cited in 4.1 (p. 36), 4.1.2 (p. 38), 4.2 (p. 43), 4.2 (p. 43), 9.1 (p. 242), 9.1 (p. 261)*

[Kri17] Fabian Krinner. *De-isobared Spin-Parity Analysis of Exclusive Diffractive Events in the $\pi^-\pi^-\pi^+$ Final-State.* Phd thesis in preparation, Technische Universität München, 2017. *cited in 9.1 (p. 204)*

[KZ07] Eberhard Klempt and Alexander Zaitsev. Glueballs, Hybrids, Multiquarks. Experimental facts versus QCD inspired concepts. *Phys.Rept.*, 454:1–202, 2007. *cited in 1.4.2 (p. 15)*

[LA88] E. Leader and M. Anselmino. A crisis in the parton model: where, oh where is the proton's spin? *Zeitschrift für Physik C Particles and Fields*, 41:239–246, 1988. 10.1007/BF01566922. *cited in 3 (p. 27)*

[Lep98] G.P. Lepage. Lattice QCD for novices. pages 49–90, 1998. *cited in 1.3 (p. 10)*

[Lie13] Stefan Lietzau. Leakage studies for the analysis of diffractive dissociation into the $\pi^-\pi^-\pi^+$ final state. Bachelor's thesis, Technische Universität München, 2013. *cited in 7.6.3 (p. 162), 9.1 (p. 261)*

[LS57] S. J. Lindenbaum and R. M. Sternheimer. Isobaric nucleon model for pion production in nucleon-nucleon collisions. *Phys. Rev.*, 105:1874–1899, Mar 1957. *cited in 6.2 (p. 77)*

[Lu05] M. et al Lu. Exotic meson decay to $\omega\pi^0\pi^-$. *Phys. Rev. Lett.*, 94:032002, Jan 2005. *cited in 1.4.2 (p. 15)*

[LY56] T. Lee and C. Yang. Charge conjugation, a new quantum number g, and selection rules concerning a nucleon-antinucleon system. *Il Nuovo Cimento (1955-1965)*, 3:749–753, 1956. 10.1007/BF02744530. *cited in 1.1.1 (p. 7)*

[LZ09] De-Min Li and Shan Zhou. On the nature of the pi(2)(1880). *Phys.Rev.*, D79:014014, 2009. *cited in 1.4.1 (p. 14), 7.5.3 (p. 134), 8.2.4 (p. 190), 8.2.4 (p. 197), 8.2.4 (p. 197), 9 (p. 201)*

[N$^+$04] V. Nikolaenko et al. Dynamical selection rule in the decays of pi(1800). *AIP Conf.Proc.*, 717:155–159, 2004. *cited in 3 (p. 105)*

[Nam66] Y. Nambu. *A systematics of hadrons in subnuclear physics*, page 133. 1966. *cited in 5 (p. 8)*

[Ne'61] Yuval Ne'eman. Derivation of strong interactions from a gauge invariance. *Nucl.Phys.*, 26:222–229, 1961. *cited in 1 (p. 6)*

[Neu12] Sebastian Neubert. *First Amplitude Analysis of Resonant Structures in the 5-Pion Continuum at COMPASS.* PhD thesis, Technische Universitat Munchen, 2012. *cited in 6.1.1 (p. 75), 6.2 (p. 77), 7.1.2 (p. 93), 7.3.2 (p. 119)*

[NN53] Tadao Nakano and Kazuhiko Nishijima. Charge independence for v-particles. *Progress of Theoretical Physics*, 10(5):581–582, 1953. *cited in 1 (p. 5)*

[Oed95] A. Oed. Properties of micro-strip gas chambers (MSGC) and recent developments. *Nucl.Instrum.Meth.*, A367:34–40, 1995. *cited in 4.1.1 (p. 37)*

[Pag98] Philip R. Page. Strong decays of hybrid mesons from the heavy quark expansion of QCD. *AIP Conf.Proc.*, 432:121–124, 1998. *cited in 1.4.1 (p. 14)*

[Per74] Martin L. Perl. *High Energy Hadron Physics.* John Wiley & Sons, Inc., 1974. ISBN 0-471-68049-4. *cited in 6.3 (p. 78), 7.4.1 (p. 126)*

[Pfl11] Stefan Pflüger. Investigations of the light meson spectrum with compass using final states containing neutral particles. Master's thesis, Technische Universität München, 2011. *cited in 9.1 (p. 261)*

[Pie72] E. Pietarinen. Dispersion relations and experimental data. *Nuovo Cim.*, A12:522–531, 1972. *cited in 9.1 (p. 205)*

[RCF+00] M. Raymond, G. Cervelli, M. French, J. Fulcher, G. Hall, et al. The CMS tracker APV25 0.25-mu-m CMOS readout chip. *Conf.Proc.*, C00091111:130–134, 2000. *cited in 4.1.2 (p. 40)*

[Ric84] Jeffrey D. Richman. An experimenter's guide to the helicity formalism. Technical report, California Institute of Techology, 1984. CALT-68-1148. *cited in 6.3 (p. 78)*

[RKP+04] L. Ropelewski, B. Ketzer, S. Paul, F. Sauli, and Q. Weitzel. Performance of triple GEM tracking detectors in the COMPASS experiment. *Nuclear Instruments and Methods in Physics Research A*, 535:314–318, 2004. *cited in 4 (p. 35), 4.1.2 (p. 38)*

[Rob12] Graig Roberts. Emergence of dses in real-world qcd, 2012. Talk given at the USCS school on non-perturbative Physics. *cited in 1.3 (p. 10)*

[Rya] Dmitri Ryabchikov. private communication. *cited in 9.1 (p. 203)*

[Sau77] Fabio Sauli. Principles of Operation of Multiwire Proportional and Drift Chambers. Technical report, CERN 77-09, 1977. *cited in 4.1.1 (p. 37)*

[Sau04] Fabio Sauli. From Bubble Chambers to Electronic Systems: 25 Years of of Evolution in Particle Detectors at CERN. In *Physics Reports, CERN 50th anniversary special issue*, 2004. *cited in 4.1.1 (p. 37)*

[Sch18] W. Schottky. Über spontane stromschwankungen in verschiedenen elektrizitätsleitern. *Annalen der Physik*, 362(23):541–567, 1918. *cited in 4.1.2 (p. 39)*

[Sch07] Florian Schneider. Construction and test of pixelgem tracking detectors. Bachelor's thesis, Technische Universität München, 2007. *cited in 4.1.2 (p. 40), 9.1 (p. 261)*

[Sch12] Tobias Schlüter. *The $\pi^-\eta$ and $\pi^-\eta'$ systems in exclusive 190 GeV π^-p reactions at COMPASS (CERN)*. PhD thesis, Ludwig-Maximilians-Universität München, 2012. *cited in 6.1.2 (p. 76), 7.3.2 (p. 119), 8.2.2 (p. 180), 9 (p. 200)*

[Sch14] Sephan Schmeing. Analysis of the mass dependence of the $\pi^-\pi^-\pi^+$ final state at compass. Master's thesis in preparation, Technische Universität München, 2014. *cited in 8.2.1 (p. 173), 8.2.1 (p. 175), 8.2.4 (p. 192), 9.1 (p. 261)*

[sci] Scintillation materials. `http://www.phenix.bnl.gov/WWW/publish/donlynch/RXNP/Safety_22_06/Kuraray-PSF-Y11.pdf`. *cited in 4 (p. 35),* **??** *(p. 36)*

[SDN02] P. Landshoff S. Donnachie, G. Dosch and O. Nachtmann. *Pomeron Physics and QCD*. Cambridge Monographs on Particle Physics, Nuclear Physics and Cosmology. Cambridge University Press, 2002. *cited in 2 (p. 17), 2.1.1 (p. 21)*

[Sim01] Frank Simon. Commissioning of the GEM Detectors in the COMPASS Experiment, 2001. Diploma Thesis. *cited in 4 (p. 35), 4.1.2 (p. 38), 4.2 (p. 43)*

[SKN12] Sebastian P. Schneider, Bastian Kubis, and Franz Niecknig. $\omega \to \pi^0\gamma^*$ and $\phi \to \pi^0\gamma^*$ transition form factors in dispersion theory. *Phys. Rev. D*, 86:054013, Sep 2012. *cited in 9.1 (p. 205)*

[SS97] Eric S. Swanson and Adam P. Szczepaniak. Hybrid decays. *Phys.Rev.*, D56:5692–5695, 1997. *cited in 1.4.1 (p. 14)*

[Ste11] Dominik Steffen. Construction of a large-sized diffusion cloud chamber. Bachelor's thesis, Technische Universität München, 2011. *cited in 9.1 (p. 262)*

[TAA97] D. R. Thompson, G. S. Adams, and Adams. Evidence for exotic meson production in the reaction $\pi^- p \to \eta\pi^- p$ at 18gev/c. *Phys. Rev. Lett.*, 79:1630–1633, Sep 1997. *cited in 1.4.2 (p. 15)*

[Tas11] Michael Tasior. Performance studies for the compass pixelgem tracking detectors and development of a modular test bench for gem detectors. Master's thesis, Technische Universität München, 2011. *cited in 4.1.2 (p. 41), 4.7 (p. 42), 4.9 (p. 44), 4.2 (p. 45), 4.10 (p. 45), 4.11 (p. 46), 4.12 (p. 47), 9.1 (p. 242), 9.1 (p. 261)*

[Uhl08] Sebastian Uhl. Construction and commissioning of the pixelgem tracking system for the compass experiment. Master's thesis, Technische Universität München, 2008. *cited in 4.1.2 (p. 38), 4.2 (p. 43), 4.2 (p. 43), 4.2 (p. 43), 9.1 (p. 261)*

[Uhl14] Sebastian Uhl. *Analysis of Exclusive Diffractive Events in the $\pi^-\pi^0\pi^0$ Final State*. Phd thesis in preparation, Technische Universität München, 2014. *cited in 9.1 (p. 203), 9.1 (p. 203)*

[Van12] Maxence Vandenbroucke. *Development and Characterization of Micro-Pattern Gas Detectors for Intense Beams of Hadrons*. PhD thesis, Technische Universität München and Universite Pierre Et Marie Curie, 2012. *cited in 4.1.1 (p. 37)*

[VHQ72] F. Von Hippel and C. Quigg. Centrifugal-barrier effects in resonance partial decay widths, shapes, and production amplitudes. *Phys.Rev.*, D5:624–638, 1972. *cited in 6.4.1 (p. 81)*

[Wei03] Quirin Weitzel. Triple gem detectors in compass. a performance study. Master's thesis, Technische Universität München, 2003. Diploma Thesis. *cited in 4 (p. 35), 4.1.2 (p. 38), 4.1.2 (p. 39)*

[Wei08] Quirin Weitzel. *Precision Meson Spectroscopy: Diffractive Production at COMPASS and Development of a GEM-based TPC for PANDA*. PhD thesis, Technische Universitat Munchen, 2008. *cited in 5.1.5 (p. 54), 5.1.5 (p. 55), 9.1 (p. 261)*

[WH93] E. J. Wolin and L. L. Ho. Covariance matrices for track fitting with the Kalman filter. 329:493–500, 1993. *cited in 3.4 (p. 31)*

[Whi08] Alan. R. White. The Past and The Future os S-Matrix Theory. *arXiv:hep-ph/0002303v1*, 2008. *cited in 2.1 (p. 17)*

[Wil74] Kenneth G. Wilson. Confinement of quarks. *Phys. Rev. D*, 10:2445–2459, Oct 1974. *cited in 1.3 (p. 10)*

[Wut07] Ch. Wuttke. Konzeption eines multiplizitätszählers für das compass experiment, 2007. *cited in 3.5 (p. 33)*

[Yao06] W.-M. et al. Yao. Review of Particle Physics. *Journal of Physics G*, 33, 2006. *cited in 1.4.1 (p. 14)*

[Yuk35] Hideki Yukawa. On the Interaction of Elementary Particles. *Proc.Phys.Math.Soc.Jap*, 17:48–56, 1935. *cited in 1 (p. 5)*

[Zai00] A. Zaitsev. Study of exotic resonances in diffractive reactions. *Nucl.Phys.*, A675:155C–160C, 2000. *cited in 1.4.2 (p. 15), 1.3c (p. 16), 7.5.2 (p. 133), 7.5.4 (p. 136), 7.5.4 (p. 140),* **??** *(p. 140), 9 (p. 200)*

[Zwe64a] G Zweig. An su_3 model for strong interaction symmetry and its breaking. oai:cds.cern.ch:352337; part i. (CERN-TH-401):24 p, Jan 1964. *cited in 1.1 (p. 6)*

[Zwe64b] G Zweig. An su_3 model for strong interaction symmetry and its breaking. oai:cds.cern.ch:570209; part ii. (CERN-TH-412):80 p, Feb 1964. *cited in 1.1 (p. 6)*

[Zwe10] G. Zweig. Memories of Murray and the Quark Model. *International Journal of Modern Physics A*, 25:3863–3877, 2010. *cited in 4 (p. 6)*

Own Contributions

This thesis followed the whole way of a hadron spectroscopy analysis, from the development and construction of suitable detector components to the spin-parity analysis and resonance parameter extraction.

Under the supervision of Bernhard Ketzer it was decided to develop and build GEM detectors of the second generation. In contrast to the first generation, which was constructed at CERN, it was planned to set up a production facility in the E18 clean rooms in Munich. A group was established in Munich and I was involved in the design of the detector as well as setting up the laboratories and the supervision of technical students. I was in charge of the construction of the prototype and installation and commissioning at COMPASS. The progress of the project had to be reported to the COMPASS collaboration and the installation and beam time had to be synchronised with other groups working at COMPASS. In the growing group several bachelor and diploma students helped to advance the design, to construct 7 detectors for use at COMPASS and to analyse detector data. Their thesis work [Sch07, Uhl08, Krä08, Aus07, Tas11] was supervised by Bernhard Ketzer and myself. As detector expert shift duties had to be taken during each beam time and additionally I served twice as weekly coordinator.

On the level of the analysis the event selection, based on the previous analysis [Wei08] was enhanced and adapted for the large amount of data and the new components of the COMPASS spectrometer. To this end a multi-purpose program was written which is able to apply an event selection for several kinds of final states. This package was also used to crosscheck the COMPASS analysis of $K^-p \to K^-\pi^+\pi^-p$ and serves as basis for the recent $\pi^-\pi^+\pi^-\pi^+\pi^-$ analysis. The software for the spin-parity analysis was originally developed by G. Ascoli in the 1970ies and further improved and maintained by Dmitri Ryabchikov. I modified this package in order to cope with the increased but necessary number of parameters and programmed new isobar parametrisations, used for this analysis. Together with Dmitri Ryabchikov the concept of the analysis was enhanced such that a two-dimensional analysis, as a function of m_X and t' was possible. The large data set made it necessary to develop a new fit model, consisting of the aforementioned enhanced event selection and isobar parametrisations and in addition the construction of a wave set including the complicated adjustment of mass thresholds. Several diploma, master and bachelor students [Lie13, Sch14, Pfl11, Dre14], working in this field at E18, were supervised by Boris Grube and myself.
I defended this analysis several times in front of the COMPASS collaboration and represented the COMPASS group as well as E18 at several international workshops and conferences by giving talks and writing proceedings.
In order to optimize the first stage of event filtering at CERN I developed a common data skim-

ming process for members of the COMPASS hadron group. A database web-frontend was developed and setup by me in order to organise talks given at the subgroup meetings or at conferences of the COMPASS hadron group.

For the 2009 COMPASS hadron run I build the inner part of the multiplicity trigger as the responsible person. Together with two technical students and Johannes Bernhard at CERN the trigger was constructed, installed and commissioned. The multiplicity counter was one of the three major trigger components in the few weeks long 'all t'' data taking campaign with a lead target.

Several times I joined the CERN student excursion as advisor, once as main organiser. In addition I was asked to support public relations of the Excellence Cluster Universe. I was sent to schools or science fairs in order to present recent science outcome to the public. As a side effect of this work I started to found, with the financial support of Stephan Paul, a project group in order to build a large-sized cloud chamber for didactic purpose. Besides the supervision of several technical students one bachelor thesis [Ste11] was the academic outcome of this project. The cloud chamber was shown at several exhibitions and will be upgraded with digital controlling in the next time.

Acknowledgments

I have been involved in several projects at E18 and the Excellence Cluster Universeover the last years, where I had the chance to work with and learn from numerous people. Thus I take the liberty of slightly extending my acknowledgments.

When I met Stephan Paul 10 years ago for the first time, I was a student teacher and looking for a topic for my master thesis. I had only one constraint: visiting CERN and working on a CERN project. Knowing that at his chair projects at CERN are undertaken, I asked for an appointment with him. During the introduction I said that I have no experience, that I am a student teacher instead diploma student but that I wanted to work at CERN. And his simple answer was 'Yes, why not'. The impartiality he showed with respect to people and new ideas and projects impressed me several times. He trusts people and gives them the freedom to try new ideas even if they are costly. This made projects like the cloud chamber possible and gave me the freedom for my PhD. I am grateful for his support which was far more than paying a salary and giving me a topic for my thesis. He helped me in some of the darkest hours of my family. Thank you.
As long as I know Stephan I know Bernhard Ketzer. He was my first supervisor and I learned from him how to work scientifically. His attitude inspired me to work harder and always try to make it better than the previous time. He is strict but I met no one else in the scientific business who is more fair than him. The most impressive moment I experienced with him was when we both saw for the first time a signal of the PixelGEM prototype on the oscilloscope after months of preparations. It was a Sunday in autumn and we were cheering and dancing in the lab. He is the prototype of a scientist, having unprecedented experience in experimental work and a fundamental understanding of physics. Thank you, Bernhard. Boris Grube was my mentor in the last years of the analysis. Regardless when you have a question or need help, Boris is there. With his calm attitude he is a pleasant conversational partner. I learned a lot discussing with him. He became a friend to me and my wife, because he is like he is. Very smart and friendly. Together with Karin Frank he is the backbone of E18. Thank you, Boris. Dmitri Ryabchikov is working since decades in the field of meson spectroscopy and the opportunity to work with him and learn from his experience and genius pushed my analysis and the whole COMPASS hadron program. I am enjoying working with him. Spasibo Dima. Karin Frank is the link between the two non-interfering worlds of administration and physics. Her job is as complicated as negotiating in the middle east. She tries to keep away all this boring but necessary administrative stuff from us and keeps things ticking over. Her job description could be read as follows: project manager, event manager, human resources manager, financial accounting manager, E18 mama, ... Thank you Karin, you made things possible. During the production of the PixelGEM, Bernhard Ketzer visited once Sebastian Uhl and me in the clean room, in order to see,

how we come along with the manufacturing. All through the whole process, Sebastian and me spoke no word, but the production went smoothly without any complications. We both understand each other without talking much. I learned a lot about programming from him, and I am always impressed of his memory and his patience and cooperativeness. Like Boris and my PhD comrades, he became a friend. Thank you, Sebastian.
I was fortunate to work with interesting PhD comrades. The passionate Sebastian Neubert; together with Thiemo Nagel he was chairing the E18 Politbüro, Quirin Weitzel, my predecessor on this analysis and Steffi Grabmüller, who made a fulminant job. Thanks for long evenings with water pipes at CERN. I have been always inspired by the efforts and work done in the E18 COMPASS group. I want to thank Florian Schneider, Alex Austregesilo, Stefan Huber, Lingxin Meng, Christian Höppner, Michael Tasior, Stefan Lietzau, Stephan Schmeing, Fabian Krinner and Sverre Dørheim. It is impressive what you have achieved in the last years. I thank Jan Friedrich and Suh Urk Chung not only for interesting ideas. Both have the ability to understand the whole without loosing sight of any detail. Their experience and understanding of physics helped me to get a deeper understanding of what we are doing. The chair E18 has its own electronic lab. I learned a lot about electronics and project management by our chief engineer Igor Konorov and his not less talented student Alexander Mann. Hadron spectroscopy means a hell of computer power. Without the extensive work of our admins I would not be where I am now. Thanks to Thiemo Nagel, Felix Böhmer and particular Markus Krämer. Not only for your technical support but also long discussions with all of you. When I came up with the mad idea to build one of the largest cloud chambers I got not only the support from Stephan Paul. This project couldn't be realised without the passion and technical cleverness of Florian Schneider and Michael Tasior, once again and Dominik Steffen and Martin Losekamm. Thank you for the team spirit. I enjoyed the discussions inside the Hadron Group and I thank Tobias Schlüter, Johannes Bernhard, Promme Jaszinski and Karin Schoenning for their work and input. I thank the COMPASS collaboration, representative the spokespersons Gerhard Mallot, Alain Magnon, Andrea Bresan and Fabienne Kunne, for the support during the last years of data taking and analysis. Martin Aigner and the workshops at the Physics Department and Vladimir Anosov and Vlatko Pesaro at COMPASS for their work far beyond their duties. I also want to thank Adam Szczepaniak for his fruitful ideas and the help with the Ascoli Deck and the $(\pi\pi)_P$ parametrisation. Beam time at a CERN experiment means stress and little sleep. I thank Elena Rocco for long walks and interesting conversations about all the world and his brother. Good luck to your family with your husband Matteo and your daughter Rebecca.

Der Zusammenhalt in meiner Familie hat mir oft den Rücken gestärkt und wie meine Eltern ihr Leben meistern, nötigt mir Respekt und Bewunderung ab. Ich hoffe, ich kann nur ansatzweise so im Leben stehen. Manches wäre mir vielleicht leichter gefallen, hätte ich die Disziplin meines Bruders. Obwohl wir uns unterschiedlich entwickelt haben, verstehen wir uns auf eine Art und Weise, die man nicht erklären kann. Du und Karen werdet grossartige Eltern. Während meiner Doktorarbeit hatte ich das Glück, eine interessante Frau und meine beste Freundin kennenzulernen. Stella, in den letzten Jahren war vieles nicht leicht, beruflich und privat, aber Du hast mir stets den Rücken frei gehalten und warst der Ruhepol. Du bist die Liebe meines Lebens und ich bin so stolz darauf, was wir zwei geschafft haben. Ich bin froh, auch Deine Familie als meine ansehen zu können. Und doch relativiert sich all das Geschaffene mit der Geburt unserer Tochter Mia Sophie. Durch sie habe ich meine wahre Berufung im Leben gefunden.

Ich liebe dich Stella und ich liebe unsere Mia